



**AFRL-RZ-ED-TR-2010-0026**

# **Hybrid Modeling of Plasma Discharges**

---

Jean-Luc Cambier

AFRL/RZSS  
1 Ara Road  
Edwards AFB, CA 93524-7013

April 2010

---

Distribution A: To be approved for Public Release; distribution unlimited

---

**AIR FORCE RESEARCH LABORATORY  
PROPULSION DIRECTORATE**

■ Air Force Materiel Command    ■ United States Air Force    ■ Edwards Air Force Base, CA 93524

**UNCLASSIFIED**

REPORT DOCUMENTATION PAGE			Form Approved OMB No. 0704-0188		
<p>Public reporting burden for this collection of information is estimated to average 1 hour per response, including the time for reviewing instructions, searching existing data sources, gathering and maintaining the data needed, and completing and reviewing this collection of information. Send comments regarding this burden estimate or any other aspect of this collection of information, including suggestions for reducing this burden to Department of Defense, Washington Headquarters Services, Directorate for Information Operations and Reports (0704-0188), 1215 Jefferson Davis Highway, Suite 1204, Arlington, VA 22202-4302. Respondents should be aware that notwithstanding any other provision of law, no person shall be subject to any penalty for failing to comply with a collection of information if it does not display a currently valid OMB control number. <b>PLEASE DO NOT RETURN YOUR FORM TO THE ABOVE ADDRESS.</b></p>					
1. REPORT DATE (DD-MM-YYYY) 7 Apr 2010		2. REPORT TYPE In-House Final Report		3. DATES COVERED (From - To) 31 Jul 2002 – 1 Feb 2010	
4. TITLE AND SUBTITLE Hybrid Modeling of Plasma Discharges			5a. CONTRACT NUMBER		
			5b. GRANT NUMBER		
			5c. PROGRAM ELEMENT NUMBER 61102F		
6. AUTHOR(S) Jean-Luc Cambier			5d. PROJECT NUMBER		
			5e. TASK NUMBER		
			5f. WORK UNIT NUMBER 23040256		
7. PERFORMING ORGANIZATION NAME(S) AND ADDRESS(ES) Air Force Research Laboratory (AFMC) AFRL/RZSS 1 Ara Road Edwards AFB CA 93524-7013			8. PERFORMING ORGANIZATION REPORT NO.		
9. SPONSORING / MONITORING AGENCY NAME(S) AND ADDRESS(ES) Air Force Research Laboratory (AFMC) AFRL/RZS 5 Pollux Drive Edwards AFB CA 93524-7048			10. SPONSOR/MONITOR'S ACRONYM(S)		
			11. SPONSOR/MONITOR'S REPORT NUMBER(S) AFRL-RZ-ED-TR-2010-0026		
12. DISTRIBUTION / AVAILABILITY STATEMENT  Approved for public release; distribution unlimited. Public Affairs # 10335.					
13. SUPPLEMENTARY NOTES					
14. ABSTRACT <p>This document describes the research performed under an AFOSR lab-task started in August 2002, and is still continuing under a different JON. Therefore, this report mostly describes results which are still preliminary. This research is aimed at investigating the difficult problem of hybridization of various physical models and numerical methods in order to more efficiently model complex, non-equilibrium plasma. We are especially interested in plasma conditions which contain a highly energetic component, here restricted to electrons. The general system under study is therefore composed of a bulk, dense fluid (which may contains electrons in equilibrium, i.e. "cold") and high-energy particles ("hot" electrons) which are either injected into the fluid or extracted by the application of high electro-magnetic fields. High-voltage pulsed discharges and laser-plasma are typical examples of such conditions, but these can be also found in sub-scale regions of other discharges. Because the "hot" component cannot be described by an equilibrium (Maxwell) distribution, one must combined essentially two numerical approaches: one for the bulk phase (Computational Fluid Dynamics – CFD – in its various formulations), and one for the high-energy component, such as Particle In Cell (PIC) or a discretized phase-space solver (Vlasov or Fokker-Planck). The latter are deemed feasible only for systems with low dimensionality – pending revolutions in computational hardware – but we are interested in eventual application to 3D problems. Thus, PIC remains the method of choice for treatment of this hot component. However, inelastic interactions are of key importance, i.e. excitation and ionization, as well as the reverse processes once the energetic component sufficiently relaxes and cools. The crux of this effort consists of developing and verifying numerical techniques which allow an efficient coupling between these two components, given the complexity of interactions and the multiple scales involved, with special emphasis on the former. This effort is also considered as a risk reduction project, in its aim at developing the basic approaches to the problem and verifying that they work accurately and efficiently, as opposed to a large-scale code development effort.</p>					
15. SUBJECT TERMS propellant; plasma; energetic; high energy; electrons; CFD; PIC; particle in cell; numerical; risk reduction					
16. SECURITY CLASSIFICATION OF:			17. LIMITATION OF ABSTRACT	18. NUMBER OF PAGES	19a. NAME OF RESPONSIBLE PERSON N/A
a. REPORT Unclassified	b. ABSTRACT Unclassified	c. THIS PAGE Unclassified			19b. TELEPHONE NO (include area code) N/A

**- STINFO COPY -**  
**NOTICE AND SIGNATURE PAGE**

Using Government drawings, specifications, or other data included in this document for any purpose other than Government procurement does not in any way obligate the U.S. Government. The fact that the Government formulated or supplied the drawings, specifications, or other data does not license the holder or any other person or corporation; or convey any rights or permission to manufacture, use, or sell any patented invention that may relate to them.

Qualified requestors may obtain copies of this report from the Defense Technical Information Center (DTIC) (<http://www.dtic.mil>).

AFRL-RZ-ED-TR-2010-0026 HAS BEEN REVIEWED AND IS APPROVED FOR PUBLICATION IN ACCORDANCE WITH ASSIGNED DISTRIBUTION STATEMENT.

FOR THE DIRECTOR:

\_\_\_\_\_/signed/\_\_\_\_\_  
JEAN-LUC J. CAMBIER  
Project Manager

\_\_\_\_\_/signed/\_\_\_\_\_  
JAMES M. HAAS  
Chief  
Spacecraft Branch

\_\_\_\_\_/signed/\_\_\_\_\_  
PHILIP A. KESSEL  
Scientific Technical Advisor  
Space & Missile Propulsion Division

This report is published in the interest of scientific and technical information exchange, and its publication does not constitute the Government's approval or disapproval of its ideas or findings.

This Page Intentionally Left Blank



## Table of Contents

1.	Introduction .....	1
2.	Objectives .....	3
3.	Challenges .....	3
4.	Approach .....	4
4.1.	Modeling Issues .....	4
4.2.	Numerical Issues .....	9
4.3.	Computational Issues .....	9
5.	Software Development .....	11
5.1.	Architecture .....	11
5.2.	Parallelization .....	12
5.3.	Data Structures .....	15
5.3.1.	Geometry .....	15
5.3.2.	Fluid .....	16
5.3.3.	Particles .....	17
5.4.	GPU programming .....	18
6.	Computational Fluid Dynamics .....	19
6.1.	Formulation .....	19
6.2.	Numerical Scheme .....	22
6.3.	Multi-Fluid .....	24
7.	Collisional-Radiative Model .....	29
8.	Particle Methods .....	40
8.1.	PIC Transport .....	40
8.2.	Particle Merging .....	41
8.3.	Lagrangian method .....	45
8.4.	Beyond PIC .....	47
8.5.	Inelastic Processes .....	49
8.6.	Remaining Issues .....	54
9.	Conclusions and Future Work .....	58
10.	References .....	60
Appendix A: Multi-Fluid Algorithm .....		A-1
Appendix B: Pseudospark Analytical Model .....		B-1
Appendix C: Electron Fluid-Element .....		C-1
Appendix D: Detailed Balance and H-theorem .....		D-1
Appendix E: A High-Order Transport Scheme for Collisional-Radiative and Nonequilibrium Plasma (Dissertation) .....		E-1
Appendix F: Particle Motion Algorithms for Arbitrary Gyro-Frequencies .....		F-1
Appendix G: Kinetic Modeling of Laser-Induced Fusion .....		G-1

## LIST OF FIGURES

Fig. No.	Page No.
1	Schematic of physical processes near cathode.....5
2	Contours of constant potential and ionization events (dots) – taken from [18].....7
3	Peak intensity of light sources and corresponding physical regimes versus history .....8
4	Possible configurations for the Client/Master/Server architecture .....11
5	Comparison of Java and C performance on floating point operations.....11
6	Screenshot of GUI with grid generation (GridPro™).....12
7	Snapshot of the evolution of a spherical explosion, computed with a second-order TVD method (ideal gas). Real time visualization using VisAD library .....13
8	Block communication using source and target patches. The dashed arrows represent referencing while the solid arrows signify remote method calls.....14
9	Preliminary scalability (CFD model) on Linux cluster.....14
10	Schematic of <i>geoCell</i> object structure .....15
11	Speed-up factor versus number of cosine operations for each particle/thread .....19
12	Temperature profiles behind strong shock with relaxation and electron heat conduction.....21
13	Results of Euler calculations on standard test case (forward step); multi-block, parallel computation (thin horizontal and vertical lines are block boundaries).....22
14	Results of AMROC code, using grid adaptation; finest resolution is equivalent to 3 times the resolution of current results shown in Figure 6.2, yet the KH instability is less resolved .....23
15	Standard CFD tests: (left) Orszag-Tang MHD vortex problem; (right) Rayleigh-Taylor instability .....23
16	Shock diffraction around a wedge; left – simulated Schlieren, right – experiment.....24
17	Shock diffraction down a step: left – simulated Schlieren, right – experiment.....25
18	Plasma oscillations (electron velocity at center of 1D box) for both explicit and implicit schemes.....26
19	Compiled multi-stage ionization rates for assumed Maxwellian distribution .....28
20	Compiled ionization rates for assumed drifting Maxwellian distribution .....28
21	Schematic of atomic levels .....29
22	Effect of upper levels on radiative cooling region; complete agreement with experimental data requires at least the 4s,4p,3d and 5s manifolds .....31
23	Temperature profiles without collisional interchange between manifolds 4s and 4p.....32
24	Temperature profiles with collisional interchange between manifolds 4s and 4p.....32
25	Steady-state profiles for complete set of reactions and complete set of levels.....33
26	Unsteady 1D profiles in shock rest frame – cyclical motion.....33
27	X-t diagram of pressure (Ma=14.7 case); shock originates from right.....34
28	X-t diagram of density (Ma=14.7 case); shock originates from right.....35
29	History of shock Mach number versus distance (top) and induction length versus time (bottom) .....35
30	2D contours of the refractive index for Ma=16.5; sequence goes top-bottom, left-right .....36
31	Comparison of experimental (left) and computed (right) interference patterns. ....37

## LIST OF FIGURES, Cont'd

Fig. No. ....	Page No.
32 Artificial “soot trace” for Ma=16.5 case, showing cell structure formed by triple points.....	37
33 Structure of “cell” in ionizing shock propagation.....	38
34 Profiles of temperature differences in shock layer around cylinder (Mach 18.1 Argon flow).....	39
35 Profiles of Argon flow simulating DLR experiment [65]. Top-left: velocity; Top-right: magnetic field; Bottom-left: heavy-particle temperature; Bottom-right: electron temperature.....	39
36 Schematic of fragmentation process in Center of Mass frame after coalescence of many individual pseudo-particles.....	42
37 Number of particles (electrons) versus time and distance, without (left, 250,000 particles) and with (right, 35,000 particles) particle coalescence.....	42
38 Electric potential in diode 10 ns after start, with and without particle coalescence .....	43
39 Particle (electron) and fluid (ions) charge densities 10 ns after start of computations, with and without pseudo-particle coalescence.....	43
40 Anode current density versus product of iteration number and discharge pressure (in Pa). Current density is normalized to initial density obtained at first iteration.....	47
41 Detail of anode current evolution in vicinity of critical pressure .....	47
42 (a) domain sub-division; (b) “quadtree” hierarchy (in 2D); (c) particle-cluster interaction .....	48
43 (a) schematic of atomic levels; (b) discretized (isotropic) energy distribution Function .....	49
44 Tests of stability of equilibrium EEDF in CR-MCC model .....	52
45 (a) verification of H-theorem during relaxation; (b) verification of energy conservation: error per time step (red) and integrated error (blue) – 0 <sup>th</sup> -order only. ....	52
46 Evolution of the EEDF as a result of collisional excitation/deexcitation only (2-level atom) by discretized kinetic solver .....	53
47 Evolution of the EEDF in similar test case as Figure 46, computed by MCC .....	54

## LIST OF TABLES

Table No. ....	Page No.
1 List of atomic levels (energy, degeneracy, and quantum numbers) for Argon.....	30

## GLOSSARY

AFOSR	Air Force Office of Scientific Research
AFRL	Air Force Research Laboratory
AMR	Adaptive mesh refinement
API	Application programming interface
ASDF	Atomic State Distribution Function
BEB	Binary encounter/Bethe
C-R	Collisional-radiative
CFD	Computational Fluid Dynamics
CPA	Chirped pulse amplification
CR	Collisional-Radiative
CUDA	Compute Unified Device Architecture
DBD	Dielectric barrier discharges
DF	Data field ? (p. 18)
DLR	German Aerospace Center (Deutschland für Luft- und Raumfahrt)
DSMC	Direct Simulation Monte-Carlo
EEDF	Electron Energy Density Function
EOS	Equation of state
F-P	Fokker-Planck
FRC	Field reversed configurations
GPGPU	General purpose computing
GPU	Graphical Processing Unit
GUI	Graphical user interface
HC	Hollow cathode
HLLE	Harten, Lax, vanLeer and Einfeldt
KE	Kinetic energy
KKRS	Kozyrev, Korolev, Rabotkin and Shemyakin
I/O	Input/output
LHS	Left-hand side
LTE	Local thermodynamic equilibrium
M&S	Modeling and Simulation
MCC	Monte-Carlo Collision
MD	Molecular Dynamics
MHD	Magneto-hydrodynamics
MP	Monotonicity preserving
MPI	Message passing interface
MURI	Multidisciplinary University Research Initiative
NIST	National Institute of Standards & Technology
ODE	Open dynamics engine
PIC	Particle in Cell
PM	Particle-mesh
POS	Plasma opening switch
PPM	Pulse-position-modulation
RAM	Random Access Memory
RF	Radio frequency

RHS	Right-hand side
RMI	Remote Method Invocation
RT	Radiation transport
SBIR	Small Business Innovation Research
SOTA	State of the art
STTR	Small Business Technology Transfer
TVD	Time-variant distortion
UCLA	University of California at Los Angeles
VDF	Velocity distribution function
VKI	Von-Karman Institute
WENO	Weighted essentially non-oscillatory

## Executive Summary

This document describes the research performed under an AFOSR lab-task started in August 2002, and is still continuing under a different JON. Therefore, this report mostly describes results which are still preliminary. We conclude it by describing the final, remaining work that must be accomplished to complete the overall research effort.

This research is aimed at investigating the difficult problem of hybridization of various physical models and numerical methods in order to more efficiently model complex, non-equilibrium plasma. We are especially interested in plasma conditions which contain a highly energetic component, here restricted to electrons. The general system under study is therefore composed of a bulk, dense fluid (which may contain electrons in equilibrium, i.e. “cold”) and high-energy particles (“hot” electrons) which are either injected into the fluid or extracted by the application of high electro-magnetic fields. High-voltage pulsed discharges and laser-plasma are typical examples of such conditions, but these can be also found in sub-scale regions of other discharges. Because the “hot” component cannot be described by an equilibrium (Maxwell) distribution, one must combined essentially two numerical approaches: one for the bulk phase (Computational Fluid Dynamics – CFD – in its various formulations), and one for the high-energy component, such as Particle in Cell (PIC) or a discretized phase-space solver (Vlasov or Fokker-Planck). The latter are deemed feasible only for systems with low dimensionality – pending revolutions in computational hardware – but we are interested in eventual application to 3D problems. Thus, PIC remains the method of choice for treatment of this hot component. However, inelastic interactions are of key importance, i.e. excitation and ionization, as well as the reverse processes once the energetic component sufficiently relaxes and cools. The crux of this effort consists of developing and verifying numerical techniques which allow an efficient coupling between these two components, given the complexity of interactions and the multiple scales involved, with special emphasis on the former<sup>1</sup>. This effort is also considered as a risk reduction project, in its aim at developing the basic approaches to the problem and verifying that they work accurately and efficiently, as opposed to a large-scale code development effort.

The principal objectives therefore were to: (a) develop detailed fluid modeling capability to handle the interaction with an energetic plasma component far from equilibrium; (b) develop efficient and highly accurate methods to treat the coupling between the two components; (c) develop and investigate new algorithms or improvements over existing algorithms for generation, transport and reactions of the energetic component; (d) investigate modern computing software and hardware technologies which can facilitate achieving the overall objective. Item (a) resulted in the development and validation of collisional-radiative fluid and multi-fluid models, the highest degree of non-equilibrium that can be achieved yet still practical and still consistent with a fluid model. Item (b) consisted in the investigation of Monte-Carlo Collision (MCC) algorithms, discretized kinetics solvers and associated techniques to handle non-Maxwellian collisional-radiative kinetics. Item (c) was limited so far to some new algorithms for particle merging and particle transport (for magnetized plasma), while item (d) saw the use of modern object-oriented programming techniques and an early investigation of Graphical Processing Unit (GPU) programming – the latter being considered of key importance, and will be a principal aspect of the future, completing research work. Along the way, other methods were investigated and deemed more or less useful, to be eventually relegated to future work – funding permitting.

The overall result is very promising, although the various research items remain disparate; it is therefore essential to complete the work by integration of the different achievements into a complete, hybrid modeling capability; this will be a focal point of the continuing research effort as well.

---

<sup>1</sup> Multi-scale techniques are envisioned as a separate research effort, once the basic physical models and numerical methods have been developed and validated.

## 1. Introduction

This research is aimed at the modeling of basic physical processes in plasma discharges characterized by non-equilibrium conditions, as a result of small spatial and temporal scales, and/or high-energy processes. These plasmas can have one or more of the following characteristics:

- Transient or steady space-charge effects that govern some critical aspects of the dynamics.
- Significant deviations from thermal (Boltzmann) and ionization (Saha) equilibrium.
- Significant deviations from a Maxwellian Electron Energy Density Function (EEDF).
- Spatial and/or temporal evolutions across several physical regimes (e.g. from continuum to rarefied, from weakly ionized to fully ionized, etc.)
- High energy (keV and relativistic) beams, externally imposed or self-generated.
- Complex coupling with bounding or embedded materials (cross-disciplinary physics).
- Microscopic sizes and/or ultra-short phenomena requiring non-continuum and complex dynamical descriptions.

Plasma discharges with such characteristics have complex properties which are difficult to predict, and yet can be of considerable importance to the Air-Force. These discharges can be used in electrical propulsion, advanced manufacturing and material processing, switches and beam sources for high-power electro-magnetic devices, power generators, advanced diagnostics, etc. The optimization of the design and operation of these devices requires a thorough knowledge of the flow and material properties, and a good predictive capability at the *engineering* level, while being able to reproduce the correct physics at the time and length scales of interest. Therefore, we need::

- A thorough understanding of the essential physical processes and scaling laws.
- An efficient and accurate modeling and simulation (M&S) approach leading to the design of appropriate M&S software.

Although the fundamental physical processes may be individually known, it is not always clear how their combination affects the overall operation, or at what level of detail this process needs to be modeled. For example, the emission of electrons from the electrode surfaces can proceed according to several mechanisms, e.g. field-emission, thermionic emission, field-enhanced thermionic emission. Each one can be modeled with reasonable accuracy, but the actual emission mechanism may depend on the surface condition, e.g. melting, irregularities, contamination, etc. Even though analytical studies can provide a guide towards the understanding of the discharge characteristics, the complex non-linear couplings between plasma, fields, and materials quickly make the problem intractable. Experimental investigations are also complicated by the transient nature of some effects and by the small characteristic length scales of the device or some of its features (sheaths, micro-protrusions). Furthermore, active diagnostic or probing techniques may in some cases perturb the system, thus preventing a clear and unambiguous measurement of the plasma properties. Therefore, modeling becomes a tool of major importance in this class of problems.

Given the current computing capabilities, it may be feasible to simulate these complex processes with great detail. Nevertheless, one must carefully consider the numerical approaches required to yield a practical M&S capability for this type of multi-scale problem. These can be categorized as belonging to three distinct classes:

- (1) fluid methods: these include single-fluid, multi-fluid, multi-temperature, and magneto-hydro-dynamics (MHD) methods
- (2) particle methods: Particle-In-Cell (PIC) [1], Direct Simulation Monte-Carlo (DSMC) [2], and Molecular Dynamics (MD) [3].

- (3) “kinetic” methods<sup>\*</sup>: these solve the fundamental equations of evolution of the distribution functions (Boltzmann equation or approximations to it) in a hyper-dimensional space [4].

The selection of either approach depends on the plasma collisionality (electron-electron, electron-ion, electron-neutral, and ion-neutral) and the ratio of length and time scales. All of these approaches aim at solving the evolution of the Boltzmann equation, in one form or another. In the general case, we have:

$$\frac{\partial}{\partial t} f + \vec{v} \cdot \vec{\nabla}_x f + \vec{a} \cdot \vec{\nabla}_v f = CR(f, f') \quad (1)$$

where  $f(t, \vec{x}, \vec{v})$  is the velocity distribution function<sup>†</sup> (VDF) and the right-hand-side (RHS) describes all exchange processes due to collisional and radiative effects. The left-hand-side (LHS) is an advection equation in a 6-dimensional space (3 for physical space and 3 for velocity space). This equation is valid for a single plasma component with no internal structure, usually electrons. If one were to consider also several ion species and internal structure (molecular modes, electronic excitation), the general distribution function would be:  $f_\alpha(t, \vec{x}, \vec{v})$  where  $\alpha$  is the component index, which can easily be within 10-100, depending on the complexity of the plasma conditions. Obviously, this is well beyond any current or near-term future computational capabilities; this is why most kinetic solvers are limited to 2D-2V or 2D-3V configurations and for a single or two plasma components. Note also that the collisional-radiative exchange term on the right-hand-side (RHS) can also be very complex and computationally very expensive. When sufficient collisions occur and are not too energetic, this collisional effect can be approximated as a diffusion process in the velocity dimensions; this leads to the Fokker-Planck (F-P) equation. Finally, if the plasma is fully ionized and very hot, it becomes collision-less, and the RHS term can be ignored; this leads to the Vlasov equation. Fortunately in most plasma discharges only the electrons, being the ones mostly affected by strong electric and magnetic fields, need to be modeled at that level of detail. It is therefore feasible to treat only the electrons by a kinetic solver and the ions with a simpler approach.

The fluid methods provide such a simplification. The hydrodynamics (Euler) equations are obtained by integrating the Boltzmann equation over the velocity space, assuming that the VDF is very close to an equilibrium Maxwell distribution. In that case, only the conserved moments of the distribution need to be modeled (mass, momentum and energy). When the internal modes are not in equilibrium (a common occurrence in plasma discharges, due to the relatively slow energy exchange rate), these can be modeled separately, leading to multi-temperature and collisional-radiative models [5-7]. The collisional-radiative (C-R) model allows a detailed description of the electronic state distribution; because of the large energy gaps involved, their distribution is more likely to deviate from a Boltzmann distribution, and because of the range of density and temperature, this distribution may be difficult to characterize simply (e.g. competition between excitation by high-energy electrons and quenching through heavy particle collisions). The main difficulty with fluids is the effect of strong fields, which can severely distort the velocity distribution (e.g. sheaths). When the collisional rate cannot maintain an equilibrium VDF, the direct kinetic solver or a particle approach must be used. Finally, the multi-fluid model also allows for separation between the mean velocities of electrons and heavy particles; this approach is important for highly dynamical situations where the bulk electrons significantly contribute to self-generated fields.

The PIC method [1] forms the basis of most plasma simulation codes that are dealing with high-temperature and/or low-density plasmas. It is the method of choice in beam simulation (e.g. RF weapons), geo-magnetic plasmas, and magnetic confinement fusion plasmas. However, it has difficulties handling dense plasmas, highly collisional plasmas, and weakly ionized plasmas. At

---

<sup>\*</sup> Strictly speaking, particle-based methods are also “kinetic” since they also aim to describe the particle distribution; we choose a nomenclature where we reserve the term “kinetic” for a method which discretizes the VDF into bins of finite width, yielding a set of integro-differential equations (Vlasov/F-P), as opposed to discretization into a random number of points (“particles”).

<sup>†</sup> The electron VDF can also be called the Electron Energy Density Function – EEDF. The latter is commonly used in the literature, but is strictly valid for isotropic distributions.



high density, the Debye length is very small and cannot be effectively resolved, yielding numerical inaccuracies (so-called numerical heating). At high collision rates, the PIC/MCC model is highly inefficient, while ionizing collisions lead to explosive growth in the number of particles. Weakly ionized plasmas would have only a small fraction of the particles contributing to the charge and current densities, and statistical noise would make the computation of electromagnetic fields highly inaccurate.

It is clear that an optimal approach consists of a *hybrid* approach, which merges two different techniques; (a) continuum, CFD methods for the equilibrium range, and (b) stochastic, particle methods for the non-equilibrium regime (although hybridization with a kinetic Vlasov or F-P method can also be considered). Hybrid methods can occur in various combinations; the most familiar one in aerospace is to consider ions as particles and electrons as a fluid. This is the case for example for the exhaust plumes of electric propulsion devices, where the density is too low for a valid CFD computation of the gas, but the electrons are relatively cold and have sufficient collisionality to maintain an approximate Maxwell distribution (as long as no strong field is applied). The opposite situation is also of interest; in that case, the density is sufficiently high that the ions (and neutrals) can be treated by a continuum approach (mean free path  $\ll$  characteristic gradient scale) while the electrons are subject to strong fields which distort the distribution function away from the equilibrium Maxwell-Boltzmann. This case is found in dense energetic plasma conditions, and is the principal aim of this project. We should also point out that in contrast to the exhaust plumes we are interested in highly dynamic situations where the location and extent of a non-equilibrium (particles) region may be changing in time. More importantly, these two components can co-exist and their interaction is of key interest.

## 2. Objectives

The overall goals of the project were as follows:

- To develop a core capability for the modeling of plasmas far from equilibrium such as high-energy and micro-discharges
- To experiment with various numerical techniques and algorithms which can facilitate and improve the development of effective hybrid modeling
- To implement a suite of object-oriented software tools that can be easily extended and maintained.
- To validate the code against experimental data and other codes for various discharges.
- To support the analysis and development of advanced plasma discharge concepts in support of future advanced war-fighting technologies (beam propagation and beam-target interactions, laser-plasma, space propulsion, hyper-spectral diagnostics, plasma-assisted hypersonics...).

It is important to emphasize that the project is mostly designed as a *risk-reduction task*, i.e. the determination of fundamental design concepts, approaches and algorithms which can make the overall goal of high-performance, hybrid modeling of complex non-equilibrium plasma possible. It is not a large-scale software development project *per se*, although software design approaches are investigated as well.

## 3. Challenges

The project is particularly challenging, requiring the implementation of complex physical models and advanced numerical methods. The general problem of interest involves the interaction of highly energetic plasma particles with a dense background, in the presence of high electromagnetic fields. It is therefore characterized by:

- Multi-scales: the high-energy plasma component can evolve on short time scales, while the dense background plasma relaxes slowly; a large hierarchy of spatial scale is also present, imposed by both physical and numerical limitations.
- Multi-physics: particle, fluid and field transport are required, collisional-radiative and ionization kinetics, along with material effects (emission, sputtering, phase change), non-ideal equation of state (EOS), Magneto-hydrodynamics (MHD) and radiation transport (RT).

- Multi-math (or multiple numerical methods): several different numerical descriptions must be combined for the Non-Maxwellian velocity distribution function (VDF) for high-energy plasma components, the continuum description of the dense background fluid, and the multi-scale models of couplings between the two components and the fields. This item is generally considered as a consequence of the first two.

Multi-scale/multi-physics problems remain one of the principal challenges in the computational community, and there is a growing body of work on fundamental approaches to those. The present project only explores a small aspect of this problem, as will be described in later sections. The level of detail implemented here into the physical models may be somewhat limited, given the resources available. However, the principal objective is to develop a core capability that can be further extended in the future to include more refined models and database. We attempted to build the software such that this extension process would be greatly facilitated.

## 4. Approach

### 4.1. Modeling Issues

In most cases of interest here, the plasma can be decomposed into a “bulk” plasma and a highly energetic component (to simplify, electrons). The general problem consists of modeling in an efficient and accurate way the dynamics of the complete distribution function of each plasma component. If the bulk plasma is strongly collisional (i.e. sufficiently dense), it can be modeled as a fluid, albeit at various levels of thermal non-equilibrium. Otherwise, one must use a particle method such as DSMC or PIC to model its dynamics. Typically, the energetic component is itself a function of time and space; for example, at the onset of the discharge there can be very few energetic particles; during a mid-phase the energetic component is at a maximum, until it finally relaxes through collisional exchange with the bulk and disappears. This would be the case of a particle “beam” (meaning any strongly non-equilibrium, energetic component) injected into a dense gas; examples of this type of problem would be the pseudospark discharge [8], laser plasma interactions [9], streamers [10], gas-filled capillary discharges [11], etc.

Because the pseudospark<sup>†</sup> is a particularly representative of the physical problem, this discharge was examined in detail in the early part of this project. A few key physical phenomena characterizing the discharge are the following (see Figure 1):

- Electrons emitted from the cathode surface inside the hollow structure are accelerated by the cathode fall potential and contribute to the ionization in the negative glow region. Some electrons cross the negative glow region and are reflected by the opposite cathode wall; these “pendular” electrons can change the potential distribution and enhance the ionization rate (note that pendular electrons cannot be described by a unique Maxwellian distribution).
- Neutral energetic particles (metastables and photons) generated in the negative glow have a higher chance of hitting a cathode surface (due to the geometrical effect), enhancing the secondary electron emission rate.
- The higher ion and neutral energies and the higher degree of confinement lead to a higher density of sputtered metallic atoms with generally lower ionization potential.

---

\* One can also envision the reverse process, where energetic particles are generated and extracted from the bulk itself (e.g. stochastic heating).

<sup>†</sup> The pseudospark device is an extension of the hollow cathode (HC) discharge, filled with a low-pressure gas (< 100 Pa), and was first developed as an accelerator at the University of Erlangen in Germany, in 1978. The discharge operation is characterized by 3 phases: (1) a very rapid current rise (up to  $10^{12}$  A/s), (2) a high intensity electron beam ( $10^9$ - $10^{12}$  W/cm<sup>2</sup>) and; (3) a super-dense glow discharge free of filaments [8]. The intense electron beam emitted in the transient phase of the discharge propagates in a self-focused manner and is rapidly space charge neutralized. The super-dense glow phase is highly conductive and the absence of filaments implies a very low erosion rate. For these reasons, the pseudospark has been mostly developed as a plasma opening switch (POS) [12]. Material processing applications may also result from the high power density electron beam [13], especially for target materials with high melting points and complex stoichiometric structures (e.g. high-temperature superconductors). Other, not well understood characteristics of the discharge may also lead to potential applications, e.g. ion beam generation [14,15] and plasma jet formation [16]. Advances in solid-state technology have limited the commercial potential of pseudosparks as opening switches; more recently, the device was investigated for its potential in high-power microwave [17].

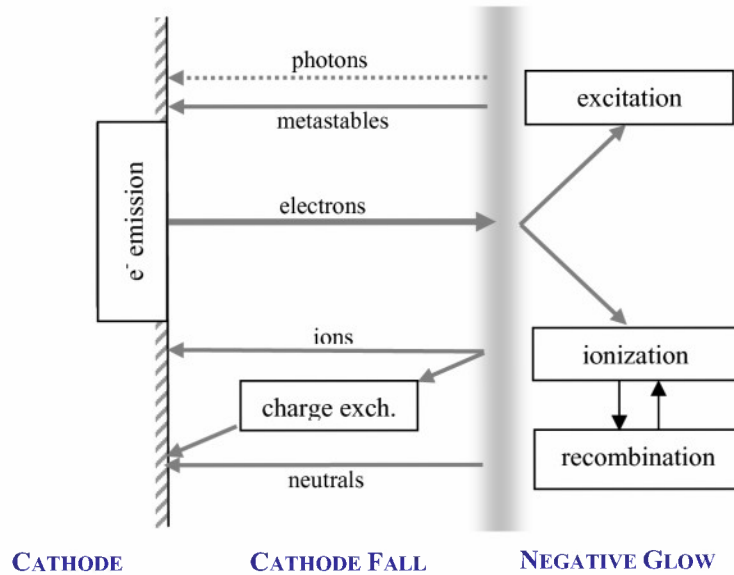


Figure 1: Schematic of physical processes near cathode

These effects combine to yield high ionization efficiencies. The electrons emitted at the cathode surface and accelerated in the cathode fall provide a “beam” component to the electron energy distribution function (EEDF). The initial phases (ignition and beam formation) of pseudospark operation were simulated by Boeuf and Litchford [18] with a hybrid code. As shown in Figure 2, the charged plasma is formed first near the anode, and when the space charge potential becomes of the same order as the applied potential, the plasma is able to propagate through the cathode hole. As the sheath contracts inside the hollow cathode, electron emission from field emission and field-enhanced thermionic emission become more important, and may eventually dominate the emission process. Hartmann and Gundersen [19] suggested a “super-emissive” state could be the result of surface heating of the cathode by ion bombardment. Eventually, as ions hit the cathode surface, sputtered atoms reaching the edge of the cathode sheath become ionized, then are accelerated again towards the cathode. Thus, a “self-sputtering” process [20] would lead to run-away ionization, and the “super-dense” glow phase is reached. Other explanations for this high-density conditions call for microscopic emission sites where explosive electron emission [21] occurs; these phenomena, extensively studied in Russia, are characterized by exponential growth of the current density from thermo-field emission at a microscopic defect (dielectric inclusion or geometric protrusion) where the electric field is concentrated, resulting in vaporization of the electrode material<sup>\*</sup> and a high density plasma plume that acts as an emission site with no work function (limit of Child-Langmuir emission). We note that the explosive electron emission process is also an excellent application of the hybrid code.

The major procedures used in [18] have significant limitations, as described below.

(a) *Ballistic Integration*

In this procedure, the trajectories of the electrons emitted from the cathode are computed from the time of emission until they are lost to the system. Along the trajectory, the ionization events are accumulated into a source term for the bulk plasma. This is valid because the fast electron motion occurs on time scales much shorter than ion drift motion (which governs the evolution of the plasma potential). However, the fields generated by the hot electrons are ignored, and cannot model the high-intensity electron beam produced in the early stage of

<sup>\*</sup> The mechanism has also been suggested for a space propulsion device.

discharge operation. A true PIC model for the high-energy electrons would be necessary to account for self-generated fields on the proper time scale.

(b) *Transfer to Bulk Plasma*

High-energy electrons are removed\* from the system when they are collected by the anode or when their total energy (kinetic + potential) falls below the ionization threshold and are then included into the bulk (fluid) plasma, i.e. the local electron density is increased by the corresponding amount given by the pseudo-particle. However, using the ionization threshold for operating the PIC-fluid transfer is somewhat arbitrary. Even at lower energies, the electrons are still capable of exciting the electronic or vibrational levels. This prevents an accurate modeling of all collisional-radiative effects in the discharge, which can be important. Furthermore, the transfer of multi-eV energy electrons would naturally distort the EEDF of the cold bulk plasma. The latter being assumed as Maxwellian, there is no possibility of accurately model this effect, unless the bulk EEDF is modeled by a Fokker-Planck. It would therefore be more accurate to perform this transfer only when the kinetic energy of the hot electrons is not too far from the *mean* energy of the bulk EEDF. Another similar problem with the model of [18] is that the secondary electrons produced by the gas from ionization by the fast (non-thermal) electrons, are themselves not treated as particles but are part of the bulk. This is inconsistent because these can have sufficient kinetic or potential energy in the discharge to produce further ionization.

(c) *Fluid Transport*

The approach of [18] describes only fluid motion through the drift approximation. Both electron and ion inertia effects are neglected, as well as the energy transport in the fluid. The neglect of ion inertia implies that the build-up of an ionic space charge near the anode cannot be accurately modeled. This effect has been considered as critical to the formation of an ion beam during the discharge ignition. Furthermore, ion and electron energy transport may also be crucial in the super-emissive glow phase, notably in controlling the heat fluxes to the cathode and material erosion. Other discharges are much more dynamic (e.g. laser-plasma plumes, plasma thrusters, etc). The solution appears straightforward, i.e. the bulk plasma model should include at least a multi-temperature, one-fluid model, and preferably a collisional-radiative model. Finally, it may also be necessary to consider at some stage the electron dynamics (inertia effects) in the bulk plasma; this requires an extension to a multi-fluid model. This would allow the description of both slow phenomena (i.e. drift model) as well as fast phenomena (Langmuir waves). More importantly, the multi-fluid model may be needed for the accurate description of dynamic double layers.

(d) *Electron emission*

The electron current from the cathode is assumed in [18] to be proportional to the ion current collected at the cathode (the discharge is initiated by seeding the gas in the discharge with electrons) (see Fig. 2). This steady-state procedure does not allow for charge build-up in the gas discharge during ignition, a problem which can be resolved by a multi-fluid model as mentioned above. Furthermore, the procedure for electron emission is quite complex, especially during the super-emissive glow phase, which cannot be modeled with this very approximate procedure. Ideally the complete plasma-material interaction physics must be modeled† i.e. (1) thermionic emission, (2) field emission, (3) field-enhanced thermionic emission, (4) photo-emission, (5) secondary emission, (6) sputtering. Note that photo-emission and the impact of metastables on electrode surface require a collisional-radiative model for the bulk plasma.

---

\* Keeping these particles in the model while they are no longer capable of ionization would be very inefficient, since their number would keep increasing during the computation.

† Even while considering all these processes, we are still limited by the model description. Emission can be significantly influenced by the local temperature of the emission spot and the state of the electrode surface; this also implies the need to model heterogeneous and multi-phase effects, as well as heat conduction in the material. Sputtering is also limited by the fact that the ions are described as a fluid, while a more accurate approach would require a PIC model *for the ions*, at least in the sheath.

We see that there is a number of modeling improvements necessary to correctly capture the physics of this discharge. In particular, in reference to the list above, we need to (a) apply the correct numerical treatment to the particles (PIC); (b) consider very carefully the exchange between fluid and the particles; (c) extend a fluid model to the appropriate non-equilibrium description (collisional-radiative); (d) implement the physically correct model of interaction with material boundaries. The last item would be a significant project in itself and is not considered here. The key issues being examined are items (b) and (c), and to a lesser extent – since current tools are well developed – item (a). The ability to exchange mass, momentum and energy between the particles and the bulk phase is a key aspect of hybrid modeling, for which innovative numerical methods must be developed and clearly the most important change that one should introduce is the ability to fully-couple a true PIC model with the fluid dynamics and the detailed, internal kinetics of ionization and excitation.

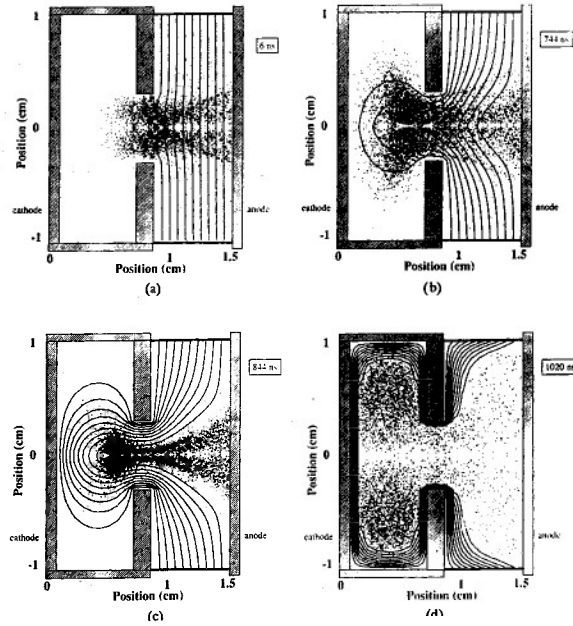
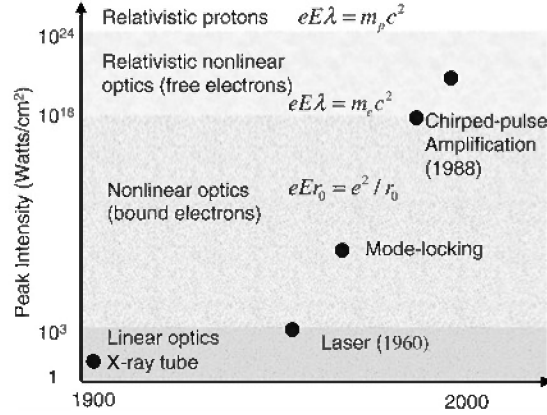


Figure 2: Contours of constant potential and ionization events (dots) - taken from [18].

Another example of plasma conditions where the hybrid model would be particularly applicable is in laser-plasma interactions. In the last decade table-top lasers have undergone several orders-of-magnitude increases in peak power using chirped pulse amplification (CPA) [22]. These systems can now easily reach intensities of  $10^{19}$  W/cm<sup>2</sup>, which is high enough to accelerate electrons to relativistic energies. Prospects for further extension to the next (nuclear) regime of relativistic effects for protons ( $10^{24}$  W/cm<sup>2</sup>) are also quite good [9,23] (see Figure 3). These ultra-intense laser pulses are also very short, in the 10-100 fs range. For pulses of such duration many of the dynamical effects are frozen, and unusual states of matter can be created. For example, ultra-short, ultra-intense laser pulses focused onto nano-clusters (1-10 nm) strip all the electrons from the clusters, while the ions are barely in motion by the time the laser pulse is completed. The ions are left with extremely high initial electrostatic potential energy, which accelerates them to extremely high velocities. This “Coulomb explosion” mechanism can produce ions with kinetic energies in the multi-keV range, sufficient even to induce nuclear fusion reactions between deuterium ions, as demonstrated in several experiments by the production of neutrons of characteristic energy [24]. Non-linear media effects are also important in this regime; for example, plasma self-focusing and relativistic self-focusing effects prevent the dispersion of the laser beam in the plasma medium, while relativistic mass shifts induce transparency and allow penetration of the laser pulse into dense plasmas [23]. These new regimes of relativistic, non-linear laser-

plasma interactions are opening new fields of research in fusion, diagnostics, and particle acceleration.



**Figure 3: Peak intensity of light sources and corresponding physical regimes versus history. Figure taken from [23].**

Of special interest are the laser interaction with dense media such as solid clusters and solid foils, but there are several issues with our understanding of the basic phenomena. First, the direct ionization process by the laser field is not fully characterized; while the basic physics are relatively well understood, the actual dynamics of the process involve complex quantum effects which make calculations of cross-sections difficult. The overall ionization also includes relativistic electron-atom collisions, while deep inelastic scattering contributes to the X-ray spectrum. The electron return current generates X-rays as well, and the electron dynamics are a very complex process involving ionization, elastic and inelastic collisions, laser propagation and absorption, self-induced electro-dynamic and magneto-hydro-dynamic fields, and radiation propagation. The states of matter involved range from dense neutral solid matter to dense continuum, collisional-radiative plasmas, relativistic particles and fully-ionized plasmas. Most of the computational studies of ultra-intense laser-plasma interactions are conducted with Particle In Cell (PIC) methods; this approach assumes that the matter is already fully ionized, and does not completely resolve the Debye length, unless fictitious problems (this may lead to significant errors in energy conservation) with scaled-down density are being considered, and does not consider collisions between particles, or long-term relaxation of the material. The extreme disparity of equations of state, time scales and energy scales implies a similar diversity of numerical methods to be employed for their modeling, i.e. a “hybrid” model. Therefore, the computational methods being researched and developed through this laboratory task could also be implemented into a sophisticated hybrid model for the detailed and accurate modeling of relativistic laser plasmas, a topic of interest to AFOSR, currently funding a MURI program on ultra-intense, ultra-short pulse lasers for hyperspectral diagnostics.

The usefulness of a hybrid model extends well beyond the two examples mentioned above; in both cases, the plasma is characterized by a dense, relatively cold gas/plasma and a highly energetic component accelerated by strong fields (non-Maxwellian electrons). The case of ultra-intense laser plasma is more severe than the pseudospark because of the energy range (relativistic) but the fundamental problems remain similar. One can also consider micro-discharges, dielectric barrier discharges (DBD), RF discharges, helicons as other examples where a hybrid model is applicable. Even relatively dense plasma which may appear fluid-like on macro-scales may require the incorporation of a kinetic model at smaller scales, e.g. reconnection of magnetized plasma near the X-point, as found in solar and geo-plasma or in high temperature field reversed configurations (FRC). The latter may require a *dynamic* hybrid model, i.e. the use of a combined fluid/kinetic model only in some regions of interest and at specific times – a generalization of adaptive mesh refinement (AMR) where the plasma inside the generated sub-grids is computed with subscale models. This additional complexity is left for the future.

## 4.2. Numerical Issues

We have indicated above the need for accurate modeling of both fast and bulk components. For the former, we have several existing tools available. The easiest and most conventional technique is the Particle-In-Cell (PIC) method [1], particularly useful for the highest degree of non-equilibrium (beams, Collisionless plasma). In the PIC method, the time-scale of electron motion is fully resolved and the electro-magnetic fields are computed at each time step by the cell-averaged distribution of particle densities and velocities. Only the shortest time-scale problems can be effectively resolved with this method, and only the plasmas with significant charge separation. The PIC method by itself is a combination of a transport algorithm (moving the particles in a field, interpolated at the particle position – “gather”) and a reconstruction algorithm (computing the field from the particle positions – “scatter”). If the time scales are short and the fields are not static, an additional step is needed to propagate the field solution, i.e. a Maxwell equations solver. Collisions (if any) are treated stochastically, i.e. by a Monte-Carlo Collision (MCC) procedure<sup>\*</sup>. The MCC computes collision events according to their probability of occurrence within the time step used [25,26]; since a given particle is either colliding or not, the accurate rates of change of the distribution function from the collisions (the right-hand-side of the Boltzmann equation) are obtained by relying on statistical averaging. For electron collisions, the procedure is similar to a test-particle Monte-Carlo: due to the difference in masses, the target atom can be assumed unperturbed during the collision. In the case where the energetic particle is an ion itself, particles must be sampled from the equilibrium bulk distribution, collided with the energetic particles, and the momentum and energy exchanged monitored; this approach does exactly conserve momentum and energy, but is expensive. Another approach is to use the more efficient “collision-field” method [25,26], which can also conserve momentum and energy but averages the velocity dependence into a collision frequency; this approach can also work for electron collisions. Finally, there is the interesting alternative of extended pseudo-particles, each one carrying its own internal distribution at an individual “temperature” [27]. This “complex particle kinetics” approach is potentially of great benefit, and we will show in a later section that the method, which involves an internal, “micro-distribution” is compatible with an algorithm for the control of particle numbers in strongly ionizing regimes.

The standard MCC can be implemented with minimal effort (although the mechanics of the procedure are simple, the database requirements of the collisional models can be significant). As will be explained in a later section, the standard MCC can have significant problems when coupling the particles to a collisional-radiative model of the bulk plasma. Therefore, special attention must be paid to developing and testing new algorithms to handle this case of detailed interaction.

## 4.3. Computational Issues

The long-term development strategy is based on the following:

- (1) Development/refinement of a software model (Object-Oriented) for a hierarchical, multi-level description of the physical processes (architecture development).
- (2) Development of new algorithms for efficient and accurate interaction of multiple physical and numerical models (procedure development).
- (3) Implementation & validation of various SOTA models aimed at solving specific problems (incremental development).
- (4) Incorporation of SOTA models and numerical techniques from other sources, whether already implemented and validated or being developed (synergetic development).
- (5) Distribution of software and extension to multiple applications (user base development and feedback)
- (6) Software optimization, refinement (user-interfaces) and collaborative maintenance.

---

<sup>\*</sup> The Direct Simulation Monte-Carlo – DSMC – method is a similar procedure [2], except that no EM fields are involved; the particles follow a straight trajectory between collision events and no moments of the distribution must be computed as source terms for the fields.

As explained earlier, this effort is mostly aimed at risk reduction, and the R&D program is focused on the first three items. Item 4 is the result of leveraged activities, while items 5 and 6 would be addressed in a follow-on program once the code has reached sufficient maturity.

Given the disparity of the modeling approaches and the complexity of the physics, it does not appear possible that all approaches can be combined into a single code *per se*. Such a code would be extremely large, difficult to use and difficult to maintain. We are mainly interested in developing a framework of data-structures, libraries, interfaces and modeling *tools*, rather than a single piece of software. This approach is already taking place for a number of scientific modeling efforts, e.g. VORPAL [28], using modern Object-Oriented architectures.

Ideally, the software should also be grid-type independent. This implies that one could at first decide to implement solvers based on structured grids, but reserving the ability to implement non-uniform grids and their solvers at a later stage. In addition, the software should have a number of features aimed at maximizing its usefulness, such as: multi-dimensional capability (1D, 2D, 3D); ability to handle complex shapes and boundary conditions; simplified maintenance and upgrade; portability; high computational efficiency, and; graphical user interface (GUI) and visualization tools. The implementation of other models developed by other teams may also be a challenge, since data-structures or even languages may be different. This integration can be achieved in steps: (a) loose coupling (legacy codes): data exchange through I/O; (b) moderate coupling: data exchange through arguments to function calls; (c) tight-coupling; re-write of additional functions. Option (a) is applicable when the legacy codes are very capable and modern, i.e. when any re-write would be a significant level of effort; this is generally not the preferred option of any software development engineer, and we have not found any existing code that merits to be included at that level. Instead, we have focused on the latter two options. Thus, various methods and codes were developed throughout this task and have yet to be integrated into the final result; these include for example a Vlasov/IC hybrid solver with a 2D Maxwell equations solver, and a grid-free, Barnes-Hut tree method. These efforts will be incorporated into the hybrid code in the next two years.

Besides efficient algorithm and software development, computational performance is another inevitable, and probably the most important issue. The multi-scale problem defies brute-force approaches; the time-scales of electron motion are simply much too small compared with hydrodynamics or MHD time-scales. Besides algorithm development to allow greater time steps on the fast scales, one should also consider multi-scale integration techniques and efficient implementation. The former is a field of study in itself and will be considered in more detail in a separate effort; presently it is sufficient to use low-order methods, e.g. sub-cycling. The latter is of special interest here, due to the recent availability of graphical processing units (GPU) for general purpose computing (so-called GPGPU). Since the start of this effort, the field of GPGPU has grown by leaps, both in terms of hardware and software development and we have refocused the effort to take advantage of it. Thus, algorithm acceleration using GPUs will also be discussed.



## 5. Software Development

### 5.1. Architecture

For several reasons, Java was the language selected for the development of the software architecture. We found Java particularly easier to use to rapidly develop bug-free software for complex object-oriented codes. Although this is still considered a *temporary* choice, a scientific code written entirely in Java is entirely possible; from all the tests performed (by us and elsewhere) the execution speed is the same as C++, and shared-memory or distributed memory parallelization is very easy to achieve with multi-threading and Remote Method Invocation (RMI). We also tested the interfacing between Java and C (using Java Native Interface – JNI), as well with CUDA, the language used for graphical processing units (GPU). Portable visualization and GUI can be completely integrated using open-source software, and there are no issues with compiler compatibilities between different vendors and platforms. Furthermore, Java allowed us to easily test various parallelization approaches across different platforms, in a way that is compatible with the modern approach of “grid-computing”. For example, we have created a client-master-server architecture (see Figure 4) with remote steering and real-time visualization. In its present stage, the “client” software allows the user to start a computing session, set-up the problem, and monitor the solution. The user can then log-off and log-on at a later time without interrupting the computations – only the visualization pipeline has been interrupted. Extensions of this approach could allow multiple sessions, encryption and user-ID checking.

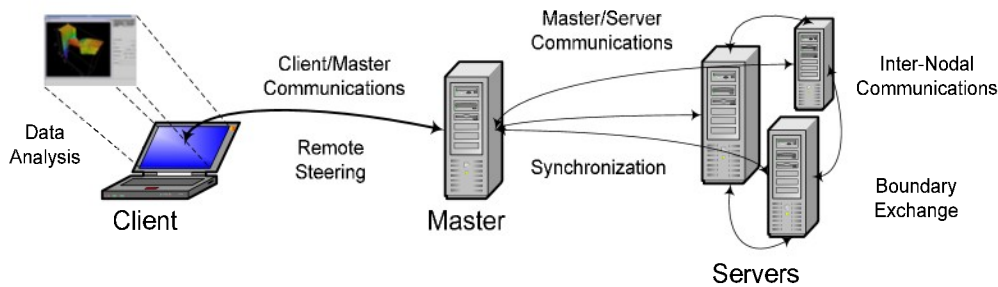


Figure 4: Possible configurations for the Client/Master/Server architecture

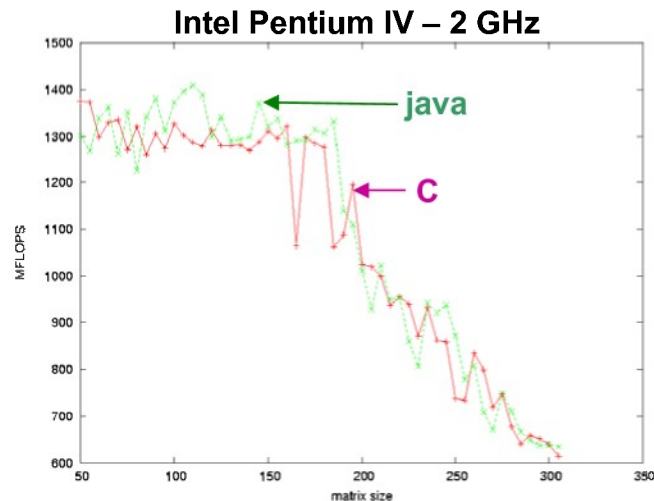
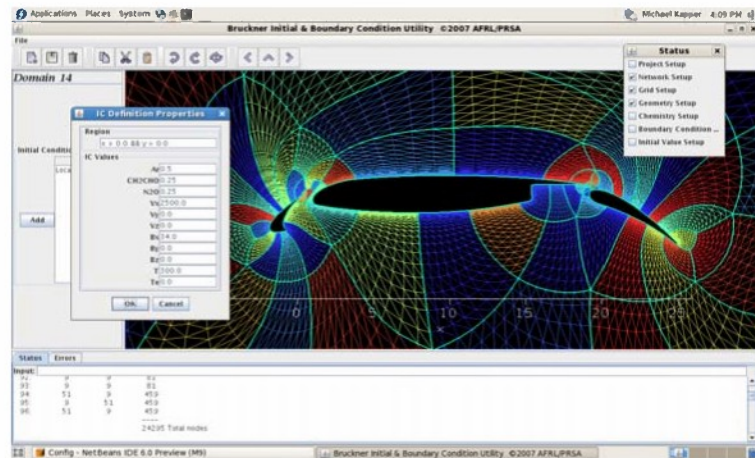


Figure 5: Comparison of Java and C performance on floating point operations

Except for a few exceptions [29-32], Java has not been considered as a viable alternative for large-scale scientific computing mostly because of a perceived lack of performance. However, as shown in Figure 5, our own tests on matrix multiplication performed a few years earlier, confirmed by third-party developers, indicate that at least on some platforms, the execution speed for simple floating-point calculations are similar to optimized C. More complete performance comparisons have been performed elsewhere with similar conclusions [33], and all our tests since have confirmed the equivalent speed of Java and C++.

The software is decomposed into various “packages” (to keep the Java terminology), or libraries that contain software objects for various purposes. Some packages deal with I/O, visualization, mathematical and physical functions, grid set-up, thermo-chemistry, particles, fluid, electro-magnetism, parallelization, and boundary conditions. A thermo-chemical database for the fluid model has been incorporated, and a separate database manager is being developed. This managing software will facilitate the addition, modification and integration of key physical and chemical data, in preparation for computations. Thus, the database manager would create files that contain data for energy levels, cross-sections, oscillator strengths, specific heats, heat of reaction, isotopic composition, etc. We have attempted to leverage other efforts into this database management; an SBIR effort delivered a preliminary version of a browser that would scan existing on-line databases (e.g. NIST) and extract relevant data into a more useful and common format. This is useful because there is a lot of currently available data which resides in various databases; agglomeration of this disparate information for immediate comparison (the cross-sections can be notably different, depending on the models of electron and atomic collisions used), selection, and manipulation for use in a CFD or hybrid code. AFRL-Kirtland (DE) also had a similar interest, but decided against a joint effort. We plan on continuing to develop this database manager through other collaborative efforts or leverage other research programs.

Problem initialization is performed through several pre-processors, for: (a) thermo-chemistry; (b) geometry; (c) initial state; (d) boundary conditions; (e) physical modeling. The latter is simply allowing the user to select which physical processes to be modeled (Fluid transport /Chemistry/ PIC / Heat conduction...). A preliminary GUI interface has been constructed to handle these pre-processors. We also included interfacing with a commercial grid generator (GridPro™) which can easily generate multi-block structured, body-fitting grids (see Figure 6), but this was principally a demonstration activity and there was no further work in that direction, the focus being placed on basic numerical and physical model development.



of 2-4 CPU each, with specialized machines having thousands of nodes. Since the start of this lab-task, GPU clusters have entered the field as a powerful alternative to these conventional Linux cluster configurations, and the use of GPU nodes for acceleration is currently under investigation. As a consequence of hardware development trends, parallelization is best accomplished through a hierarchy of levels, including both distributed memory architecture at the coarse grain (multi-CPU clusters), shared memory at the finer grain (multi-core architecture at each server), and another distributed memory level yet possible at the finest scale (multiple GPU boards at each server).

Distributed memory parallelization (across several servers/nodes) is accomplished with Java's remote method invocation (RMI) for all inter-processor communications [34] (in standard C++/Fortran this would be done with MPI). Java-RMI allows for the manipulation of remote objects on a local machine. As an example, and according to the architecture described in the previous section and in Figure 4, the client can invoke remote methods on the master, asking the remote method to return an object to the client, such as the computation data for visualization. The RMI architecture of the code therefore consists of those three levels—client, master, and server. The code is initialized on the master with a list of server(s) that will handle the computations. A "server" is a single-term denomination that can physically be, for example, a single-processor or multi-processor workstation, or a node in a Linux cluster<sup>†</sup>. Once the master has been initialized, the client can establish a connection to it<sup>‡</sup>. The client can then perform preprocessing operations such as set-up of the grid, boundary conditions, chemistry, etc, to initialize the computations and engage in real-time visualization as data is being computed (see Figure 7).

Shared memory parallelization (inside each server/node) is done by multi-threading (in C++ this would be done with OpenMP). Each "server" can compute several blocks (subsets of the computational domain), each block running in its own thread. The synchronization of all iterations and communications is the responsibility of the master node. Various locks and associated *wait/notify* methods determine when all of the servers have finished their computation and communication iterations and to cue them so that they may proceed with the next iteration. The master is also in charge of global data which is processed from local data from each block, such as the time step, or data that must be visualized. The client code provides a graphical user interface from which the code can be controlled and data can be viewed in real-time. The client can make requests to the master to grab data from the servers as it is being computed and display it in real-time with VisAD—a Java visualization API (freeware) built upon Java3D [35,36].

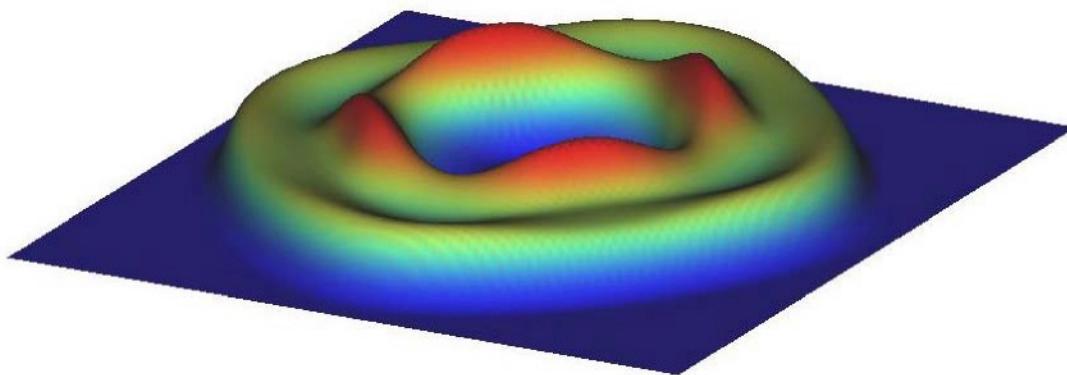


**Figure 7: Snapshot of the evolution of a spherical explosion, computed with a second-order TVD method (ideal gas). Real time visualization using VisAD library.**

<sup>†</sup> One should think of the "server" as a computational unit that provides a "service" (computations). There is a-priori no reason why the "server" cannot by itself further distribute the computational load to other service providers, although this recurrent (multi-level) parallelization has not been tested.

<sup>‡</sup> The master is a command and control center, responsible for gathering and distributing information to the servers and client, scheduling the tasks, providing critical I/O, and monitoring commands from the client.

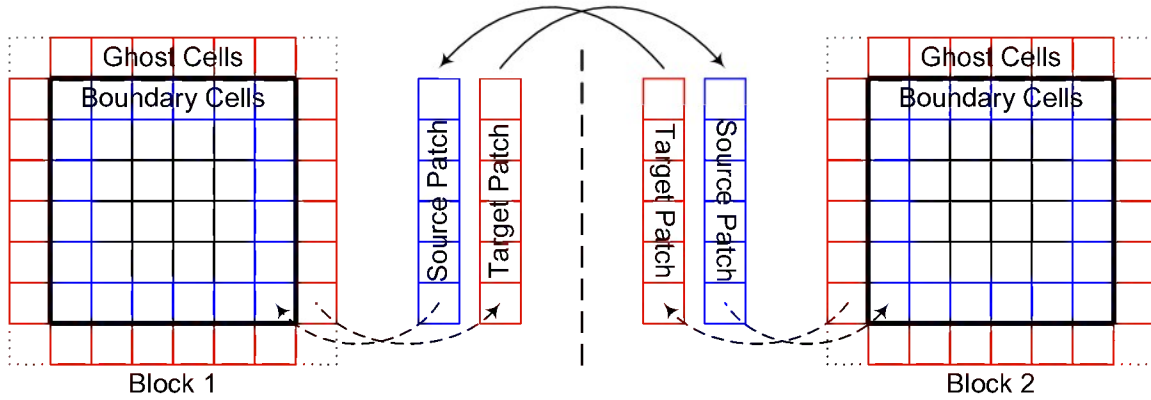


**Figure 8: Block communication using source and target patches. The dashed arrows represent referencing while the solid arrows signify remote method calls.**

The most crucial concern regarding communication overhead is the optimization of the intra-/inter-server communications. At every time-step, it is necessary for each block in the domain to share its information with one or more neighboring blocks. If two neighboring blocks are being computed on the same server, the communication can be handled by standard local method calls. However, if two neighboring blocks are computed on different servers, then inter-server communication is involved and it becomes necessary to use Java-RMI or other suitable message passing protocol. Figure 8 illustrates how two neighboring blocks communicate with each other. There are two types of patches which allow data transfer between two blocks. The first of these being the source patch is an array of objects which contain references to data available in the boundary layer of cells. The data references are depicted by the dashed arrows in Figure 8. The second is the target patch from which the ghost layer of cells receives its information.

During block communication, there is a method call for each source/target patch pair in which the target patch is filled with the information from its neighboring block's source patch. The method calls are depicted by the solid arrows which can either be a local call if both blocks are on the same server or an RMI call if each block is on a separate server. The exchange of boundary condition information between servers is done without involving the master: this prevents a bottleneck when scaling to a large number of processors. Figure 9 shows preliminary results of scalability tests of a fluid computation (CFD model) on a Linux cluster as function of the number of nodes (static domain decomposition). The overall parallelization efficiency is very good (systematically > 90%) for this test case, although the current measurements were limited by the number of processors available.

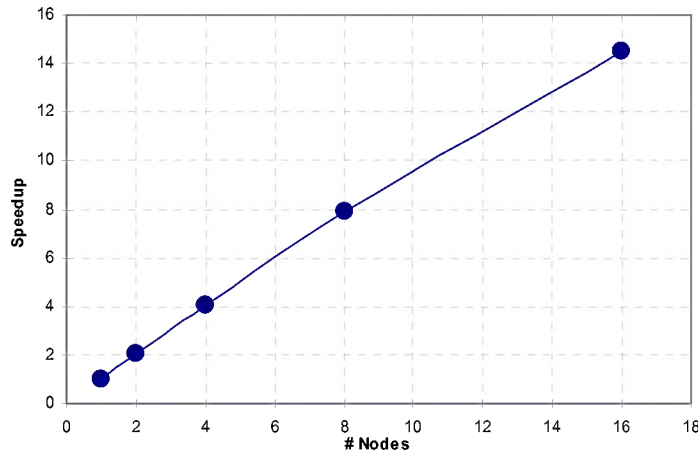


**Figure 9: Preliminary scalability (CFD model) on Linux cluster.**

### 5.3. Data Structures

#### 5.3.1. Geometry

Ideally, the software should be grid-independent; this implies that one could at first decide to implement solvers based on structured grids, while reserving the ability to implement unstructured grids and their solvers at a later stage. All numerical approaches described above make use of a discretized space: besides the self-evident case of Computational Fluid Dynamics (CFD), PIC is a typical particle-mesh method, and DSMC needs a mesh to determine collision partners. Grids can be described with the following categories: (1) Structured (constant number of grid points in each direction), or (2) Unstructured (triangles, tetrahedra). The former also has the following sub-cases: (1-a) Cartesian ( $\Delta x$ ,  $\Delta y$ ,  $\Delta z$  are constants); (1-b) Uniform (spacings are not constants); (1-c) Curvilinear, or “body-fitted” (not necessarily orthogonal). Structured grids can be described by multi-dimensional arrays of given dimensions ( $Q[][][]$ ), i.e. any grid point can be addressed by a set of indices ( $i,j,k$  in 3D). In unstructured grids there is no such ordering, and the grid connectivity (i.e. how to access another point from the current one) requires a list of pointers between grid elements. Despite the apparent difference between the two descriptions, one can use the same approach in representing the grid data and connectivity. Thus, one can define an object *geoNode* to represent a grid point (a node in the mesh); each *geoNode* contains the coordinates of the point (in real or transformed space), as well as a list of pointers (addresses in the memory where the data is located, or integer indices that indicate a position in an array) to the neighboring points. The same goes for object of type “*geoCell*”, which describes the volume enclosed by the grid lines or grid surfaces. Thus one can walk through the connected list of nodes and cells to reach every point, whether the grid is structured or not. Of course, the structured case has the additional advantage that one could also directly address a given node or cell from the set of indices ( $i,j,k$ ). However, instead of forcing the data to be stored in a structured form, it is just as easy to have a method that provides the memory location of a node/cell with those particular indices. Thus, the data structure (a one-dimensional list of objects) can remain the same to describe both structured and unstructured grids, while the additional methods “*getNodeIndex*” and “*getCellIndex*” allow a mapping between the structured indices ( $i,j,k$ ), arguments to the method, and the one-dimensional list. Such a mapping is of course void in the unstructured case.

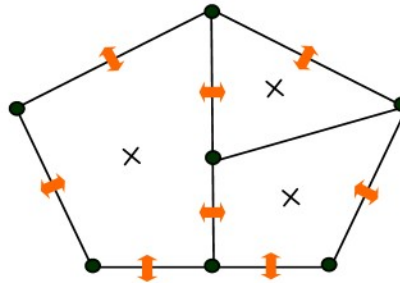


**Figure 10: Schematic of *geoCell* object structure.**

Each *geoCell* is defined by a variable number of nodes, faces, with corresponding pointers to the attached *geoNode* and *geoFace* objects, and to the neighboring *geoCells*. The cell also includes variables such as center position, volume, and metric.

Within this approach a “*Mesh*” object is defined as a list (or 1D array) of cells, nodes and surfaces, with pointers to connected objects (see Figure 10). If a structured solver is being used, one must address information on either side of a cell or surface by the pointers to the corresponding objects; for example in 2D, the variable on the left ( $U[i-1][j]$ ) is accessed as  $U[ncL]$ , with  $ncL=pointer\_2leftcell(nc)$ . This procedure has two disadvantages with respect to a simple multi-dimensional data structure (e.g.  $U[][]$ ): (a) there is redundant information being stored in the *Mesh* object; however, the information is contained in a few



variables and does not constitute any significant penalty; (b) there is additional overhead in, for example, the method call “*getCellIndexI*”, which maps the one-dimensional index of the list of cells with the structured indices  $(i,j,k)$ ; however, one can easily construct algorithms such that this method call is relatively infrequent and the cost is minimal compared to the large number of operations involved in a flow or field solver, for example. The major advantage is that this approach allows the same data-structure to be used for any type of grid structure. The *Mesh* object can be sufficiently general that each cell has an arbitrary connectivity, while some variables used only for some types of grids may remain un-instantiated for others. For example, a structured grid may need a metric for some solvers; this metric may be computed and stored in that case, but is empty when the grid is unstructured. Similarly, some techniques of dynamic grid adaptation may be valid only for some types of grids (e.g. octree subdivision for Cartesian grids) and not on others. Each *Mesh* object is therefore flagged by a few Boolean variables (e.g. Cartesian / Curvilinear / Unstructured), so that one could match appropriate solvers and methods to the types of grids being used. Even if not all solvers are immediately implemented, future extensions are facilitated because the geometry infrastructure can support it. This is the approach used here: while the current focus is on developing solvers for structured, body-fitted grids, unstructured grid implementations will be facilitated in the future, using solvers and grid generators (which must provide the connectivity information) from external providers.

Structured, body-fitted grids are efficient for CFD, especially when boundary layers are present; in that case, cells can be stretched to match the preferred direction of the gradients (normal to the body surface), while allowing efficient tri-diagonal implicit solvers and increasing the accuracy of dimensionally-split high-order schemes. This approach may also be efficient for plasma sheaths, since again the thermal, plasma composition and plasma potential gradients are aligned with the normal to the body surface. On the other hand, Cartesian grids are preferable for particle transport, the construction of simple high-order schemes (e.g. for the Maxwell equations), Fourier-transformed schemes, and dynamic cell adaptation. If the grid is Cartesian, it is extremely easy to keep track of the cell to which the particle belongs, given its position, e.g.  $i = x / \Delta x$ . This can be important for a large number of non-interacting particles, where transport (particle “pusher”) is the major computational activity. However, this is true mostly for collision-less plasmas in simple geometries<sup>†</sup>. When the plasma is collisional, most of the computational cost is in the MCC procedure. In those cases, the additional cost in determining the relative particle position with respect to the cells (i.e. cell-indexing the particle) for non-Cartesian geometries becomes a negligible fraction. This extra-cost is typically a few arithmetic operations, and is roughly of the same order for body-fitted grids (using metric-transformed variables) and unstructured grids (computing relative distances), as long as the particle moves at most to neighboring cells. This last limitation is also not a restriction for collisional plasmas, since it is important for solution accuracy. One should point-out that the two approaches can be effectively combined, by using body-fitted grids near the body and in collisional regions, while Cartesian grids are used away from the body and in collisionless regions. The ability to handle any grid type, as described above, is essential to this optimization scenario. Therefore, there is no need to be restricted to Cartesian meshes, as most PIC solvers are.

### 5.3.2.Fluid

The data-structure for the fluid and plasma variables must also be highly flexible. The fluid can be described at various levels of non-equilibrium, corresponding to various relaxation time-scales. By assumption, the velocity distribution of the fluid-like plasma components remains Maxwellian, the collisional momentum exchange between particles of similar masses being the fastest relaxation process. However, electrons and ions may have different velocity distributions (i.e. different translational temperatures), and internal modes may not follow identical equilibrium distributions, or may significantly deviate from Boltzmann distributions. This hierarchy of non-equilibrium descriptions results in a variety of multi-temperature models. The hierarchy for atomic plasmas

---

<sup>†</sup> When complex 3D shapes are involved, Cartesian cells must be “cut” near the boundary, yielding complex tetrahedral shapes. High accuracy near the boundaries becomes more difficult to achieve, and different solvers must be used.

would be single-temperature, two-temperature ( $T_h - T_e$ ), three-temperature ( $T_h - T_e - T_x$ ), and Collisional-Radiative (C-R) models, where  $T_h$  is the translational temperature of heavy particles,  $T_e$  is the temperature of the free electrons, and  $T_x$  is the temperature of the (assumed) Boltzmann distribution of electronic excited states. In the two-temperature model, the bound electronic states are assumed to be in a Boltzmann distribution at the temperature  $T_e$ ; this is usually valid in cases where the electron collisions dominate over atomic collisions. In low-density cases, when radiative rates are comparable to collisional or atomic quenching becomes significant, the electronic states cannot be described by a Boltzmann distribution; in this regime the C-R model is required.

The ability to generate a variety of non-equilibrium descriptions is another important aspect of the code flexibility. One can determine from the input conditions which model is necessary, and also easily perform parametric studies to verify assumptions regarding the state of the plasma, or evaluate the importance of non-equilibrium effects. Furthermore, it is also desirable in some circumstances to adjust the level of description according to the *local* conditions. This would maximize efficiency, since higher levels of non-equilibrium imply higher computational costs. The software is currently being configured to allow different non-equilibrium fluid models in different regions; this feature is currently limited to static and pre-determined conditions, but it is theoretically feasible to extend this capability to automatic and time-dependent determination of the non-equilibrium model. This capability implies that boundary conditions between contiguous domains automatically transform the data between lower and higher-levels of thermodynamic description. Therefore, key methods to be implemented in the library for fluid modeling are for the *contraction* (from higher- to lower level) and *expansion* of information. An example of the former would be the grouping of all excited levels from a C-R model into a Boltzmann distribution and the forcing of equilibrium with the free electrons (from C-R to 2-T model); an example of the latter would be the generation of an additional variable for the electron energy from the single fluid equations (from 1-T to 2-T). Preliminary tests of these procedures have been performed successfully. Of course, the procedures are accurate as long as the conditions permit it, i.e. are such that the higher level of description (e.g. 2-T model) is compatible with local thermodynamic equilibrium (LTE) for the mode being expanded or contracted ( $T_e \approx T_h$ ). This approach yields maximal benefits when the high level of thermodynamic description is very expensive to maintain in near-equilibrium conditions; this would be the case of the C-R model, for example, since it requires a solver for the master equations of collisional and radiative excitation and de-excitation, and mass conservation equations for all levels. Similar benefits could be found for molecular plasmas. Note also that a similar procedure applied to translational modes (i.e. velocity DF) would allow the transition between CFD in dense fluid regions and DSMC in transitional or rarefied regions.

Finally, one should also point out that atomic electronic states are too numerous to be treated independently inside a C-R model; the usual procedure consists of grouping together electronic states which are close together in the energy spectrum.

### 5.3.3. Particles

Particles usually have a very simple structure: they must contain a minimum of information, since accurate simulations requiring  $10^6$ - $10^7$  particles or more would consume an inordinate amount of memory if each particle object contained an excessive amount of data. The minimum information is: (a) a particle type identifier (this can be the species number); (b) particle coordinates ( $x, y, z$ ); (c) particle velocity ( $v_x, v_y, v_z$ ). The rest, i.e. charge, mass, etc, can be obtained from the species information. Additional information may include: (d) particle statistical weight; (e) cell number to which the particle belongs, but also; (f) transformed local coordinates ( $\xi, \eta, \zeta$ ) which are especially useful for monitoring whether a particle crosses into an adjacent cell in body-fitted grids, and; (g) time scale – this has been explained further in Section 5.1. The statistical weight (each simulated particle is a “pseudo-particle” and represents a large number  $\varpi$  of real particles) could be made species-dependent only, in which case it would not need to be included as item

(d) in the particle data-structure, but there are several reasons why this may be beneficial: (1) when particles are injected from time-dependent boundary conditions (e.g. electrons from cathodes) a higher accuracy could be obtained by varying the statistical weight in addition to, or instead of, varying the number of pseudo-particles; (2) chemical reactions can be more accurately computed using variable statistical weights; (3) higher statistical accuracy can be achieved when the particle density varies by several orders of magnitude across the computational domain, by duplicating particles that move into low-density regions. These issues are common to DSMC simulations, where the use of variable statistical weights is very frequent [2].

Since some of these quasi-particles may describe gas species with internal structure (electronic, vibrational and rotational states), there may also be some information required to describe these modes. Ideally, to each particle would be associated a unique state; however, to accurately (i.e. with low statistical noise) describe the complete DF, one would require an extraordinarily large number of particles. One must instead attribute a distribution of internal states, e.g. a simulated molecule could have its own rotational temperature, indicating how these modes are populated. During a collisional energy exchange, one can compute and modify the overall internal energy associated with that mode, and assign again a temperature. The disadvantage of this approach is that one potentially neglects correlations between internal and translational modes. For example, if situations occur where most of the excited states (indicated by a quantum number  $\ell$ ) are associated with particles moving at high-velocity in the z-direction, the statistical correlation  $\langle \ell | v_z \rangle$  can be high when both  $\ell$  and  $v_z$  are high, and this effect would not be reproduced if internal energy distributions are stored for each particle. Such situations can occur in special cases (beam interactions) and although molecular plasmas are not currently being considered, it is prudent to design the software with both potential approaches in mind; the data-structure can simply have un-instantiated arrays of levels or distribution parameters, which can be used for whichever model becomes implemented.

This approach also could be extended to the velocity distribution, i.e. the particle data includes also a velocity distribution. This approach is particularly interesting when dealing with the problem of particle coalescence, to be described later.

#### 5.4. GPU programming

Within the course of the lab-task we have acquired workstations with GPU cards from NVIDIA; one workstation with 2 Tesla C870, and another one with 2 Tesla C1060 cards. The C870 was another model which allows floating-point operations only, but is sufficient for preliminary development and testing purposes. Both cards support some version of CUDA [37], the C-like language from NVIDIA for GPU programming. The technology evolves very fast and at the time of this writing, a newer technology yet has been developed, the Tesla "Fermi" card (C2050/C2070) which allows C++ programming. Further testing of the Fermi card will be done in the next 2 years. Various algorithms were tested on the GPU. First, we implemented a generic particle transport and Monte-Carlo collision algorithm; the particle transport is extremely simple and involved only a few floating-point operations; the collision algorithm selected pairs of particles in each cell and collided them elastically with a 50% probability. We found that the GPU was slightly slower than the CPU (Quad-core Xeon) if only the move algorithm was performed. When the collision algorithm was added, the GPU was faster by a factor of about 4\*. Considering that the MC algorithm is stochastic and that the threads must be synchronized, this result is quite good. These results include the time required to transfer data between the CPU and GPU. The reason the move+collide algorithm was so much more efficient presumably lies in the fact that many more operations are needed to compute the post-collision velocities. To test this idea further, we implemented a generic "workload" for each particle, by computing a cosine function a certain number of times. The speed-up was very clear: Figure 11 shows the speed-up compared to the CPU, as function of the number of cosine function calls. This acceleration factor was computed

---

\*Up to 16 million particles were tested; the number of particles in each cell was varied but the results were not significantly affected.



for several cases of the total number of particles/threads and found to be almost independent of the number of threads (above 1 million). We conclude that the optimal approach to using the GPU is to maximize the amount of independent work; thus the GPU may not be profitable for problems with simple physics, but may allow rapid computation of much more challenging problems. An obvious application, for example, would be an exact relativistic particle pusher which involves many more flops than the standard, approximate Boris algorithm [38]. The complex system of collisions between particles and fluid in a collisional-radiative kinetics model should also greatly benefit from GPU technology. These will be investigated in the near future.

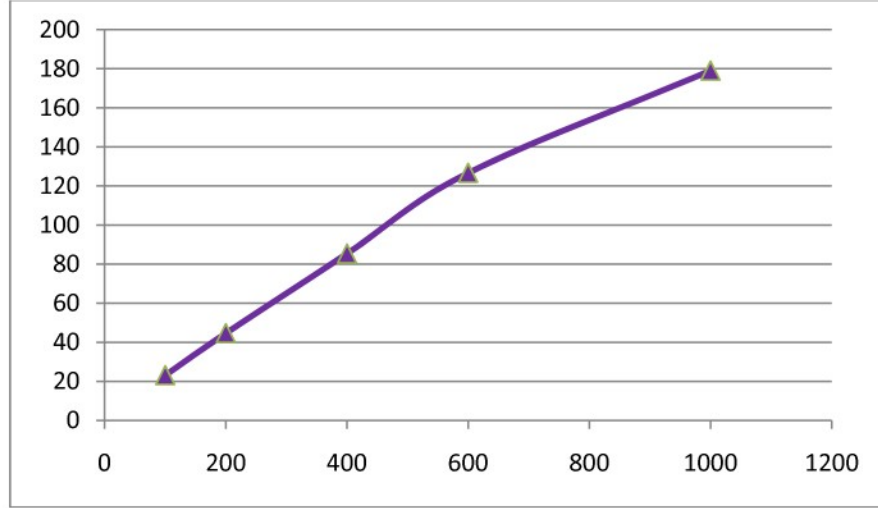


Figure 11: Speed-up factor versus number of cosine operations for each particle/thread

For fluid modeling, we investigated what seemed to be the easiest parallelization task with the greatest benefits, i.e. implementation of the chemical kinetics on the GPU. Since most of the cost is found in the solution of a linear algebra problem for the point-implicit kinetics, the focus was on developing an efficient version of a Gaussian elimination/back-substitution algorithm on the GPU. The problem is divided into 2 scales: the number of “species”  $N_s$  at each cell, and the number of cells  $N_c$ . The linear algebra problem consists of solving  $A \cdot \underline{x} = \underline{b}$  for  $\underline{x}$ , a vector of length  $N_s$ . The number of operations scales as  $N_s^3$ , so one can easily obtain a large workload for each cell/thread. However, a naïve implementation of the algorithm led to poor performance (speed-up  $< 1$ ). It turns out that a critical factor here is the size of the problem. At each cell, the matrix  $A$  of size  $N_s \times N_s$  is too large for the small cache memory of the GPU, and data must constantly be transferred between the ALU and the global memory (RAM) on the GPU; this can create bottlenecks and increase the operation count very easily. We were able to obtain a speed-up of about 8 (for  $N_s = 128$ ) by careful choice of memory stride. Later, the speed-up was increased to about 11 by using the limited shared memory available on the GPU device. This is still a significant acceleration, but less than we originally expected. There are several approaches to further improving this situation, such as using iterative solvers, or multi-scale schemes which would reduce the problem size and complete unrolling of the algorithm. Furthermore, the computation of the source terms (reaction rates) and jacobian matrix  $A$  is also intensive and when ported to the GPU can lead to significant speed-up. All of these approaches are currently being investigated.

## 6. Computational Fluid Dynamics

### 6.1. Formulation

The simplest models for the convection of the plasma fluid variables are finite-volume based; in this approach, the fluxes are evaluated at the cell interfaces and Gauss law is used to compute the changes in the cell-averaged variables. This so-called conservative form can be written as:

$$\frac{\partial \mathbf{Q}}{\partial t} + \vec{\nabla} \cdot \vec{\mathbf{F}} = \dot{\mathbf{Q}} \quad (2)$$

with  $\mathbf{Q}$  the array of conserved variables,  $\mathbf{F}$  the array of convective fluxes and  $\dot{\mathbf{Q}}$  the array of local source and exchange terms. For convection processes only (i.e. the Euler equations) and ignoring the source terms due to collisional exchanges of mass (chemistry) and energy (relaxation), we have:

$$\mathbf{Q} = \begin{bmatrix} \rho_s \\ \rho u^\alpha \\ \vdots \\ E \\ \tilde{E}_e \end{bmatrix} \quad \mathbf{F}^\beta = \begin{bmatrix} \rho_s u^\alpha \\ \bar{P}_{\alpha\beta} \\ \vdots \\ u^\beta (E+P) \\ u^\beta \tilde{E}_e \end{bmatrix} \quad \dot{\mathbf{Q}} = \begin{bmatrix} 0 \\ 0 \\ \vdots \\ 0 \\ -P_e \vec{\nabla} \cdot \vec{u} \end{bmatrix} \quad (3)$$

The total energy  $E$  of the plasma includes a purely thermal component  $\tilde{E}$  and the kinetic energy.  $E = \tilde{E} + 1/2 \rho \vec{u}^2$ . The pressure tensor can be defined as the sum of two contributions:

$$\bar{P}_{\alpha\beta} = P \delta_{\alpha\beta} + \rho u_\alpha u_\beta \quad (4)$$

For a two-temperature plasma [5], there are two contributions to the pressure and to the plasma internal energy, i.e.  $P = P_h + P_e$ , with  $(\gamma_e \equiv 5/3)$ :  $P_h = (\gamma_h - 1) \tilde{E}_h$ ;  $P_e = (\gamma_e - 1) \tilde{E}_e$ . This implies that a jump in pressure across a cell interface can be expressed by:

$$\Delta P = (\gamma_h - 1)(\Delta E - \Delta E_K - \Delta \tilde{E}_e) + (\gamma_e - 1) \Delta \tilde{E}_e, \quad (5)$$

where:

$$\Delta E_K = \vec{u} \cdot \Delta(\rho \vec{u}) - \frac{\vec{u}^2}{2} \Delta \rho = \rho \vec{u} \cdot \Delta \vec{u} + \frac{\vec{u}^2}{2} \Delta \rho. \quad (6)$$

The linearization  $\Delta F = A \circ \Delta Q$  forms the basis of numerical schemes based on approximate Riemann solvers [39] (Godunov schemes [40]). Note that equation (2) contains a source term on the Right Hand Side (RHS) for the electron energy equation – a consequence of the one-fluid approximation – that is responsible for the adiabaticity of the electron gas component. Notably, since the electron gas is always subsonic, there is no shock heating of the electrons across a viscous shock, where there can be a considerable jump in ion temperature [41]. The complete equation for the electron energy, combined with the conservation of mass for the electrons, leads to:  $T_e^{-1} (D_t T_e) = (2/3) n_e^{-1} (D_t n_e)$ , with  $D_t \equiv \partial_t + \vec{u} \cdot \vec{\nabla}$  the covariant derivative. Therefore the electron heating (cooling) obtained as a result of compression (expansion) is *always adiabatic*:  $\log(T_e) = (\gamma_e - 1) \log(n_e)$ . A modified formulation using an entropy-like variable [42] leads to a simpler and more accurate treatment. We define<sup>†</sup>:

$$S_e = \frac{P_e}{\rho^{\gamma_e - 1}} \quad ; \quad \hat{s}_e = \frac{P_e}{\rho^{\gamma_e}} \quad (7)$$

The convection of this quantity yields:

$$\partial_t \left[ \rho \frac{P_e}{\rho^{\gamma_e}} \right] + \vec{\nabla} \cdot \left[ \rho \vec{u} \frac{P_e}{\rho^{\gamma_e}} \right] = (\gamma_e - 1) \rho^{1-\gamma_e} \left[ \partial_t \tilde{E}_e + \vec{\nabla} \cdot (\vec{u} \tilde{E}_e) \right] + (1 - \gamma_e) \frac{P_e}{\rho^{\gamma_e}} \left[ -\rho \vec{\nabla} \cdot \vec{u} \right] \quad (8)$$

Using the equation for the electron thermal energy  $\partial_t \tilde{E}_e + \vec{\nabla} \cdot (\vec{u} \tilde{E}_e) = -p_e (\vec{\nabla} \cdot \vec{u})$ , we can easily verify that the modified electron entropy satisfies a simple conservation equation, i.e.:

$$\partial_t S_e + \vec{\nabla} \cdot (\vec{u} S_e) = 0 \quad (9)$$

The use of the entropy variable may be convenient for the convective processes, but not for electron heat conduction and inelastic energy exchanges. The latter make it more appropriate to

<sup>†</sup>  $\rho_e$  was used in the original formulation [42], in which case  $\hat{s}_e$  was the true electron entropy, but the advantage here is that the variables in (6-5) remain finite when the ionization fraction goes to zero ( $\rho_e \rightarrow 0$ ).

retain the electron thermal energy as the conserved variable. However, the operator-splitting approach allows us to compute the convective processes differently. Thus, the change in the modified entropy variable can be written as:

$$S_e^{(n+1)} = S_e^{(n)} + \delta S_e = S_e^{(n)} - \frac{\Delta t}{\Delta V} \left[ \sum_{surfaces} F \right]_{TVD} \quad (10)$$

Where the term in brackets is the change due to convection (using for example a TVD scheme [43]). A corresponding change in electron thermal energy due to convection can be computed:

$$\delta \tilde{E}_e = \left[ \rho^{(n)} + \delta \rho \right]^{\gamma_e - 1} \frac{S_e^{(n)} + \delta S_e}{\gamma_e - 1} - \left[ \rho^{(n)} \right]^{\gamma_e - 1} \frac{S_e^{(n)}}{\gamma_e - 1} \quad (11)$$

where  $\delta \rho, \delta S_e$  are the results of *convection only*. This overall approach is quite accurate; the relative errors for the same cases of shock and rarefaction waves are of the order of  $10^{-3}$  for a shock and  $3 \times 10^{-5}$  across a rarefaction.

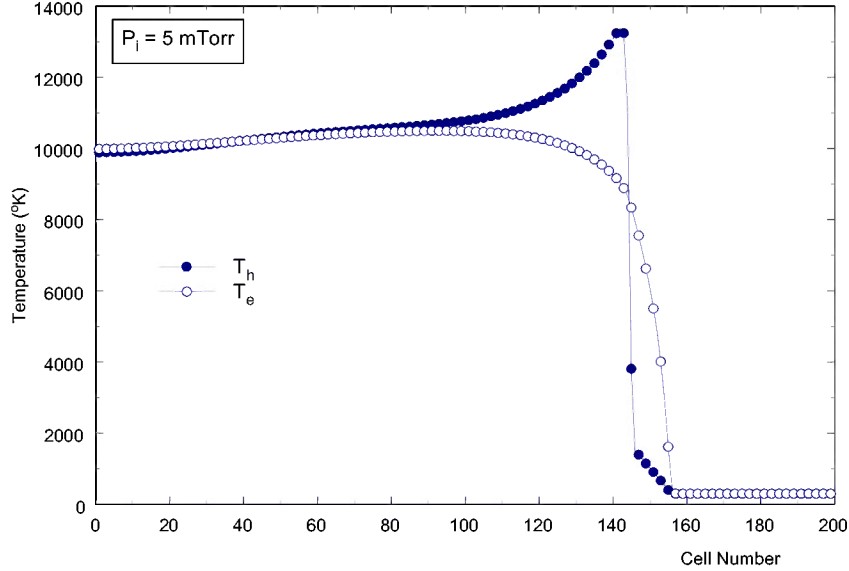


**Figure 12: Temperature profiles behind strong shock with relaxation and electron heat conduction**

The other approach consists of using  $S_e$  as the fundamental conserved variable and expressing all other terms (fluxes, jacobian, EOS) as function of this variable. This is the approach taken in the course of this lab-task, and described in detail in Appendix E (thesis). Figure 12 shows an example of a test of the multi-temperature model, including relaxation effects and precursor heat conduction, which have also been implemented.

The 2T formulation described above has been extended to the ideal MHD equations; since the magnetic field can perform rotations of the plasma velocity, it is always necessary in the MHD system to consider the 3 components of the velocity, as well as 3 components of the magnetic field, even if the simulations are performed on 1D or 2D grids. The main difficulties with the MHD system are related to the divergence-free property of the magnetic field, i.e.  $\vec{\nabla} \cdot \vec{B} = 0$ , one of Maxwell equations. This reduces the number of independent variables in the system (and the number of eigenvalues), making the system non-homogeneous. Various numerical approaches have been used to guarantee the divergence-free property in ideal MHD simulations, e.g. a

corrective step [44], adding an equation for the divergence itself (Powell's method [45]), or constraining the fluxes to guarantee this property (the constrained transport approach [46]).

The fluid component can have various levels of non-equilibrium, depending on the relaxation time-scales. A hierarchy of descriptions ensues, for example: single-temperature (1T), two-temperature ( $T_h - T_e$ ), three-temperature ( $T_h - T_e - T_x$ ), and Collisional-Radiative (CR) models. We have previously developed these versions, and the current focus is on a more detailed CR model. We have also experimented with code design to allow a seamless transition between these various levels of description. This would allow us to adjust the complexity of the code according to local conditions, e.g. starting from a 1T model in a very dense (equilibrium) region, to multi-T then to a CR model as the density is lowered. The chosen procedure was to devise methods for *contraction* (from higher- to lower level) and *expansion* of thermodynamic information at the boundary between domains. An example of the former would be the grouping of all excited levels from a C-R model into a Boltzmann distribution and the forcing of equilibrium with the free electrons (from C-R to 2-T model); an example of the latter would be the generation of an additional variable for the electron energy from the single fluid equations (from 1-T to 2-T). Preliminary tests of these procedures have been performed successfully, but have not yet been implemented on a final version of the code.

## 6.2. Numerical Scheme

We have implemented and tested a variety of Godunov schemes for the Euler equations, with variable order of accuracy, starting from a 2<sup>nd</sup>-order TVD method [43], to 5<sup>th</sup>-order WENO schemes [47]. Various limiters have also been investigated, and these variations have been compared on well-known, published test cases. When used in conjunction with the HLLC Godunov-type flux as the building block, the WENO scheme has proven to be very robust for numerous conditions. The WENO schemes require Runge-Kutta time discretization for time-accurate solutions, which has led to the implementation of second- and third-order versions in temporal accuracy. The 2<sup>nd</sup>-order time discretization requires two-thirds as many computations without significantly reducing the stability limits. After all tests were performed, the selection was made to use a 3<sup>rd</sup>-order variant of the MP scheme of Huynh [55], which showed the best combination of accuracy and stability, and an Adams-Bashford time-stepping algorithm, which provided some memory savings compared to a Runge-Kutta approach.

A first example of such a numerical test is shown in Figure 13 (the Emery wind tunnel problem [48], consisting of a Mach 3 flow and a step); by comparison, the results of another state of the art numerical scheme are shown in Figure 14. Interestingly, the current results are more accurate (for same grid resolution) than the AMROC code [49], and more accurate than the PPM scheme used in the FLASH code [50] from the University of Chicago (not shown), used in astrophysics calculations.

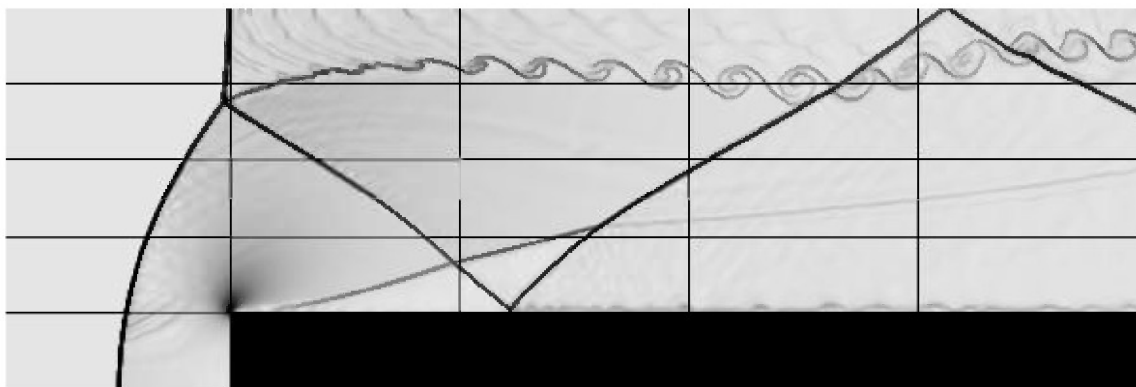


Figure 13: Results of Euler calculations on standard test case (forward step); multi-block, parallel computation (thin horizontal and vertical lines are block boundaries)

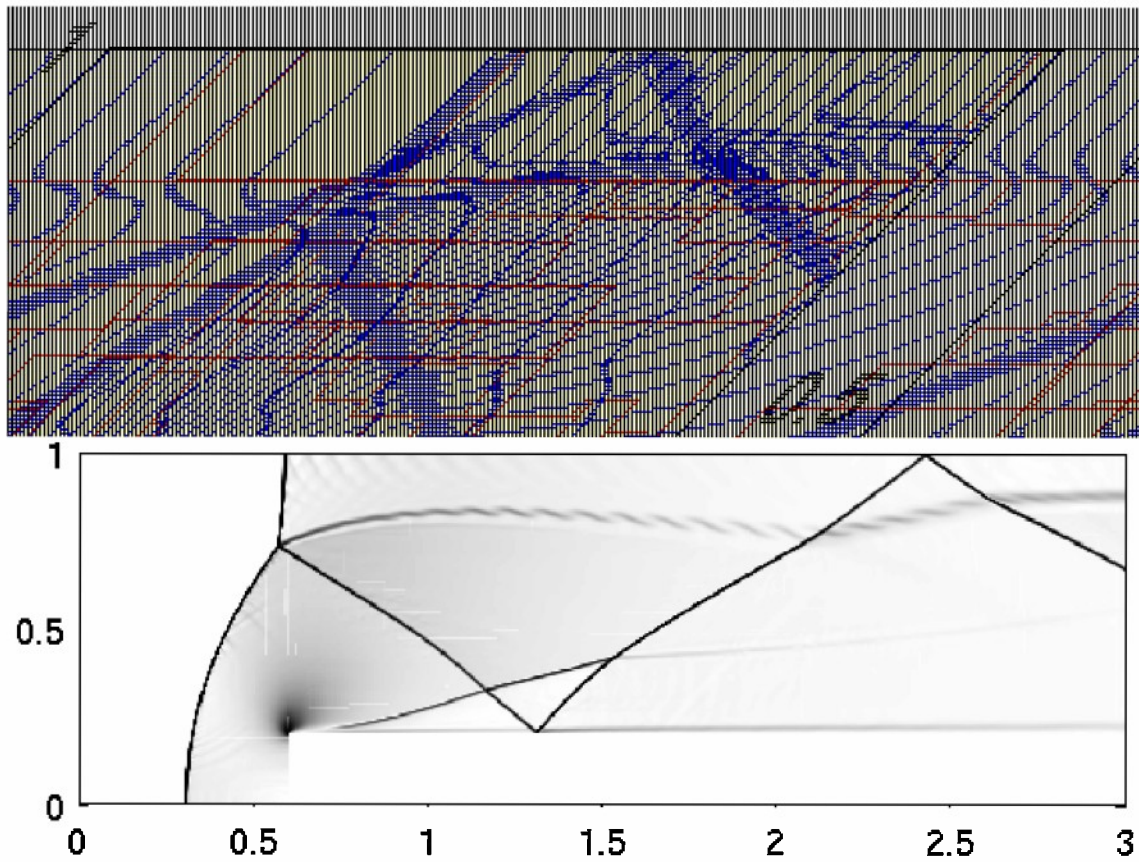


Figure 14: Results of AMROC code, using grid adaptation; finest resolution is equivalent to 3 times the resolution of current results shown in Figure 13, yet the KH instability is less resolved.

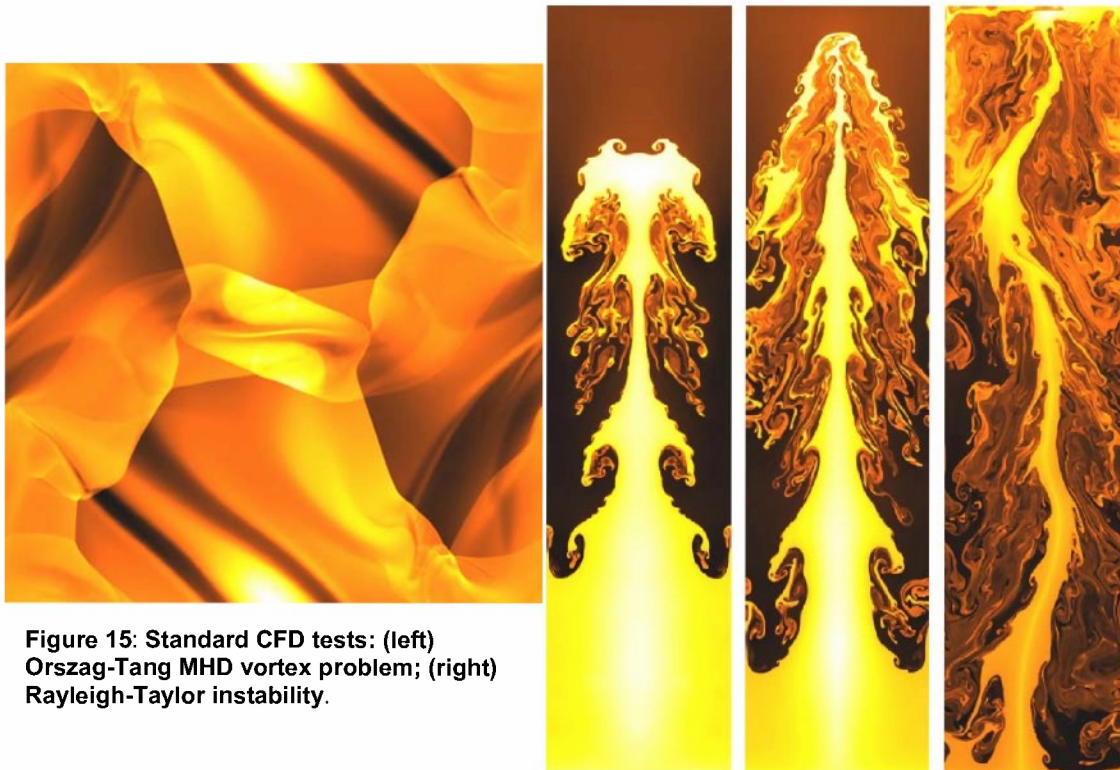
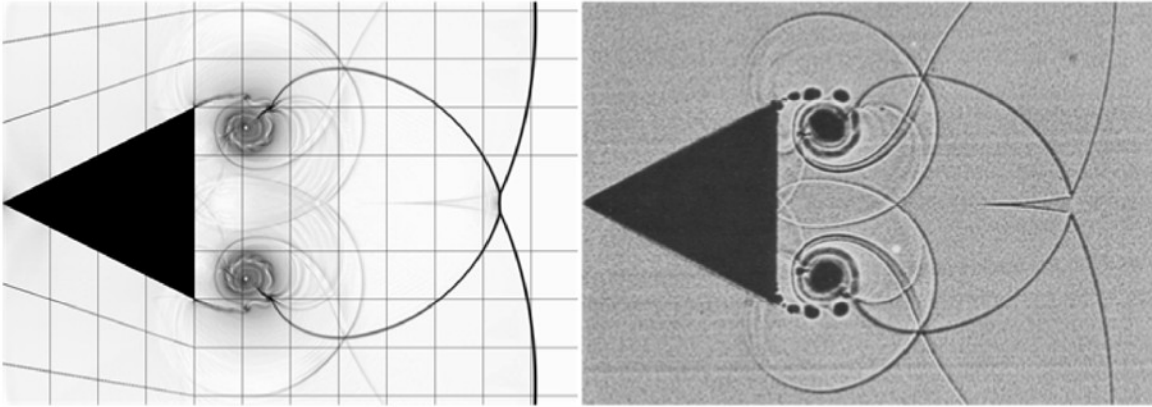


Figure 15: Standard CFD tests: (left) Orszag-Tang MHD vortex problem; (right) Rayleigh-Taylor instability.



The MHD version of the code was also tested against the Brio and Wu problem [51] and the Orszag-Tang MHD vortex [52], both of which are standard benchmarks in the MHD fluid community; the latter is shown in Figure 15-left. On the right of the same figure is a standard Rayleigh-Taylor instability test computed on a 400x1600 grid; the resolution of the contact surface is maintained very well throughout the simulation. In Figure 16 we show a comparison of the computational – left side – and experimental – right side – results of a shock diffraction around a wedge, the so-called Schardin’s problem [53]. The grid-like structure on the left indicates the boundaries of computational domains.



**Figure 16: Shock diffraction around a wedge: left-simulated Schlieren, right-experiment**

Finally, we show in Figure 17 a similar comparison for a problem of shock diffraction down a step. Other standard test cases included the Shu-Osher shock-entropy wave interaction problem [54] and the Woodward-Colella blast wave problem [48]; these can be found in the PhD thesis of Dr. M. Kapper, provided in Appendix E. Clearly the basic method is capable of very good accuracy, and we found the 3<sup>rd</sup>-order MP method (MP3) arguably superior to even higher-order schemes like the popular 5<sup>th</sup>-order WENO. While further refinements of the basic method could be obtained with further research, there is a point of diminishing return on the investment in time and effort, i.e. higher-order accuracy and improved stability can always be implemented at a later stage. The present scheme is considered sufficiently accurate and fast for the present purposes. Thus, the next steps consist of implementing the physical models for non-equilibrium dynamics, i.e. a Collisional-Radiative model. Note however that this basic scheme provides a single-fluid solution, with or without plasma effects. The next section discusses an early investigation whereby the description is being extended to multiple fluids.

### 6.3. Multi-Fluid

As an alternative to a PIC model for the energetic electrons, one can envision separating the electrons from the rest of the plasma while keeping a continuum model. This is the basis of the multi-fluid model; it assumes that the electrons are sufficiently collisional within themselves to maintain a distribution function that is close to a Maxwellian, drifting at a mean velocity governed by both inertial and electrostatic effects. The main advantage is that computations can be much faster than with a PIC model, while still being able to account for space-charge effects. The disadvantage is that the time scale is governed by a combination of the mean electron velocity and the speed of sound in the electron gas. Therefore, for this approach to be useful, an implicit fluid solver must be devised for the electrons, coupled to the electric field. A first attempt at devising such a scheme was made. Two versions of the scheme have been designed; one which entails the inversion of 7x7 matrices, and is linear-order in the time step  $\delta t$ ; a second version that uses 4x4 matrices, but is a second-order expansion, i.e. includes terms proportional to  $(\delta t)^2$ . Both algorithms were implemented and tested, and are described in more detail in Appendix A.

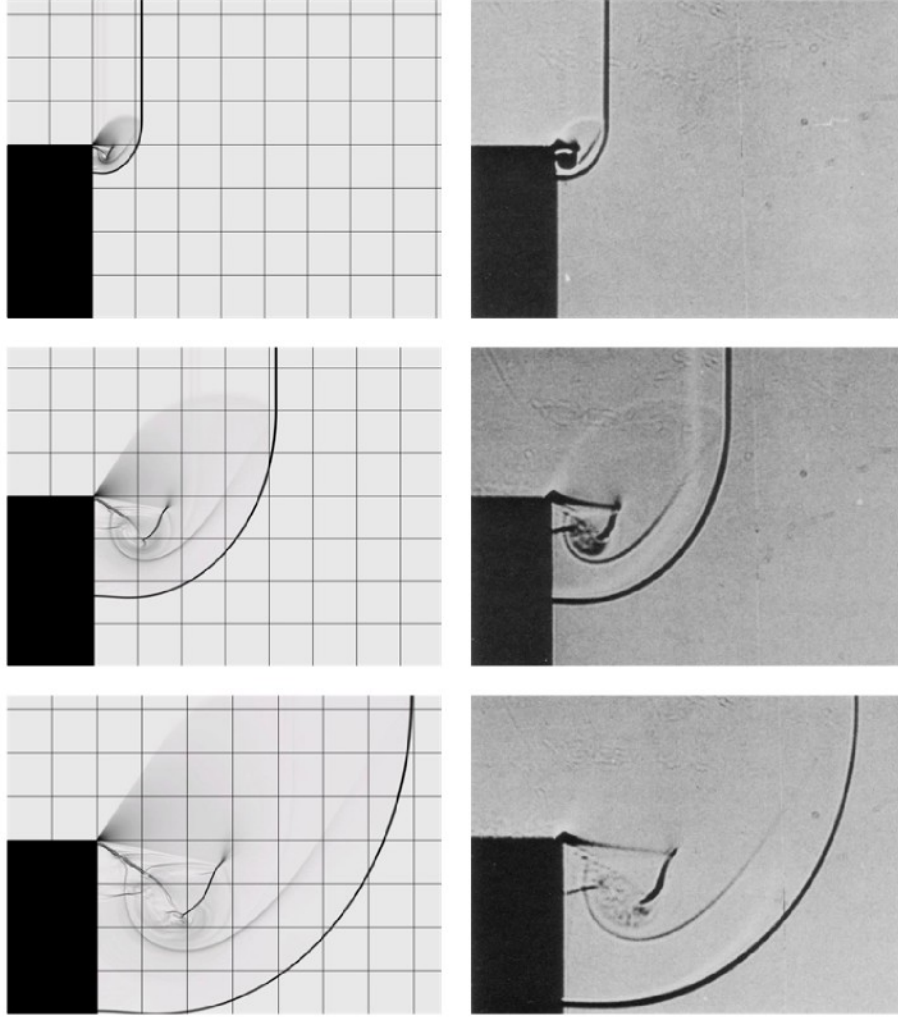


**Figure 17: Shock diffraction down a step: left – simulated Schlieren, right – experiment**

To verify the algorithm, we used a simple test case consisting of a one-dimensional plasma with reflecting boundaries (“plasma in a box”); the initial state was a fully ionized, non-reacting plasma with all the electrons moved to the left half of the box. This generated a large internal electric field which accelerated the electrons towards the right side. Without dissipation, the electron motion leads to an oscillatory behavior, as the electrons accumulate on the right side, create a restoring field that accelerates back the other way, and so on. This test case is similar to the one studied in [76] but with a much more severe initial condition, since in [76] there is only a *slight* perturbation of the space charge. The plasma oscillations in our case have much larger amplitudes, and non-linear effects (steepening of the profiles) can be detected; nevertheless, Figure 18 shows an excellent agreement with theory, and negligible dispersive errors. The stability of the algorithms is also severely tested. Indeed, it was found that the 7x7 algorithm would occasionally fail when the time step was too large compared to the plasma frequency or the Courant condition  $(|u| + c)\delta t < \Delta x$ . The second-order expansion scheme provided greater stability, and strongly damped the oscillations when the time step was such that  $(|u| + c)\delta t > \Delta x$  and  $\omega_{pe}\delta t \gg 1$ . However, there is some residual damping for time steps just below the Courant condition, which is not yet understood. Development of this scheme is continuing, and will also include effects of a magnetic field.

$$\omega_{pe}^{-1} = 226.4 \pm 0.5 \text{ ps} \quad (\text{theor.} = 226.7 \text{ ps})$$

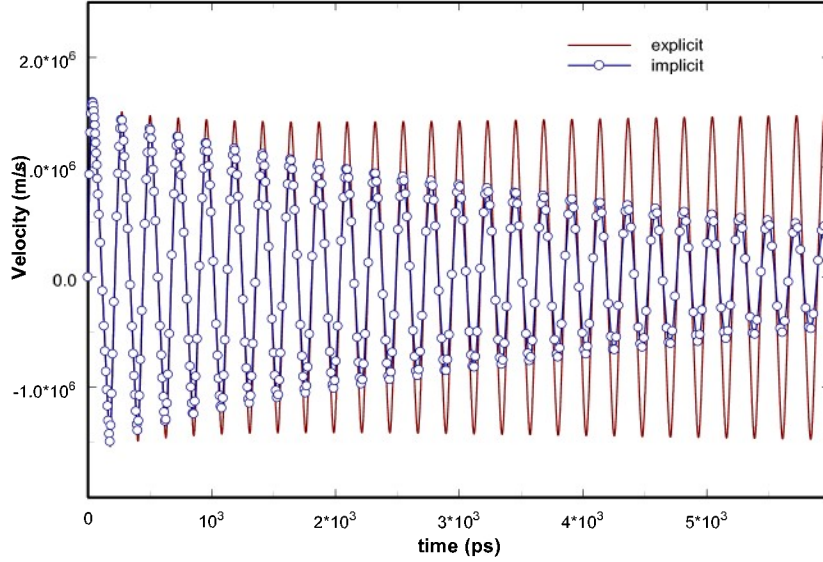


**Figure 18: Plasma oscillations (electron velocity at center of 1D box) for both explicit and implicit schemes**

A multi-fluid model also involves the presence of coupling terms on the right-hand-side. The scheme described in Appendix A is actually a reduced version of the complete set; it involves the strong coupling between electron fluid motion and electrostatic field from charge separation. This fast scale motion involves two equations for the electron density and velocity; the energy (temperature) is constant.

The use of a multi-fluid model involves collisional interactions between the fluids; averaging over the Boltzmann equations, we can write for each fluid component  $\alpha$  a set of Euler equations:

$$\frac{\partial}{\partial t} n_\alpha + \vec{\nabla} \cdot (n_\alpha \vec{u}_\alpha) = 0 \quad (12a)$$

$$\frac{\partial}{\partial t} (m_\alpha n_\alpha u_\alpha^i) + \nabla^j (\bar{P}_\alpha^{ij} + m_\alpha n_\alpha u_\alpha^i u_\alpha^j) = Z_\alpha e n_\alpha (E + u \times B)^i + \sum_\beta R_{\alpha\beta}^i \quad (12b)$$

$$\frac{\partial}{\partial t} E_\alpha + \nabla^j \{ (E_\alpha \delta^{ij} + \bar{P}_\alpha^{ij}) u_\alpha^j + q_\alpha^j \} = Z_\alpha e n_\alpha u_\alpha^j E_\alpha^j + \sum_\beta (Q_{\alpha\beta} + u_\alpha^j R_{\alpha\beta}^j) \quad (12c)$$

Where summation over repeated indices is implied (Einstein notation), and  $i, j$  are geometrical indices;  $E_\alpha = \frac{3}{2} n_\alpha T_\alpha + \frac{1}{2} m_\alpha n_\alpha u_\alpha^2$  is the total energy of the plasma component. These equations are the conservative form<sup>†</sup> of the well-known Braginskii equations [56]. The  $\vec{R}_{\alpha\beta}$  is the resistance force and  $Q_{\alpha\beta}$  is the energy exchange term, for both of which Braginskii provides approximate forms. Ignoring the thermal resistance effect [56], the friction force between two components  $\alpha, \beta$  is:

$$\vec{R}_{\alpha\beta} = m_\alpha n_\alpha \nu_{\alpha\beta} (\vec{u}_\beta - \vec{u}_\alpha) \quad (13)$$

while the energy exchange term:

$$Q_{\alpha\beta} = \frac{m_\beta}{m_\alpha + m_\beta} (\vec{u}_\beta - \vec{u}_\alpha) \cdot \vec{R}_{\alpha\beta} + \frac{3}{2} n_\alpha \nu_{\alpha\beta}^E (T_\beta - T_\alpha) \quad (14)$$

Here,  $\nu_{\alpha\beta}$  and  $\nu_{\alpha\beta}^E$  are the collision frequencies for momentum exchange and energy exchange respectively, which obey the symmetry properties:

<sup>†</sup> Here we use the notation of Decoster [57], where  $Q_{\alpha\beta}$  is the  $Q_\Delta$  of Braginskii.



$$m_\alpha n_\alpha v_{\alpha\beta} = m_\beta n_\beta v_{\beta\alpha} \quad (15)$$

and

$$n_\alpha v_{\alpha\beta}^E = n_\beta v_{\beta\alpha}^E \quad (16)$$

For energy exchange and small velocity differences:

$$v_{\alpha\beta}^E = \frac{2m_\alpha}{m_\alpha + m_\beta} v_{\alpha\beta} \quad (17)$$

Note that  $v_{\alpha\beta}$  is not a symmetric quantity.

It must be emphasized here that these formulations are obtained strictly for elastic collisions; this is clearly seen in equation (6-10a) which does not involve any exchange of mass between the components (ionization/recombination). To go beyond fully-ionized plasma conditions (commonly found in fusion or astrophysical applications, for which the multi-fluid equations have been developed) we must also include the inelastic collision terms, which generate additional source terms in the fluid equations, for all three quantities: mass, momentum and energy. Consider for example ionization by electron impact. There is a corresponding source term for the number density  $\Gamma_e$ , and there is obviously an energy loss; since the conservation equation of the electron fluid applies to the total energy, i.e. kinetic and thermal, the energy loss rate is:  $\Gamma_e \epsilon^*$ , where  $\epsilon^*$  is the ionization threshold. However, this does not provide sufficient information to distinguish between the loss of mean kinetic energy and thermal energy. If we write again the momentum exchange rate due to inelastic collisions as a frictional force, i.e.  $\zeta \Gamma_e (\vec{u}_n - \vec{u}_e)$  where  $\vec{u}_n, \vec{u}_e$  are the neutral and electron fluid velocities and  $\zeta$  is a constant. Therefore, we have:

$$\frac{dn_e}{dt} = \Gamma_e \quad (18a)$$

$$\frac{d}{dt}(n_e \vec{u}_e) = -\zeta \Gamma_e \vec{u}_e \quad (18b)$$

$$\frac{d}{dt}\left(\frac{3}{2}n_e kT_e + \frac{1}{2}m_e n_e \vec{u}_e^2\right) = -\Gamma_e \epsilon^* \quad (18c)$$

where we have neglected  $\vec{u}_n$  to simplify the notation. The system (18) yields two different solutions for the rate of loss of kinetic energy in the limit  $kT_e \ll m_e \vec{u}_e^2/2$ :

$$n_e \frac{d}{dt}\left(\frac{u_e^2}{2}\right) = -(1 + \zeta) u_e^2 \frac{dn_e}{dt} \quad (19a)$$

$$n_e \frac{d}{dt}\left(\frac{u_e^2}{2}\right) = -(\epsilon^* + u_e^2/2) \frac{dn_e}{dt} \quad (19b)$$

Obviously, these cannot be both satisfied for any value of kinetic energy. Thus, the source terms of (6-16) are inconsistent. This is not all too surprising, since the microscopic collision process between two particles can yield complex dependences when the two particles in question belong to different statistical distributions which are not in equilibrium. To obtain a self-consistent model of the coupling terms in a multi-fluid description due to inelastic collisions, it is necessary to evaluate these terms from first principles, i.e. starting from the microscopic level and averaging over the respective distribution functions of each component. We can start from a detailed model of the inelastic collisions, using multiply-differentiated cross-sections, and integrate over a known distribution (here Maxwellian) to obtain the rates (see Figure 19). Figure 20 shows the same results for a drifting Maxwellian, in which case both relative mean velocity (kinetic energy – KE) and thermal velocity (temperature) can contribute. This is especially important for multi-fluid models, for which the relative velocity can be large. From the detailed cross-section information, one can also compute additional moments of the collision operator, such as momentum and energy transferred, to derive effective friction and energy exchange terms, i.e. the equivalent to the terms of the Bragiński equations for inelastic collisions and unrestricted velocity differences. A description of the approach developed so far is given in Appendix C. We have developed and tested the procedure for the forward rates and need to do the same for the reverse reactions. This work is currently on-going and we expect it to be completed by end of CY 2010.

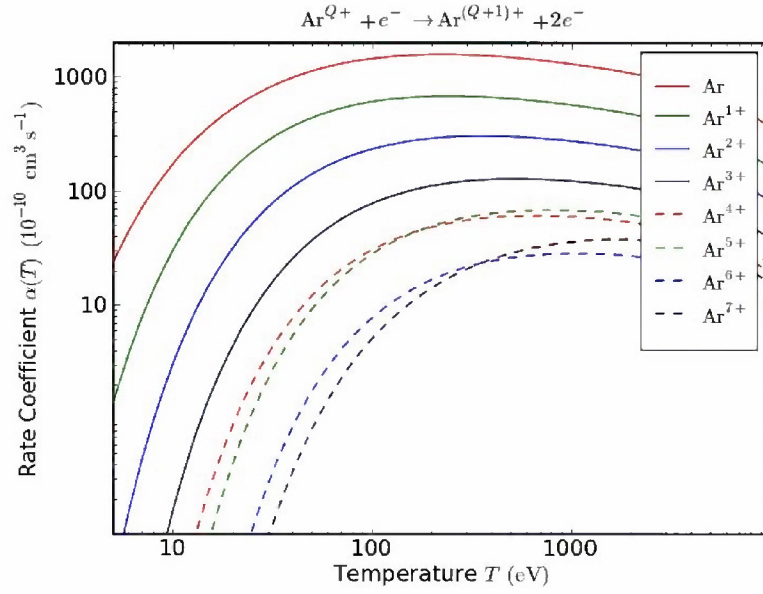


Figure 19: Compiled multi-stage ionization rates for assumed Maxwellian distribution

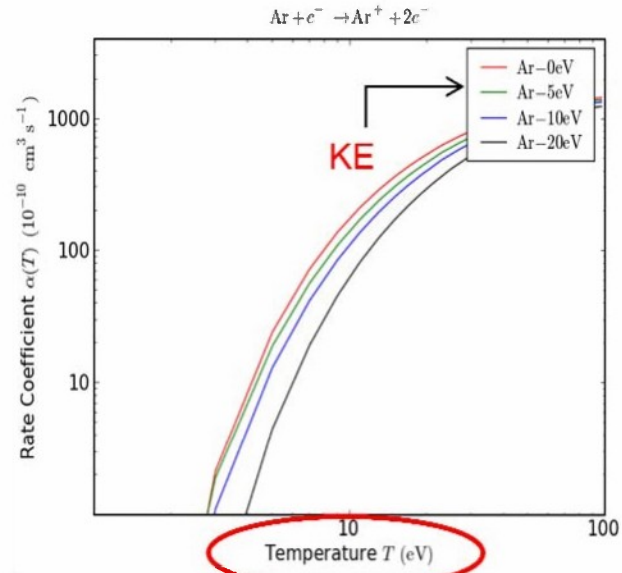


Figure 20: Compiled ionization rates for assumed drifting Maxwellian distribution

## 7. Collisional-Radiative Modeling

Starting from the multi-species 2T and MHD equations (see Section 6.1), it is straightforward to consider species as individual electronic states. For a molecular plasma, this requires that we modify the EOS and thermodynamic database to have a separate specific heat and internal energy for each of these electronic states (the internal energy being a combination of vibrational and rotational states). We currently restrict ourselves to atomic plasma only, in which case the EOS becomes very simple (the adiabatic index is a constant,  $\gamma \equiv 5/3$ ). The main difficulties in the CR fluid model are in generating the database of state properties and reaction rates (or cross-sections), and the management of the complexity of the internal states. Theoretically, there is an infinite number of bound electronic states and obviously one must limit that number to a practical value. The truncation of the series is currently done on a fixed basis, which is the common practice in CR models; in other words, we consider a fixed number of states starting from the ground level. The argument is that the upper states lying very close to the ionization limit are very thinly populated or eliminated altogether, due to the effective lowering of the ionization potential by the ambient micro-field and non-ideal effects (highly excited states, or Rydberg states, have a radius that becomes comparable to the average inter-atomic spacing). There is more work that could be done to treat this truncation issue more accurately, including dynamic truncation, i.e. depending on the actual plasma conditions; this is an issue that may be investigated at a later stage. The second way to resolve the problem of the very large number of states is “grouping”, i.e. to combined individual states into a new one with average properties (energy, decay rate); this is implicitly done anyway, since the levels obtained from a typical database are degenerate levels with respect to spin and orbital quantum numbers; this degeneracy is lifted, for example, when strong fields are applied (Stark and Zeeman effects. Grouping levels at a coarser levels makes sense for levels close together in energy and with similar radiative decay rates. The optimal way to perform this grouping remains an issue that deserves more attention, along with a more complete and practical database for species and physical conditions of interest.

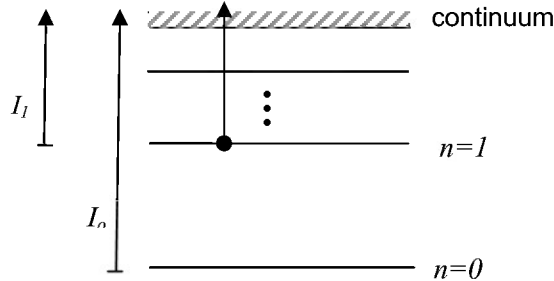


Figure 21: Schematic of atomic levels

Consider then a simplified set of atomic levels; the populations (normalized number densities) of all states form a discrete phase space, the Atomic State Distribution Function (ASDF). The evolution of this ASDF is obtained by summation of all collisional and radiative transitions, yielding an ODE of the form:

$$\begin{aligned} \frac{dn_k}{dt} = & \sum_{j < k} \{ C_{kj}^{ex} n_e n_j - C_{jk}^{ed} n_e n_k - R_{jk} \} + \sum_h \sum_{j > k} \{ C_{kj}^{ed} n_e n_j - C_{jk}^{ex} n_e n_k + R_{kj} \} \\ & \sum_{j < k} \{ C_{kj}^{hx} n_h n_j - C_{jk}^{hd} n_h n_k \} + \sum_h \sum_{j > k} \{ C_{kj}^{hd} n_h n_j - C_{jk}^{hx} n_h n_k \} \\ & - C_k^{ei} n_e n_k + C_k^{er} n_e^2 n_i - \sum_h C_k^{hi} n_h n_k + \sum_h C_k^{hr} n_e n_h n_i + R_k n_e n_i \end{aligned} \quad (20)$$

The collisional rates in (20) are indicated as  $C_{jk}^{\alpha T}$ , where  $\alpha = e, h$  is the collisional partner responsible for the transition (electron-impact or heavy particle impact) and  $T = x, d, i, r$  indicates

the type of event, respectively excitation, deexcitation, ionization and recombination. There can be several types of heavy particles present, so the index  $h$  must be summed (including neutral atoms and ions). The radiative rates are present for line emission and radiative capture; there are no rates of photo-ionization or line absorption, which would depend on the radiation energy density, and would include some model of radiation transport. Instead, we use an effective rate for the line emission, corrected by an escape probability factor  $\Lambda$ , i.e.:

$$R_{jk} = (1 - \Lambda_{jk})A_{jk} \quad (21)$$

Where  $A_{jk}$  is the average Einstein coefficient of spontaneous emission. Complex models can be used to evaluate the escape probability, but we use here a simplified model, i.e.  $\Lambda_{jk} = 0,1$ ; in the former case the plasma is transparent, in the latter case the radiation is completely self-absorbed. In the validation case studied (ionizing shock wave in Argon), the density gradients are not sufficiently large that a complex model [58,59] must be used, or that the radiation transport (RT) equation must be solved; instead, we find from calculation of the radiation mean-free paths that the transitions to the ground state are self-absorbed, while the plasma is completely transparent to transitions to any other state.

We focused the development of the CR model on the case of an Argon plasma; the reasons were two-fold: (a) the Argon system is well-known, yet complex enough to provide a good benchmark of a CR model; (b) there are multiple experiments in Argon with spectroscopic data which can be used for validation. We chose a set of experimental tests of ionizing shock waves in Argon to validate the model. This was also the objective of a prior study [7], limited to 1D simulations; with the advances in computational power, we demonstrated that this type of problem can now be simulated in 2D with modest computational power (32 node Linux cluster), indicating that even 3D problems could be handled by the current large-scale resources.

**Table 1: List of atomic levels (energy, degeneracy, and quantum numbers) for Argon**

$i$	$\varepsilon(i)$ [eV]	$g_i$	$j_c$	$n\ell[K]_J$	$i$	$\varepsilon(i)$ [eV]	$g_i$	$j_c$	$n\ell[K]_J$
1	0	1	1.5	[Mg]3p <sup>6</sup>	18	13.903	5	1.5	3d[3/2] <sub>2</sub>
2	11.548	5	1.5	4s[3/2] <sub>2</sub>	19	13.979	9	1.5	3d[7/2] <sub>4</sub>
3	11.624	3	1.5	4s[3/2] <sub>1</sub>	20	14.013	7	1.5	3d[7/2] <sub>3</sub>
4	11.723	1	0.5	4s'[1/2] <sub>0</sub>	21	14.063	5	1.5	3d[5/2] <sub>2</sub>
5	11.828	3	0.5	4s'[1/2] <sub>1</sub>	22	14.068	5	1.5	3d[3/2] <sub>1</sub>
6	12.907	3	1.5	4p[1/2] <sub>1</sub>	23	14.090	3	1.5	5s[3/2] <sub>2</sub>
7	13.076	7	1.5	4p[5/2] <sub>3</sub>	24	14.099	7	1.5	5s[5/2] <sub>3</sub>
8	13.095	5	1.5	4p[5/2] <sub>2</sub>	25	14.153	3	1.5	3d[3/2] <sub>1</sub>
9	13.153	3	1.5	4p[3/2] <sub>1</sub>	26	14.214	5	0.5	5s'[1/2] <sub>0</sub>
10	13.172	5	1.5	4p[3/2] <sub>2</sub>	27	14.234	5	0.5	3d'[5/2] <sub>2</sub>
11	13.273	1	1.5	4p[1/2] <sub>0</sub>	28	14.236	7	0.5	5s'[1/2] <sub>1</sub>
12	13.283	3	0.5	4p'[3/2] <sub>1</sub>	29	14.241	1	0.5	3d'[3/2] <sub>2</sub>
13	13.302	5	0.5	4p'[3/2] <sub>2</sub>	30	14.255	3	0.5	3d'[5/2] <sub>3</sub>
14	13.328	3	0.5	4p'[1/2] <sub>1</sub>	31	14.304	3	0.5	3d'[3/2] <sub>1</sub>
15	13.480	1	0.5	4p'[1/2] <sub>0</sub>	$\infty$	15.760	4	1.5	[Mg]3p <sup>5</sup>
16	13.845	1	1.5	3d[1/2] <sub>0</sub>	$\infty'$	15.937	2	0.5	[Mg]3p <sup>5</sup>
17	13.864	3	1.5	3d[1/2] <sub>1</sub>					

The basic numerical methods and formulation developed for the Argon test cases are equally valid for any other atomic plasma and once the database for say, Xenon, is compiled one can readily apply the model to that problem as well. In fact, there are similar experimental studies of ionizing shocks and MHD shocks in Xenon which could be investigated in the future. We chose a final set of 31 levels to describe the ASDF in Argon (see Table 1). Note that the levels are decomposed into 2 sub-sets according to the value of the total spin of the core:  $j_c = \{\frac{1}{2}, \frac{3}{2}\}$ . Although the energy levels of the respective sets can be very close, transitions between levels of different  $j_c$  are generally forbidden, and one must account for this restriction appropriately by

considering the two sub-groups. It also means that there are two ionization potentials, and equivalently, two ground-states for the ion  $Ar^+$ . Mode details of the CR model and its validation are given in the PhD thesis by M. Kapper, provided in Attachment A.

The system (20) is augmented by equations for the electron energy and heavy particle translational energy, to account for the energy exchanged during inelastic collisions; in the single-fluid model, these terms can be easily derived and no source term is required for momentum exchange, as opposed to the multi-fluid case. In addition to the inelastic collisions listed in (20), one can also include other reactions involving  $Ar_2^+$ , or dielectronic recombination (inverse Auger process); the former was added to the model and showed little influence in our test case, but may contribute in other plasma discharges. The latter may be relevant in low-density, high-temperature plasma. The most uncertain aspect of the CR model concerns the cross-sections for excitation and ionization; data is poor or non-existent for collisions involving excited states and one relies on simplified models of collision physics – such as the Binary Encounter/Bethe (BEB) and its variants [60-61] – or quantum (R-matrix) calculations when feasible. These can provide a good estimate of the cross-sections, but valid only for electron-impact. Atomic collisions such as  $Ar + Ar \rightarrow Ar^* + Ar$  can be important, yet the cross-sections are not well-known; standard models (see [62]) have been used in the community, yet more precise calculations would be very beneficial, especially for the type of weakly ionized plasma found in aerospace applications\*. We will see that in the chosen test case of ionizing shock, the heavy-particle impact is important immediately behind the shock, since the electron density is still very low; these rates are therefore mostly responsible for the shock structure, i.e. the “induction” zone separating the shock and a region where rapid ionization occurs (“avalanche”) and the electron-impact processes take-over. This type of experiment can be very useful in calibrating the heavy-particle impact inelastic cross-sections, through parametric studies.

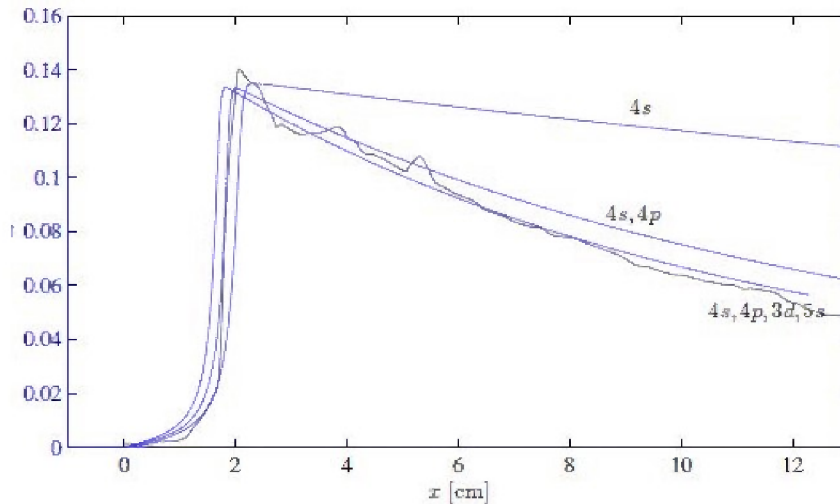


**Figure 22: Effect of upper levels on radiative cooling region; complete agreement with experimental data requires at least the 4s,4p,3d and 5s manifolds**

In addition to the cross-sections, one must also consider a minimum number of levels; this can be clearly seen in Figure 22 which shows different profiles of the ionization fraction in the relaxation region (“radiative cooling”), past the peak ionization. In that figure, the flow goes from left to right and the shock is at  $x=0$ . The profiles are computed with a steady-state, space-marching scheme in the rest frame of the shock. The fluctuating curve is the experimental data, while the smooth profiles are the computed solutions, for several cases of sets of atomic levels. Thus, if only the 4s states are considered, the solution is significantly in error. Adding the 4p levels improves the accuracy, but one needs at least the levels up to 5s to reproduce the correct rate of recombination. The collisional exchange between upper states is also important; for example,

\* At significant ( $>10^{-3}$ ) ionization fractions, the electron-impact processes completely dominate the kinetics.

Figure 23 shows the temperature profiles of heavy particle ( $T_h$ ), electron ( $T_e$ ), and bound states<sup>†</sup>  $4s$  and  $4p$ , when no inelastic collisions between these two sets are included. One can clearly see a separation between the two behind the shock. In Figure 24, the excitation and deexcitation processes between levels of these two sets are included, and the two manifolds clearly come into fast equilibrium with respect to each other. Note, however, that the temperature of the excited states is not the same as that of the free electrons. The latter is also changed when the inter-manifold collisions are included (red curve).

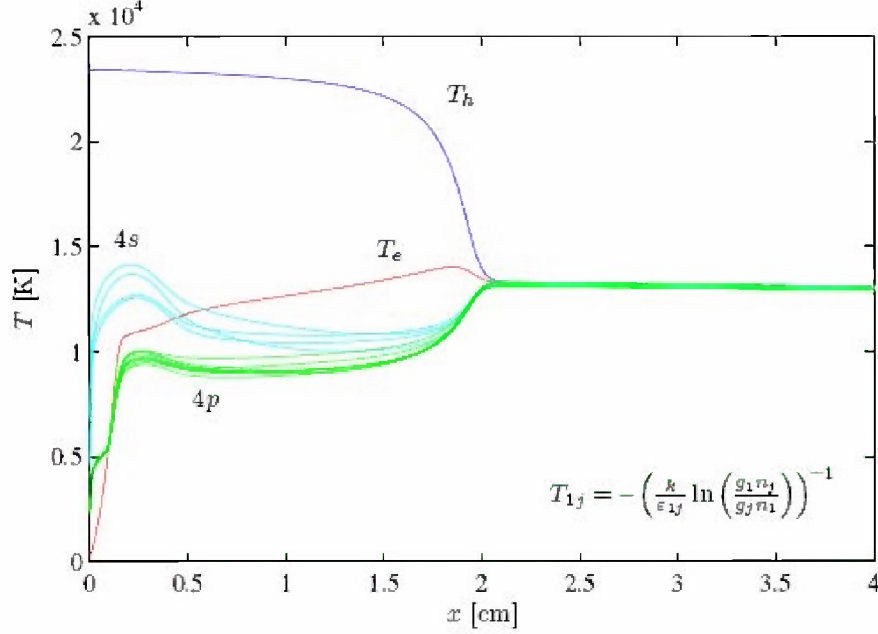


**Figure 23: Temperature profiles without collisional interchange between manifolds  $4s$  and  $4p$**

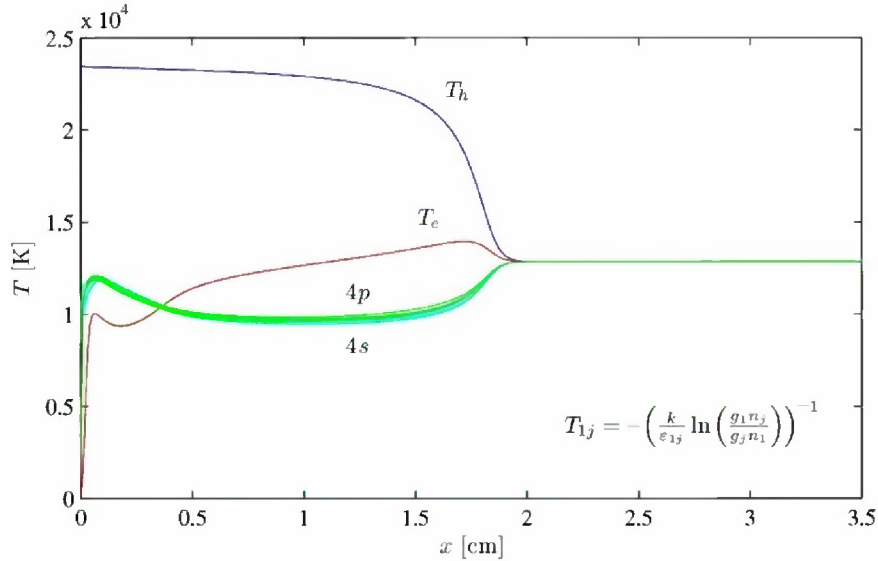


**Figure 24: Temperature profiles with collisional interchange between manifolds  $4s$  and  $4p$**

<sup>†</sup> The "temperature" of an excited level is obtained as the equivalent temperature which would satisfy a Boltzmann equilibrium relation with respect to the ground state.

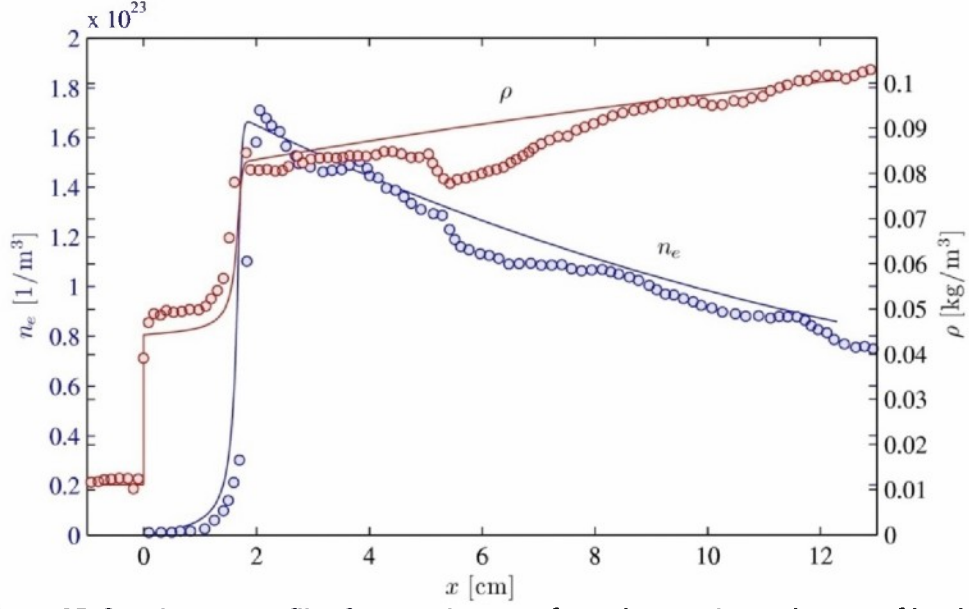


Figure 25: Steady-state profiles for complete set of reactions and complete set of levels

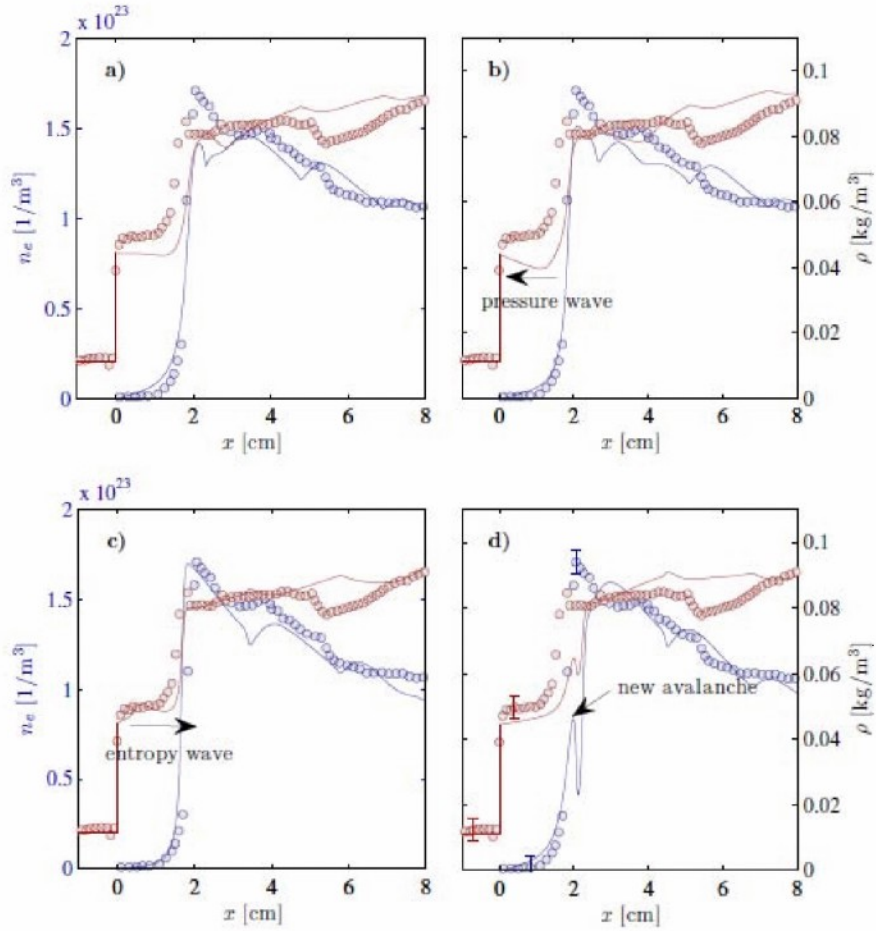


Figure 26: Unsteady 1D profiles in shock rest frame – cyclical motion



The final steady-state profiles are shown in Figure 25 and compared with the data from the ionizing shock wave data in [63]; the comparison is for the case of an initial Mach number 15.9 (similar agreement is found for other cases of Mach number, except for the lowest  $Ma=13.6$  case, for which boundary effects become important and are not considered here). However, the flow is not steady-state; this can be clearly seen in Figure 26, which shows a sequence of profiles in the rest-frame of the shock, obtained from a time-accurate 1D simulation. From a) to b) a pressure wave develops, which propagates towards the shock front; in c) the wave is reflected as an entropy wave (contact) propagating back towards the avalanche region. The higher temperature associated with the entropy wave triggers in d) a new position for the electron avalanche. The new position of the peak generates a new pressure wave and the sequence repeats itself. Figure 27 shows the x-t diagram of the pressure: the shock moves from right to left and is the leftmost trace; the avalanche is seen as the secondary trace also moving right to left (the right boundary is a reflecting wall and the free stream is from the left). One can also see the pressure waves generated at the avalanche and catching up with the shock, while a simultaneous wave propagates in the other direction (and is eventually reflected at the wall). Figure 28 shows the x-t diagram of the total density; the same pressure waves can be seen but this time the contact wave reflected at the shock and propagating back to the right can be clearly observed; this difference confirms the identification of this wave as an entropy/contact wave.

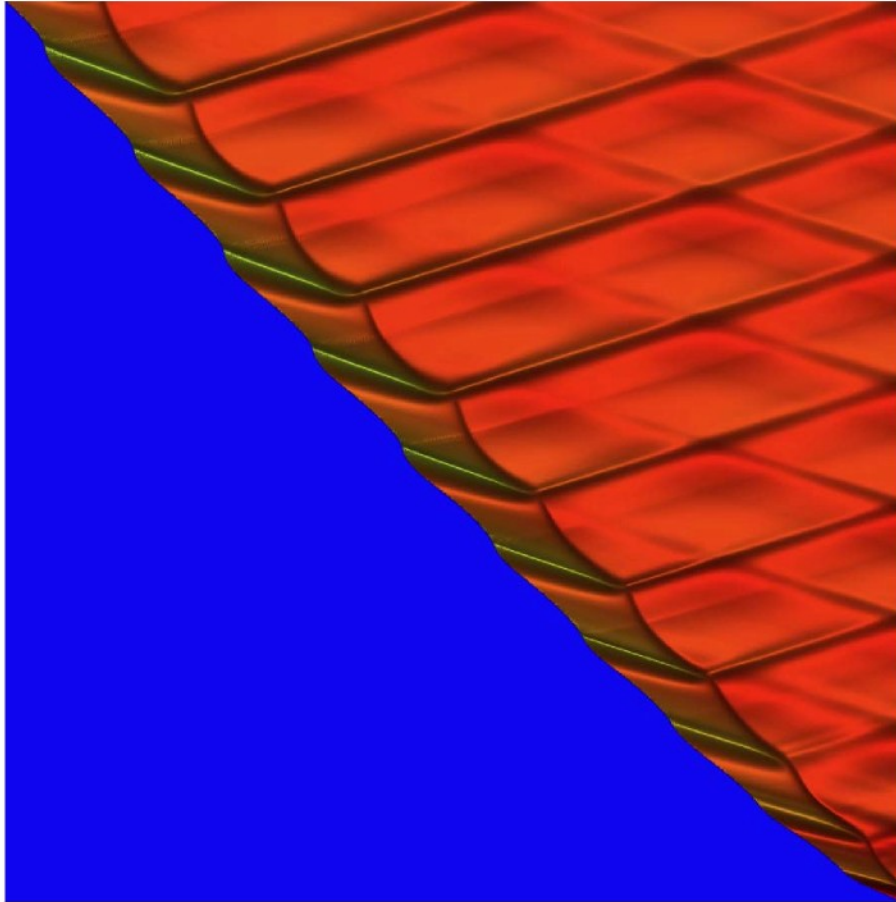


Figure 27: X-t diagram of pressure ( $Ma=14.7$  case); shock originates from right



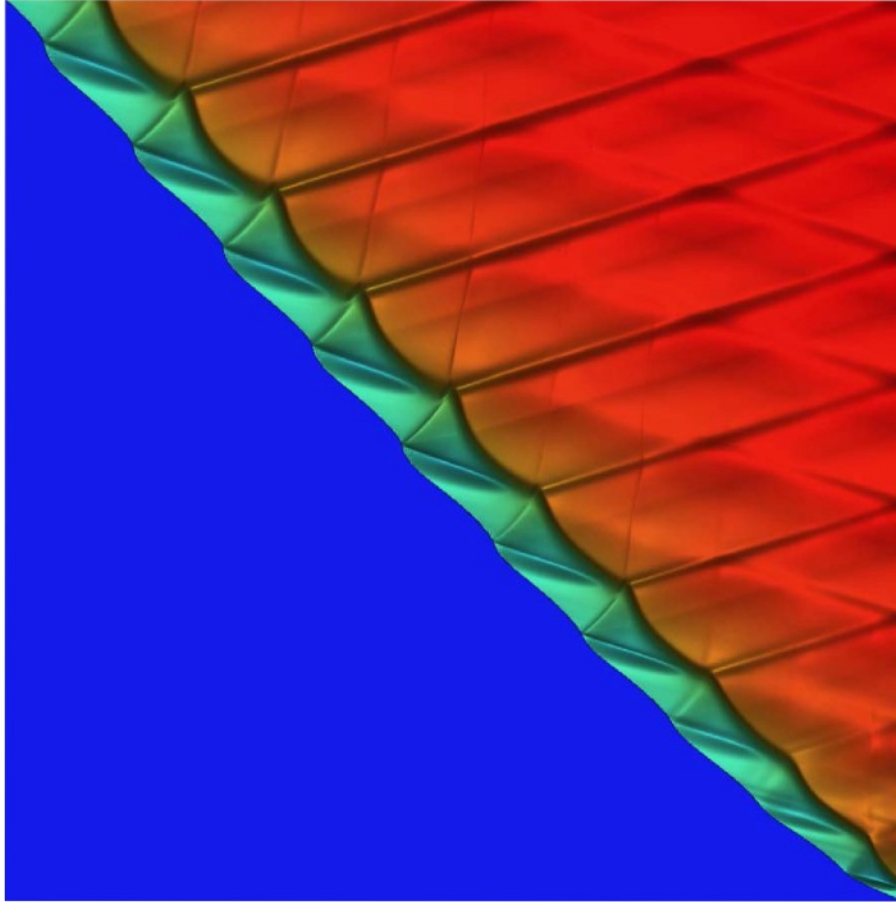


Figure 28: X-t diagram of density (Ma=14.7 case); shock originates from right

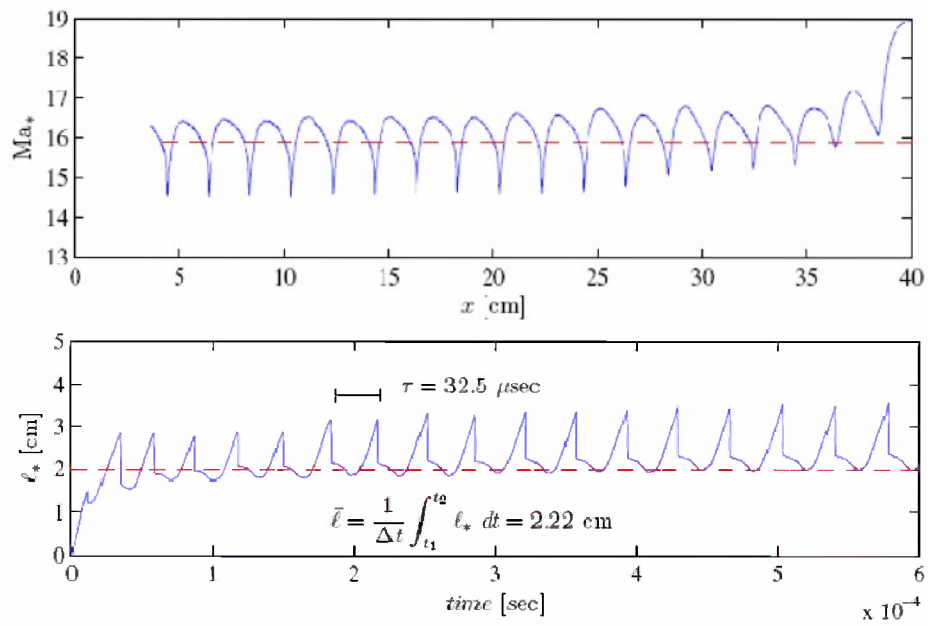


Figure 29: History of shock Mach number versus distance (top) and induction length versus time (bottom).

The periodicity of the dynamics inside the induction zone can be seen by monitoring key global parameters, such as instantaneous shock Mach number and induction length – the distance between shock front and avalanche region; the latter is defined as the location of the first peak ionization fraction. Both quantities are shown in Figure 29 for the Ma=15.9 case (dashed line in top figure); the experimental value of the induction length is 2 cm (dashed line in bottom figure). Note that a better agreement could be obtained with a better definition of the induction length (distance to the region of maximum curvature in the electron density profile). Using the argument first given in [6], one can match the periodicity with the time taken by the pressure wave and reflected wave to travel back and forth within the induction length, i.e.:

$$\tau = \bar{\ell} \left( \frac{1}{a_2 - u_2} + \frac{1}{u_2} \right) \quad (22)$$

where  $a_2, u_2$  are respectively the speed of sound and flow velocity (with respect to the shock) in the post-shock region. We found from Figure 29 a periodicity of 32.5  $\mu\text{sec}$ , while expression (22) yields 31.4  $\mu\text{sec}$ ; the agreement is fairly good, and repeated for most Mach numbers studied. Additional cases are found in Appendix E.

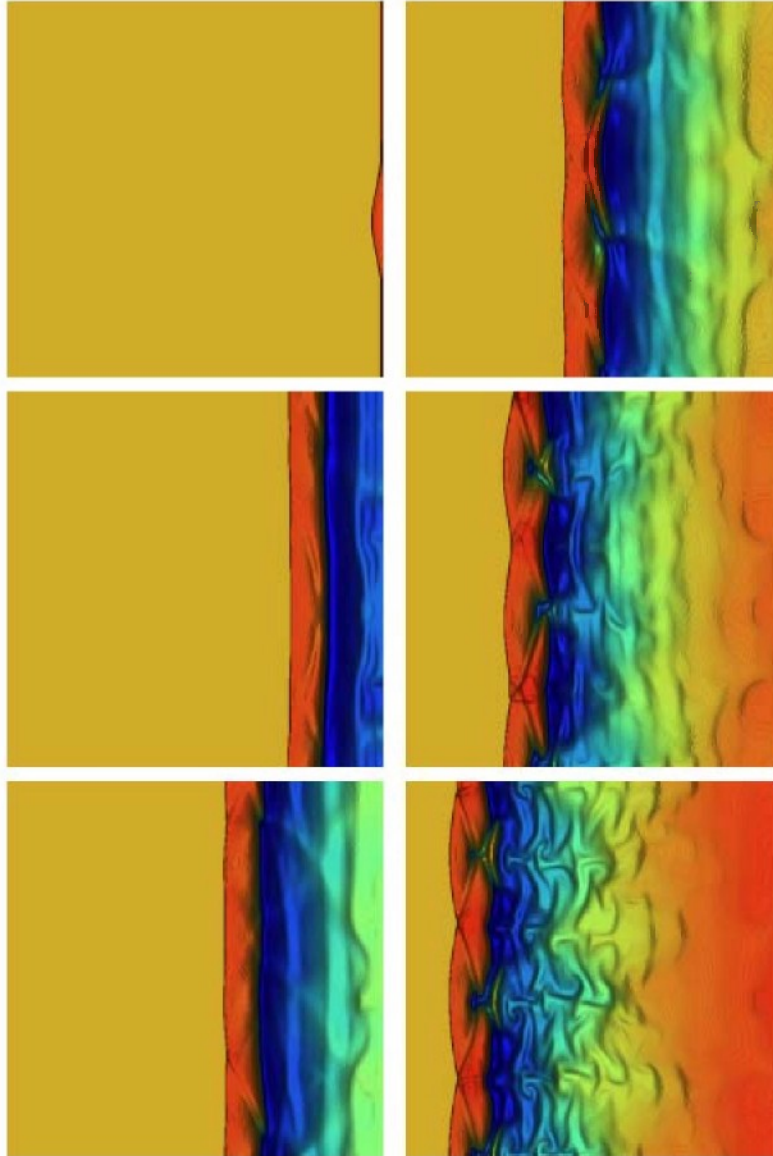
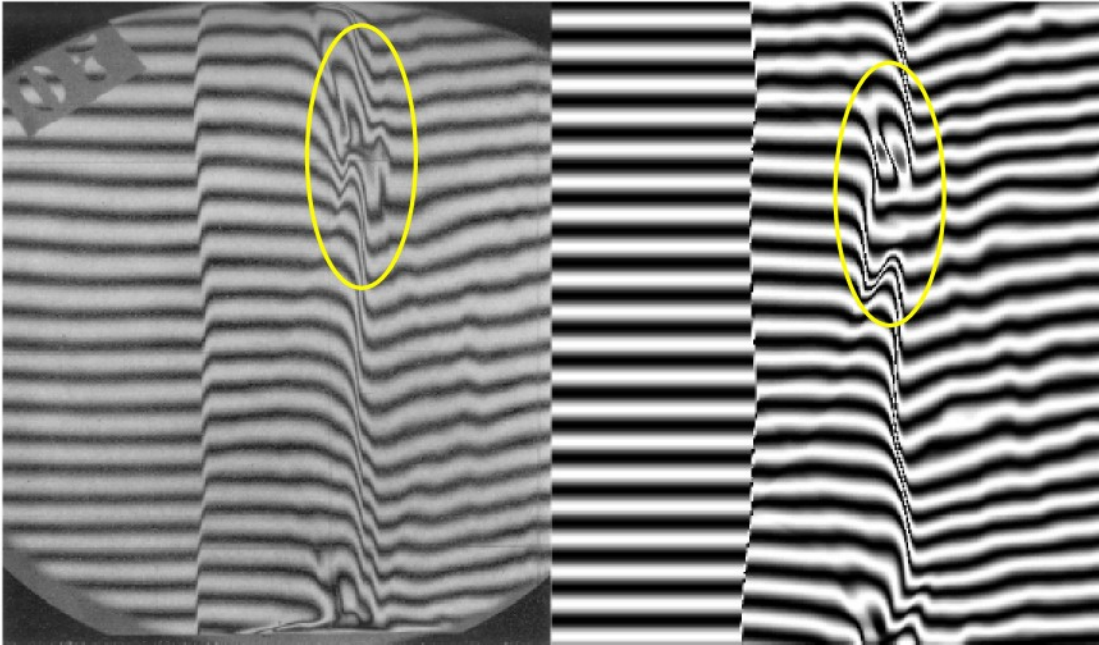
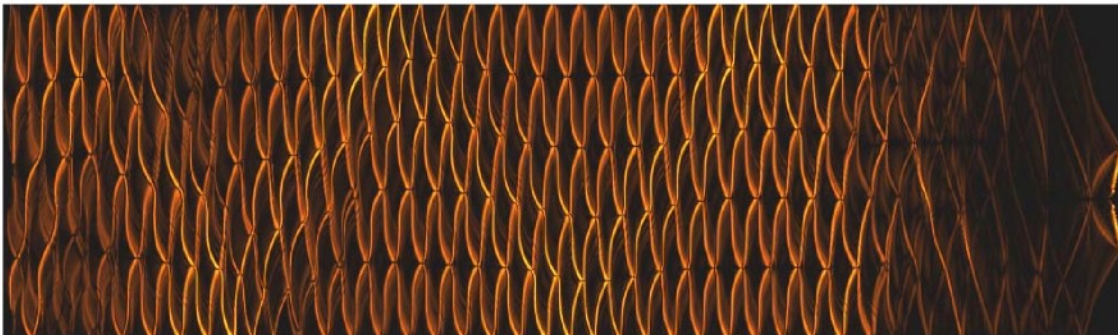


Figure 30: 2D contours of the refractive index for Ma=16.5; sequence goes top-bottom, left-right

We expect that the wave motion seen in 1D simulations will transform into a transverse pattern in multi-dimensions. Previous limitations on computing power prevented us from verifying this conjecture [6], but it was found that 2D simulations could now easily be performed with a 32 node cluster. Figure 30 shows the 2D profiles obtained for the  $Ma=16.5$  case. The 2D cases were initialized as in 1D – flow reflecting off a wall on the right – but with a small sinusoidal perturbation (see top-left panel in Figure 30). This allowed us to immediately trigger transverse instabilities, which developed into a regular pattern. The number of nodes in the transverse direction depends on the ratio of the tube height (18 cm) and the induction length (function of Mach number). This pattern could also be obtained without the initial perturbation, but after further distance. To accelerate the computations the sinusoidal perturbation was kept for all cases studied, and the results were verified to be independent of the characteristics of that perturbation. We can now compute a simulated interferogram from the 2D profiles. Figure 31 shows the comparison between the experimental (left) and computed (right) fringe patterns for  $Ma=14.7$ . The characteristics are very similar; we are able to see both the smooth, low amplitude wave-like fluctuation of the shock front position, the regions of peak avalanche at the regions where the transverse waves interact (yellow circles), and the gradual shift of lines past the avalanche region due to the radiative cooling. Thus, we have been able to reproduce the key features of these experiments and interpret them as the result of periodic fluctuations of the induction region between shock front and electron avalanche, coupled by pressure and contact waves.



**Figure 31: Comparison of experimental (left) and computed (right) interference patterns**



**Figure 32: Artificial "soot trace" for  $Ma=16.5$  case, showing cell structure formed by triple points**

This pattern of interacting waves between a shock and reaction front is entirely similar to the mechanism of detonation wave propagation [64]. To emphasize this similarity, we can produce a standard experimental result of detonation studies, the soot-trace resulting from the passage of triple points (interaction points between transverse waves), which generate high peak pressure and vorticity (erasing the soot, thus leaving a trace on the surface). We can relatively easily monitor this region of peak vorticity and generate a computational equivalent of the soot pattern, as shown in Figure 32. The structure of the “detonation” cell for the ionizing shock is shown in Figure 33. The analogy with detonation wave structure was also conjectured in [6] and is now firmly established with these 2D results.

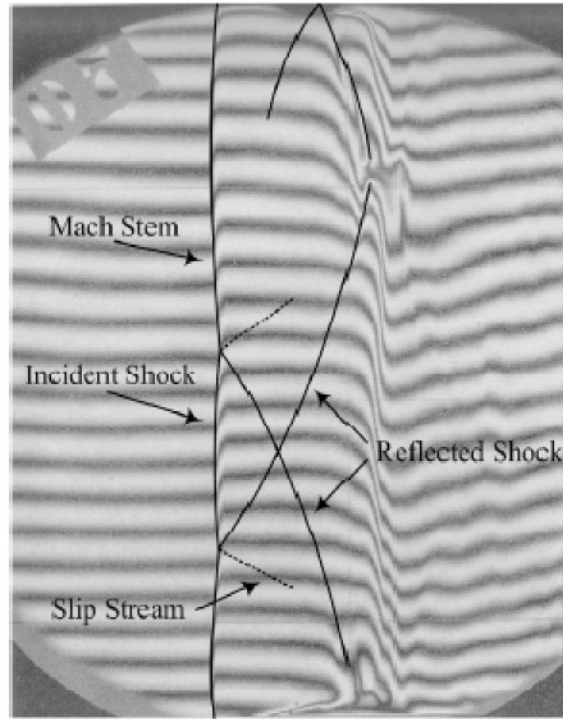


**Figure 33: Structure of “cell” in ionizing shock propagation**

The CR code was also applied to other problems such as shock layer around shaped bodies; the flow was still Argon, which is a common feedstock in plasma-discharges for hypersonic wind tunnels for testing of thermal protection system (TPS) materials. Typical profiles obtained for flow around a cylinder are shown in Figure 34;  $T_{12}$  is the equivalent temperature of the first excited level, and the difference between the excitation temperature and translational (both heavy and electron) temperatures are shown. As in the shock-tube studies, there is a significant induction region where  $T_h$  remains much higher than either  $T_{12}$  or  $T_e$ ; the electron temperature remains closer to the excitation temperature, as expected from the profile of Figure 24. We also performed some initial computations of an experiment performed at the DLR [65] which showed unexpected results in the heat transfer to the surface. DLR organized a workshop with selected participants (with relevant modeling capabilities) to try to understand the results; despite the very short time available and the need to implement additional physics (and model the entire wind tunnel to better characterize the flow), our calculations showed the best agreement with the observed shock standoff distance, an indication of the accurate reproduction of the non-equilibrium kinetics in the flow. Figure 35 shows some profiles obtained from the calculation, which involve a strong applied magnetic field. Preliminary extension of the code to the multi-fluid regime was initiated but there was not sufficient time to complete that effort. Future development of this multi-D CR code will include additional MHD physics, multi-fluid effects and molecular plasma. The latter will be performed in collaboration with Von-Karman Institute (VKI).



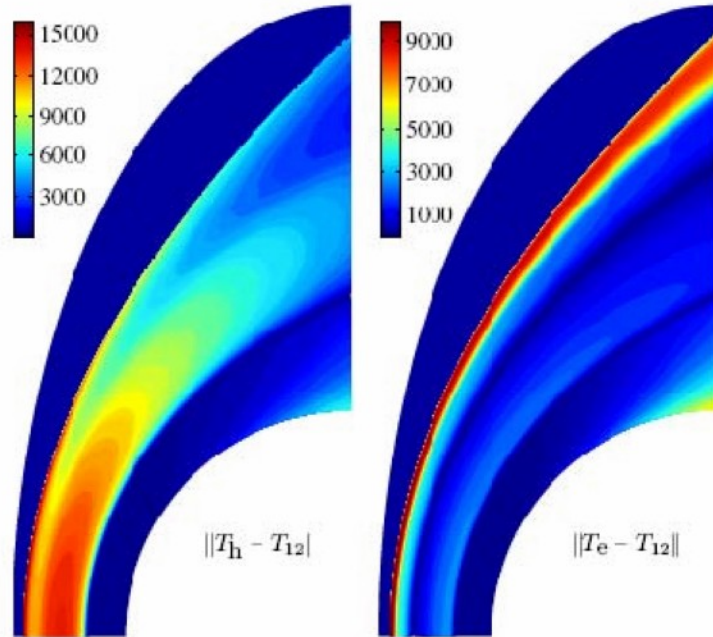


Figure 34: Profiles of temperature differences in shock layer around cylinder (Mach 18.1 Argon flow)

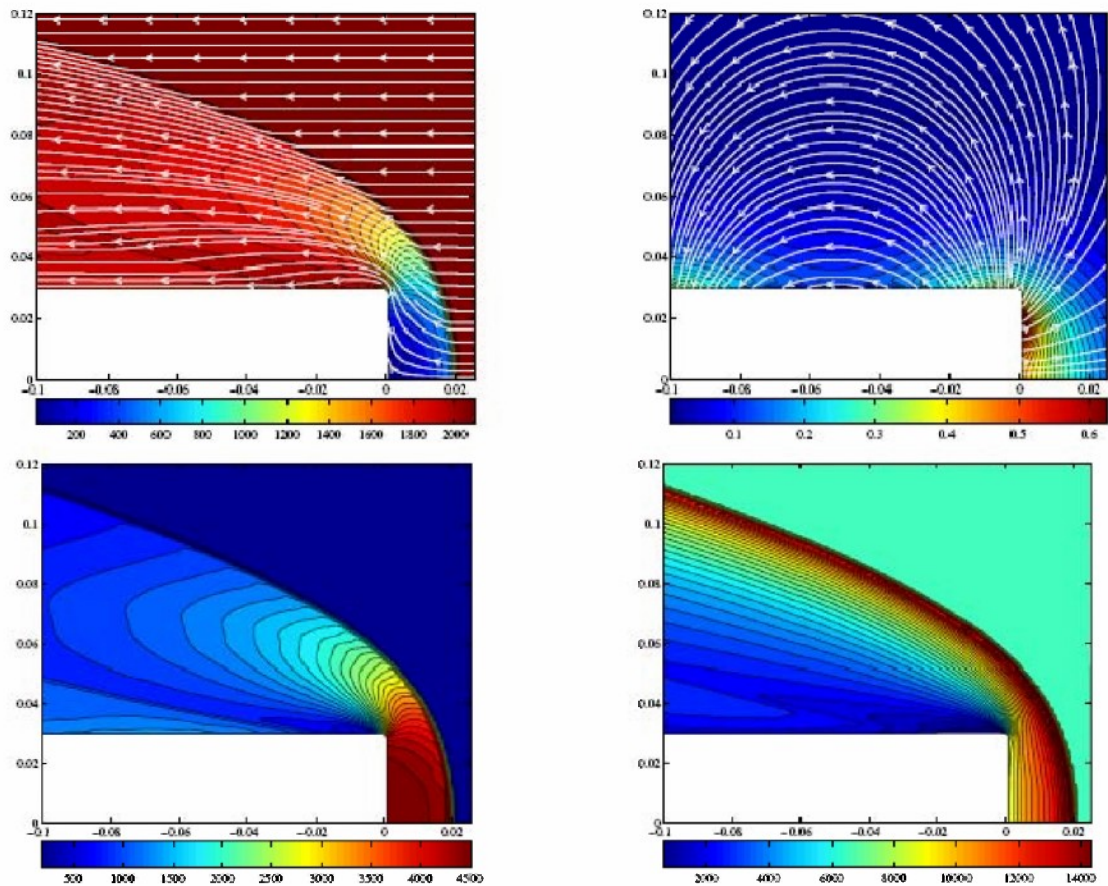


Figure 35: Profiles of Argon flow simulating DLR experiment [65]. Top-left: velocity; Top-right: magnetic field; Bottom-left: heavy-particle temperature; Bottom-right: electron temperature.

## 8. Particle Methods

### 8.1. PIC transport

The PIC model currently in place is a simple electrostatic, non-relativistic model. Particles are generated with variable statistical weight; this is useful in cases where emission is variable, i.e. depends on the plasma and field conditions near the cathode. Only electrons are presently implemented in the PIC model, and electrode boundary conditions are limited to a couple of simplified models. Electrons are “pushed” in three partial steps: first, the velocity is advanced to the time level  $(n+1/2)$ ; second, the particle position is changed using the updated velocity; third, the particle velocity is advanced again to the next time level  $(n+1)$ . This is the simplest form of a second-order symplectic integration scheme [66]. Note that the velocity must be evaluated at time level  $(n+1)$  if one wants to evaluate the current density and inelastic collision rates appropriately at that level. The global time step is of the order of the average time taken by a particle to move by the characteristic length of a cell. There is no strict Courant-like condition for the particles, but that in average the particles will not cross more than one cell per time-step. Exception is made for the particles in cells lying next to a boundary, as explained below.

The “move” is in itself decomposed into several phases. Each particle data-structure contains the time left to the particle for executing its move. At the start of each iteration, this time-left is increased by the global time step  $\Delta t$ . During the first phase, only the particles that belong to cells near a boundary are being moved (this is a cell-based operation, which obviously requires that the cell contains a list of particles inside the cell). For these, the exact time at which the particle hits the boundary (if at all) is determined, and these particle positions are advanced up to that time; this implies that the time-left is decreased by the corresponding amount. These particles are then flagged and treated by the particle boundary condition procedure. For example, if the boundary is a solid wall, the particle velocity is reflected, and if the boundary is a patch to another grid, the particle is buffered for transmission to another processor. Finally, the particles are moved again by the remaining time-left individual to each particle. This last phase includes a check on the new cell position; if it appears that a particle crosses into a boundary (i.e. it was two-layers removed from the boundary, and therefore not considered by the cell-based pre-positioning), its trajectory is re-computed with a smaller elapsed time until it end-up within the computational domain. This procedure prevents the loss of particles from the system; it would affect only a few particles, and only if the global time step is chosen relatively large, and therefore is not a significant computational penalty. Note that such particles would end-up with some time remaining, which will be processed at the *next* time-step. The use of a time-left variable for each particle allows some flexibility in the particle transport, avoiding the processors to spend extraneous time attempting to synchronize all particles.

The PIC method uses the same grid as the CFD; thus, the 2D cells are quadrilateral but not necessarily rectangular. This may generate a small, spurious force on the particles; this is a well-known problem in PIC for non-cartesian grid, which may be noticeable mostly for collisionless plasma. We believe there is a simple solution to this problem, which will be tried-out in the future. Extending the PIC to the magnetostatic case requires to add a rotation of the particle around the field line (the Lorentz force). The standard method is to use the Boris algorithm [38] which for non-relativistic plasma (as is the case here) is a very simple and fast algorithm. Although the Boris algorithm is stable for large time steps, it is not accurate for  $\omega_c \Delta t \gg 1$ . This can be problematic for magnetized plasma, since accuracy (especially energy conservation) would require very small time steps. We have developed a more efficient algorithm for this important case; so far, the algorithm works for uniform magnetic field, but we believe it can be extended to the non-uniform case, provided the variation is smooth (the case of a magnetic field discontinuity would require further thought). This would allow the more efficient study of magnetic mirror configurations, for example. Nevertheless, even the case of a strong uniform field is of interest. The new algorithm is described in detail in Appendix F.

## 8.2. Particle Merging

A critical issue in the problems of interest is the high rate of ionization that can be obtained when the energetic particles interact with a dense gas. If each ionization event from a simulated collision of a particle with atoms of the background fluid generates additional particles, the number of particles can grow exponentially, leading to a commensurate growth in computational work. To prevent this, one must devise an algorithm for particle coalescence. Let us first consider the merging of two particles of identical type (and mass  $m$ ) into a single pseudo-particle of combined statistical weight  $\varpi_{ab} = \varpi_a + \varpi_b$ , and a combined velocity  $\vec{u}_{ab} = (\varpi_a \vec{p}_a + \varpi_b \vec{p}_b) / (m \varpi_{ab})$ . This procedure conserves momentum, but the sum of the kinetic energies of the individual constituents differs from the mean kinetic energy:

$$\begin{aligned} \delta E_K &= E_{Ka} + E_{Kb} - E_{Kab} = \varpi_a \frac{\vec{p}_a^2}{2m} + \varpi_b \frac{\vec{p}_b^2}{2m} - \varpi_{ab} \frac{m}{2} \vec{u}_{ab}^2 \\ &= \frac{\varpi_{ab}}{2m} \frac{\varpi_a \varpi_b}{(\varpi_a + \varpi_b)^2} \left[ p_a^2 + p_b^2 - 2 p_a p_b \cos \theta_{ab} \right] \end{aligned} \quad (23)$$

Note that  $\delta E_K$  is always positive:

$$\frac{\varpi_a \varpi_b}{\varpi_{ab}} \frac{(p_a - p_b)^2}{2m} \leq \delta E_K \leq \frac{\varpi_a \varpi_b}{\varpi_{ab}} \frac{(p_a + p_b)^2}{2m} \quad (24)$$

Therefore, to conserve both momentum and energy during the coalescence process, a quasi-internal energy is created, which contains the randomized components of the kinetic energies of the initial particles. This is equivalent to describing the pseudo-particle with a distribution of velocities, such that the temperature of an equivalent Maxwellian distribution is:  $\delta E_K = \frac{3}{2} kT$ . One could add to the description of the particle this “thermal” component, and there are a number of arguments in favor of such a modification. A very sophisticated model based on this approach has been described by Hewett [27], and demonstrated high accuracy with a fewer number of particles. Besides the reduction in computational cost, there is another potential advantage in having internal velocity DF in the pseudo-particle data structure. When dealing with collisional plasmas, the rates of excitation and ionization are very sensitive to the energy distribution function near the inelastic thresholds, and can be a critical part of the overall plasma dynamics. Using a MCC method with only a few particles may generate an unacceptable level of stochastic noise; if each pseudo-particle also contains its own velocity DF, a smoother and more accurate evaluation of these rates could possibly be obtained. Assuming a Gaussian distribution centered on the mean particle velocity and using a Taylor expansion of the cross-section around that velocity, one can easily evaluate the inelastic rate as function of the pseudo-particle temperature. However, a succession of merging processes would eventually lead to excessive internal DF temperatures, and assigning dynamics based on the mean velocity only (i.e. particle trajectories) leads to inaccuracies. In the absence of the internal DF of each pseudo-particle, it is clear from the discussion above that one cannot combine two particles into a single one while conserving mass, momentum and energy. There have been various schemes [67,68] proposed to minimize the energy error, but the one described below provides an exact conservation scheme.

Let us first consider the more general process of combining an arbitrarily large number of particles, and to consider the energy in the center of mass (CM) frame. Combining  $N$  identical particles, we get a total mass  $M = \sum_i \varpi_i m$ , and a total momentum  $\vec{P} = \sum_i \vec{p}_i$ . The velocity of the center of mass is:  $\vec{U}_{CM} = \vec{P} / M$ . Denoting by a prime the variables in that CM reference frame, the individual constituents have a momentum:  $\vec{p}'_i = \vec{p}_i - m \vec{U}_{CM}$ , and contribute a kinetic energy  $\varepsilon'_i = (\vec{p}'_i)^2 / 2m$  to the “thermal” energy. The latter can be expressed as the difference between the total energy contributions of all constituents and the kinetic energy of the center of mass, i.e.:

$$\delta E_K = \sum_i \varpi_i \frac{\vec{p}_i^2}{2m} - \frac{\vec{P}^2}{2M} = \sum_i \varpi_i \frac{\vec{p}'_i^2}{2m} \quad (25)$$

This particle distribution can now be split into two pseudo-particles with half the statistical weight of the entire system. Furthermore, this can be done while transforming the thermal energy into the relative kinetic energy of the two “children”. Again, consider the split in the CM frame, into two pseudo-particles of mass  $M / 2$  with equal and opposite momentum  $\delta\vec{p}'$  (see Figure 36).

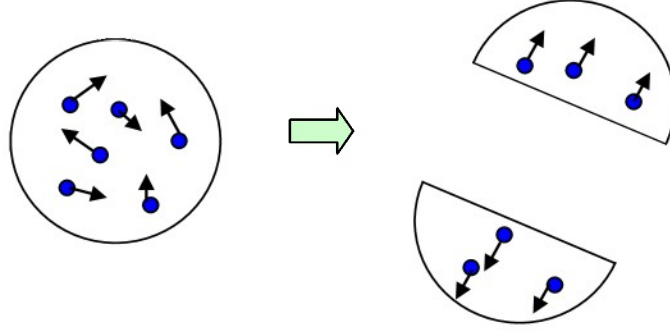


**Figure 36: Schematic of fragmentation process in Center of Mass frame after coalescence of many individual pseudo-particles**

The total kinetic energy is now:

$$2 \times \frac{(\delta\vec{p}')^2}{2(M/2)} = \delta E_K \quad (26)$$

Therefore, one can generate two pseudo-particles with half the mass and statistical weight of the center-of-mass, and with equal and opposite momentum in the CM frame, where the magnitude is given by (26), i.e.:

$$|\delta\vec{p}'| = \sqrt{M\delta E_K/2} \quad (27)$$

and with an orientation chosen at random along the unit solid angle. Note that there is no need for a formal transformation to the CM rest frame; the quantities of interest can be evaluated directly, using (25) for the thermal energy, with post-fragmentation momentums:  $\frac{1}{2} \vec{P} \pm \delta\vec{p}'$ , using (27).

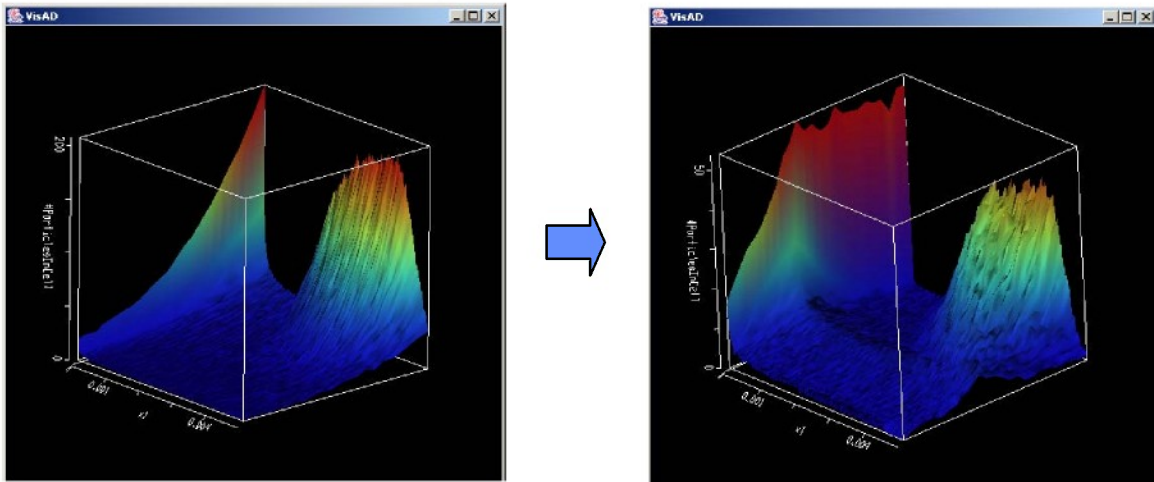


**Figure 37: Number of particles (electrons) versus time and distance, without (left, 250,000 particles) and with (right, 35,000 particles) particle coalescence.**

Notice the exponential growth of electrons emitted by the cathode and generated in the ionization region. On the right, particle coalescence automatically controls the number of electrons in each cell; the true physical quantities (e.g. current densities) remain the same.



The procedure generates two particles from  $N$  particles without creating internal energies, while exactly conserving mass, momentum and energy. As long as  $N > 2$ , there is an effective reduction in the number of particles, and while there is no conservative process to coalesce 2 particles into 1, the process of merging 4 into 2 is equivalent. The reduction factor achieved here can take all values  $(n+2)/2$  starting from  $n=1$ , and is quite efficient for high values of  $n$ .

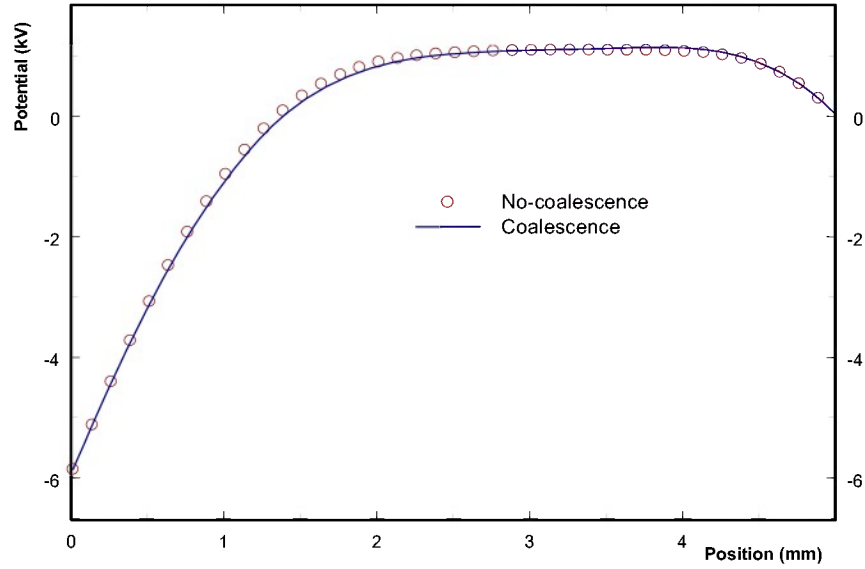


**Figure 38: Electric potential in diode 10 ns after start, with and without particle coalescence**

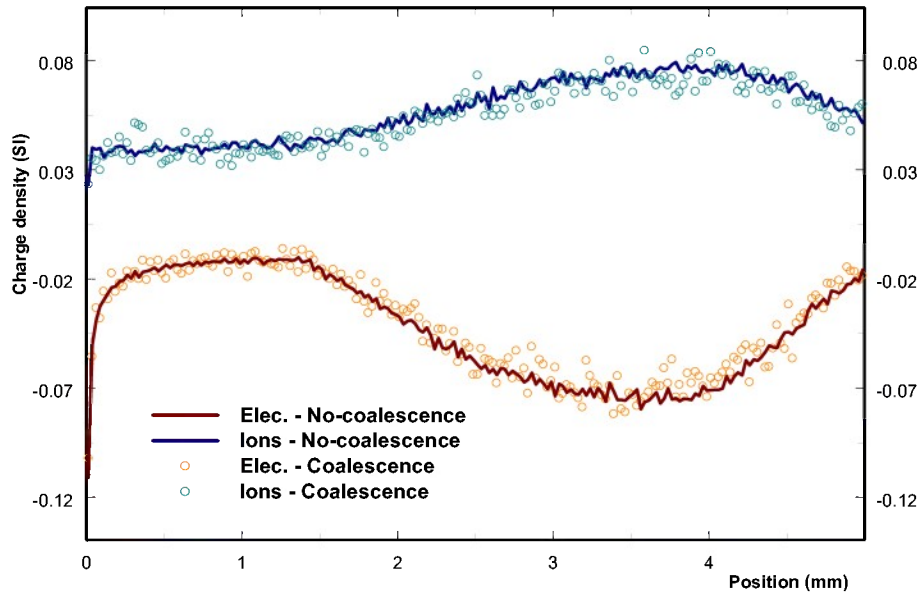


**Figure 39: Particle (electron) and fluid (ions) charge densities 10 ns after start of computations, with and without pseudo-particle coalescence.**  
Reduced statistical fluctuations in the former case indicate the approximately 9-times larger number of simulated particles.

We conducted preliminary tests of this procedure on a simple planar diode case. Without particle merging, the ionization of the gas rapidly leads to exponential growth in the number of simulated electrons. With an aggressive coalescence process in place, we were able to reduce the number of particles from 250,000 to 35,000 with no significant losses in accuracy of the results (see Figure 37). Figures 38 and 39 show the potential profiles and particle charge densities obtained in both cases at the same simulated time. Note that from an initially linear profile, the potential has developed a virtual anode that partially traps electrons and slowly migrates towards the cathode (the ions are immobile in this simulation: the apparent motion is a shift in the ionization front). This also causes the field at the cathode to increase, and the electron emission rate to increase as well. This profile is in agreement with analytical models [69]. Because the potential is obtained as a result of solving Poisson's equation, which filters-out short-wavelength fluctuations, a better test is the comparison of the charge densities themselves. Although Figure 39 shows that the statistical noise is slightly higher in the merging case – as expected given the reduction in the number of particles – the results are in excellent agreement.

Not only does the coalescence procedure conserve momentum and kinetic energy, but it also preserves the electrostatic energy to 1<sup>st</sup>-order. The electrostatic energy of the initial particles being coalesced is:

$$E_{ES} = \sum_i \varpi_i Z_i e \phi(\vec{x}_i) \quad (28)$$

where the electric potential field  $\phi(\vec{x})$  is a global field, resulting from space charges in the complete domain. Assume first that this field is constant. After coalescence, the electrostatic energy can now be written as:

$$E_{ES} = \frac{\Omega}{2} Ze \phi(\vec{x}_+) + \frac{\Omega}{2} Ze \phi(\vec{x}_-) \quad (29)$$

We have used the fact that all particles are similar (same charge), and  $\vec{x}_\pm = \vec{x}_c \pm \delta\vec{x}$  are the positions of the two new pseudo-particles that replace the coalesced ensemble;  $\vec{x}_c$  is the centroid of the ensemble. To first-order (dipole) approximation, we have:

$$\phi(\vec{x}_\pm) = \phi(\vec{x}_c) \pm \vec{E} \cdot \delta\vec{x} + o(2) \quad (30)$$

The first-order terms cancel out in (8-8), and after equating (8-6) and (8-7) we find that:

$$\Omega \phi(\vec{x}_c) = \sum_i \varpi_i \phi(\vec{x}_i) \quad (31)$$

This equation defines the centroid: the conservation of momentum and kinetic energy does not place restrictions on the positions of the new pseudo-particles, only their momentum. The centroid position can be approximately defined as:

$$\vec{x}_c = \Omega^{-1} \sum_i \varpi_i \vec{x}_i \quad (32)$$

For particles of identical masses, this is equivalent to the center-of-gravity of the ensemble. The approximation of constant scalar potential  $\phi(\vec{x})$  can also be justified. Since it is obtained by solution of Poisson's equation:

$$\vec{\nabla}^2 \phi = - \frac{\tilde{\rho}}{\epsilon_0} \quad (33)$$

where  $\tilde{\rho} = e(Z_i n_i - n_e)$  is the charge density, it is enough to verify that the latter is approximately conserved during the coalescence procedure. In fact, both the charge density and the current density are conserved, since for a given cell of volume  $Vol$ :

$$\tilde{\rho} = \frac{\sum_i \varpi_i Z_i e}{Vol} = \frac{\Omega}{Vol} Ze \quad (34a)$$

$$\vec{j} = \frac{\sum_i (Z_i e m_i) \varpi_i \vec{p}_i}{Vol} = \frac{Ze}{m} \frac{\vec{P}}{Vol} = \tilde{\rho} \vec{U}_{CM} \quad (34b)$$

Solving a discretized version of Poisson's equation (33) with the charge density defined at the cell centers, one obtains the same source field, and therefore the same scalar potential field. Note also that the same solution is obtained even if one deposits the space charge on the nodes of the cell (a common practice in PIC). The charge density at a node  $\mathbf{x}_v$  is defined as:

$$\phi_v = Ze \sum_i w_i W_v(\tilde{\mathbf{x}}_i) \approx Ze \Omega W_v(\tilde{\mathbf{x}}_v) + Ze (\bar{\nabla} W_v) \sum_i w_i (\tilde{\mathbf{x}}_i - \tilde{\mathbf{x}}_v) + \dots \quad (35)$$

where  $W_v$  is a normalized weighting function, such that the contributions over all nodes add-up to 1, and  $\tilde{\mathbf{x}}_v$  is the node position. The weighting function evaluated at the node position itself is of course 1; after using the definition of the centroid, (8-13) becomes:

$$\phi_v \approx Ze \Omega \left[ 1 + (\bar{\nabla} W_v)(\tilde{\mathbf{x}}_c - \tilde{\mathbf{x}}_v) + \dots \right] \quad (36)$$

After coalescence, the contribution of the two resulting pseudo-particles to the same node is now:

$$\phi_v = \frac{Ze \Omega}{2} W_v(\tilde{\mathbf{x}}_+) + \frac{Ze \Omega}{2} W_v(\tilde{\mathbf{x}}_-) \approx Ze \Omega + \frac{Ze \Omega}{2} (\bar{\nabla} W_v)(\tilde{\mathbf{x}}_+ + \tilde{\mathbf{x}}_- - 2\tilde{\mathbf{x}}_v) \quad (37)$$

which is clearly the same as (36). Therefore, up to the dipole approximation, the new coalescence procedure conserves both kinetic and electrostatic energy, and conserves charge density, current density, and electrostatic and magnetic potential fields.

We believe this approach is significant and very capable; further extensions will include a selective algorithm which combines particles which have relatively similar properties, i.e. their relative distance in phase space is small. This would prevent the systematic combinations of particles of opposite and large velocities, such as in the case of beam-beam interactions. Without a selective algorithm, the coalescence could lead to an artificial thermalization. We also plan to test the procedure on a large variety of discharge conditions.

### 8.3. Lagrangian method

In addition to Eulerian fluid models, we have also devised a Lagrangian “fluid-element” model, where the fluid solution is obtained at each spatial position in the steady-state approximation. The fluid element is advected as a pseudo-particle, but yet has internal properties such as density and temperature. In the limit of no internal temperature, this corresponds to the “ballistic” integration procedure used in [18] and in several electron gun codes. This work was initiated as an attempt to gain a better understanding of the essential physics of pseudospark ignition. In particular, Kozyrev, Korolev, Rabotkin and Shemyakin (KKRS) [69] developed a pseudo-analytical model of pseudospark ignition by treating the problem as one-dimensional, i.e. as a planar diode, and looked at the conditions for electron avalanche in the inter-electrode gap. The model introduced by KKRS uses a modified version of the Child-Langmuir discharge [70] that takes into account the build-up of ion density within the discharge gap. This model is summarized in Appendix B, starting with a review of the standard Child-Langmuir discharge.

The KKRS model provides an interesting insight in the physics of the discharge initiation; however it is very approximate and not entirely self-consistent. Notably, although the potential is space-dependent, the electron current density and both ion and electron densities are assumed *independent* of position, and the ion outflow time is also constant. The details of the model could be improved by: (a) including all spatial dependences; (b) including elastic collisions; (c) including non-fluid effects. The model also is based on the Child-Langmuir emission rate (i.e. space-charge limited only), which assumes that there is no cathode work function. The effect of an actual work function should also be investigated. The non-fluid effects would aim at accounting for the effect of pendular electrons in the potential trap mentioned above.

Before using the full hybrid model in this planar diode case, we thought it worthwhile to investigate first if the KKRS model could simply improved by using the Lagrangian, fluid-element model mentioned above. This basic hydrodynamic model is described in detail in Appendix C, and was implemented into a simple Java code. The fluid-element approach is different from the

KKRS analytical model and offers an alternative approach to testing the validity of the physical model. In the first application we neglect elastic collisions and recombination, and replace the spatially varying ion density with its spatial average, thus bringing the electron-fluid element model closer to the KKRS assumptions. The first numerical results were obtained for the case of spatially-averaged ion density, with the same discharge conditions as described in [69]. In addition to the fluid element solution for the electrons, described in the previous section, there are also two other critical variations in the overall model. First, the ion density obeys an equation of the form:

$$\frac{\partial N_i}{\partial t} = \nu^i n_e - \frac{N_i}{\tau} \quad (38)$$

where  $\nu^i$  is the ionization frequency mentioned in the previous section. The decay time-scale  $\tau$  represents the sum of all contributions to ion removal. At low gas pressures, recombination would proceed at slow rates, but ion diffusion to the walls would be more important. In the KKRS model, this time scale is determined by the minimum ion time of flight, i.e.:

$$\tau = \frac{L}{v_i} = \frac{L}{\sqrt{2eV_o/M_i}} \quad (39)$$

and is independent of the gas pressure. Second, the current emitted at the cathode is modified as the space charge builds-up inside the gap and the electric field at the cathode increases. Instead of equation (B11) of Appendix B, the cathode current density becomes:

$$j_e^{cat} = \frac{4}{9\epsilon_o} \left( \frac{2e}{m_e} \right)^{1/2} \frac{|E|^{3/2}}{L^{1/2}} \quad (40)$$

As the ion density increases as a result of gas ionization, the slope of the electrostatic potential (i.e. the electric field) increases at the cathode after each iteration and the current emitted at the next iteration is correspondingly increased. It is important to emphasize that:

1. without the increase of the cathode current, i.e. the feedback from the space charge onto the boundary condition, there *never* is exponential growth of the current density in the discharge.
2. without the loss of ions, but with the cathode current increase described in item 1 above, there is *always* an exponential growth of the current density inside the discharge.

With both features present, it is possible to find a critical regime. By varying the gas pressure, one can obtain the series of curves shown in Figure 8-5a.

Typically, the anode current increases by several orders of magnitude, achieving extremely high values for high gas pressures. The initial value is usually of the same order as the cathode current. The rate of increase is dependent on the pressure, but does not exactly scale linearly with the gas pressure (in which case the position of the maximum would be at the same location in Figure 40). The decrease following this maximum is due to the fact that: (1) the gas becomes fully ionized, and; (2) the ion removal rate removes gas without replenishment; at the end, there is pure vacuum in the discharge and the anode current becomes the same as the cathode current (pure vacuum diode, with Child-Langmuir emission). It may appear difficult to determine a transition point from the curves of Figure 40, although one can conclude that, based on the maximum values of the anode current, the 0.7Pa case does not yield to discharge ignition while the 1 Pa case does. A clearer picture emerges when looking at the initial slopes of the current growth curve at relatively early times. As shown in Figure 41, there is a clear difference in behavior as the pressure is lowered below 0.8 Pa, which is estimated as the critical pressure. This is slightly greater than the 0.6 Pa value obtained from KKRS for the discharge conditions being examined (6 kV applied voltage), but of the same order of magnitude. Thus, despite the differences in numerical approaches, we obtain similar results as the analytical model of [69]. From this point, several assumptions can be re-examined and relaxed, to better examine the qualitative effect on the discharge ignition. For example, the effect of spatial variation of the ion density (Figures 40 and 41 are obtained for an average ion density as source term to Poisson's equation), elastic collisions, recombinations and more realistic models of ion diffusion and

cathode emission. These effects could be examined in the future. Note also that the fundamental study of the planar diode can lead to a number of very interesting physical phenomena [71,72], despite the apparent simplicity of the device. The combination of rich physics and simple geometry make it a very good test case for the hybrid model.

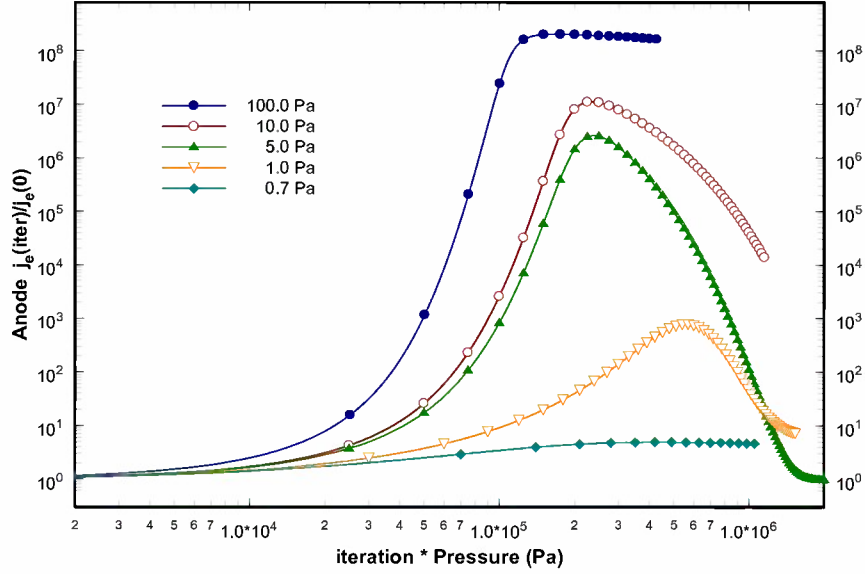


Figure 40: Anode current density versus product of iteration number and discharge pressure (in Pa). Current density is normalized to initial density obtained at first iteration.

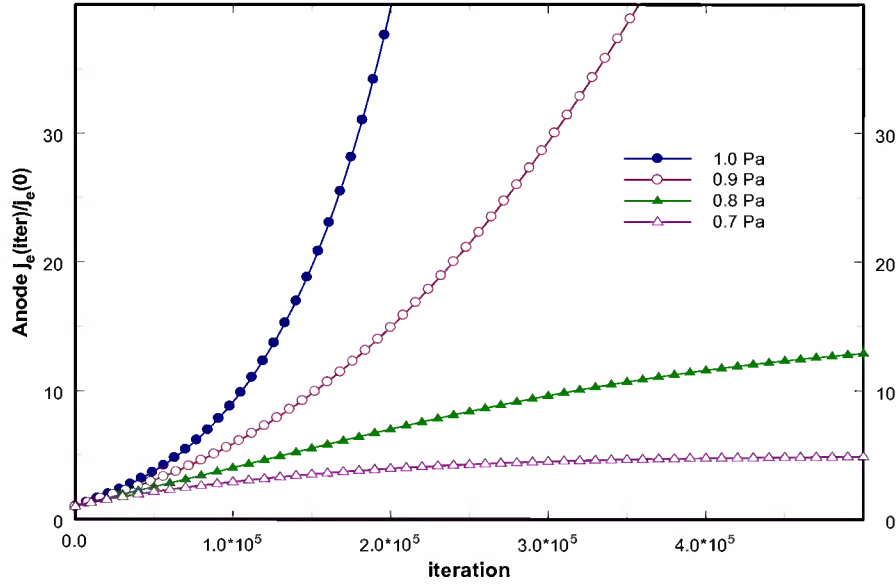


Figure 41: Detail of anode current evolution in vicinity of critical pressure

#### 8.4. Beyond PIC

In a prior state-of-the-art in hybrid modeling of pseudospark discharges [18], the particles become part of the bulk when their total (potential + kinetic) energy falls below the ionization threshold. While this technique correctly accounts for the true ionization rate, it does not allow an accurate determination of the excitation rates, and is rather coarse (particles just below excitation

thresholds may still have significantly more energy than the mean bulk plasma electrons). We suggest that a more accurate approach could be developed, based on comparison of moments of distribution functions; in that scheme, a particle is more likely to be absorbed by the bulk if its properties are close to the bulk-average, while particles can be sampled from the bulk as well, thus allowing a two-way transfer. This can be made possible by allowing particles (actually “pseudo-particles”, which statistically describe a large number of physical particles) to have an internal distribution function, i.e. a micro-VDF similar to the prior work of Coppa et al. [73] or Hewett [27]. This option was briefly mentioned in Section 8.2 while describing a newly developed particle-merging algorithm. This extension of standard PIC can be considered as a simple generalization of the method which already treats the pseudo-particles as regions of finite extent in space, in order to smooth the distribution of charges and currents onto the grid. A finite extent in velocity space seems a straightforward idea. Furthermore, using a Maxwellian form for the micro-VDF allows us to directly compare the non-equilibrium component and a bulk (fluid) plasma, determining with precision when and where to change the nature of the component (see section 4.1, Transfer to Bulk Plasma). This approach may be investigated in the future.

The transport of particles is traditionally handled by a Particle-In-Cell (PIC) method; indeed, a simple preliminary PIC model (electrostatic, non-relativistic) has been implemented in the code. PIC falls in the category of particle-mesh (PM) methods, which avoid the  $\mathcal{O}(N^2)$  problem of direct summation of particle-particle interactions (force evaluation) by first computing a field on a mesh, then computing the force on any particle from this field. The method has two interpolation steps (the so-called “gather-scatter”): first to interpolate the particle charge onto mesh points to define a charge density field; second, to compute the force at the particle location from the field defined at mesh points. Furthermore, the PIC method does not account for particle interactions at close range, since the mesh spacing provides a filtering length scale; thus, when the Debye length is unresolved the PIC calculations are notoriously inaccurate, and suffer from “numerical heating”, a manifestation of poor total energy conservation. This is particularly problematic for dense plasmas (especially for laser-target interactions), since the Debye length becomes very small, and an extraordinarily large number of grid points would be required. This is an important issue and although there are various options we have been contemplating, this issue may require a separate, focused research effort.

Therefore, we have also been looking at alternatives to the standard PIC as the fundamental particle transport solver. One promising approach is the grid-free approach (see e.g. Christlieb et al. [74]), which relies on binary decomposition of the domain into clusters containing particles, followed by a multipole expansion to compute the particle-cluster interactions. The approach is a derivation of the Barnes-Hut [75] tree-code method; each domain is recursively divided (forming an “octree” in 3D) into boxes until each box (cluster) contains less than a given number of particles. Figure 42 shows the process in 2D, starting from a subdivision into 4 quadrants (A-D), followed by further sub-division (B yielding sub-quadrants 3,4,7,8); sub-quadrant 7 does not contain particles and therefore can be eliminated from the tree-structure. The force at particle location  $\mathbf{x}_i$  (red dot) has contributions from clusters 3,4, and 8, each one acting as a distributed source.

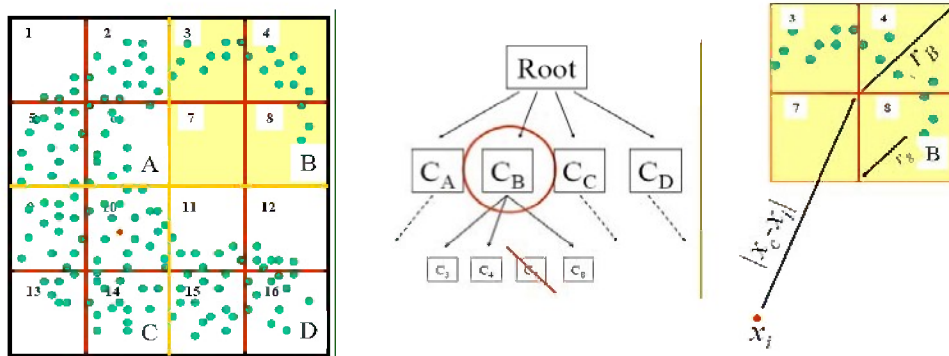


**Figure 42: (a) domain sub-division; (b) “quadtree” hierarchy (in 2D); (c) particle-cluster interaction**

This numerical approach is of order  $N \ln N$ , i.e. is computationally efficient. By using the particle-cluster computation only for distant interactions and direct summation within the cluster for a small number of particles, higher accuracy can be obtained by accounting for short-range interactions exactly. The grid-free method also uses boundary integrals to account for both Dirichlet and Neumann boundary conditions. One of the advantages of the approach is that the tree-code approach automatically adapts to the local conditions; thus, there is no conflict between grid requirements for a CFD calculation and a PIC calculation. We should emphasize that this approach allows us to use non-Cartesian grids for particle transport and avoid the self-force problem in PIC methods; we plan on implementing a variation of the Barnes-Hut method specifically for this purpose.

The grid-free/octree method is probably an excellent approach when dealing with flows with considerable variation in density scale, e.g. backflow from thruster exhaust in space environment. We have so far concluded that the basic Barnes-Hut tree method has a lot to offer, but the overall procedure can be greatly simplified by using a grid. This is no-longer a “grid-free” method, but since we need a grid for the fluid (CFD) component anyway, this is not an issue. The cells of the grid provide a natural way to compute a source for the multipole expansion, without having to recursively construct a quad-tree (octree in 3D). This allows us to apply more effective parallelization procedures. While the basic method has been developed and tested, implementation into the general hybrid code has been delayed due to lack of sufficient manpower, and will be attempted during the remainder of the project.

### 8.5. Inelastic Processes

Inelastic collisions are especially important for the problems of interest. The degree of deviation from Boltzmann and Saha equilibrium for the excited and ionized states respectively is especially important, since the population densities of these excited states and ions impact a number of other processes (radiation, material coupling, etc). Thus a detailed and non-Maxwellian collisional-radiative model of the excited and ionized states is very much desired. Again, the collisions of the non-Maxwellian component (particles) is typically treated by a stochastic approach (Monte-Carlo Collisions – MCC), while the inelastic processes within the fluid description are treated by a set of ODE, the master rate equations. The combination of the two approaches into a unified framework can however be problematic.

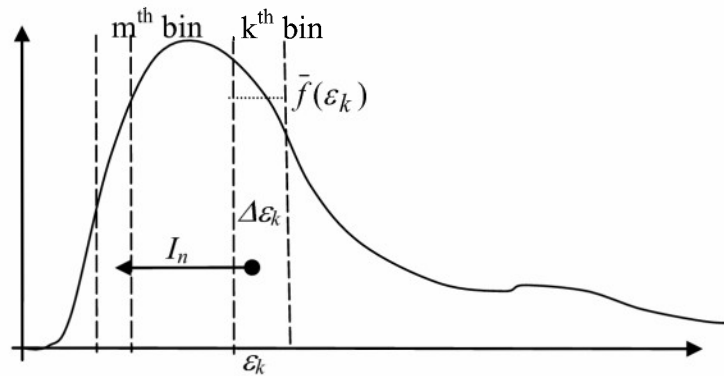


Figure 43: (a) schematic of atomic levels; (b) discretized (isotropic) energy distribution function

Consider for example collisional ionization from an atomic level  $n$  by electron impact.  $I_n$  is the ionization potential of the level, and let us assume that the bound-free transition leaves an ejected electron with a negligible kinetic energy. The rate of ionization by electrons from this level is:

---

\* This is far from being accurate at high initial electron energies; one of the key tasks currently under-way is to implement a systematic model to account for variable energy transferred to the bound electrons, and the tabulation of the appropriate differential cross-sections and collision probabilities.

$$\frac{\partial N_i}{\partial t} = N_n \int_{I_n}^{\infty} d\varepsilon \cdot \sigma(\varepsilon) v \cdot f(\varepsilon) \quad (41)$$

where  $\varepsilon$  is the kinetic energy of the electron,  $v$  the velocity, and  $f(\varepsilon)$  the distribution function. Assuming that the electron energy distribution function (EEDF) is discretized into B bins of variable spacing  $\Delta\varepsilon_k$ , the rate of change is:

$$\frac{\partial N_i}{\partial t} \approx N_n \sum_k \Delta\varepsilon_k \bar{f}(\varepsilon_k) \cdot \sigma(\varepsilon_k) \cdot \sqrt{2\varepsilon_k/m} \quad (42a)$$

which we re-write as: 
$$\frac{\partial N_i}{\partial t} \approx N_n \sum_k \bar{k}_{i(k)} \cdot \bar{n}_{e(k)} \quad (42b)$$

where 
$$\bar{n}_{e(k)} = \Delta\varepsilon_k \bar{f}(\varepsilon_k) = \int_{\Delta\varepsilon_k} d\varepsilon f(\varepsilon) \quad (43)$$

and 
$$k_{i(k)} = \sigma(\varepsilon_k) \cdot \sqrt{2\varepsilon_k/m} \quad (44)$$

The rate of change is obtained as the sum of elementary processes, such that electrons from  $k^{\text{th}}$ -bin are moved to another energy bin  $m$  such that:

$$\varepsilon_k - \varepsilon_m = I_n \quad (45)$$

For each *elementary* process, we have:

$$\frac{\partial N_i}{\partial t} = -\frac{\partial N_n}{\partial t} = +k_{i(k)} \cdot \bar{n}_{e(k)} \cdot N_n \quad (46a)$$

$$\frac{\partial \bar{n}_{e(k)}}{\partial t} = -k_{i(k)} \cdot \bar{n}_{e(k)} \cdot N_n \quad (46b)$$

$$\frac{\partial \bar{n}_{e(m)}}{\partial t} = +k_{i(k)} \cdot \bar{n}_{e(k)} \cdot N_n \quad (46c)$$

$$\frac{\partial \bar{n}_{e(0)}}{\partial t} = +k_{i(k)} \cdot \bar{n}_{e(k)} \cdot N_n \quad (46d)$$

The last equation indicates the production of electrons with zero kinetic energy (the ejected atomic electron). The interesting aspect of equations (46a-d) is that one can construct a complete system of kinetic equations and solve implicitly:

$$\begin{bmatrix} 1 + \sum \nu_k \delta t & -\sum \nu_k \delta t & \dots \\ \dots & 1 + \sum \nu'_k \delta t & \dots \\ \vdots & \vdots & \ddots \\ & & & 1 + \sum \nu''''_k \delta t \end{bmatrix} \otimes \begin{bmatrix} \delta N_i \\ \delta N_n \\ \delta \bar{n}_{e(k)} \\ \vdots \end{bmatrix} = \begin{bmatrix} rhs_i \\ rhs_n \\ rhs_{e(k)} \\ \vdots \end{bmatrix} \quad (47)$$

One can use time scales larger than the characteristic time scale of ionization/recombination, and by extension, excitation/de-excitation for a full Collisional-Radiative model. There are, however, some remaining issues with this description:

- (1) The elementary ionization process transfers electrons from  $k^{\text{th}}$ -bin to  $m^{\text{th}}$  bin, but if the initial and final electron energies are such that equation (47) is not exactly satisfied, a systematic error would be introduced in the energy conservation.
- (2) Even if the bins are defined such that energy conservation is guaranteed, according to item 41 above, the scheme replaces the varying EEDF inside a bin by a constant (average) value; this is a zero-th order approximation, which needs to be extended to higher-order for improved accuracy.



- (3) If the distribution is not isotropic the situation becomes more complicated; the inelastic jump would produce changes from all cells<sup>†</sup> lying along a circle of radius  $v = \sqrt{2\varepsilon/m}$  into all cells that intersect a circle of radius  $\sqrt{2(\varepsilon - I_n)/m}$ . Again, one would need to compute the fractional cell area of the discretized phase space on either side of this circle.

The formulation (47) is a path towards an implicit MCC procedure, described in a later section; we have not yet implemented it but have been making progress towards developing the basic MCC procedure for collisional-radiative kinetics, a significant task in itself.

The MCC model must guarantee energy conservation and detailed balance. The latter is obtained when the cross-sections for the forward and reverse processes satisfy certain relationships; the *Fowler* relation for ionization/recombination:

$$g_0 \varepsilon d\sigma^{ion}(\varepsilon; \varepsilon' \varepsilon'') = \frac{16\pi m_e}{h^3} g_u \varepsilon' \varepsilon'' d\sigma^{rec}(\varepsilon', \varepsilon''; \varepsilon) \quad (48)$$

and the *Klein-Rosseland* relation for excitation/de-excitation:

$$g_l \varepsilon d\sigma_{ul}^{\uparrow}(\varepsilon) = g_u \varepsilon' d\sigma_{ul}^{\downarrow}(\varepsilon') \quad (49)$$

These relations have been used to guarantee detailed balance in the implementation of a collisional-radiative MCC algorithm; this work was performed in collaboration with R. Caflisch of UCLA. The implementation of the reverse process is not necessarily an easy task, and to our knowledge there has never been a fully-consistent collisional-radiative MCC model. One problem is the implementation of the recombination process; as can be derived from the Fowler relation, the recombination cross-section has an infrared divergence<sup>‡</sup> which leads to practical problems in a standard Monte-Carlo procedure. So far, a standard set of techniques have been used to compute the recombination; more sophisticated approaches will be used in the next year. One may ask why a stochastic (MCC) model should be used for recombination, since this is usually a process that becomes important only at high density, for which a continuum model may be more appropriate; there are several reasons:

- (1) Any process must satisfy detailed balance; if recombination is not included, one may obtain inaccurate and inconsistent results.
- (2) Beam particles can be energized in one region and transported to another region where they can lose energy and recombine; this would be the case, for example, of electrons ejected from a target by a ponderomotive force and returning to the target.
- (3) There is no guarantee that a hybrid methodology would be able to “capture” all thermalized particles into a fluid component, albeit desirable this may be.
- (4) Electrons can suddenly lose most of their energy by an excitation/ionization process, making them good candidates for recombination.

Although we have only recently done some basic verification tests, the completion of the basic collisional-radiative model is a significant step. The tests performed include the evolution of the electronic state populations towards Boltzmann equilibrium, stability of the equilibrium distribution function (see Figure 44) and we have developed and verified (see Figure 45) the correct expression for the H-theorem in collisional-radiative plasma – to the best of our knowledge, this is the first time the H-theorem was derived for this case – details are provided in Appendix D. Further developments will focus on improved techniques for dealing with the stiffness of recombination, and extension to implicit MCC procedures and particle kinetics with micro-VDF.

We have also completed a discretized phase space approach for the inelastic collisions (i.e. kinetic solver, following the steps described in Equations 46a-d). Again, basic tests have recently performed to verify the accuracy (such as consistency of the rates); the H-theorem was again verified, and the dynamics of the relaxation were verified against the MCC algorithm (for excitation/de-excitation only). During these tests we discovered an interesting aspect of the dynamics which suggests a breakdown of ergodicity under specific conditions (again, an effect

<sup>†</sup> Momentum conservation is assured by the heavy particle.

<sup>‡</sup> This divergence at zero-energy of the incident electrons is also reflected in the divergence at low temperature of the Maxwellian rate.

verified by the MCC model). Figure 46 shows the evolution of the EEDF when relaxing as a consequence of inelastic (excitation/deexcitation only) collisions. Note that in the absence of elastic e-atom and e-e collisions, the EEDF develops discontinuities occurring at multiples of the energy gap of the bound-bound atomic transition. This feature was also found in the MCC algorithm after computing the relaxation for longer times than previously tests. This shows that the discretized phase-space kinetics is a much faster algorithm which easily allows us to compute the dynamics over a longer time scale, but also that the physics are correctly implemented, since the two independent models cross-validate each other. The final version of this discretized solver works for arbitrary binning of the EEDF, also works for ionization and recombination (the latter involving transitions from two different bins into one). The current scheme also *exactly* conserves mass and energy (momentum is not conserved for electron-impact inelastic collisions, since the heavy particle can absorb an arbitrary of momentum; this is an approximation of order  $m_e/M$ ).

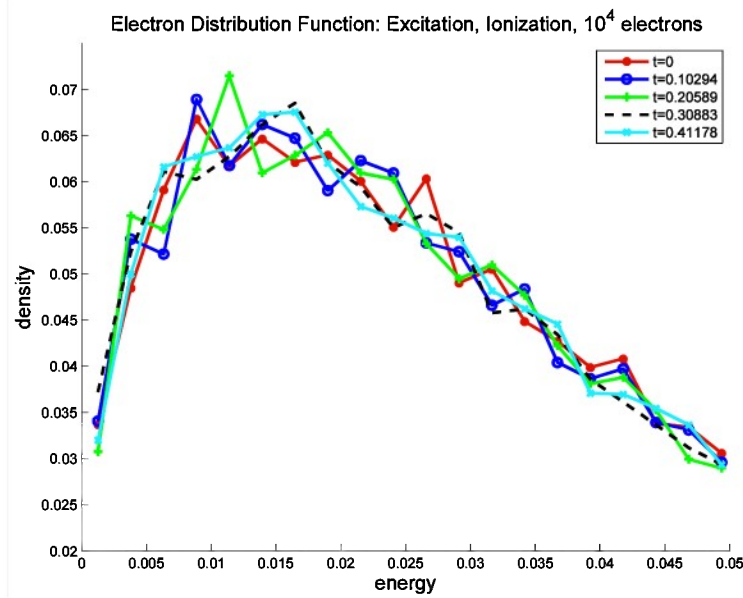


Figure 44: Tests of stability of equilibrium EEDF in CR-MCC model

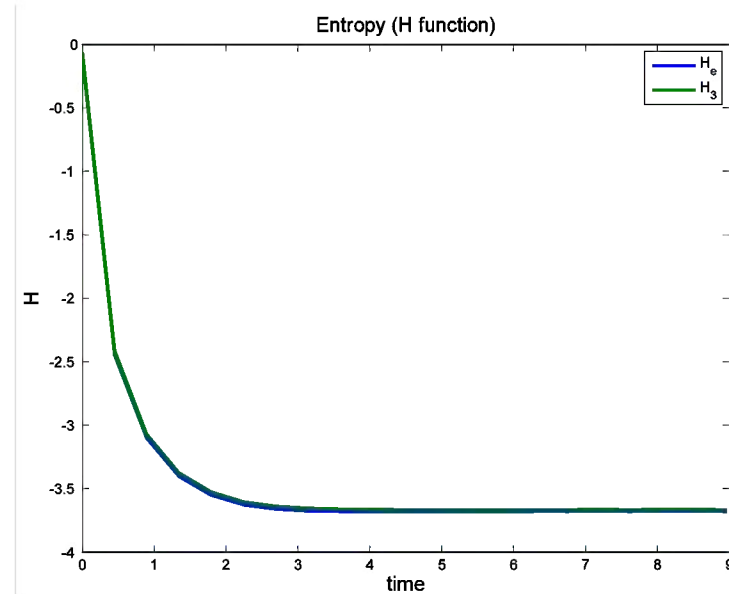
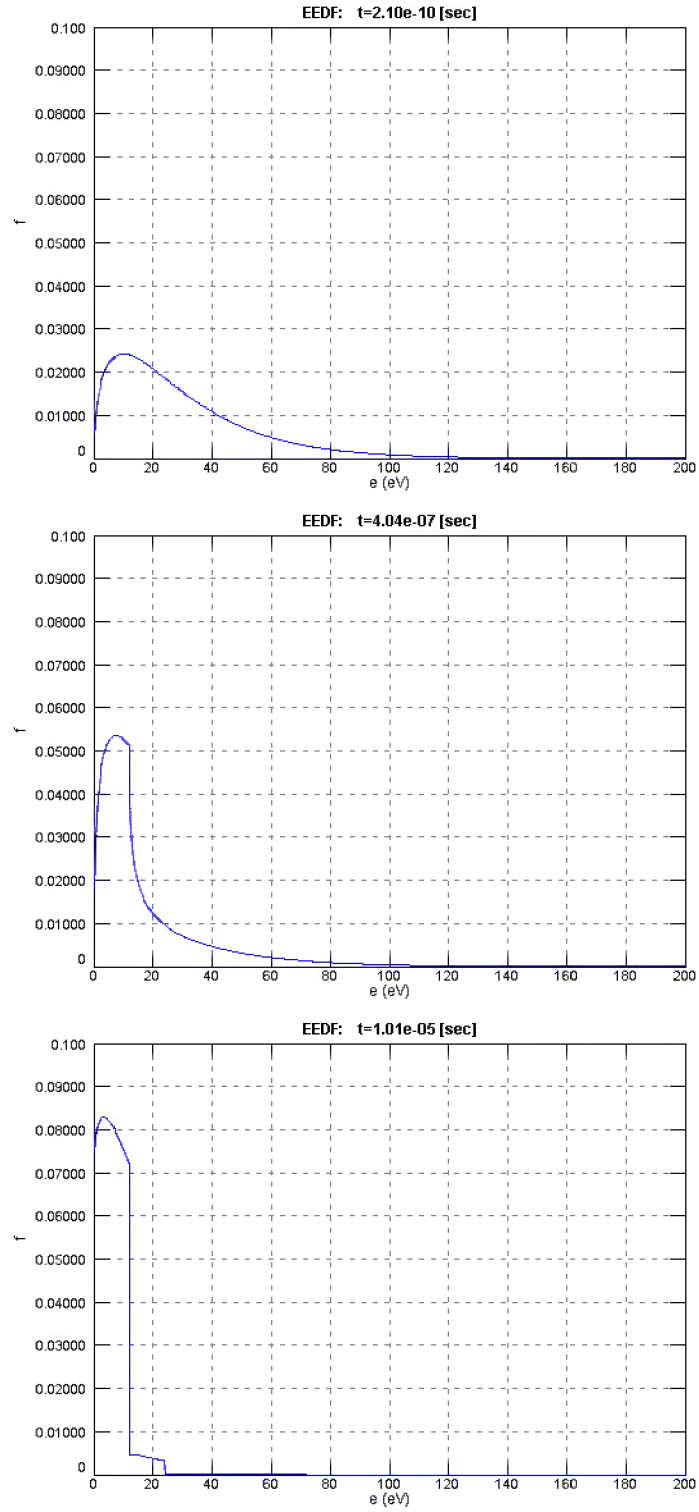
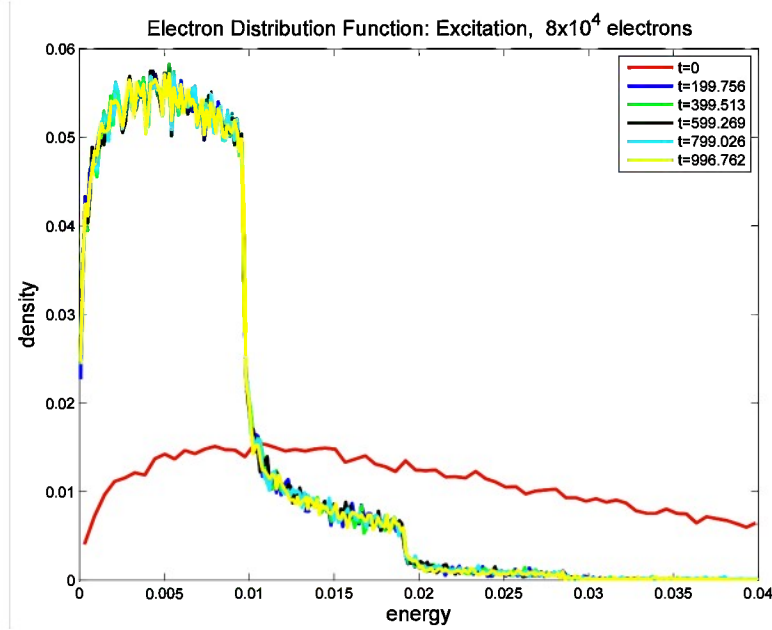


Figure 45: (a) verification of H-theorem during relaxation; (b) verification of energy conservation: error per time step (red) and integrated error (blue) – 0<sup>th</sup>-order only



**Figure 46: Evolution of the EEDF as a result of collisional excitation/deexcitation only (2-level atom) by discretized kinetic solver**



**Figure 47: Evolution of the EEDF in similar test case as Figure 46, computed by MCC.**

A summary report describing this kinetic solver is being completed. The phase-space approach was investigated because (a) it provides a means of verification for the Monte-Carlo model; (b) it is an alternative approach to the non-Maxwellian CR kinetics. The latter would be especially relevant when combined with a Fokker-Planck model for elastic collisions, and a Vlasov step for transport. This will be investigated in the future.

### 8.6. Remaining Issues

The standard MCC procedure is to draw a random number, compare it to the probabilities of various events and decide on accepting or rejecting an event. This makes the low-probability events very noisy (poor statistics), and if improbable events are occasionally selected, the statistical weight of the particles can make it such that unphysical values (negative) of population densities can be obtained. This can easily be seen as follows. The stochastic equivalent of (42a) or (46a) is:

$$\frac{\partial N_i}{\partial t} = N_n \frac{\varpi_p}{V} \sigma(\varepsilon_p) \cdot \sqrt{\frac{2\varepsilon_p}{m}} = k_{i(p)} N_n \frac{\varpi_p}{V} \quad (50)$$

where  $\varpi_p$  is the statistical weight of the pseudo-particle and  $V$  is the cell volume. The expression  $\varpi_p / V = \tilde{n}_p$  is an equivalent density (per unit volume) of physical particles with the same properties (momentum, energy). The equivalent of (46b) is:

$$\frac{\partial \tilde{n}_p}{\partial t} = -k_{i(p)} \cdot N_n \cdot \tilde{n}_p \quad (51)$$

In the standard MCC, the probability of the ionization event is obtained:

$$P_i = 1 - e^{-v_i \Delta t} \approx v_i \Delta t = k_{i(p)} N_n \Delta t \quad (52)$$

and if the event is accepted, the particle is destroyed, i.e.  $d\varpi_p = -\varpi_p$ . The stochastic solution is equivalent to the differential (continuous) solution (51) *in average*, since the probability of the event is related to the rate of change by (52). However, when the event occurs, there must be a

corresponding change in the level population, i.e.  $dN_n = -\tilde{n}_p$ . For large statistical weights and low population densities ( $N_n < \tilde{n}_p$ ), this may result in unphysical, *negative* population densities.

Instead, if the incremental change is applied to the level at all times, i.e.  $dN_n = -k_{i(p)} \cdot N_n \cdot \tilde{n}_p \Delta t$  but the change in the statistical weight (i.e. particle destruction) is applied once, conservation of mass and energy is obtained at best only in average. In fact, the situation is worse, because small changes in level population are due to collisions with specific particles, while the change in particle density occurs once for a different particle. Thus, this approach is definitely not desirable.

Let us examine in more detail the collisional process by pseudo-particles. Let us borrow the syntax of quantum mechanics and write the transition from a state  $|p, n\rangle$  to a state  $|p', f\rangle$ , where:  $p$  is the state of an incident particle,  $p'$  is the final state of the same particle,  $n$  is the electronic level of the target atom, and  $f$  describes a free (ionized) state. This describes the collisional ionization of an atom by a particle. It is important that the final state  $p'$  is the result of both the initial particle state and the initial electronic level; therefore,  $p'$  depends on both  $p$  and  $n$ . The rate of depletion of level  $n$  and the rate of change of the particle density are written as:

$$\frac{dN_n}{dt} = -\sum_p \langle p', f | \sigma v | p, n \rangle N_n \tilde{n}_p \quad (53a)$$

$$\frac{d\tilde{n}_p}{dt} = -\sum_n \langle p', f | \sigma v | p, n \rangle N_n \tilde{n}_p \quad (53b)$$

Equation (8-31a) contains a summation over initial particles, while (8-31b) is a summation over levels, not particles. The rate of production of a product particle  $p'$  is:

$$\frac{d\tilde{n}_{p'}}{dt} = + \langle p', f | \sigma v | p, n \rangle N_n \tilde{n}_p \quad (54)$$

No summation is involved in (8-32), since  $p'$  corresponds to a unique combination of  $(p, n)$ . The total system is composed of  $L$  equations for the level populations,  $P$  equations for the incident particle densities ( $P$ =number of pseudo-particles in cell), and  $L \times P$  equations for the particles resulting from each interacting combination  $(p, n)$ . Whatever scheme is used to solve the kinetics, it is important to conserve mass, i.e. to satisfy the following properties:

$$\sum_n \delta N_n = \sum_p \delta \tilde{n}_p = - \sum_{(p,n)} \delta \tilde{n}_{p'} \quad (55)$$

The master kinetic equations lead to an implicit formulation:

$$\left[ 1 + \sum_p \underbrace{\langle p', f | \sigma v | p, n \rangle \tilde{n}_p}_{v_p} \delta t \right] \delta N_n + \sum_p \underbrace{\langle p', f | \sigma v | p, n \rangle N_n}_{v_n} \delta t \delta \tilde{n}_p = - \sum_p \underbrace{\langle p', f | \sigma v | p, n \rangle N_n \tilde{n}_p}_{r_{pn}} \delta t \quad (56a)$$

$$\left[ 1 + \sum_n v_n \delta t \right] \delta \tilde{n}_p + \sum_n v_p \delta t \delta N_n = - \sum_n r_{pn} \delta t \quad (56b)$$

The implicit C-R system results in the following linear problem:

$$\begin{bmatrix} \ddots & \vdots & \vdots & \vdots & \vdots \\ \cdots & 1 + \sum_p v_p \delta t & \cdots & v_n \delta t & \cdots \\ \cdots & \vdots & \ddots & \vdots & \vdots \\ \cdots & v_p \delta t & \cdots & 1 + \sum_n v_n \delta t & \cdots \\ \cdots & \cdots & \cdots & \cdots & \ddots \end{bmatrix} \otimes \begin{bmatrix} \delta N_n \\ \vdots \\ \delta \tilde{n}_p \\ \vdots \end{bmatrix} = - \begin{bmatrix} \vdots \\ \sum_p r_{pn} \delta t \\ \vdots \\ \sum_n r_{pn} \delta t \\ \vdots \end{bmatrix} \quad (57)$$

Note that this system is a *reduced* version of the full C-R kinetics which also include the produced particles. If one uses detailed balance and solve for the reverse processes ( $|p', f\rangle \mapsto |p, n\rangle$ ), the

dependence of the rates on  $\tilde{n}_{p'}$ , would imply that the matrix on the LHS would be extended and be of a size:  $(L+P+L \cdot P)^2$ . Typically, with 10 electronic levels and 40 particles per cell, this would imply inverting a 450×450 matrix at each cell. This is clearly too expensive to consider, at least with a standard Gauss algorithm. Even in its reduced form, the inversion of the matrix is very expensive. An approximate solution which still guarantees the conservation properties is to use a global rate reduction by the factor:

$$1 + \sum_p \nu_p \delta t + \sum_n \nu_n \delta t \quad (58)$$

Thus we obtain:

$$\delta N_n = - \frac{\sum_p r_{pn} \delta t}{1 + \sum_p \nu_p \delta t + \sum_n \nu_n \delta t} = -N_n \frac{\sum_p \nu_p \delta t}{1 + \sum_p \nu_p \delta t + \sum_n \nu_n \delta t} \quad (58a)$$

$$\delta \tilde{n}_p = -\tilde{n}_p \frac{\sum_n \nu_n \delta t}{1 + \sum_p \nu_p \delta t + \sum_n \nu_n \delta t} \quad (58b)$$

This approach guarantees that  $N_n$  and  $\tilde{n}_x$  remain positive, and that the conservation laws remain satisfied. With this global time scale reduction, each rate is replaced by:

$$\hat{K}_{p,n}^{p',f} = \frac{\langle p', f | \sigma v | p, n \rangle}{1 + \sum_p \nu_p \delta t + \sum_n \nu_n \delta t} \quad (59)$$

From this, the produced particle has an equivalent density:

$$\delta \tilde{n}_{p'} = + \frac{r_{pn} \delta t}{1 + \sum_p \nu_p \delta t + \sum_n \nu_n \delta t} \quad (60)$$

One can then generate  $L \times P$  particles with the statistical weights corresponding to Equation (60) above, and rely on a global cell-based particle coalescence technique to limit the total number of particles to a reasonable size. This coalescence scheme has been developed within the previous year; it is a unique (and deceptively simple) algorithm to combine particles and exactly conserve all quantities (mass, momentum and energy) in the process – important features that have not been reproduced in prior particle merging schemes. Furthermore, it also conserves electrostatic and magnetostatic energy to first order, while higher-order corrections could presumably be achieved with a slight increase in algorithm complexity.

There is yet an alternative to the generation of scores of particles (each with small statistical weight), which is to construct an average product particle:

$$|p'\rangle = \frac{\sum_n (\delta \tilde{n}_{p'}) |p'\rangle}{\delta \tilde{n}_p} \quad (61)$$

This indicates that all conserved properties are averaged, i.e. momentum and kinetic energy (particles have the same mass). Note that the average product particle contains a micro-VDF with a given total density, mean velocity and energy spread (first three moments of the micro-VDF). Therefore, if micro-VDF is implemented as an essential feature of the new, “extended” particle transport method, the inelastic collisions automatically require the construction of such an extended particle as an average product of collisions. If the micro-VDF is not implemented, or if the micro-VDF of the product particle is too diffuse (hot), it is necessary to split this average into several (at least two) particles with no micro-VDF or smaller (colder) internal distributions. This process is equivalent to the particle coalescence algorithm, which was developed earlier to control the number of particles generated by an ionization avalanche.

The most important points can be summarized as follows:

- (a) Some of the key machinery for the advanced particle methods have been (particle coalescence) or are currently being implemented (collisional-radiative MCC); these have

important applications beyond the pure hybrid simulation problem, i.e. can be applied to other, more traditional particle solvers (PIC). The next step will consist of developing a *complete* complex particle model for inelastic collisions and compare with the standard MCC that has just been tested, and the phase-space kinetic solvers.

- (b) The overall approach is very synergetic; advanced methods for particle-based collisional-radiative models are also relevant to particle-fluid coupling (thermalization), particle transport (higher accuracy with extended particles), and hybrid MCC/kinetic solvers, as mentioned above.
- (c) The most urgent and key problems have been identified and are being systematically attacked; both the phase-space and Monte-Carlo methods can be used to provide the basis of a detailed non-Maxwellian collisional-radiative model and to study the dynamics of beam particles in dense media. This non-Maxwellian model will extend the fluid/Maxwellian model that is currently being developed (see next section).
- (d) There is parallel work being performed to develop a database and cross-section models, as explained in the next section. This is needed to guarantee consistency between the various levels of description, e.g. non-Maxwellian and Maxwellian models.
- (e) Further work is required for the transport problem; implementation of the grid-based tree method as described earlier; automatic grid adaptation for high dynamic gradients (based on tree-code method); incorporation of radiative coupling such as ponderomotive force and non-perturbative effects such as above-threshold-ionization; radiation transport (for which we will leverage an STTR effort).

We expect to continue work on the phase-space CR kinetics solver and investigate the implicit MCC described above in more detail.

While the implicit MCC offers a potentially intriguing solution to the problem at hand, the use of a phase-space kinetics solver is still very attractive due to its speed and easy handling of low densities, which would have poor statistical significance in a Monte-Carlo procedure. However, the discretized phase is impractical for particle transport except in the cases of lower-dimensionality problems. There is, however a third approach: hybridization of kinetic (phase-space) and Monte-Carlo/PIC method. This approach has been used in a restricted fashion by O. Batishchev at MIT, with whom we have been collaborating. In this approach, the kinetic phase space is generated on the spot from the set of existing particles in a PIC simulation, and all collisional processes are solved through the kinetic solver. This has two main advantages (a) an implicit solver can readily be used, reducing the effective stiffness of the problem; (b) gradual changes in population densities can be computed, eliminating the problem of potentially unphysical results (see discussion below). The disadvantages are the additional cost of mapping the particles to the phase space and back (presumably more than compensated by using a kinetic solver instead of an MCC), and statistical noise generated during the mapping process (a finite number of particles having a limited amount of information, and a slow statistical convergence as  $1/\sqrt{N}$ ). The latter issue could potentially be alleviated by using complex particles, with internal distribution function and variable statistical weight. Alternatively, we can use multiple samplings of the phase-space and multiple “histories” of the particle trajectories, thus smoothing out statistical fluctuations and allowing higher precision on populations with low statistics. This will be examined as a high-priority item in the future.

## 9. Conclusions and Future Work

As explained in the executive summary, this report is a preliminary document regarding the work performed under the lab-task on hybrid modeling, and was principally concerned with the investigation of some fundamental techniques to advance the state of the art in complex, multi-physics simulations of non-equilibrium plasma. Considerable progress has been made in several areas, but the work remains incomplete. To summarize the accomplishments:

- We have developed a new object-oriented software infrastructure in Java, easily parallelized and applicable to any platform including heterogeneous computing. The platform is complete with in-house real-time, 3D visualization and preliminary GUI to facilitate problem set-up. The data-structures are flexible and can easily accommodate future extensions to more complex problems.
- We have developed a Lagrangian method and used it to study the dynamics of the space charge layer and explosive emission in a model pseudospark discharge.
- We have investigated several, finite-volume numerical schemes for CFD and developed a compact 3<sup>rd</sup>-order scheme which provides an optimal balance between accuracy and stability, yields excellent resolution of contact discontinuities, and has been thoroughly validated. The scheme was extended to ideal 2T-MHD equations and to the Collisional-Radiative equations for atomic plasma. Details of the numerical scheme are provided in Appendix E.
- We have validated the Collisional-Radiative fluid model against a series of experiments and proven that the mechanism behind fluctuations of the dynamics of ionizing shock waves in noble gases can be explained by the theory of detonation cells.
- We have developed a preliminary version of a multi-fluid scheme, with implicit coupling of the electron fluid motion and electrostatic fields.
- We have developed and implemented a basic hybrid model with an electrostatic PIC model and a simple MCC algorithm for ionization to test the fundamental issues with hybridization.
- We have developed a new algorithm for particle merging that for the first time, simultaneously conserves mass, momentum and energy, allowing control of the number of particles.
- We have developed a new algorithm that computes particle trajectories in the highly magnetized case rapidly and accurately when E and B fields are both present.
- We have developed a basic MCC procedure for Collisional-Radiative kinetics, verified it and proven the corresponding H-theorem for plasma with excitation and ionization reactions.
- We have developed an implicit kinetics solver for non-Maxwellian collisional-radiative kinetics using discretized energy phase space (another first) that works with non-uniform gridding and guarantees energy conservation in a single step.
- We have performed preliminary tests of GPU acceleration by porting some key algorithms and examined performance results to better understand how to maximize the impact of GPU programming on future large-scale simulations.

There are, however, some remaining issues and work to complete. In the near-future, we propose to accomplish the following:

1. Extend the CR fluid code to include the complete MHD physics (resistive and Hall) in 3D.
2. Extend the CR fluid code to include molecular plasma; this work will be accomplished in collaboration with VKI.
3. Implement the fluid code and Maxwellian kinetics on the GPU.
4. Complete the phase-space discretized solver for non-Maxwellian CR kinetics by adding elastic collisions and implement procedures to minimize memory requirements; the latter will allow future generalization to non-isotropic distribution functions.
5. Complete the particle merging algorithm by adding automatic generation of discretized VDF to improve sampling of candidate particles for merging (using an octree algorithm);



- this will considerably generalize the applicability of the scheme and prevent artificial thermalization in some conditions.
6. Complete the particle-push algorithm for magnetized conditions in E and B fields to allow smooth variation of fields; this algorithm can then be used to efficiently study a wide range of magnetized plasma conditions with PIC, such as magnetic mirrors and cusped field thrusters.
  7. Finally, implement the improved PIC, the phase-space kinetics solver and the MHD fluid code into a new version of the multi-D hybrid code, and demonstrate it on a generic discharge (e.g. beam energy deposition or pseudospark).

This program is mostly aimed at completing the items already initiated in this lab-task. Other issues, e.g. the implicit MCC technique, the micro-VDF, the multi-fluid algorithms, may be investigated as well by leveraging other activities or another research task.

The fluid-PIC hybridization we have been focusing about implies that there exists a plasma component that is close to equilibrium (the “cold” fluid). In some cases, the dense bulk may not be describable by a fluid model. This is the case for example of high energy plasma obtained from ultra-intense, ultra-fast laser interactions. There may even be an additional “hot” component, which characteristic energy well beyond the range of the bulk plasma. This is the case, for example, of fusion products. We have been able to investigate some aspects of this problem with standard PIC techniques (see Appendix G), but the limitations of the approach are very clear: multiple scales, spatial (unresolved Debye length) and temporal (hot particles move on much smaller time scales). The same problem occurs here, i.e. the hot electrons (modeled by a PIC method) have much faster dynamics than the bulk fluid. Inevitably, we need to investigate advanced multi-scale methods, which would be the subject of a different research effort.

## 10. References

- [1] C. K. Birdsall and A. B. Langdon, *Plasma Physics via Computer Simulation*, Institute of Physics publ., 1991.
- [2] G.A. Bird, *Molecular Gas Dynamics and the Direct Simulation of Gas Flows*, Oxford Univ. Press, 1994.
- [3] P. Balbuena, J. Seminario eds., *Molecular Dynamics: From Classical to Quantum Methods*, Elsevier, Amsterdam, 1999.
- [4] H. Risken, *The Fokker-Planck Equation*, Springer-Verlag, Berlin, 1996.
- [5] J.-L. Cambier, "Numerical Methods for TVD Transport and Coupled Relaxing Processes in Gases and Plasmas," AIAA 90-1464.
- [6] J. L. Cambier. M. Carroll and M. Kapper, "Development of a Hybrid Model for Non-Equilibrium High Energy Plasmas," AIAA 2004-2166
- [7] J.-L. Cambier, "Numerical Simulations of a non-equilibrium Argon plasma in a shock-tube experiment," AIAA 91-1464
- [8] M. Gundersen and G. Schaefer eds. , *Physics and Applications of Pseudosparks*, NATO ASI Series, vol. **219**, Plenum Press, New-York (1990).
- [9] G. Mourou and D. Umstadter, *Scientific American*, May 2002.
- [10] A.A. Kulikovskiy, *J. Phys.* **D33**, 1514 (2000); A. Luque, U Ebert, C. Montijn and W. Hundsdoerfer, *Appl. Phys. Lett.* **90**, 081501 (2007)
- [11] Y. Wang et al., *Phys. Rev.* **E72**, 026413 (2005)
- [12] V. D. Bochkov et al., *IEEE Trans. Plasma Sci.*, **29**, 802-808 (2001).
- [13] R. Stark et al., *IEEE Trans. Plasma Sci.*, **23**(3), 258 (1995).
- [14] K. K. Jain and P. K. Sharma, *App. Phys. Lett.* **62**, 1466-1468, (1993).
- [15] C.G. Cain et al., *Rev. Sci. Instrum.* **71**, 675-677 (2000).
- [16] W. Bauer et al, *Proc. 6<sup>th</sup> Pulsed Power Conf.* (Arlington, VA), 1987, B. Bernstein and P. Turchi eds.
- [17] A. W. Cross et al., *J. Phys.* **D40**, 1953 (2007)
- [18] J.-P. Boeuf, L. C. Pitchford, *IEEE Trans. Plasma Sci.*, vol. **19**, No 2 (1991), 286.
- [19] W. Hartmann and M. A. Gundersen, *Phys. Rev. Lett.* **60**, 2371-2374 (1988)
- [20] A. Anders, S. Anders, M. A. Gundersen and A. M. Martsinovskii, *IEEE Trans. Plasma Sci.*, **23** 275-282 (1995).
- [21] G.A. Mesyats, *Physics-Uspekhi* **38**(6), 567-591 (1995)
- [22] P. Maine, D. Strickland, P. Bado, M. Pessot, and G. Mourou, *IEEE J. Quantum Electron.* **24**, 398 (1988)
- [23] D. Umstadter, *Phys. of Plasmas* **8**, 1774 (2001)
- [24] J. Zweibak et al., *Phys. of Plasmas* **9**, 3108 (1997).
- [25] M. E. Jones et al., *J. Comp. Phys.*, **123**, 169 (1996)
- [26] D. J. Larson, *J. Comp. Phys.*, **188**, 123 (2003)
- [27] D. W. Hewett, *J. Comp. Phys.* **189**, 390 (2003).
- [28] <http://www.txcorp.com/products/VORPAL/>
- [29] J. Hauser et al., "A Pure Java Parallel Flow Solver," AIAA paper 99-0549.
- [30] S. Markidis, G. Lapenta and W. B. Vanderheyden, "Parsek: Object Oriented particle-in-Cell Implementation and performance Issues," Proc. 2002 Joint CM-ISCOPE Conf. on Java Grande, Seattle, Wa (2002)
- [31] <http://www.philippsen.com/JGI2001/finalpapers/18500143.pdf>; see also Proceedings of the ACM Workshop on Java for High Performance Network Computing, Stanford University, Palo-Alto, CA, Feb. 28-Mar-1, 1998;
- [32] D. Genovesi and L. Long, [A Java-Based Direct Monte Carlo Simulation of a Nano- Scale Pulse Detonation Engine](#) 23rd Rarefied Gas Dynamics Conf., Whistler, BC, Canada, July, 2002.
- [33] <http://math.nist.gov/scimark>; J. P. Lewis and U. Neumann, "Performance of Java versus C++," <http://www.idiom.com/~zilla/Computer/JavaCbenchmark.html>. J. M. Moreira et al., IBM Research report RC 21166; J. M. Moreira et al., IBM Research report RC 21255; J.M. Moreira et al., *IBM Systems Journal* **39** (2000).

- [34] <http://java.sun.com/javase/technologies/core/basic/rmi/index.jsp>
- [35] <http://www.ssec.wisc.edu/~billh/visad.html>
- [36] <http://www.java3d.org/>
- [37] [http://www.nvidia.com/object/cuda\\_home\\_new.html](http://www.nvidia.com/object/cuda_home_new.html)
- [38] J.P. Boris, *Proc. 4<sup>th</sup> Conf. Num. Simulations of Plasma*, pp. 3-67, J.P. Boris and R.A. Shanny eds., Naval Res. Lab., Washington D.C., Nov. 1970.
- [39] P. Roe, *Ann Rev. Fluid Mech.* **18**, 337 (1986).
- [40] S. Godunov, *Math. Sb.* **47**, 271 (1959).
- [41] Y. Zeldovich and Y. Raizer, *Physics of Shock Waves and High Temperature Hydrodynamic Phenomena*, vol. II, Academic Press, New-York, 1967.
- [42] H. S. Reksoprodjo and R. Agarwal, "A Kinetic Scheme for Numerical Solution of Ideal Magnetohydrodynamics Equations with a Bi-Temperature Model," AIAA 2000-0448.
- [43] A. Harten, *J. Comp. Physics* **49**, 357 (1983).
- [44] J. U. Brackbill and D. C. Barnes, *J. Comp. Phys.* **35**, 426 (1980)
- [45] K. G. Powell et al., *J. Comp. Phys.* **154**, 284 (1999)
- [46] G. Toth, *J. Comp. Phys.* **161**, 605 (2000)
- [47] X-D Liu, S. Osher and T. Chan, *J. Comp. Phys.* **115**, 200 (1994)
- [48] P. Colella and P. R. Woodward, *J. Comp. Phys.* **54**, 174 (1984)
- [49] <http://amroc.sourceforge.net>
- [50] <http://flash.uchicago.edu/website/home/>
- [51] M. Brio and C. C. Wu, *J. Comp. Phys.* **75**, 400 (1987)
- [52] A. Orszag and C. M. Tang, *J. Fluid Mech.* **90**, 129 (1979)
- [53] M. van Dyke, *An Album of Fluid Motion*, Parabolic Press, Stanford, 1982.
- [54] C-W Shu and S. Osher, *J. Comp. Phys.* **145**, 458 (1998)
- [55] H. T. Huynh, *SIAM J. Num. Analysis* **32**(5), 1565 (1995)
- [56] S. I. Braginskii, in *Review of Plasma Physics*, vol. 1, ed. M. A. Leontovich, Consultants Bureau, New-York, 1965.
- [57] A. Decoster et al., *Modeling of Collisions*, Elsevier, Amsterdam, 1998.
- [58] P. Segur et al., *Plasma Sources Sci. Techn.* **15**(4), 648 (2006)
- [59] A. Bourdon et al., *Plasma Sources Sci. Techn.* **16**(3), 656 (2007)
- [60] Y-K Kim, *Phys. Rev.* **A50**(5), 3954 (1994)
- [61] Y-K Kim, *Phys. Rev.* **A64**, 032713 (2001)
- [62] J. Vlček, *J. of Phys.* D22, 623 (1989)
- [63] I. I. Glass and W. S. Liu, *J. Fluid Mech.* **84**, 55 (1978)
- [64] R. L. Alpert and T. Y. Toong, *Acta Astronautica* **17**, 538 (1972)
- [65] A. Gülhan et al., *J. Spacecraft & Rockets* **46**(2), 274 (2009)
- [66] H. Yoshida, *Phys. Lett.* **A150**, 262 (1990).
- [67] F. Assous, T. Pougeard-Dulimbert, J. Segre, *J. Comp. Phys.* **187**, 550 (2003).
- [68] T. Bagdonat and U. Motschmann, *J. Comp. Phys.* **183**, 470 (2002).
- [69] A. V. Kozyrev et al., *J. Appl. Phys.* **74** (1993), 5366 (1993).
- [70] R. C. Davidson, *Introduction to the Physics of Nonneutral Plasmas*, Addison-Wesley,
- [71] P. V. Akimov et al., *Phys. Plasmas* **8**, 3788 (2001).
- [72] P.V. Akimov and H. Schamel, *J. App. Phys.* **92**, 1690 (2002).
- [73] G. G. M. Coppa et al., *J. Comp. Phys.* **127**, 268 (1996)
- [74] A. J. Christlieb, R. Krasny and J. P. Verboncoeur, *IEEE Trans. Plasma Sci.* **32** (2004), 384-389
- [75] J. Barnes and P. Hut, *Nature*, vol. **324** (1986), pp. 446-449.
- [76] U. Shumlak, J. Loverich, *J. Comp. Phys.* **187**, 620 (2003).

This page intentionally blank

## Appendix A: Multi-Fluid Algorithm

Consider the conservation equations for density and momentum only in one -direction:

$$\partial_t n + \partial_x(nu) = 0 \quad (\text{A1})$$

$$\partial_t(nu) + \partial_x(nu^2 + p_e/m_e) = 0 \quad (\text{A2})$$

define an eigenvalue:  $c_e^2 = kT_e / m_e$  which is the speed of sound in an isothermal gas. Then (A1) and (A2) can be written as  $\partial_t Q + \partial_x F = 0$ , where  $Q$  is the vector of conserved variables and  $F$  is the flux in conservative form:

$$\partial_t \begin{pmatrix} n \\ nu \end{pmatrix} + \partial_x \begin{pmatrix} nu \\ n(u^2 + c_e^2) \end{pmatrix} = 0 \quad (\text{A3})$$

We define the transformation matrices:

$$X = \begin{bmatrix} -\frac{u-c}{2c} & +\frac{1}{2c} \\ +\frac{u+c}{2c} & -\frac{1}{2c} \end{bmatrix} \quad (\text{A4a})$$

$$X^{-1} = \begin{bmatrix} 1 & 1 \\ u+c & u-c \end{bmatrix} \quad (\text{A4b})$$

and the diagonal eigenvalue matrix:

$$\Lambda = \begin{bmatrix} u+c & 0 \\ 0 & u-c \end{bmatrix} \quad (\text{A4c})$$

The Jacobian of the system (A3) is obtained as:  $A = X^{-1} \cdot \Lambda \cdot X$ . The characteristic jumps are:

$$\alpha = X \cdot \Delta Q = \begin{pmatrix} -\left(\frac{u-c}{2c}\right)\Delta n + \frac{\Delta(nu)}{2c} \\ +\left(\frac{u+c}{2c}\right)\Delta n - \frac{\Delta(nu)}{2c} \end{pmatrix} \quad (\text{A5})$$

In order to construct a Godunov scheme that uses flux-limiters on the characteristic variables, it is necessary to verify that: (a)  $\Delta Q = X^{-1} \cdot \alpha$ ; and (b)  $\Delta F = X^{-1} \cdot \Lambda \cdot \alpha$ . The first relation is trivial to verify. For the second, we first note that:

$$\Lambda \cdot \alpha = \begin{pmatrix} -\frac{u^2-c^2}{2c}\Delta n + \frac{u+c}{2c}\Delta(nu) \\ +\frac{u^2-c^2}{2c}\Delta n - \frac{u-c}{2c}\Delta(nu) \end{pmatrix} \quad (\text{A6})$$

Then, after some algebra:

$$X^{-1} \cdot \Lambda \cdot \alpha = \begin{pmatrix} \Delta(nu) \\ -(u^2-c^2)\Delta n + 2u\Delta(nu) \end{pmatrix} = \begin{pmatrix} \Delta(nu) \\ \Delta(nu^2) + c^2\Delta n \end{pmatrix} \quad (\text{A7})$$

The second term is equal to the flux component of (A3) as long as  $c^2$  is invariant, in which case  $c^2\Delta n \equiv \Delta(nc^2)$ . This is true because the system (A1-A2) describes an isothermal gas: the pressure is controlled by the temperature, which is an external variable here: there is no equation of state (EOS) that determines the temperature from only  $n, u$ , and there is no conservation equation for the energy or pressure. The system can be generalized to more than one dimension, where (A2) extends to:

$$\partial_t(nu^\alpha) + \partial_\beta(nu^\alpha u^\beta + \delta^{\alpha\beta} p_e/m_e) = 0 \quad (\text{A8})$$

The system (A3) becomes:

$$\partial_t \begin{pmatrix} n \\ nu_x \\ nu_y \\ nu_z \end{pmatrix} + \partial_x \begin{pmatrix} nu_x \\ n(u_x^2 + c^2) \\ nu_x u_y \\ nu_x u_z \end{pmatrix} + \partial_y \begin{pmatrix} nu_y \\ nu_x u_y \\ n(u_y^2 + c^2) \\ nu_y u_z \end{pmatrix} + \partial_z \begin{pmatrix} nu_z \\ nu_x u_z \\ nu_y u_z \\ n(u_z^2 + c^2) \end{pmatrix} = 0 \quad (\text{A9})$$

The flux along a direction  $\hat{n}$  (with  $\hat{t}, \hat{s}$  the correspondingly rotated unit vectors normal to  $\hat{n}$ ) can be obtained through the following matrix definitions:

$$X = \begin{bmatrix} -\frac{(u_n - c)}{2c} & \frac{\hat{n}_x}{2c} & \frac{\hat{n}_y}{2c} & \frac{\hat{n}_z}{2c} \\ +\frac{(u_n + c)}{2c} & -\frac{\hat{n}_x}{2c} & -\frac{\hat{n}_y}{2c} & -\frac{\hat{n}_z}{2c} \\ -u_t & \hat{t}_x & \hat{t}_y & \hat{t}_z \\ -u_s & \hat{s}_x & \hat{s}_y & \hat{s}_z \end{bmatrix} \quad (\text{A10a})$$

$$X^{-1} = \begin{bmatrix} 1 & 1 & 0 & 0 \\ u_x + \hat{n}_x c & u_x - \hat{n}_x c & \hat{t}_x & \hat{s}_x \\ u_y + \hat{n}_y c & u_y - \hat{n}_y c & \hat{t}_y & \hat{s}_y \\ u_z + \hat{n}_z c & u_z - \hat{n}_z c & \hat{t}_z & \hat{s}_z \end{bmatrix} \quad (\text{A10b})$$

and the eigenvalue matrix is:

$$\Lambda = \begin{bmatrix} u_n + c & 0 & 0 & 0 \\ 0 & u_n + c & 0 & 0 \\ 0 & 0 & u_n & 0 \\ 0 & 0 & 0 & u_n \end{bmatrix} \quad (\text{A10c})$$

With these matrices, the flux-limited solver can be constructed. An implicit algorithm can also be constructed, such that:

$$\begin{bmatrix} \ddots & \ddots & 0 & 0 \\ -A_{i-1}^+ & I + A_i^+ - A_i^- & A_{i+1}^- & 0 \\ 0 & -A_{i-1}^+ & I + A_i^+ - A_i^- & A_{i+1}^- \\ 0 & 0 & \ddots & \ddots \end{bmatrix} \cdot \begin{bmatrix} \delta Q_{i-1} \\ \delta Q_i \\ \delta Q_{i+1} \end{bmatrix} = \begin{bmatrix} \Delta F_{i-2} \\ \Delta F_{i-1} \\ \Delta F_i \\ \Delta F_{i+1} \end{bmatrix} \quad (\text{A11})$$

where  $A^+, A^-$  are the Jacobians for positive and negative eigenvalues only. They are constructed by  $A^\pm = X^{-1} \cdot \Lambda^\pm \cdot X$ , with:  $\Lambda^+ = \{\dots, \max(0, \lambda^a), \dots\}$ , and  $\Lambda^- = \{\dots, \min(0, \lambda^a), \dots\}$ .

We can now turn our attention to the right-hand sides of the conservation equations, which have been ignored so far. We will consider first the electrostatic approximation, which implies that only an electric field is present, and all magnetic fields can be neglected. The conservation equation (A1) does not change, but the momentum equation is now:

$$\partial_t(n_e u_e^\alpha) + \partial_\beta \left( n_e u_e^\alpha u_e^\beta + n_e \frac{kT_e}{m_e} \right) = -\frac{e}{m_e} E^\alpha + \frac{(R_T^\alpha + R_U^\alpha)}{m_e} \quad (\text{A12})$$

where  $\vec{R}_T \approx -0.71 \cdot n_e \vec{\nabla}(kT_e)$  is a thermal force and

$$\vec{R}_U = m_e n_e \cdot \left[ \nu_{en} (\vec{U}_n - \vec{u}_e) + \nu_{ei} (\vec{U}_i - \vec{u}_e) \right] \quad (\text{A13})$$

is the frictional force and  $\nu_{en}, \nu_{ei}$  are the collisional frequencies for momentum exchange. The latter can be simplified when the ions and neutrals are both at the same velocity  $\vec{U}$ ; if the plasma is at sufficiently low density for an ion-slip to occur, the approach described below can easily be extended to the more general case. For simplification, we also neglect the thermal force, which can also be easily added later on.

The second term on the left-hand-side is the advection term which was treated in the previous section. The contributions of each term on the RHS can be examined one by one. The easiest is the collisional momentum exchange. One can write this contribution as follows:

$$\delta(n_e \vec{u}_e^\alpha) = \delta t \cdot \nu_{eh} [n_e U^\alpha - (n_e u_e^\alpha)] \quad (\text{A14})$$

Evaluating terms on the RHS at the *advanced* time level will yield:

$$\delta(n_e u_e^\alpha) = \delta t \cdot \nu_{eh} [n_e U^\alpha - (n_e u_e^\alpha)] + (\delta t \cdot \nu_{eh} U^\alpha) \delta n_e - (\delta t \cdot \nu_{eh}) \delta(n_e u_e^\alpha) \quad (\text{A15})$$

The term involving the electric field can be written in a similar form,

$$\delta(n_e u_e^\alpha) = -\delta t \frac{e}{m_e} n_e E^\alpha - \delta t \frac{e}{m_e} n_e \cdot \delta E^\alpha - \delta t \frac{e}{m_e} E^\alpha \delta n_e \quad (\text{A16})$$

and we need only to express the change in the electric field. Using one of Maxwell's equations:

$$\epsilon_o \frac{\partial \vec{E}}{\partial t} + \vec{j} = \frac{\vec{\nabla} \times \vec{B}}{\mu_o} \quad (\text{A17})$$

and neglecting the magnetic field (electrostatic approximation), this leads to:

$$\epsilon_o \partial_t E^\alpha = -e(Z_i n_i U_i^\alpha - n_e u_e^\alpha) \quad (\text{A18})$$

Again, expressing the RHS at the advanced time level yields:

$$\delta E^\alpha = -\frac{e}{\epsilon_o} \delta t (Z_i n_i U_i^\alpha - n_e u_e^\alpha) + \frac{e}{\epsilon_o} \delta t \delta(n_e u_e^\alpha) \quad (\text{A19})$$

One can therefore construct a point-implicit solution of the form:

$$\begin{bmatrix} 1 & 0 & 0 \\ +\frac{eE^\alpha \delta t}{m_e} - \delta t \cdot \nu_{eh} U^\alpha & 1 + \delta t \cdot \nu_{eh} & +\frac{en_e \delta t}{m_e} \\ 0 & -e\delta t/\epsilon_o & 1 \end{bmatrix} \otimes \begin{pmatrix} \delta n_e \\ \delta(n_e u_e^\alpha) \\ \delta E^\alpha \end{pmatrix} = \begin{pmatrix} 0 \\ \delta t \cdot \nu_{eh} n_e (U^\alpha - u_e^\alpha) - \frac{en_e \delta t}{m_e} E^\alpha \\ -e\delta t/\epsilon_o (Z_i n_i U_i^\alpha - n_e u_e^\alpha) \end{pmatrix} \quad (\text{A20})$$

Note that this is a point-implicit part due to the Taylor expansion of the RHS. One should also include the advection process, i.e. the matrices defined in (A11). Without the energy conservation equation, this would lead to a 7x7 matrix system: 3(momentum) + 3(electric field) + 1(density). However, since the evolution of the electric field does not involve neighboring points, it would be simpler to solve for the change in electric field, and include this solution into the evolution of the momentum. Inserting (A19) into (A16), we obtain:

$$[1 + \omega_{pe}^2 \delta t^2] \cdot \delta(n_e u_e^\alpha) = -\left(\frac{e\delta t}{m_e}\right) n_e E^\alpha + \omega_{pe}^2 \delta t^2 (Z_i n_i U_i^\alpha - n_e u_e^\alpha) - \left(\frac{e\delta t}{m_e}\right) E^\alpha \delta n_e \quad (\text{A21})$$

and using  $J^\alpha = e(Z_i n_i U_i^\alpha - n_e u_e^\alpha)$ , (A20) becomes:

$$\begin{bmatrix} 1 & 0 \\ +\frac{e\delta t}{m_e} E^\alpha - \delta t \cdot \nu_{eh} U^\alpha & 1 + \nu_{eh} \delta t + \omega_{pe}^2 \delta t^2 \end{bmatrix} \otimes \begin{pmatrix} \delta n_e \\ \delta(n_e u_e^\alpha) \end{pmatrix} = \begin{pmatrix} 0 \\ -\frac{e\delta t}{m_e} n_e E^\alpha + \omega_{pe}^2 \delta t^2 \left(\frac{J^\alpha}{e}\right) \end{pmatrix} \quad (\text{A22})$$

This page intentionally blank



## Appendix B: Pseudospark Analytical Model

Consider the flow in the planar diode with a gap  $L$ , with  $\Phi = 0$  on the left side (cathode), and  $\Phi = +V_o$  on the right-side (anode). Let us now consider a cold fluid ( $T_e \equiv 0$ ) model without ionization and without elastic losses ( $v_m \equiv 0, v^i \equiv 0, v^r \equiv 0$ ). The conservation equations

$$\frac{\partial n_e}{\partial t} + \frac{\partial}{\partial x}(n_e u_e^x) = 0 \quad (B1)$$

$$\frac{\partial(n_e u_e^x)}{\partial t} + \frac{\partial}{\partial x}(n_e u_e^x u_e^x) = -\frac{e}{m_e} n_e E^x \quad (B2)$$

along with Poisson's equation for the electro-static field:

$$\vec{\nabla} \cdot \vec{E} = \varepsilon_o e (\bar{Z}_i n_i - n_e) \quad (B3)$$

describe the evolution of the system. Using  $\vec{E} = -\vec{\nabla}\Phi$  the steady-state solution is given by:

$$\frac{\partial^2}{\partial x^2} \Phi = e \varepsilon_o n_e \quad (B4)$$

$$n_e u_e^x = -\frac{j_e}{e} = C^{te} \quad (B5)$$

$$n_e m_e u_e^x \frac{\partial u_e^x}{\partial x} = +e \frac{\partial \Phi}{\partial x} \quad (B6)$$

The latter can be integrated to yield:

$$\varepsilon_e^T = \frac{1}{2} m_e (u_e^x)^2 - e \Phi = C^{te} \quad (B7)$$

The value of this constant can be estimated by considering the emission process at the cathode, where  $\Phi \equiv 0$ . The electrons within the cathode have to overcome a potential barrier (the work function), and this potential energy becomes the electron kinetic energy away from the cathode surface. Therefore, the constant is approximately equal to the work function  $eW$ . In the case of space-charge limited flow (see [70], Chap. 8), the work function is assumed to be  $W \equiv 0$ , and the cathode is an unlimited supply of electrons. The physical basis for this approximation relies on explosive electron emission from micro-tips. If we denote the spatial derivative of the potential as  $\Phi' \equiv d\Phi/dx$ , Poisson's equation becomes:

$$\Phi'' = -j_e \varepsilon_o \left[ \frac{m_e}{2e(\Phi + W)} \right]^{1/2} \quad (B8)$$

Multiplying (B8) by  $\Phi'$  and integrating, we obtain:

$$\frac{1}{2} (\Phi')^2 = \frac{1}{2} (\Phi'|_0)^2 - j_e \varepsilon_o \left( \frac{2m_e}{e} \right)^{1/2} [(\Phi + W)^{1/2} - W^{1/2}] \quad (B9)$$

In the case of unlimited electron emission  $W \equiv 0$  and the electric field at the cathode is assumed to be vanishing, i.e.  $\Phi'|_0 = 0$ . In that case, (B9) can be integrated to yield:

$$\Phi(x) = \left[ -\frac{9j_e \varepsilon_o}{8} \left( \frac{2m_e}{e} \right)^{1/2} L^2 \right]^{2/3} \left( \frac{x}{L} \right)^{4/3} \quad (B10)$$

Enforcing  $\Phi(L) = V_o$ , one can invert (B10) to obtain the current density:

$$j_e^{CL} = \frac{4}{9\varepsilon_o} \left( \frac{2e}{m_e} \right)^{1/2} \frac{V_o^{3/2}}{L^2} \quad (B11)$$

This is the Child-Langmuir (CL) current density, obtained for steady-state, space-limited vacuum discharges with infinite cathode emissivity. Given the spatial dependence (B10) of the electrostatic potential, solving Poisson's equation for the electron density yields:

$$n_e^{CL} = \frac{4}{9} \frac{V_o}{e\epsilon_o L^2} \left( \frac{x}{L} \right)^{-2/3} \quad (B12)$$

Equations (B11) and (B12) can also be used to determine the electron velocity profile. Note that the density becomes infinite as  $x \rightarrow 0$  in (B12). This is because in the CL model the electrons are injected at zero velocity, while the electron current density is assumed constant. In a real world scenario, at least one of these assumptions is broken.

The KKRS model extends the CL solution by including ionization. The continuity equation for the ion density is:

$$\frac{\partial n_i}{\partial t} + \vec{\nabla}(n_i \vec{u}_i) = \nu^i n_n - \nu^r n_i \quad (B13)$$

Kozyrev *et al.* assume that the ion density is independent of space. In that case, one can integrate (B13) with respect to  $x$  and obtain a time-dependence only of the gap-averaged ion density:

$$\frac{\partial \bar{n}_i}{\partial t} + \frac{\bar{n}_i}{d} \left( \frac{2\bar{Z}_i e}{M} V_o \right)^{1/2} = n_h n_e <\sigma^i v> - \nu^r \bar{n}_i \quad (B14)$$

The ionization term (first on the RHS) can be approximated, for a cold electron fluid, as:

$$<\sigma^i v> \approx \bar{\sigma}^i u_e \quad (B15)$$

and (B14) can be re-written as:  $\frac{\partial \bar{n}_i}{\partial t} + \frac{\bar{n}_i}{\tau_o} = n_h \bar{\sigma}^i \left( -\frac{j_e}{e} \right)$  (B16)

with  $\tau_o^{-1} = \left( \frac{2\bar{Z}_i e}{M} \frac{V_o}{L^2} \right)^{1/2} + \nu^r$  (B17)

Since  $j_e < 0$  the term on the RHS of (B16) is a positive source. The solution of (B16) is:

$$\bar{n}_i(t) = \left( -\frac{n_h \bar{\sigma}^i}{e} \right) e^{-t/\tau_o} \int_0^t dt' e^{+t'/\tau_o} j_e(t') \quad (B18)$$

The electron density in the KKRS model is then obtained from the Child-Langmuir value. Using (B11) and (B12), one can write the electron density profile as:

$$n_e^{CL} = \frac{1}{e} \left( \frac{2m_e}{9e\epsilon_o} \right)^{1/3} \left( \frac{j_e}{x} \right)^{2/3} \quad (B19)$$

Both solutions for the ion and electron densities can now be entered into Poisson's equation:

$$\frac{\partial^2 \Phi}{\partial x^2} = \epsilon_o \left( \frac{2m_e}{9e\epsilon_o} \right) \left( \frac{j_e(t)}{x} \right)^{2/3} + (n_h \bar{\sigma}^i \bar{Z}_i \epsilon_o) e^{-t/\tau_o} \int_0^t dt' e^{+t'/\tau_o} j_e(t') \quad (B20)$$

After normalization:  $\Phi = V_o \phi$  ;  $x = L\xi$  ;  $t = \tau_o \zeta$  ;  $j_e = j_e^{CL} \iota_e$  we have:

$$\frac{\partial^2 \phi}{\partial \xi^2} = \frac{4}{9} \left[ \left( \frac{\iota_e}{\xi} \right)^{2/3} - A e^{-\zeta} \int_0^\zeta \iota_e(\zeta') e^{\zeta'} d\zeta' \right] \quad (B21)$$

with:

$$A = \bar{\sigma}^i n_h L \left( \frac{\bar{Z}_i M}{m_e} \right)^{1/2} \frac{1}{1 + \nu^r \left( \frac{2 \bar{Z}_i e V_o}{M L^2} \right)^{-1}} \quad (\text{B22})$$

Equation (B21) is similar to equation (10) of [69], except that here the constant  $A$  includes an additional term due to recombination. Following KKRS, integration of (B21) yields the solution:

$$\varphi = t_e^{2/3} \xi^{4/3} - \frac{2}{9} A \xi^2 e^{-\xi} \int_0^\xi t_e(\xi') e^{\xi'} d\xi' \quad (\text{B23})$$

Taking the value at the anode ( $\varphi(l) = 1$ ) and differentiating with respect to time:

$$\frac{\partial}{\partial \xi} (t_e^{2/3}) = \frac{2A}{9} t_e - t_e^{2/3} + 1 \quad (\text{B24})$$

Again following the analysis by KKRS, one can observe that the normalized current density can grow indefinitely with time, signaling the breakdown and pseudospark initiation. This occurs when  $A > \sqrt{3}$ , or when the density is above a critical value (neglecting the recombination frequency):

$$n > n_{cr} = \left( \frac{3m}{\bar{Z}_i M} \right)^{1/2} (\bar{\sigma}^i L)^{-1} \quad (\text{B25})$$

The physical interpretation is as follows: when the ionization process is sufficiently large compared to the ion removal rate, there is an excess positive charge being built-up in the discharge gap. The electrostatic potential has a maximum at some location within the gap and the electric field is correspondingly increased, which in turn increases the electron current density.

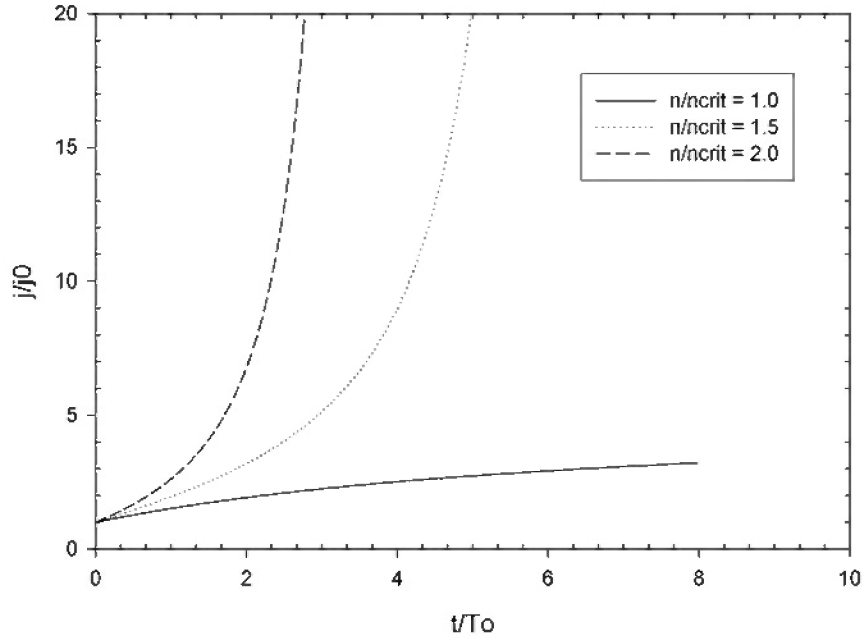


**Figure B-1:** Non-dimensional current density solution versus time for three cases of gas density in inter-electrode gap.

The non-dimensional current is shown in Figure B-1. Here we see that for  $n > n_{cr}$  a discharge is formed in the gap and the current increases faster than exponentially, the asymptote occurring closer to the cathode the higher the density is that the critical density. The non-dimensional potential is shown in Figures B-2a/c. In Figure B-2a,  $n = n_{cr}$  and we see a monotonic increase in potential through the gap from cathode to anode. In Figures B-2b and B-2c we see a non-monotonic potential variation through the gap with a potential maximum that increases with  $n/n_{cr}$ . Kozirev *et al.* [69] explain this region as being a result of the electrons having insufficient energy to overcome the potential barrier and reach the anode, thus producing a “potential trap” in the gap.

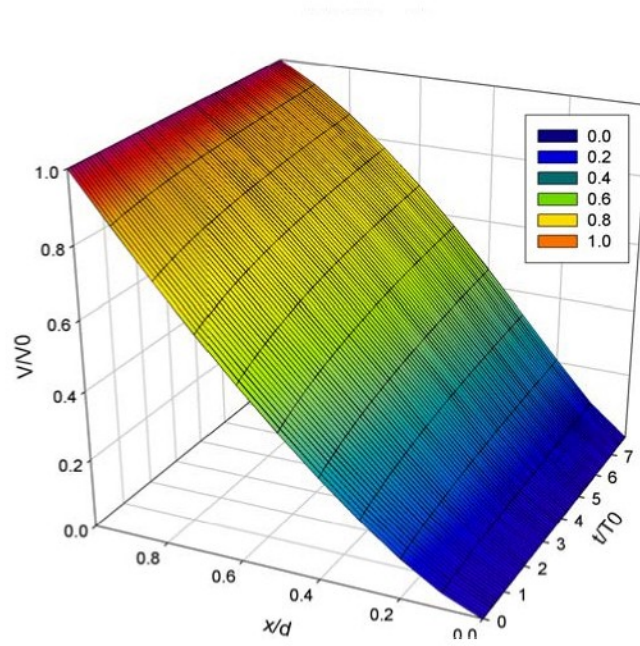


**Figure B-2a:** Non-dimensional electrostatic potential solution versus time and distance; 1<sup>st</sup> case of number density.

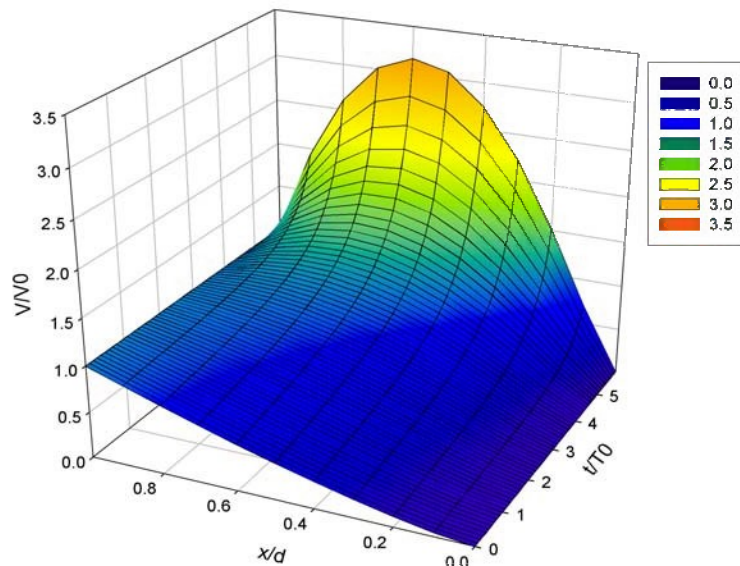


**Figure B-2b:** Non-dimensional electrostatic potential solution versus time and distance; 2<sup>nd</sup> case of number density.

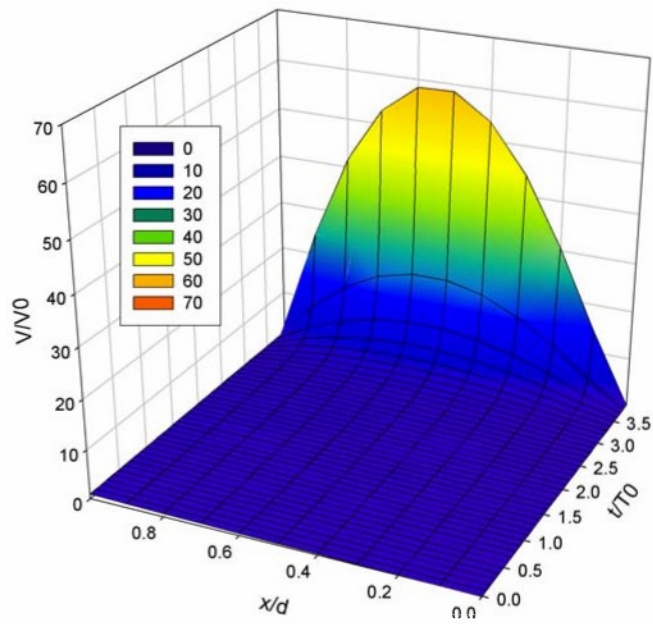


**Figure B-2c:** Non-dimensional electrostatic potential solution versus time and distance; 3<sup>rd</sup> case of number density.

This page intentionally blank

## Appendix C: Electron Fluid-Element Model

The basic equations to solve are:

$$\frac{\partial n_e}{\partial t} + \vec{\nabla} \cdot (n_e \vec{u}_e) = \dot{\Omega}_e \quad (C1)$$

$$\frac{\partial (n_e m_e u_e^\alpha)}{\partial t} + \nabla^\beta (p_e \delta_\beta^\alpha + n_e m_e u_e^\alpha u_e^\beta) = -en_e E^\alpha - n_e m_e v_m u_e^\alpha \quad (C2)$$

$$\begin{aligned} \frac{\partial}{\partial t} \left[ \frac{3}{2} n_e k T_e + \frac{n_e m_e u_e^2}{2} \right] + \nabla^\beta \left[ u_e^\beta \left( \frac{5}{2} n_e k T_e + \frac{n_e m_e u_e^2}{2} \right) \right] = \\ -en_e (E^\alpha u_e^\alpha) - n_e m_e v_m (u_e^\alpha u_e^\alpha) - \dot{\Omega}_e I \end{aligned} \quad (C3)$$

where  $\alpha = x, y, z$ ,  $\delta_\beta^\alpha$  is the Kronecker symbol and summation over repeated indices is assumed.

$I$  is the ionization potential and  $\dot{\Omega}_e$  is the rate of change of electron density due to ionization and recombination:

$$\dot{\Omega}_e = n_e n_n \langle \sigma^i v \rangle - n_e n_i \langle \sigma^r v \rangle = n_e (v^i - v^r) \quad (C4)$$

where  $\sigma^{i(r)}$  is the cross-section for ionization (recombination),  $v$  is the electron velocity and the brackets  $\langle \rangle$  denote statistical averaging. Combining the first two equations (C1-2) one obtains:

$$\frac{\partial u_e^\alpha}{\partial t} + u_e^\beta \nabla^\beta (u_e^\alpha) = -\frac{e}{m_e} E^\alpha - \frac{\nabla^\alpha p_e}{n_e m_e} - (v_m + v^i - v^r) u_e^\alpha \quad (C5)$$

The energy conservation equation (C4) can then be written as:

$$\frac{3}{2} \frac{k}{m_e} \frac{dT_e}{dt} + \frac{d}{dt} \left( \frac{u_e^2}{2} \right) = -\frac{e}{m_e} (E u_e) - \frac{\nabla^\alpha (p_e u_e^\alpha)}{n_e m_e} - v_m u_e^2 - (v^i - v^r) \left( \frac{u_e^2}{2} + \frac{I}{m_e} + \frac{3}{2} \frac{k T_e}{m_e} \right) \quad (C6)$$

where we have used the covariant derivative:

$$\frac{d}{dt} = \frac{\partial}{\partial t} + u_e^\alpha \nabla^\alpha \quad (C7)$$

The last term on the RHS of (C6) indicates the amount of energy (kinetic, potential and thermal) that is exchanged during ionization and recombination processes. Using (C5) one can extract an equation for the thermal energy alone, i.e.:

$$\begin{aligned} \frac{3}{2} \frac{k}{m_e} \frac{dT_e}{dt} = - \underbrace{\frac{p_e (\nabla^\alpha u_e^\alpha)}{n_e m_e}}_{\text{adiabatic heating}} + \underbrace{v_m \left( \frac{u_e^2}{2} \right)}_{\text{Ohmic heating}} - \underbrace{(v^i - v^r) \frac{k}{m_e} \left( \theta^i + \frac{3}{2} T_e \right)}_{\text{endo/exo-thermicity}} \end{aligned} \quad (C8)$$

Note that we have neglected the ion velocity, so that  $j \approx j_e = -en_e u_e$ .

Equations (C1), (C5) and (C8) fully describe the electrons as a fluid. In the case of negligible thermal energy, only (C1) and (C5) need to be solved and the pressure gradient in (C5) can be neglected. In the steady state, (C5) can be re-written as:

$$\frac{d}{dx} \varepsilon_e = -eE - \frac{1}{n_e} \frac{dp_e}{dx} - (v_m + v^i - v^r) (m_e u_e) \quad (C9)$$

where  $\varepsilon_e = m_e u_e^2 / 2$  and for simplification we have assumed variation with respect to only one spatial direction ( $x$ ).

Let us define the total non-thermal energy:  $\varepsilon_e^T = m_e u_e^2 / 2 - e\Phi$ , which includes the kinetic and potential energies,  $\vec{v} = v_m + v^i - v^r$  and a time scale  $d\tau = dx / u_e$ . Equation (C9) becomes:

$$\frac{d\varepsilon_e^T}{dx} = -\bar{v} \left[ 2m_e (\varepsilon_e^T + e\Phi) \right]^{1/2} - kT_e \frac{d \ln n_e}{dx} - k \frac{dT_e}{dx} \quad (C10)$$

and after Taylor expansion of the RHS:

$$(1 + \bar{v} d\tau) d\varepsilon_e^T + kT_e d \ln n_e + kdT_e = -2(\bar{v} d\tau) (\varepsilon_e^T + e\Phi) \quad (C11)$$

Note also that we have neglected the non-linear functional dependence of the frequencies  $\nu_m$ ,  $\nu^i$  on the electron energy  $\varepsilon_e$ . One could derive a full 3-dimensional system of equations with respect to the variables  $n_e$ ,  $\varepsilon_e^T$  and  $T_e$ , to be solved implicitly. This is not necessary at this stage, and a simple forward integration or a predictor-corrector method are considered sufficient. The steps to the solution are as follows:

1. determine a spatial step  $dx$ :
2. solve for the total "cold" energy ("predictor step")
3. determine velocity at new position
4. solve for density and temperature
5. obtain new values for energy and velocity ("corrector step")
6. obtain new values for density and temperature
7. replace old values with new and advance position

The first step can be easily accomplished as follows:

$$d\tau = \min \left( \frac{(n\%)}{\nu_m + |\nu^i - \nu^r|}, \frac{L-x}{u_e} \right), \quad dx = u_e d\tau \quad (C12)$$

The  $(n\%)$  factor is a restrictive parameter that must be much smaller than 1 (e.g.  $\approx 0.1$ ). The second step in the numerical scheme is done by solving (C11), neglecting the changes in density and temperature:

$$\tilde{\varepsilon}_e^T = \varepsilon_e^T + d\varepsilon_e^T \quad \text{with} \quad d\varepsilon_e^T = -2 \frac{(\bar{v} d\tau)}{1 + (\bar{v} d\tau)} (\varepsilon_e^T + e\Phi) \quad (C13)$$

The predicted velocity (third step) and its gradients can then be found:

$$\tilde{u}_e(x+dx) = \left[ \frac{2}{m_e} (\tilde{\varepsilon}_e^T + e\tilde{\Phi}(x+dx)) \right]^{1/2} \quad (C14)$$

Note that we use the knowledge of the potential at the advanced position ( $\tilde{\Phi}$ ) to determine the acceleration due to the electric field. If the potential is known only at specific locations (i.e. on the nodes of a grid), it is necessary to interpolate to obtain its value at any position. Step 4 can be obtained by solving the following two equations:

$$d \ln n_e + d \ln u_e = (\nu^i - \nu^r) d\tau \quad (C15)$$

$$\text{and} \quad \left[ 1 + (\nu^i - \nu^r) d\tau \right] dT_e = \nu_m d\tau \left[ \frac{2}{3k} (\tilde{\varepsilon}_e^T + e\tilde{\Phi}) \right] - (\nu^i - \nu^r) d\tau \left( \frac{2\theta^i}{3} + T_e \right) \quad (C16)$$

knowing that  $d \ln u_e = \ln \tilde{u}_e(x+dx) - \ln u_e(x)$ . Once  $d \ln n_e$  and  $dT_e$  are known, they can be used in step 5 to obtain a "corrected" value for the total cold energy,  $\varepsilon_e^T(x+dx) = \varepsilon_e^T(x) + d\varepsilon_e^T$  with:

$$d\varepsilon_e^T = -2 \frac{(\bar{v} d\tau)}{1 + (\bar{v} d\tau)} (\hat{\varepsilon}_e^T + e\hat{\Phi}) - \frac{kT_e d \ln n_e + kdT_e}{1 + (\bar{v} d\tau)} \quad (C17)$$

and where  $\hat{\varepsilon}_e^T = (\varepsilon_e^T + \tilde{\varepsilon}_e^T) / 2$  and  $\hat{\Phi} = \Phi(x+dx/2)$  ("centered" variables). A final value of the velocity at position  $(x+dx)$  can then be obtained, and used in step 6 to determine again the gradients of density and temperature and the values  $n_e(x+dx)$  and  $T_e(x+dx)$ . Finally (step 7), the solution can be displayed or stored, and the following replacements are made:

- $u_e(x+dx) \rightarrow u_e(x)$



- $n_e(x+dx) \rightarrow n_e(x)$
- $T_e(x+dx) \rightarrow T_e(x)$
- $\varepsilon_e^T(x+dx) \rightarrow \varepsilon_e^T(x)$
- $x + dx \rightarrow x$

The procedure is repeated until the complete solution is obtained for the total inter-electrode gap.

This page intentionally blank

## Appendix D: Detailed Balance and H-Theorem

Consider an electron induced collisional ionization from an atomic level  $k$ :

$$[e, A_k \rightarrow e', e'', A^+] = w_{(e, A_k \rightarrow e', e'', A^+)} \cdot N(A_k)N(e)G(e')G(e'')G(A^+) \quad (D1)$$

where  $w_{(path)}$  is the rate of the given reaction path,  $N(s)$  is the number of particles of type  $s$ , and  $G(s)$  is the total degeneracy of that particle. Following (II.26), the total degeneracy for electrons is

$$G(\epsilon)d\epsilon = \mathcal{V}g \frac{2^{5/2}\pi m^{3/2}}{h^3} \epsilon^{1/2} d\epsilon \quad (D2)$$

while the degeneracy of the atom or the ion is ( $\alpha = k, +$ ):

$$G(A_\alpha) = \mathcal{V}g_\alpha G_{trans}(\epsilon_\alpha) \quad (D3)$$

Strictly speaking, the degeneracy due to the translational degrees of freedom for the heavy particles should be included; however, the mass difference between electrons and atoms implies that the center-of-mass is approximately co-located with the atom and ion, whose kinetic energy  $\epsilon_\alpha$  changes little. Therefore, one can ignore these translational degrees of freedom (they are a constant) in the formulation which follows.

The corresponding number of particles is:

$$N(\epsilon)d\epsilon = \eta(\epsilon)G(\epsilon)d\epsilon \quad (D4)$$

where

$$\eta(\epsilon) = \zeta e^{-\beta\epsilon}$$

is the mean occupation number; here,  $\beta = 1/kT$  and for electrons the normalization constant is:

$$\zeta = \frac{1}{g_s} \frac{N}{\mathcal{V}} \lambda_T^3 \quad (D5)$$

with

$$\lambda_T = \frac{h}{(2\pi m k T)^{1/2}} \quad (D6)$$

the thermal deBroglie wavelength. One can also define variables per unit volume, i.e. total density  $n = N/\mathcal{V}$ , differential density  $\hat{n}(\epsilon) = N(\epsilon)/\mathcal{V}$ , and the energy distribution function:

$$f(\epsilon) = \frac{N(\epsilon)}{N} \quad \text{with} \quad \int_0^\infty f(\epsilon)d\epsilon \equiv 1 \quad (D7)$$

Note that

$$\hat{n}(\epsilon) = n f(\epsilon) \quad (D8)$$

And that one can also define an energy-dependent degeneracy:

$$g(\epsilon) = g_s \left( \frac{4\pi m^2}{h^3} \right) \left( \frac{2\epsilon}{m} \right)^{1/2} \quad (D9)$$

such that  $\hat{n}(\epsilon) = \eta(\epsilon)g(\epsilon)$ . The equilibrium distribution is the Maxwellian:

$$f_M(\epsilon)d\epsilon = \frac{2\pi\epsilon^{1/2}}{(\pi k T)^{3/2}} e^{-\epsilon/kT} d\epsilon \quad (D10)$$

And one can also write the distribution function as function of the velocity,

$$f(v)d^3v \equiv \left( \frac{2\epsilon}{m} \right)^{1/2} \frac{d\epsilon d\Omega}{m} f(\epsilon) \quad (D11)$$

for which the equilibrium (Maxwellian) distribution is:

$$f_M(v)d^3v = \left( \frac{m}{2\pi k T} \right)^{3/2} e^{-mv^2/2kT} d^3v \quad (D12)$$

One must also specify the Boltzmann equilibrium relation between levels:

$$\frac{N_\ell}{N_k} = \frac{n_\ell}{n_k} = \frac{g_\ell}{g_k} e^{-\Delta\epsilon_{k\ell}/kT} \quad (D13)$$

And the Saha equation for ionization equilibrium:

$$\left( \frac{n_e n_+}{n_k} \right)^* = \frac{g_+}{g_k} \mathbb{Z}_e e^{-I_k/kT} \quad (D14)$$

Where the \* denotes equilibrium values and where

$$\mathbb{Z}_e = 2 \left( \frac{2\pi m k T}{h^2} \right)^{3/2} \quad (D15)$$

is the partition function for the electrons.

The forward rate of the ionization (D1) is proportional to:

$$n_k \hat{n}(v_0) v_0 d\sigma_{(k,\epsilon_0 \rightarrow +, \epsilon_1, \epsilon_2)}^i \delta(\epsilon_0 - \epsilon_1 - \epsilon_2 - I_k) d^3v_0 d^3v_1 d^3v_2 \quad (D16)$$

To simplify the notation, we used  $\hat{n}_0 = \hat{n}(v_0)$ , and  $\delta(\{\epsilon\})$  to represent respectively the density of particles with a given velocity or energy, and the Dirac delta-function imposing energy conservation. Note that momentum conservation is not specified as the heavy atom can absorb any amount of momentum, due to the small mass ratio  $m_e/M_A$ . We also eliminate the subscript in the cross-section, since the reaction path is well understood. Similarly, the backward rate (3-body recombination) is:

$$n_+ \hat{n}(v_1) \hat{n}(v_2) v_1 v_2 d\sigma^r \delta(\{\epsilon\}) d^3v_0 d^3v_1 d^3v_2 \quad (D16)$$

At equilibrium the forward and reverse rates are equal; using  $\hat{n}(v) = n_e f(v)$  and the Maxwellian distributions (D11), we find:

$$\left(\frac{m}{2\pi kT}\right)^{\frac{3}{2}} \left(\frac{n_+ n_e}{n_k}\right)^* e^{-\beta(\epsilon_1 + \epsilon_2 - \epsilon_0)} v_1 v_2 d\sigma^r = v_0 d\sigma^i \quad (D17)$$

Using the Saha equation (D14), this expression simplifies to:

$$g_k v_0 d\sigma^i = \left(\frac{2m^3}{h^3}\right) g_+ v_1 v_2 d\sigma^r \quad (D18)$$

Expression (D18) is the *Fowler* relation.

The elementary cross-sections  $d\sigma^i, d\sigma^r$  are functions of the *velocities* (or momenta), and include all angular variables; they are triply-differentiated cross-sections, of the form:

$$d\sigma^i \equiv \frac{d^3\sigma}{d\epsilon dW d\Omega} \quad (D19)$$

Where  $W$  is the energy transferred by the incident electron to the target atom. One can also express the rates as function of the doubly-differential cross-sections, averaging over the angular variables. The forward and backward rates become:

$$R^{ion} = n_k \hat{n}_0 v_0 d\bar{\sigma}^i \delta(\{\epsilon\}) d\epsilon_0 d\epsilon_1 d\epsilon_2 \quad (D20a)$$

$$\text{and} \quad R^{rec} = n_+ \hat{n}_1 \hat{n}_2 v_1 v_2 d\bar{\sigma}^r \delta(\{\epsilon\}) d\epsilon_0 d\epsilon_1 d\epsilon_2 \quad (D20b)$$

At equilibrium, we now find, using (D10) and (D14):

$$g_k \epsilon_0 d\bar{\sigma}^i = \left(\frac{16\pi m}{h^3}\right) g_+ \epsilon_1 \epsilon_2 d\bar{\sigma}^r \quad (D21)$$

This is another form of the Fowler relation, for cross-sections averaged over angular variables. We will use this expression below, as well as the rate expressions (D20a-b).

For an ensemble of  $N$  particles, the (classical) number of independent micro-states available and compatible with a given total energy is:

$$G = \frac{G^N}{N!} \quad (D22)$$

The entropy is given by (see 5.1.1 and 5.1.9 of [1])

$$S = k \ln G \quad (D23)$$

And therefore, using the Stirling formula  $\ln(N!) \approx N \ln N - N$ :

$$S \approx k[N \ln G - N \ln N + N] = -kN \left[ \ln\left(\frac{N}{G}\right) - 1 \right] \quad (D24)$$

The time-derivative of the entropy for particles of a given type is therefore:

$$\frac{\partial S}{\partial t} = -k \left( \frac{\partial N}{\partial t} \right) \left[ \ln\left(\frac{N}{G}\right) - 1 \right] - k \left( \frac{\partial N}{\partial t} \right)$$

or, recalling the definition of the mean occupation number (D4):

$$\frac{\partial S}{\partial t} = -k \left( \frac{\partial N}{\partial t} \right) \ln(\eta) \quad (D25)$$

Equation (D25) shows that the only time variation of the entropy is contained in the number of particles, weighted by the logarithm of the occupation number. Consider now the change in

entropy from the collisional ionization and the reverse process. Since  $N = n\mathcal{V}$ , the change in entropy can be written as:

$$\frac{\partial}{\partial t} \delta S = -k\mathcal{V} \left\{ \frac{\partial \hat{n}(\epsilon_0)}{\partial t} \ln \eta(\epsilon_0) + \frac{\partial \hat{n}(\epsilon_1)}{\partial t} \ln \eta(\epsilon_1) + \frac{\partial \hat{n}(\epsilon_2)}{\partial t} \ln \eta(\epsilon_2) \right. \\ \left. + \frac{\partial n_i}{\partial t} \ln \eta_i + \frac{\partial n_k}{\partial t} \ln \eta_k \right\} \quad (D26)$$

The rates of change can be obtained from the rates of ionization and recombination, i.e.  $\frac{\partial n}{\partial t} \sim R^{ion} - R^{rec}$ ; after simplifying the notation by using  $\hat{n}_0 = \hat{n}(\epsilon_0)$ , we obtain:

$$\frac{\partial}{\partial t} \delta S = +k\mathcal{V} \left\{ (R^{rec} - R^{ion}) \ln \left[ \frac{\eta_1 \eta_2}{\eta_0} \frac{\eta_i}{\eta_k} \right] \right\} \quad (D27)$$

The first term in brackets is:

$$[...] = [n_+ \hat{n}_1 \hat{n}_2 v_1 v_2 d\bar{\sigma}^r - n_k \hat{n}_0 v_0 d\bar{\sigma}^i] \delta(\{\epsilon\}) d\epsilon_0 d\epsilon_1 d\epsilon_2 \quad (D28)$$

From the Fowler relation (D21), we have:

$$d\bar{\sigma}^r = \frac{g_k}{g_i} \left( \frac{h^3}{16\pi m} \right) \left( \frac{\epsilon_0}{\epsilon_1 \epsilon_2} \right) d\bar{\sigma}^i \quad (D29)$$

Which we can use to re-write the first term in brackets on the RHS of (D28):

$$n_i \hat{n}_1 \hat{n}_2 \left( \frac{2\epsilon_1}{m} \right)^{\frac{1}{2}} \left( \frac{2\epsilon_2}{m} \right)^{\frac{1}{2}} d\bar{\sigma}^r = d\bar{\sigma}^i \frac{g_k}{g_i} \left( \frac{h^3}{8\pi m^2} \right) (\epsilon_1 \epsilon_2)^{\frac{1}{2}} \left( \frac{\epsilon_0}{\epsilon_1 \epsilon_2} \right) \eta_1 \eta_2 g(\epsilon_1) g(\epsilon_2)$$

Using (4.9):

$$= d\bar{\sigma}^i \frac{g_k}{g_i} \left( \frac{h^3}{8\pi m^2} \right) \left( \frac{8\pi m^2}{h^3} \right)^2 \left( \frac{2\epsilon_0}{m} \right) \eta_1 \eta_2 \\ = d\bar{\sigma}^i \frac{g_k}{g_i} \left( \frac{2\epsilon_0}{m} \right)^{\frac{1}{2}} \left[ \left( \frac{8\pi m^2}{h^3} \right) \left( \frac{2\epsilon_0}{m} \right)^{\frac{1}{2}} \right] \eta_1 \eta_2 \quad (D30)$$

The expression (D28) can now be re-written as:

$$[...] = d\bar{\sigma}^i \left[ \left( \frac{8\pi m^2}{h^3} \right) \left( \frac{2\epsilon_0}{m} \right) \right] \left[ \frac{n_i}{g_i} g_k \eta_1 \eta_2 - n_k \eta_0 \right] \delta(\{\epsilon\}) d\epsilon_0 d\epsilon_1 d\epsilon_2 \quad (D31a)$$

or

$$[...] = d\bar{\sigma}^i [v_0 g_k g(\epsilon_0)] \left[ \frac{n_i}{g_i} \eta_1 \eta_2 - \frac{n_k}{g_k} \eta_0 \right] \delta(\{\epsilon\}) d\epsilon_0 d\epsilon_1 d\epsilon_2 \quad (D31b)$$

Thus the rate of entropy change (D27) becomes:

$$\frac{\partial(\delta S)}{\partial t} = k\mathcal{V} \left\{ d\bar{\sigma}^i [v_0 g_k g(\epsilon_0)] [\eta_i \eta_1 \eta_2 - \eta_k \eta_0] \ln \left[ \frac{\eta_1 \eta_2}{\eta_0} \frac{\eta_i}{\eta_k} \right] \right\} \delta(\{\epsilon\}) d\epsilon_0 d\epsilon_1 d\epsilon_2 \quad (D32)$$

This rate is of the form

$$\frac{\partial(\delta S)}{\partial t} \propto (x - y) \ln \left( \frac{x}{y} \right) \quad (D33)$$

With all other pre-factors being positive quantities, this expression is always positive when either  $x > y$  or  $x < y$ , and is zero when  $x = y$ . Thus the entropy always increases during relaxation, and equilibrium is reached when

$$\eta_k \eta(\epsilon_0) = \eta_i \eta(\epsilon_1) \eta(\epsilon_2) \quad (D34)$$

This result is an expression of the H-theorem for the collisional ionization/recombination process.

A similar procedure can be used for the excitation/de-excitation. In that case, the rates of excitation and de-excitation can be written as:

$$R^x = n_k n_e f_e(v) f_A(v_k) c d\sigma_{(k,v \rightarrow \ell, v')}^x d^3 v d^3 v_k \quad (D35a)$$

$$R^d = n_\ell n_e f_e(v') f_A(v_\ell) c' d\sigma_{(\ell, v' \rightarrow k, v)}^d d^3 v' d^3 v_\ell \quad (D35b)$$

Where  $\vec{c} = \vec{v} - \vec{v}_k$  and  $\vec{c}' = \vec{v}' - \vec{v}_\ell$  are the relative velocities between electron and atom. Kinematics show that

$$\frac{d^3 v d^3 v_k}{c} = \frac{d^3 v' d^3 v_\ell}{c'} \quad (D36)$$

while the conservation of energy implies that  $\epsilon = \epsilon' + \Delta_{k\ell}$ . The forward rates being equal at equilibrium, using (D13) and  $c dc = c' dc'$  we find:

$$g_k c^2 d\bar{\sigma}_{(k,v \rightarrow \ell, v')}^x = g_\ell c'^2 d\bar{\sigma}_{(\ell, v' \rightarrow k, v)}^d \quad (D37)$$

This is the *Klein-Rosseland* relation. Again, using cross-sections averaged over the angular variables and expressing the distribution functions in term of energy alone, we find a similar relation:

$$g_k \epsilon d\bar{\sigma}_{(k, \epsilon \rightarrow \ell, \epsilon')}^x = g_\ell \epsilon' d\bar{\sigma}_{(\ell, \epsilon' \rightarrow k, \epsilon)}^d \quad (D38)$$

The change in entropy due to this reaction is:

$$\frac{\partial}{\partial t} \delta S = +kV \left\{ (R^d - R^x) \ln \left[ \frac{\eta_e(\epsilon')}{\eta_e(\epsilon)} \frac{\eta_\ell}{\eta_k} \right] \right\} \quad (D39)$$

Using the Klein-Rosseland relation (D37), this leads to:

$$\frac{\partial}{\partial t} \delta S \propto d\bar{\sigma}^x \left\{ \frac{\eta_\ell}{g_\ell} \hat{n}(\epsilon) \sqrt{\epsilon'} g_k \left( \frac{\epsilon}{\epsilon'} \right) - n_k \hat{n}(\epsilon) \sqrt{\epsilon} \right\} \ln \left[ \frac{\eta_e(\epsilon')}{\eta_e(\epsilon)} \frac{\eta_\ell}{\eta_k} \right]$$

or

$$\frac{\partial}{\partial t} \delta S \propto g_k \epsilon d\bar{\sigma}^x \{ \eta_\ell \eta_e(\epsilon') - \eta_k \eta_e(\epsilon) \} \ln \left[ \frac{\eta_e(\epsilon')}{\eta_e(\epsilon)} \frac{\eta_\ell}{\eta_k} \right] \quad (D40)$$

This result is also of the form (D33) and also implies that entropy increases during relaxation until equilibrium is satisfied by the relation between the mean occupation numbers,  $\eta_\ell \eta_e(\epsilon') = \eta_k \eta_e(\epsilon)$ .

## References

[1] J. Oxenius, *Kinetic Theory of Particles and Photons*, Springer-Verlag, Berlin, 1986.

A HIGH-ORDER TRANSPORT SCHEME FOR  
COLLISIONAL-RADIATIVE AND NONEQUILIBRIUM PLASMA

DISSERTATION

Presented in Partial Fulfillment of the Requirements for  
the Degree of Philosophy in the Graduate  
School of the Ohio State University

By

Michael Gino Kapper, M.S.

\* \* \* \* \*

The Ohio State University  
2009

Dissertation Committee:

Professor John Yu, Adviser

Professor Walter Lempert

Professor Igor Adamovich

Professor Mohammed Samimy

Dr. Jean-Luc Cambier

Approved by

---

Adviser

Mechanical Engineering Graduate Program

Copyright by  
Michael Gino Kapper  
2009



## ABSTRACT

A series of shock tube experiments performed in the 1970s at the Institute for Aerospace Studies, University of Toronto, led in the discovery of instabilities in relaxing shock structures in noble gases under hypervelocity conditions. The instabilities were oscillatory in nature and found to affect the entire shock structure including the translational front, induction zone, and electron avalanche. Theoretical models were first developed in order to reproduce the length and time scales of the observed quasi-equilibrium state, and later extended to include unsteady plasmadynamic simulations that verified the influence of pressure oscillations in one dimension. Despite these attempts, a complete explanation for the oscillations nor a quantitative analysis of the multi-dimensional shock structure has been provided to date.

This dissertation builds upon previous modeling efforts, extending the numerical simulations to a high level of accuracy and detail so that coupling of complex wave phenomena and nonequilibrium effects can be well resolved. This has necessitated the development of a numerical capability aimed at relaxing shock layers and other unsteady, high-enthalpy nonequilibrium plasmas and is the focus of much of this work. The plasma is described as a two-temperature, single fluid with the electronic states convected as separate species. Solution of the convective transport is handled via upwind shock-capturing techniques, extended to third-order on general curvilinear meshes. A collisional-radiative model describing the kinetics of excitation and ionization and reverse processes allows for a non-Boltzmann distribution of the excited levels. The solver is developed within a parallelized software architecture, implemented entirely in Java and capable of execution on distributed memory machines.

The numerical solver is developed in a systematic fashion with much emphasis placed

---

Distribution A: Approved for public release; distribution is unlimited.

on code validation. The transport schemes are benchmarked using standard test cases. The collisional-radiative model is benchmarked as well on a steady flow fields before considering unsteady calculations.

Numerical simulations of ionizing shocks in argon are conducted to gain insight to the shock structure and help determine the source of the oscillations observed in the experiment. Solutions presented in the form of simulated interferograms provide a direct comparison with experimental interferograms enabling identification of key wave structures. Results show that the instabilities are caused by a resonance pattern of longitudinal and transverse waves that give rise to ionization cells that are analogous to detonation cells. Furthermore, a mechanism is proposed for the oscillations which takes into account the unsteady wave phenomena coupled with the collisional-radiative kinetics.

## ACKNOWLEDGMENTS

I would like to acknowledge the many people who have helped in making this dissertation possible. I would first like to thank my adviser Prof. John Yu for his help and support during my time at OSU. He has proved to be a respectable running partner whether it be jogging around Antrim Park Lake or running laps at Jesse Owens Memorial Stadium. I would also like to thank Prof. Walter Lempert, Prof. Igor Adamovich, and Prof. Mohammed Samimy for serving on my committee and their valuable input to my research. I am grateful to Dr. Jean-Luc Cambier, who has given my research a sense of direction, allowing me to tackle problems of real interest. His attention to detail and discerning eye has served to greatly improve the quality of my work. He has also been an excellent teacher, always willing to sharing his experiences and wisdom.

I would like to acknowledge the various professors and colleagues who have inspired me to achieve more, including Prof. Periklis Papadopoulos of SJSU for being my first CFD professor and helping to spring-board my career in numerical methods as well as Prof. Edward Overmann of the OSU math department for his contagious enthusiasm for numerical methods. I would like to thank Dr. Hung T. Huynh of NASA Glenn Research Center for sharing his clear and elegant description of Riemann solvers, reconstruction methods, and limiters. I thank AFRL alumnus Mr. Jay Levine for his deep interest and support of CFD at the AFRL. I would also like to acknowledge Mr. Levine as being the first to inspire me to pursue a doctorate. I thank Dr. Leonid Pekker for many enlightening discussions about physics.

This research was supported by AFOSR laboratory task 02PR05COR.

## VITA

January 15, 1978.....	Born in Hayward, California
June, 2000.....	B.S., Chemistry University of California at Berkeley
October, 2000–June, 2003.....	Engineer, Guerra Technologies, Inc San José, CA
June, 2005.....	M.S., Mechanical Engineering San José State University San José, CA
July, 2003–present.....	Mechanical engineer Air Force Research Laboratory Edwards AFB, CA

## PUBLICATIONS

M. Kapper and J.-L. Cambier. A High-Order Scheme for Collisional-Radiative and Non-Equilibrium Plasma. In *Proceedings of the 3rd International Workshop of High Temperature Gases in Atmospheric Entry*, Heraklion, Greece, 30 September–3 October 2008 (ESA SP-667, January 2009).

J.-L. Cambier, M. Carroll, and M. Kapper. Development of a Hybrid Model for Nonequilibrium High-Energy Plasmas. In *Proceedings of the 35th Plasmadynamics and Lasers Conference*, Portland, OR, June 2004. AIAA.

## FIELDS OF STUDY

Major Field: Mechanical engineering

## TABLE OF CONTENTS

Abstract . . . . .	ii
List of Tables . . . . .	x
List of Figures . . . . .	xiv
List of Symbols . . . . .	xv
<b>1 Introduction</b>	<b>1</b>
1.1 UTIAS experiments . . . . .	2
1.2 Scope and overview . . . . .	6
<b>2 Governing Equations</b>	<b>8</b>
2.1 Conservative formulation . . . . .	9
2.1.1 Hyperbolic terms . . . . .	10
2.2 Two-temperature model . . . . .	12
2.2.1 Two-fluid equations . . . . .	12
2.2.2 Generalized Ohm's law . . . . .	14
2.2.3 Electron fluid . . . . .	14
2.2.4 Thermophysical properties . . . . .	20
2.2.5 Two-temperature eigensystem . . . . .	25
2.3 Two-Temperature MHD Model . . . . .	25
2.4 Eigensystem . . . . .	27
<b>3 Numerical Formulation</b>	<b>28</b>
3.1 Finite-volume formulation . . . . .	28
3.2 Semi-discete approach . . . . .	29
3.3 Time-Marching . . . . .	31

<b>4</b>	<b>Reconstruction</b>	<b>33</b>
4.1	One-dimensional formulation . . . . .	34
4.2	Two-dimensional formulation . . . . .	38
4.2.1	Flux Calculation . . . . .	40
4.3	Limiters . . . . .	40
<b>5</b>	<b>Numerical Stability</b>	<b>42</b>
5.1	Finite-difference approximation . . . . .	43
5.2	1D stability . . . . .	44
5.3	2D stability . . . . .	48
<b>6</b>	<b>Benchmarks</b>	<b>53</b>
6.1	Woodward-Colella blastwave . . . . .	53
6.2	Shu-Osher shock-entropy wave interaction . . . . .	55
6.3	Emery wind tunnel . . . . .	56
6.4	Schardin's problem . . . . .	58
6.5	Shock diffraction down a step . . . . .	58
6.6	Rayleigh-Taylor instability . . . . .	59
6.7	Brio-Wu MHD shocktube . . . . .	60
6.8	Orszag-Tang MHD vortex . . . . .	60
<b>7</b>	<b>Diffusion Processes</b>	<b>65</b>
7.1	Governing equations . . . . .	65
7.2	One-dimensional case . . . . .	66
7.3	Stability . . . . .	69
7.4	Thermal conductivity . . . . .	71
7.5	Benchmarks . . . . .	71
<b>8</b>	<b>Near-Vacuum Flows</b>	<b>74</b>
8.1	Formulation . . . . .	75
8.2	Benchmarks . . . . .	77

<b>9</b>	<b>Collisional-Radiative Model</b>	<b>81</b>
9.1	Rate equations . . . . .	81
9.1.1	Atom impact processes . . . . .	85
9.1.2	Electron impact processes . . . . .	87
9.1.3	Pressure ionization . . . . .	89
9.2	Photorecombination . . . . .	89
9.3	Bremsstrahlung emission . . . . .	90
9.4	Bound-bound transitions . . . . .	91
9.5	Elastic collisions . . . . .	92
9.6	Numerical formulation . . . . .	93
<b>10</b>	<b>UTIAS Shock Tube Experiments</b>	<b>97</b>
10.1	Steady-state simulations . . . . .	98
10.1.1	Effect of upper levels . . . . .	100
10.1.2	Shock structure . . . . .	103
10.2	Unsteady 1D simulations . . . . .	106
10.2.1	Fluctuation mechanism . . . . .	108
10.2.2	Sensitivity to cross sections . . . . .	108
10.3	Unsteady 2D simulations . . . . .	112
10.4	Mach 16.5 case . . . . .	113
10.5	Mach 14.7 case . . . . .	116
10.5.1	Cell size approximation . . . . .	117
<b>11</b>	<b>Ionizing Flow Past a Circular Cylinder</b>	<b>119</b>
11.1	Numerical results . . . . .	119
11.2	Excitation temperatures . . . . .	122
<b>12</b>	<b>Parallel Framework</b>	<b>125</b>
12.1	Introduction . . . . .	125
12.2	Architecture . . . . .	126
12.2.1	Client . . . . .	127
12.2.2	Server . . . . .	127

12.2.3	Tree Model . . . . .	128
12.3	Communication . . . . .	129
12.3.1	Boundary Communication . . . . .	130
12.4	Synchronization . . . . .	134
<b>13</b>	<b>Conclusions</b>	<b>145</b>
13.1	Achievements and contributions . . . . .	145
13.2	Suggestions for future work . . . . .	146
<b>A</b>	<b>Eigensystem</b>	<b>149</b>
A.1	Two-Temperature eigensystem . . . . .	149
A.2	Two-Temperature MHD eigensystem . . . . .	156
<b>B</b>	<b>Isoparametric Elements</b>	<b>163</b>
B.1	One-Dimensional Shape Functions . . . . .	163
B.1.1	Linear Elements . . . . .	163
B.2	Two-Dimensional Shape Functions . . . . .	164
B.2.1	Bilinear Elements . . . . .	164
<b>C</b>	<b>Visualization</b>	<b>167</b>
<b>D</b>	<b>Implicit CR Formulation</b>	<b>169</b>
D.1	Jacobian Elements . . . . .	174
D.2	Conditioning . . . . .	176
<b>E</b>	<b>Additional Steady-State Results</b>	<b>178</b>
	<b>Bibliography</b>	<b>193</b>



## LIST OF TABLES

1.1	Atom-atom cross section parameters used in previous research. . . . .	4
9.1	Rate coefficients for collisional-radiative model . . . . .	83
9.2	Argon levels considered in current CR model . . . . .	84
9.3	Atom impact excitation parameters for allowed transitions from ground state Ar. . . . .	86
9.4	Atom impact excitation parameters for intra-4s transitions. . . . .	86
9.5	Electron-impact ionization parameters. . . . .	88
9.6	Radii of <i>Ar</i> valence electron and reduced weighting factors. . . . .	88
9.7	Estimated mean-free paths for bound-bound transitions to ground state. . . .	91
10.1	Shock tube cases studied by Glass and Liu. . . . .	99
10.2	Comparison between experimental and steady-state numerical relaxation lengths for ionizing shock in argon. . . . .	100
10.3	Tuned atom impact excitation parameters for allowed transitions from ground state Ar. . . . .	100

## LIST OF FIGURES

1.1	Temperatures and ionization distribution in a shock wave in argon. . . . .	4
1.2	Experimental interferogram of argon shock structure at Ma 14.7. . . . .	5
4.1	Numerical approach . . . . .	34
4.2	One-dimensional parabolic interpolation . . . . .	35
4.3	General area representation based on arbitrary point. . . . .	38
4.4	Two-dimensional interpolation stencil. . . . .	39
4.5	Two-dimensional quadric surface interpolation on a uniform mesh. . . . .	41
5.1	Modified wave number and phase error for 3 <sup>rd</sup> -order backward difference op- erator. . . . .	45
5.2	Stability plot for the 1D MP3-AB2 scheme with CFL= 0.58. . . . .	46
5.3	Stability plot for the 1D MP3-AB2 scheme with CFL= 0.1. . . . .	47
5.4	Stability plot for the 1D MP3-RK2 scheme with CFL= 0.9. . . . .	47
5.5	Stability plot for the 1D MP3-RK2 scheme with CFL= 0.1. . . . .	48
5.6	Stability plot for the 2D AB2-MP3 scheme with CFL= 0.29. . . . .	50
5.7	Stability plot for the 2D AB2-MP3 scheme with CFL= 0.05. . . . .	50
5.8	Stability plot for the 2D MP3-RK2 scheme with CFL= 0.45. . . . .	51
5.9	Stability plot for the 2D RK2-MP3 scheme with CFL= 0.05. . . . .	51
6.1	Woodward-Colella blastwave. . . . .	54
6.2	Shu-Osher problem. . . . .	55
6.3	Emery solution at $t = 1$ . . . . .	57
6.4	Emery solution at $t = 2$ . . . . .	57
6.5	Emery solution at $t = 3$ . . . . .	57
6.6	Emery solution at $t = 4$ . . . . .	58

6.7	Simulated Schlieren ( <i>left</i> ) of Schardin's problem as compared with experiment ( <i>right</i> ) from [36]. . . . .	58
6.8	Mach 5.09 shock diffracting down a $90^\circ$ step . . . . .	59
6.9	Rayleigh-Taylor instability . . . . .	61
6.10	Brio-Wu MHD shocktube . . . . .	62
6.11	Orszag-Tang MHD vortex. . . . .	63
7.1	Thermal diffusion benchmarks. . . . .	72
8.1	Solution to Einfeldt's 1-2-3 problem as obtained with conservation of energy. . . . .	79
8.2	Solution to Einfeldt's 1-2-3 problem as obtained with conservation of entropy. . . . .	80
9.1	Partial Grotrian diagram for neutral argon. . . . .	82
9.2	Electron-neutral collision rate as computed from the theoretical cross sections . . . . .	92
10.1	Comparison of experimental and numerical results for Ma 15.9 shock in argon taking into account only levels of the $4s$ manifold. . . . .	101
10.2	Comparison of experimental and numerical results for Ma 15.9 shock in argon taking into account levels of the $4s$ and $4p$ manifolds. . . . .	102
10.3	Comparison of experimental and numerical results for Ma 15.9 shock in argon taking into account levels of the $4s$ , $4p$ , $5s$ , and $3d$ manifolds. . . . .	102
10.4	Effect of upper levels on the ionizing shock structure as indicated by the ionization fraction. . . . .	103
10.5	Details of the Mach 15.9 ionizing shock structure in terms of electron, heavy particle, and equivalence temperatures. . . . .	104
10.6	Numerical setup for 1D unsteady shock tube simulations. . . . .	106
10.7	Instantaneous Mach number as a function of distance from wall. . . . .	107
10.8	Instantaneous induction length as a function of time for Mach 15.9 case. . . . .	107
10.9	$x - t$ diagrams for 1D Ma 14.7 case. . . . .	109
10.10	Dynamic evolution of 1D ionizing shock structure. . . . .	110
10.11	Sensitivity of 1D ionizing shock oscillation dynamics to cross sections. . . . .	111
10.12	Numerical setup for 2D unsteady shock tube simulations. . . . .	113

10.13	Evolution of Mach 16.5 shock, showing transition from 2D planar shock to oscillating shock. . . . .	114
10.14	Simulated interferogram and refractive index for 2D Mach 16.5 shock. . . .	115
10.15	Trace of triple points for Mach 16.5 case, exposing ionizing cell structure. . .	115
10.16	Simulated interferogram and refractive index for 2D Mach 14.7 shock. . . .	116
10.17	Numerical soot trace for Mach 14.7 case, exposing ionizing cell structure. . .	117
10.18	Direct comparison of experimental and numerical results for Mach 14.7 shock.	117
10.19	Details of the 2D ionizing shock structure for the Mach 14.7 case. . . . .	118
11.1	Lehr's detonation experiment of a projectile traveling through hydrogen-oxygen mixture. . . . .	120
11.2	Mesh used in computation of flow around cylinder and simulated interferogram.	120
11.3	Heavy particle and electron temperatures and ionization fraction for flow around cylinder. . . . .	121
11.4	Temperature profiles and ionization fraction taken at $\theta = 0$ for flow past cylinder. . . . .	122
11.5	Equivalence temperatures of the first four excited levels relative to the ground state. . . . .	124
12.1	Domain decomposition process. Solution domain is decomposed into multiple computation domains from which new threads are created. . . . .	126
12.2	Master-slave configurations. In (a), a single Master node distributes workload among 3 slaves. In (b), Master 2 controls Slaves 1 and 2, but is itself a slave to Master 1. . . . .	128
12.3	Tree abstraction. (a) <i>Root</i> , <i>Branch</i> , and <i>Leaf</i> are subclasses of <i>Node</i> . (b) Example configuration: A represents the <i>Root</i> node; B, C, D, E, F, I, L, and M represent <i>Branch</i> nodes; and J, G, H, K, N, O, and P represent <i>Leaf</i> nodes.	129
12.4	Domain Buffers are used to transfer data from the boundary layers of the source domain over the network and into the ghost layers of the target domain.	131
12.5	Push vs. Pull. Domain buffers can be transferred by either (a) a <i>pull</i> from the source domain by the target domain or (b) a <i>push</i> from the source domain to the target domain. . . . .	133

12.6	FIFO buffer queue. FIFO buffer queues on the receiving end of a push from the source domain are used to ensure correct synchronization of data between iterations. . . . .	134
12.7	Synchronization convention. Synchronization calls between a child node and its parent are accomplished through the <i>Sync</i> implementation on the parent and the <i>Sync</i> interface of the child. . . . .	141
12.8	Global cycle. Interaction between <i>Root</i> and <i>Leaf</i> nodes and associated <i>Domains</i> during a global cycle. . . . .	143
C.1	Generalized visualization setup and geometric schematic. . . . .	167
E.1	Ionizing shock structure as detailed by (a) $\rho$ and $n_e$ , and (b) $\alpha$ for case 2: $p_o = 5.15$ torr, $T_o = 295.9$ K, $Ma = 16.1$ . . . . .	179
E.2	Ionizing shock structure as detailed by (a) $\rho$ and $n_e$ , and (b) $\alpha$ for case 3: $p_o = 5.12$ torr, $T_o = 296.6$ K, $Ma = 16.5$ . . . . .	180
E.3	Ionizing shock structure as detailed by (a) $\rho$ and $n_e$ , and (b) $\alpha$ for case 4: $p_o = 5.01$ torr, $T_o = 296.6$ K, $Ma = 13.0$ . . . . .	181

## LIST OF SYMBOLS

### Latin Symbols

$a$	thermal sound speed, abscissa for Gaussian quadrature, specific Helmholtz function
$A$	flux Jacobian matrix, Helmholtz function per unit volume
$\mathcal{A}$	area
$B$	banded matrix
$\vec{B}$	magnetic flux density (magnetic induction)
$c$	speed of light in vacuum
$c_a$	Alfvén wave speed
$c_f$	fast magnetosonic wave speed
$c_p$	specific heat at constant pressure
$c_s$	slow magnetosonic wave speed
$c_v$	specific heat at constant volume
$E$	energy density
$\vec{E}$	electric field
$\vec{E}^*$	electric field including pondermotive force, i.e. $\vec{E} + \vec{u} \times \vec{B}$
$f$	distribution function, oscillator strength
$F$	vector flux density of the fluid
$\mathbb{F}$	DFT matrix
$\ddot{F}$	tensor flux density of the fluid
$g$	specific Gibbs function, degeneracy
$g_{ij}$	covariant metric coefficient
$g^{ij}$	contravariant metric coefficient
$\bar{g}$	gaunt factor

$\vec{g}_i$	covariant basis vector
$\vec{g}^i$	contravariant basis vector
$G$	Gibbs function density
$h$	Planck constant, specific enthalpy
$H$	enthalpy density
$\vec{H}$	magnetic field strength
$h_o$	specific stagnation enthalpy
$H_o$	stagnation enthalpy density
$h_f$	specific enthalpy of formation
$\hbar, \hbar$	Planck constant
$I$	identity matrix, ionization potential
$J$	Jacobian matrix, angular momentum quantum number
$\vec{j}$	electric current
$k_B$	Boltzmann constant
$K$	quantum number
$\vec{l}$	left eigenvector
$\ell$	length
$L$	matrix of left eigenvectors
$m$	mass
$\vec{m}$	momentum density
$M$	similarity transformation matrix
$n$	number density, principal quantum number
$\vec{P}$	momentum transfer operator
$p$	pressure
$p_o$	sum of thermal and magnetic pressures
$Q$	vector of conserved quantities
$\vec{r}$	right eigenvector
$R$	gas constant, matrix of right eigenvectors
$\mathcal{R}$	universal gas constant
$S$	entropy density

$s$	specific entropy
$t$	time
$u$	velocity component in $x$ -direction
$\vec{u}$	mass-average velocity
$v$	specific volume, velocity component in $y$ -direction
$V$	vector of primitive variables, Vandermonde matrix
$\vec{V}$	diffusion velocity field
$\mathcal{V}$	volume
$w$	velocity component in $z$ -direction, weight for Gaussian quadrature
$\vec{w}$	velocity w.r.t. laboratory coordinates
$W$	vector of characteristic variables
$\vec{W}$	relative velocity field
$x$	specie mole fraction
$y$	specie mass fraction
$Z$	particle charge, partition function

## Greek Symbols

$\alpha$	characteristic wave strength, ionization fraction, plasma diffusivity
$\vec{\beta}$	normalized magnetic field
$\epsilon_0$	dielectric constant, permittivity of vacuum
$\eta$	plasma diffusivity
$\delta$	finite-difference approximation
$\Delta$	forward-difference operator: $(\cdot)_R - (\cdot)_L$
$\eta$	plasma diffusivity
$\gamma$	adiabatic exponent (ratio of specific heats)
$\kappa$	thermal diffusivity, wave number
$\lambda$	eigenvalue
$\lambda_D$	Debye length
$\Lambda$	diagonal matrix of eigenvalues, optical escape factor
$\mu$	momentum transfer operator



$\mu_o$	magnetic permeability
$\nu_{rs}$	collision frequency between species $r$ and $s$
$\omega$	plasma frequency, general source term
$\Omega$	vector of source terms
$\ddot{\Pi}$	tensor momentum flux density of the fluid (Maxwell stress tensor)
$\rho$	mass density, plasma resistivity
$\dot{\rho}$	rate of density change
$\sigma$	collision cross section, plasma conductivity
$\tau$	relaxation time scale
$\varepsilon$	specific internal energy
$\xi$	number of optical electrons

### Superscripts

$'$	rate of energy density production/destruction
$*$	excited state
$^\circ$	standard reference state
$n$	time level
$A$	allowed transition
$F$	forbidden transition
$P$	parity-forbidden transition
$S$	spin-forbidden transition

### Subscripts

$c$	conservative form, capture
$e$	electron specie component
$i$	mesh index in $x$ - or $\xi$ -direction, ion specie component
$j$	mesh index in $y$ - or $\eta$ -direction
$k$	mesh index in $z$ - or $\zeta$ -direction
$h$	heavy (atom) specie component

$n$	specie component, normal component
$N$	north
$p$	primitive form, periodic
$s$	general specie component
$L$	left state
$R$	right state
$\nu$	photon
$x$	vector component in $x$ -direction
$y$	vector component in $y$ -direction
$z$	vector component in $z$ -direction
$\xi$	vector component in $\xi$ -direction
$\eta$	vector component in $\eta$ -direction
$\zeta$	vector component in $\zeta$ -direction
$\parallel$	parallel component
$\perp$	perpendicular component

## CHAPTER 1

### INTRODUCTION

As a proven complement to experimental results, flowfield simulation has become an integral component in the engineering process, providing valuable insight to observed phenomena. In particular, modeling of nonequilibrium plasma flows has emerged as a key technology for many critical aerospace applications, including aerodynamic flow control, re-entry and hypersonic air-breathing vehicles, as well as capillary discharge and electric propulsion devices. As applied to such cases, modeling can aid in improved aerodynamic performance, thermal protection systems, combustion enhancement, and thruster efficiency among others.

The complexity of such high enthalpy flows is as vast as the range of characterizing conditions, from highly collisional regimes encountered in shock layers, to supersonic base flows that give rise to near-vacuum states. These flows are dominated by nonlinear wave phenomena and nonequilibrium plasma conditions, requiring an accurate description of the transport processes along with generalized equations of state that can account for a non-Boltzmann distribution of states.

In relaxing shock layers, for example, plasma transport through the nonlinear compression shock results in conversion of bulk kinetic energy to random thermal energy which is then distributed between the various internal modes of the plasma through collisions. If the time scales of such collisions are comparable to the convective times scales to be resolved, then the resulting nonequilibrium states of the plasma must be evaluated through the use of kinetic models.

In stark contrast to collision-dominated shocks, flows through nonlinear rarefaction waves can be nearly collisionless, resulting in a cold plasma. While such plasmas may be unable to relax through collisions, radiation emission and absorption becomes important and must

be accounted for.

Furthermore, when unsteady flow effects are considered, coupling between the plasma transport and nonequilibrium effects becomes especially important. In many cases the dynamics of the flow can depend heavily upon accurate treatment of the thermophysical properties, requiring accurate and complete descriptions of the equation of state. The sensitivity can be quite pronounced, as nonlinearities can amplify small changes. The equation of state in turn depends on the local conditions as determined by the transport, for which correct temperature jumps through shocks and temperature drops in rarefactions, for example, should be accurately computed.

With this in mind, it is the focus of this research not to include as much nonequilibrium complexity as possible, but rather to focus on developing a relatively complete model of the nonequilibrium effects considered and to ensure proper coupling with transport phenomena. In particular, the current work is limited to monatomic gases so that nonequilibrium effects of the electronic states can be studied in some detail. The approach will be very systematic, starting from an accurate treatment of the plasma transport, described by a two-temperature, single-fluid model, which is then coupled with a collisional-radiative model that includes the kinetics of excitation and ionization and all reverse processes, allowing a non-Boltzmann distribution of the bound electronic states. Particular emphasis will be placed on validation through benchmarks, ensuring proper coupling between transport and kinetics. In particular, the numerical model developed in this work will be validated against the shock tube studies described in the following section.

### **1.1 UTIAS experiments**

Shock tubes have been and continue to be an invaluable tool in providing thermochemical data for gases under non-equilibrium conditions. They are able to generate gasdynamic phenomena with time scales on the order of relaxation times necessary to achieve thermodynamic equilibrium. For gasdynamic processes occurring more rapidly than relaxation processes, the gas will be left in a state of non-equilibrium, thereby allowing measurement of reaction rates and collision cross sections in a controlled environment.

Due to its simplicity as a monatomic gas and its relative abundance, argon in particular has extensively been studied in the context of shock tubes. Without an energy sink for

rotational or vibrational modes or dissociative processes, high shock speeds and associated temperature jumps are easily attainable, making it ideal to study electronic excitation and ionization kinetics. The first experiments on ionization relaxation in argon were carried out by Petschek and Byron [85], the results of which were used to benchmark theoretical models in subsequent work. The structure of an ionizing shock wave in argon was first calculated by Biberman and Yakubov [11] whose results are shown in Figure 1.1. These results indicate a compression shock at  $x = 0$  cm through which the argon gas is rapidly heated (within several mean-free paths) to temperatures above 2 eV. At these temperatures, there exist atoms with sufficient thermal energy to excite and ionize other argon atoms through inelastic collisions. The electrons produced by these collisions are then heated through thermalization with ground state atoms, indicated by the initial sharp gradient of  $T_e$  from 0–0.75 cm. Once a sufficient number of *priming* electrons have been liberated, they themselves begin to dominate inelastic collisions due to their high velocity in comparison with that of the atoms. Electron production and temperature steadily increase until just before 4 cm, at which point the rate of inelastic collisions increases exponentially, resulting in an electron avalanche. The distance between the compression shock and the peak ionization fraction in the avalanche is known as the relaxation or induction length. The heavy-particle temperature then rapidly drops due to the large number of electrons and the large cross section for thermalization through Coulomb collisions.

Combination of such experimental data with theoretical calculations has yielded approximate values for cross sections and rates associated with excitation and ionization. Knowledge of key parameters from experimental data such as the relaxation length and ionization fraction allow for the tailoring of rates used in theoretical calculations until agreement is achieved. In particular, it has been found that atom-atom cross sections for excitation from ground state have the greatest influence on the shock structure and the relaxation length. Since the gas down stream of the shock is not ionized, atom-atom collisions immediately following the compression shock generate the initial priming electrons which in turn become the dominant ionizing species once sufficient number densities have been obtained. Table 1.1 offers some values of the atom-atom cross sections used in previous studies. The range of values exceeds an order of magnitude and indicates the relative uncertainty in this particular cross section.

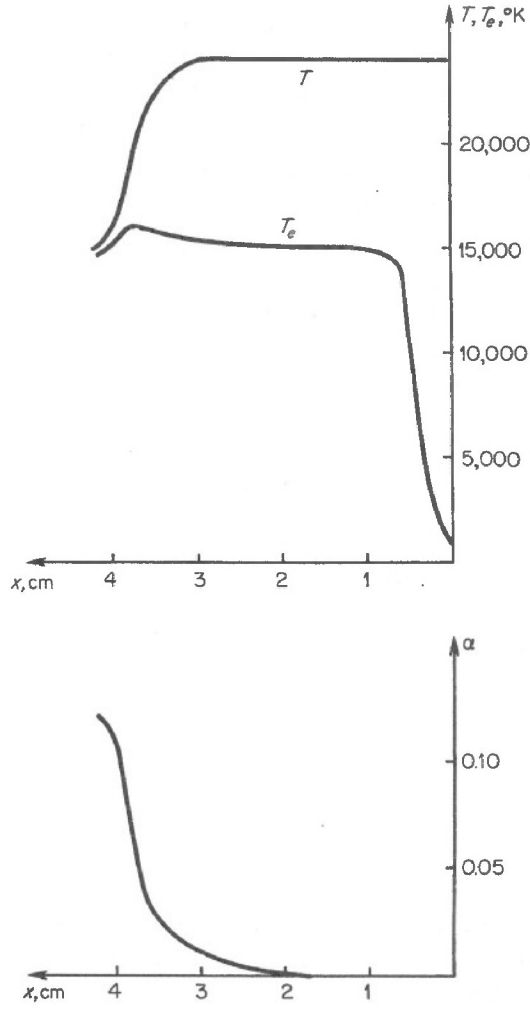


Figure 1.1: Distribution of electron and atom temperatures and degree of ionization in a shock wave in argon on the assumption that the initial electrons are formed by atom-atom collisions. The Mach number is 16, the pressure ahead of the shock 10 mm Hg, and the initial temperature 293 K. Taken from [128].

Authors	$\sigma^a$ [ $\text{m}^2/\text{eV}$ ]
Harwell and Jahn [49]	$7 \times 10^{-23}$
Morgan and Morrison [80]	$7 \times 10^{-24}$
Kelly [60]	$1.2 \times 10^{-23}$
Merilo and Morgan [76]	$1.2 \times 10^{-23}$
McLaren and Hobson [72]	$2.5 \times 10^{-24}$
Glass and Liu [42]	$1 - 2 \times 10^{-23}$

Table 1.1: Atom-atom cross section parameters for excitation from ground state used in various attempts to reproduce the shock structure in argon.

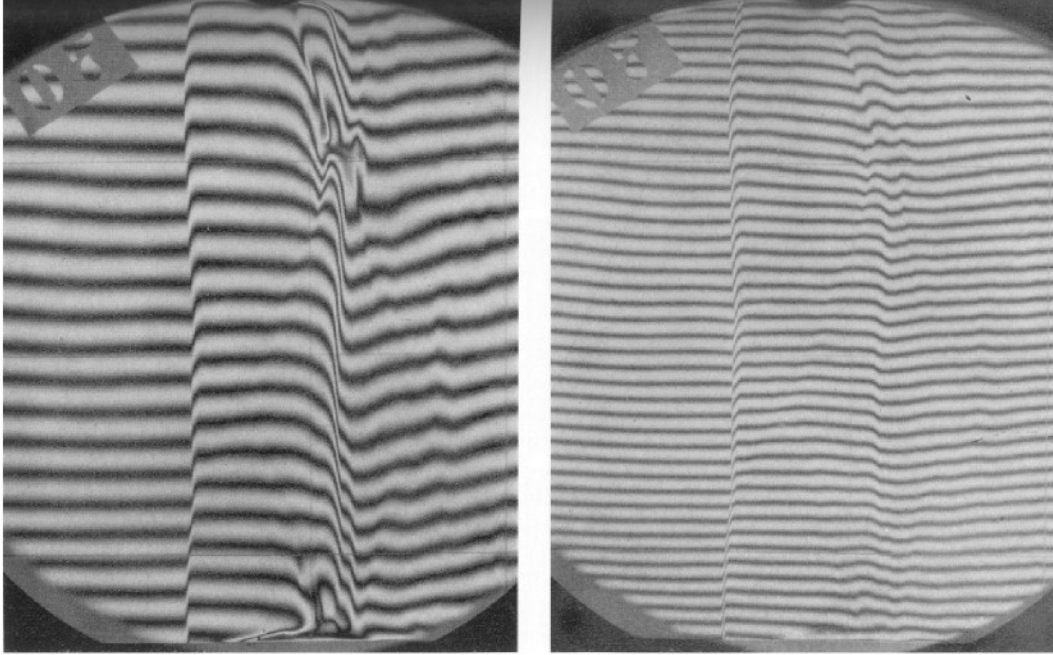


Figure 1.2: Experimental interferogram of argon shock structure at Ma 14.7 from [42]. First fringe shift from the left is the compression shock which is followed by the electron avalanche approximately 4.4 cm upwind. Flow is from right to left.

Of the numerous studies conducted and results obtained, it was not until the shock tube experiments conducted at the Institute for Aerospace Studies, University of Toronto, [42] showed that under certain conditions, a definite dynamical behavior could be associated with a strong ionizing shock in argon. It was discovered that the translational shock front propagating in pure argon “develops sinusoidal instabilities which affect the entire shock structure including the ionization relaxation region, the electron cascade front, and the final quasi-equilibrium state” (cf. Figure 1.2). The authors noted similarities between the oscillating shock front of the ionizing argon shock and detonation shock waves and sought techniques for suppressing the ionization instabilities that could also be applicable to detonation waves. While it was found that small amounts of impurities including molecular hydrogen, nitrogen, and oxygen were suitable in quenching the oscillations, a valid explanation for their existence nor a concrete link to detonation phenomena was found.

Attempts to duplicate these anomalies numerically were not made until the transient, one-dimensional simulations of Cambier [21] were able to show a definite coupling between the ionization kinetics and the gasdynamics through pressure sources. It was found that

pressure spikes in the electron avalanche region are reflected down stream to the compression shock, thereby causing fluctuations in the shock temperature and speed. This mechanism is similar to that found in detonation waves, furthering the case for a link between the two. The further significance is that it introduced yet another criterion to gauge the quality of theoretical models against experimental data. An accurate model should be able to reproduce the oscillations of the experimental results to the same degree. Despite these efforts, the work was never extended to simulate the instabilities of a multi-dimensional ionizing shock.

## 1.2 Scope and overview

It is the primary focus of this work to develop a numerical method for the transport of nonequilibrium plasma as described by a collisional-radiative model that can be applied to study the structure of multidimensional ionizing shocks in argon. Modeling such a structure requires high-order transport solvers to resolve the dynamical nature of the shock structure as well as a detailed chemical kinetics scheme to solve the processes of nonequilibrium ionization. The ability to accurately do so would be a significant contribution to the coupling of gasdynamic and collisional-radiative modeling. This would also open the door to many problems of interest including re-entry dynamics including base flows, rapid expansion of plasmas, RF plasmas, laser-plasma interaction, etc.

The plasma is described by the two-temperature, single-fluid equations with treatment of the electronic states as individual as formulated in Chapter 2. A numerical formulation based on a finite-volume discretization is given in Chapter 3. Treatment of the convective transport is discussed in some detail, beginning in Chapter 4 with a third-order reconstruction scheme for which the stability analysis in Chapter 5 is performed. The convection scheme is benchmarked against several standard test cases in Chapter 6 as applied to the Euler and ideal MHD equations. The collisional-radiative model developed for argon is presented in Chapter 9.

Numerical results of the Glass and Liu shock tube experiments are presented in Chapter 10 in terms of one- and two-dimensional simulations. Both steady and unsteady 1D simulations are used to establish the cross sections and rates that are best able to reproduce the experimental relaxation length and ionization fractions. Two-dimensional simulations



are then performed to determine the actual shock structure. As an extension to external flow, the solver is then applied to flow around a circular cylinder in Chapter 11.

The parallel framework that serves as the backbone of the numerical solver is presented in Chapter 12. It is developed entirely in Java and is capable of execution on distributed memory machines.

## CHAPTER 2

### GOVERNING EQUATIONS

The governing set of equations at the foundation of the current research are presented in this chapter. They include all of the relevant physics to be modeled, including convective and diffusive transport, wave (acoustic) phenomena, chemical kinetics, and so on. Of critical importance is the coupling of these effects and how they are accounted for in the formulation and resulting numerical implementation.

In particular, a self-consistent formulation between convective transport and wave phenomena is crucial. This is important, for example, to ensure proper jump conditions across shock waves and other discontinuities that are necessary for accurate calculation of the reaction rates needed for the collisional-radiative model. As a result, added emphasis will be placed on accurate treatment of the convective terms.

The plasmas to be investigated are assumed to be sufficiently collisional such that the continuum hypothesis is valid. As a result, a Maxwellian distribution of the velocity is taken, allowing a fluid description of the plasma. The resulting fluid equations are presented here in conservation form and are hyperbolic in nature. It is from the hyperbolic nature of these equations that numerical formulations will be developed. The diffusive and kinetic processes will be treated as source terms that can be updated independently<sup>1</sup> of the convective terms.

We begin by introducing the general form of the governing equations and some properties. We then get into the specifics in which we introduce the two-temperature (2T) equations which we finally couple with electromagnetic effects.

---

<sup>1</sup>Within a time step.

## 2.1 Conservative formulation

The governing equations are presented here in differential form to facilitate their derivation. They will be cast into integral form in the following chapter which will serve as the basis for the numerical finite-volume formulation. The flow equations in divergence form can be expressed as

$$\frac{\partial Q}{\partial t} + \nabla \cdot \bar{\bar{F}} = \dot{\Omega}, \quad (2.1)$$

where  $Q$  is the vector of conserved quantities,  $\bar{\bar{F}}$  is a second-order tensor containing the flux density of  $Q$ , and  $\dot{\Omega}$  is a vector of source terms. The convention adopted in this work is that the mathematical nature of the left-hand side (LHS) of Eq. (2.1) will be strictly hyperbolic while  $\dot{\Omega}$  contains all terms to the contrary. These terms may include diffusive, dispersive, chemical kinetics and other such processes, each of which must be dealt with appropriately. In particular, these processes may have associated time scales much smaller than that of the convective processes, and temporal resolution of these scales in both an efficient and accurate manner requires operator-splitting techniques to be employed. That is, the transport equations are solved independently of the source terms, which are in turn solved independently of each other. In such an approach, a change is computed for the convective contribution,

$$\left. \frac{\partial Q}{\partial t} \right|_{\text{conv}} = -\nabla \cdot \bar{\bar{F}} \quad (2.2)$$

followed by the contribution from the various source terms,

$$\left. \frac{\partial Q}{\partial t} \right|_{\text{cond}} = \dot{\Omega}_{\text{cond}}, \quad \left. \frac{\partial Q}{\partial t} \right|_{\text{diff}} = \dot{\Omega}_{\text{diff}}, \quad \left. \frac{\partial Q}{\partial t} \right|_{\text{chem}} = \dot{\Omega}_{\text{chem}}, \dots \quad (2.3)$$

the combined sum of which gives the total change of the conserved variables,

$$\frac{\partial Q}{\partial t} = \left. \frac{\partial Q}{\partial t} \right|_{\text{conv}} + \left. \frac{\partial Q}{\partial t} \right|_{\text{cond}} + \left. \frac{\partial Q}{\partial t} \right|_{\text{diff}} + \left. \frac{\partial Q}{\partial t} \right|_{\text{chem}} + \dots \quad (2.4)$$

### 2.1.1 Hyperbolic terms

Operator-splitting can be used to analyze individual contributions to the governing equations. In particular, operator-splitting is applied here to isolate the hyperbolic contribution to the governing equations, resulting in

$$\frac{\partial Q}{\partial t} + \nabla \cdot \bar{\bar{F}} = 0. \quad (2.5)$$

Taking the directional derivative of the LHS of Eq. (2.5) along an arbitrary direction  $\hat{n}$  gives,

$$\frac{\partial Q}{\partial t} + \nabla_{\hat{n}} \cdot \bar{\bar{F}} = 0, \quad (2.6)$$

or equivalently,

$$\frac{\partial Q}{\partial t} + \nabla \cdot F_n = 0, \quad (2.7)$$

where  $F_n = \hat{n} \cdot \bar{\bar{F}}$  is the vector of flux density in the  $n$ -direction. This form is particularly useful in the analysis of the governing equations and will be used extensively throughout this work. Upon application of the chain rule,

$$\frac{\partial F(Q)}{\partial n} = \left[ \frac{\partial F}{\partial Q} \right] \frac{\partial Q}{\partial n} = A \frac{\partial Q}{\partial n}, \quad (2.8)$$

Eq. (2.6) can be expressed as

$$\frac{\partial Q}{\partial t} + A_n \frac{\partial Q}{\partial n} = 0, \quad (2.9)$$

where  $A = \partial F / \partial Q$ . This system is classified as hyperbolic if all eigenvalues of the Jacobian matrix  $A$  are real and has a complete set of right eigenvectors,  $\vec{r}_i$ . This work will deal only with systems for which the flux Jacobian matrix  $A$  can be diagonalized as,

$$A = R\Lambda L, \quad (2.10)$$

where  $\Lambda$  is a diagonal matrix of *real* eigenvalues and  $R$  and  $L$  are matrices of right and left eigenvectors, respectively. In general, diagonalization of the Jacobian matrix when expressed

in terms of the conserved quantities can be fairly complex. To facilitate diagonalization, the Jacobian is re-expressed through a similarity transformation,

$$A = \frac{\partial Q}{\partial V} \frac{\partial V}{\partial Q} \frac{\partial F}{\partial V} \frac{\partial V}{\partial Q} \quad (2.11)$$

$$= M A_p M^{-1} \quad (2.12)$$

provided by the transformation matrices,

$$M = \partial Q / \partial V \quad (2.13)$$

$$M^{-1} = \partial V / \partial Q. \quad (2.14)$$

Because  $A$  and  $A_p$  are similar, they share the same eigenvalues, although their eigenvectors span different eigenspaces. Their eigenvectors are related by

$$R = M R_p, \quad L = L_p M^{-1}. \quad (2.15)$$

The vector  $V$  can arbitrarily be defined, but will be taken as the vector of primitive variables as will later be shown (hence the subscript  $p$  in Eq. (2.12)). With such a diagonalization, Eq. (2.9) can be cast into characteristic form as,

$$\frac{\partial W}{\partial t} + \Lambda_n \frac{\partial W}{\partial n} = 0, \quad (2.16)$$

with  $W = LQ$  and assuming  $A$  to be constant. In the transformation from Eq. (2.9) to Eq. (2.16), the hyperbolic system has been decoupled, and as a result, each characteristic equation can be solved independently of each other.<sup>2</sup> The exact form of  $Q$ ,  $V$ , and  $F$ , as well as their resulting diagonalization, to be used in the current research are the subject of the following sections, which include the basic flow equations coupled with the bi-temperature and magnetohydrodynamic models, for which the form of  $\dot{\Omega}$  will also be derived.

---

<sup>2</sup>This is a necessary step if the solution technique involves nonlinear operators, such as limiters.

## 2.2 Two-temperature model

For flows that can be described by very high Mach numbers, the air may become appreciably ionized. For such cases in which ionization results from a hot plasma, an equation for the electron energy is also required. As the atoms in the fluid are ionized and an electron gas is formed, electrons rapidly thermalize with each other, and a Maxwellian distribution and associated electron temperature  $T_e$  can be assumed if the electrons are sufficiently collisional. The slow energy exchange between electrons and the heavy particles, however, means that the two species, in general, cannot be described by the same temperature. As a result, a two-temperature (2T) model in which the electron thermal energy is convected independently of the total energy is necessary.

Such a model can be achieved by augmenting the governing equations for the bulk fluid with the electron fluid equations. Incorporation of the full electron mass, momentum, and energy equations leads to a two-fluid (2F) description of the plasma. This can be computationally restrictive as the electron conservation equations introduce the electron thermal velocity,  $a_e$ , which can be several orders of magnitude greater than that of the heavy particles and must be resolved nonetheless. In the single-fluid (1F) approach, on the other hand, the electron momentum equation is used to simplify the electron energy equation to a linear convection equation. As a result, the electron momentum equation is implicitly satisfied and the electron thermal velocity vanishes. In order to highlight key assumptions, the single-fluid, two-temperature model is derived here from the full two-fluid description of the plasma.

### 2.2.1 Two-fluid equations

For collision-dominated flows, the heavy particles are well-defined by a single fluid, with continuity, momentum, and energy equations,

$$\frac{\partial \rho_s}{\partial t} + \nabla \cdot (\rho_h \vec{u}_h) = \dot{\rho}_s \quad (2.17)$$

$$\frac{\partial \rho_h \vec{u}_h}{\partial t} + \nabla \cdot (\rho_h \vec{u}_h \vec{u}_h) + \nabla p_h = \vec{\mu}_{eh} + n_i e Z_i (\vec{E} + \vec{u}_h \times \vec{B}) \quad (2.18)$$

$$\begin{aligned} \frac{\partial}{\partial t} \left[ \rho_h \left( \varepsilon_h + \frac{1}{2} \vec{u}_h \cdot \vec{u}_h \right) \right] + \nabla \cdot \left[ \rho_h \vec{u}_h \left( \varepsilon_h + \frac{1}{2} \vec{u}_h \cdot \vec{u}_h \right) \right] + \nabla \cdot (\vec{u}_h p_h) \\ = \vec{u}_h \cdot \vec{\mu}_{eh} - n_i e Z_i \vec{u}_h \cdot \vec{E} - \nabla \cdot (\bar{\kappa}_h \nabla T_h) - \dot{q}_h^{\text{CR}} \end{aligned} \quad (2.19)$$

respectively. Each heavy particle specie  $s$  contributes to the total mass density,

$$\rho_h = \sum_{s \neq e} \rho_s \quad (2.20)$$

which in this work can be an atom, ion, or electronically-excited level. Thermal conductivity is given by  $\kappa$  and  $\dot{q}_h^{\text{CR}}$  denotes energy changes dues to collisional-radiative processes, while  $\vec{\mu}$  is the momentum transfer function between heavy particles and electrons.

The continuity, momentum, and energy equations for the electron fluid are given by

$$\frac{\partial \rho_e}{\partial t} + \nabla \cdot (\rho_e \vec{u}_e) = \dot{\rho}_e \quad (2.21)$$

$$\frac{\partial \rho_e \vec{u}_e}{\partial t} + \nabla \cdot (\rho_e \vec{u}_e \vec{u}_e) + \nabla p_e = \vec{\mu}_{he} + n_e e (\vec{E} + \vec{u}_e \times \vec{B}) \quad (2.22)$$

$$\begin{aligned} \frac{\partial}{\partial t} \left[ \rho_e \left( \varepsilon_e + \frac{1}{2} \vec{u}_e \cdot \vec{u}_e \right) \right] + \nabla \cdot \left[ \rho_e \vec{u}_e \left( \varepsilon_e + \frac{1}{2} \vec{u}_e \cdot \vec{u}_e \right) \right] + \nabla \cdot (\vec{u}_e p_e) \\ = \vec{u}_e \cdot \vec{\mu}_{he} - n_e e \vec{u}_e \cdot \vec{E} - \nabla \cdot (\bar{\kappa}_e \nabla T_e) - \dot{q}_e^{\text{CR}} \end{aligned} \quad (2.23)$$

respectively. Here,  $\vec{\mu}_{he}$  is the momentum transfer function between electrons and heavy particles which is equal in magnitude but opposite in sign to  $\vec{\mu}_{eh}$ .

The key assumption in the two-temperature model is that both the heavy particle and electron bulk velocities can be described by the same velocity, i.e.  $u \approx u_e \approx u_h$ . This assumption is a direct consequence of charge neutrality and is valid when considering length scales greater than the Debye length. Making use of this condition, the overall continuity equation becomes

$$\frac{\partial \rho}{\partial t} + \nabla \cdot (\rho \vec{u}) = 0 \quad (2.24)$$

while the heavy-particle and electron momentum equations can be combined into an overall momentum equation,

$$\frac{\partial \rho \vec{u}}{\partial t} + \nabla \cdot (\rho \vec{u} \vec{u}) + \nabla p = Q \vec{E} + \vec{j}_c \times \vec{B}, \quad (2.25)$$

with the total mass density  $\rho = \rho_e + \rho_h$  and the total charge density  $Q = en_e + e \sum n_i Z_i$ . Furthermore, the heavy-particle and electron energy equations can be combined into an overall energy equation,

$$\frac{\partial E}{\partial t} + \nabla \cdot (\vec{u} H_o) + \nabla p = \vec{j}_c \cdot \vec{E} - \nabla \cdot (\bar{\kappa}_h \nabla T_h) - \nabla \cdot (\bar{\kappa}_e \nabla T_e) - \dot{q}_{CR} \quad (2.26)$$

where  $E$  is the total energy,

$$E = \varepsilon_h + \varepsilon_e + \frac{1}{2} \rho \vec{u} \cdot \vec{u} \quad (2.27)$$

and  $H_o = E + p$  is the stagnation enthalpy density.

### 2.2.2 Generalized Ohm's law

Although the assumption of charge neutrality in the 2T model precludes the possibility of convection currents, conduction currents can still be present due to variations in the specie drift velocities. As derived from the 2F equations, the generalized Ohm's law provides an expression for the conduction current [109],

$$\vec{j}_c = \sigma \left\{ \vec{E} + \vec{u} \times \vec{B} + \frac{\nabla p_e}{n_e e} - \frac{\vec{j} \times \vec{B}}{n_e e} \right\}. \quad (2.28)$$

### 2.2.3 Electron fluid

Note that the electron energy equation is a function of the electron pressure  $p_e$ . The eigenvalues of such a system includes the thermal sound speed of the electron gas which is prohibitively stiff. It is therefore necessary to remove this dependency and reduce the electron energy equation to a linear advection equation in eigenspace. We begin this process by first recasting the electron continuity and momentum equations in non-conservative form which will then be used to simplify the electron energy equation. Furthermore, electromagnetic



effects will be neglected.

### Conservation of electron mass

The electron continuity equation in divergence form is given by Eq. (2.21),

$$\frac{\partial \rho_e}{\partial t} + \nabla \cdot (\rho_e \vec{u}) = \dot{\rho}_e \quad (2.29)$$

where  $\dot{\rho}_e$  is the rate of change of electron density due to ionization and recombination.

Expanding the divergence term,

$$\frac{\partial \rho_e}{\partial t} + \vec{u} \cdot \nabla \rho_e + \rho_e \nabla \cdot \vec{u} = \dot{\rho}_e, \quad (2.30)$$

the non-conservative form is found to be

$$\frac{D \rho_e}{Dt} + \rho_e \nabla \cdot \vec{u} = \dot{\rho}_e \quad (2.31)$$

with the material derivative defined as

$$\frac{D}{Dt} \equiv \frac{\partial}{\partial t} + \vec{u} \cdot \nabla. \quad (2.32)$$

### Conservation of electron momentum

The momentum equation in divergence form is given by

$$\frac{\partial \rho_e \vec{u}}{\partial t} + \nabla \cdot (\rho_e \vec{u} \vec{u}) + \nabla p_e = \vec{\mu}_{he}. \quad (2.33)$$

where  $\vec{\mu}_e$  is the momentum transfer function between the electron and heavy species. Substitution into the momentum equation and carrying out the indicated operations on the LHS yields

$$\rho_e \frac{\partial \vec{u}}{\partial t} + \vec{u} \frac{\partial \rho_e}{\partial t} + \rho_e (\vec{u} \cdot \nabla) \vec{u} + \vec{u} \nabla \cdot (\rho_e \vec{u}) + \nabla p_e = \vec{\mu}_{he} \quad (2.34)$$

in which the second and fourth terms are the convective terms of the continuity equation, Eq. (2.31), yielding

$$\rho_e \frac{D\vec{u}}{Dt} + \nabla p_e = \vec{\mu}_{he} - \dot{\rho}_e \vec{u}. \quad (2.35)$$

### Conservation of electron energy

The energy equation is represented in divergence form as

$$\begin{aligned} \frac{\partial}{\partial t} \left[ \rho_e \left( \varepsilon_e + \frac{1}{2} \vec{u} \cdot \vec{u} \right) \right] + \nabla \cdot \left[ \rho_e \left( \varepsilon_e + \frac{1}{2} \vec{u} \cdot \vec{u} \right) \vec{u} \right] + \nabla \cdot (\vec{u} p_e) \\ = \vec{u}_{he} \cdot \vec{\mu} - \nabla \cdot \vec{q}_e - \dot{q}_{CR} \end{aligned} \quad (2.36)$$

where  $\nabla \cdot \vec{q}_e$  is the electron heat conduction. Separating the internal energy from the kinetic energy, for which the indicated operations are carried out,

$$\begin{aligned} \frac{\partial}{\partial t} (\rho_e \varepsilon_e) + \nabla \cdot (\rho_e \varepsilon_e \vec{u}) + \frac{1}{2} (\vec{u} \cdot \vec{u}) \frac{\partial \rho_e}{\partial t} + \frac{1}{2} \rho_e \frac{\partial}{\partial t} (\vec{u} \cdot \vec{u}) \\ + \frac{1}{2} \rho_e \vec{u} \cdot \nabla (\vec{u} \cdot \vec{u}) + \frac{1}{2} (\vec{u} \cdot \vec{u}) \nabla \cdot (\rho_e \vec{u}) + p_e \nabla \cdot \vec{u} + \vec{u} \cdot \nabla p_e \\ = \vec{u}_{he} \cdot \vec{\mu} - \nabla \cdot \vec{q}_e - \dot{q}_{CR} \end{aligned} \quad (2.37)$$

and upon regrouping terms,

$$\begin{aligned} \frac{\partial}{\partial t} (\rho_e \varepsilon_e) + \nabla \cdot (\rho_e \varepsilon_e \vec{u}) + \frac{1}{2} (\vec{u} \cdot \vec{u}) \left[ \frac{\partial \rho_e}{\partial t} + \nabla \cdot (\rho_e \vec{u}) \right] + \frac{1}{2} \rho_e \frac{D}{Dt} (\vec{u} \cdot \vec{u}) + \vec{u} \cdot \nabla p_e + p_e \nabla \cdot \vec{u} \\ = \vec{u}_{he} \cdot \vec{\mu} - \nabla \cdot \vec{q}_e - \dot{q}_{CR} \end{aligned} \quad (2.38)$$

and noting that

$$\frac{1}{2} \rho_e \frac{D}{Dt} (\vec{u} \cdot \vec{u}) = \vec{u} \cdot \rho_e \frac{D\vec{u}}{Dt}$$

$$\begin{aligned}
\frac{\partial}{\partial t}(\rho_e \varepsilon_e) + \nabla \cdot (\rho_e \varepsilon_e \vec{u}) + \frac{1}{2}(\vec{u} \cdot \vec{u}) \left[ \frac{\partial \rho_e}{\partial t} + \nabla \cdot (\rho_e \vec{u}) \right] + \vec{u} \cdot \left[ \rho_e \frac{D\vec{u}}{Dt} + \nabla p_e \right] + p_e \nabla \cdot \vec{u} \\
= \vec{u}_{he} \cdot \vec{\mu} - \nabla \cdot \vec{q}_e - \dot{q}_{CR} \quad (2.39)
\end{aligned}$$

it is found that the third and fourth terms on the LHS of Eq. (2.39) contain expressions involving the continuity and momentum equations, (2.29) and (2.35), respectively. Making the appropriate substitutions, the energy equation reduces to

$$\frac{\partial}{\partial t}(\rho_e \varepsilon_e) + \nabla \cdot (\rho_e \varepsilon_e \vec{u}) = -p_e \nabla \cdot \vec{u} + \dot{\omega} \quad (2.40)$$

where

$$\dot{\omega} = \frac{1}{2} \dot{\rho}_e \vec{u} \cdot \vec{u} - \nabla \cdot \vec{q}_e - \dot{q}_{CR} \quad (2.41)$$

in which the second term has been obtained under the assumption,  $\vec{V}_e \gg \vec{u}$ .

The result is that the electron energy equation has been reduced to a linear convection equation, for which the electron sound speed does not play a role. The trade-off, however, is that the source term containing the velocity divergence  $p_e \nabla \cdot \vec{u}$  is in non-conservative form, and may present severe numerical difficulties where the flow gradients are not resolved, degrading solutions at shocks and other discontinuities. A solution to this problem is possible and was first presented in [15]. Expressing the LHS of Eq. (2.40) in non-conservative form with the aid of Eq. (2.31),

$$\rho_e \frac{D\varepsilon_e}{Dt} + p_e \nabla \cdot \vec{u} = \dot{\omega} - \dot{\rho}_e \varepsilon_e \quad (2.42)$$

and noting that the from the continuity equation Eq. (2.31),

$$\begin{aligned}
\nabla \cdot \vec{u} &= -v_e \frac{D\rho_e}{Dt} + v_e \dot{\rho}_e \\
&= \rho_e \frac{Dv_e}{Dt} + v_e \dot{\rho}_e \quad (2.43)
\end{aligned}$$

where  $v_e$  is the specific electronic volume, the velocity divergence term can be eliminated from Eq. (2.42), yielding

$$\rho_e \frac{D\varepsilon_e}{Dt} + \rho_e p_e \frac{Dv_e}{Dt} = \dot{\omega} - \varepsilon_e \dot{\rho}_e - \frac{p_e}{\rho_e} \dot{\rho}_e \quad (2.44)$$

The LHS of Eq. (2.44) can be related to the entropy through the 1<sup>st</sup> law of thermodynamics in advection form, namely

$$\rho_e \frac{D\varepsilon_e}{Dt} + \rho_e p_e \frac{Dv_e}{Dt} = \rho_e T_e \frac{Ds_e}{Dt} \quad (2.45)$$

resulting in

$$\rho_e T_e \frac{Ds_e}{Dt} = \dot{\omega} - \dot{\rho}_e h_e, \quad (2.46)$$

where  $h_e = \varepsilon_e + p_e/\rho_e$  is the specific electronic enthalpy. Dividing through by  $T_e$ ,

$$\rho_e \frac{Ds_e}{Dt} = \frac{1}{T_e} (\dot{\omega} - \dot{\rho}_e h_e) \quad (2.47)$$

and adding the continuity equation Eq. (2.31) with a factor  $s_e$ ,

$$\rho_e \frac{\partial s_e}{\partial t} + \rho_e \vec{u} \cdot \nabla s_e + s_e \left[ \frac{\partial \rho_e}{\partial t} + \nabla \cdot (\rho_e \vec{u}) - \dot{\rho}_e \right] = \frac{1}{T_e} (\dot{\omega} - \dot{\rho}_e h_e) \quad (2.48)$$

the conservative formulation is obtained for  $\rho_e s_e$ ,

$$\frac{\partial \rho_e s_e}{\partial t} + \nabla \cdot (\rho_e s_e \vec{u}) = \frac{1}{T_e} (\dot{\omega} - \dot{\rho}_e h_e) + \dot{\rho}_e s_e \quad (2.49)$$

This form of the energy equation is free of any non-conservative spatial operators and so is best-suited for shock-capturing schemes. The electron entropy function is given by the ideal gas isentropic relation,

$$s_e \equiv \frac{p_e}{\rho_e^{\gamma_e}} = \text{constant} \quad (2.50)$$

since electrons lack an internal structure and the assumption of constant specific heats is valid.

The electron entropy above presents a problem as it is ill-defined for cases in which the ionization fraction tends to zero. This can be remedied by introducing a pseudo-entropy variable defined as

$$\hat{s}_e \equiv \frac{p_e}{\rho^{\gamma_e}} \quad (2.51)$$

which is well-defined for all ionization fractions. Since the electron gas is calorically-perfect,

$$p_e = (\gamma_e - 1)\rho_e \varepsilon_e, \quad (2.52)$$

so that  $\hat{s}_e$  can also be defined as

$$\hat{s}_e \equiv (\gamma_e - 1) \frac{\rho_e \varepsilon_e}{\rho^{\gamma_e}} \quad (2.53)$$

The replacement of  $\rho_e s_e$  with  $\rho \hat{s}_e$  as a conserved variable is trivial as can be seen when inserted into the convection equation, (and can be verified by direct calculation)

$$\begin{aligned} \frac{\partial \rho \hat{s}_e}{\partial t} + \nabla \cdot (\rho \hat{s}_e \vec{u}) &= \frac{\partial}{\partial t} \left( \frac{p_e}{\rho^{\gamma_e-1}} \right) + \nabla \cdot \left( \frac{p_e}{\rho^{\gamma_e-1}} \vec{u} \right) \\ &= (1 - \gamma_e) \frac{p_e}{\rho^{\gamma_e}} \frac{\partial \rho}{\partial t} + \frac{1}{\rho^{\gamma_e-1}} \frac{\partial p_e}{\partial t} + \vec{u} \cdot \nabla \frac{p_e}{\rho^{\gamma_e-1}} + \frac{p_e}{\rho^{\gamma_e-1}} \nabla \cdot \vec{u} \\ &= (1 - \gamma_e) \frac{p_e}{\rho^{\gamma_e}} \frac{D\rho}{Dt} + \frac{\gamma_e - 1}{\rho^{\gamma_e-1}} \left( \frac{\partial E_e}{\partial t} + \nabla \cdot \vec{u} E_e \right) \\ &= \frac{\gamma_e - 1}{\rho^{\gamma_e-1}} \dot{\omega} \end{aligned} \quad (2.54)$$

where the overall momentum equation,  $D\rho/Dt + \rho \nabla \cdot \vec{u} = 0$ , has been used as well as Eq. (2.40) in conjunction with Eq. (2.52). Note that in addition to being better conditioned, Eq. (2.54) has the advantage of also being a simpler expression than Eq. (2.49). This results from the fact that  $d\rho = 0$  while  $d\rho_e \neq 0$ . Thus if the source terms are computed with  $\rho_e \varepsilon$  as the conservative variable, an update to the electronic entropy function may be obtained after the source term is multiplied by the factor  $(\gamma_e - 1)/\rho^{\gamma_e-1}$ . This result is verified by differentiating Eq. (2.53), i.e.

$$d(\rho \hat{s}_e) = \frac{(\gamma_e - 1)}{\rho^{\gamma_e - 1}} d(\rho_e \varepsilon_e) \quad (2.55)$$

## 2.2.4 Thermophysical properties

With the electron entropy equation, Eq. (2.54), combined with the bulk equations of motion and total energy, the two-temperature model takes the following form,

$$Q = \begin{pmatrix} \rho_1 \\ \vdots \\ \rho_n \\ \rho u \\ \rho v \\ \rho w \\ E \\ \rho \hat{s}_e \end{pmatrix}, \quad V = \begin{pmatrix} \rho_1 \\ \vdots \\ \rho_n \\ u \\ v \\ w \\ p \\ p_e \end{pmatrix}, \quad F_n = \begin{pmatrix} \rho_1 v_n \\ \vdots \\ \rho_n v_n \\ \rho u v_n + n_x p \\ \rho v v_n + n_y p \\ \rho w v_n + n_z p \\ (E + p) v_n \\ \rho \hat{s}_e v_n \end{pmatrix} \quad (2.56)$$

In order to close the 2T system, the thermal pressure must be related to the conserved quantities via appropriate equations of state (EOS). The relations are paramount in determining the differential relations that are necessary to develop the flux Jacobian matrix and corresponding eigensystem. First, the partial derivatives of the total and electron thermal pressures with respect to the conserved quantities are derived, followed by the partial derivatives of the total energy and electron entropy function with respect to the primitive variables.

### Pressure derivatives

The plasma is assumed to behave as an ideal gas in which case an exact expression for the total pressure of all species is obtained from Dalton's law of partial pressures,

$$p = p_h + p_e, \quad (2.57)$$

where the heavy particles obey a thermally-perfect EOS,

$$p_h = T_h \sum_{s \neq e} \rho_s R_s, \quad (2.58)$$

while a direct relationship between the electron pressure and entropy function has previously been defined (cf. Eq. (2.51)), giving

$$p_e = S_e \rho^{\gamma_e - 1}. \quad (2.59)$$

Differentiating Eqs. (2.58) and (2.59),

$$dp_h = dT_h \sum_{s \neq e} \rho_s R_s + T_h \sum_{s \neq e} R_s d\rho_s \quad (2.60)$$

$$dp_e = \rho^{\gamma_e - 1} dS_e + (\gamma_e - 1) \frac{p_e}{\rho} d\rho, \quad (2.61)$$

and combining with Eq. (2.57),

$$dp = dT_h \sum_{s \neq e} \rho_s R_s + T_h \sum_{s \neq e} R_s d\rho_s + \rho^{\gamma_e - 1} dS_e + (\gamma_e - 1) \frac{p_e}{\rho} d\rho, \quad (2.62)$$

an expression for the differential pressure is obtained. While the electron pressure has been expressed solely in terms of the conserved quantities, the heavy species contain a temperature dependence, which must be expressed in terms of the energy—a conservative variable. The total energy is expressed as the sum of the specie internal energies, kinetic energy, and, in the presence of magnetic fields, the magnetic pressure.

$$E = \sum_{s \neq e} \rho_s \varepsilon_s + \rho_e \varepsilon_e + \frac{\vec{m} \cdot \vec{m}}{2\rho} + \frac{\vec{B} \cdot \vec{B}}{2\mu_o} \quad (2.63)$$

Since the electrons lack an internal structure, the electron fluid obeys a calorically-perfect EOS, permitting a direct relationship between the electron internal energy and pressure,

$$\rho_e \varepsilon_e = \frac{p_e}{\gamma_e - 1}, \quad (2.64)$$

which, in combination with Eq. (2.63), gives

$$E = \sum_{s \neq e} \rho_s \varepsilon_s + \frac{p_e}{\gamma_e - 1} + \frac{\vec{m} \cdot \vec{m}}{2\rho} + \frac{\vec{B} \cdot \vec{B}}{2\mu_o} \quad (2.65)$$

Differentiating this expression,

$$dE = \sum_{s \neq e} \rho_s d\varepsilon_s + \sum_{s \neq e} \varepsilon_s d\rho_s + \frac{dp_e}{\gamma_e - 1} + \vec{u} \cdot d\vec{m} - \frac{1}{2} \vec{u} \cdot \vec{u} d\rho + \frac{1}{\mu_o} \vec{B} \cdot d\vec{B}, \quad (2.66)$$

and noting that for the (thermally-perfect) heavy species,

$$c_{v,s} = \left( \frac{\partial \varepsilon_s}{\partial T_h} \right)_v \xrightarrow[\text{ideal gas}]{c_{v,s}=f(T)} d\varepsilon_s = c_{v,s} dT_h \quad (2.67)$$

the desired differential form of  $T_h$  is found to be

$$dT_h = \frac{1}{\sum_{s \neq e} \rho_s c_{v,s}} \left[ dE + \frac{1}{2} \vec{u} \cdot \vec{u} d\rho - \vec{u} \cdot d\vec{m} - \frac{1}{\mu_o} \vec{B} \cdot d\vec{B} - \sum_{s \neq e} \varepsilon_s d\rho_s - \frac{dp_e}{\gamma_e - 1} \right] \quad (2.68)$$

Inserting Eq. (2.68) into (2.62) and again applying (2.61), the expression for the differential pressure can finally be expressed entirely in terms of the conserved quantity differentials,

$$dp = (\gamma_h - 1) \left[ dE + \frac{1}{2} \vec{u} \cdot \vec{u} d\rho - \vec{u} \cdot d\vec{m} - \frac{1}{\mu_o} \vec{B} \cdot d\vec{B} - \sum_{s \neq e} \varepsilon_s d\rho_s - \frac{\rho^{\gamma_e - 1}}{\gamma_e - 1} dS_e \right] \\ + T_h \sum_{s \neq e} R_s d\rho_s + \rho^{\gamma_e - 1} dS_e + (\gamma_e - \gamma_h) \frac{p_e}{\rho} d\rho \quad (2.69)$$

where

$$\gamma_h - 1 \equiv \frac{\sum_{s \neq e} \rho_s R_s}{\sum_{s \neq e} \rho_s c_{v,s}} \quad (2.70)$$

From Eqs. (2.61) and (2.69), the resulting pressure derivatives can now be defined.

$$P_E \equiv \left( \frac{\partial p}{\partial E} \right)_{q \neq E} = \gamma_h - 1 \quad (2.71)$$



$$P_{S_e} \equiv \left( \frac{\partial p}{\partial S_e} \right)_{q \neq S_e} = \rho^{\gamma_e - 1} \left( 1 - \frac{\gamma_h - 1}{\gamma_e - 1} \right) \quad (2.72)$$

$$P_{\vec{m}} \equiv \left( \frac{\partial p}{\partial \vec{m}} \right)_{q \neq \vec{m}} = -(\gamma_h - 1) \vec{u} \quad (2.73)$$

$$P_{\vec{B}} \equiv \left( \frac{\partial p}{\partial \vec{B}} \right)_{q \neq \vec{B}} = -(\gamma_h - 1) \frac{\vec{B}}{\mu_o} \quad (2.74)$$

$$P_{\rho_e} \equiv \left( \frac{\partial p}{\partial \rho_e} \right)_{q \neq \rho_e} = (\gamma_e - \gamma_h) \frac{p_e}{\rho} + \frac{1}{2} (\gamma_h - 1) \vec{u} \cdot \vec{u} \quad (2.75)$$

$$P_{\rho_{s \neq e}} \equiv \left( \frac{\partial p}{\partial \rho_{s \neq e}} \right)_{q \neq \rho_{s \neq e}} = P_{\rho_e} - (\gamma_h - 1) \varepsilon_s + \frac{p_s}{\rho_s} \quad (2.76)$$

$$P_\rho \equiv \left( \frac{\partial p}{\partial \rho} \right)_{q \neq \rho} = \sum y_s P_{\rho_s} = P_{\rho_e} - (\gamma_h - 1) \sum_{s \neq e} y_s \varepsilon_s + \frac{p - p_e}{\rho} \quad (2.77)$$

### Energy derivatives

Similar to the approach taken in the previous section, we can find the partial derivatives of the total energy and electron entropy function with respect to the primitive variables. Contrary to inserting the expression found for  $dT_h$  from the energy equation into the pressure equation, the pressure equation is rearranged to find  $dT_h$  which is then inserted into the energy equation. Differentiating the energy equation with respect to the primitive variables  $(\rho_s, \vec{u}, \vec{B}, p, p_e)$ , the following expression is obtained.

$$dE = dT_h \sum_{s \neq e} \rho_s c_{v,s} + \sum_{s \neq e} \varepsilon_s d\rho_s + \frac{dp_e}{\gamma_e - 1} + \rho \vec{u} \cdot d\vec{u} + \frac{1}{2} \vec{u} \cdot \vec{u} d\rho + \frac{1}{\mu_o} \vec{B} \cdot d\vec{B} \quad (2.78)$$

Rearranging the primitive variable equivalent of Eq. (2.62),

$$dT_h = \frac{1}{\sum_{s \neq e} \rho_s R_s} \left[ dp - T_h \sum_{s \neq e} R_s d\rho_s - dp_e \right] \quad (2.79)$$

and inserting into Eq. (2.78),

$$dE = \frac{1}{\gamma_h - 1} \left[ dp - T_h \sum_{s \neq e} R_s d\rho_s - dp_e \right] + \sum_{s \neq e} \varepsilon_s d\rho_s + \frac{dp_e}{\gamma_e - 1} + \rho \vec{u} \cdot d\vec{u} + \frac{1}{2} \vec{u} \cdot \vec{u} d\rho + \frac{1}{\mu_o} \vec{B} \cdot d\vec{B}, \quad (2.80)$$

an expression for the differential energy is obtained from which the partial derivatives of the total energy with respect to the primitive variables are defined.

$$E_p \equiv \left( \frac{\partial E}{\partial p} \right)_{v \neq p} = \frac{1}{\gamma_h - 1} \quad (2.81)$$

$$E_{p_e} \equiv \left( \frac{\partial E}{\partial p_e} \right)_{v \neq p_e} = \frac{1}{\gamma_e - 1} - \frac{1}{\gamma_h - 1} \quad (2.82)$$

$$E_{\vec{u}} \equiv \left( \frac{\partial E}{\partial \vec{u}} \right)_{v \neq \vec{u}} = \rho \vec{u} \quad (2.83)$$

$$E_{\vec{B}} \equiv \left( \frac{\partial E}{\partial \vec{B}} \right)_{v \neq \vec{B}} = \frac{1}{\mu_o} \vec{B} \quad (2.84)$$

$$E_{\rho_e} \equiv \left( \frac{\partial E}{\partial \rho_e} \right)_{v \neq \rho_e} = \frac{1}{2} \vec{u} \cdot \vec{u} \quad (2.85)$$

$$E_{\rho_{s \neq e}} \equiv \left( \frac{\partial E}{\partial \rho_{s \neq e}} \right)_{v \neq \rho_{s \neq e}} = E_{\rho_e} + \varepsilon_s - \frac{p_s}{(\gamma_h - 1)\rho_s} \quad (2.86)$$

### Electron pressure and entropy function derivatives

The electron pressure derivatives,

$$P_{eS_e} \equiv \left( \frac{\partial p_e}{\partial S_e} \right)_{q \neq S_e} = \rho^{\gamma_e - 1} = \frac{p_e}{S_e} \quad (2.87)$$

$$P_{e\rho_s} \equiv \left( \frac{\partial p_e}{\partial \rho_s} \right)_{q \neq \rho_s} = (\gamma_e - 1) \frac{p_e}{\rho} \quad (2.88)$$

$$P_{e\rho} \equiv \left( \frac{\partial p_e}{\partial \rho} \right)_{q \neq \rho} = P_{e\rho_s} \quad (2.89)$$

$$P_{e\vec{m}} \equiv \left( \frac{\partial p_e}{\partial \vec{m}} \right)_{q \neq \vec{m}} = 0 \quad (2.90)$$

$$P_{e\vec{B}} \equiv \left( \frac{\partial p_e}{\partial \vec{B}} \right)_{q \neq \vec{B}} = 0 \quad (2.91)$$

$$P_{eE} \equiv \left( \frac{\partial p_e}{\partial E} \right)_{q \neq E} = 0 \quad (2.92)$$

and entropy function derivatives,

$$S_{e\rho_s} \equiv \left( \frac{\partial S_e}{\partial \rho_s} \right)_{v \neq \rho_s} = (1 - \gamma_e) \frac{p_e}{\rho^{\gamma_e}} = (1 - \gamma_e) \frac{S_e}{\rho} \quad (2.93)$$

$$S_{e\rho} \equiv \left( \frac{\partial S_e}{\partial \rho} \right)_{v \neq \rho} = S_{e\rho_s} \quad (2.94)$$

$$S_{ep_e} \equiv \left( \frac{\partial S_e}{\partial p_e} \right)_{v \neq p_e} = \rho^{1-\gamma_e} \quad (2.95)$$

$$S_{e\vec{u}} \equiv \left( \frac{\partial S_e}{\partial \vec{u}} \right)_{v \neq \vec{u}} = 0 \quad (2.96)$$

$$S_{e\vec{B}} \equiv \left( \frac{\partial S_e}{\partial \vec{B}} \right)_{v \neq \vec{B}} = 0 \quad (2.97)$$

$$S_{ep} \equiv \left( \frac{\partial S_e}{\partial p} \right)_{v \neq p} = 0 \quad (2.98)$$

are defined via Eq. (2.61).

### 2.2.5 Two-temperature eigensystem

With the thermodynamics properties derived, it is now possible to derive the eigensystem for the two-temperature model. The complete 2T eigensystem is given in Appendix A.

## 2.3 Two-Temperature MHD Model

With the presence of electrically charged species, the fluid has the ability to conduct electricity, and in the presence of electromagnetic fields, body forces which act on the fluid will be created and energy will be exchanged within the fluid. In order to take these effects into account, the bi-temperature fluid transport equations Eqs. (2.1) and (2.56) and must be coupled with Maxwell's equations,

$$\nabla \cdot \vec{E} = \frac{\rho_e}{\epsilon_o} \quad (2.99)$$

$$\nabla \cdot \vec{B} = 0 \quad (2.100)$$

$$\nabla \times \vec{E} = \frac{\partial \vec{B}}{\partial t} \quad (2.101)$$

$$\nabla \times \vec{B} = \mu_o \vec{J} + \mu_o \epsilon_o \frac{\partial \vec{E}}{\partial t} \quad (2.102)$$

The resulting two-temperature MHD equations can be expressed in the following vector form ([65],[15]),

$$Q = \begin{pmatrix} \rho_1 \\ \vdots \\ \rho_n \\ \rho u \\ \rho v \\ \rho w \\ B_x \\ B_y \\ B_z \\ E \\ \rho \hat{s}_e \end{pmatrix}, \quad V = \begin{pmatrix} \rho_1 \\ \vdots \\ \rho_n \\ u \\ v \\ w \\ B_x \\ B_y \\ B_z \\ p \\ p_e \end{pmatrix}, \quad F_n = \begin{pmatrix} \rho_1 v_n \\ \vdots \\ \rho_n v_n \\ \rho u v_n + n_x p_o - B_x B_n / \mu_o \\ \rho v v_n + n_y p_o - B_y B_n / \mu_o \\ \rho w v_n + n_z p_o - B_z B_n / \mu_o \\ v_n B_x - u B_n \\ v_n B_y - v B_n \\ v_n B_z - w B_n \\ v_n (E + p_o) - B_n (\vec{v} \cdot \vec{B}) / \mu_o \\ v_n S_e \end{pmatrix} \quad (2.103)$$

where  $p_o$  is the sum of the thermal and magnetic pressures,

$$p_o = p + \frac{\vec{B} \cdot \vec{B}}{2\mu_o}, \quad (2.104)$$

and the total energy is given by

$$E = \sum_{s \neq e} \rho_s \varepsilon_s + \rho_e \varepsilon_e + \frac{\vec{m} \cdot \vec{m}}{2\rho} + \frac{\vec{B} \cdot \vec{B}}{2\mu_o}. \quad (2.105)$$

## 2.4 Eigensystem

As done for the two-temperature hydrodynamic equations, the 2T MHD eigensystem is presented in Appendix A.

## CHAPTER 3

### NUMERICAL FORMULATION

With the governing equations detailed in the previous chapter, attention is here turned to developing a suitable numerical formulation. In particular, the discretization approach resulting from a finite-volume (FV) formulation is described. Focus will then be extended to the hyperbolic convection terms and the shock-capturing method will be detailed. Solution techniques for the diffusion terms and chemical kinetics will be described in Chapters 7 and 9, respectively.

#### 3.1 Finite-volume formulation

While their derivation was carried out in divergence form, the governing equations are here cast into integral form to ensure a conservative discretization. From Reynold's transport theorem,

$$\int_{V(t_2)} Q dV - \int_{V(t_1)} Q dV + \int_{t_1}^{t_2} \oint_{S(t)} \hat{n} \cdot \bar{\bar{F}} dS dt = \int_{t_1}^{t_2} \int_{V(t)} \dot{\Omega} dV dt, \quad (3.1)$$

the integral form of the governing equations is obtained. Defining

$$F_n \equiv \hat{n} \cdot \bar{\bar{F}} = n_x F_x + n_y F_y + n_z F_z \quad (3.2)$$

as the flux normal to the surface described by the unit vector,  $\hat{n}$ , and assuming that all variables are continuous in time, Eq. 3.1 reduces to

$$\frac{d}{dt} \int_V Q dV + \oint_S F_n dS = \int_V \dot{\Omega} dV. \quad (3.3)$$

Introducing the volume-average quantities,

$$\bar{Q} \equiv \frac{1}{V} \int_V Q dV, \quad \dot{\bar{Q}} \equiv \frac{1}{V} \int_V \dot{Q} dV, \quad (3.4)$$

further simplification can be made, yielding

$$\frac{dQ}{dt} + \frac{1}{V} \oint_S F_n dS = \dot{Q}, \quad (3.5)$$

in which the bars have been dropped with the implication that all quantities are volume averages. Equation (3.5) serves as the basis for finite-volume (FV) schemes adopted in this work.

Before proceeding, Eq. (3.5) is *operator split* such that the contribution of the source terms to the change in the conserved quantities will be treated independently of the contribution of the convective terms. The splitting results in two equations,

$$\left. \frac{dQ}{dt} \right|_{\text{conv}} = -\frac{1}{V} \oint_S F_n dS \quad \text{and} \quad \left. \frac{dQ}{dt} \right|_{\text{src}} = \dot{Q}, \quad (3.6)$$

the combination of which yields the total change in  $Q$ ,

$$\frac{dQ}{dt} = \left. \frac{dQ}{dt} \right|_{\text{conv}} + \left. \frac{dQ}{dt} \right|_{\text{src}}. \quad (3.7)$$

### 3.2 Semi-discete approach

Although a number of techniques exist to discretize Eq. (3.5), the one adopted here is a term-by-term treatment, in which the spatial operator is discretized first followed by the temporal derivative. Known as the semi-discrete approach, it is straight-forward, allowing flexibility. We begin by discretizing the spatial domain into  $N$ -sided polyhedra<sup>1</sup> which we refer to here as cells, such that the surface integral can be replaced by the summation,

$$\oint_S F_n dS \rightarrow \sum_{s=1}^N F_s A_s \quad (3.8)$$

where  $F_s$  is the flux normal to surface  $s$  and  $A_s$  is the area of surface  $s$ . This results in a coupled system of ODE's of the form

---

<sup>1</sup>Polyhedra in 3D, polygons in 2D, etc.

$$\frac{dQ}{dt} = -\frac{1}{V} \sum_s F_s A_s \quad (3.9)$$

for all cells in the domain. The flux function  $F_s$  at the surface between two cells,  $L$  and  $R$ , may be approximated via a numerical flux function,

$$\hat{F}_s = \frac{1}{2}(F_L + F_R) - \Phi, \quad (3.10)$$

which is a combination of a nondissipative centered approximation and a numerical diffusion function,  $\Phi$ . The numerical flux function can be tailored depending on the form of  $\Phi$ . In particular, an *upwind* bias may be introduced by letting  $\Phi$  take the form

$$\Phi = \frac{1}{2}|A_s|(Q_R - Q_L) \quad (3.11)$$

with the flux Jacobian as defined through the diagonalization

$$|A_s| \equiv R|\Lambda|L \quad (3.12)$$

as detailed in Chapter 2. The exact form of  $|A_s|$  follows from the necessary condition for pure upwinding,

$$F_s = \begin{cases} F_L & \text{if } |\Lambda| = \Lambda \\ F_R & \text{if } |\Lambda| = -\Lambda \end{cases}, \quad (3.13)$$

which can be achieved only in the case that  $A_s$  from Eq. (3.11) satisfies

$$F_R - F_L = A_s(Q_R - Q_L), \quad (3.14)$$

the solution of which yields the Roe-average states [96]. Such a linearization of the flux Jacobian also satisfies the Rankine-Hugoniot jump conditions and is able to capture stationary discontinuities exactly. Note that the Roe-average values are obtainable for the bi-temperature gasdynamic equations in the case that all species can be described by a calorically-ideal EOS. The bi-temperature MHD equations are further restricted to polytropic species with an adiabatic exponent of 2 [17], which consequently represents a phys-



ically meaningless state. However, approximations are available and can have a negligible effect as determined through numerical experiments.

As with all numerical flux functions, the upwind approximation does have its share of shortcomings, requiring special attention under certain flow conditions. Although details are not provided here, stabilizing techniques similar to the approaches found in [25], [92], and [47] have been implemented in this work.

### 3.3 Time-Marching

Once the spatial fluxes have been evaluated, the conserved quantities can be integrated in time via an appropriate time-marching method. While implicit integration techniques will be applied to the various source terms (c.f. Chapters 7 and 9), integration of the convective terms has been limited to explicit methods. Several such time-marching methods have been implemented and tested, including multi-step and predictor-corrector schemes. Introducing the operator  $L(Q) = -1/V \sum_s F_s A_s$ , Eq. (3.1) can be expressed as

$$\frac{dQ}{dt} = L(Q). \quad (3.15)$$

Integration from discrete time levels  $n$  to  $n + 1$ ,

$$\int_{t_n}^{t_{n+1}} (dQ = L(Q)dt), \quad (3.16)$$

can be approximated in a number of ways, several of which are provided as follows.

#### Explicit Euler

The explicit Euler scheme given by

$$Q^{n+1} = Q^n + \Delta t L(Q^n) \quad (3.17)$$

is perhaps the simplest integration techniques, resulting in global first-order accuracy.

#### Adams-Bashforth

The second-order Adams-Bashforth (AB2) scheme is given by

$$Q^{n+1} = Q^n - \frac{1}{2}\Delta t L(3Q^n - Q^{n-1}) \quad (3.18)$$

can provide better stability than the Euler explicit method, especially in convection-dominated problems. The AB2 scheme requires the storage of the solution at two distinct time levels,  $n$  and  $n+1$ . One possible implementation approach is to store  $Q^n$  explicitly, while  $Q^{n-1}$  is stored implicitly in the linear combination,  $3Q^n - Q^{n-1}$ . This can present advantages over storing as the fluxes must be evaluated for  $3Q^n - Q^{n-1}$  as opposed to  $Q^{n-1}$ .

### Runge-Kutta

Runge-Kutta schemes are of the predictor-corrector type which require multiple evaluations of the operator  $L$  per time step. This may be undesirable in a parallel implementation as each evaluation of  $L$  requires communication between blocks in order to update information at the boundaries. The second-order variant (RK2), also known as modified Euler, is given below.

$$\tilde{Q}^{n+1} = Q^n + \Delta t L(Q^n), \quad (3.19a)$$

$$Q^{n+1} = Q^n + \frac{1}{2}\Delta t L(Q^n + \tilde{Q}^{n+1}). \quad (3.19b)$$

$$(3.19c)$$

## CHAPTER 4

### RECONSTRUCTION

Accurate solution of the transport equations is necessary in order to reproduce such complex wave structures such as those seen in the argon shock tube results as discussed in Chapter 1. In particular, the ionization begins with a small but significant number of priming electrons just after the compression shock. The convection of these priming electrons and excited species farther upstream of the shock is determined by the evaluation of the flux  $F$  in Eq. (2.1). A low-order evaluation of the flux may lead to excessive diffusion of these species, resulting in a delay in the electron avalanche, thereby altering the induction length. Therefore it is desirable to have an advection scheme which introduces as minimal amount of diffusion as possible, while maintaining a numerically stable and oscillation-free solution.

The approach taken here begins with the finite-volume method described in the previous chapter and proceeds via the steps outlined in Figure 4.1. In the standard finite-volume approach, the conservative variables are stored as averaged values over each computational cell. These values are then used to *reconstruct* higher-order representations based on polynomial, logarithmic, and other such approximations. The reconstruction determines the overall accuracy of the scheme and therefore is a key element of the numerical transport process. The principle function of the reconstruction scheme is to obtain accurate values at the interfaces between cells. These values, combined with an appropriate Riemann solver, are used to evolve the variables in characteristic phase-space, giving a flux quantity at each cell interface. Once the flux values have been determined, the variables are then projected to the new time level via a time-marching scheme.

The purpose of the chapter is to describe the reconstruction scheme to be used in the present research. A one-dimensional formulation is presented first, followed by a two-

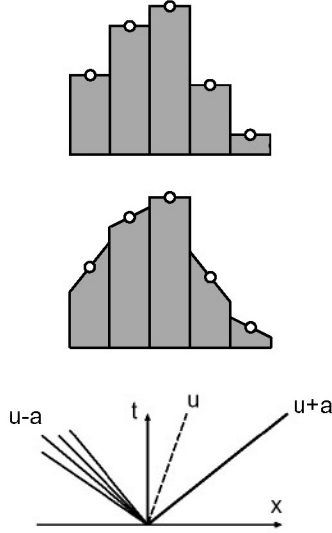


Figure 4.1: Numerical approach: projection, reconstruction, and evolution (taken from [89]).

dimensional extension based on piecewise-quadric surfaces. Formulated from the method of undetermined coefficients, the proposed reconstruction scheme can provide true multi-dimensional reconstruction on arbitrary meshes. Implementation of boundary conditions is briefly considered along with limiters.

#### 4.1 One-dimensional formulation

As applied to a three-point stencil from a 1D finite-volume discretization, the method of undetermined coefficients seeks a fit of the cell average values to a quadratic polynomial which defines the profile of the parabola,

$$u(x) = c_1 + c_2x + c_3x^2, \quad (4.1)$$

as determined by the following conditions,

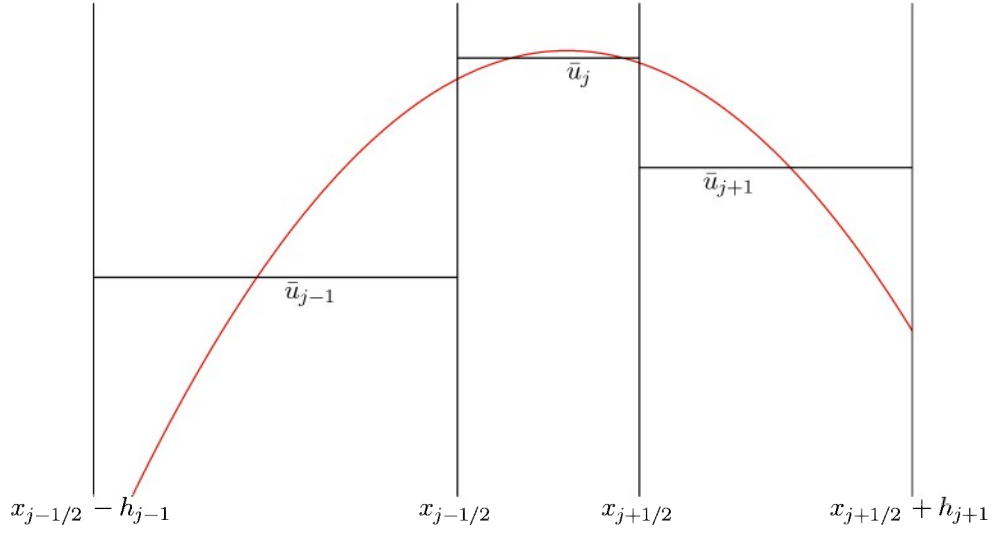


Figure 4.2: One-dimensional parabolic interpolation on a non-uniform mesh.

$$\frac{1}{h_{j+1}} \int_{x_{j+1/2}}^{x_{j+1/2} + h_{j+1}} u(x) dx = \bar{u}_{j+1} \quad (4.2a)$$

$$\frac{1}{h_j} \int_{x_{j-1/2}}^{x_{j+1/2}} u(x) dx = \bar{u}_j \quad (4.2b)$$

$$\frac{1}{h_{j-1}} \int_{x_{j-1/2} - h_{j-1}}^{x_{j-1/2}} u(x) dx = \bar{u}_{j-1}, \quad (4.2c)$$

where  $h_j$  is the width of cell  $j$  as illustrated in Figure 4.1. Introducing normalization parameters based on the ratio of the left and right cell widths *w.r.t.* that of the center cell,

$$r_{j-1} = \frac{h_{j-1}}{h_j} \quad r_{j+1} = \frac{h_{j+1}}{h_j},$$

the system can be rewritten as

$$\frac{1}{2r_{j+1}} \int_1^{1+2r_{j+1}} u(\xi) d\xi = \bar{u}_{j+1} \quad (4.3a)$$

$$\frac{1}{2} \int_{-1}^1 u(\xi) d\xi = \bar{u}_j \quad (4.3b)$$

$$\frac{1}{2r_{j-1}} \int_{-1-2r_{j-1}}^{-1} u(\xi) d\xi = \bar{u}_{j-1} \quad (4.3c)$$

with corresponding polynomial,  $u(\xi) = c_1 + c_2\xi + c_3\xi^2$ . This leads to the following linear system which must be solved for each cell  $I_j$ .

$$\begin{bmatrix} 1 & -1 - r_{j-1} & 1 + 2r_{j-1} + \frac{4}{3}r_{j-1}^2 \\ 1 & 0 & \frac{1}{3} \\ 1 & 1 + r_{j+1} & 1 + 2r_{j+1} + \frac{4}{3}r_{j+1}^2 \end{bmatrix} \begin{bmatrix} c_1 \\ c_2 \\ c_3 \end{bmatrix} = \begin{bmatrix} \bar{u}_{j-1} \\ \bar{u}_j \\ \bar{u}_{j+1} \end{bmatrix} \quad (4.4)$$

The first term on the LHS is the corresponding Vandermonde coefficient matrix,  $V$ , which can easily be inverted to obtain

$$V_j^{-1} = \begin{bmatrix} -\frac{1+r_{j+1}}{3|V|} & 1 - \frac{2+r_{j-1}+r_{j+1}}{3|V|} & -\frac{1+r_{j-1}}{3|V|} \\ -\frac{2(1+r_{j+1})(1+2r_{j+1})}{3|V|} & -\frac{2(r_{j-1}-r_{j+1})(3+2r_{j-1}+2r_{j+1})}{3|V|} & \frac{2(1+r_{j-1})(1+2r_{j-1})}{3|V|} \\ \frac{1+r_{j+1}}{|V|} & -\frac{2+r_{j-1}+r_{j+1}}{|V|} & \frac{1+r_{j-1}}{|V|} \end{bmatrix} \quad (4.5)$$

with determinant,

$$|V| = \frac{4}{3}(1+r_{j-1})(1+r_{j+1})(1+r_{j-1}+r_{j+1}). \quad (4.6)$$

Obtaining the coefficients of the reconstruction polynomial then becomes a simple matrix-vector multiplication,

$$\begin{bmatrix} c_1 \\ c_2 \\ c_3 \end{bmatrix} = \begin{bmatrix} V_j^{-1} \end{bmatrix} \begin{bmatrix} \bar{u}_{j-1} \\ \bar{u}_j \\ \bar{u}_{j+1} \end{bmatrix}. \quad (4.7)$$

An example reconstruction polynomial obtained from Eq. (4.7) is plotted in figure 4.1.

Since constructing the fluxes at the cell interfaces (cf. Eq. (3.10)) is of primary concern,

the value of the interpolated polynomial at the locations  $u_{j\pm n/2}$ ,  $n = 1, 2, \dots$  is desired. In the normalized reference frame, the values of the polynomial at the faces of cell  $j$  are defined by

$$u_{L,j} \equiv u_{j-1/2} = u(-1) = c_1 - c_2 + c_3, \quad (4.8)$$

$$u_{R,j} \equiv u_{j+1/2} = u(+1) = c_1 + c_2 + c_3, \quad (4.9)$$

where  $u_{L,j}$  is the interpolated value at the left cell interface, resulting from the interpolation based in cell  $j$ , while  $u_{R,j}$  is the interpolated value at the right cell interface, resulting from the interpolation based in cell  $j$ . Vectorization is accomplished via

$$u_j^L = \begin{bmatrix} 1 & 1 & 1 \end{bmatrix} \begin{bmatrix} V_j^{-1} \end{bmatrix} \begin{bmatrix} \bar{u}_{j-1} \\ \bar{u}_j \\ \bar{u}_{j+1} \end{bmatrix}, \quad (4.10)$$

$$u_j^R = \begin{bmatrix} 1 & -1 & 1 \end{bmatrix} \begin{bmatrix} V_j^{-1} \end{bmatrix} \begin{bmatrix} \bar{u}_{j-1} \\ \bar{u}_j \\ \bar{u}_{j+1} \end{bmatrix}. \quad (4.11)$$

### Uniform mesh

In the case of uniform mesh spacing, the Vandermonde matrix reduces to

$$V = \begin{bmatrix} 1 & -2 & \frac{13}{3} \\ 1 & 0 & \frac{1}{3} \\ 1 & 2 & \frac{13}{3} \end{bmatrix}, \quad V^{-1} = \begin{bmatrix} -\frac{1}{24} & \frac{13}{12} & -\frac{1}{24} \\ -\frac{1}{4} & 0 & \frac{1}{4} \\ \frac{1}{8} & -\frac{1}{4} & \frac{1}{8} \end{bmatrix} \quad (4.12)$$

yielding left and right states,

$$u_L = \frac{1}{6}(2\bar{u}_{j-1} + 5\bar{u}_j - \bar{u}_{j+1}), \quad (4.13)$$

$$u_R = \frac{1}{6}(2\bar{u}_{j+1} + 5\bar{u}_j - \bar{u}_{j-1}). \quad (4.14)$$

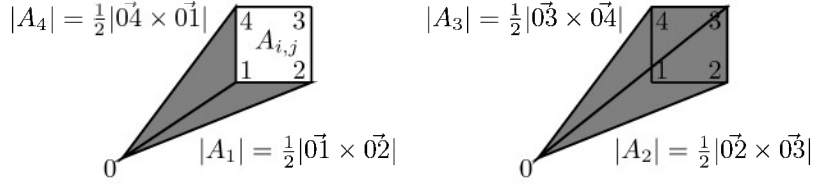


Figure 4.3: General area representation based on arbitrary point. Shaded regions are absolute values of the areas  $A_1 \dots A_4$ .

This formulation is equivalent to the fourth scheme of van Leer (cf. [115, 54]).

## 4.2 Two-dimensional formulation

The method of undetermined coefficients is easily generalized to 2D. The second-order polynomial which defines a quadric paraboloid in two dimensions is given by

$$u(x, y) = c_1 + c_2x + c_3y + c_4x^2 + c_5y^2 + c_6xy. \quad (4.15)$$

To determine the coefficients, this polynomial is integrated over each cell in the stencil.

$$\frac{1}{A_{i,j}} \int_{I_{i,j}} u(x, y) dx dy = \bar{u}_{i,j} \quad (4.16)$$

To evaluate the integral, we rely on a coordinate transformation from the physical to the natural domain using isoparametric elements defined by bi-linear shape functions as given in Appendix B. The integral in Eq. (4.16) is transformed to

$$\frac{1}{A_{i,j}} \int_{-1}^1 \int_{-1}^1 u(\xi, \eta) |J_{i,j}| d\xi d\eta = \bar{u}_{i,j} \quad (4.17)$$

with associated polynomial,

$$u(\xi, \eta) = c_1 + c_2\xi + c_3\eta + c_4\xi^2 + c_5\eta^2 + c_6\xi\eta. \quad (4.18)$$

Integration of Eq. (4.17) with Eq. 4.18 yields

$$\bar{u}_{i,j} = \sum_{k=1}^6 c_k v_k, \quad (4.19)$$

where



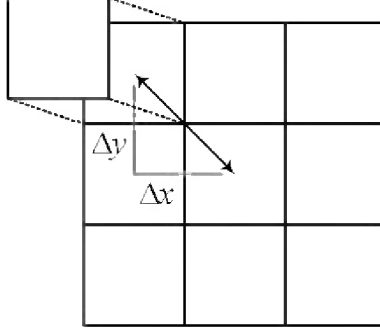


Figure 4.4: Two-dimensional interpolation stencil.

$$v_1 = 1 \quad (4.20a)$$

$$v_2 = \frac{1}{3A_{i,j}} \sum_{n=1}^4 A_n (x_n + x_{n+1}) \quad (4.20b)$$

$$v_3 = \frac{1}{3A_{i,j}} \sum_{n=1}^4 A_n (y_n + y_{n+1}) \quad (4.20c)$$

$$v_4 = \frac{1}{12A_{i,j}} \sum_{n=1}^4 A_n [x_n^2 + x_{n+1}^2 + (x_n + x_{n+1})^2] \quad (4.20d)$$

$$v_5 = \frac{1}{12A_{i,j}} \sum_{n=1}^4 A_n [y_n^2 + y_{n+1}^2 + (y_n + y_{n+1})^2] \quad (4.20e)$$

$$v_6 = \frac{1}{12A_{i,j}} \sum_{n=1}^4 A_n [x_n y_n + x_{n+1} y_{n+1} + (x_n + x_{n+1})(y_n + y_{n+1})] \quad (4.20f)$$

with  $\sum A_n$  being equivalent to the cell area,

$$A_{i,j} = \underbrace{\frac{1}{2}(\vec{01} \times \vec{02})}_{A_1} + \underbrace{\frac{1}{2}(\vec{02} \times \vec{03})}_{A_2} + \underbrace{\frac{1}{2}(\vec{03} \times \vec{04})}_{A_3} + \underbrace{\frac{1}{2}(\vec{04} \times \vec{01})}_{A_4} \quad (4.21)$$

A geometric description of  $A$  is provided in Figure 4.2 which can be determined from any arbitrary point  $P_0$ .

In order to establish a well-defined system, a stencil of six cells is necessary—one cell for each coefficient. However, in order to preserve symmetry on a logically-indexed mesh, a nine cell stencil as illustrated in Figure 4.4 is chosen, resulting in the linear system,

$$\begin{bmatrix} v_{1,i-1,j-1} & v_{2,i-1,j-1} & \cdots & v_{6,i-1,j-1} \\ \vdots & \vdots & & \vdots \\ v_{1,i,j} & v_{2,i,j} & \cdots & v_{6,i,j} \\ \vdots & \vdots & & \vdots \\ v_{1,i+1,j+1} & v_{2,i+1,j+1} & \cdots & v_{6,i+1,j+1} \end{bmatrix} \begin{bmatrix} c_1 \\ c_2 \\ c_3 \\ c_4 \\ c_5 \\ c_6 \end{bmatrix} = \begin{bmatrix} \bar{u}_{i-1,j-1} \\ \bar{u}_{i,j-1} \\ \bar{u}_{i+1,j-1} \\ \bar{u}_{i-1,j} \\ \bar{u}_{i,j} \\ \bar{u}_{i+1,j} \\ \bar{u}_{i-1,j+1} \\ \bar{u}_{i,j+1} \\ \bar{u}_{i+1,j+1} \end{bmatrix}. \quad (4.22)$$

The above system is over-determined, which can be solved using a least-squares formulation,

$$V\vec{c} = \vec{u} \quad (4.23)$$

$$V^T D V \vec{c} = V^T D \vec{u} \quad (4.24)$$

$$\vec{c} = (V^T D V)^{-1} V^T D \vec{u} \quad (4.25)$$

where,  $D$  is a diagonal matrix of weights to apply to each cell in the stencil. The elements of  $D$  have been chosen such that the diagonal cells of the stencil are given minimal weight, while maintaining a well-conditioned system. Once the coefficients have been determined, the quadric surface results from Eq. 4.18. A generic example is provided in Figure 4.5.

#### 4.2.1 Flux Calculation

Once the quadric surface has been determined, evaluation of the interface values becomes a simple line integral of the parabolic function resulting from the intersection of the quadric surface with the cell interface. Since the parabolas are determined using second-order polynomials, the integrals can be evaluated exactly using three-point Gaussian quadratures.

### 4.3 Limiters

When applied to highly nonlinear wave phenomena such as shocks, the interpolation scheme will inherently develop oscillations leading to catastrophic failure of the reconstruction. To

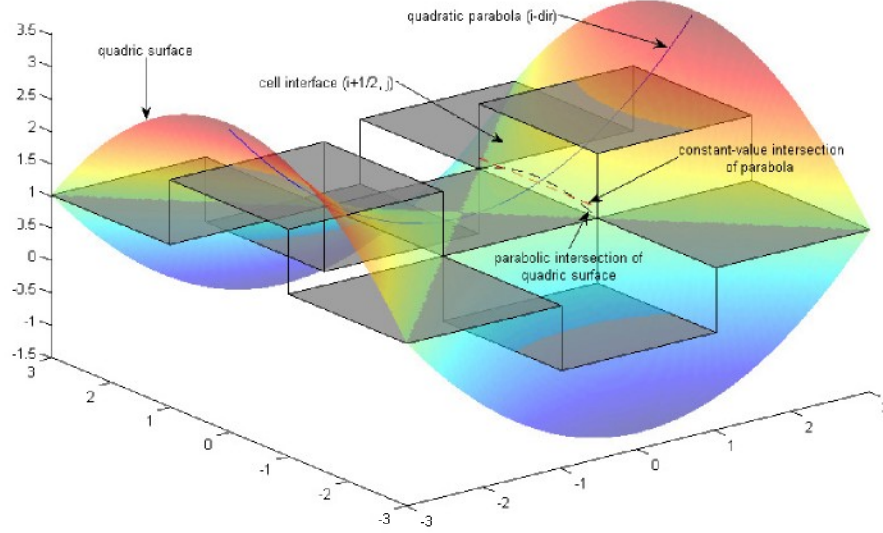


Figure 4.5: Two-dimensional quadric surface interpolation on a uniform mesh.

remedy this, the monotonicity-preserving (MP) limiters of Suresh and Huynh [107] have been implemented in the reconstruction. MP limiters enforce monotonicity in the reconstruction scheme by modifying interpolated point values at cell interfaces. As applied to the 1D interpolation on a uniform mesh, the reconstructed value  $u_L$  in Eq. (4.13) is modified according to

$$u_L \leftarrow \text{median}(u_L, \bar{u}_j, u^{\text{MP}}) \quad (4.26)$$

with  $u^{\text{MP}} = \bar{u}_j + \text{minmod}[\bar{u}_{j+1} - \bar{u}_j, \alpha(\bar{u}_j - \bar{u}_{j-1})]$ . The MP limiter has been implemented in the current work with  $\alpha = 2$ .

## CHAPTER 5

### NUMERICAL STABILITY

The reconstruction procedure detailed in the previous chapter is just one component of the semi-discrete approach. In order to complete the numerical convection scheme, the reconstruction must be combined with an appropriate time-marching method. The suitability of the integration scheme is dependent upon the spatial discretization, making it necessary to analyze the numerical scheme as a whole. In general it must be determined if the given scheme is consistent with the physical model and under what conditions it is stable—only then can convergence be ensured.

In particular, the stability analysis performed here will be based on discretization of the model linear advection equation,

$$\frac{\partial u}{\partial t} + a \frac{\partial u}{\partial x} + a \frac{\partial u}{\partial y} = 0, \quad (5.1)$$

with a constant advection speed  $a > 0$ . Consistent with the semi-discrete approach, the spatial derivatives of Eq. (5.1) will first be discretized,

$$\frac{d\vec{u}}{dt} = L\vec{u}, \quad (5.2)$$

requiring a vectorization of the reconstruction scheme. It is important to note that when combined with the monotonicity-preserving limiters discussed in Chapter 4 Section 4.3, the reconstruction scheme cannot be linearized. However, the base interpolation scheme will be considered independently of the limiters, resulting in two coupled sets of ODE's that will be analyzed separately. The ODE's will then be discretized in time yielding the desired set of OΔE's,

$$\bar{u}^{n+1} = S\bar{u}^n. \quad (5.3)$$

to advance the solution from time level  $n$  to  $n + 1$ . The conditions for stability of Eq. 5.3 as based on the Lax-Richtmyer theorem require the eigenvalue of maximum magnitude of  $S$  be bounded by the unit circle,

$$\sigma_{\max} \leq 1. \quad (5.4)$$

In what follows, the form of  $L$  will be determined along with its eigenvalues,  $\lambda$ . Making use of the so-called  $\lambda - \sigma$  relation [68], the eigenvalues of  $S$  will be derived without the explicit form of  $S$ . To facilitate analysis, all discretizations are performed on equispaced Cartesian grids with periodic boundary conditions.

### 5.1 Finite-difference approximation

A finite-difference (FD) approximation to the spatial derivatives of Eq. (5.1) can be made based on the reconstruction procedure of the previous chapter. In particular, an upwind approximation results from differencing the interpolated cell interface values given by Eq. 4.13,

$$\left(\frac{\partial u}{\partial x}\right)_j = u_{R,j} - u_{R,j-1} + O(\Delta x^2) \quad (5.5)$$

$$= \frac{1}{6\Delta x} [2\bar{u}_{j+1} + 5\bar{u}_j - \bar{u}_{j-1} - (2\bar{u}_j + 5\bar{u}_{j-1} - \bar{u}_{j-2})] + O(\Delta x^2) \quad (5.6)$$

$$= \frac{1}{6\Delta x} (2\bar{u}_{j+1} + 3\bar{u}_j - 6\bar{u}_{j-1} + \bar{u}_{j-2}) + O(\Delta x^2). \quad (5.7)$$

The truncated term in Eq. 5.7 can be found from Fourier error analysis by comparing the exact derivative of  $u = e^{i\kappa x}$ ,

$$\frac{\partial e^{i\kappa x}}{\partial x} = i\kappa e^{i\kappa x}, \quad (5.8)$$

with the approximate derivate of discrete function  $u_j = e^{i\kappa j\Delta x}$ ,

$$(\delta_x e^{i\kappa j \Delta x})_j = \frac{2e^{i\kappa \Delta x(j+1)} + 3e^{i\kappa \Delta x(j)} - 6e^{i\kappa \Delta x(j-1)} + e^{i\kappa \Delta x(j-2)}}{6\Delta x} \quad (5.9)$$

$$= \frac{(e^{-i\kappa 2\Delta x} - 6e^{-i\kappa \Delta x} + 3 + 2e^{i\kappa \Delta x})e^{i\kappa j \Delta x}}{6\Delta x}. \quad (5.10)$$

where  $\kappa$  is the modified wave number. Comparing the right-hand sides of Eqs. 5.8 and 5.10 yields a modified wave number,

$$\kappa^* = \frac{3 + \cos 2\kappa \Delta x - 4 \cos \kappa \Delta x + i(8 \sin \kappa \Delta x - \sin 2\kappa \Delta x)}{6i\Delta x}, \quad (5.11)$$

that approximates the exact wave number to third order accuracy as revealed by the series expansion of Eq. 5.11,

$$\kappa^* = \kappa + \frac{\kappa^4 \Delta x^3}{12i} + \dots, \quad (5.12)$$

confirming third-order accuracy of Eq. (5.7). As such, the scheme including monotonicity-preserving limiters shall be referred to as MP3.

The modified wave number along with the modified phase speed,  $a^*/a = \kappa^*/\kappa$ , are plotted in Figure 5.1. The third-order scheme requires approximately 19 points per wavelength (PPW) to maintain an error in phase speed of less than 0.1% or 10 PPW for an error of less than 1%.

## 5.2 1D stability

Spatial discretization of the model equation using Eq. (5.7) on an uniform 1D mesh with  $M$  cells results in the spatial discretization operator,

$$L = \frac{a}{\Delta x} \frac{1}{6} \begin{bmatrix} -3 & -2 & & -1 & 6 \\ 6 & -3 & -2 & & -1 \\ -1 & 6 & -3 & -2 & \\ & \ddots & \ddots & \ddots & \ddots \\ & & -1 & 6 & -3 & -2 \\ -2 & & & -1 & 6 & -3 \end{bmatrix} \quad (5.13)$$

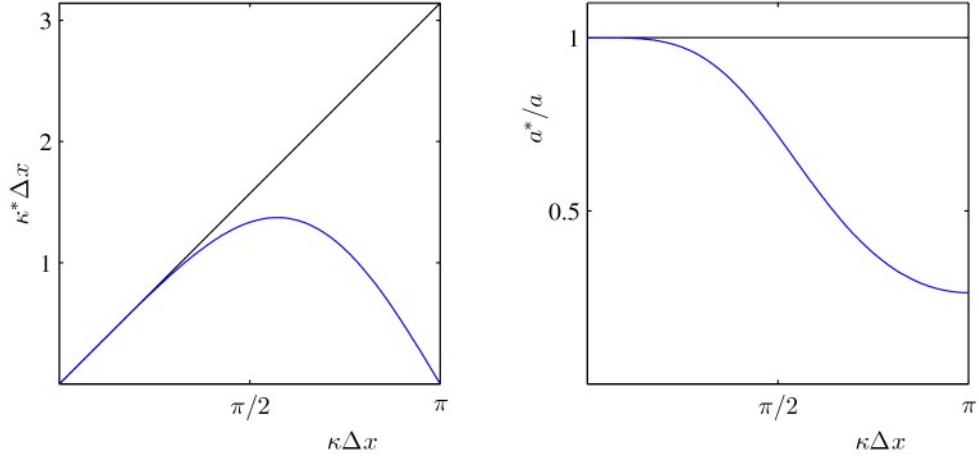


Figure 5.1: Modified wave number and phase error for 3<sup>rd</sup>-order backward difference operator.

which may conveniently be expressed in banded matrix notation as

$$L = \frac{a}{\Delta x} \frac{1}{6} B_p(M : -1, 6, -3, -2, 0), \quad (5.14)$$

in which  $B_p$  denotes a periodic banded or circulant matrix. Because it is circulant, the eigenvalues of  $L$  can be found from a 1D discrete Fourier transform (DFT),

$$\lambda_j = \sum_{m=0}^{M-1} e^{-2\pi i j m / M} L_{1j}, \quad j = 0, 1, \dots, M-1. \quad (5.15)$$

The linear operator resulting from the MP limiter is also considered here and is given by

$$L = \frac{a}{\Delta x} \frac{1}{6} \begin{bmatrix} -3 & & & -2 & 5 \\ 5 & -3 & & & -2 \\ -2 & 5 & -3 & & \\ & \ddots & \ddots & \ddots & \ddots \\ & & -2 & 5 & -3 \\ & & & -2 & 5 & -3 \end{bmatrix} \quad (5.16)$$

Though not detailed here, its derivation is similar to that of the third-order FD approximation.

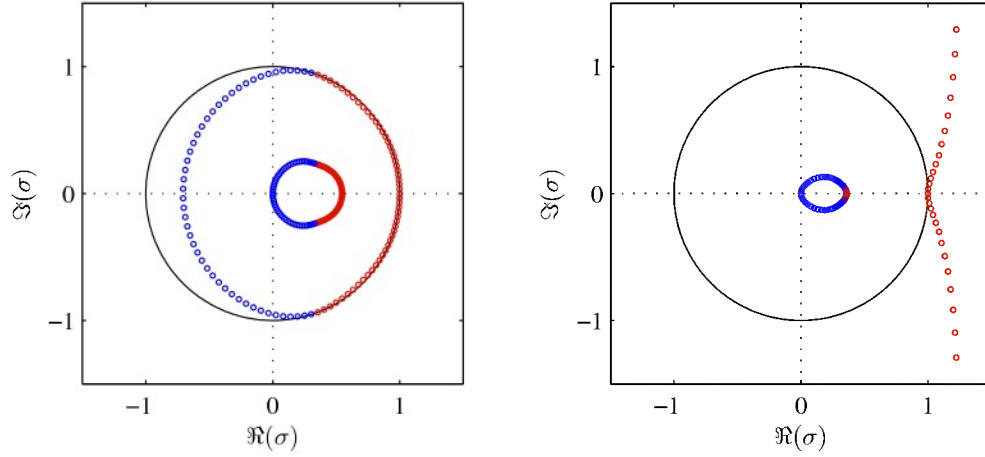


Figure 5.2: Stability plot for the 1D MP3-AB2 scheme with CFL= 0.58. The 3<sup>rd</sup>-order interpolation is stable (*left*), while the limiter is not (*right*).

### 2<sup>nd</sup>-order Adams-Bashforth

Once the eigenvalues of  $L$  have been computed, the eigenvalues of  $S$  follow from the  $\lambda - \sigma$  relation, which are given by

$$\sigma^2 - \left(1 + \frac{3}{2}\lambda\Delta x\right)\sigma + \frac{1}{2}\lambda\Delta x = 0. \quad (5.17)$$

for the 2<sup>nd</sup>-order Adams-Bashforth (AB2) scheme [68]. As a multi-step scheme, AB2 gives rise to two  $\sigma$ -eigenvalues for each  $\lambda$ -eigenvalue.

The eigenvalues for the 1D AB2-MP3 scheme have been plotted for a CFL number of 0.58 in Figure 5.2 and for a CFL number of 0.1 in Figure 5.3. The base interpolation scheme is clearly stable for CFL= 0.58 as all of the eigenvalues lie within the unit circle in the complex plane. The MP limiter function, on the other hand, is not stable at this CFL number. Even as the CFL number is decreased to 0.1, the limiter function is still unstable, with eigenvalues from the principle  $\sigma$ -root lying outside the unit circle.

### 2<sup>nd</sup>-order Runge-Kutta

The second-order Runge-Kutta (RK2) scheme is a two-step, predictor-corrector scheme which has one principal  $\sigma$  root given by



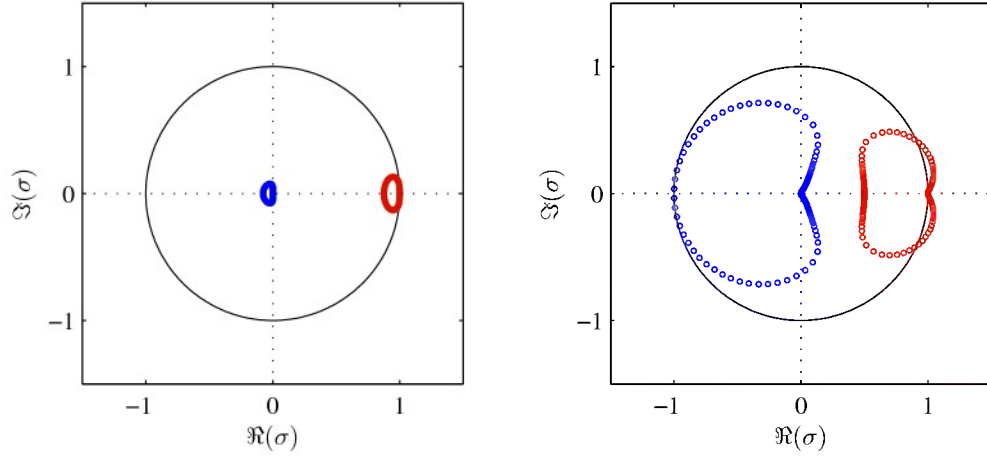


Figure 5.3: Stability plot for the MP3-AB2 scheme with CFL= 0.1. Despite the small value of the CFL number, the limiter (*right*) remains unstable, although mildly so. It is interesting to note that the spurious root is stable while the principal root is not. The 3<sup>rd</sup>-order interpolation is given on the left.

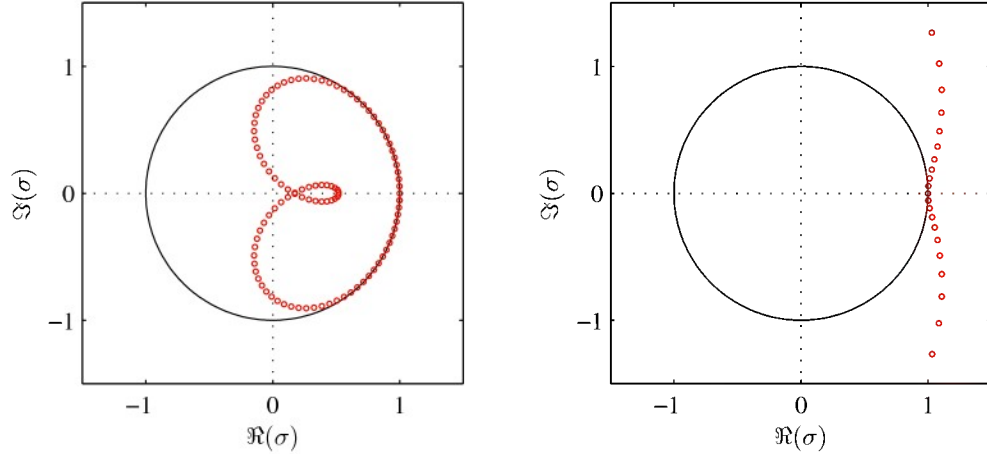


Figure 5.4: Stability plot for the 1D RK2-AB2 scheme with CFL= 0.1. The 3<sup>rd</sup>-order interpolation is stable (*left*), while the limiter is not (*right*).

$$\sigma - 1 - \lambda\Delta x - \frac{1}{2}\lambda^2\Delta x^2 = 0. \quad (5.18)$$

From Figures 5.4 and 5.5, the base interpolation scheme is stable for CFL= 0.9. As with the AB2 scheme, the MP limiter function is not stable, even as the CFL number is decreased to 0.1.

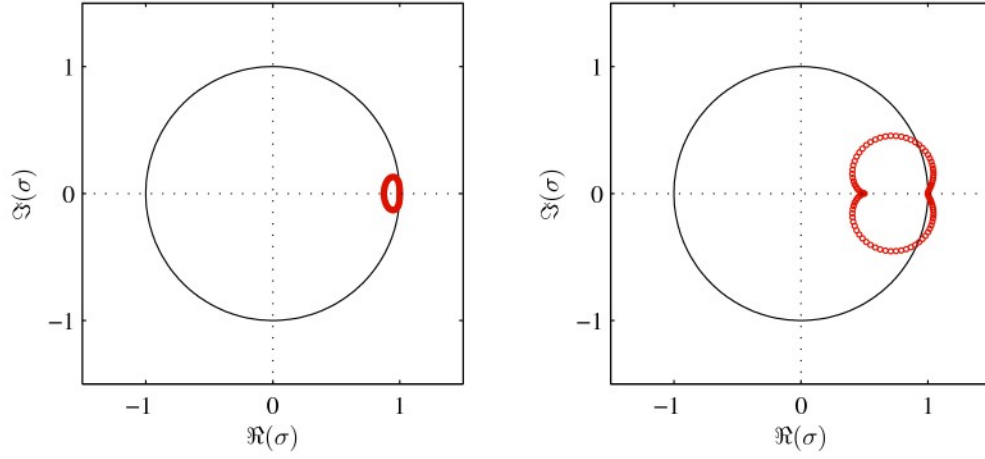


Figure 5.5: Stability plot of the 3<sup>rd</sup>-order interpolation scheme with RK2 for CFL= 0.1. Despite the small value of the CFL number, the limiter (*right*) remains unstable, although mildly so. The 3<sup>rd</sup>-order interpolation is given on the left.

### 5.3 2D stability

As applied to an  $M \times M$  mesh with  $\Delta x = \Delta y$  and periodic boundary conditions, vectorization of the 2D reconstruction scheme results in a  $M^2 \times M^2$  block circulant matrix with circulant blocks (BCCB),

$$C = \begin{pmatrix} C_0 & C_1 & & & C_{M-2} & C_{M-1} \\ C_{M-1} & C_0 & C_1 & & & C_{M-2} \\ C_{M-2} & C_{M-1} & C_0 & C_1 & & \\ & \ddots & \ddots & \ddots & \ddots & \\ & & C_{M-2} & C_{M-1} & C_0 & C_1 \\ C_1 & & & C_{M-2} & C_{M-1} & C_0 \end{pmatrix}, \quad (5.19)$$

where  $C_{M-2} = -\frac{1}{6}I_M$ ,  $C_{M-1} = I_M$ ,  $C_1 = -\frac{1}{3}I_M$ , and

$$C_0 = \frac{1}{6}B_p(M : -1, 6, -6, -2, 0), \quad (5.20)$$

for the third-order FD approximation ( $I_M$  indicates a  $M \times M$  identity matrix). Diagonalization of a BCCB is given by ([32])

$$C = (\mathbb{F}_M \otimes \mathbb{F}_M)^{-1} \Lambda (\mathbb{F}_M \otimes \mathbb{F}_M) \quad (5.21)$$

where  $\Lambda$  is the diagonal matrix of eigenvalues of  $C$  and  $\mathbb{F}_M$  is the  $M \times M$  discrete Fourier transform (DFT) matrix,

$$\mathbb{F}_M = \begin{bmatrix} 1 & 1 & \cdots & 1 \\ 1 & w^1 & \cdots & w^{M-1} \\ 1 & w^2 & \cdots & w^{2(M-1)} \\ \vdots & \vdots & & \vdots \\ 1 & w^{M-1} & \cdots & w^{(M-1)(M-1)} \end{bmatrix} \quad (5.22)$$

where  $w = e^{-2\pi i/M}$ . The eigenvalues of  $C$  can be found from the 2D DFT,

$$\sigma_{jk} = \sum_{n=0}^{M-1} \sum_{m=0}^{M-1} e^{-2\pi i j n/M} e^{-2\pi i k m/M} g_{nm}, \quad n, m = 0, 1, \dots, M-1 \quad (5.23)$$

where  $g_{nm}$  are the elements of matrix  $G$ , of which the  $n^{\text{th}}$  row corresponds to the first row of the  $n^{\text{th}}$  circulant matrix  $C_n$  in Eq. 5.19,

$$G = \begin{pmatrix} C_{0,11} & C_{0,12} & \cdots & C_{0,1M} \\ C_{1,11} & C_{1,12} & \cdots & C_{1,1M} \\ 0 & 0 & \cdots & 0 \\ \vdots & \vdots & & \vdots \\ 0 & 0 & \cdots & 0 \\ C_{M-2,11} & C_{M-2,12} & \cdots & C_{M-2,1M} \\ C_{M-1,11} & C_{M-1,12} & \cdots & C_{M-1,1M} \end{pmatrix} \quad (5.24)$$

The matrix operator for the limiter function can be found in a similar manner.

## 2<sup>nd</sup>-order Adams-Bashforth

The results for the 2D AB2-MP3 scheme plotted in Figures 5.6 and 5.7 indicate that stability decreases by a factor of two for all cases as compared with the 1D scheme.

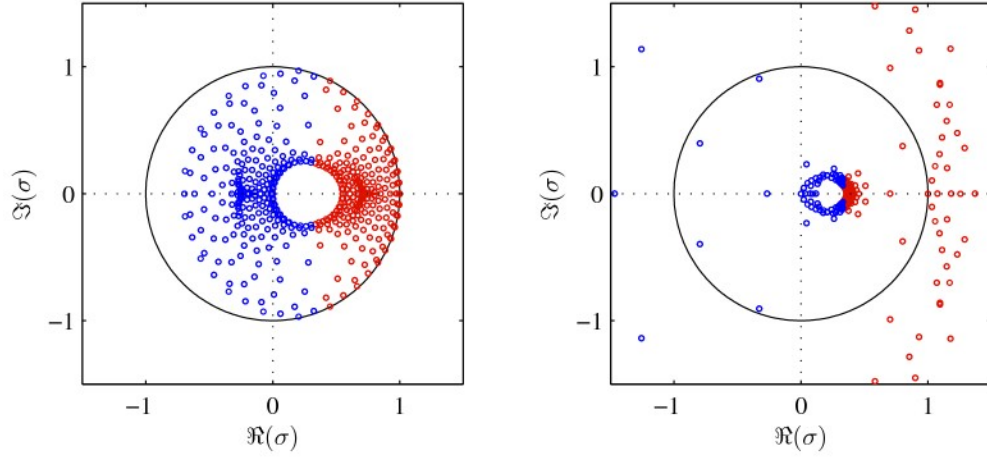


Figure 5.6: Stability plot for the 2D AB2-MP3 scheme with CFL= 0.29. The 3<sup>rd</sup>-order interpolation is stable (*left*), while the limiter is not (*right*).

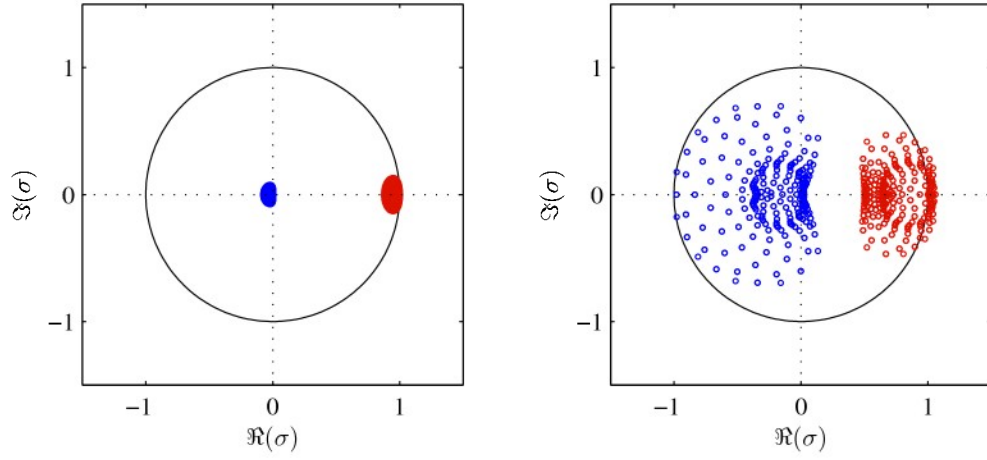


Figure 5.7: Stability plot for the 2D AB2-MP3 scheme with CFL= 0.05. The limiter (*right*) remains unstable at this CFL number. The 3<sup>rd</sup>-order interpolation is given on the left.

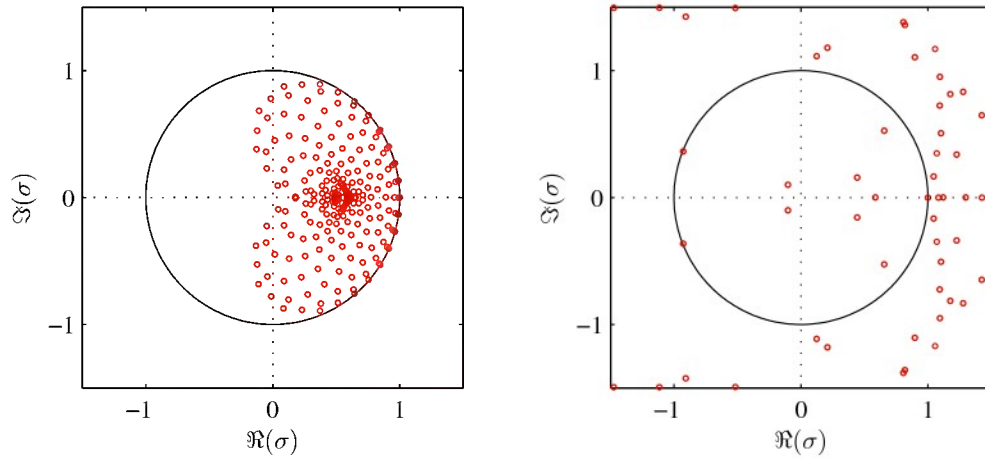


Figure 5.8: Stability plot for the 2D RK2-MP3 scheme with CFL= 0.45.

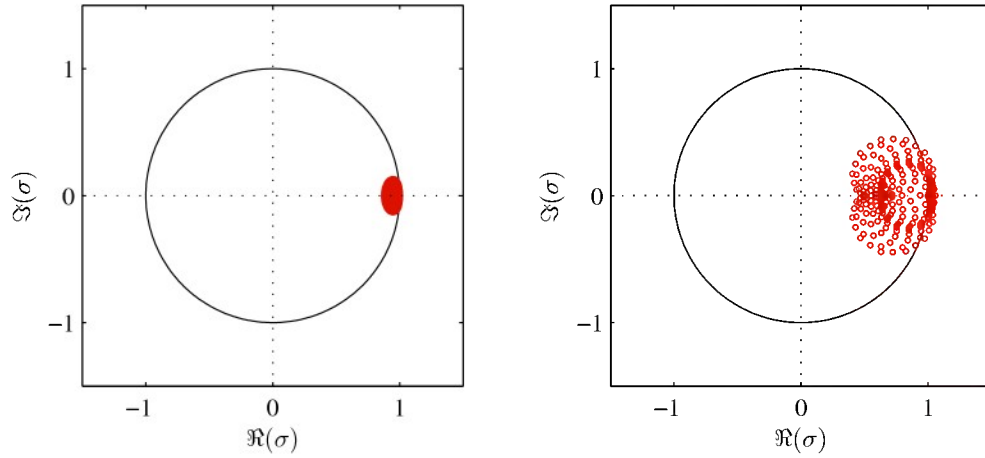


Figure 5.9: Stability plot for the 2D RK2-MP3 scheme with CFL= 0.05. The limiter (*right*) remains unstable at this CFL number. The 3<sup>rd</sup>-order interpolation is given on the left.

## 2<sup>nd</sup>-order Runge-Kutta

The stability plots for the 2D MP3-RK2 scheme are given in Figures 5.8 and 5.9. As for the 2D AB2-MP3 scheme, the 2D RK2-MP3 scheme is stable up to only half the value of the CFL number as found for its 1D counterpart.

While these results demonstrate a clear advantage of the AB2-MP3 scheme over the RK2-MP3 scheme based on the third-order differencing scheme, the results are inconclusive with respect to the MP limiters in regards to their stability. This has warranted numerical

experiments that have indicated the AB2-MP3 scheme to be more efficient when considering multiple factors, including parallelization implementation and communication overhead. As such, the AB2-MP3 scheme has been applied to the convective transport equations in the current research.

## CHAPTER 6

### BENCHMARKS

Benchmarks are essential in validating the performance of the numerical algorithms as applied to physical processes under known and controlled conditions. Assembled here is a collection of one- and two-dimensional test cases that have been well-documented in the literature. All problems have been solved using upwind Riemann solvers and the 3<sup>rd</sup>-order scheme detailed in Chapter 4 to increase accuracy. Problems in gasdynamics are presented first followed by two magnetohydrodynamic cases.

#### 6.1 Woodward-Colella blastwave

Blastwaves can generally be described as a strong and sudden release of energy, resulting in regions characterized by extreme temperatures and pressures. The severity of the conditions is further compounded when two blastwaves interact. The reconstruction scheme must deal with pressure and temperature jumps of several orders of magnitude while preserving monotonicity and preserving critical features. In particular, when the shock fronts of the blastwaves interact, the resulting contact discontinuity is difficult to resolve. The initial conditions for the left, middle, and right states are given by,

$$\begin{pmatrix} \rho_L \\ u_L \\ p_L \end{pmatrix} = \begin{pmatrix} 1 \\ 0 \\ 10^3 \end{pmatrix}, \quad \begin{pmatrix} \rho_M \\ u_M \\ p_M \end{pmatrix} = \begin{pmatrix} 1 \\ 0 \\ 10^{-2} \end{pmatrix}, \quad \begin{pmatrix} \rho_R \\ u_R \\ p_R \end{pmatrix} = \begin{pmatrix} 1 \\ 0 \\ 10^2 \end{pmatrix} \quad (6.1)$$

for a polytropic gas with an adiabatic exponent of 7/5. As can be seen in Figure 6.1, the middle contact is well resolved by the scheme with the use of a slope-steepening technique

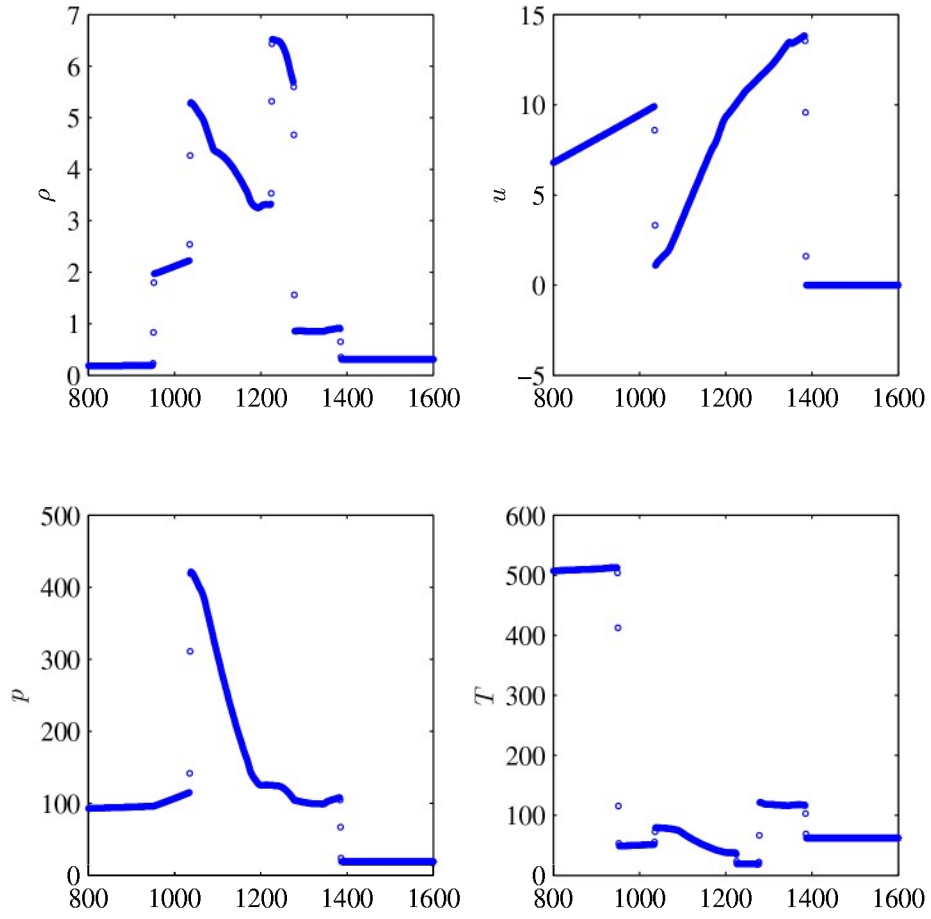


Figure 6.1: Numerical solution of Woodward-Colella blastwave problem as computed with 1600 cells.



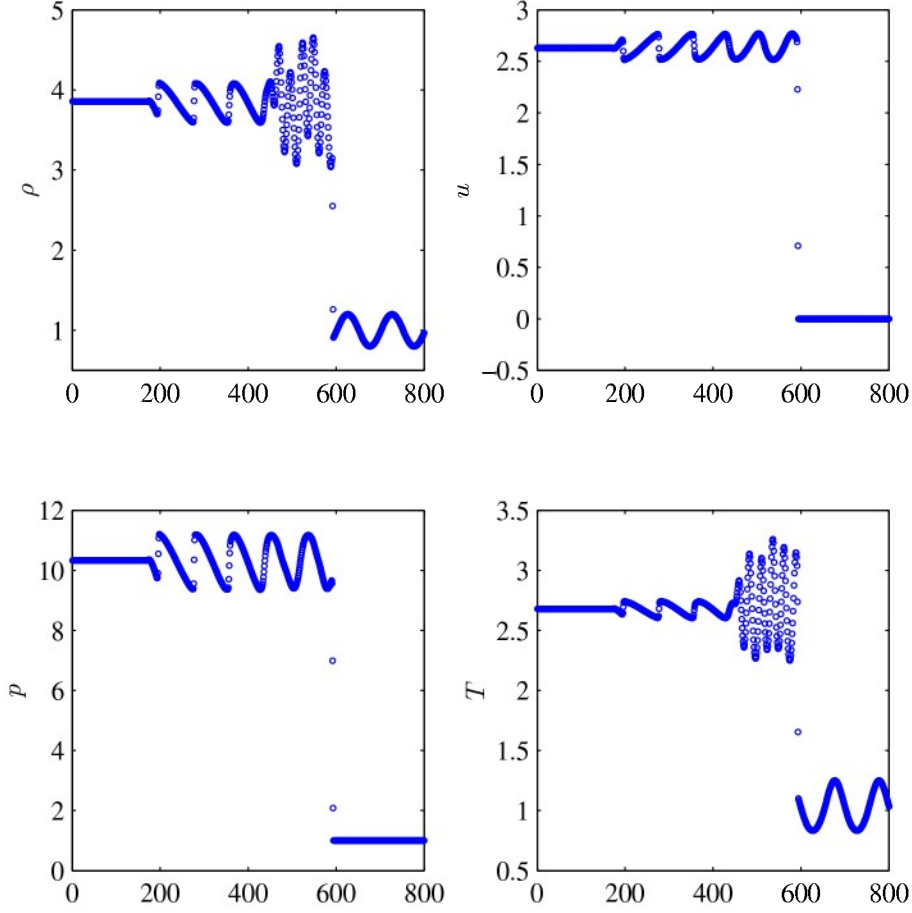


Figure 6.2: Numerical solution of the Shu-Osher problem as computed with 800 cells.

similar to that of [25] and [54].

## 6.2 Shu-Osher shock-entropy wave interaction

The ability of a numerical scheme to resolve smooth flow disturbances is also of concern. This becomes especially critical in boundary layers and other highly turbulent regions where entropy waves are prevalent. The Shu-Osher problem [104] has extensively been used to simulate a shock passing through an entropy disturbance which can be thought of as a one-dimensional analog to the shock-vortex interaction problem. The initial conditions for the

left and right states are given by,

$$\begin{pmatrix} \rho_L \\ u_L \\ p_L \end{pmatrix} = \begin{pmatrix} 3.857143 \\ 2.629369 \\ 10.33333 \end{pmatrix}, \quad \begin{pmatrix} \rho_R \\ u_R \\ p_R \end{pmatrix} = \begin{pmatrix} 1 + 0.2 \sin(5x - 25) \\ 0 \\ 1 \end{pmatrix} \quad (6.2)$$

for a polytropic gas with an adiabatic exponent of 7/5. As can be seen in Figure 6.2, the entropy waves are well-defined after compression by the shock.

### 6.3 Emery wind tunnel

Another case popularized by Colella and Woodward [25], this problem has been simulated extensively in the literature to test various solvers' ability to properly capture the flow around the 90° corner of a forward-facing step. The resultant sonic rarefaction fan emanating from this corner flow may be strong enough to produce negative densities if a positivity-preserving scheme is not utilized. The standard Harten-type entropy fix [100] is sufficient to ensure positivity as well as avoid sonic rarefactions. An key feature of this problem is the Kelvin-Helmoltz (KH) instabilities which originate at the triple point of the Mach stem. While the KH structures themselves are physical in nature, it is how they are initiated that is an artifact of the numerical solver. The inability of Riemann solvers to capture slow-moving shocks exactly creates oscillations which serve as a forcing function that acts as artificial turbulence. These features are purely numerical in nature and result from the inability of Riemann solvers to capture slow-moving shocks exactly. Despite artificial dissipation as prescribed in [25], the oscillations and subsequent vortices persist.

The initial conditions are everywhere identical, with a Mach 3 flow described by a polytropic gas with an adiabatic exponent of 7/5 traversing from the left inlet to the sonic outflow boundary at the opposite end. Results are presented in Figures 6.3–6.6 in the form of infinite-fringe interferograms and were obtained using a total of 252 computational domains, each consisting of  $75 \times 75$  cells for which  $\Delta x = \Delta y$ .

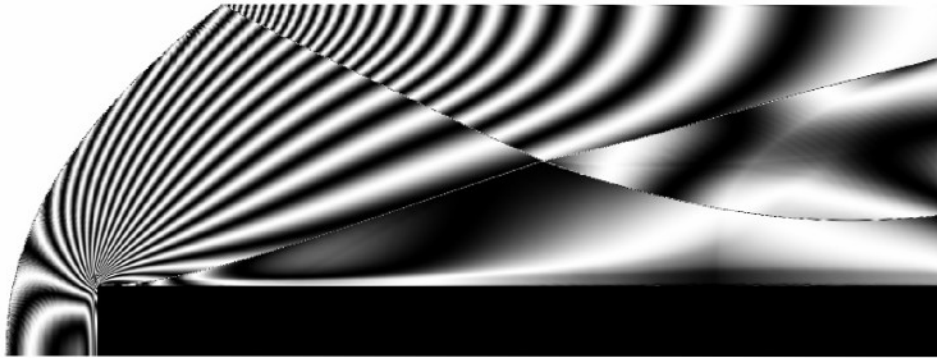


Figure 6.3: Emery solution at  $t = 1$ .

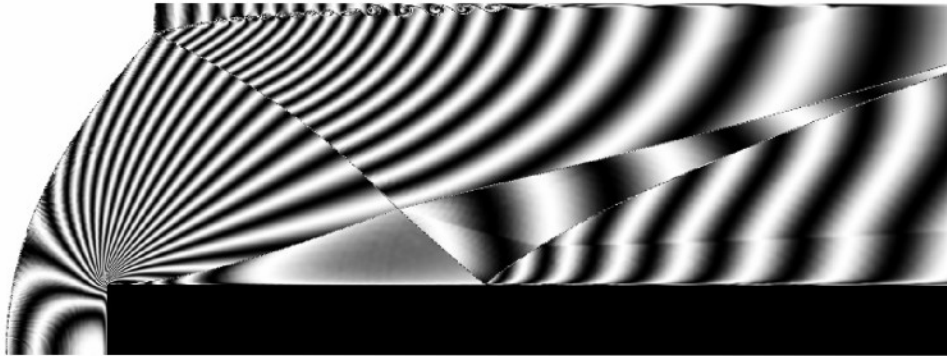


Figure 6.4: Emery solution at  $t = 2$ .

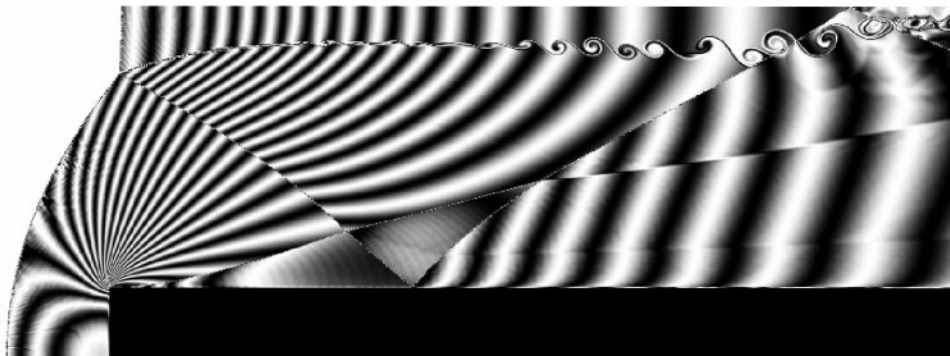


Figure 6.5: Emery solution at  $t = 3$ .

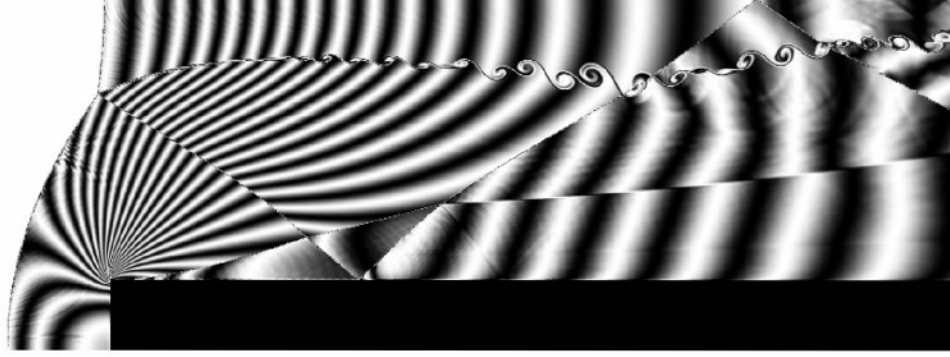


Figure 6.6: Emery solution at  $t = 4$ .

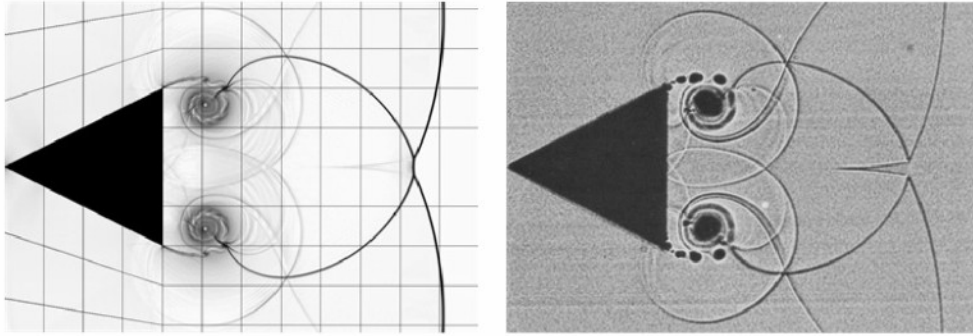


Figure 6.7: Simulated Schlieren (*left*) of Schardin's problem as compared with experiment (*right*) from [36].

#### 6.4 Schardin's problem

Schardin's problem involves air flow past a symmetric wedge at Mach 1.3. This problem has been simulated using a polytropic gas with an adiabatic exponent of  $7/5$  on a mesh with  $400k$  cells that included half of the wedge. The numerical Schlieren in Figure 6.7 shows excellent agreement with the experimental results.

#### 6.5 Shock diffraction down a step

Shock diffraction down a  $90^\circ$  step has been a popular problem for comparing numerical and experimental results. This particular problem chosen here is due to Bazhenova [10], involving a Mach 5.09 shock. The numerical results presented in Figure 6.8 have been computed assuming an adiabatic exponent of  $7/5$ . The numerical results are able to reproduce all of the experimental flow features accurately. Solutions were obtained on a 1.2M cell mesh with

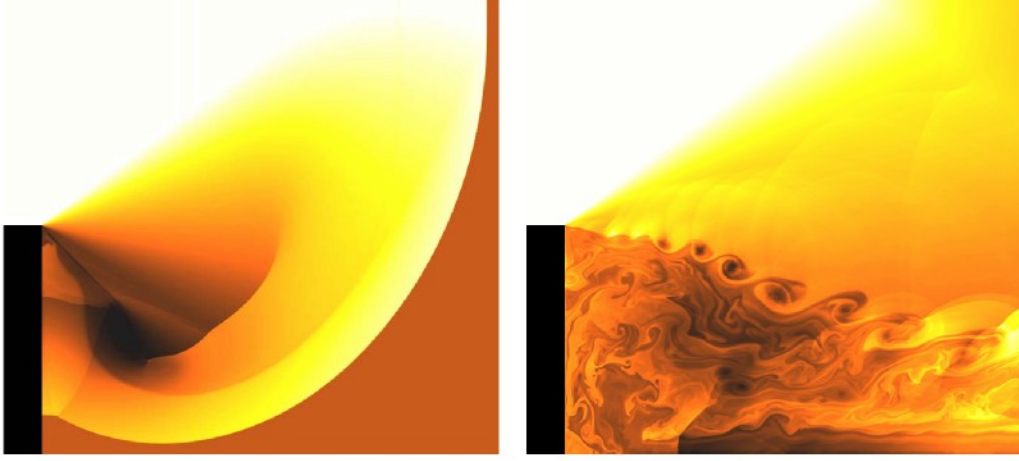


Figure 6.8: Density plot of a Mach 5.09 shock diffracting down a 90° step. Results (*left*) compare favorably with experimental results [10] and previous numerical simulations [92]. The right frame shows the intricate flow field at a much later time. Colormap:  $\rho_{min}$   $\rho_{max}$

$$\Delta x = \Delta y.$$

## 6.6 Rayleigh-Taylor instability

Rayleigh-Taylor instability can occur at the interface of two fluids of differing densities if the heavier fluid is accelerated into the lighter one. The instabilities are initiated here at a contact surface, across which the fluid pressure is constant but mass density is discontinuous. The initial conditions are given by

$$\begin{pmatrix} \rho_L \\ u_L \\ v_L \\ p_L \end{pmatrix} = \begin{pmatrix} 2 \\ 0 \\ -0.025 \cos(8\pi x) \\ 2y + 1 \end{pmatrix}, \quad \begin{pmatrix} \rho_U \\ u_U \\ v_U \\ p_U \end{pmatrix} = \begin{pmatrix} 1 \\ 0 \\ -0.025a \cos(8\pi x) \\ y + 3/2 \end{pmatrix} \quad (6.3)$$

on the domain  $0 \leq x \leq 1/4$ ,  $0 \leq y \leq 1$  where the subscripts  $U$  and  $L$  denote the upper and lower fluids respectively. The numerical setup here is slightly different from similar RT simulations presented in the literature (see [122]), in that the left and right boundaries here are periodic, while the top and bottom boundaries are reflecting. The results in Figure 6.6 show many fine-scale structures emanating from the contact surface. As the flow develops,

and mixing increases, Kelvin-Helmholtz instabilities are also apparent as shear layers develop. While the flow is undoubtedly unstable, it is unclear to what extent, if any, these structures are numerical in origin. It has been stated that higher complexity of the fine-scale structures is an indication of less diffusive solvers [122], but the work of [98] may suggest other influences, including numerical effects (e.g. grid effects).

## 6.7 Brio-Wu MHD shocktube

The Brio-Wu shock tube problem [17] is a magnetohydrodynamic extension of Sod's gas-dynamic problem. Magnetic fields both normal and tangential to the flow generate several MHD wave structures, including fast and slow magnetosonic shocks and rarefactions as well as a compound wave. This problem demonstrates the true complexity of the fact that the waves cannot all be described as strictly being either linearly degenerate or genuinely nonlinear. From Figure 6.10 it can be seen that the solver has problems capturing the compound wave structure as well as the tail of the slow rarefaction wave, typical of compressive limiters. Also noteworthy is the ability of the slope-steepening to capture the contact in 2 cells.

## 6.8 Orszag-Tang MHD vortex

When considering MHD problems in more than one spatial dimension, enforcement of  $\nabla \cdot \vec{B}$  is no longer automatic and may require special attention. The Orszag-Tang MHD vortex is one example of a problem which has been used to test a solver's ability to satisfy the divergence-free condition. The solution is obtained on the domain  $0 \leq x \leq 1, 0 \leq y \leq 1$  with the density and pressure initially equal everywhere with values  $25/36\pi$  and  $5/12\pi$ , and the velocity and magnetic fields described by  $[-\sin(2\pi y), \sin(2\pi y)]$  and  $[-\sin(2\pi y), \sin(4\pi x)]$ , respectively. The magnetic fields specified by the initial conditions are able to twist the fluid into a vortical structure via the Lorentz force. The boundary conditions are periodic. Critical to this problem is enforcement of the  $\nabla \cdot \vec{B}$  condition as required by the MHD equations. While there are several well-known methods for implementing this condition, including Hodge projection ([14]), constrained transport ([38]), and the 8-wave formulation ([87],[86]), the solution presented in Figure 6.11 was obtained without using any of these methods. In this particular test case, the standard Roe FDS approximate Riemann solver

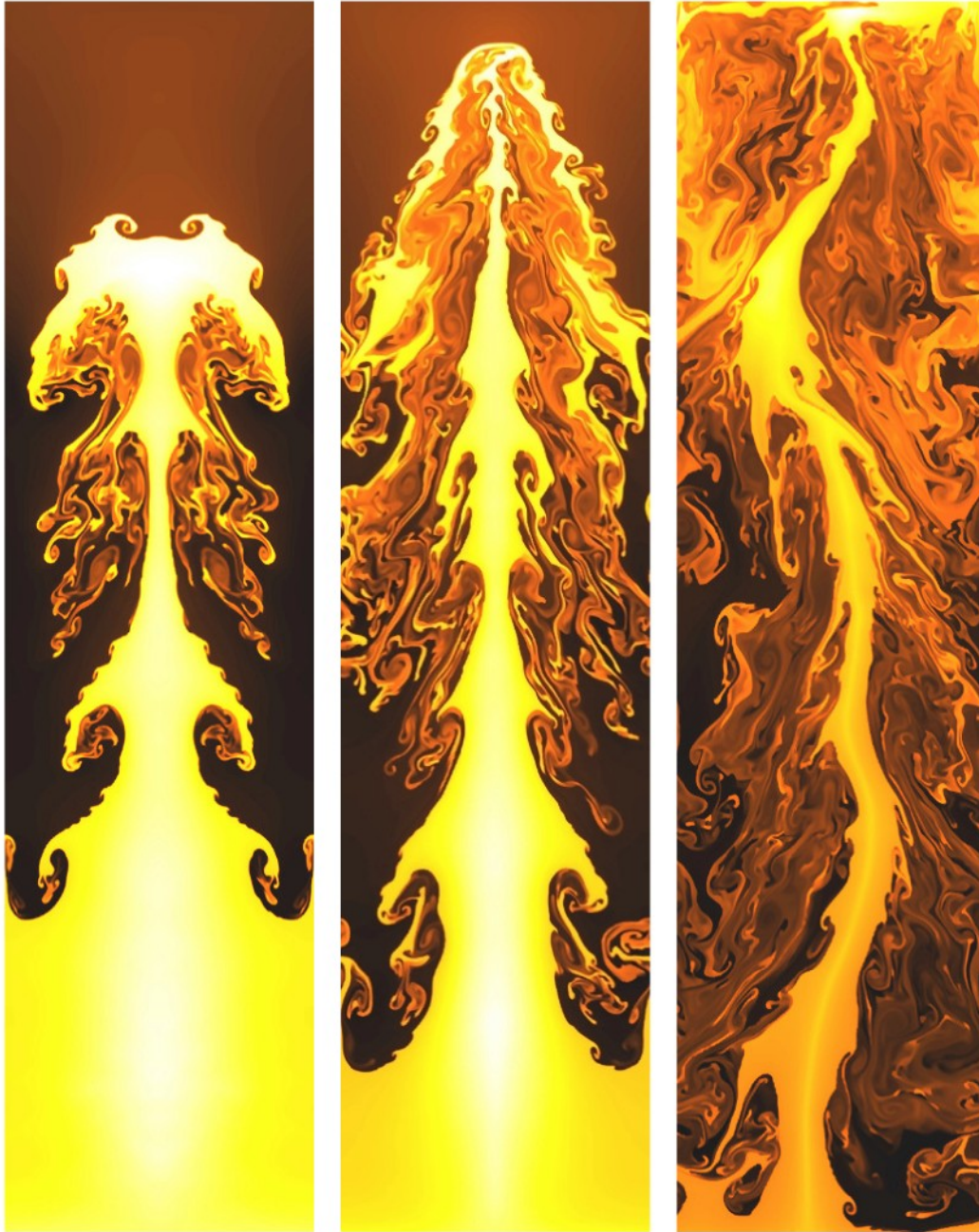



Figure 6.9: Rayleigh-Taylor instability at three different times as computed on a  $400 \times 1600$  cell mesh with  $\Delta x = \Delta y$ . In the third frame, portions of the contact surface have reflected from the upper boundary. Colormap:  $\rho_{min}$    $\rho_{max}$



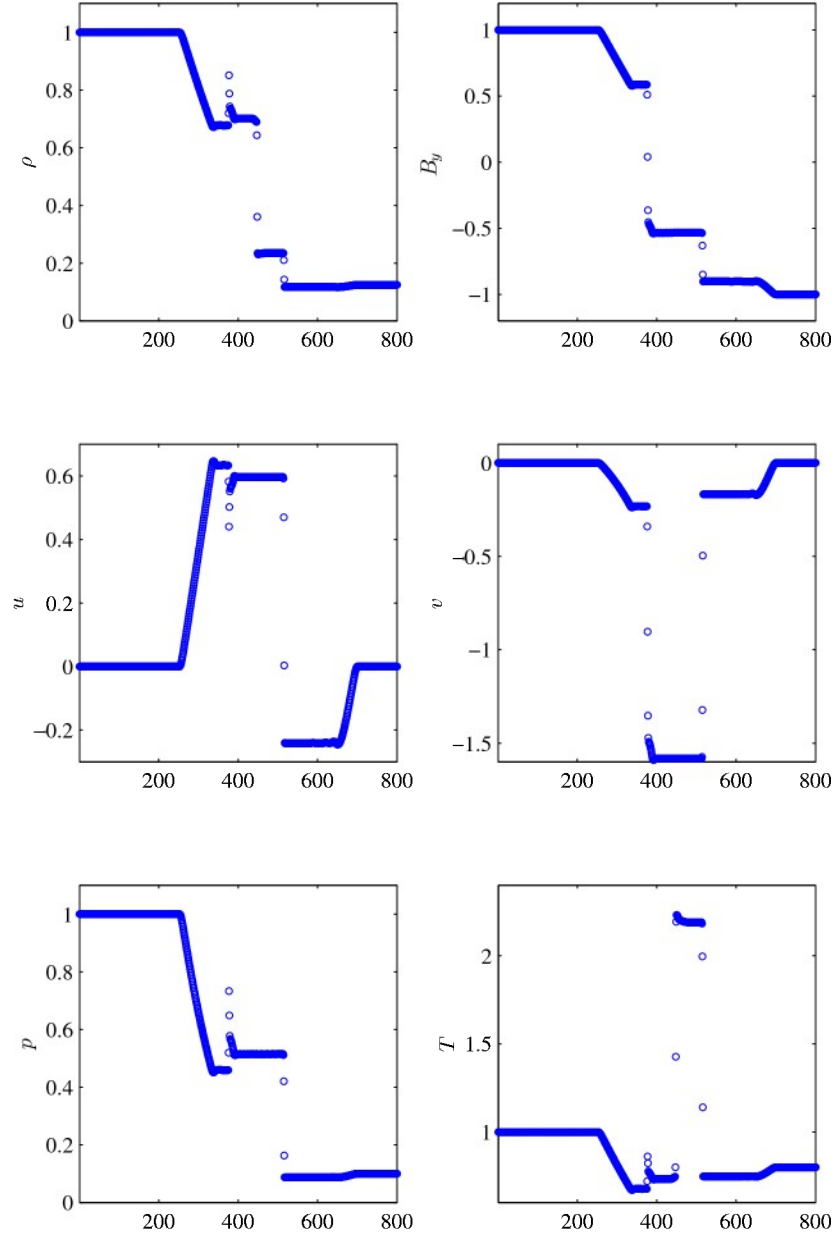


Figure 6.10: Numerical results for Brio-Wu MHD shocktube as computed with 800 cells.



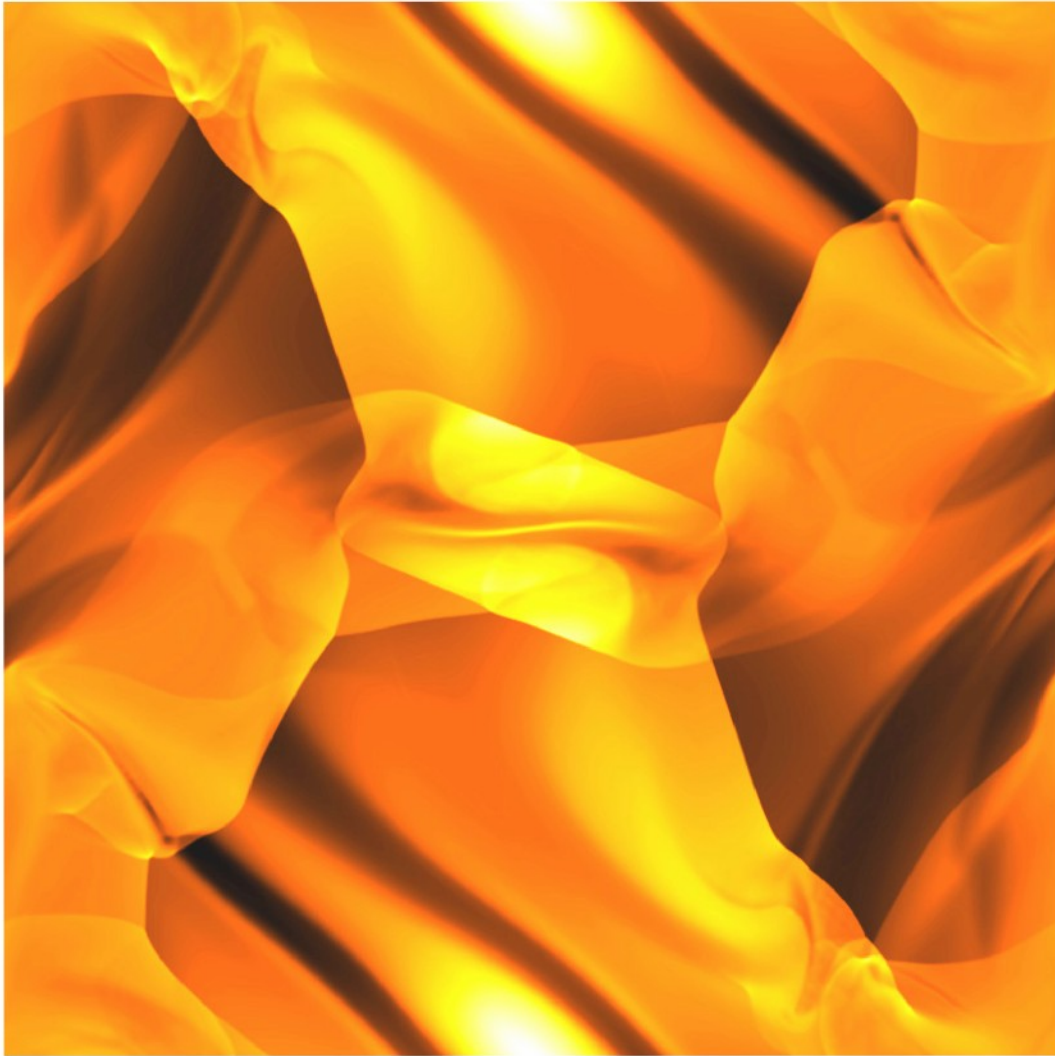



Figure 6.11: Orszag-Tang MHD vortex as computed on an  $800 \times 800$  cell mesh with  $\Delta x = \Delta y$ .  
 Colormap:  $\rho_{min}$    $\rho_{max}$

has been replaced with the highly diffusive HLLE [37] Riemann solver. It is well known that errors in the divergence of the magnetic flux density can be artificially diffused away [69]. The HLLE solver provides a significant amount of diffusion, effectively stabilizing the solution.

## CHAPTER 7

### DIFFUSION PROCESSES

It has been shown to be a natural conclusion to separate the physical models based on their mathematical classification as being hyperbolic, parabolic, etc. The individual processes resulting from this decomposition are then solved independently of each other using the operator splitting technique. In this chapter, attention is shifted from the convective terms of the governing equations to the source terms. In particular, diffusion processes are parabolic in nature and are considered here. In particular, an implicit solver for electron heat conduction is detailed.

#### 7.1 Governing equations

Relative to the convective speeds studied in this work, thermal diffusion of the heavy particles is negligible. The diffusion speed of electrons on the other hand may be significant as a result of their large thermal velocity. As such, all diffusion processes involving electrons must be considered. This includes thermal diffusion, the governing equations of which may be expressed as a finite-volume discretization,

$$\frac{\partial E}{\partial t} = \frac{1}{V} \sum_s F_{n_s} A_s \quad (7.1)$$

with the flux  $F_{n_s}$  normal to cell interface  $s$  given by

$$F_{n_s} = \kappa_s \frac{\partial T}{\partial \hat{n}_s} \quad (7.2)$$

with  $\kappa_s$  being the scalar thermal conductivity taken at  $s$ . The difference is approximated using the states immediately to the left and right of  $s$ ,

$$\frac{\partial T}{\partial \hat{n}_s} \approx \frac{(T_R - T_L)}{\Delta n} \quad (7.3)$$

while the thermal conductivity at  $s$  is taken as a simple arithmetic average,

$$\kappa_s \approx \frac{1}{2}(\kappa_L + \kappa_R). \quad (7.4)$$

In the following sections, the one- and two-dimensional form of the governing equations are derived, assuming the conductivity to be a function of temperature. The exact form of the thermal conductivity for an electron fluid will be given in Section 7.4.

## 7.2 One-dimensional case

The one-dimensional heat equation will be described here in detail. To facilitate analysis, the heat equation is recast into differential form, yielding

$$\frac{\partial E}{\partial t} = \frac{\partial}{\partial x} \left( \kappa_s \frac{\partial T}{\partial x} \right) \quad (7.5)$$

and upon application of the chain rule to the LHS, an expression for the time rate of change of the temperature is obtained,

$$\frac{\partial E}{\partial T} \frac{\partial T}{\partial t} = \frac{\partial}{\partial x} \left( \kappa_s \frac{\partial T}{\partial x} \right) \quad (7.6)$$

Assuming a one-dimensional discretization on a uniformly-spaced mesh, the spatial derivatives can be approximated by finite-differences, thereby reducing the PDE to a system of ODE's,

$$\frac{dT_i}{dt} = \frac{(E_T)_i^{-1}}{\Delta x} \left[ \kappa_{i+1/2} \frac{(T_{i+1} - T_i)}{\Delta x} + \kappa_{i-1/2} \frac{(T_i - T_{i-1})}{\Delta x} \right] \quad (7.7)$$

for  $i = 1, 2, \dots, M$  where

$$E_T = \text{diag} \left( \dots, \frac{dE_i}{dT_i}, \dots \right) \quad (7.8)$$

For an ideal gas, the definition of the specific heat yields  $dE_i/dT_i = \rho_i c_{v,i}$ . Rearranging,

$$\frac{dT_i}{dt} = \frac{(E_T)_i^{-1}}{\Delta x^2} [\kappa_{i-1/2} T_{i-1} - (\kappa_{i-1/2} + \kappa_{i+1/2}) T_i + \kappa_{i+1/2} T_{i+1}] \quad (7.9)$$

the system of equations can be written in matrix notation as

$$\frac{\partial \vec{T}}{\partial t} = \Phi \vec{T} \quad (7.10)$$

where  $\Phi$  is a tridagonal matrix and  $\vec{T}$  is the spatial vector of temperatures,

$$\Phi = \frac{E_T^{-1}}{\Delta x^2} \begin{bmatrix} \ddots & & & & \\ & \ddots & & & \\ & & \ddots & & \\ & & & \ddots & \\ & & & & \ddots \end{bmatrix}, \quad \vec{T} = \begin{bmatrix} \vdots \\ T_{i-1} \\ T_i \\ T_{i+1} \\ \vdots \end{bmatrix} \quad (7.11)$$

The above discretization has resulted in a reduction of the original PDE into a system of ODE's. The choice for discretization in time, however, is still open to consideration. Since electron diffusion is such a rapid process, the above system is stiff in comparison with the bulk convection. This implies that an implicit time marching scheme can be advantageous. Evaluating the RHS of Eq. (7.10) at time  $t + \Delta t$ ,

$$\frac{\Delta \vec{T}}{\Delta t} = \Phi^{n+1} \vec{T}^{n+1} \quad (7.12)$$

a temporal discretization is obtained, where  $T^n = T(t)$ ,  $T^{n+1} = T(t + \Delta t)$ , and  $\Phi^{n+1} = \Phi(\vec{T}^{n+1})$ . As usual,  $\Delta$  is the forward difference operator. Linearization of the RHS is obtained through a Taylor series expansion, yielding

$$\frac{\Delta \vec{T}}{\Delta t} = \Phi \vec{T} + \frac{\partial(\Phi \vec{T})_i}{\partial T_j} \Delta \vec{T} \quad (7.13)$$

in which the superscripts have been dropped with the implication that all terms are evaluated at time  $n$ . Isolating the energy difference,

$$\Delta \vec{T} = (I - \Delta t J)^{-1} \Delta t \Phi \vec{T} \quad (7.14)$$

the final expression is obtained which is used to compute the change in energy. The Jacobian,  $J = \partial(\Phi \vec{T})_i / \partial T_j$  is a tridiagonal matrix,

$$J = \begin{bmatrix} & & & & \\ & \ddots & & & \\ & & \ddots & & \\ & & & \ddots & \\ & & & & \ddots \\ & & a_i & b_i & c_i \\ & & & \ddots & \ddots & \ddots \end{bmatrix} \quad (7.15)$$

with elements

$$a_i = \frac{E_T^{-1}}{\Delta x^2} \left[ \frac{\partial \kappa_{i-1/2}}{\partial T_{i-1}} (T_{i-1} - T_i) - \kappa_{i-1/2} \right] \quad (7.16)$$

$$b_i = \frac{E_T^{-1}}{\Delta x^2} \left[ \frac{\partial \kappa_{i-1/2}}{\partial T_{i-1}} (T_{i-1} - T_i) - \kappa_{i-1/2} + \frac{\partial \kappa_{i+1/2}}{\partial T_i} (T_{i+1} - T_i) - \kappa_{i+1/2} \right] \quad (7.17)$$

$$c_i = \frac{E_T^{-1}}{\Delta x^2} \left[ \frac{\partial \kappa_{i+1/2}}{\partial T_{i+1}} (T_{i+1} - T_i) - \kappa_{i+1/2} \right] \quad (7.18)$$

Note that the Jacobian can also be expressed in terms of  $\Phi$  and  $Q$  only,

$$J = \Phi + \frac{\partial \Phi}{\partial Q} Q \quad (7.19)$$

Defining  $\Psi \equiv (\partial \Phi / \partial Q) Q$ , the Jacobian can compactly be expressed as

$$J = \Phi + \Psi \quad (7.20)$$

with the explicit form of  $\Psi$  easily found by subtracting  $\Phi$  from  $J$ ,

$$\Psi = \frac{E_T^{-1}}{\Delta x^2} \begin{bmatrix} \ddots & & \ddots & & \ddots \\ & \frac{\partial \kappa_{i-1/2}}{\partial T_{i-1}} (T_{i-1} - T_i) & \left( \frac{\partial \kappa_{i-1/2}}{\partial T_i} (T_{i-1} - T_i) + \frac{\partial \kappa_{i+1/2}}{\partial T_i} (T_{i+1} - T_i) \right) & \frac{\partial \kappa_{i+1/2}}{\partial T_{i+1}} (T_{i+1} - T_i) & \\ & & \ddots & & \\ & & & \ddots & \\ & & & & \ddots \end{bmatrix} \quad (7.21)$$

This splitting of the Jacobian is key to developing a condition for stability as derived in the following section.

### 7.3 Stability

The practical reason for using an implicit method is for its added stability over explicit methods, thereby allowing the solution to be advanced by larger time steps per iteration. Since the thermal diffusion equation is nonlinear, however, stability is not unconditional. Linearization has precluded the solution from being advanced to regions beyond which such an approximation is valid. As such, a criterion for an optimal time step must be determined as to maximize solver efficiency while avoiding oscillations or even catastrophic instability.

The solution of Eq. (7.14) at time  $t + \Delta t$  is given by

$$\vec{T}^{n+1} = (I - \Delta t J)^{-1} [I - \Delta t J + \Delta t \Phi] \vec{T}^n \quad (7.22)$$

or equivalently

$$\vec{T}^{n+1} = (I - \Delta t (\Phi + \Psi))^{-1} [I - \Delta t \Psi] \vec{T}^n \quad (7.23)$$

after application of Eq. (7.19). Introducing  $\Theta \equiv (I - \Delta t (\Phi + \Psi))^{-1} [I - \Delta t \Psi]$  such that

$$\vec{T}^{n+1} = \Theta \vec{T}^n, \quad (7.24)$$

it is evident that stability of the above system can only be guaranteed if the eigenvalues of  $\Theta$ ,

$$\lambda_i^\Theta = \frac{1 - \Delta t \lambda_i^\Phi}{1 - \Delta t (\lambda_i^\Phi + \lambda_i^\Psi)} \quad (7.25)$$

satisfy the condition

$$|\lambda_i^\Theta| \leq 1, \forall i \quad (7.26)$$

The strict evaluation of this criterion requires the eigenvalues of  $\Phi$  and  $\Psi$  be determined from recursion formulas, adding severe complexity to the analysis. This is avoidable, however, as a reasonable estimate can readily be found by assuming that the function  $\kappa_i, \forall i$  in  $\Phi$  as well as the function  $\partial \kappa_{i+1/2} / \partial T_i (T_{i+1/2} - T_{i+1/2}), \forall i$  in  $\Psi$  can be replaced by *representative*<sup>1</sup> constant parameters  $\phi$  and  $\psi$ , such that

$$\Phi \rightarrow \phi \frac{E_T^{-1}}{\Delta x^2} B(M : 1, -2, 1), \quad \Psi \rightarrow \psi \frac{E_T^{-1}}{\Delta x^2} B(M : 1, -2, 1). \quad (7.27)$$

The eigenvalues of Eq. (7.25) can then be approximated as

$$\lambda_i^\Phi \approx -4\phi \frac{E_T^{-1}}{\Delta x^2} \left[ \sin^2 \left( \frac{i\pi}{2(M+1)} \right) \right], \quad \lambda_i^\Psi \approx -4\psi \frac{E_T^{-1}}{\Delta x^2} \left[ \sin^2 \left( \frac{i\pi}{2(M+1)} \right) \right] \quad (7.28)$$

where  $B(M : 1, -2, 1)$  is banded matrix notation for a tridiagonal matrix with the main diagonal composed of 2's while the entries of both the subdiagonal and superdiagonal are 1. Note that  $\phi$  is necessarily positive while  $\psi$  is not. Returning to the stability condition,

$$-1 \geq \frac{1 - \Delta t \lambda_i^\Psi}{1 - \Delta t (\lambda_i^\Phi + \lambda_i^\Psi)} \leq 1 \quad (7.29)$$

it is now evident that for  $\lambda_i^\Phi > 0$ ,

$$-1 \geq \frac{1 - \Delta t |\lambda_i^\Psi|}{1 - \Delta t |\lambda_i^\Psi| + \Delta t |\lambda_i^\Phi|} \leq 1 \quad (7.30)$$

the system is unconditionally stable, while for  $\lambda_i^\Psi < 0$ ,

---

<sup>1</sup>This approach can be found in [106] for example.



$$-1 \geq \frac{1 + \Delta t |\lambda_i^\Psi|}{1 + \Delta t |\lambda_i^\Psi| + \Delta t |\lambda_i^\Phi|} \leq 1 \quad (7.31)$$

it is found that

$$\Delta t \leq \frac{2}{2|\lambda_i^\Psi| - |\lambda_i^\Phi|} \quad (7.32)$$

which holds true *iff* the denominator is positive, i.e.  $2|\lambda_i^\Psi| > |\lambda_i^\Phi|$ . In other words, as  $|\lambda_i^\Phi| \rightarrow 2|\lambda_i^\Psi|$ ,  $\Delta t \rightarrow 0$ , and as a result,  $|\lambda_i^\Phi|$  can safely be neglected. Neglecting this eigenvalue greatly simplifies the condition, but the drawback is a more restrictive time step. The condition can be restated as

$$\Delta t \leq \frac{1}{|\lambda_i^\Psi|} \quad (7.33)$$

for which Eq. (7.28) can be applied, yielding

$$\Delta t \leq \frac{1}{\left| -4\psi \frac{E_T^{-1}}{\Delta x^2} \sin^2 \left( \frac{i\pi}{2(M+1)} \right) \right|}. \quad (7.34)$$

#### 7.4 Thermal conductivity

Constitutive equations for the thermal conductivity are necessary to obtain closure for the diffusion equation. In the case of electron heat transfer, the thermal conductivity for a fully-ionized plasma takes the form

$$\kappa_e \approx 1.44 \times 10^{-10} \frac{T_e^{5/2}}{\ln \Lambda} \text{ [W/m} \cdot \text{K]} \quad (7.35)$$

with the Coulomb logarithm given by

$$\Lambda = 1.24 \times 10^7 \frac{T_e^{3/2}}{n_e^{1/2}}. \quad (7.36)$$

#### 7.5 Benchmarks

In order to validate the thermal diffusion solver, a test problem was created which demonstrates the importance of electron heat conduction in a fully-ionized plasma. The problem

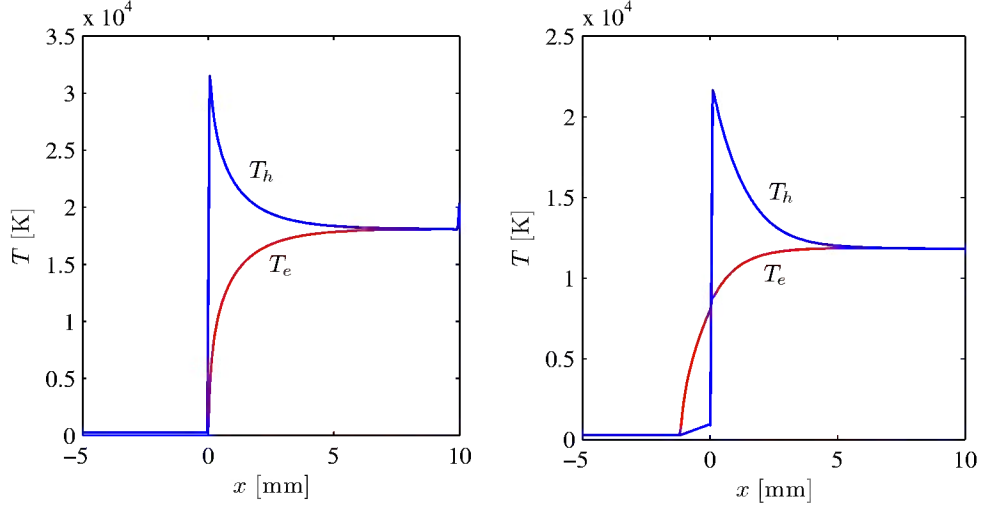


Figure 7.1: Thermal diffusion benchmarks—fully-ionized argon plasma ( $Ar^+$ ,  $e^-$ ) without (*left*) and with (*right*) electron heat conduction. The shock is created by reflection of a uniform flow from an adiabatic wall located at  $x = 10$  mm

setup consists of a uniform one-dimensional flow field described by

$$\begin{pmatrix} p_\infty \\ u_\infty \\ T_\infty \end{pmatrix} = \begin{pmatrix} 4.13 \text{ Pa} \\ 4700 \text{ m/s} \\ 275 \text{ K} \end{pmatrix} \quad (7.37)$$

composed of  $e^-$  and  $Ar^+$  species with equal number densities (fully ionized) impinging upon an adiabatic wall<sup>2</sup>. The shock structure resulting from the reflection of the plasma from the wall is given in Figure 7.5 for cases with and without electron heat conduction. The results show that without conduction, the shock travels at approximately Mach 19 while with conduction, this value decreases to approximately 16. This is a significant difference and demonstrates the amount of thermal energy that is diffused by the electrons across the shock. The pre-shock electron temperature profile reflects the nonlinear dependence ( $\kappa \sim T_e^{5/2}$ ) and is consistent with the analytical solutions presented in [128].

A point of interest is the plasma *overheating* that results when the shock reflects from the wall for the case without heat conduction. This is purely a numerical anomaly and results from a known deficiency of approximate Riemann solvers (cf. [82] and [75]). Although its treatment is not addressed nor implemented here, the electron heat conduction is significant

<sup>2</sup>Coulombic thermalization is also considered and is detailed in Section 9.5.

enough to diffuse away this anomaly and minimize any adverse effects.

Also noteworthy is the discontinuous profile of the electron temperature across the shock. While adiabatic compression of the electrons across the shock may lead to such a jump, thermal diffusion should be significant enough to smooth out the profile. It has yet to be determined whether this jump is indeed physical in nature or is a numerical artifact.

## CHAPTER 8

### NEAR-VACUUM FLOWS

Under certain flow conditions, a situation may occur in which the internal energy becomes a small fraction of the total energy. For example, in cases of rapid expansions, the kinetic energy may dominate the total energy of the system as the internal energy quickly drops. As the kinetic energy is subtracted from the total energy, substantial errors in the internal energy and subsequent pressure may result<sup>1</sup>. This problem is further compounded in cases in which the density approaches zero, as small fluctuations in this variable can lead to large errors in the fluid temperature.

While the choice of solver can have some impact in such cases [81], the root of the problem lies in the conditioning of the governing equations. This problem has been addressed in the literature with several approaches being proposed. In [24], the internal energy is convected independently of the total energy which is a technique that can be found in mature CFD codes. The drawback is that the formulation is no longer conservative and can result in significant errors.

Another approach has been to modify the reconstruction scheme to include a bound on the internal and kinetic energies [51]. While this technique is able to preserve positivity of the governing equations, it does not address the conditioning problem of the system.

The approach taken here is to augment the transport equations with entropy conservation in a similar fashion as done in [62]. This in effect is a way to convect the internal energy independently of the total energy while preserving the conservation property of the governing equations. Such an approach, however, is limited to flows that are isentropic, namely non-shocked polytropic gases. However, this approach can be extended to include real gas effects

---

<sup>1</sup>This problem can be even more dramatic if the MHD equations are considered with a strong magnetic field, in which case the magnetic pressure can be a dominant term as well.

through the inclusion of relaxation parameters, assuming near-equilibrium conditions. The formulation of the governing equations are presented first followed by benchmarks on a standard rarefaction test case.

### 8.1 Formulation

The purpose of this section is to augment the the continuity, momentum, and energy equations with an entropy equation in conservation form. The derivation is entirely analogous to that of the electron energy equation for the 2T model presented in Chapter 2. For simplicity, a single component fluid will be considered. For a polytropic gas, the entropy equation can be expressed in conservative form as

$$\frac{\partial \rho s}{\partial t} + \nabla \cdot (\vec{u} \rho s) = 0 \quad (8.1)$$

with  $s = p/\rho^\gamma$ . Incorporating this into the governing equations, the entropy-augmented Euler equations can be expressing in vector form as

$$\frac{\partial Q}{\partial t} + \nabla \cdot F_n = 0 \quad (8.2)$$

where

$$Q = \begin{pmatrix} \rho_1 \\ \vdots \\ \rho_n \\ \rho u \\ \rho v \\ \rho w \\ E \\ S \end{pmatrix}, \quad V = \begin{pmatrix} \rho_1 \\ \vdots \\ \rho_n \\ u \\ v \\ w \\ p \\ p \end{pmatrix}, \quad F_n = \begin{pmatrix} v_n \rho_1 \\ \vdots \\ v_n \rho_n \\ v_n \rho u + n_x p \\ v_n \rho v + n_y p \\ v_n \rho w + n_z p \\ v_n (E + p) \\ v_n S \end{pmatrix} \quad (8.3)$$

and  $S = \rho s$ . The flux Jacobian of the system is analogous to Eq. (A.4) and is given by

$$A_x = \frac{\partial F}{\partial Q} = \begin{pmatrix} u(1-y_1) & \dots & -uy_1 & y_1 & 0 & 0 & 0 & 0 \\ \vdots & \ddots & \vdots & \vdots & \vdots & \vdots & \vdots & \vdots \\ -uy_n & \dots & u(1-y_n) & y_n & 0 & 0 & 0 & 0 \\ -uv & \dots & -uv & v & u & 0 & 0 & 0 \\ -uw & \dots & -uw & w & 0 & u & 0 & 0 \\ P_{\rho_1} - \vec{u} \cdot \vec{u} & \dots & P_{\rho_n} - \vec{u} \cdot \vec{u} & P_{m_x} + 2u & P_{m_y} & P_{m_z} & P_E & P_S \\ \mathcal{A}_{\rho_1,E} & \dots & \mathcal{A}_{\rho_n,E} & \mathcal{A}_{m_x,E} & uP_{m_y} & uP_{m_z} & u(1+P_E) & uP_S \\ -uS/\rho & \dots & -uS/\rho & S/\rho & 0 & 0 & 0 & u \end{pmatrix}$$

where

$$\mathcal{A}_{\rho_i,E} = uP_{\rho_i} - u(E+p)/\rho,$$

$$\mathcal{A}_{m_x,E} = uP_{m_x} + (E+p)/\rho.$$

The similarities with the 2T extend to the diagonalization of the flux Jacobian, resulting in an analogous eigensystem as well. The right and left eigenvectors for the entropy-augmented Euler equations can be deduced from Eqs. (A.11) and (A.15), respectively. In addition, the Roe-averaged states  $\tilde{Q}$  can be found from a linearization of the definition of the flux Jacobian,

$$\Delta F = A(\tilde{Q})\Delta Q, \quad (8.4)$$

and are given by

$$\tilde{\rho} = \sqrt{\rho_L \rho_R} \quad (8.5)$$

$$\tilde{u} = \frac{\sqrt{\rho_L} u_L + \sqrt{\rho_R} u_R}{\sqrt{\rho_L} + \sqrt{\rho_R}} \quad (8.6)$$

$$\tilde{h}_o = \frac{\sqrt{\rho_L} h_{oL} + \sqrt{\rho_R} h_{oR}}{\sqrt{\rho_L} + \sqrt{\rho_R}} \quad (8.7)$$

$$\tilde{S} = \frac{\sqrt{\rho_L} S_R + \sqrt{\rho_R} S_L}{\sqrt{\rho_L} + \sqrt{\rho_R}} \quad (8.8)$$

Note that with the inclusion of both the energy and entropy equations, there are two distinct possibilities for computing the Roe-average pressure and sound speed for isentropic flows. The first option is to compute the sound speed and pressure from the stagnation enthalpy according to

$$\tilde{a} = (\gamma - 1) \left( \tilde{h}_o - \frac{1}{2} \tilde{u}^2 \right)^{1/2} \quad (8.9)$$

$$\tilde{p} = \frac{\tilde{\rho} \tilde{a}^2}{\gamma}. \quad (8.10)$$

Alternatively, the values may be derived from the entropy,

$$\tilde{p} = \tilde{S} \tilde{\rho}^{\gamma-1} \quad (8.11)$$

$$\tilde{a} = \left( \frac{\gamma \tilde{p}}{\tilde{\rho}} \right)^{1/2} \quad (8.12)$$

To ensure consistency, Eq. (8.11) must be used if the left and right pressure states were computed from the entropy variable as well. If the left and right pressure states were computed from the internal energy, on the other hand, the sound speed should be derived from the Roe average stagnation enthalpy.

## 8.2 Benchmarks

One of the most common benchmarks to test a solver's ability to properly capture high velocity/low density flows is the *1-2-3* problem, so-called due to the initial ratio of density

to momentum to energy, respectively [37]. This test case simulates two retracting pistons and the low pressure/density region that results. The left and right states are defined by,

$$\begin{pmatrix} \rho_L \\ u_L \\ p_L \end{pmatrix} = \begin{pmatrix} 1 \\ -2 \\ 0.4 \end{pmatrix}, \quad \begin{pmatrix} \rho_R \\ u_R \\ p_R \end{pmatrix} = \begin{pmatrix} 1 \\ 2 \\ 0.4 \end{pmatrix} \quad (8.13)$$

for a polytropic gas with an adiabatic exponent of  $5/3$ . The deficiency of numerical solvers in duplicating the exact solution is a conditioning problem inherent in the governing equations. At very low densities, relatively small changes in the pressure and density can lead to large errors in temperature as can be seen in Figure 8.2. However, if the pressure is obtained directly from the entropy function,  $p/\rho^{\gamma-1}$ , this problem is essentially eliminated as can be seen in Figure 8.2.



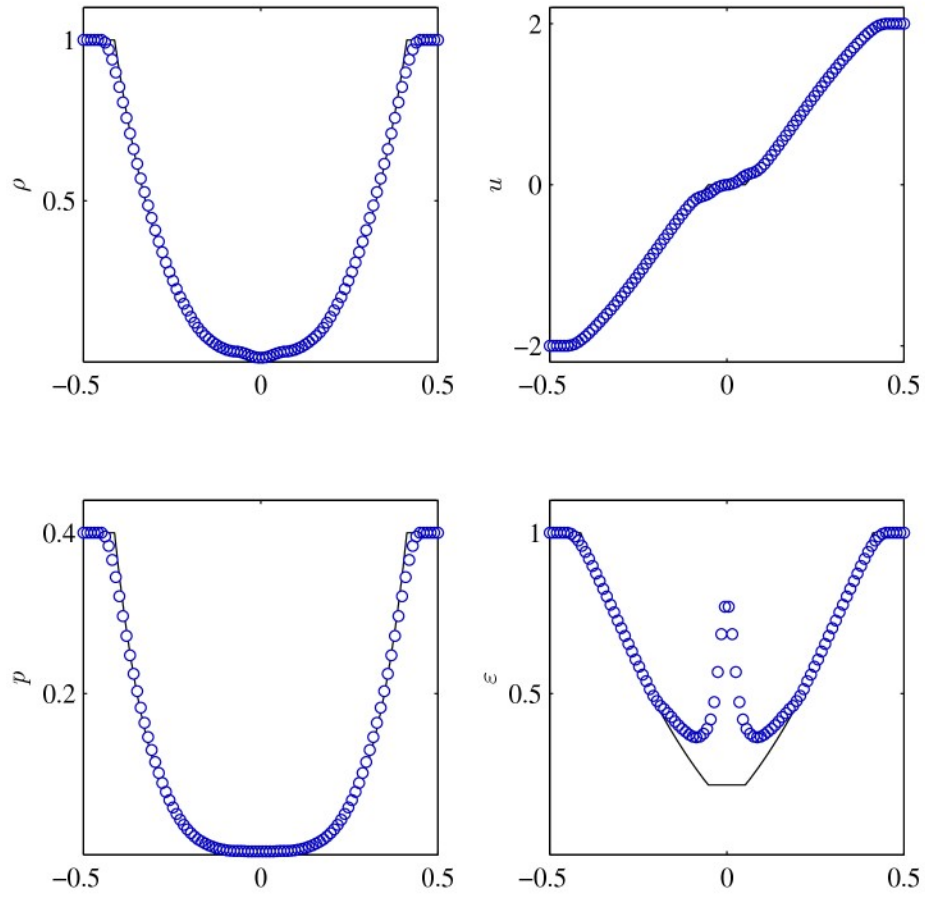


Figure 8.1: Solution to Einfeldt's 1-2-3 problem as obtained with conservation of energy. Symbols ( $\circ$ ) denote numerical solution while solid line ( $—$ ) is the exact solution.

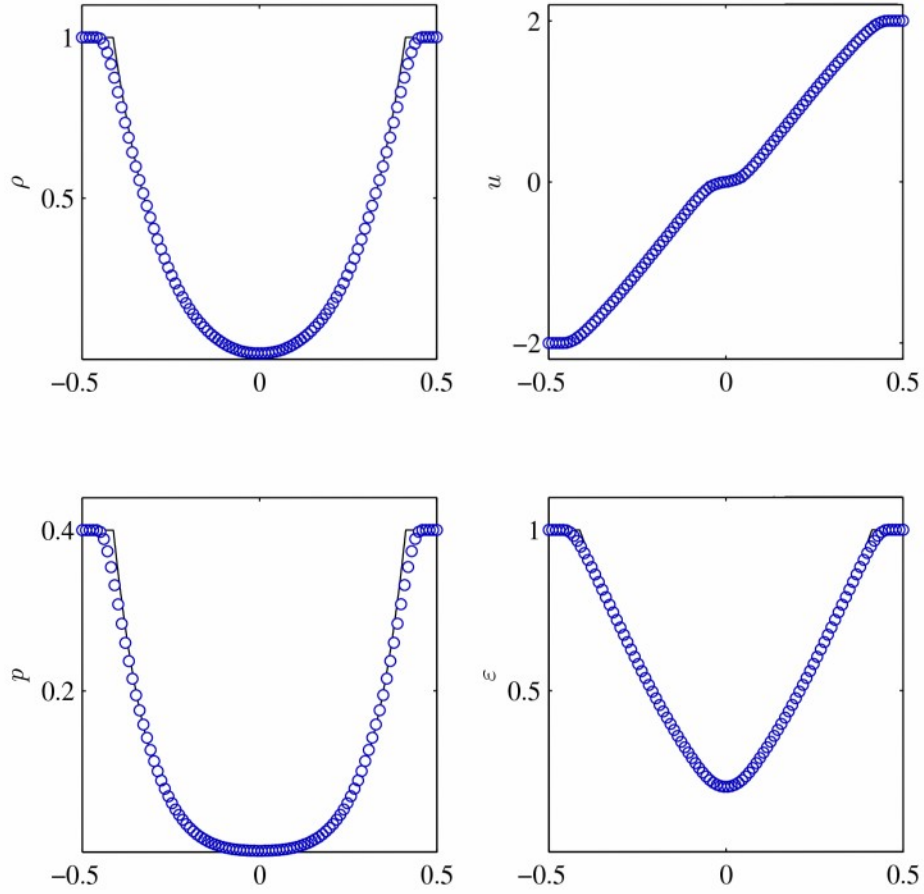


Figure 8.2: Solution to Einfeldt's 1-2-3 problem as obtained with conservation of entropy. Symbols ( $\circ$ ) denote numerical solution while solid line ( $—$ ) is the exact solution.

## CHAPTER 9

### COLLISIONAL-RADIATIVE MODEL

In this chapter, the collisional-radiative model developed for monatomic argon is detailed. The CR model functions as a generalized equation of state for the electronic energy modes. It is used to compute the populations of the excited levels through detailed kinetic relations for excitation and ionization, and reverse processes, allowing for non-Boltzmann distribution of bound electronic states. Rates are computed from collision cross sections of the associated processes under the assumption of a Maxwellian electron energy distribution function (EEDF).

The CR model presented here draws upon the previous work of Vlček [117] and Bultel *et al.* [19] both of which are specific to argon. The model includes the first 31 excited levels of neutral argon, for which a partial Grotrian is provided in Figure 9.1, as well as the ground states of the singly-charged ion. Population of the states beyond the lower lying levels is negligible for the plasma conditions considered, as verified by equilibrium considerations. Level grouping is not considered, as the approach here is to look in detail at the influence of the lower lying states.

As the CR model will be validated on the UTIAS shock tube experiments in the following chapter, assumptions made herein are based on the plasma conditions of the experiments where ever necessary. This includes number densities up to  $10^{24}$  [m<sup>-3</sup>] and temperatures just above 1 eV.

#### 9.1 Rate equations

The processes to be included can be represented by the following rate equations,

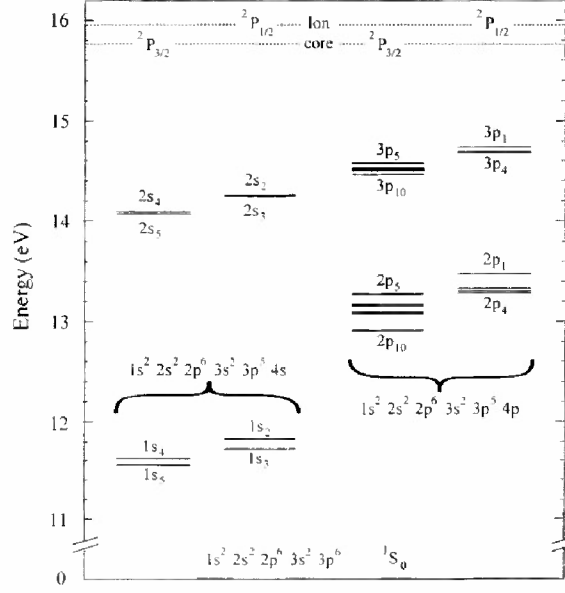


Figure 9.1: Partial Grotrian diagram for neutral argon taken from [99].

$$Ar(i) + e^- \xrightleftharpoons[F_{ji}]{C_{ij}} Ar(j) + e^- \quad (9.1)$$

$$Ar(i) + Ar(1) \xrightleftharpoons[L_{ji}]{K_{ij}} Ar(j) + Ar(1) \quad (9.2)$$

$$Ar(i) + e^- \xrightleftharpoons[O_i]{S_i} Ar^+ + e^- + e^- \quad (9.3)$$

$$Ar(i) + Ar(1) \xrightleftharpoons[W_i]{V_i} Ar^+ + Ar(1) + e^- \quad (9.4)$$

$$Ar(i) + h\nu_{ij} \xrightleftharpoons[A_{ij}]{(1-\Lambda_{ij})A_{ij}} Ar(j) \quad (9.5)$$

$$Ar(i) + h\nu \xrightleftharpoons[R_i]{(1-\Lambda_i)R_i} Ar^+ + e^- \quad (9.6)$$

where the rate coefficients defined in [117] are summarized in Table 9.1. The convention has been adopted that takes  $j > i$  so that  $C_{ij}$  and  $K_{ij}$  represent the rates for excitation from level  $i$  to  $j$  while  $F_{ji}$  and  $L_{ji}$  are the rates for de-excitation from level  $j$  to  $i$ . The levels considered in the present model include only those up to the  $3p^5 3d$  and  $3p^5 5s$  manifolds (cf. Table 9.2). This implies that ionization and recombination should proceed from and to only these low-lying levels; although levels beyond this manifold are more than 1 eV away

Rate Coefficient	Process
$C_{ij}$	collisional excitation by electrons
$K_{ij}$	collisional excitation by ground state atoms
$F_{ji}$	collisional de-excitation by electrons
$L_{ji}$	collisional de-excitation by ground state atoms
$S_i, V_i$	collisional ionization
$O_i, W_i$	three-body recombination
$R_i$	radiative recombination
$A_{ij}$	transition probability/spontaneous emission (Einstein coefficient)
$\Lambda_{ij}$	bound-bound optical escape factor
$\Lambda_i$	bound-free optical escape factor
$k_{ei}$	electron-ion collisions
$k_{en}$	electron-neutral collisions
$k_{\text{brems}}$	bremsstrahlung emission

Table 9.1: Rate coefficients for collisional-radiative model.

from the ionization limit, the combination of small energy gap and large cross-section makes the ionization from these levels extremely rapid, certainly with time scales much below the time resolution needed in the current research. Thus the lower-lying states provide the bottleneck to the ionization regime and most of the energy in bound states.

Note that neutral argon has two ionization potentials owing to the fact that the levels of argon are split according to two possible configurations for the core angular momentum  $j_c$ .

Neutral argon has two ionization potentials corresponding to two possible configurations for the core angular momentum  $j_c$ . As ionization and recombination can proceed only between levels having the same value of  $j_c$ , the populations of the two lowest lying levels of  $\text{Ar}^+$  must be accounted for individually. In the current model, these two levels are treated as separate species and convected as such.

Considered here are plasmas for which a Maxwellian electron energy distribution function (EEDF) is valid,

$$f(\varepsilon) d\varepsilon = \frac{2}{\pi^{1/2}} \frac{\varepsilon^{1/2}}{(k_B T_e)^{3/2}} e^{-\varepsilon/k_B T_e} d\varepsilon, \quad (9.7)$$

which has been normalized according to

$$\int_0^\infty f(\varepsilon) d\varepsilon = 1. \quad (9.8)$$

$i$	$\varepsilon(i)$ [eV]	$g_i$	$j_c$	$n\ell[K]_J$	$i$	$\varepsilon(i)$ [eV]	$g_i$	$j_c$	$n\ell[K]_J$
1	0	1	1.5	[Mg]3p <sup>6</sup>	18	13.903	5	1.5	3d[3/2] <sub>2</sub>
2	11.548	5	1.5	4s[3/2] <sub>2</sub>	19	13.979	9	1.5	3d[7/2] <sub>4</sub>
3	11.624	3	1.5	4s[3/2] <sub>1</sub>	20	14.013	7	1.5	3d[7/2] <sub>3</sub>
4	11.723	1	0.5	4s'[1/2] <sub>0</sub>	21	14.063	5	1.5	3d[5/2] <sub>2</sub>
5	11.828	3	0.5	4s'[1/2] <sub>1</sub>	22	14.068	5	1.5	3d[3/2] <sub>1</sub>
6	12.907	3	1.5	4p[1/2] <sub>1</sub>	23	14.090	3	1.5	5s[3/2] <sub>2</sub>
7	13.076	7	1.5	4p[5/2] <sub>3</sub>	24	14.099	7	1.5	5s[5/2] <sub>3</sub>
8	13.095	5	1.5	4p[5/2] <sub>2</sub>	25	14.153	3	1.5	3d[3/2] <sub>1</sub>
9	13.153	3	1.5	4p[3/2] <sub>1</sub>	26	14.214	5	0.5	5s'[1/2] <sub>0</sub>
10	13.172	5	1.5	4p[3/2] <sub>2</sub>	27	14.234	5	0.5	3d'[5/2] <sub>2</sub>
11	13.273	1	1.5	4p[1/2] <sub>0</sub>	28	14.236	7	0.5	5s'[1/2] <sub>1</sub>
12	13.283	3	0.5	4p'[3/2] <sub>1</sub>	29	14.241	1	0.5	3d'[3/2] <sub>2</sub>
13	13.302	5	0.5	4p'[3/2] <sub>2</sub>	30	14.255	3	0.5	3d'[5/2] <sub>3</sub>
14	13.328	3	0.5	4p'[1/2] <sub>1</sub>	31	14.304	3	0.5	3d'[3/2] <sub>1</sub>
15	13.480	1	0.5	4p'[1/2] <sub>0</sub>	$\infty$	15.760	4	1.5	[Mg]3p <sup>5</sup>
16	13.845	1	1.5	3d[1/2] <sub>0</sub>	$\infty'$	15.937	2	0.5	[Mg]3p <sup>5</sup>
17	13.864	3	1.5	3d[1/2] <sub>1</sub>					

Table 9.2: Argon levels considered in current CR model.

The rate coefficients are computed using the EEDF according to

$$k = \frac{\bar{v}}{(k_B T)^2} \int_{\varepsilon_o}^{\infty} \sigma(\varepsilon) \varepsilon e^{-\varepsilon/k_B T} d\varepsilon \quad (9.9)$$

where  $\varepsilon_o$  is the threshold energy and  $\bar{v}$  is the mean thermal velocity,

$$\bar{v} = \left( \frac{8k_B T}{\pi \mu} \right)^{1/2}, \quad (9.10)$$

with  $\mu$  being the reduced mass. The reverse rates are then computed from the principle of detailed balance. For excitation processes this takes the form

$$k_{ji} = k_{ij} \frac{g_i}{g_j} e^{\varepsilon_{ij}/k_B T} \quad (9.11)$$

where  $\varepsilon_{ij} = \varepsilon_j - \varepsilon_i$  is the energy difference of the upper and lower levels. The temperature in Eq. (9.11) is taken to be that of the the impact species. For processes involving a third body, the reverse rates are computed via

$$k_i^r = k_i \frac{Z_i}{Z_+ Z_e} \quad (9.12)$$

where  $Z_e$  is the electron partition function,

$$Z_e = 2 \left( \frac{2\pi m_e k_B T_e}{h^2} \right)^{3/2} \quad (9.13)$$

while the ratio of partition functions for  $Ar$  and  $Ar^+$  can be approximated as<sup>1</sup>

$$\frac{Z_i}{Z_+} \approx \frac{g_i}{g_+} e^{I_i/k_B T} \quad (9.14)$$

with  $I_i$  being the ionization potential of the  $i^{\text{th}}$  excited state, allowing Eq. (9.12) to be written as

$$k_i^r = k_i \frac{g_i}{g_+} \frac{1}{2} \left( \frac{h^2}{2\pi m_e k_B T_e} \right)^{3/2} e^{I_i/k_B T}. \quad (9.15)$$

Note that the exponential temperature dependence in Eq. (9.15) is a function of the third body— $T$  is taken to be either the electron or heavy particle temperature for cases in which the third body is an electron or atom, respectively.

In addition to species production rates, the second moment with respect to energy is also necessary as it determines the energy production rate for a given process,

$$k' = \frac{\bar{v}}{(k_B T)^2} \int_{\varepsilon_0}^{\infty} \sigma(\varepsilon) \varepsilon^2 e^{-\varepsilon/k_B T} d\varepsilon \quad (9.16)$$

In practice, all rate coefficients and their derivatives are computed *a priori* and tabulated as a function of temperature which is used in the code. This is possible due to the assumption of a known distribution function.

The remainder of this section is devoted to calculation of the cross sections and associated rates used in the CR model. For further details, the reader is directed to [19] and [117].

### 9.1.1 Atom impact processes

Cross sections for atom-atom collisions are typically several orders of magnitude less than their electron-atom counterpart since for a given translational temperature,  $\bar{v}_e \gg \bar{v}_a$ . However, with the absence of electrons immediately behind the compression shock, atom-atom collisions are the only means for initial electron production and result in the necessary

---

<sup>1</sup>Assuming  $m_{Ar} \approx m_{Ar^+}$ .

$i$	$j$	$\beta_{ij}^* [\text{m}^2/\text{eV}]$	$f_{ij}$
1	3	$1.10 \times 10^{-23}$	$6.78 \times 10^{-02}$
1	5	$3.95 \times 10^{-23}$	$2.56 \times 10^{-01}$
1	17	$9.58 \times 10^{-26}$	$1.00 \times 10^{-03}$
1	23	$3.10 \times 10^{-24}$	$3.40 \times 10^{-02}$
1	25	$8.55 \times 10^{-24}$	$9.51 \times 10^{-02}$
1	30	$1.59 \times 10^{-24}$	$1.80 \times 10^{-02}$
1	31	$6.92 \times 10^{-24}$	$7.94 \times 10^{-02}$

Table 9.3: Atom impact excitation parameters for allowed transitions from ground state Ar.

$i$	$j$	$\beta_{ij}^* [\text{m}^2/\text{eV}]$
2	3	$1.79 \times 10^{-24}$
2	4	$4.80 \times 10^{-26}$
2	5	$4.80 \times 10^{-26}$
3	4	$4.80 \times 10^{-26}$
3	5	$4.80 \times 10^{-26}$
4	5	$1.79 \times 10^{-24}$

Table 9.4: Atom impact excitation parameters for intra-4s transitions.

priming electrons that eventually trigger inelastic electron collisions.

Excitation from ground state in particular plays a significant role in determining the overall induction length, i.e. the distance between shock-front and electron avalanche. In addition, the excitation rates have a profound influence on the dynamics of the simulation. It will be shown that pressure waves initiated at the electron avalanche are exacerbated for undervalued cross sections while excessive values can lead to over damping of the system. The sharp sensitivity of the convection-kinetics coupling highlights the need for accurate determination of the heavy particle cross sections.

The cross sections for excitation from ground state have been determined from Drawin's model,

$$\sigma_{ij}^a(\varepsilon) = 4\pi a_0^2 \left( \frac{\varepsilon_1^H}{\varepsilon_{ij}} \right)^2 \frac{m_{Ar}}{m_H} \xi^2 f_{ij} \frac{2m_e}{m_{Ar} + m_e} \frac{\varepsilon/\varepsilon_{ij} - 1}{\left( 1 + \frac{2m_e}{m_{Ar} + m_e} (\varepsilon/\varepsilon_{ij} - 1) \right)^2} \quad (9.17)$$

where  $I_H$  is the ionization potential of the hydrogen atom and  $\xi$  is the number of optical electrons. For the energy ranges under consideration, Eq. (9.17) is well-approximated by a



linear function,

$$\sigma_{1j}^a(\varepsilon) = \beta_{1j}^*(\varepsilon - \varepsilon_{ij}), \quad (9.18)$$

where

$$\beta_{1j}^* = 4\pi a_0^2 \frac{(\varepsilon_1^H)^2}{\varepsilon_{ij}^3} \xi^2 f_{ij} \frac{2m_e}{m_H} \quad (9.19)$$

The inner  $3p^5 4s$  manifold transitions, however, take the form [19]

$$\sigma_{ij}^a(\varepsilon) = \beta_{ij}^* \frac{\varepsilon - \varepsilon_{ij}}{\varepsilon_{ij}^{2.26}} \quad (9.20)$$

All necessary parameters are given in Table 9.3.

Less sensitive are the ionization cross sections—we remark that decreasing these values by an order of magnitude did not have any significant effect on the induction length or flow dynamics. The cross section for ionization from ground state argon is taken from [50],

$$\sigma_1^a(\varepsilon) = 1.8 \times 10^{-25} (\varepsilon - 15.760)^{1.3} \text{ [m}^2\text{]}, \quad (9.21)$$

while the formula of Drawin has been applied for all other levels,

$$\sigma_i^a(\varepsilon) = 4\pi a_0^2 \left( \frac{I_H}{I_i} \right)^2 \frac{m_{Ar}}{m_H} \xi^2 \frac{2m_e}{m_{Ar} + m_e} \frac{\varepsilon/I_i - 1}{\left( 1 + \frac{2m_e}{m_{Ar} + m_e} (\varepsilon/I_i - 1) \right)^2}. \quad (9.22)$$

### 9.1.2 Electron impact processes

Once a sufficient number of priming electrons have been generated by heavy particle impact and their temperature increased by thermalization, electron impact processes begin to become important and eventually dominate the kinetics. The rates associated with processes are critical in determining the magnitude of the electron avalanche and associated ionization fraction. The cross sections for ionization and excitation processes can be computed using Drawin's formulas,

The cross sections for electron-impact excitation are due to Zatsarinny and Bartschat [126],[125]. These include excitation from the ground and  $4s$  levels to all levels below the

	$s$	$p$	$d$	$f$
$a$	1.06	2	3/2	3/2
$b$	0.23	1	3	1
$c$	1	1	2/3	2/3
$d$	1	1	1	1

Table 9.5: Electron-impact ionization parameters as taken from [35].

Valence electron		
shell, $n\ell$	$r_{n\ell}$ [m]	$g_{n\ell} \times I_{n\ell}$ [eV]
$4s$	$2.49 \times 10^{-10}$	7.40
$5s$	$6.35 \times 10^{-10}$	6.35
$4p$	$3.40 \times 10^{-10}$	31.00
$3d$	$4.36 \times 10^{-10}$	13.60

Table 9.6: Radii of  $Ar$  valence electron and reduced weighting factors for  $\xi = 1$  as taken from [35] and [34].

$5p$  manifold. For all other transitions, Drawin's formulas

$$\sigma_{ij}^e(\varepsilon) = 4\pi a_o^2 \begin{cases} \alpha_{ij}^A f_{ij}(u_{ij} - 1)/u_{ij}^2 (I_H/\varepsilon_{ij})^2 \ln(1.25\beta_{ij}u_{ij}) & \text{allowed} \\ \alpha_{ij}^P (u_{ij} - 1)/u_{ij}^2 & \text{parity forbidden} \\ \alpha_{ij}^S (u_{ij}^2 - 1)/u_{ij}^5 & \text{spin forbidden} \end{cases} \quad (9.23)$$

have been used systematically with  $\alpha_{ij}^A f_{ij} = 1$ ,  $\alpha_{ij}^P = 1$ , and  $\alpha_{ij}^S = 1$ .

Cross sections for electron-impact ionization from the excited levels have been determined based on the work of Deutsch *et al.* [34] via

$$\sigma_i(\varepsilon) = g_{n\ell} \pi r_{n\ell}^2 \xi_{n\ell} f(\varepsilon) \quad (9.24)$$

where  $g_{n\ell}$  are the reduced weighting factors,  $r_{n\ell}$  are the radii of the valence electron, and

$$f_i(\varepsilon) = d \frac{I_i}{\varepsilon} \left( \frac{\varepsilon/I_i - 1}{\varepsilon/I_i + 1} \right)^a \left[ b + c \left( 1 - \frac{I_i}{2\varepsilon} \right) \ln(2.7 + (\varepsilon/I_i - 1)^{1/2}) \right]. \quad (9.25)$$

The necessary parameters for Eqs. (9.24) and (9.25) are given in Tables 9.5 and 9.6.

### 9.1.3 Pressure ionization

Particular attention must be paid when considering ionization and recombination in plasmas defined by relatively high densities. This is due to nonideal effects for which interactions between particles can lead to an effective lowering of the ionization potential. As a consequence, the rates must be considered as functions of pressure as well. Griem [44] used Debye theory to predict a decrease in the ionization potential that is inversely proportional to the Debye length,

$$\Delta\varepsilon_{\infty,m} = \frac{(m+1)e^2}{4\pi\epsilon_0\lambda_D}, \quad (9.26)$$

where  $\lambda_D$  is the Debye length<sup>2</sup>,

$$\lambda_D = \left( \frac{\epsilon_0 k_B T_e}{N_e e^2} \right)^{1/2}. \quad (9.27)$$

For the shock tube conditions under consideration, the lowering of the ionization potential was found to be small, yielding a drop of 0.08 eV for an electron temperature of 1 eV and number density of  $10^{23} \text{ m}^{-3}$ . As a result, the effects of pressure ionization were not accounted for.

## 9.2 Photorecombination

In the absence of a third body, the energy released in recombination is liberated as radiation. Photorecombination is a significant loss mechanism and plays an important role in radiative cooling. The cross section for photorecombination can be found from the cross section for photoionization under equilibrium conditions [128],

$$\sigma_{c,i}(\nu) = \frac{g_n}{g_+} \frac{h^2 \nu^2}{m_e^2 v_e^2 c^2} \sigma_{\nu,i}(\nu). \quad (9.28)$$

Utilizing the relation  $h\nu = m_e v^2/2 + \varepsilon_i = \varepsilon + \varepsilon_i$ , the cross section associated with the ground state is given by

---

<sup>2</sup>neglecting the effect of ions

$$\sigma_1(\varepsilon) = \frac{g_1}{g_+} \frac{(\varepsilon + \varepsilon_1)^2}{2\varepsilon m_e c^2} \begin{cases} 3.5 \times 10^{-21} & 0 \leq \varepsilon \leq 2\varepsilon_1^H - \varepsilon_1 \\ 2.8 \times 10^{-20} \left( \frac{\varepsilon_1^H}{\varepsilon + \varepsilon_1} \right)^3 & \varepsilon > 2\varepsilon_1^H - \varepsilon_1 \end{cases} \quad (9.29)$$

while all others are computed using

$$\sigma_i(\varepsilon) = \gamma_i(n_{pq n, \ell}) \frac{g_i}{g_+} \frac{(\varepsilon + \varepsilon_i)^2}{2\varepsilon m_e c^2} \begin{cases} 2 \times 10^{-22} & 0 \leq \varepsilon \leq 0.59\varepsilon_1^H - \varepsilon_i \\ 7.91 \times 10^{-22} \left( \frac{\varepsilon_i}{\varepsilon_1^H} \right)^{5/2} \left( \frac{\varepsilon_1^H}{\varepsilon + \varepsilon_i} \right)^3 & \varepsilon > 0.59\varepsilon_1^H - \varepsilon_i \end{cases}. \quad (9.30)$$

The parameter  $\gamma_i(n_{pq n, \ell})$  takes the values 0.0763, 0.0458, 0.0305, and 0.0915 for  $i = 2, 3, 4$ , and 5, respectively [117].

Estimation of the mean-free path as based on the representative shock tube plasma conditions indicates that radiation from bound-free transitions to the ground state are absorbed locally while the mean-free paths for transitions to the 4s manifold are greater by several orders of magnitude. Thus, radiation from bound-free transitions is assumed to escape completely.

### 9.3 Bremsstrahlung emission

Free-free transitions have been incorporated in the model via Kramer's formula [128] for *Bremsstrahlung* emission,

$$\frac{\partial E_e}{\partial t} = -\frac{16\pi^2}{3\sqrt{3}} \frac{\bar{v}_e Z_{\text{eff}}^2 e^6 \bar{g}}{m_e h (4\pi\epsilon_0 c)^3} n_+ n_e \quad (9.31)$$

$$= -1.42 \times 10^{-40} Z_{\text{eff}}^2 T_e^{1/2} n_+ n_e \quad [\text{J} \cdot \text{m}^{-3} \cdot \text{s}^{-1}] \quad (9.32)$$

where  $\bar{g}$  is the gaunt factor taken to be unity and the effective charge  $Z_{\text{eff}}^2$  is taken to be 1.67 [42]. Bremsstrahlung emission resulting from neutral atoms is 1-2 orders of magnitude less than for ions and has therefore been neglected. The plasma is assumed to be optically thin to all Bremsstrahlung emission.

lower level	upper level	mean-free path [m]
$3p^6$	$4s[1/2]_1$	$3.59 \times 10^{-2}$
$3p^6$	$4s'[1/2]_1$	$9.47 \times 10^{-3}$
$3p^6$	$3d[1/2]_1$	2.41
$3p^6$	$5s[3/2]_1$	$7.11 \times 10^{-2}$
$3p^6$	$3d[3/2]_1$	$2.54 \times 10^{-2}$
$3p^6$	$5s'[1/2]_1$	$1.34 \times 10^{-1}$
$3p^6$	$3d'[3/2]_1$	$3.05 \times 10^{-2}$

Table 9.7: Estimated mean-free paths for bound-bound transitions to ground state for  $T = 1$  eV and  $n_{3p^6} = 10^{24} \text{ m}^{-3}$ .

#### 9.4 Bound-bound transitions

In addition to photorecombination and Bremsstrahlung, bound-bound transitions are a significant source of radiative cooling of the plasma. The photoionization cross section for a given bound-bound transition may be estimated by [128],

$$\sigma_{ij} = \frac{1}{\nu_{ij}} \int \sigma_{\nu,ij} d\nu = 2.65 \times 10^{-6} \frac{f_{ij}}{\nu_{ij}} [\text{m}^2] \quad (9.33)$$

where the absorption oscillator strength is given by

$$f_{\text{abs}} = \frac{g_j}{g_i} \frac{A_{ji}}{3\gamma}. \quad (9.34)$$

Contributions to the parameter  $\gamma$  have been assumed to result from a combination of natural and pressure line broadening,

$$\gamma = \gamma_{\text{nat}} + \gamma_{\text{col}} \quad (9.35)$$

given by

$$\gamma_{\text{nat}} = \frac{8\pi^2 e^2 \nu^2}{3mc^3} = 2.47 \times 10^{-22} \nu^2 [\text{s}^{-1}] \quad (9.36)$$

and

$$\gamma_{\text{col}} = \frac{2}{\tau_{\text{col}}} = 2\sigma\bar{v}n \quad (9.37)$$

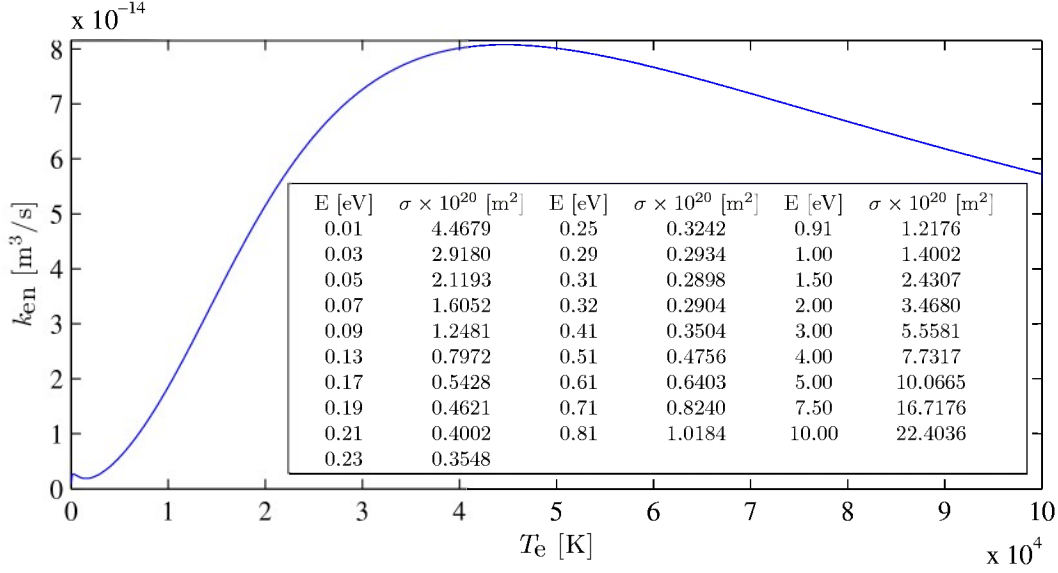


Figure 9.2: Electron-neutral collision rate as computed from the theoretical cross sections (table) computed in [71].

respectively. The collision periodicity  $\tau_{\text{col}}$  and the collision cross section  $\sigma$  have been tallied for neutral argon-argon collisions. The radiation cross sections Eq. (9.33) have been estimated using the oscillator strengths and transition probabilities from [95] along with representative plasma conditions of the shock tube experiments. The resulting mean-free paths for bound-bound transitions to ground state given in Table 9.7 are below the length scales of the shock tube dimensions for most of the levels. It has therefore been assumed that all bound-bound radiation to the ground level from the excited states is absorbed. For all other transitions, the mean-free path is several orders of magnitude greater than the dimensions of the shock tube and the associated radiation is assumed to escape.

## 9.5 Elastic collisions

Elastic collisions are incorporated into the CR implicit solver as well. This strong coupling permits more accurate and stable calculations. The energy transfer between electrons and neutrals is computed as

$$\frac{\partial E_e}{\partial t} = -\frac{\partial E_h}{\partial t} = n_e n_n \frac{3}{2} k_B (T_h - T_e) \frac{2m_e}{m_{Ar}} k_{en} \quad (9.38)$$

For electron-neutral collisions, the theoretical cross section of McEachran and Stauffer [71] have been utilized. These are reproduced in Figure 9.2 along with the associated rates. The Coulomb collision rates,  $\bar{k}_{ei}$ , have been computed using the energy-averaged properties [78],

$$\frac{\partial E_e}{\partial t} = -\frac{\partial E_h}{\partial t} = n_e n_n \frac{3}{2} k_B (T_h - T_e) \frac{2m_e}{m_{Ar}} k_{en} \quad (9.39)$$

$$\bar{k}_{ei} = \bar{v}_e \bar{Q}_{ei} \quad (9.40)$$

$$\bar{Q}_{ei} = 5.85 \times 10^{-10} \frac{\ln \Lambda}{T_e^2} [\text{m}^2] \quad (9.41)$$

$$\Lambda = 1.24 \times 10^7 \left( \frac{T_e^3}{n_e} \right)^{1/2} \quad (9.42)$$

where  $\bar{Q}_{ei}$  is the momentum-averaged cross section, and  $\Lambda$  is the Coulomb logarithm. The energy transfer equation for electron-ion collisions is similar to Eq. 9.39 and is given by

$$\frac{\partial E_e}{\partial t} = -\frac{\partial E_h}{\partial t} = n_e n_i \frac{3}{2} k_B (T_h - T_e) \frac{2m_e}{m_{Ar^+}} k_{ei} \quad (9.43)$$

## 9.6 Numerical formulation

The coupled system of linear rate equations for the CR model is expressed in vector form via

$$\frac{dQ_{CR}}{dt} = \dot{\Omega} \quad (9.44)$$

where

$$Q_{CR} = \begin{pmatrix} n_{3p^6} \\ n_{4s[3/2]_2} \\ n_{4s[3/2]_1} \\ \vdots \\ n_{n\ell[K]_J} \\ n_{Ar^+(j_c=3/2)} \\ n_{Ar^+(j_c=1/2)} \\ E_h \\ E_e \end{pmatrix}, \quad \dot{\Omega} = \begin{pmatrix} \dot{\omega}_{3p^6} \\ \dot{\omega}_{4s[3/2]_2} \\ \dot{\omega}_{4s[3/2]_1} \\ \vdots \\ \dot{\omega}_{n\ell[K]_J} \\ \dot{\omega}_{Ar^+(j_c=3/2)} \\ \dot{\omega}_{Ar^+(j_c=1/2)} \\ \dot{\omega}_{E_h} \\ \dot{\omega}_{E_e} \end{pmatrix} \quad (9.45)$$

Note that the conservative variables used in the CR formulation are not the same as those previously detailed in Chapter 2. However, conversion between the two vectors is accomplished via the simple transformation,

$$Q = MQ_{CR} \quad (9.46)$$

where

$$M = \begin{pmatrix} m_{Ar} & & & & & & & & \\ & \ddots & & & & & & & \\ & & m_{Ar} & & & & & & \\ & & & m_{Ar^+} & & & & & \\ & & & & m_{Ar^+} & & & & \\ & & & & & m_{Ar^+} & & & \\ & & & & & & 1 & 1 & \\ & & & & & & & \frac{\gamma_e-1}{\rho^{\gamma_e-1}} & \end{pmatrix} \quad (9.47)$$

The components of  $\dot{\Omega}$  are obtained after combining the rate equations for all processes, the exact form of which are as follows.



### Ar levels

$$\begin{aligned}
\dot{\omega}_{n_k} \equiv \frac{\partial n_k}{\partial t} = & \sum_{i < k} n_i (n_e C_{ik} + n_1 K_{ik} + (1 - \Lambda_{ki}) A_{ki}) - \sum_{j < k} n_k (n_e F_{kj} + n_1 L_{kj} + A_{kj}) \\
& - \sum_{j > k} n_k (n_e C_{kj} + n_1 K_{kj} + (1 - \Lambda_{jk}) A_{jk}) + \sum_{i > k} n_i (n_e F_{ik} + n_1 L_{ik} + A_{ik}) \\
& + n_+ n_e (n_1 W_k + n_e O_k + R_k) - n_k (n_e S_k + n_1 V_k + (1 - \Lambda_k) R_k)
\end{aligned} \tag{9.48}$$

### Ar<sup>+</sup>

$$\dot{\omega}_{n_+} \equiv \frac{\partial n_+}{\partial t} = \sum_i n_i (n_e S_i + n_1 V_i + (1 - \Lambda_i) R_i) - n_+ n_e \sum_i (n_1 W_i + n_e O_i + R_i) \tag{9.49}$$

### Heavy-particle energy

$$\begin{aligned}
\dot{\omega}_{E_h} \equiv \frac{\partial E_h}{\partial t} = & n_1 \sum_i \sum_{j > i} \varepsilon_{ij} (n_j L_{ji} - n_i K_{ij}) && \text{from (9.2)} \\
& + n_1 \sum_i I_i (n_e n_+ W_i - n_i V_i) && \text{from (9.4)} \\
& - 3\rho_e n_n k_B (T_h - T_e) \frac{k_{en}}{m_{Ar}} && \text{from (9.39)} \\
& - 3\rho_e n_+ k_B (T_h - T_e) \frac{\bar{k}_{ei}}{m_{Ar^+}} && \text{from (9.43)}
\end{aligned} \tag{9.50}$$

### Electron energy

$$\begin{aligned}
\dot{\omega}_{E_e} \equiv \frac{\partial E_e}{\partial t} = & n_e \sum_i \sum_{j > i} \varepsilon_{ij} (n_j F_{ji} - n_i C_{ij}) && \text{from (9.1)} \\
& + n_e \sum_i I_i (n_e n_+ O_i - n_i S_i) && \text{from (9.3)} \\
& + \sum_i ((n_i (1 - \Lambda_i) - n_e n_+) R'_i) && \text{from (9.6)} \\
& - n_+ n_e \frac{16\pi^2}{3\sqrt{3}} \frac{\bar{v}_e Z_{e\Pi}^2 e^6 \bar{g}}{m_e h (4\pi\epsilon_0 c)^3} && \text{from (9.31)} \\
& + 3\rho_e n_n k_B (T_h - T_e) \frac{k_{en}}{m_{Ar}} && \text{from (9.39)} \\
& + 3\rho_e n_+ k_B (T_h - T_e) \frac{\bar{k}_{ei}}{m_{Ar^+}} && \text{from (9.43)}
\end{aligned} \tag{9.51}$$

A necessary condition in closure of the above system is the assumption of quasi-neutrality,

which in this instance takes the form

$$n_e = n_{Ar^+(j_c=3/2)} + n_{Ar^+(j_c=1/2)}. \quad (9.52)$$

It is important to note that since ionization and recombination proceed to and from either  $Ar^+(j_c = 3/2)$  or  $Ar^+(j_c = 1/2)$ , the rates associated with such processes are functions of  $j_c$  as well, such that

$$S_i, O_i, W_i, V_i, R_i = f(j_c). \quad (9.53)$$

Due to inevitable stiffness in the above system, the CR kinetics are solved implicitly, the algorithm for which is detailed in Appendix D.

## CHAPTER 10

### UTIAS SHOCK TUBE EXPERIMENTS

While conducting shock tube experiments at the Institute for Aerospace Studies, University of Toronto (UTIAS), Brimelow [16] discovered instabilities in the translational shock front of a strong ionizing shock in argon. The discovery set off a series of experiments that extended the research to various Mach numbers and other noble gases, including krypton and xenon. The UTIAS experiments were unique in that it was the first time instabilities were observed in an ionizing shock. The instabilities, which were observed as aberrations in the translational shock front and electron avalanche, were labeled as *sinusoidal* and an explanation for their existence was not determined.

These experiments provided invaluable data for which to benchmark theoretical and numerical models, including databases. Measurements were taken in the form of interferograms from which the total mass and electron number densities were derived. From this data, key parameters for describing the shock structure can be ascertained, including the peak ionization fraction,  $\alpha$ , and the relaxation length,  $\ell$ , as measured from the shock front to the location of peak ionization.

Glass and Liu [42] provided a theoretical model that was used in the analysis of the resulting shock structure based on the conditions of several of the UTIAS experiments. In particular, they determined the relaxation length to be a function of the excitation cross sections by atom-atom,  $\sigma^a$ , and electron-atom,  $\sigma^e$ , impact; the elastic cross sections for electron-neutral,  $\sigma^{en}$ , and Coulomb,  $\sigma^{ei}$  collisions; and the combined radiation losses,  $q_{\text{rad}}$ :

$$\ell = \ell(\sigma^a, \sigma^e, \sigma^{en}, \sigma^{ei}, q_{\text{rad}}) \quad (10.1)$$

Of these, the atom-atom excitation cross sections were found to have the largest influence

on the relaxation length, which currently maintain an association with the largest amount of uncertainty.

The work of Cambier [21] extended the model to include one-dimensional transient effects and found that pressure pulses initiated by the electron avalanche would propagate downstream, increasing the pressure of the compression shock. The consequential increase in shock intensity was found to shorten the relaxation length and raise the peak ionization fraction. This phenomenon necessitated the addition of a new parameter  $\tau$  to describe the periodicity of shock fluctuations.

Here, the collisional-radiative model detailed in the previous chapter is combined with the transport equations in order to match the experimental results of the UTIAS shock tube experiments presented by Glass and Liu. We proceed by first simplifying the governing equations to a steady-state form to develop a baseline for the collisional-radiative cross sections. Transient simulations are then performed in one- and two-dimensions to determine the effect of the cross sections on the dynamical behavior of the ionizing shock.

## 10.1 Steady-state simulations

Although the data provided by the UTIAS experiments are *snapshots* of dynamic behavior, steady-state calculations can nonetheless provide valuable insight to the shock structure. Such numerical experiments were carried out in [42] and are important in the current analysis as well to determine the atom-atom impact excitation cross sections.

With the conditions downstream of the shock known along with the shock Mach number, the Rankine-Hugoniot relations were applied to determine the post shock conditions. A shooting method was then used to determine the steady-state shock structure, with the post shock conditions serving as the initial values.

The steady-state form can be found by canceling the time-dependent term from the differential form of the governing equations (cf. Eq. (2.9)),

$$\frac{\partial Q}{\partial t} + A \frac{\partial F}{\partial x} = \dot{\Omega}, \quad (10.2)$$

reducing the system to a set of ODE's,

Case	Reference	$\text{Ma}_s$	$p_o$ [torr]	$T_o$ [K]	$\ell$ [cm]	$\alpha$
1	1	15.9	5.14	293.6	2.00	0.14
2	2	16.1	5.15	295.9	1.90	0.15
3	3	16.5	5.12	296.6	1.80	0.16
4	4	13.0	5.01	296.6	8.90	0.06
7	7	14.7	4.08	297.8	4.40	0.106

Table 10.1: Shock tube cases studied by Glass and Liu.

$$\frac{dQ}{dx} = A^{-1}\dot{\Omega}. \quad (10.3)$$

The inverse of the flux Jacobian in Eq. (10.3) can be computed efficiently if the analytical form of the eigensystem is known (see Appendix A), such that

$$\frac{dQ}{dx} = R\Lambda^{-1}L\dot{\Omega}. \quad (10.4)$$

The matrix product on the RHS of Eq. (10.4) can be computed in approximately  $2N^2$  operations. The inverse of  $\Lambda$  is well-defined as long as the flow velocity does not approach zero.

Glass and Liu applied their steady-state model in the analysis of four different cases in pure argon which are summarized in Table 10.1<sup>1</sup>. In a similar fashion, Eq. (10.4) has been applied to the same four cases, the results of which are presented in terms of total mass density  $\rho$ , electron number density  $n_e$ , and ionization fraction  $\alpha$ . As there exists a fair amount of uncertainty associated with the atom-atom excitation cross sections  $\sigma^a$ , these were varied until an acceptable agreement between the theoretically-predicted and experimentally-observed relaxation lengths was achieved. Exact agreement for all cases could not be achieved with a fixed value for  $\sigma^a$ . However, good agreement was obtained for the intermediate cases, corresponding to Mach numbers 14.7, 15.9, and 16.1, the results of which are summarized in Table 10.2.

As mentioned in Section 9.1.1, the atom-atom impact excitation cross sections have been approximated as linear functions of energy as based on the model of Drawin. Tuning these cross sections was therefore a matter of modifying their slopes. This was accomplished by

<sup>1</sup>Although not modeled by Glass and Liu, information was provided on the relaxation length and ionization fraction of a Mach 14.7 shock that we also consider here as case 7.

Case	Experiment [cm]	Theory [cm]
1	2.00	2.09
2	1.90	1.88
3	1.80	1.61
4	8.90	10.6
7	4.40	4.48

Table 10.2: Comparison between experimental and steady-state numerical relaxation lengths for ionizing shock in argon.

$i$	$j$	$\beta_{ij}^*$ [m <sup>2</sup> /eV]
1	3	$9.35 \times 10^{-25}$
1	5	$3.36 \times 10^{-24}$
1	17	$8.14 \times 10^{-27}$
1	23	$2.64 \times 10^{-25}$
1	25	$7.27 \times 10^{-25}$
1	30	$1.35 \times 10^{-25}$
1	31	$5.88 \times 10^{-25}$

Table 10.3: Tuned atom impact excitation parameters for allowed transitions from ground state Ar.

multiplying  $\beta_{1j}^*$  in Eq. 9.18 by a factor of 0.085. That is, the current results indicate that Drawin’s model over-predicts these cross sections by more than a factor of 10. The modified parameters are summarized in Table 10.3. In comparison with values previously obtained in the literature (cf. Table 1.1), it is evident that the cross sections used here are at the lower end of the spectrum, matching most closely with the values obtained by McLaren and Hobson [72].

### 10.1.1 Effect of upper levels

In an effort to quantify the influence of the upper levels on the overall shock structure, simulations were first performed taking into account the  $4s$  manifold of  $Ar$  exclusively, followed by systematic inclusion of higher manifolds, including the  $4p$ ,  $5s$  and  $3d$ . Numerical results obtained with levels of only the  $4s$  manifold given in Figure 10.1 show satisfactory prediction of the induction length, but poor reproduction of the radiative cooling region as indicated by the slow drop-off in electron number density, indicating an under-prediction in radiative losses. This is as expected as the the plasma has been assumed to be optically-thick for all transitions to ground state  $Ar$  (cf. Section 9.4), resulting in no radiative losses due to

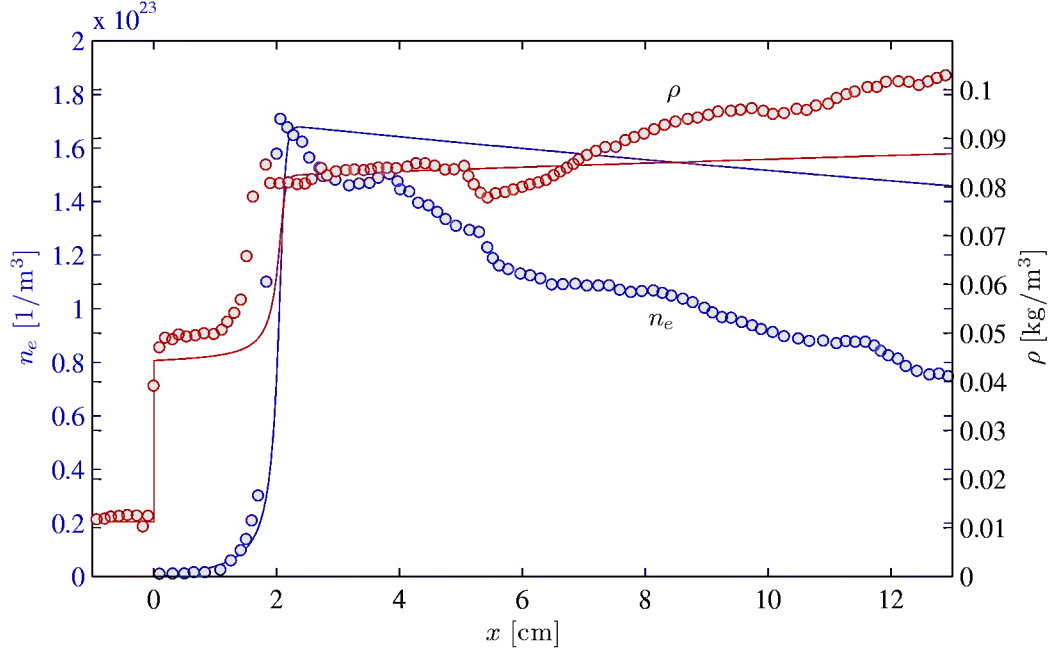


Figure 10.1: Comparison of experimental (o) and numerical (–) results for Ma 15.9 shock in argon in terms of total mass density  $\rho$  and electron number density  $n_e$ . Numerical results were obtained using only levels of the  $4s$  manifold of  $Ar$ .

bound-bound transitions since intra- $4s$  transitions are forbidden. As a result, all radiative losses in this case are due to free-free and free-bound transitions only.

When the levels of the  $4p$  manifold are included in the CR model, the numerical prediction of the radiative cooling region drastically improves as indicated by the results in Figure 10.2. The difference clearly represents the direct influence of the 32 allowed transitions within the  $4p$  manifold as well as those between the  $4s$  and  $4p$  manifolds on the radiative cooling region.

Figure 10.2 illustrates the effects of additional levels, this time with inclusion of levels from the  $5s$  and  $3d$  manifolds. The results clearly indicate an asymptotic approach of the numerical solution to the experimental results as more levels are included and hence the full extent of radiative losses due to bound-bound transitions are realized.

Similar behavior can also be observed through the influence of additional levels on the ionization fraction as evident in Figure 10.4. As more levels are added, the ionization fraction approaches the experimentally-observed value. Also apparent is the effect of the upper levels on the induction length. Addition of the upper levels increases radiation losses in

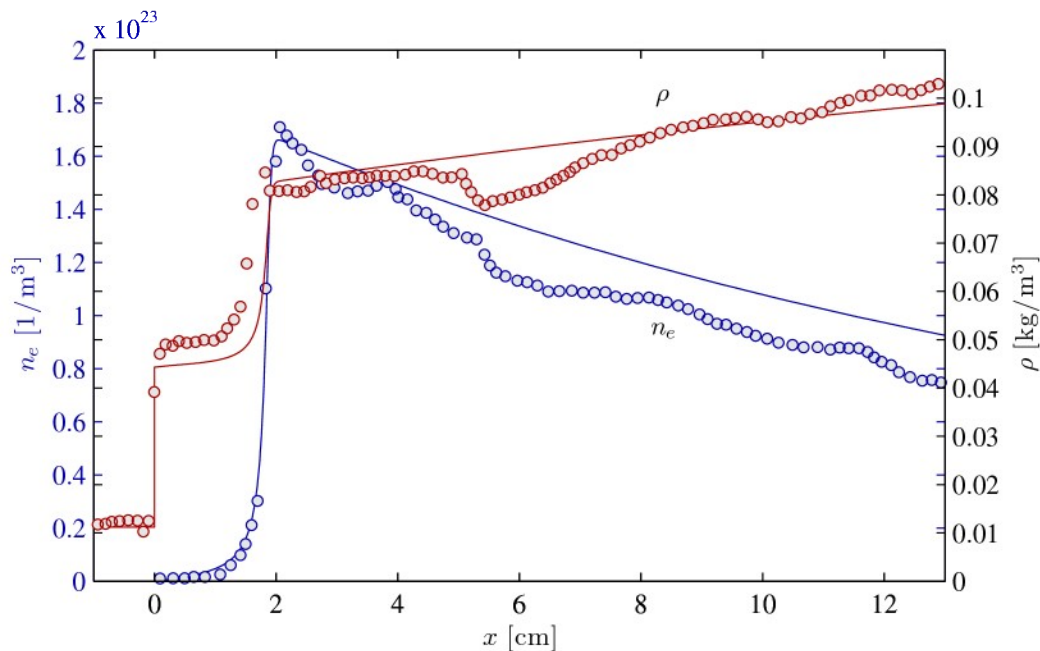


Figure 10.2: Comparison of experimental (○) and numerical (—) results for Ma 15.9 shock in argon in terms of total mass density  $\rho$  and electron number density  $n_e$ . Numerical results were obtained using levels of the  $4s$  and  $4p$  manifolds of  $Ar$ .

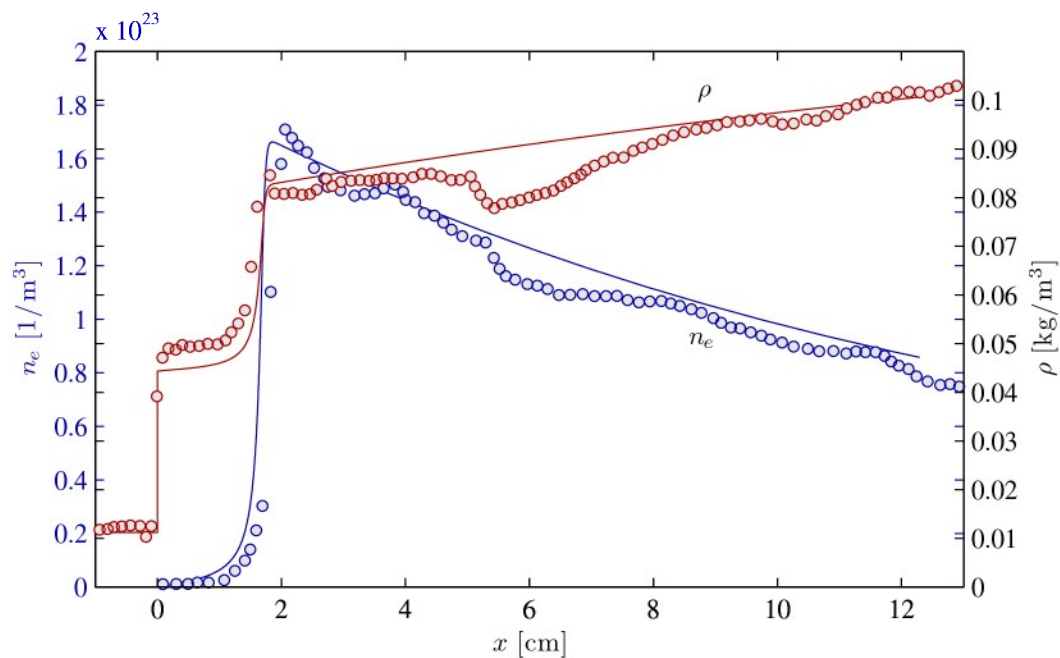


Figure 10.3: Comparison of experimental (○) and numerical (—) results for Ma 15.9 shock in argon in terms of total mass density  $\rho$  and electron number density  $n_e$ . Numerical results were obtained using levels of the  $4s$ ,  $4p$ ,  $5s$ , and  $3d$  manifolds of  $Ar$ .



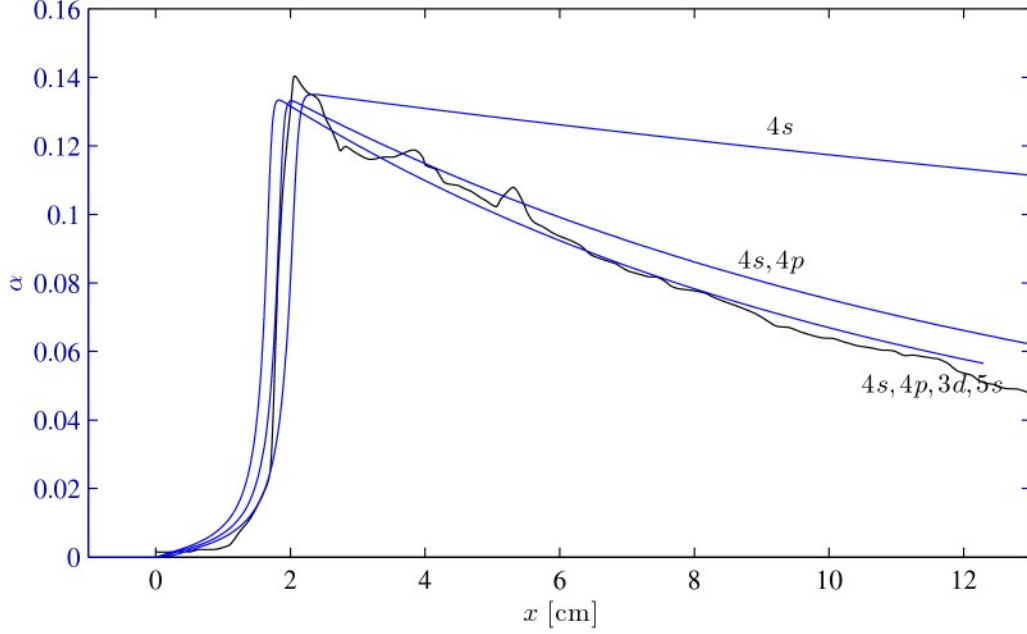


Figure 10.4: Effect of upper levels on the ionizing shock structure as indicated by the ionization fraction. With the inclusion of more levels, the numerical ionization fraction (—) approaches the experimental results (—).

the induction region, thereby delaying the onset of the electron avalanche. It should be noted that the ionization fractions as derived from the experimental data for this particular case,  $Ma = 15.9$ , as well as for the case of  $Ma = 16.1$  in [42] do not coincide with the respective total mass and electron number densities provided. As a consequence, the experimental ionization fractions plotted for comparison have been computed directly from the plasma densities. Results for the remaining three cases (2,3,4) have been provided in Appendix E.

### 10.1.2 Shock structure

Details of the electron and heavy-particle temperature profiles along with the Boltzmann and Saha equivalence temperatures provided in Figure 10.4 help illustrate the influence of the various CR processes and to separate the shock structure into several distinct regions. The first region, easily identifiable by a sharp spike in electron temperature just behind the compression shock, indicates the initial production of priming electrons which are rapidly thermalized by the heavy particles. The excitation temperatures based on a Boltzmann distribution,

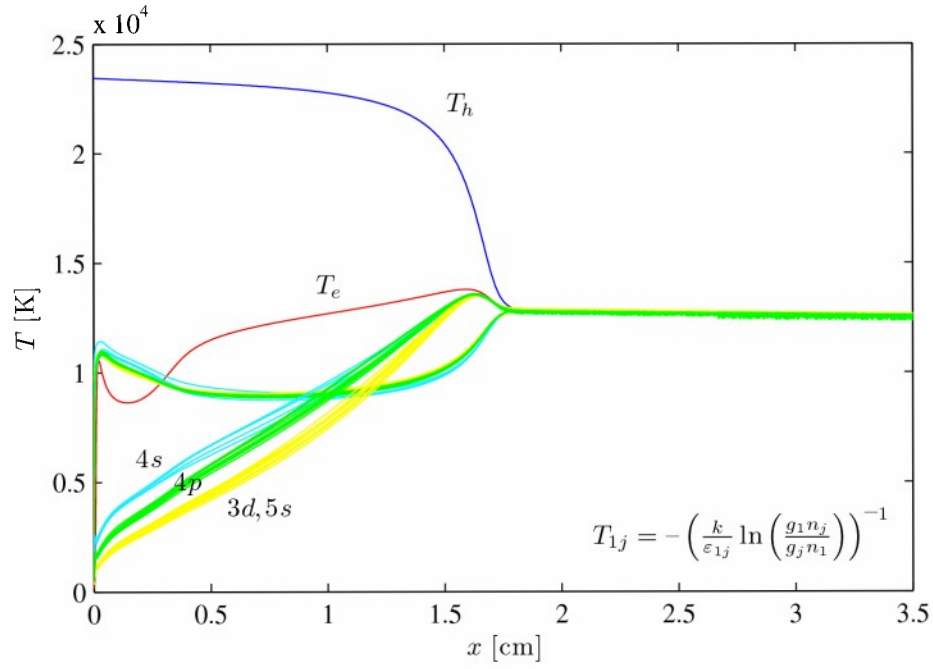


Figure 10.5: Details of the Mach 15.9 ionizing shock structure in terms of electron, heavy particle, and excitation temperatures. The bottom profiles labeled  $4s$ ,  $4p$ , and  $3d, 5s$  are of the Saha equivalence temperatures of the respective manifolds, while the upper profiles, characterized by a sharp rise accompanied by an overshoot, are of the Boltzmann equivalence temperatures.

$$T_{1j} \equiv - \left( \frac{k_B}{\varepsilon_{1j}} \ln \left( \frac{g_1 n_j}{g_j n_1} \right) \right)^{-1}, \quad (10.5)$$

surpass the electron temperature, indicating over-population of the excited states and confirming that the priming electrons are generated via *Ar-Ar* inelastic collisions.

The spike is quickly followed by a dip in electron temperature, signaling a shift from heavy-particle dominated kinetics to electron-impact processes. That is, as the electron population becomes more significant, the electrons themselves become responsible for the bulk of excitation and ionization processes. As a result, thermal energy of the free electrons is transferred to the bound electronic modes as well as liberating more electrons. The dip is the result of this energy transfer which cannot be compensated for by thermalization with heavy-particles. The excitation temperature declines as well, and stabilizes significantly below the electron temperature. This indicates that ionization is rapid from the excited levels under these conditions, causing an under-population of the excited levels, and hence the deviation from  $T_e$ .

After this, the electron temperature recovers from the dip and increases steadily as energy is transferred from the heavy-particles to the free electrons at a slightly higher rate than which the electrons lose energy through inelastic collisions. In this region, electron production begins to ramp up exponentially, triggering rapid thermalization with the heavy-particles and the resulting electron avalanche. The avalanche results in complete thermalization between the heavy-particles and electrons, as the energy reserves of the heavy particles becomes exhausted. All levels finally reach Boltzmann and Saha equilibrium and the plasma is well-described by a single temperature.

It is worth noting that the spread of excitation temperatures throughout the shock structure is quite small, indicating Boltzmann equilibrium among the excited levels with respect to the ground state. This indicates a rapid exchange between the excited levels, with the result that the plasma may be approximated by a three-temperature model under such conditions.

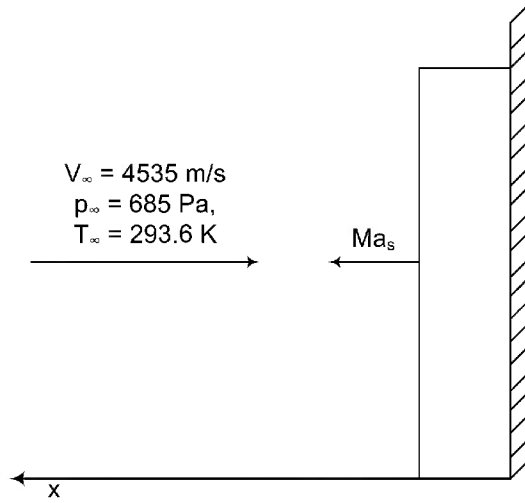


Figure 10.6: Numerical setup for unsteady 1D shock tube simulations.

## 10.2 Unsteady 1D simulations

With the CR model validated against experimental data for the steady-state case, the unsteady solver was then applied to determine the effect of the kinetics on the dynamic behavior of the system. Initial work on such unsteady effects verified the existence of oscillations in the form of longitudinal pulsations in the direction of flow [21]. Building upon this work, similar numerical experiments are carried out here, albeit with the more detailed CR model.

The conditions of the shock tube experiments were simulated numerically by impinging argon gas upon a wall, thereby initiating a shock that would propagate against the oncoming flow as illustrated in Figure 10.6. The freestream conditions provided in the figure were those used to reproduce the Mach 15.9 shock of case 1. Note that such conditions correspond to a shock with an initial strength of Mach 19. As the shock reflects from the wall, its Mach number decreases as the thermal energy is quickly converted to electronic energy in the form of bound excited states as well as free electrons, until a quasi-steady limit is reached.

The results in Figures 10.7 and 10.8 clearly show oscillations, characteristic of the experimental results, that appear as undamped, periodic fluctuations in both the shock Mach number as well as the induction length, with a periodicity of approximately  $32.5 \mu\text{sec}$ . The oscillations do not vary smoothly as evident in the discontinuous shifts of the induction length, signaling strong non-linear behavior. In fact, this behavior is well approximated by

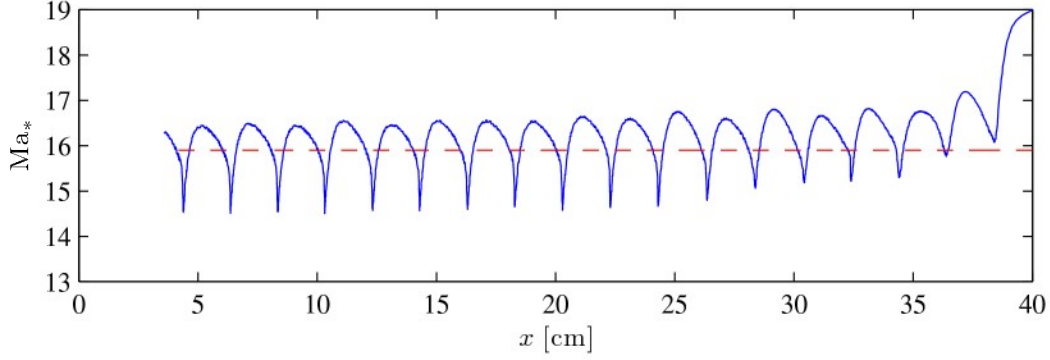


Figure 10.7: Instantaneous Mach number as a function of distance from the wall located at 40 cm for Mach 15.9 case.

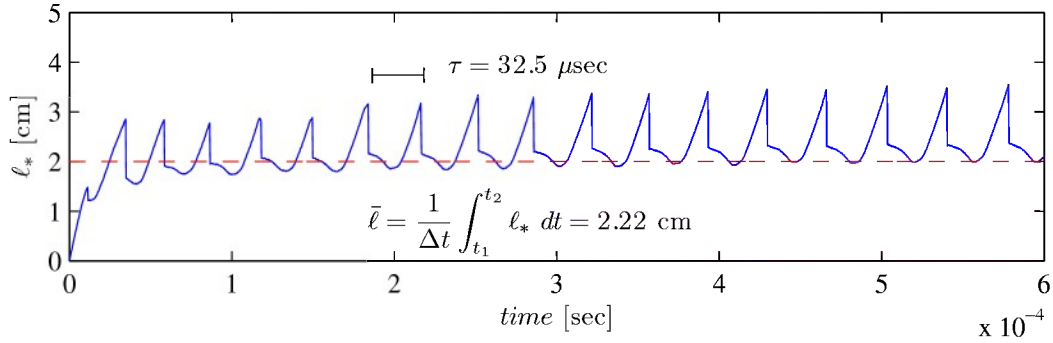


Figure 10.8: Instantaneous induction length as a function of time for Mach 15.9 case. Dashed red line indicates the experimentally observed value of 2 cm. The fluctuation periodicity is 32.5  $\mu\text{sec}$ , with an induction length of 2.22 cm averaged over one period.

the square-wave model for detonations [39] in which the kinetics are assumed to be frozen below a certain threshold, but infinitely fast above, reaching equilibrium instantaneously. This necessitates introduction of an average induction length defined over one period,

$$\bar{\ell} = \frac{1}{\Delta t} \int_{t_1}^{t_2} \ell_* dt, \quad (10.6)$$

with  $\ell_*$  being the instantaneous induction length. In regards to the discontinuous change in the induction length exhibited in this particular case, there is evidence that these anomalies have a physical origin. From the experimental results, it can be seen that in certain regions the ionization fraction rises before taking a sharp dip after which it spikes until the peak of the avalanche is realized.

### 10.2.1 Fluctuation mechanism

A semiquantitative description of the fluctuations can be extracted from the space-time plots given in Figure 10.2.1 as well as several snapshots illustrated in Figure 10.2.1. The plots clearly show pressure waves emerging from the electron avalanche that travel both towards and away from the compression shock. This is taken as the initiation of the fluctuation cycle. The forward-moving wave overtakes the shock, thereby increasing its temperature and speed.<sup>2</sup> The resulting high temperature region generated behind the shock is separated from the previous post-shock region by a contact wave that can be seen as traveling away from the shock as it accelerates. Identification of the contact waves is trivial as they are present in the mass density plot but absent in the pressure plot.

The temperature jump across the contact wave is crucial. Due to the exponential dependence on temperature, a relatively small jump can accelerate the kinetics and cause the electron avalanche to form much sooner than its quasi-equilibrium position. This discontinuous shift in the electron avalanche evident in Figure 10.2.1 is entirely analogous to the mechanism for detonation wave fluctuations proposed by Alpert and Toong [2].

This theory of the fluctuation mechanism can be confirmed by a simple estimation of the periodicity of the oscillations from basic wave theory. In [21] it was shown that the period can be approximated by

$$\tau = \bar{\ell} \left( \frac{1}{a_2 - u_2} + \frac{1}{u_2} \right), \quad (10.7)$$

assuming that the pressure wave travels towards the shock with the nonlinear wave speed  $a_2 - u_2$ , while the entropy wave reflected from the shock travels with velocity  $u_2$ , where the subscript 2 denotes the post-shock state. With  $u_2 = 1284\text{m/s}$  and  $a_2 = 2852\text{m/s}$  taken as the post-shock fluid and sound speeds respectively, the estimated periodicity is  $31.4\mu\text{sec}$  which agrees well with the observed value of  $32.5\mu\text{sec}$  (cf. Figure 10.8).

### 10.2.2 Sensitivity to cross sections

Knowing the effect of the cross sections on the dynamics of the oscillations is crucial to a stability analysis. While an analytical approach to stability is not pursued here, semi-

---

<sup>2</sup>The interaction also produces a rarefaction wave due to the acceleration of the shock which is too weak to notice here.

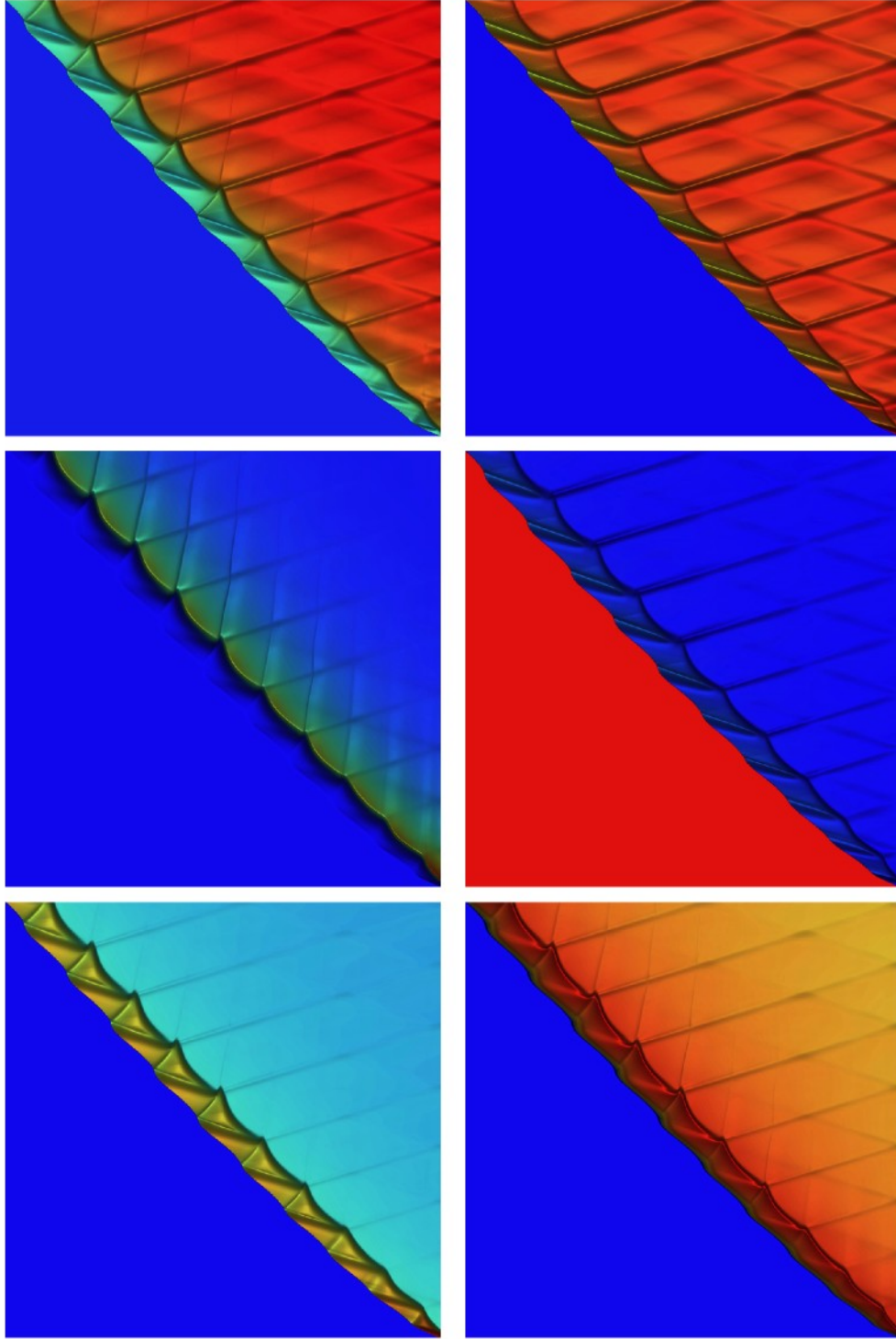



Figure 10.9:  $x$ - $t$  diagrams for 1D Ma 14.7 case. Clockwise from top left: total density, total pressure, velocity, electronic temperature, heavy-particle temperature, and ionization fraction. Gradients are enhanced through shading effects. Colormap:  $\min$    $\max$

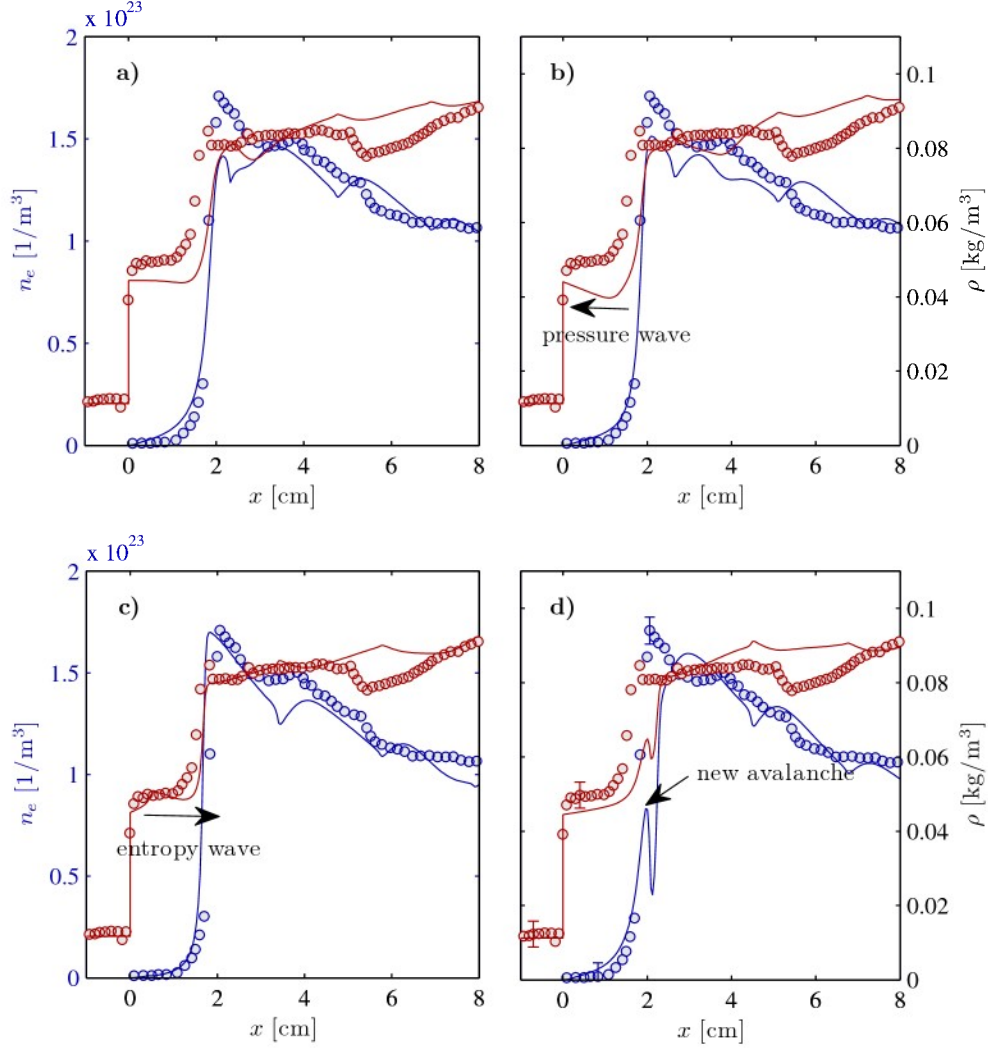


Figure 10.10: Dynamic evolution of 1D ionizing shock structure: a) quasi-equilibrium state b) pressure wave initiated at electron avalanche travels towards compression shock c) after overtaking shock, pressure wave is reflected as an entropy wave due to strengthening of shock d) sensitivity of excitation and ionization rates to temperature jump across entropy wave results in earlier onset of electron avalanche. The process then repeats.



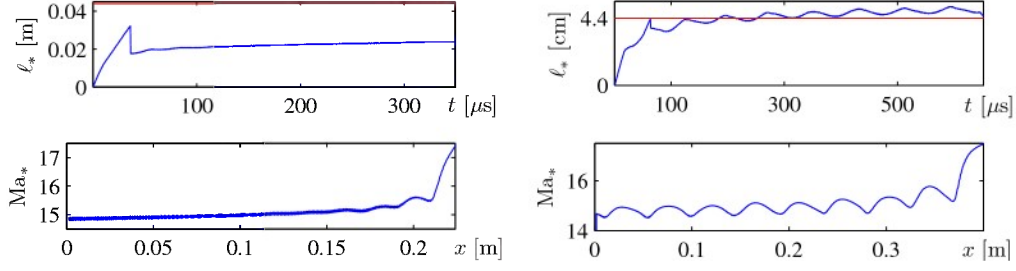


Figure 10.11: Sensitivity of 1D ionizing shock oscillation dynamics to cross sections. Left: Results using Drawin’s atom-atom impact excitation cross sections. Right: Results obtained after decreasing electron-atom impact excitation cross sections by a factor of ten.

empirical considerations can serve as a valuable precursor to such studies.

As a first test, the Mach 14.7 case was run using the atom-atom impact excitation cross sections as computed from Drawin’s formula, Eq. (9.17), without modification. As a reminder, the resulting rates are more than a factor of ten greater than those used to obtain the solutions with the experimentally-observed induction length. The results shown in Figure 10.2.2 indicate that increasing the atom-impact excitation cross sections by an order of magnitude, essentially halves the induction length. Furthermore, the influence on the oscillations is pronounced, resulting in significant damping to the point that the oscillations can no longer be sustained. The explanation for this is as follows. As the pressure wave emanating from the electron avalanche overtakes the compression shock, the heavy particle temperature increases. This in turn increases the atom-impact inelastic processes accordingly to their exponential dependence on  $T_h$ . The atom-impact inelastic processes thus act as an energy sink, effectively absorbing energy from the pressure wave and damping the oscillations.

In a separate test, the electron-atom impact excitation cross sections were reduced by a factor of ten. In this case the atom-atom impact excitation cross sections were also modified so that the induction length was close to 4.4 cm as seen in Figure 10.2.2. While the oscillations still persist in this case, a key observation is that the discontinuous change in the induction length (cf. Figure 10.7) has disappeared. Instead, the oscillations vary smoothly over the entire period of the fluctuation. The discontinuous shift is a nonlinear effect caused by the exponential temperature dependence of the rate equations and is well-approximated by the square-wave model for detonation phenomena as previously noted.

As the electron-impact cross sections are decreased, this nonlinear effect diminishes, and is overshadowed by other processes, such as thermalization. This slows the rate of onset of the electron avalanche and gives the fluid more time to “react” to the kinetics.

### 10.3 Unsteady 2D simulations

With a general understanding of the oscillation mechanism and resulting wave pattern observed in the unsteady 1D simulations, focus was then set upon extending the simulations and theory to a two-dimensional shock tube. With a second dimension, the oscillations observed in the 1D simulations are no longer confined to the longitudinal direction, leading to the possibility of transverse waves. While this opens the door to more complex wave interactions and structures, a systematic approach that extends the ideas of the previous section in a straight-forward manner is taken here.

The 2D simulations were conducted on the domain  $0 \leq x \leq 54$  cm,  $0 \leq y \leq 18$  cm, with a depth of 10 cm<sup>3</sup>. A general schematic is provided in Figure 10.3. The simulations were initiated in the same manner as the 1D simulations, with a high speed flow impinging upon a wall, resulting in a shock propagating in the opposite direction. The difference being, however, that the 2D simulations required an initial perturbation to initiate *disturbances* in the transverse direction. While such disturbances can have any number of origins in an actual shock tube<sup>4</sup>, such disturbances must be explicitly included in the numerical experiment as small perturbations. Such perturbations must be sufficiently random and weak as to not overshadow the dynamics inherent in the model, yet strong enough to initiate pressure disturbances that can essentially be picked up and amplified by the (GE).

Simulations have been performed for two of the cases, including Mach 14.7 and 16.5. All simulations shown were run on a Cartesian mesh with  $\Delta x = \Delta y = 0.33$  mm and have taken into account excited levels from only the 4s manifold of neutral argon. It was shown in the 1D simulations that although higher levels are required to obtain good agreement in the radiative cooling region, the induction zone is for the most part unaffected. Therefore, neglecting the levels beyond those contained in the 4s manifold should have negligible effect on the overall dynamics.

---

<sup>3</sup>The actual width of the UTIAS shock tube was 17.78 cm with a depth of 10.16 cm [18].

<sup>4</sup>Including turbulence, boundary layer effects, wall irregularities, etc.

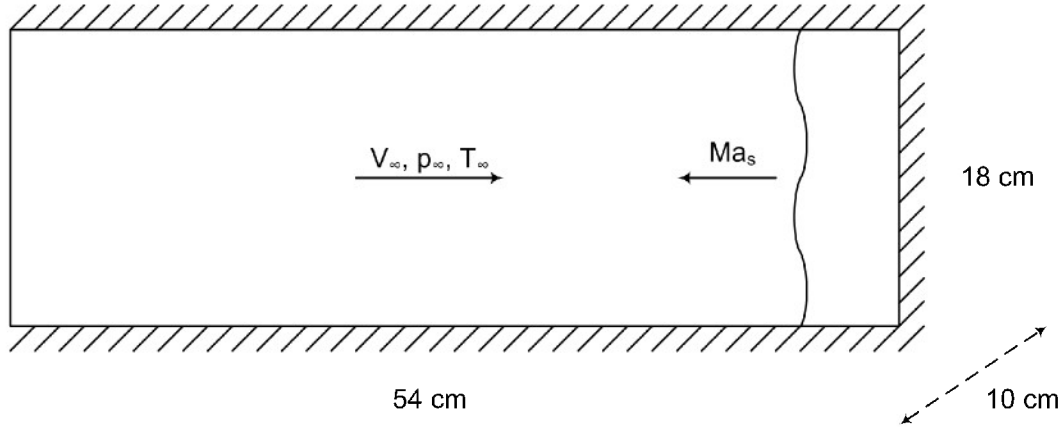


Figure 10.12: Numerical setup for 2D unsteady shock tube simulations.

#### 10.4 Mach 16.5 case

Figure 10.13 shows the evolution of the Mach 16.5 ionizing shock from a nearly planar wave to a self-sustaining oscillating pattern. The initial perturbation, visible as a half-sine wave bulge in the shock front, generates transverse waves that are apparently random in nature. After propagating a few centimeters, however, the waves begin to oscillate with a resonant frequency, creating the strong incident and reflected shock pattern that is clearly visible.

Figure 10.4 provides snapshots of the same simulation at a later time as generated by two different visualization techniques. From the finite-fringe interferogram, it is clear that the simulations have produced corrugations in the shock front similar to the UTIAS experiments. The refractive index plot further reveals a well-defined structure behind the shock, having a periodic nature in the transverse direction. From an investigation of the wave structure it was determined that the shock front actually consists of incident and reflected shocks as well as Mach stems, the intersection of which forms a series of triple points. These nodes appear in a quite regular pattern in both the longitudinal and transverse directions, indicating a resonant phenomenon. The triple points are a source of significant vorticity, the trace of which, given in Figure 10.15, highlights a cellular structure, remarkably similar to detonation cells. These analogous *ionization* cells, bounded by the trace of triple points, initiate at the intersection of two triple points which causes a high-temperature node. This node can be thought of as a two-dimensional analog to the one-dimensional electron avalanche. The resulting pressure wave generated by the increase in electron number density at this point

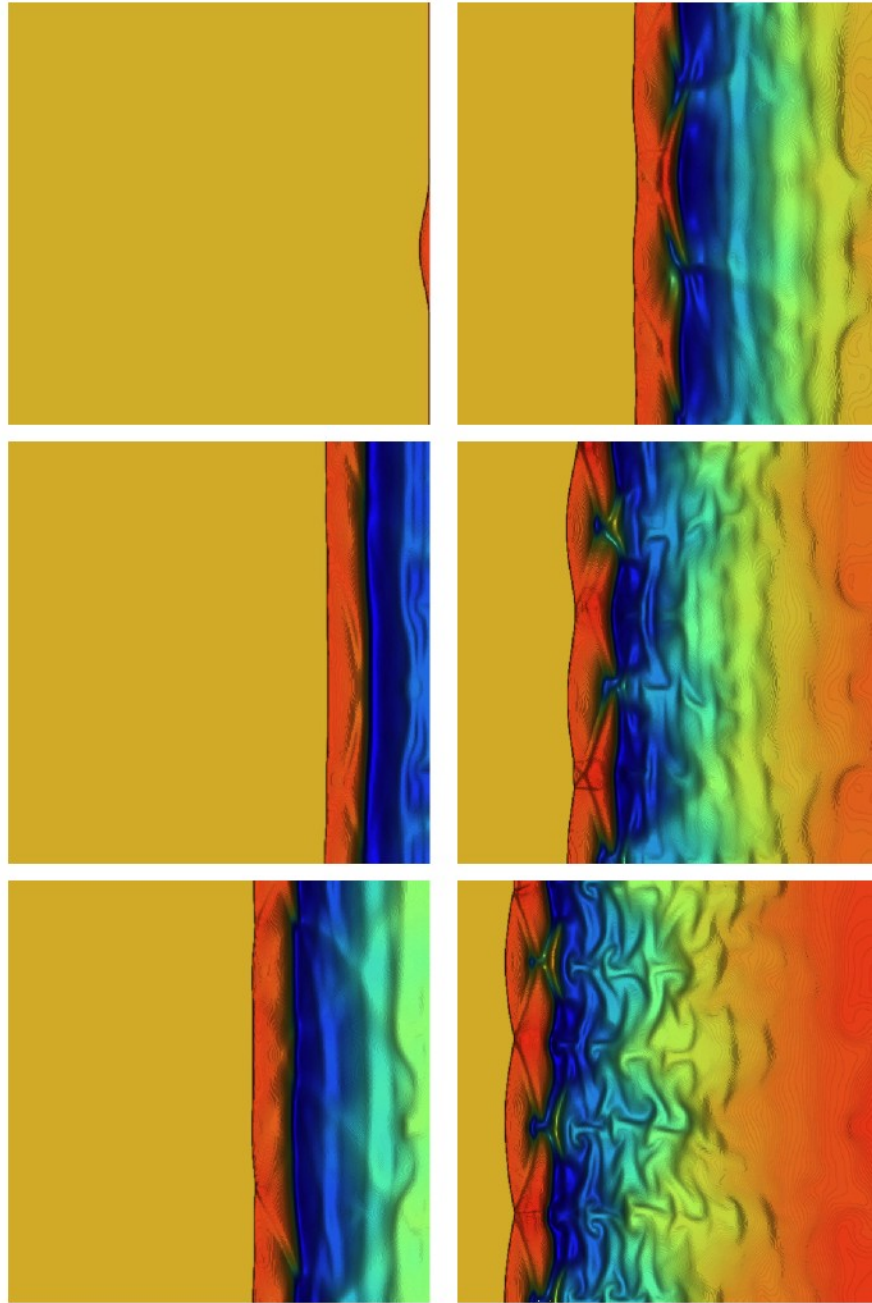



Figure 10.13: Evolution of Mach 16.5 shock, showing transition from 2D planar shock to oscillating shock. The perturbation seen in the first frame triggers transverse waves that initially appear random, but develop into a definite. Colormap: *min*  *max*

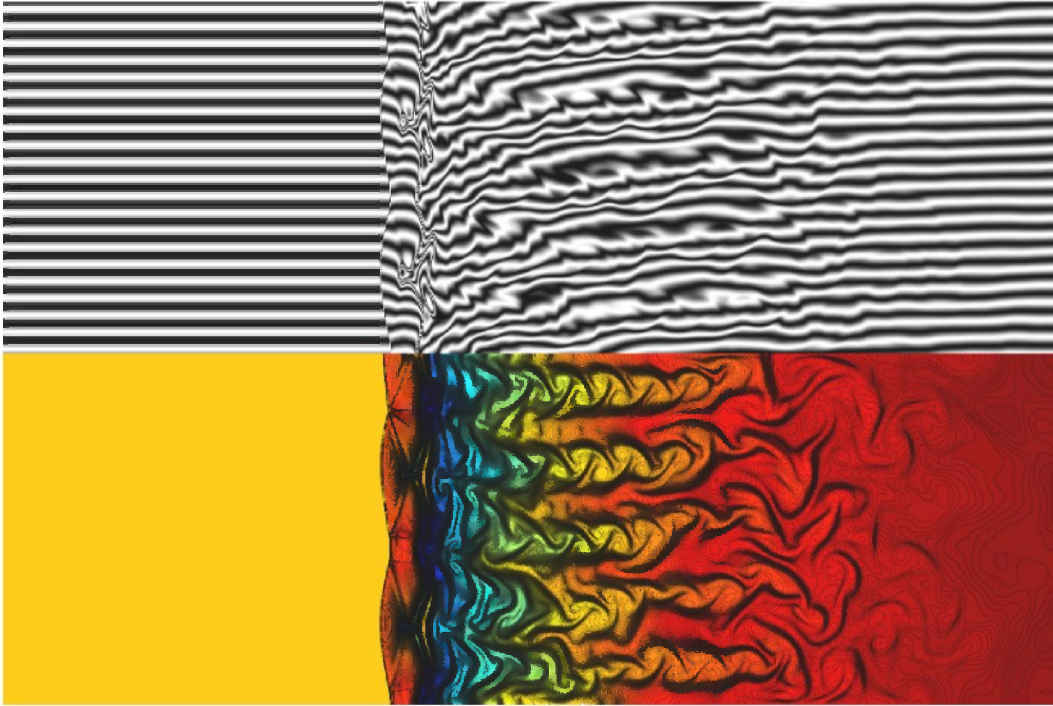



Figure 10.14: Simulated interferogram and refractive index for 2D Mach 16.5 shock. The shock front consists of incident and reflected shock waves. Colormap: *min*  *max*

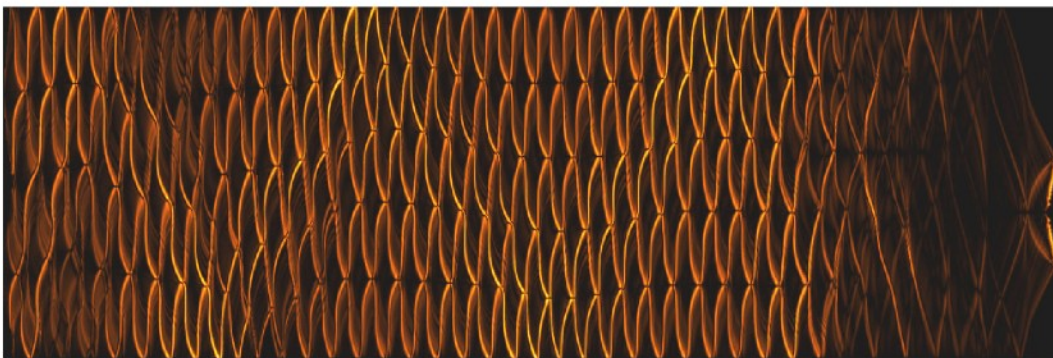


Figure 10.15: Trace of triple points for Mach 16.5 case exposing ionizing cell structure. Brighter regions correspond to stronger flow vorticity.



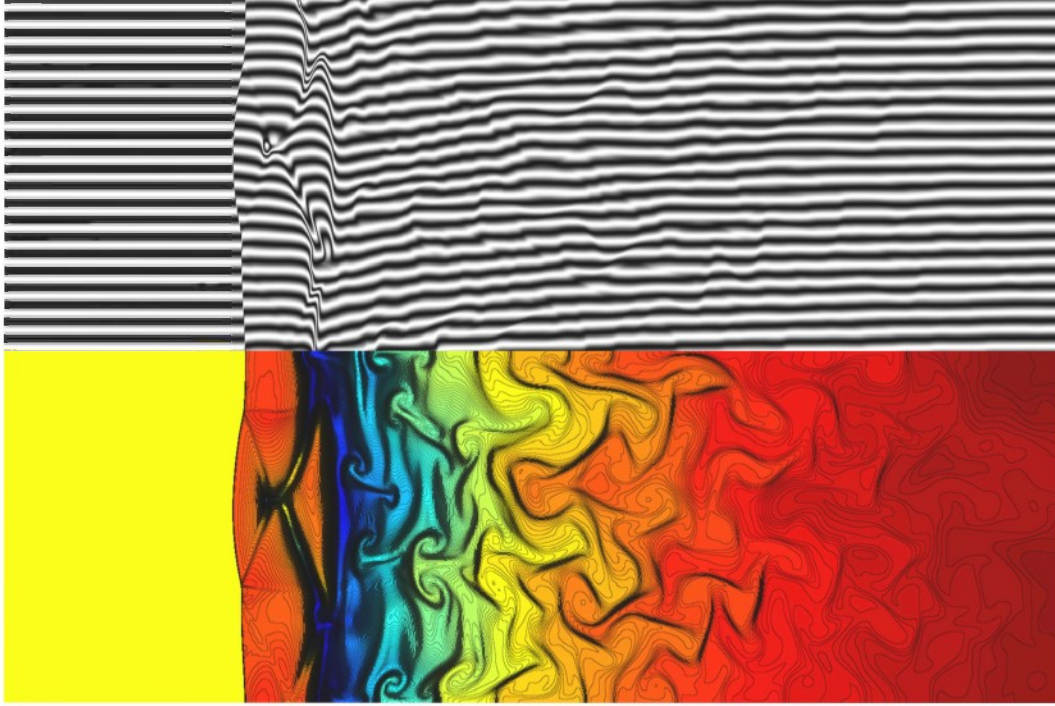



Figure 10.16: Simulated interferogram and refractive index for 2D Mach 14.7 shock. Colormap: *min*  *max*

travels radially outward, as indicated by the trace of triple points.

### 10.5 Mach 14.7 case

The case of a Mach 14.7 shock was also simulated, and from the snapshots in Figure 10.16, as well as the simulated soot trace in Figure 10.5, it is clear that decreasing the Mach number has increased the cell size in both the longitudinal and transverse directions. A direct comparison of the experimental and simulated results for the Mach 14.7 case is presented in Figure 10.5. As can be seen, the shock structure is well-predicted by the numerical simulations, with similar relaxation lengths and discontinuous gradients in the electron avalanche region along the transverse direction.

A comparison between the shock structure of the refractive index and features of the experimental interferogram in Figure 10.19 indicate the two match well. Well enough, in fact, that a similar shock structure can be overlaid upon on the experimental results showing excellent agreement and compatibility with the visible structures. In particular, the pattern

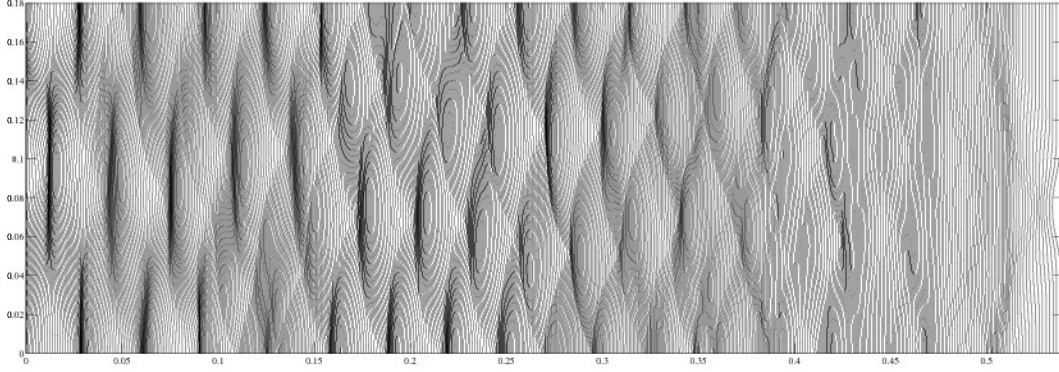


Figure 10.17: Numerical soot trace for Mach 14.7 case, exposing ionizing cell structure. Image was made by super-imposing instantaneous snapshots of the shock front.

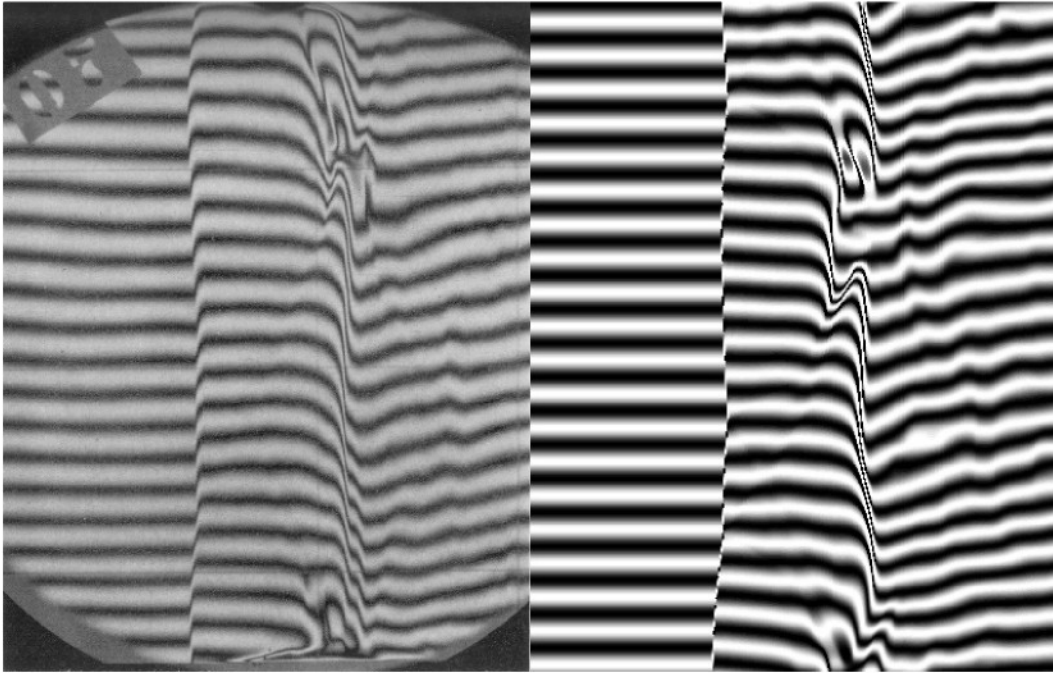


Figure 10.18: Direct comparison of experimental and numerical results for Mach 14.7 shock. Clearly evident are the corrugations in the compression shock as well as unique formation patterns in the electron avalanche which are accurately reproduced by the solver.

of incident and reflected shocks is clear in the fringe shifts of the interferogram.

### 10.5.1 Cell size approximation

Estimation of the 2D cell size was also provided in [21], based on an extension of the 1D periodicity calculation. In particular, it was determined that the longitudinal periodicity

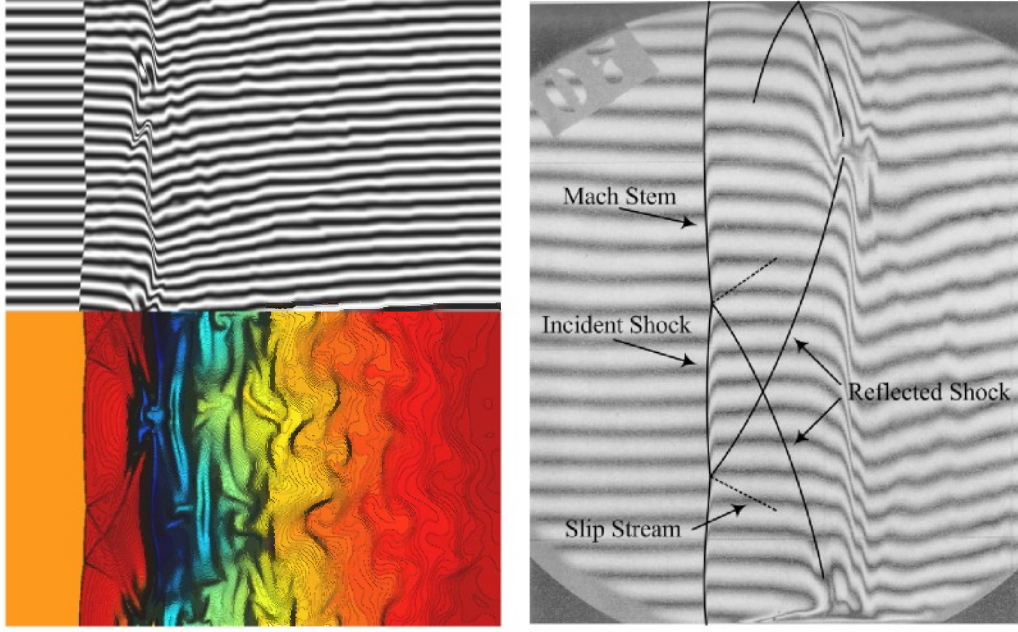


Figure 10.19: Details of the 2D ionizing shock structure for the Mach 14.7 case. The experimental shock structure can be inferred from a comparison of the simulated interferogram and refractive index plots. Incident and reflected shocks are evident in the shift in fringes in the induction zone.

must equal the transverse wave propagation time across the height ( $y$ -dir) of one complete cell. The cell width can therefore be estimated by

$$\delta \approx (a_2 + v_2^0)\tau, \quad (10.8)$$

where the bulk velocity in the transverse direction behind the shock,  $v_2$ , is assumed to be zero. Using the periodicity as determined in the 1D Mach 15.9 simulations, the periodicity of the Mach 14.7 and 16.5 cases can roughly be approximated by

$$\tau' \simeq \frac{Ma}{Ma'} \frac{\ell'}{\ell} \tau. \quad (10.9)$$

From this it is found  $\tau'_{Ma14.7} \simeq 77 \mu\text{sec}$  and  $\tau'_{Ma16.5} \simeq 28 \mu\text{sec}$ . Plugging these values into Eq. 10.8 gives  $\delta_{Ma14.7} \simeq (2658 \text{ m/s})(77 \mu\text{sec}) \simeq 20 \text{ cm}$  and  $\delta_{Ma16.5} \simeq (2973 \text{ m/s})(28 \mu\text{sec}) \simeq 8.3 \text{ cm}$ . The predicted cell height for the Mach 16.5 case agrees favorably with the numerically-observed value of 7.2 cm, while there is a bit of over-prediction for the Mach 14.7 case with a maximum observed value of just under 14 cm.



## CHAPTER 11

### IONIZING FLOW PAST A CIRCULAR CYLINDER

Furthermore, with similar structures between ionizing shocks and detonation waves,

With the numerical solver proven capable of reproducing the detailed shock structure and dynamic behavior observed in the UTIAS shock tube experiments, it was a natural progression to apply the solver to other flow configurations. Of particular interest, an extension of the solver to external flows is suggested by a series of experiments performed by Lehr [64] of a projectile fired into a hydrogen-oxygen mixture, producing a detonation shock front with nearly identical oscillating wave patterns as that of the 1D ionizing shock simulations (cf. Figure 11.1). With such similar behavior between detonations and ionizing shocks as detailed in the previous chapter, the Lehr experiments open the possibility of oscillating ionizing shock fronts in external flow cases.

#### 11.1 Numerical results

To test this theory, the flow solver has been applied to a single quadrant of a circular cylinder with a mesh defined by the transformation,

$$x = (R_x - (R_x - R_o)\xi) \cos \theta \quad (11.1)$$

$$y = (R_y - (R_y - R_o)\xi) \sin \theta \quad (11.2)$$

on the domain  $\xi = [0, 1]$ ,  $\theta = [\pi, 3\pi/2]$ , with  $R_x = 0.075$  m,  $R_y = 0.14$  m, and  $R_o = 0.05$  m. While relatively simple in nature, this particular transformation demonstrates the potential of the solver to handle non-orthogonal, curvilinear geometries. The topology of the grid and

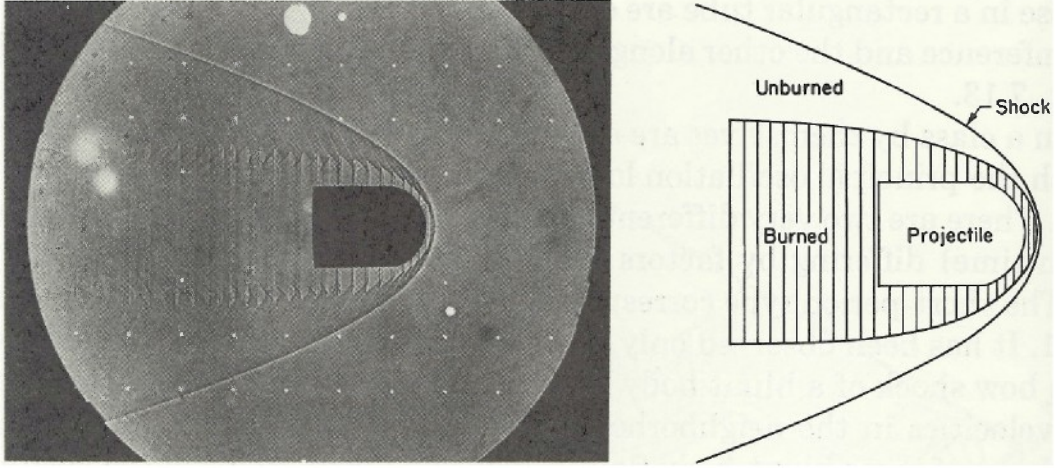


Figure 11.1: Lehr's detonation experiment of a projectile traveling through hydrogen-oxygen mixture. Taken from [39].

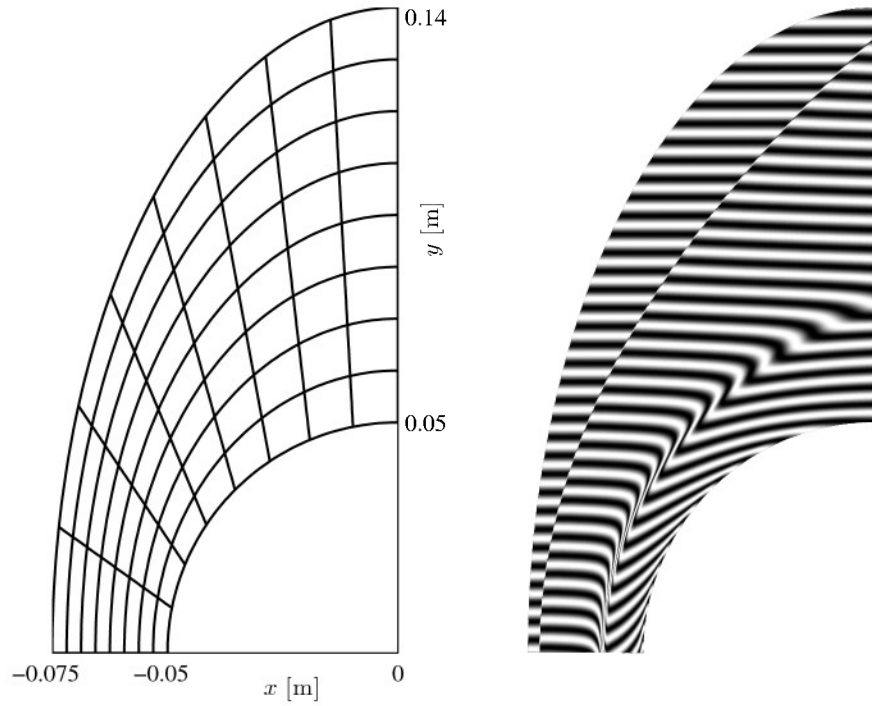


Figure 11.2: Mesh used in computation of flow around cylinder and simulated interferogram.

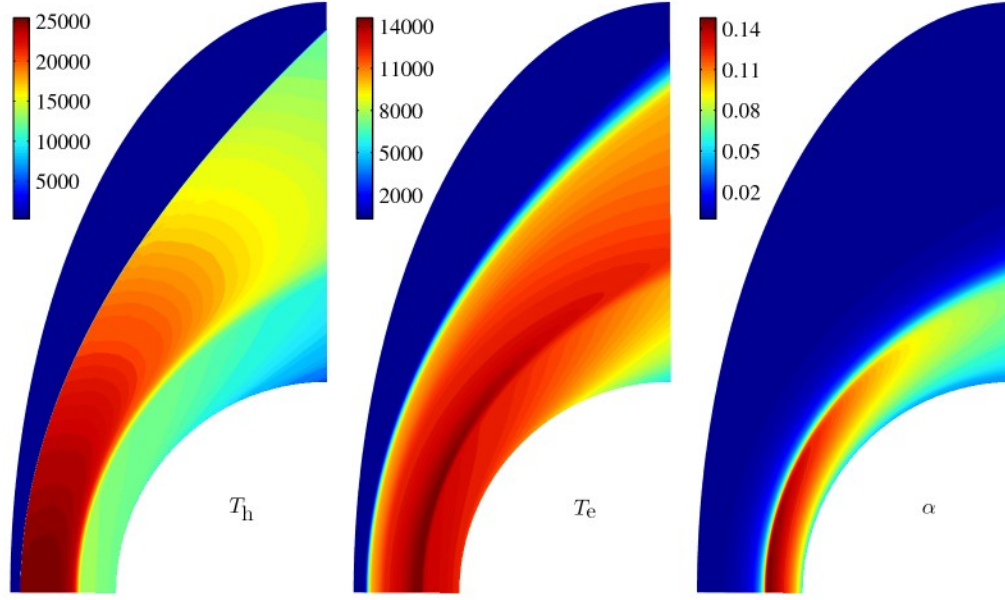


Figure 11.3: Heavy particle and electron temperatures and ionization fraction for flow around cylinder.

resulting domain decomposition are given in Figure 11.2. The actual mesh consisted of 144 domains, each containing  $50 \times 50$  cells.

Results for a shock of Mach 18.1 are given in Figure 11.3 for which the free stream conditions are given by

$$\begin{pmatrix} u_{\infty} \\ p_{\infty} \\ T_{\infty} \end{pmatrix} = \begin{pmatrix} 5292 \text{ [m/s]} \\ 4.08 \text{ [torr]} \\ 297.8 \text{ [K]} \end{pmatrix}. \quad (11.3)$$

The simulation was performed taking into account only the 4s manifold as in the 2D unsteady shock tube experiments presented in the previous chapter. The conditions result in a relaxation length of 1.45 cm along the stagnation line as seen in Figure 11.4.

The results in Figures 11.3 represent a truly steady-state solution in which there are no oscillations or fluctuations. Such a steady solution is not entirely unexpected and may be described as follows. As compared with the pressure waves generated by the heat release and specie production in the Lehr experiments, the pressure waves generated by the electron avalanche are relatively weak. As a consequence, any pressure disturbances are quickly convected past the cylinder, without the possibility of interacting with the compression

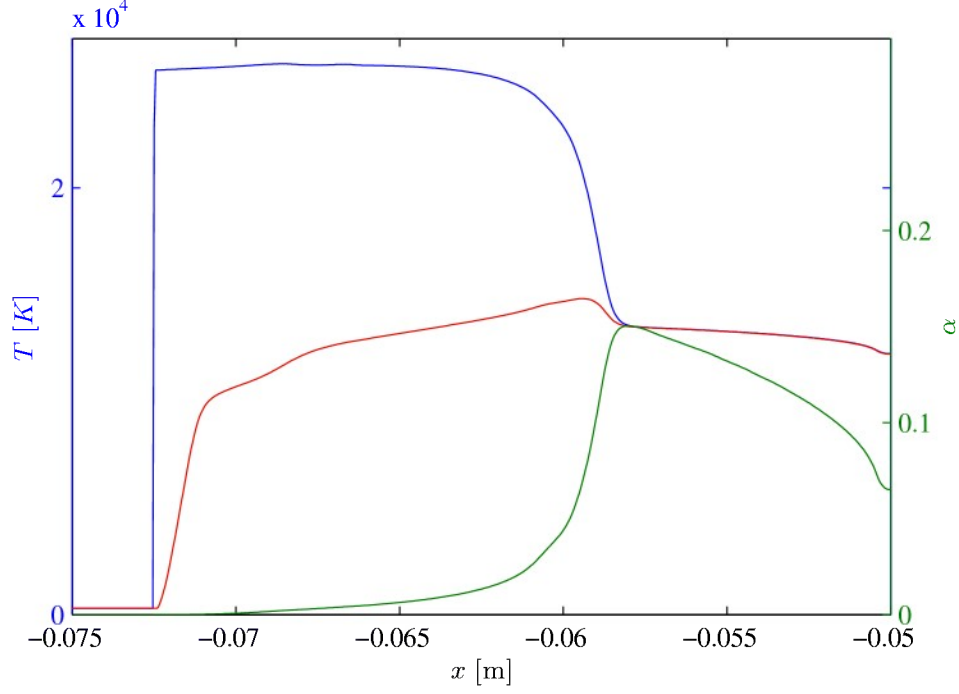


Figure 11.4: Temperature profiles and ionization fraction taken at  $\theta = 0$  for flow past cylinder.

shock. This result, however, does not preclude the possibility of such oscillations for external flows involving other geometries. Increasing the bluntness of the geometry may serve to *trap* the pressure waves so that they are able to overtake the shock. Investigation of alternate geometries is planned as a part of future work.

## 11.2 Excitation temperatures

With the number densities of all the excited states known, the degree of non-equilibrium can be assessed in terms of the excitation temperature between levels  $i$  and  $j$  as defined in terms of the Boltzmann distribution,

$$T_{ij} \equiv - \left( \frac{k_B}{\varepsilon_{ij}} \ln \left( \frac{g_i n_j}{g_j n_i} \right) \right)^{-1} \quad (11.4)$$

As can be seen from Figure 11.5, the excited states are over-populated just behind the compression shock but quickly reach near equilibrium with the electron temperature shortly thereafter. Equilibrium holds constant until the flow passes near the top of the cylinder at

which point the plasma cools as it expands, resulting in an over-population of the excited states once again.

Although not modeled beyond the apex of the cylinder, the flow will continue to expand rapidly in such a region, resulting in a cold plasma far from equilibrium conditions. The rapid expansion will lead to near-vacuum conditions, making the CR model especially important as the population of the levels will be far from Boltzmann equilibrium. Accurate simulation of the flow conditions in this radiative cooling region is not trivial and, if not treated properly, the governing equations may lead to erroneous temperature prediction. This is a result of the near-vacuum conditions leading to poor conditioning of the governing equations as discussed in Chapter 8. Application of the techniques discussed therein to this problem is planned as a part of future work.

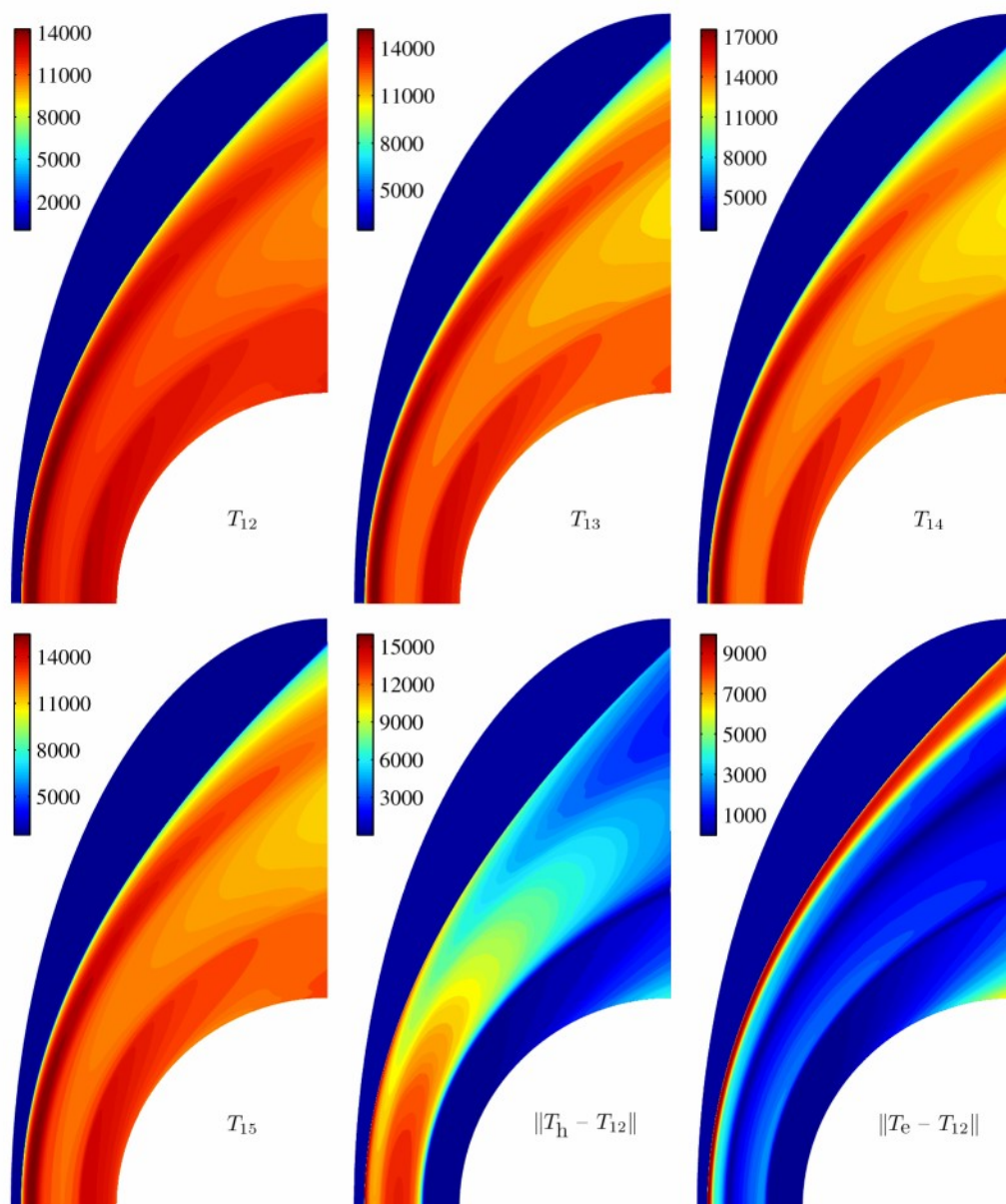


Figure 11.5: Equivalence temperatures of the first four excited levels relative to the ground state.

## CHAPTER 12

### PARALLEL FRAMEWORK

#### 12.1 Introduction

Java is a highly attractive language for developing high performance computing (HPC) applications. Extensive thread support is built into the language, allowing programs to harness the power of multi-core and symmetric multiprocessing (SMP) hardware. The Remote Method Invocation (RMI) API allows seamless interaction with remote objects, simplifying the development of distributed applications. Java is inherently object-oriented, allowing key abstraction of various network environments. And its platform independence makes it ideal for distributing applications over heterogeneous computing platforms, thus maximizing hardware resources.

Making extensive use of these features, we have developed a distributed framework tailored for explicitly parallel, Single Program, Multiple Data (SPMD) programming applications on clustered networks. In particular, the framework is aimed at solving hyperbolic conservation laws and other problems in which parallelization can be accomplished via domain decomposition—the process by which the physical or solution domain is divided into multiple computation domains (see Figure 12.1). These computation domains encompass instruction sets necessary for advancing the solution in time or achieving a steady-state solution and are executed concurrently and asynchronously through an iterative cycle with only periodic communication and synchronization requirements. Furthermore, the domain decomposition is overlapping such that each domain can communicate by exchanging boundary information with its neighbors.

The framework is implemented 100% in Java, maintaining independence of computing platforms for which the Java Virtual Machine (JVM) is available. This maximizes available

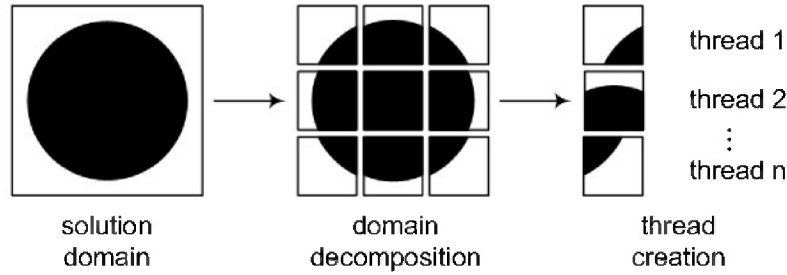


Figure 12.1: Domain decomposition process. Solution domain is decomposed into multiple computation domains from which new threads are created.

computing resources with a minimum of programming effort and required maintenance. The framework relies upon Java threads in order to optimize performance on shared-memory machines. Each computation domain executes within its own lightweight process (LWP), created by spawning new threads. The resulting threadpool is distributed over multiple servers. Communication between different servers is based on the client-server paradigm and relies upon the Remote Method Invocation (RMI) API for network-based communication. RMI is used to exchange boundary information from one domain object to another over the network. Communication must be synchronized and is implemented using concurrency constructs that encapsulate Java monitors.

## 12.2 Architecture

Java's distributed computing model is based upon the client-server paradigm. Objects distributed over client and server machines communicate with each other through Remote Method Invocation (RMI) protocols, allowing seamless interaction between applications. Programming with distributed objects greatly simplifies the development process and provides a natural extension of object-oriented programming to distributed environments. Because of its inherent simplicity, RMI is used as the basis for designing the framework around the client-server paradigm. Employing a request-response protocol, orchestrated with the aide of concurrency constructs, the framework allows interaction and communication between computation domains distributed over a network. Here we discuss the roles of clients and servers within the framework and extensions to a multi-tier implementation.



### 12.2.1 Client

From the user's point-of-view, the client is the access point into the entire framework. By means of a Graphical User Interface (GUI), the client allows remote-steering of simulations by the user. The user is able to configure, modify, and visualize the problem and solution in real time, all in a user-friendly environment. Before a simulation is initiated, problem-dependent tasks such as the set-up and initialization of boundary conditions, initial conditions, and numerical solvers can be configured through the client.

### 12.2.2 Server

Servers are responsible for the relevant program execution. This entails funneling critical I/O, communication between domains, synchronization, and execution of the domain threads. These tasks are divided between two different types of servers, masters and slaves. Master servers accept incoming requests and initialize slave servers for the client. Their primary function is to distribute the computation domains to slave servers and provide periodic barrier synchronization between iteration cycles. Masters in turn initialize slave servers that respond to synchronization signals from their master to begin a cycle of program execution, returning signals when completed.

A simple master-slave interaction is demonstrated in Figure 12.2. A master server distributes computation domains among multiple slave machines and requests for the advancement of the solution for a given time step. During this time, the servers may communicate with each other, requesting critical I/O such as domain boundary information. The client then awaits for their successful completion via signals from each of the servers, at which time it may request for solution results. The entire process is then repeated until the final solution is achieved.

This two-tier model demonstrates horizontal scalability, in which the bottom tier is expanded to accommodate the computational load requested by the master. This assumes that the master has direct access to all possible hardware resources. However, this may not always be the case. A master may want to tap into the resources of a Beowulf cluster for example, but may only do so through the head node of the cluster. In such a scenario, the head node assumes a dual role of accepting part of the computational workload from

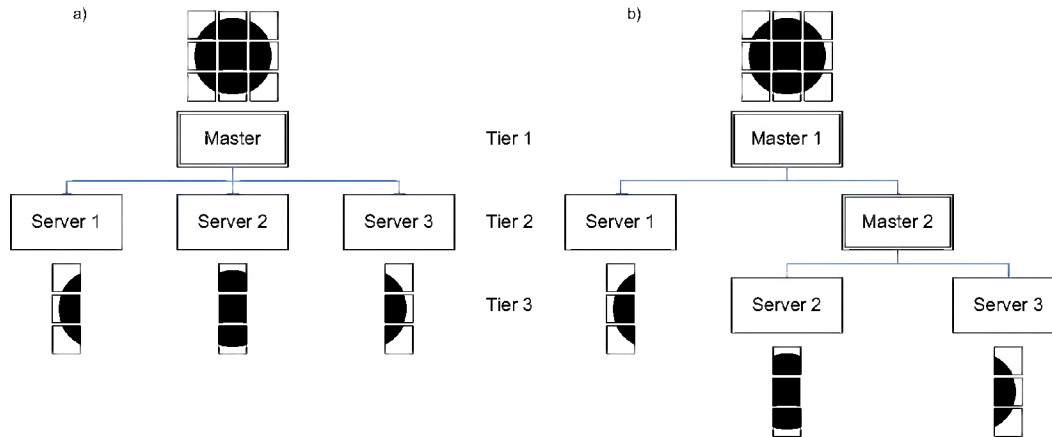


Figure 12.2: Master-slave configurations. In (a), a single Master node distributes workload among 3 slaves. In (b), Master 2 controls Slaves 1 and 2, but is itself a slave to Master 1.

the master as well as distributing the load to its available nodes. This is an example of a three-tier model and is depicted in 12.3 below.

In order to support both horizontal and vertical scalability, the framework has been generalized to a multi-tiered, client-master-slave model. In a multi-tier network, servers can simultaneously function as both masters and slaves, far more hardware and networking environments can be used. Furthermore, horizontal scalability cannot be sustained indefinitely, and will eventually present a bottleneck for massively-parallel applications. Vertical scalability can be used to funnel I/O through multiple tiers, effectively reducing I/O bandwidth at each tier. The disadvantage is that multiple requests may need to be made in order to obtain the same response, increasing network latency time.

### 12.2.3 Tree Model

In the current architecture, the multi-tier client-server paradigm is implemented through a tree-based abstraction. As illustrated in Figure 12.3, each node in the system can be represented as either a *Root*, *Branch*, or *Leaf* object. The standard tree terminology is also adopted in the following descriptions, including parent, child, sibling, etc.

#### Root

The *Root* node is the information focal point of the tree data structure. As such, for every network tree there can exist a single root node. It functions as a global master by

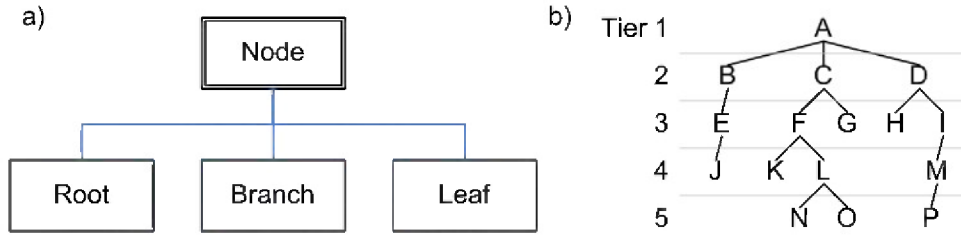


Figure 12.3: Tree abstraction. (a) *Root*, *Branch*, and *Leaf* are subclasses of *Node*. (b) Example configuration: A represents the *Root* node; B, C, D, E, F, I, L, and M represent *Branch* nodes; and J, G, H, K, N, O, and P represent *Leaf* nodes.

synchronizing its child nodes. It is also the access point for the client to the entire framework. The root node can have as children any combination of branches or leaves. The root node has no parents but listens for data requests from the client for such tasks as visualization. The Root node is used as a central location for configuration files as well as mapping information about which domains belong to which servers.

### Leaf

Terminal nodes in the network tree are called leaves and cannot have child Nodes. The primary function of a leaf is to host computational domains which handle the computational workload.

### Branch

A branch assumes the same responsibilities as those of both root and leaf nodes. The branch must wait until signaled by its parent node (either a *Root* or *Branch* node) and in turn must signal its child nodes (either *Leaf* or other *Branch* nodes) and finally wait for its children to finish their tasks. While it is possible, it is not necessary for a branch node to have computational domains. If it does, however, it must also signal and wait for the domains.

## 12.3 Communication

With computation domains distributed over a multi-tiered, heterogeneous network, communication becomes of critical importance. In the current framework, there are three primary types of information which must be communicated between different nodes in the network. These include

- (i) boundary information shared between domains
- (ii) global information
- (iii) signals for thread communication and cooperation

In all three cases, Java RMI is the protocol used to establish a connection between the nodes, allowing objects to interact and share data. Here we provide details on the exchange process of boundary and global data. Thread communication is an integral part of the synchronization process and is discussed in the next section.

### 12.3.1 Boundary Communication

Continuity of the solution domain is left fragmented after the domain decomposition process. To restore continuity, each computation domain must exchange its boundary information with its neighbors during program execution. For time-accurate simulations, this translates into one or more boundary communications per time step.

In the current framework, boundary information is passed from one domain to another within buffer objects. Source buffers are used to store boundary information which originates on the local domain and is to be sent to the remote domain. The domain on the receiving end of the source buffer stores it locally as a "target" buffer. The information from the target buffer is then used to fill the ghost cells of that domain. This process is illustrated in Figure 12.4.

A partial listing of the Buffer class implemented in the current framework is given below. Along with fields for storing the boundary information of the domain, the Buffer class also contains all necessary information to ensure that data is transferred and received in the proper order. This includes information about the source and target pairs for the domain, cell, and face indices. Encapsulating this information within the Buffer class greatly simplifies implementation of dynamic load balancing. Sending this information each exchange may seem extraneous and unnecessary, but the overhead is negligible since the performance limitation is based on the time it takes to make a remote call overshadows the time it takes to transfer the extra data. This "connectivity" information tells the local domain how to fill the buffer and how the remote domain extracts data from the buffer is determined a priori

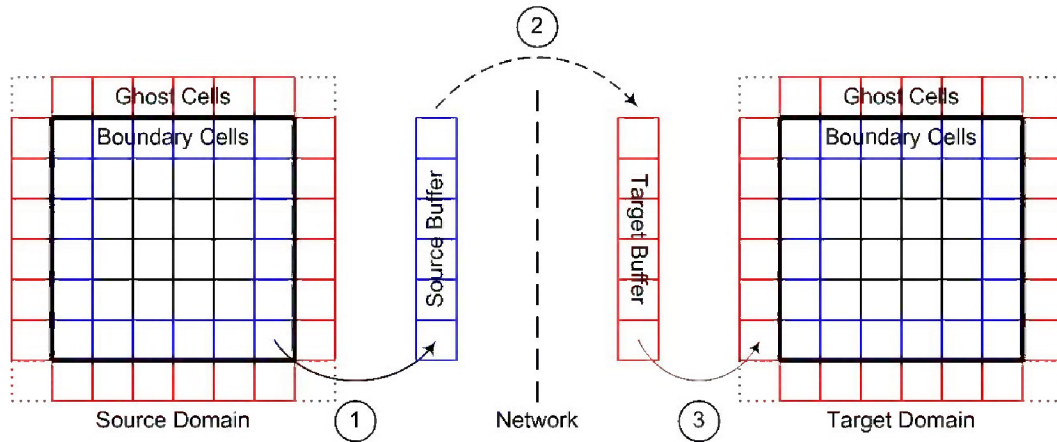


Figure 12.4: Domain Buffers are used to transfer data from the boundary layers of the source domain over the network and into the ghost layers of the target domain.

by the preprocessor. To be transferable via the RMI protocol, the *Buffer* class implements *java.io.Serializable*.

Before a method call is made to transfer the data, a check is in place to determine if the source and target domains exist within the same JVM. If so, a remote method call is initiated, otherwise a local call is made.

---

Listing 12.1: Buffer

---

```
public class DomainBuffer implements java.io.Serializable
{
    public int sourceDomain;
    public int targetDomain;

    public int sourceFace [];
    public int targetFace [];

    public int sourceCell [][];
    public int targetCell [][];

    public double [] [] [] [] Q;

    ...
}
```

}

---

*Buffer* objects can either be pushed from the source domain to the target domain by a *set()* method or pulled from the source domain by the target domain by a *get()* method. This may seem like a trivial choice, but proper implementation of the two methods can be quite different, with one resulting in performance gains over the other. To analyze the differences between a push and a pull, we present two scenarios. The first case represents a push by the source domain while the second is a pull by the target domain. Both cases represent the steps taken by each domain during a complete time step with all domains assumed to be synchronized at the start the iteration.

Cycle I:

- (i) Begin time step n.
- (ii) Fill ghost cells with target buffer data.
- (iii) Advance solution to time n+1
- (iv) Fill source buffer with boundary cell data corresponding to time level n+1.
- (v) Send source buffer to target domains.
- (vi) End Iteration.

Cycle II:

- (i) Begin time step n.
- (ii) Get buffer from source domain.
- (iii) Fill ghost cells with target buffer data.
- (iv) Advance solution to time n+1
- (v) Fill source buffer with boundary cell data corresponding to time level n+1.
- (vi) End Iteration.

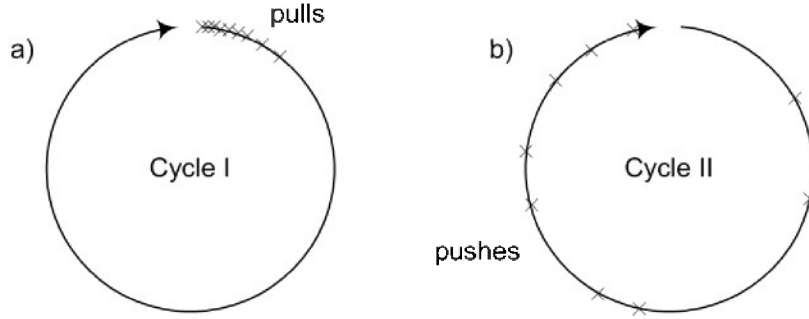


Figure 12.5: Push vs. Pull. Domain buffers can be transferred by either (a) a *pull* from the source domain by the target domain or (b) a *push* from the source domain to the target domain.

Note that the *push* at the end of the iteration by the source domain in Cycle I becomes a *pull* by the target domain at the beginning of the iteration in Cycle II. For the pull taking place at the beginning of the time step, it is more likely that all domains will attempt to get their boundary information at the same time, leading to a possible I/O bottleneck. This is less of an issue for a push, however, since it is less probable that all domains will finish their cycle at the exact same moment. This means that the domains will likely perform the push during a time when they would otherwise be idle, waiting for the final domain to finish its cycle. The chances for the remote calls being staggered in time is much greater, thus maintaining a higher level of asynchronicity. The degree of this effect is dependent upon how many domain threads are executing on each server and the thread scheduling characteristics of the operating system.

It is important to note that there exists the potential for synchronization issues with both of the above schemes. If either of the cases are not implemented properly, a critical race condition may ensue. In both scenarios, it is possible for the source domain to have completed its iteration before the target domain has even begun. In this situation, the target domain will attempt to fill its ghost cells with buffer data from an incorrect time step—the next one ( $n+1$ ).

This race condition can be remedied by storing the buffers on each domain in a First-In-First-Out (FIFO) queue as illustrated in Figure 12.6. For Cycle I, as 12.6 illustrates, as source buffers are pushed to the target domain, they are added to the top of the buffer queue. The target domain then extracts these buffers from the bottom of the queue, ensuring

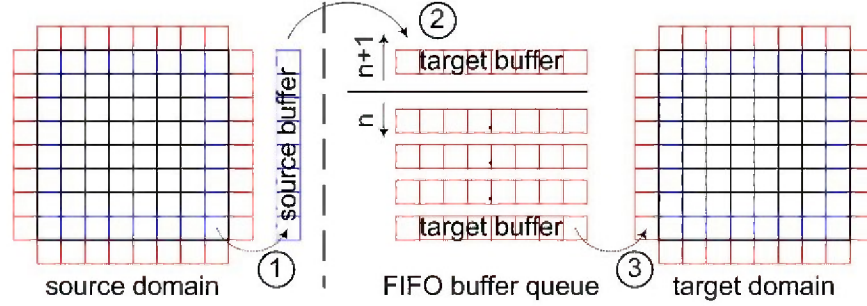


Figure 12.6: FIFO buffer queue. FIFO buffer queues on the receiving end of a push from the source domain are used to ensure correct synchronization of data between iterations.

that buffers of different time steps are effectively separated. The fix for Cycle II is similar, necessitating a FIFO buffer queue on the source domain from which the target domain *pulls*.

In the current framework, the buffer queue is implemented with the *java.util.LinkedList* class that provides such FIFO access. Since the object can be accessed by more than one thread, we must ensure that its methods are synchronized. This is accomplished by creating the *LinkedList* object in conjunction with the *java.util.Collections.synchronizedList()* static method.

## 12.4 Synchronization

The end of Moore's Law has ushered in a new era of symmetric multiprocessor (SMP) and multi-core platforms. As a result, successful applications must be able to exploit inherent parallelism to take advantage of the processing power available from all cores/processors. As a thread-based language with support for mutual exclusion and thread cooperation built in, Java is ideal for developing parallel applications on shared-memory machines. Any object (and corresponding class) can be locked by a thread that enters either a synchronized method or synchronized statement of that object. Once inside a synchronized region, a thread blocks all others from accessing any field or method. While a thread maintains a lock on an object, inter-thread communication and coordination is possible through the wait/notify mechanism. A thread can either invoke the *wait()* method, in which case the thread releases its hold on the object and allows for the possibility that another thread may enter and obtain a lock, or it can invoke the *notify()* method as it leaves the synchronized region, to signal to awaiting threads that the object has become available.



The *wait/notify* mechanism provides the essentials for thread coordination, provided that critical sections are encapsulated within a synchronized region. For a domain decomposition-based parallelization scheme, a particular example of a critical section is code that accesses the buffer data objects. Since multiple buffers are accessed by multiple threads through *get/set* methods, explicitly encapsulating this critical code in synchronized regions can quickly lead to a complicated implementation that is difficult to understand. Furthermore, the *wait/notify* mechanism is a low level concurrency construct which does not guarantee against deadlock conditions.

As an alternative, the *wait/notify* mechanism itself can be encapsulated within a higher-level lock construct. Critical code can then interact with this construct, thereby invoking the *wait/notify* mechanism implicitly. The lock construct implemented in the current work is based on the BooleanLock utility of Paul Hyde [55]. BooleanLock is a shared class that encapsulates a boolean variable that can be accessed only through several synchronized methods. The boolean variable is a thread-safe condition variable upon which threads can wait for other thread to change its state to either true or false. Encapsulation of the *wait/notify* mechanism is provided in such a way that it is also thread safe, eliminating the possibility of deadlock conditions.

---

Listing 12.2: BooleanLock Utility

---

```
public class BooleanLock
{
    private boolean value;

    public synchronized boolean get()
    {
        return value;
    }

    public synchronized void set(boolean value)
    {
        this.value = value;
        notifyAll();
    }

    public synchronized void waitUntil(boolean value)
```

```

        throws InterruptedException
    {
        while( this.value != value )
            wait();
    }
}

```

---

Within the framework, *BooleanLock* is used to synchronize several processes including initialization of the simulation, computation cycles, and visualization just to name a few. A unique lock is associated with each process for each thread. *BooleanLock* is further encapsulated within the *NodeSync* class listed below which is used directly within the framework. It provides methods to set, query, and wait on the state of individual threads as well as groups of threads. The *NodeSync* class also allows locks to be stored in *java.util.TreeMaps* so that they can easily be accessed through unique IDs.

Upon the completion of an iteration, each domain must wait for the final domain to complete its computations before the cycle can continue. This form of barrier synchronization is implemented by looping over all domain locks and waiting until each lock has been released. This is accomplished in the code by invoking *waitUntil(DOMAINS, RUNNING, false)* at any point in the code where all domains must be synchronized together.

---

Listing 12.3: NodeSync

---

```

public class NodeSync implements NodeSyncInterface
{
    private int Nchildren;
    private int Ndomains;
    private int Nproxies;

    private Lock[] clientLock;
    private Lock[] localLock;

    private Map<Integer, Lock[]> childLock =
                                new TreeMap<Integer, Lock[]>();
    private Map<Integer, Lock[]> domainLock =

```

```

new TreeMap<Integer , Lock[] >();

private Map<Integer , Lock[] > proxyLock =
    new TreeMap<Integer , Lock[] >();

...

public void set(Identifier identifier , int state , boolean value)
    throws RemoteException
{
    switch(identifier)
    {
        case CLIENT:
            clientLock[state].set(value);
            break;
        case LOCAL:
            localLock[state].set(value);
            break;
        case CHILDREN:
            for(Lock[] lock : childLock.values())
                lock[state].set(value);
            break;
        case DOMAINS:
            for(Lock[] lock : domainLock.values())
                lock[state].set(value);
            break;
        case PROXIES:
            for(Lock[] lock : proxyLock.values())
                lock[state].set(value);
    }
}

public void set(Identifier identifier ,
    int index , int state , boolean value)
    throws RemoteException

```

```

{
    switch(identifier)
    {
        case CHILD:
            childLock.get(index)[state].set(value);
            break;
        case DOMAIN:
            domainLock.get(index)[state].set(value);
            break;
        case PROXY:
            proxyLock.get(index)[state].set(value);
            break;
    }
}

public boolean is(Identifier identifier, int state)
    throws RemoteException
{
    switch(identifier)
    {
        case CLIENT:
            return clientLock[state].get();
        case PARENT:
            return parentLock[state].get();
        case LOCAL:
            return localLock[state].get();
    }
}

public boolean is(Identifier identifier, int index, int state)
    throws RemoteException
{
    switch(identifier)
    {
        case CHILD:
            return childLock.get(index)[state].get();
    }
}

```

```

        case DOMAIN:
            return domainLock.get(index)[state].get();
        case PROXY:
            return proxyLock.get(index)[state].get();
    }
}

```

```

public boolean are(Identifier identifier , int state)
    throws RemoteException
{
    switch(identifier)
    {
        case CHILDREN:
            for(Lock[] lock : childLock.values())
                if( !lock[state].get() )
                    return false;
            return true;
        case DOMAINS:
            for(Lock[] lock : domainLock.values())
                if( !lock[state].get() )
                    return false;
            return true;
        case PROXIES:
            for(Lock[] lock : proxyLock.values())
                if( !lock[state].get() )
                    return false;
            return true;
    }
}

```

```

public void waitUntil(Identifier identifier ,
    int state , boolean value)
    throws RemoteException , InterruptedException
{

```

```

switch(identifier)
{
    case CLIENT:
        clientLock[state].waitUntil(value);
        break;
    case LOCAL:
        localLock[state].waitUntil(value);
        break;
    case CHILDREN:
        for(Lock[] lock : childLock.values())
            lock[state].waitUntil(value);
        break;
    case DOMAINS:
        for(Lock[] lock : domainLock.values())
            lock[state].waitUntil(value);
        break;
    case PROXIES:
        for(Lock[] lock : proxyLock.values())
            lock[state].waitUntil(value);
}
}

public void waitUntil(Identifier identifier ,
    int index, int state, boolean value)
    throws RemoteException, InterruptedException
{
    switch(identifier)
    {
        case CHILD:
            childLock.get(index)[state].waitUntil(value);
            break;
        case DOMAIN:
            domainLock.get(index)[state].waitUntil(value);
            break;
        case PROXY:

```

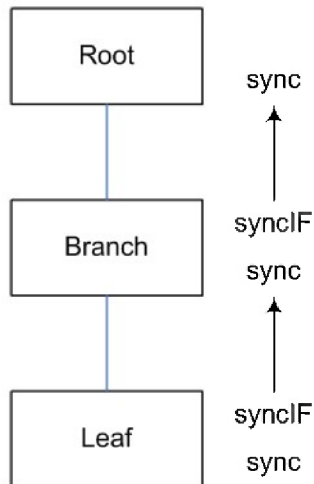


Figure 12.7: Synchronization convention. Synchronization calls between a child node and its parent are accomplished through the *Sync* implementation on the parent and the *Sync* interface of the child.

```

        proxyLock.get(index)[state].waitUntil(value);
    }
}
}
}

```

---

The elegance of the *BooleanLock/NodeSync* combination is that it not only simplifies local thread coordination (reducing the chances of error-prone code), but it is easily extended to coordinate communication between remote threads via RMI. As can be seen from the *NodeSync* listings above, *NodeSyncInterface* extends `java.rmi.Remote`, making its implemented methods invocable from remote JVMs. Threads on one JVM can transparently set, query, and wait for thread states on an entirely different JVM. The *NodeSync* class is the basis for distributed-shared memory (DSM) computing in the current architecture.

Each Node in the network has its own local instance of *NodeSync* as well as a *NodeSyncInterface* proxy corresponding to the *NodeSync* implementation of its parent Node. As illustrated in the Figure 12.7, the convention adopted in the framework is for a Node to communicate with its parent through a *NodeSyncInterface* proxy. A Node then communicates with its child through its local *NodeSync* instance.

*BooleanLock* is just one example of a concurrency construct for barrier synchronization.

The following *IntegerLock* could also be used to synchronize multiple domains by incrementing an integer value as each domain obtains a lock and then decrementing the value upon release of the lock. This could result in a more efficient implementation.

Listing 12.4: IntegerLock

---

```
public class IntegerLock
{
    private int value;

    public synchronized int get()
    {
        return value;
    }

    public synchronized void set(int value)
    {
        this.value = value;
        notifyAll();
    }

    public synchronized void increment()
    {
        value++;
        notifyAll();
    }

    public synchronized void decrement()
    {
        value--;
        notifyAll();
    }

    public synchronized void waitUntil(int value)
        throws InterruptedException
    {
        while( this.value != value )
            wait();
    }
}
```



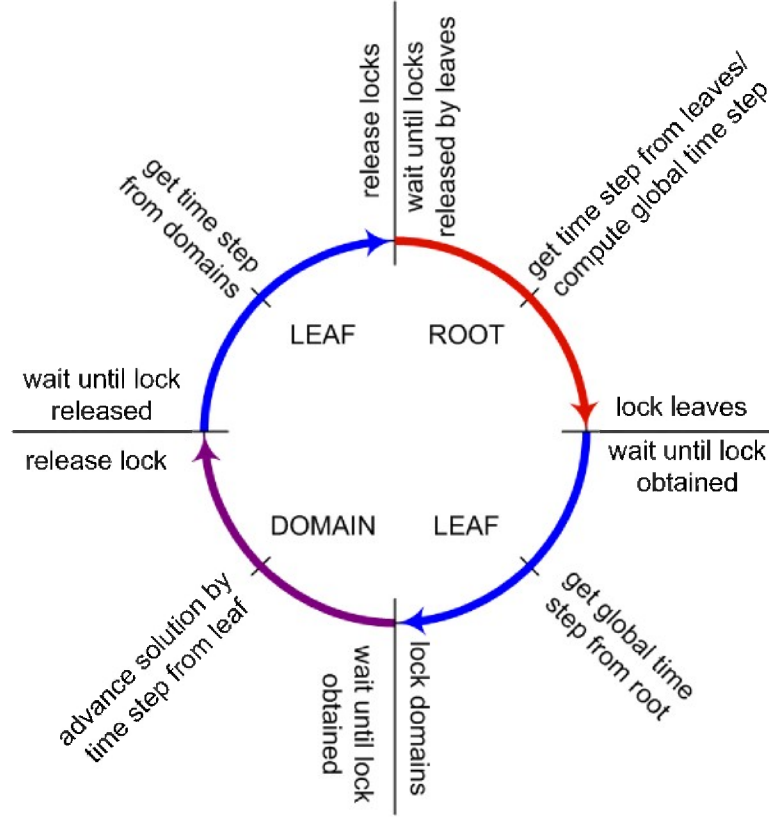


Figure 12.8: Global cycle. Interaction between *Root* and *Leaf* nodes and associated *Domains* during a global cycle.

}

To demonstrate the usage of the *NodeSync* class, we detail a computation cycle in the current framework for a given network configuration. The example considered is a two-tier network structure, consisting of a *Root* node, a *Leaf* node, and multiple *Domains* as illustrated in Figure 12.8. The stages along with the corresponding methods invoked in *NodeSync*.

ROOT THREAD:

- (i) wait until proxies have released their locks  $\rightarrow \text{sync.waitUntil}(\text{PROXIES}, \text{RUNNING}, \text{false})$
- (ii) get time step from proxies and compute global time step
- (iii) lock each proxy  $\rightarrow \text{sync.set}(\text{PROXIES}, \text{RUNNING}, \text{true})$

PROXY THREAD:

- (i) wait until lock is obtained  $\rightarrow \text{sync.waitUntil}(\text{PROXY}, 0, \text{RUNNING}, \text{true})$
- (ii) get global time step
- (iii) lock child Node (Leaf)  $\rightarrow \text{sync.set}(\text{CHILD}, 0, \text{RUNNING}, \text{true})$
- (iv) wait until child has released its lock  $\rightarrow \text{sync.waitUntil}(\text{CHILD}, 0, \text{RUNNING}, \text{true})$
- (v) get time step from child
- (vi) release lock  $\rightarrow \text{sync.set}(\text{PROXY}, 0, \text{RUNNING}, \text{false})$

LEAF THREAD:

- (i) wait until lock is obtained  $\rightarrow \text{syncIF.waitUntil}(\text{CHILD}, 0, \text{RUNNING}, \text{true})$
- (ii) get global time step
- (iii) lock domains  $\rightarrow \text{sync.set}(\text{DOMAINS}, \text{RUNNING}, \text{true})$
- (iv) wait until domains release their locks  $\rightarrow \text{waitUntil}(\text{DOMAINS}, \text{RUNNING}, \text{false})$
- (v) get time step from domains
- (vi) release lock  $\rightarrow \text{syncIF.set}(\text{CHILD}, 0, \text{RUNNING}, \text{false})$

DOMAIN THREADS:

- (i) wait until lock is obtained  $\rightarrow \text{sync.waitUntil}(\text{DOMAIN}, n, \text{RUNNING}, \text{true})$
- (ii) get global time step
- (iii) fill ghost cells from target buffers
- (iv) advance solution by time step and calculate new time step
- (v) fill source buffers with boundary data and push to neighbor domains
- (vi) release lock  $\rightarrow \text{sync.set}(\text{DOMAIN}, n, \text{RUNNING}, \text{false})$

## CHAPTER 13

### CONCLUSIONS

#### 13.1 Achievements and contributions

The achievements of the present work can be distinctly categorized in terms of both capability and application. In the case of the former, this work has been successful in introducing a numerical capability for plasmadynamic simulation that can resolve both transport phenomena and nonequilibrium effects to a high level of degree. Many advanced ideas have been incorporated including nonstandard formulations of the governing equations, such as entropy transport, with the aim of obtaining as accurate a solution as possible. A fluid description of the plasma has allowed solution of the convective transport by shock-capturing Riemann solvers extended to third-order, thus enabling resolution of highly nonlinear wave phenomena. The third-order reconstruction scheme has been extended to two-dimensional general curvilinear coordinates, allowing reconstruction of the data by quadric surfaces. A collisional-radiative model for atomic argon has yielded a database for both elastic and inelastic collisions that incorporates the latest cross section data available in the literature.

Development of the code has been systematic, relying heavily upon benchmarks and stability analysis. Stability analysis has further led to better choices for numerical algorithms, in terms of efficiency and robustness. Performance has also been addressed and a novel parallel framework in Java has been developed in conjunction with the governing equations used in this work.

In regards to application, the current work has made significant contributions to the modeling of ionizing shock instabilities. In particular, the current research marks the first time that the instabilities in a two-dimensional ionizing shock have been verified through direct simulation. Simulations have produced details of the shock structure, previously

unknown, revealing structures that are nearly identical to detonation waves. This opens the door for further comparisons between the two phenomena, with the potential to increase understanding of

This has only been possible through a strong coupling between transport and kinetics, verifying the capability of the solver to resolve such flows. The instabilities have been shown to result from a sensitivity of the kinetics to local changes in the flow properties, and hence must be modeled with an accurate treatment of both unsteady transport phenomena and nonequilibrium kinetics.

The same cellular structure resulting from a highly exothermic detonation wave can be observed in an endothermic system. In a detonation system the temperature increase in the induction zone is provided by the energy release from the chemical bonds. In an ionizing shock, however, the heavy particles act as the source of energy that enables the rise in electron temperature. In either case it is this temperature rise to which the kinetics are sensitive to.

The numerical experiments have also resulted in an improved description of the kinetics. While previous attempts to model relaxing shocks in argon have relied on limited kinetic models, this work has applied a fairly detailed collisional-radiative model that has enabled some key conclusions to be drawn. While assuming the argon plasma to be optically-thin to all radiative transitions except to the ground state, it has been found that inclusion of excited levels from the  $4s$ ,  $4p$ ,  $5s$ , and  $3d$  manifolds is sufficient to obtain excellent agreement with the experimental results for the radiative-cooling region. Results for the induction zone and electron avalanche regions, however, indicate that the levels beyond the  $4s$  manifold have very little effect.

### **13.2 Suggestions for future work**

While the solver has been applied to unsteady ionizing shock phenomena with excellent results, there is still room for improvement starting with the collisional-radiative model. In particular, it was shown in [19] that molecular argon processes including associative ionization, atomic-to-molecular ion conversion, and dissociative recombination can have a large effect on the overall kinetics. Such processes are sure to influence the relaxation scales associated with relaxing shock layers, including the relaxation length in the current

simulations. This is especially important when considering the atom-atom impact excitation cross sections. The two-step process of atom-atom impact excitation followed by atom-atom ionization is the only method considered in the current work for generating priming electrons just behind the compression shock. Inclusion of the molecular argon processes are sure to require modifications to the atom-atom impact cross sections and should be done so before any claims as to the proper value of the atom-atom impact excitation cross sections can be made.

Improvements can also be made to the collisional-radiative model by extending its nonequilibrium effects to include a non-Maxwellian electron energy distribution function. This may be important for a more accurate representation of the high-energy region (11–16 eV) of the distribution function from which electrons are selectively removed as determined by excitation and ionization thresholds.

Also an open issue is the opacity of the plasma to the various radiation sources involved. It has been assumed that all radiation from higher states to the ground level of argon are absorbed locally while radiation resulting from all other transitions escapes the system. These assumptions have been based on rough estimates of the radiation mean-free path, and in order to validate or nullify these assumptions, solution of the radiation transport equations should be coupled with the solver. While this can be quite a challenge even in two dimensions (let alone 3D), a one-dimensional implementation may be all that is necessary to verify these assumptions or to determine the proper escape factors if necessary.

Glass and Liu noted that with the existence of similar instabilities in both ionizing shocks and detonation waves, developing a stabilizing mechanism for one system may lead to similar for the other. While doping with hydrogen and other impurities were shown both experimentally and numerically [21] to suppress these instabilities, it would be of interest to determine if other approaches can lead to the same effect. In particular, studies can be done to determine if magnetohydrodynamic effects can be applied suppress these oscillations.

An attempt has been made to induce the same type of instabilities in an external flow situation. Although unsuccessful, an extension to alternate geometries could prove successful in generating oscillations and could lead to open the door to a new set of experiments for further code validation.

The UTIAS experiments also resulted in unique boundary layer phenomena caused by

the interaction of viscous and nonequilibrium effects. While water vapor impurities on the surface of the shock tube were known to exacerbate these effects [], a straight-forward inclusion of the viscous terms in the governing equations should allow for the direct simulation of the boundary layer. Reproducing such effects and validating a viscous solver can result in a capability for accurate determination of boundary layers necessary for prediction of heat fluxes, drag, etc.

## APPENDIX A

### EIGENSYSTEM

#### A.1 Two-Temperature eigensystem

With the thermodynamics properties derived, it is now possible to derive the eigensystem for the two-temperature model. The final vector form of the two-temperature model results when the electron energy equation is combined with the overall conservation equations,

$$Q = \begin{pmatrix} \rho_1 \\ \vdots \\ \rho_n \\ \rho u \\ \rho v \\ \rho w \\ E \\ \rho \hat{s}_e \end{pmatrix}, \quad V = \begin{pmatrix} \rho_1 \\ \vdots \\ \rho_n \\ u \\ v \\ w \\ p \\ p_e \end{pmatrix}, \quad F_n = \begin{pmatrix} \rho_1 v_n \\ \vdots \\ \rho_n v_n \\ \rho u v_n + n_x p \\ \rho v v_n + n_y p \\ \rho w v_n + n_z p \\ (E + p) v_n \\ \rho \hat{s}_e v_n \end{pmatrix} \quad (\text{A.1})$$

With these vectors, the determination of the flux Jacobian matrix  $A$  and its corresponding eigensystem (cf. Eq.(2.10)) can be found in a staright-forward manner. The similarity matrices defined by Eqs. (2.14) and (2.14) are found to be

$$M = \frac{\partial Q}{\partial V} = \begin{pmatrix} 1 & \dots & 0 & 0 & 0 & 0 & 0 & 0 \\ \vdots & \ddots & \vdots & \vdots & \vdots & \vdots & \vdots & \vdots \\ 0 & \dots & 1 & 0 & 0 & 0 & 0 & 0 \\ u & \dots & u & \rho & 0 & 0 & 0 & 0 \\ v & \dots & v & 0 & \rho & 0 & 0 & 0 \\ w & \dots & w & 0 & 0 & \rho & 0 & 0 \\ E_{\rho_1} & \dots & E_{\rho_n} & E_u & E_v & E_w & E_p & E_{p_e} \\ S_{e\rho_1} & \dots & S_{e\rho_n} & S_{eu} & S_{ev} & S_{ew} & S_{ep} & S_{ep_e} \end{pmatrix} \quad (\text{A.2})$$

and

$$M^{-1} = \frac{\partial V}{\partial Q} = \begin{pmatrix} 1 & \dots & 0 & 0 & 0 & 0 & 0 & 0 \\ \vdots & \ddots & \vdots & \vdots & \vdots & \vdots & \vdots & \vdots \\ 0 & \dots & 1 & 0 & 0 & 0 & 0 & 0 \\ -u/\rho & \dots & -u/\rho & 1/\rho & 0 & 0 & 0 & 0 \\ -v/\rho & \dots & -v/\rho & 0 & 1/\rho & 0 & 0 & 0 \\ -w/\rho & \dots & -w/\rho & 0 & 0 & 1/\rho & 0 & 0 \\ P_{\rho_1} & \dots & P_{\rho_n} & P_{m_x} & P_{m_y} & P_{m_z} & P_E & P_{S_e} \\ P_{e\rho_1} & \dots & P_{e\rho_n} & P_{em_x} & P_{em_y} & P_{em_z} & P_{eE} & P_{eS_e} \end{pmatrix} \quad (\text{A.3})$$

The conservative variable flux Jacobian matrix is found to be



$$A_x = \frac{\partial F}{\partial Q} = \begin{pmatrix} u(1-y_1) & \dots & -uy_1 & y_1 & 0 & 0 & 0 & 0 \\ \vdots & \ddots & \vdots & \vdots & \vdots & \vdots & \vdots & \vdots \\ -uy_n & \dots & u(1-y_n) & y_n & 0 & 0 & 0 & 0 \\ -uv & \dots & -uv & v & u & 0 & 0 & 0 \\ -uw & \dots & -uw & w & 0 & u & 0 & 0 \\ P_{\rho_1} - \vec{u} \cdot \vec{u} & \dots & P_{\rho_n} - \vec{u} \cdot \vec{u} & P_{m_x} + 2u & P_{m_y} & P_{m_z} & P_E & P_{S_e} \\ \mathcal{A}_{\rho_1, E} & \dots & \mathcal{A}_{\rho_n, E} & \mathcal{A}_{m_x, E} & uP_{m_y} & uP_{m_z} & u(1+P_E) & uP_{S_e} \\ -uS_e/\rho & \dots & -uS_e/\rho & S_e/\rho & 0 & 0 & 0 & u \end{pmatrix} \quad (\text{A.4})$$

where

$$\mathcal{A}_{\rho_i, E} = uP_{\rho_i} - u(E+p)/\rho$$

$$\mathcal{A}_{m_x, E} = uP_{m_x} + (E+p)/\rho.$$

from which the primitive variable Jacobian can be obtained using the similarity transformation,

$$A_{p_x} = M^{-1}A_xM = \begin{pmatrix} u & \dots & 0 & \rho_1 & 0 & 0 & 0 & 0 \\ \vdots & \ddots & \vdots & \vdots & \vdots & \vdots & \vdots & \vdots \\ 0 & \dots & u & \rho_n & 0 & 0 & 0 & 0 \\ 0 & \dots & 0 & u & 0 & 0 & 1/\rho & 0 \\ 0 & \dots & 0 & 0 & u & 0 & 0 & 0 \\ 0 & \dots & 0 & 0 & 0 & u & 0 & 0 \\ 0 & \dots & 0 & \rho a^2 & 0 & 0 & u & 0 \\ 0 & \dots & 0 & \gamma_e p_e & 0 & 0 & 0 & u \end{pmatrix} \quad (\text{A.5})$$

Since the eigenvalues of  $A_{p_x}$  are  $u, u \pm a$ , the thermal speed of sound can be determined using the following matrix identity,

$$|A_x| = |A_{p_x}| = \prod_i^n \lambda_i = u^{n-2}(u+a)(u-a) \longrightarrow a^2 = u^2 - \frac{|A_{xp}|}{u^{n-2}} \quad (\text{A.6})$$

yielding,

$$a^2 = \sum y_s P_{\rho_s} + (\varepsilon + p/\rho - \vec{u} \cdot \vec{u}/2) P_E + \hat{s}_e P_{S_e} \quad (\text{A.7})$$

The subsequent right eigenvectors are given by

$$R_p = \begin{pmatrix} 1 & \dots & 0 & y_1 & 0 & 0 & y_1 & 0 \\ \vdots & \ddots & \vdots & \vdots & \vdots & \vdots & \vdots & \vdots \\ 0 & \dots & 1 & y_n & 0 & 0 & y_n & 0 \\ 0 & \dots & 0 & -a/\rho & 0 & 0 & a/\rho & 0 \\ 0 & \dots & 0 & 0 & 1 & 0 & 0 & 0 \\ 0 & \dots & 0 & 0 & 0 & 1 & 0 & 0 \\ 0 & \dots & 0 & a^2 & 0 & 0 & a^2 & 0 \\ 0 & \dots & 0 & \gamma_e p_e/\rho & 0 & 0 & \gamma_e p_e/\rho & 1 \end{pmatrix} \quad (\text{A.8})$$

which can be inverted to obtain the left eigenvectors,

$$L_p = \begin{pmatrix} 1 & \dots & 0 & 0 & 0 & 0 & -y_1/a^2 & 0 \\ \vdots & \ddots & \vdots & \vdots & \vdots & \vdots & \vdots & \vdots \\ 0 & \dots & 1 & 0 & 0 & 0 & -y_n/a^2 & 0 \\ 0 & \dots & 0 & -\rho/2a & 0 & 0 & 1/2a^2 & 0 \\ 0 & \dots & 0 & 0 & 1 & 0 & 0 & 0 \\ 0 & \dots & 0 & 0 & 0 & 1 & 0 & 0 \\ 0 & \dots & 0 & \rho/2a & 0 & 0 & 1/2a^2 & 0 \\ 0 & \dots & 0 & 0 & 0 & 0 & -\gamma_e p_e/\rho a^2 & 1 \end{pmatrix} \quad (\text{A.9})$$

The eigenvalues which are identical for both the conservative and primitive Jacobians are given by

$$\Lambda = \begin{pmatrix} u & \dots & 0 & 0 & 0 & 0 & 0 & 0 \\ \vdots & \ddots & \vdots & \vdots & \vdots & \vdots & \vdots & \vdots \\ 0 & \dots & u & 0 & 0 & 0 & 0 & 0 \\ 0 & \dots & 0 & u-a & 0 & 0 & 0 & 0 \\ 0 & \dots & 0 & 0 & u & 0 & 0 & 0 \\ 0 & \dots & 0 & 0 & 0 & u & 0 & 0 \\ 0 & \dots & 0 & 0 & 0 & 0 & u+a & 0 \\ 0 & \dots & 0 & 0 & 0 & 0 & 0 & u \end{pmatrix} \quad (\text{A.10})$$

The eigensystem is transformed from the primitive back to the conservative formulation once again using the similarity matrices. The conservative right eigenvectors are found to be

$$R_n = T^{-1}R_x = \begin{pmatrix} 1 & \dots & 0 & y_1 & 0 & 0 & y_1 & 0 \\ \vdots & \ddots & \vdots & \vdots & \vdots & \vdots & \vdots & \vdots \\ 0 & \dots & 1 & y_n & 0 & 0 & y_n & 0 \\ u & \dots & u & u - \xi_x a & \eta_x \rho & \zeta_x \rho & u + \xi_x a & 0 \\ v & \dots & v & v - \xi_y a & \eta_y \rho & \zeta_y \rho & v + \xi_y a & 0 \\ w & \dots & w & w - \xi_z a & \eta_z \rho & \zeta_z \rho & w + \xi_z a & 0 \\ E_{\rho_1} & \dots & E_{\rho_n} & \mathcal{H}^- & E_{v_\eta} & E_{v_\zeta} & \mathcal{H}^+ & E_{p_e} \\ S_{e\rho_1} & \dots & S_{e\rho_n} & \mathcal{H}_e & 0 & 0 & \mathcal{H}_e & S_{ep_e} \end{pmatrix} \quad (\text{A.11})$$

where

$$\mathcal{H}^\pm = \sum y_s E_{\rho_s} + \frac{\gamma_e p_e}{\rho} E_{p_e} + a^2 E_p \pm \frac{a}{\rho} E_{v_\xi} \quad (\text{A.12})$$

and

$$\mathcal{H}_e = \sum y_s S_{e\rho_s} + \frac{\gamma_e p_e}{\rho} S_{ep_e} = \frac{S_e}{\rho} \quad (\text{A.13})$$

while the conservative left eigenvectors take the form,

Conservative left eigenvector matrix ( $x$ -dir)

$$L_x = L_{p_x} M^{-1} =$$

$$\begin{pmatrix} 1 - y_1 \frac{P_{\rho_1}}{a^2} & \dots & -y_1 \frac{P_{\rho_n}}{a^2} & -y_1 \frac{P_{m_x}}{a^2} & -y_1 \frac{P_{m_y}}{a^2} & -y_1 \frac{P_{m_z}}{a^2} & -y_1 \frac{P_E}{a^2} & -y_1 \frac{P_{S_e}}{a^2} \\ \vdots & \ddots & \vdots & \vdots & \vdots & \vdots & \vdots & \vdots \\ -y_n \frac{P_{\rho_1}}{a^2} & \dots & 1 - y_n \frac{P_{\rho_n}}{a^2} & -y_n \frac{P_{m_x}}{a^2} & -y_n \frac{P_{m_y}}{a^2} & -y_n \frac{P_{m_z}}{a^2} & -y_n \frac{P_E}{a^2} & -y_n \frac{P_{S_e}}{a^2} \\ \frac{P_{\rho_1} + au}{2a^2} & \dots & \frac{P_{\rho_n} + au}{2a^2} & \frac{P_{m_x} - a}{2a^2} & \frac{P_{m_y}}{2a^2} & \frac{P_{m_z}}{2a^2} & \frac{P_E}{2a^2} & \frac{P_{S_e}}{2a^2} \\ -v/\rho & \dots & -v/\rho & 0 & 1/\rho & 0 & 0 & 0 \\ -w/\rho & \dots & -w/\rho & 0 & 0 & 1/\rho & 0 & 0 \\ \frac{P_{\rho_1} - au}{2a^2} & \dots & \frac{P_{\rho_n} - au}{2a^2} & \frac{P_{m_x} + a}{2a^2} & \frac{P_{m_y}}{2a^2} & \frac{P_{m_z}}{2a^2} & \frac{P_E}{2a^2} & \frac{P_{S_e}}{2a^2} \\ P_{e\rho_1} - \frac{\gamma_e p_e P_{e\rho_1}}{\rho a^2} & \dots & P_{e\rho_n} - \frac{\gamma_e p_e P_{e\rho_n}}{\rho a^2} & -\frac{\gamma_e p_e P_{m_x}}{\rho a^2} & -\frac{\gamma_e p_e P_{m_y}}{\rho a^2} & -\frac{\gamma_e p_e P_{m_z}}{\rho a^2} & -\frac{\gamma_e p_e P_E}{\rho a^2} & P_{eS_e} - \frac{\gamma_e p_e P_{S_e}}{\rho a^2} \end{pmatrix} \quad (\text{A.14})$$

Conservative left eigenvector matrix ( $n$ -dir)

$$L_n = L_x T = \begin{pmatrix} 1 - y_1 \frac{P_{\rho 1}}{a^2} & \dots & -y_1 \frac{P_{e n}}{a^2} & -y_1 \frac{P_{m x}}{a^2} & -y_1 \frac{P_{m y}}{a^2} & -y_1 \frac{P_{m z}}{a^2} & -y_1 \frac{P_E}{a^2} & -y_1 \frac{P_{S_e}}{a^2} \\ \vdots & \ddots & \vdots & \vdots & \vdots & \vdots & \vdots & \vdots \\ -y_n \frac{P_{\rho 1}}{a^2} & \dots & 1 - y_n \frac{P_{e n}}{a^2} & -y_n \frac{P_{m x}}{a^2} & -y_n \frac{P_{m y}}{a^2} & -y_n \frac{P_{m z}}{a^2} & -y_n \frac{P_E}{a^2} & -y_n \frac{P_{S_e}}{a^2} \\ \frac{P_{\rho 1} + av_\xi}{2a^2} & \dots & \frac{P_{e n} + av_\xi}{2a^2} & \frac{P_{m x} - \xi_x a}{2a^2} & \frac{P_{m y} - \xi_y a}{2a^2} & \frac{P_{m z} - \xi_z a}{2a^2} & \frac{P_E}{2a^2} & \frac{P_{S_e}}{2a^2} \\ -v_\eta / \rho & \dots & -v_\eta / \rho & \eta_x / \rho & \eta_y / \rho & \eta_z / \rho & 0 & 0 \\ -v_\zeta / \rho & \dots & -v_\zeta / \rho & \zeta_x / \rho & \zeta_y / \rho & \zeta_z / \rho & 0 & 0 \\ \frac{P_{\rho 1} - av_\xi}{2a^2} & \dots & \frac{P_{e n} - av_\xi}{2a^2} & \frac{P_{m x} + \xi_x a}{2a^2} & \frac{P_{m y} + \xi_y a}{2a^2} & \frac{P_{m z} + \xi_z a}{2a^2} & \frac{P_E}{2a^2} & \frac{P_{S_e}}{2a^2} \\ P_{e \rho 1} - \frac{\gamma_e p_e P_{\rho 1}}{\rho a^2} & \dots & P_{e \rho n} - \frac{\gamma_e p_e P_{e n}}{\rho a^2} & -\frac{\gamma_e p_e P_{m x}}{\rho a^2} & -\frac{\gamma_e p_e P_{m y}}{\rho a^2} & -\frac{\gamma_e p_e P_{m z}}{\rho a^2} & -\frac{\gamma_e p_e P_E}{\rho a^2} & P_{e S_e} - \frac{\gamma_e p_e P_{S_e}}{\rho a^2} \end{pmatrix} \quad (\text{A.15})$$

## A.2 Two-Temperature MHD eigensystem

As done for the two-temperature hydrodynamic equations, the eigensystem is now presented for the two-temperature MHD equations. Although not strictly hyperbolic, the MHD equations are always diagonalizable. In the absence of magnetic fields, the fast magnetoacoustic waves become thermal acoustic waves while the Alfvén waves collapse onto the slow magnetoacoustic waves, producing the shear waves of the basic fluid equations [97]. This may lead to singularities in the eigensystem and was first addressed by Brio and Wu [17] in their development on an upwind solver. Renormalization parameters were introduced that were further refined by Roe and Balsara *et. al.* [97] and Barth [6].

$$Q = \begin{pmatrix} \rho_1 \\ \vdots \\ \rho_n \\ \rho u \\ \rho v \\ \rho w \\ B_x \\ B_y \\ B_z \\ E \\ S_e \end{pmatrix}, \quad V = \begin{pmatrix} \rho_1 \\ \vdots \\ \rho_n \\ u \\ v \\ w \\ B_x \\ B_y \\ B_z \\ p \\ p_e \end{pmatrix}, \quad F_n = \begin{pmatrix} \rho_1 v_n \\ \vdots \\ \rho_n v_n \\ \rho u v_n + n_x p_o - B_x B_n / \mu_o \\ \rho v v_n + n_y p_o - B_y B_n / \mu_o \\ \rho w v_n + n_z p_o - B_z B_n / \mu_o \\ v_n B_x - u B_n \\ v_n B_y - v B_n \\ v_n B_z - w B_n \\ v_n (E + p_o) - B_n (\vec{v} \cdot \vec{B}) / \mu_o \\ v_n S_e \end{pmatrix} \quad (\text{A.16})$$

# Similarity transformation matrices

$$M = \frac{\partial Q}{\partial V} = \begin{pmatrix} 1 & \dots & 0 & 0 & 0 & 0 & 0 & 0 & 0 & 0 & 0 \\ \vdots & \ddots & \vdots & \vdots & \vdots & \vdots & \vdots & \vdots & \vdots & \vdots & \vdots \\ 0 & \dots & 1 & 0 & 0 & 0 & 0 & 0 & 0 & 0 & 0 \\ u & \dots & u & \rho & 0 & 0 & 0 & 0 & 0 & 0 & 0 \\ v & \dots & v & 0 & \rho & 0 & 0 & 0 & 0 & 0 & 0 \\ w & \dots & w & 0 & 0 & \rho & 0 & 0 & 0 & 0 & 0 \\ 0 & \dots & 0 & 0 & 0 & 0 & 1 & 0 & 0 & 0 & 0 \\ 0 & \dots & 0 & 0 & 0 & 0 & 0 & 1 & 0 & 0 & 0 \\ 0 & \dots & 0 & 0 & 0 & 0 & 0 & 0 & 1 & 0 & 0 \\ E_{\rho_1} & \dots & E_{\rho_n} & E_u & E_v & E_w & E_{B_x} & E_{B_y} & E_{B_z} & E_p & E_{p_e} \\ S_{e\rho_1} & \dots & S_{e\rho_n} & S_{eu} & S_{ev} & S_{ew} & S_{eB_x} & S_{eB_y} & S_{eB_z} & S_{ep} & S_{ep_e} \end{pmatrix} \quad (\text{A.17})$$

$$M^{-1} = \frac{\partial V}{\partial Q} = \begin{pmatrix} 1 & \dots & 0 & 0 & 0 & 0 & 0 & 0 & 0 & 0 & 0 \\ \vdots & \ddots & \vdots & \vdots & \vdots & \vdots & \vdots & \vdots & \vdots & \vdots & \vdots \\ 0 & \dots & 1 & 0 & 0 & 0 & 0 & 0 & 0 & 0 & 0 \\ -\frac{u}{\rho} & \dots & -\frac{u}{\rho} & \frac{1}{\rho} & 0 & 0 & 0 & 0 & 0 & 0 & 0 \\ -\frac{v}{\rho} & \dots & -\frac{v}{\rho} & 0 & \frac{1}{\rho} & 0 & 0 & 0 & 0 & 0 & 0 \\ -\frac{w}{\rho} & \dots & -\frac{w}{\rho} & 0 & 0 & \frac{1}{\rho} & 0 & 0 & 0 & 0 & 0 \\ 0 & \dots & 0 & 0 & 0 & 0 & 1 & 0 & 0 & 0 & 0 \\ 0 & \dots & 0 & 0 & 0 & 0 & 0 & 1 & 0 & 0 & 0 \\ 0 & \dots & 0 & 0 & 0 & 0 & 0 & 0 & 1 & 0 & 0 \\ P_{\rho_1} & \dots & P_{\rho_n} & P_{m_x} & P_{m_y} & P_{m_z} & P_{B_x} & P_{B_y} & P_{B_z} & P_p & P_{p_e} \\ P_{e\rho_1} & \dots & P_{e\rho_n} & P_{em_x} & P_{em_y} & P_{em_z} & P_{eB_x} & P_{eB_y} & P_{eB_z} & P_{ep} & P_{ep_e} \end{pmatrix} \quad (\text{A.18})$$

# Conservative flux Jacobian matrix

$$A = \frac{\partial F}{\partial Q} = \begin{pmatrix} u(1-y_1) & \dots & -uy_1 & y_1 & 0 & 0 & 0 & 0 & 0 & 0 & 0 \\ \vdots & \ddots & \vdots & \vdots & \vdots & \vdots & \vdots & \vdots & \vdots & \vdots & \vdots \\ -uy_n & \dots & u(1-y_n) & y_n & 0 & 0 & 0 & 0 & 0 & 0 & 0 \\ P_{\rho_1} - u^2 & \dots & P_{\rho_n} - u^2 & P_{m_x} + 2u & P_{m_y} & P_{m_z} & P_{B_x} - \frac{B_x}{\mu_o} & P_{B_y} + \frac{B_y}{\mu_o} & P_{B_z} + \frac{B_z}{\mu_o} & P_E & P_{S_e} \\ -uw & \dots & -uw & v & u & 0 & -\frac{B_y}{\mu_o} & -\frac{B_x}{\mu_o} & 0 & 0 & 0 \\ -uw & \dots & -uw & w & 0 & u & -\frac{\mu_o}{B_z} & 0 & 0 & 0 & 0 \\ \frac{vB_x - uB_y}{\rho} & \dots & \frac{vB_x - uB_y}{\rho} & \frac{B_y}{\rho} & -\frac{B_x}{\rho} & 0 & -v & u & 0 & 0 & 0 \\ \frac{wB_x - uB_z}{\rho} & \dots & \frac{wB_x - uB_z}{\rho} & \frac{B_z}{\rho} & 0 & -\frac{B_x}{\rho} & -w & 0 & u & 0 & 0 \\ -\frac{u}{\rho} S_e & \dots & -\frac{u}{\rho} S_e & \frac{1}{\rho} S_e & \longleftarrow \partial f_E / \partial Q & 0 & 0 & 0 & 0 & 0 & u \end{pmatrix} \quad (\text{A.19})$$

where

$$\frac{\partial f_E}{\partial Q} = \begin{pmatrix} uP_{\rho_1} - [u(E + p_o) - B_x(\vec{u} \cdot \vec{B})/\mu_o]/\rho & \vdots & \\ uP_{\rho_n} - [u(E + p_o) - B_x(\vec{u} \cdot \vec{B})/\mu_o]/\rho & & \\ uP_{m_x} + (E + p_o - B_x^2/\mu_o)/\rho & & \\ uP_{m_y} - \frac{\rho\mu_o B_y}{B_x B_z} & & \\ uP_{m_z} - \frac{\rho\mu_o B_z}{B_x B_y} & & \\ uP_{B_x} - \vec{u} \cdot \vec{B}/\mu_o & & \\ u(P_{B_y} + B_y/\mu_o) - vB_x/\mu_o & & \\ u(P_{B_z} + B_z/\mu_o) - wB_x/\mu_o & & \\ u(1 + P_E) & & \\ uP_{S_e} & & \end{pmatrix}^T$$



## Primitive flux Jacobian matrix

$$A_{p_x} = M^{-1} A_x M = \begin{pmatrix} u & \dots & 0 & \rho_1 & 0 & 0 & 0 & 0 & 0 & 0 & 0 \\ \vdots & \ddots & \vdots & \vdots & \vdots & \vdots & \vdots & \vdots & \vdots & \vdots & \vdots \\ 0 & \dots & u & \rho_n & 0 & 0 & 0 & 0 & 0 & 0 & 0 \\ 0 & \dots & 0 & u & 0 & 0 & 0 & \frac{B_y}{\rho\mu_o} & \frac{B_z}{\rho\mu_o} & \frac{1}{\rho} & 0 \\ 0 & \dots & 0 & 0 & u & 0 & 0 & -\frac{B_x}{\rho\mu_o} & 0 & 0 & 0 \\ 0 & \dots & 0 & 0 & 0 & u & 0 & 0 & -\frac{B_x}{\rho\mu_o} & 0 & 0 \\ 0 & \dots & 0 & 0 & 0 & 0 & u & 0 & 0 & 0 & 0 \\ 0 & \dots & 0 & B_y & -B_x & 0 & 0 & u & 0 & 0 & 0 \\ 0 & \dots & 0 & B_z & 0 & -B_x & 0 & 0 & u & 0 & 0 \\ 0 & \dots & 0 & \rho a^2 & 0 & 0 & 0 & 0 & 0 & u & 0 \\ 0 & \dots & 0 & \gamma_e p_e & 0 & 0 & 0 & 0 & 0 & 0 & u \end{pmatrix} \quad (\text{A.20})$$

where  $a^2$  is the thermal sound speed and is independent of the magnetic pressure,

$$a^2 = \sum y_s P_{\rho_s} + (\varepsilon + p/\rho - \vec{u} \cdot \vec{u}/2) P_E + \hat{s}_e P_{S_e} \quad (\text{A.21})$$

Diagonal matrix of eigenvalues

$$\Lambda = \begin{pmatrix} u & \dots & 0 & 0 & 0 & 0 & 0 & 0 & 0 & 0 & 0 & 0 & 0 \\ \vdots & \ddots & \vdots & \vdots & \vdots & \vdots & \vdots & \vdots & \vdots & \vdots & & & \\ 0 & \dots & u & 0 & 0 & 0 & 0 & 0 & 0 & 0 & 0 & 0 & 0 \\ 0 & \dots & 0 & u & 0 & 0 & 0 & 0 & 0 & 0 & 0 & 0 & 0 \\ 0 & \dots & 0 & 0 & u - c_s & 0 & 0 & 0 & 0 & 0 & 0 & 0 & 0 \\ 0 & \dots & 0 & 0 & 0 & u + c_s & 0 & 0 & 0 & 0 & 0 & 0 & 0 \\ 0 & \dots & 0 & 0 & 0 & 0 & u - c_f & 0 & 0 & 0 & 0 & 0 & 0 \\ 0 & \dots & 0 & 0 & 0 & 0 & 0 & u + c_f & 0 & 0 & 0 & 0 & 0 \\ 0 & \dots & 0 & 0 & 0 & 0 & 0 & 0 & u - \frac{B_x}{\sqrt{\rho}} & 0 & 0 & 0 & 0 \\ 0 & \dots & 0 & 0 & 0 & 0 & 0 & 0 & 0 & u + \frac{B_x}{\sqrt{\rho}} & 0 & 0 & 0 \\ 0 & \dots & 0 & 0 & 0 & 0 & 0 & 0 & 0 & 0 & u & 0 & 0 \\ 0 & \dots & 0 & 0 & 0 & 0 & 0 & 0 & 0 & 0 & 0 & u & 0 \end{pmatrix} \quad (\text{A.22})$$

Conservative right eigenvector matrix

$$R_n = \begin{pmatrix} 1 & \dots & 0 & 0 & \alpha_f y_1 & \alpha_f y_1 & \alpha_s y_1 & 0 & 0 & 0 \\ \vdots & \ddots & \vdots & \vdots & \vdots & \vdots & \vdots & \vdots & \vdots & \vdots \\ 0 & \dots & 1 & 0 & \alpha_f y_n & \alpha_s y_n & \alpha_s y_n & 0 & 0 & 0 \\ u & \dots & u & 0 & \alpha_f u + \mathcal{A}_f^x & \alpha_f u - \mathcal{A}_f^x & \alpha_s u - \mathcal{A}_s^x & -(\hat{n} \times \vec{\beta})_x & (\hat{n} \times \vec{\beta})_x & 0 \\ v & \dots & v & 0 & \alpha_f v + \mathcal{A}_f^y & \alpha_f v - \mathcal{A}_f^y & \alpha_s v - \mathcal{A}_s^y & -(\hat{n} \times \vec{\beta})_y & (\hat{n} \times \vec{\beta})_y & 0 \\ w & \dots & w & 0 & \alpha_f w + \mathcal{A}_f^z & \alpha_f w - \mathcal{A}_f^z & \alpha_s w - \mathcal{A}_s^z & -(\hat{n} \times \vec{\beta})_z & (\hat{n} \times \vec{\beta})_z & 0 \\ 0 & \dots & 0 & 0 & \sqrt{\frac{\mu_0}{\rho}} \mathcal{G}_f^x & \sqrt{\frac{\mu_0}{\rho}} \mathcal{G}_f^x & \sqrt{\frac{\mu_0}{\rho}} \mathcal{G}_s^x & \sqrt{\frac{\mu_0}{\rho}} (\hat{n} \times \vec{\beta})_x & \sqrt{\frac{\mu_0}{\rho}} (\hat{n} \times \vec{\beta})_x & n_x \\ 0 & \dots & 0 & 0 & \sqrt{\frac{\mu_0}{\rho}} \mathcal{G}_f^y & \sqrt{\frac{\mu_0}{\rho}} \mathcal{G}_f^y & \sqrt{\frac{\mu_0}{\rho}} \mathcal{G}_s^y & \sqrt{\frac{\mu_0}{\rho}} (\hat{n} \times \vec{\beta})_y & \sqrt{\frac{\mu_0}{\rho}} (\hat{n} \times \vec{\beta})_y & n_y \\ 0 & \dots & 0 & 0 & \sqrt{\frac{\mu_0}{\rho}} \mathcal{G}_f^z & \sqrt{\frac{\mu_0}{\rho}} \mathcal{G}_f^z & \sqrt{\frac{\mu_0}{\rho}} \mathcal{G}_s^z & \sqrt{\frac{\mu_0}{\rho}} (\hat{n} \times \vec{\beta})_z & \sqrt{\frac{\mu_0}{\rho}} (\hat{n} \times \vec{\beta})_z & n_z \\ E_{\rho_1} & \dots & E_{\rho_n} & E_{p_e} & \mathcal{H}_f^+ & \mathcal{H}_f^- & \mathcal{H}_s^+ & (\vec{v} \times \vec{\beta}) \cdot \hat{n} & -(\vec{v} \times \vec{\beta}) \cdot \hat{n} & B_x \\ S_{e\rho_1} & \dots & S_{e\rho_n} & S_{ep_e} & \mathcal{H}_e & \mathcal{H}_e & \mathcal{H}_e & 0 & 0 & 0 \end{pmatrix} \quad (\text{A.23})$$

161

$$(\text{A.24})$$

$$(\text{A.25})$$

$$(\text{A.26})$$

$$(\text{A.27})$$

$$(\text{A.28})$$

$$(\text{A.29})$$

$$(\text{A.30})$$

$$\vec{\mathcal{A}}_{f,s} = \hat{n} \alpha_{f,s} c_{f,s} \mp \alpha_{s,f} c_{s,f} (\vec{\beta} - \hat{n} \beta_n) \text{sgn}(B_n), \quad \vec{\mathcal{G}}_{f,s} = \pm \alpha_{s,f} a (\vec{\beta} - \hat{n} \beta_n)$$

$$\mathcal{H}^\pm = \alpha \left( \sum y_s E_{\rho_s} + \frac{\gamma_e p_e}{\rho} E_{p_e} + a^2 E_p + c^2 - a^2 \right) \pm \vec{v} \cdot \vec{\mathcal{A}}, \quad \mathcal{H}_e = \sum y_s S_{e\rho_s} + \frac{\gamma_e p_e}{\rho} S_{ep_e} = \hat{s}_e$$

$$B_n = \hat{n} \cdot \vec{B}, \quad B^2 = B_x^2 + B_y^2 + B_z^2, \quad B_\perp = \sqrt{B^2 - B_n^2}$$

$$\vec{\beta} = \vec{B}/B_\perp, \quad \beta_n = B_n/B_\perp$$

$$a_*^2 = a^2 + \frac{B^2}{\rho \mu_0} = c_f^2 + c_s^2, \quad c_a^2 = \frac{B_n^2}{\rho \mu_0}$$

$$c_{f,s}^2 = \frac{1}{2} \left( a_*^2 \pm \sqrt{a_*^4 - 4a^2 c_a^2} \right)$$

$$\alpha_f^2 = \frac{a^2 - c_s^2}{c_f^2 - c_s^2}, \quad \alpha_s^2 = \frac{c_f^2 - a^2}{c_f^2 - c_s^2}$$

E-182

## APPENDIX B

### ISOPARAMETRIC ELEMENTS

In order to obtain a high-order solution in the finite-volume scheme, it is necessary to *reconstruct* the cell-average values to obtain more an accurate representation of the data. The method of undetermined coefficients is one such technique, that requires the basis functions to be integrated over the area of the cell. In general coordinates or on unstructured meshes, integration over irregular cells becomes a necessity which can be handled by the use of shape functions, which are used to transform between the physical and natural coordinate systems,

$$\int_{x_1}^{x_2} u(x) \, dx \xleftrightarrow[\text{physical}]{\text{natural}} \int_{-1}^1 u(\xi) |J| \, d\xi. \quad (\text{B.1})$$

#### B.1 One-Dimensional Shape Functions

##### B.1.1 Linear Elements

The shape functions for the linear isoparametric element are as follows.

$$H_1(\xi) = \frac{1}{2}(1 - \xi) \quad (\text{B.2a})$$

$$H_2(\xi) = \frac{1}{2}(1 + \xi) \quad (\text{B.2b})$$

A point  $\xi$  within the natural element is mapped into a point  $x$  within the physical element using the shape functions given in Eq. B.2.

$$x = H_1(\xi)x_1 + H_2(\xi)x_2 \quad (\text{B.3a})$$

$$= \frac{1}{2}(1 - \xi)x_1 + \frac{1}{2}(1 + \xi)x_2 \quad (\text{B.3b})$$

The Jacobian is given by

$$J = \frac{dx}{d\xi} = \sum_{i=1}^2 \frac{dH_i(\xi)}{d\xi} x_i = \frac{1}{2}(x_2 - x_1). \quad (\text{B.4})$$

## B.2 Two-Dimensional Shape Functions

### B.2.1 Bilinear Elements

The shape functions for the bilinear isoparametric element are given below.

$$H_1(\xi, \eta) = \frac{1}{4}(1 - \xi)(1 - \eta) \quad (\text{B.5a})$$

$$H_2(\xi, \eta) = \frac{1}{4}(1 + \xi)(1 - \eta) \quad (\text{B.5b})$$

$$H_3(\xi, \eta) = \frac{1}{4}(1 + \xi)(1 + \eta) \quad (\text{B.5c})$$

$$H_4(\xi, \eta) = \frac{1}{4}(1 - \xi)(1 + \eta) \quad (\text{B.5d})$$

A point  $(\xi, \eta)$  within the natural element is mapped into a point  $(x, y)$  within the physical element using the shape function given in Eq. B.5.

$$x = \sum_{i=1}^4 H_i(\xi, \eta)x_i \quad (\text{B.6a})$$

$$y = \sum_{i=1}^4 H_i(\xi, \eta)y_i \quad (\text{B.6b})$$

Similarly, any physical variable can be interpolated using the same shape functions.

$$\phi = \sum_{i=1}^4 H_i(\xi, \eta)\phi_i \quad (\text{B.7})$$

The Jacobian matrix is given by

$$J = \begin{pmatrix} \frac{\partial x}{\partial \xi} & \frac{\partial y}{\partial \xi} \\ \frac{\partial x}{\partial \eta} & \frac{\partial y}{\partial \eta} \end{pmatrix}, \quad (\text{B.8})$$

with Jacobian,

$$|J| \equiv \det(J) = \frac{\partial x}{\partial \xi} \frac{\partial y}{\partial \eta} - \frac{\partial y}{\partial \xi} \frac{\partial x}{\partial \eta}. \quad (\text{B.9})$$

The components of the Jacobian matrix are as follows:

$$J_{11} = \frac{\partial x}{\partial \xi} = \sum_{i=1}^4 \frac{\partial H_i(\xi, \eta)}{\partial \xi} x_i \quad (\text{B.10a})$$

$$J_{12} = \frac{\partial y}{\partial \xi} = \sum_{i=1}^4 \frac{\partial H_i(\xi, \eta)}{\partial \xi} y_i \quad (\text{B.10b})$$

$$J_{21} = \frac{\partial x}{\partial \eta} = \sum_{i=1}^4 \frac{\partial H_i(\xi, \eta)}{\partial \eta} x_i \quad (\text{B.10c})$$

$$J_{22} = \frac{\partial y}{\partial \eta} = \sum_{i=1}^4 \frac{\partial H_i(\xi, \eta)}{\partial \eta} y_i \quad (\text{B.10d})$$

$$J_{11} = -\frac{1}{4}(1-\eta)x_1 + \frac{1}{4}(1-\eta)x_2 + \frac{1}{4}(1+\eta)x_3 - \frac{1}{4}(1+\eta)x_4 \quad (\text{B.11a})$$

$$J_{12} = -\frac{1}{4}(1-\eta)y_1 + \frac{1}{4}(1-\eta)y_2 + \frac{1}{4}(1+\eta)y_3 - \frac{1}{4}(1+\eta)y_4 \quad (\text{B.11b})$$

$$J_{21} = -\frac{1}{4}(1-\xi)x_1 + \frac{1}{4}(1+\xi)x_2 + \frac{1}{4}(1+\xi)x_3 - \frac{1}{4}(1-\xi)x_4 \quad (\text{B.11c})$$

$$J_{22} = -\frac{1}{4}(1-\xi)y_1 + \frac{1}{4}(1+\xi)y_2 + \frac{1}{4}(1+\xi)y_3 - \frac{1}{4}(1-\xi)y_4 \quad (\text{B.11d})$$

$$J_{11} = \frac{1}{4}[(1 - \eta)(x_2 - x_1) + (1 + \eta)(x_3 - x_4)] \quad (\text{B.12a})$$

$$J_{12} = \frac{1}{4}[(1 - \eta)(y_2 - y_1) + (1 + \eta)(y_3 - y_4)] \quad (\text{B.12b})$$

$$J_{21} = \frac{1}{4}[(1 - \xi)(x_4 - x_1) + (1 + \xi)(x_3 - x_2)] \quad (\text{B.12c})$$

$$J_{22} = \frac{1}{4}[(1 - \xi)(y_4 - y_1) + (1 + \xi)(y_3 - y_2)] \quad (\text{B.12d})$$

This leads to a more precise form of the Jacobian,

$$\begin{aligned} |J| = & A + (x_1y_4 - x_1y_3 + x_2y_3 + x_4y_2 - x_2y_4 + x_3y_1 - x_4y_1 - x_3y_2)\xi \\ & + (x_4y_2 - x_3y_1 + x_1y_3 - x_1y_2 - x_2x_4 + x_3y_4 + x_2y_1 - x_4y_3)\eta, \end{aligned} \quad (\text{B.13})$$

or

$$|J| = \frac{1}{8}[2A + (\vec{12} \times \vec{43})\xi + (\vec{23} \times \vec{14})\eta], \quad (\text{B.14})$$

where the area,  $A$ , is given by the cross product

$$A = \frac{1}{2}(\vec{13} \times \vec{24}). \quad (\text{B.15})$$



## APPENDIX C

### VISUALIZATION

Many of the two-dimensional numerical results in the work have been presented in the form of Schlierens and interferograms. Such visualization techniques not only accentuate key flow features such as strong gradients but also allow direct comparison with experimental results (see Figure C.1).

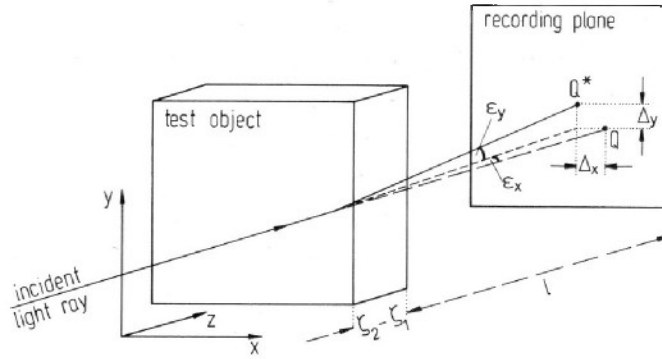


Figure C.1: Generalized visualization setup and geometric reference. Taken from [77].

Such techniques are based on gradients of the refractive index of the fluid and for a plasma, the electron contribution is significant and must be accounted for. The composite refractive index can be found from a linear combination of all species<sup>1</sup>,

$$n - 1 = \sum \rho_i K_i \quad (\text{C.1})$$

For a singly-ionized, monatomic plasma, we have

$$n - 1 = \rho \{ (1 - \alpha) K_a + \alpha K_i \} + N_e K'_e \quad (\text{C.2})$$

<sup>1</sup>Here  $n$  is used to denote the refractive index while  $N$  denotes the number density.

and specifically for argon, we have  $K_{Ar^+} = \frac{2}{3}K_{Ar}$  ([77]),

$$n - 1 = \rho K(1 - \alpha/3) - 4.46 \times 10^{-16} \lambda^2 N_e \quad (\text{C.3})$$

with the electronic refractive index,

$$n_e - 1 = -4.46 \times 10^{-16} \lambda^2 N_e \quad (\text{C.4})$$

With the refractive index computed from a numerical snapshot, a simulated interferogram can easily be calculated from

$$\frac{\Delta\phi}{2\pi} = \frac{1}{\lambda} \int_{\zeta_1}^{\zeta_2} \{n(x, y, z) - n_\infty\} dz. \quad (\text{C.5})$$

Alternatively, the refractive index can be used to construct a simulated Schlieren by computing its gradient throughout the flowfield by

$$\frac{\Delta I}{I} = \int_{\zeta_1}^{\zeta_2} \frac{1}{n} \frac{\partial n}{\partial y} dz. \quad (\text{C.6})$$

## APPENDIX D

### IMPLICIT CR FORMULATION

The collisional-radiative source term is integrated independently of the convective terms at each time step, assuming the conserved variables to be frozen within the time step. The governing equations for the CR kinetics then reduce to a system of ODE's,

$$\left(\frac{dQ}{dt}\right)_{CR} = \dot{\Omega}, \quad (\text{D.1})$$

that can be integrated in time using a standard Euler implicit method,

$$\left(\frac{\Delta Q}{\Delta t}\right)_{CR} = \dot{\Omega}^{n+1}. \quad (\text{D.2})$$

Upon expanding the RHS via a Taylor series expansion,

$$\left(\frac{\Delta Q}{\Delta t}\right)_{CR} = \dot{\Omega}^n + \frac{\partial \dot{\Omega}^n}{\partial Q^n} (Q^{n+1} - Q^n) \quad (\text{D.3})$$

an expression is obtained for that change in conserved quantities<sup>1</sup>,

$$\Delta Q = (I - \Delta t J)^{-1} \Delta t \dot{\Omega}, \quad (\text{D.4})$$

with the Jacobian,

$$J = \frac{\partial \dot{\Omega}}{\partial Q}. \quad (\text{D.5})$$

As was done for the case of heat conduction<sup>2</sup>, the source term may be expressed as a

---

<sup>1</sup>Note that the subscript  $n$  has been dropped.

<sup>2</sup>To facilitate derivation of the stability condition (see Chapter 7)

matrix-vector product,

$$\dot{\Omega} = \Phi Q \quad (\text{D.6})$$

such that the Jacobian can also be written as

$$J = \frac{\partial(\Phi Q)}{\partial Q} \quad (\text{D.7})$$

$$= \Phi + \frac{\partial \Phi}{\partial Q} Q \quad (\text{D.8})$$

$$= \Phi + \Psi, \quad (\text{D.9})$$

the elements of which take on the following form,

$$J = \left( \begin{array}{ccc|cc} \ddots & \vdots & \ddots & \vdots & \vdots \\ \dots & \frac{\partial \dot{\omega}_{n_i}}{\partial n_j} & \dots & \frac{\partial \dot{\omega}_{n_i}}{\partial E_h} & \frac{\partial \dot{\omega}_{n_i}}{\partial E_e} \\ \ddots & \vdots & \ddots & \vdots & \vdots \\ \hline \dots & \frac{\partial \dot{\omega}_{E_h}}{\partial n_j} & \dots & \frac{\partial \dot{\omega}_{E_h}}{\partial E_h} & \frac{\partial \dot{\omega}_{E_h}}{\partial E_e} \\ \dots & \frac{\partial \dot{\omega}_{E_e}}{\partial n_j} & \dots & \frac{\partial \dot{\omega}_{E_e}}{\partial E_h} & \frac{\partial \dot{\omega}_{E_e}}{\partial E_e} \end{array} \right). \quad (\text{D.10})$$

This leads to a natural block matrix decomposition of the Jacobian,

$$J = \begin{pmatrix} J^{(1)} & J^{(2)} \\ J^{(3)} & J^{(4)} \end{pmatrix} = \begin{pmatrix} \Phi^{(1)} & \Phi^{(2)} \\ \Phi^{(3)} & \Phi^{(4)} \end{pmatrix} + \begin{pmatrix} \Psi^{(1)} & \Psi^{(2)} \\ \Psi^{(3)} & \Psi^{(4)} \end{pmatrix} \quad (\text{D.11})$$

In what follows, the form of matrix  $\Phi$  is given along with the components of the Jacobian  $J$ . The matrix  $\Psi$  can be found by subtracting  $\Phi$  from  $J$ . It is emphasized here that the rates associated with ionization and recombination processes are functions of  $j_c$ , such that

$$S_i, O_i, W_i, V_i, R_i = f(j_c). \quad (\text{D.12})$$

Also, the electron density is given from consideration of charge neutrality,  $n_e = n_{Ar^+(j_c=3/2)} + n_{Ar^+(j_c=1/2)}$ .

Sub-matrices of  $\Phi$

$$\Phi^{(2)} = \begin{pmatrix} & & \\ & \vdots & \vdots \\ & 0 & 0 \\ & \vdots & \vdots \end{pmatrix} \quad (\text{D.13})$$

$$\Phi^{(4)} = \begin{pmatrix} n_e \frac{2m_e}{m_{Ar}} ((\alpha - 1)k_{en} - \alpha k_{ei}) & \frac{2m_e}{m_{Ar}} (n_n k_{en} + n_e k_{ei}) \\ -n_e \frac{2m_e}{m_{Ar}} ((\alpha - 1)k_{en} - \alpha k_{ei}) & -\frac{2m_e}{m_{Ar}} (n_n k_{en} + n_e k_{ei}) \\ & -9.5 \times 10^{-41} \frac{n_e Z_{\text{eff}}^2}{(k_B T_e)^{1/2}} \end{pmatrix}, \quad \alpha = \frac{n_e}{n_h} \quad (\text{D.14})$$

$$\Phi^{(1)} = \begin{pmatrix}
-\sum_{i \neq 1} A_{i1}^{(1)} & n_e F_{21} + n_1 L_{21} & n_e F_{31} + n_1 L_{31} & n_e F_{41} + n_1 L_{41} & n_e (n_1 W_1 & n_e (n_1 W_1 \\
& + A_{21} & + A_{31} & + A_{41} & + n_e O_1 + R_1) \\
n_e C_{12} + n_1 K_{12} & -\sum_{i \neq 2} \Phi_{i2}^{(1)} & n_e F_{32} + n_1 L_{32} & n_e F_{42} + n_1 L_{42} & n_e (n_1 W_2 & n_e (n_1 W_2 \\
+ (1 - \Lambda_{21}) A_{21} & & + A_{32} & + A_{42} & + n_e O_2 + R_2) \\
n_e C_{13} + n_1 K_{13} & n_e C_{23} + n_1 K_{23} & -\sum_{i \neq 3} \Phi_{i3}^{(1)} & n_e F_{43} + n_1 L_{43} & n_e (n_1 W_3 & n_e (n_1 W_3 \\
+ (1 - \Lambda_{31}) A_{31} & + (1 - \Lambda_{32}) A_{32} & & + A_{43} & + n_e O_3 + R_3) \\
n_e C_{14} + n_1 K_{14} & n_e C_{24} + n_1 K_{24} & n_e C_{34} + n_1 K_{34} & -\sum_{i \neq 4} \Phi_{i4}^{(1)} & n_e (n_1 W_4 & n_e (n_1 W_4 \\
+ (1 - \Lambda_{41}) A_{41} & + (1 - \Lambda_{42}) A_{42} & + (1 - \Lambda_{42}) A_{42} & & + n_e O_4 + R_4) \\
n_e S_1 + n_1 V_1 & n_e S_2 + n_1 V_2 & n_e S_3 + n_1 V_3 & n_e S_4 + n_1 V_4 & -\sum_{i \neq 5} \Phi_{i5}^{(1)} & 0 \\
+ (1 - \Lambda_i) R_1 & + (1 - \Lambda_i) R_2 & + (1 - \Lambda_i) R_3 & + (1 - \Lambda_i) R_4 & & \\
n_e S_1 + n_1 V_1 & n_e S_2 + n_1 V_2 & n_e S_3 + n_1 V_3 & n_e S_4 + n_1 V_4 & 0 & -\sum_{i \neq 6} \Phi_{i6}^{(1)} \\
+ (1 - \Lambda_i) R_1 & + (1 - \Lambda_i) R_2 & + (1 - \Lambda_i) R_3 & + (1 - \Lambda_i) R_4 & & 
\end{pmatrix}$$

(D.15)

$$\Phi^{(3)} = \begin{pmatrix}
-n_1 \sum_{j>1} \varepsilon_{1j} K_{1j} & n_1 \sum_{i<2} \varepsilon_{i2} L_{2i} & n_1 \sum_{i<3} \varepsilon_{i3} L_{3i} & n_1 \sum_{i<4} \varepsilon_{i4} L_{4i} & n_1 n_e \sum_k I_k W_k & n_1 n_e \sum_k I_k W_k \\
-n_1 I_1 V_1 & -n_1 \sum_{j>2} \varepsilon_{2j} K_{2j} & -n_1 \sum_{j>3} \varepsilon_{3j} K_{3j} & -n_1 I_4 V_4 & n_1 n_e \sum_k I_k W_k & n_e n_e \sum_k I_k O_k \\
-n_1 I_2 V_2 & -n_1 I_2 V_2 & -n_1 I_3 V_3 & n_e \sum_{i<2} \varepsilon_{i2} F_{2i} & n_e n_e \sum_k I_k O_k & n_e n_e \sum_k I_k O_k \\
-n_e \sum_{j>1} \varepsilon_{1j} C_{1j} & -n_e \sum_{j>2} \varepsilon_{2j} C_{2j} & -n_e \sum_{j>3} \varepsilon_{3j} C_{3j} & -n_e I_4 S_4 & -n_e R'_k & -n_e R'_k \\
-n_e I_1 S_1 & -n_e I_2 S_2 & -n_e I_3 S_3 & -n_e I_4 S_4 & -n_e R'_k & -n_e R'_k
\end{pmatrix} \quad (\text{D.16})$$

## D.1 Jacobian Elements

$$\frac{\partial \dot{\omega}_{Ar^+}}{\partial n_1} = n_1 V_1 + \sum_k n_k V_k + n_e S_1 - n_e \sum_k n_{Ar^+} W_k + (1 - \Lambda_1) R_1 \quad (D.17)$$

$$\begin{aligned} \frac{\partial \dot{\omega}_{i>1}}{\partial n_1} = & \sum_{k<i} (n_k K_{ki} - n_i K_{ik}) + \sum_{k>i} (n_k L_{ki} \\ & + n_1 K_{1i} - n_i K_{ik}) - n_i V_i + n_e n_{Ar^+} W_i + n_e C_{1i} + n_1 K_{1i} + (1 - \Lambda_{i1}) A_{i1} \end{aligned} \quad (D.18)$$

$$\frac{\partial \dot{\omega}_{Ar^+(j_c)}}{\partial n_{j>1}} = n_e S_j(j_c) + n_1 V_j + (1 - \Lambda_j) R_j \quad (D.19)$$

$$\frac{\partial \dot{\omega}_i}{\partial n_{j>1}} = n_e F_{ji} + n_1 L_{ji} + A_{ji} \quad (D.20)$$

$$\frac{\partial \dot{\omega}_{i>j}}{\partial n_{j>1}} = n_e C_{ji} + n_1 K_{ji} + (1 - \Lambda_{ij}) A_{ij} \quad (D.21)$$

$$\begin{aligned} \frac{\partial \dot{\omega}_i}{\partial n_{Ar^+}} = & \sum_{k>i} (n_k F_{ki} - n_i C_{ik}) + \sum_{k<i} (n_k C_{ki} - n_i F_{ik}) \\ & + 2n_e n_{Ar^+} O_i + n_{Ar^+} R_i - n_1 S_i + n_1 n_{Ar^+} W_i + n_e^2 O_i + n_e R_i + n_1 n_e W_i \end{aligned} \quad (D.22)$$

$$\begin{aligned} \frac{\partial \dot{\omega}_{E_e}}{\partial n_j} = & n_+ \sum_{k<j} \varepsilon_{kj} F_{jk} - n_+ \sum_{k>j} \varepsilon_{jk} C_{jk} - n_+ S_j \varepsilon_j \\ & + 3\rho_e k_B (T_h - T_e) \frac{k_{en}}{m_j} + \sum_i ((1 - \Lambda_i) R'_i) \end{aligned} \quad (D.23)$$



$$\begin{aligned} \frac{\partial \dot{\omega}_{E_e}}{\partial n_+} = & \sum_k \varepsilon_k (3n_+^2 O_k - n_k S_k) + \sum_i \sum_{j>i} \varepsilon_{ij} (n_j F_{ji} - n_i C_{ij}) \\ & + 3\rho_e k_B (T_h - T_e) \frac{\bar{k}_{ei}}{m_{Ar^+}} - 2n_e \sum_i R'_i \quad (D.24) \end{aligned}$$

$$\begin{aligned} \frac{\partial \dot{\omega}_{E_e}}{\partial E_e} = & \frac{2}{3} \frac{1}{k_B} \sum_i \sum_{j>i} \varepsilon_{ij} \left( n_j \frac{\partial F_{ji}}{\partial T_e} - n_i \frac{\partial C_{ij}}{\partial T_e} \right) + \frac{2}{3} \frac{1}{k_B} \sum_i \varepsilon_i \left( n_e n_+ \frac{\partial O_i}{\partial T_e} - n_i \frac{\partial S_i}{\partial T_e} \right) \\ & + n_n \frac{2m_e}{m_{Ar}} \left( (T_h - T_e) \frac{\partial k_{en}}{\partial T_e} - k_{en} \right) + n_e \frac{2m_e}{m_{Ar^+}} \left( (T_h - T_e) \frac{\partial \bar{k}_{ei}}{\partial T_e} - \bar{k}_{ei} \right) \\ & + \sum_i \left( (n_i(1 - \Lambda_i) - n_e n_+) \frac{\partial R'_i}{\partial T_e} \frac{2}{3} \frac{1}{n_e k_B} \right) - 4.75 \times 10^{-41} \frac{Z_{\text{eff}}^2}{k_B T_e^{1/2}} n_+ \quad (D.25) \end{aligned}$$

$$\frac{\partial \dot{\omega}_{E_e}}{\partial E_h} = \frac{n_e n_n}{n_h} \frac{2m_e}{m_{Ar}} k_{en} + \frac{n_e^2}{n_h} \frac{2m_e}{m_{Ar^+}} \bar{k}_{ei} \quad (D.26)$$

$$\begin{aligned} \frac{\partial \dot{\omega}_{E_h}}{\partial n_1} = & \sum_i \sum_{j>i} \varepsilon_{ij} (n_j L_{ji} - n_i K_{ij}) - \sum_{j>1} \varepsilon_{1j} (n_1 K_{1j}) \\ & + \sum_i \varepsilon_i (n_e n_+ W_i - n_i V_i) - n_1 V_1 \varepsilon_1 \\ & - \frac{3}{2} n_e k_B (T_h - T_e) \frac{2m_e}{m_{Ar}} k_{en} \quad (D.27) \end{aligned}$$

$$\frac{\partial \dot{\omega}_{E_h}}{\partial n_k} = n_1 \sum_{i<k} L_{ki} \varepsilon_{ik} - n_1 \sum_{j>k} K_{kj} \varepsilon_{kj} - n_1 V_k \varepsilon_k - \frac{3}{2} n_e k_B (T_h - T_e) \frac{2m_e}{m_{Ar}} k_{en} \quad (D.28)$$

$$\frac{\partial \dot{\omega}_{E_h}}{\partial n_+} = 2n_1 n_+ \sum_i \varepsilon_i W_i - \frac{3}{2} n_n k_B (T_h - T_e) \frac{2m_e}{m_{Ar}} k_{en} - 3n_e k_B (T_h - T_e) \frac{2m_e}{m_{Ar^+}} \bar{k}_{ei} \quad (D.29)$$

$$\begin{aligned} \frac{\partial \dot{W}_{E_h}}{\partial E_e} = & \frac{2n_1 n_+^2}{3k_B} \sum_i \varepsilon_i \frac{\partial W_i}{\partial T_e} - n_n \frac{2m_e}{m_{Ar}} \left( (T_h - T_e) \frac{\partial k_{en}}{\partial T_e} - k_{en} \right) \\ & - n_e \frac{2m_e}{m_{Ar^+}} \left( (T_h - T_e) \frac{\partial \bar{k}_{ei}}{\partial T_e} - \bar{k}_{ei} \right) \end{aligned} \quad (D.30)$$

$$\begin{aligned} \frac{\partial \dot{W}_{E_h}}{\partial E_h} = & \frac{2n_1}{3k_B} \sum_i \sum_{j>i} \varepsilon_{ij} \left( n_j \frac{\partial L_{ji}}{\partial T_h} - n_i \frac{\partial K_{ij}}{\partial T_h} \right) \\ & + \frac{2n_1}{3k_B} \sum_i \varepsilon_i \left( n_e n_+ \frac{\partial W_i}{\partial T_h} - n_i \frac{\partial V_i}{\partial T_h} \right) \\ & - \frac{n_e n_n}{n_h} \frac{2m_e}{m_{Ar}} k_{en} - \frac{n_e^2}{n_h} \frac{2m_e}{m_{Ar^+}} \bar{k}_{ei} \end{aligned} \quad (D.31)$$

## D.2 Conditioning

Note that matrices  $J^{(1)}$  and  $J^{(4)}$  are nondimensional. This is an ideal situation for optimal numerical condition of the Jacobian matrix. Matrices  $J^{(2)}$  and  $J^{(3)}$ , however, have units of Joules and Joules<sup>-1</sup>, respectively, which may lead to an ill-conditioned Jacobian under certain conditions. To remedy this, these matrices are normalized by a scaling factor which leaves the Jacobian well-conditioned for numerical inversion while simultaneously maintaining diagonal dominance<sup>3</sup>. The scaling factor, which can be thought of as an idealized energy unit, takes the form

$$SF = \left( \frac{\max J^{(2)}}{\max J^{(3)}} \right)^{1/2} \quad (D.32)$$

which is used to update  $J^{(2)}$  and  $J^{(3)}$  according to

$$J^{(2)} \rightarrow J^{(2)} / SF \quad (D.33)$$

$$J^{(3)} \rightarrow J^{(3)} \cdot SF. \quad (D.34)$$

---

<sup>3</sup>A necessary condition for Gaussian elimination without partial pivoting.

In addition, the energy source terms Eqs. (??) must also be transformed,

$$\dot{\omega}_{E_h} \rightarrow \dot{\omega}_{E_h} \cdot SF \quad (\text{D.35})$$

$$\dot{\omega}_{E_e} \rightarrow \dot{\omega}_{E_e} \cdot SF. \quad (\text{D.36})$$

Once the changes in the heavy particle and electron energies have been obtained, the units are transformed back to Joules via

$$\Delta E_h \rightarrow \Delta E_h / SF \quad (\text{D.37})$$

$$\Delta E_e \rightarrow \Delta E_e / SF. \quad (\text{D.38})$$

## APPENDIX E

### ADDITIONAL STEADY-STATE RESULTS

Results of the Mach 16.1, 16.5, and 13.0 ionizing shock test cases as computed under steady-state conditions are provided here.

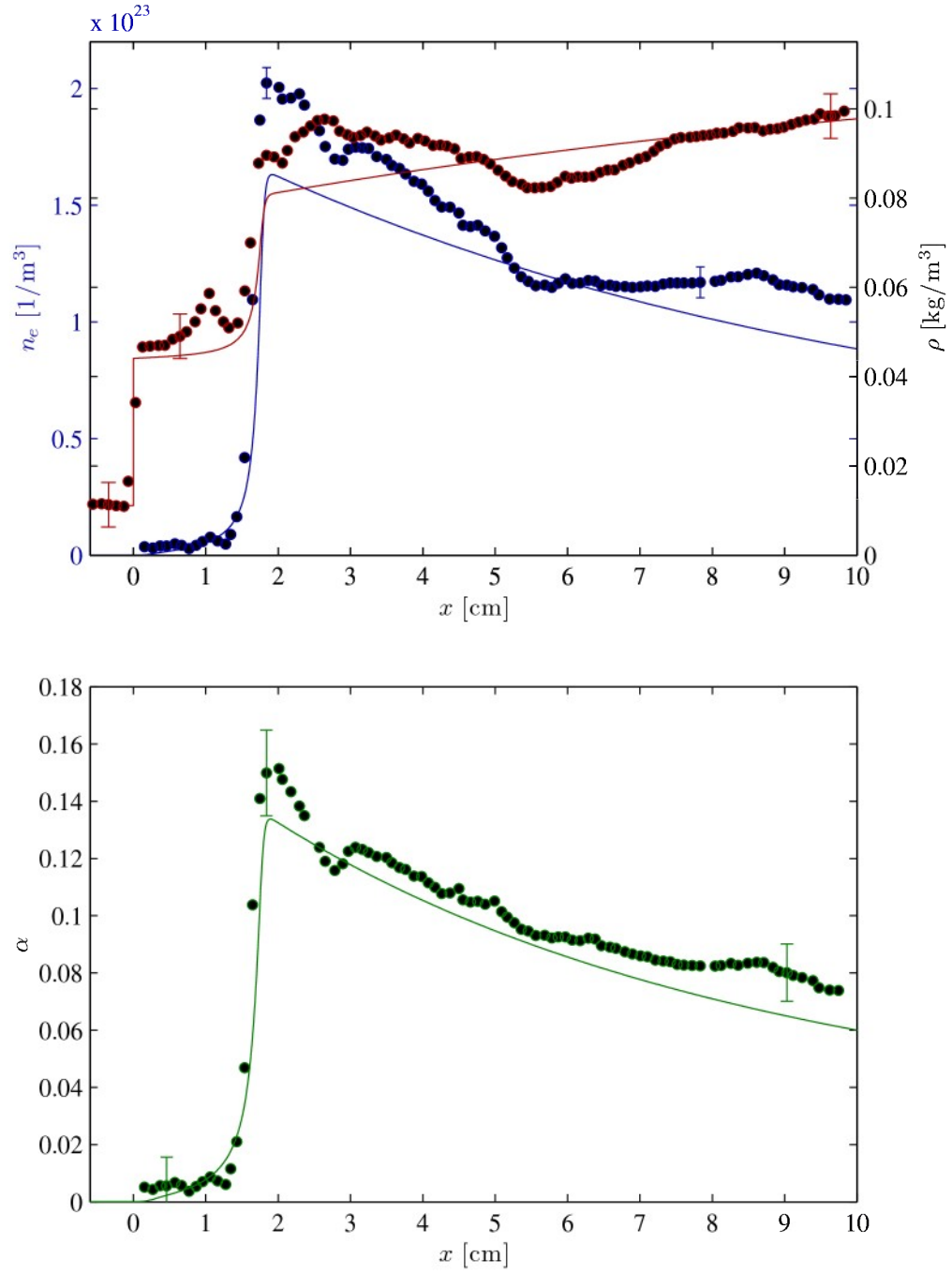


Figure E.1: Ionizing shock structure as detailed by (a)  $\rho$  and  $n_e$ , and (b)  $\alpha$  for case 2:  $p_o = 5.15 \text{ torr}$ ,  $T_o = 295.9 \text{ K}$ ,  $\text{Ma} = 16.1$ .

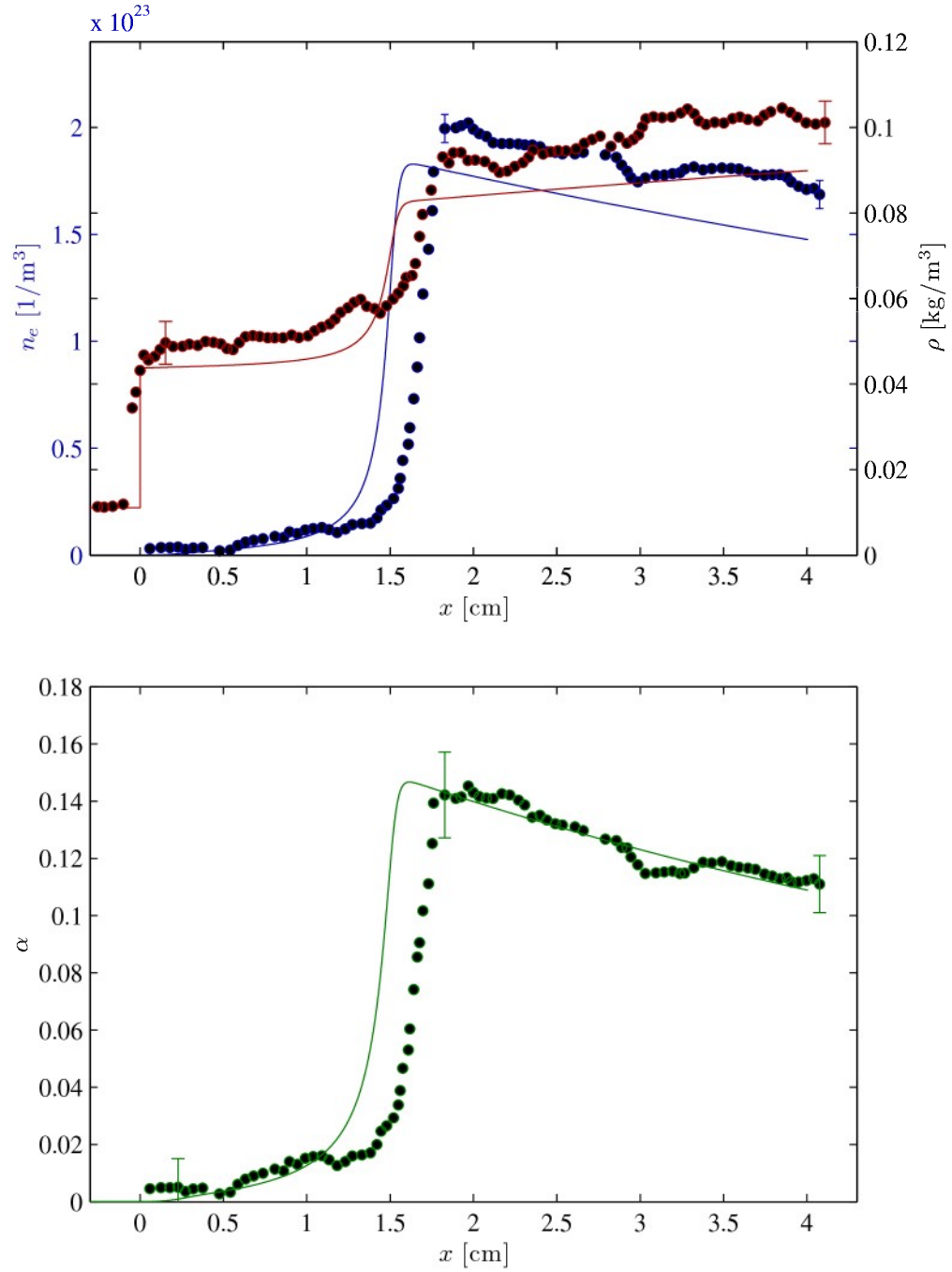


Figure E.2: Ionizing shock structure as detailed by (a)  $\rho$  and  $n_e$ , and (b)  $\alpha$  for case 3:  $p_o = 5.12$  torr,  $T_o = 296.6$  K,  $Ma = 16.5$ .

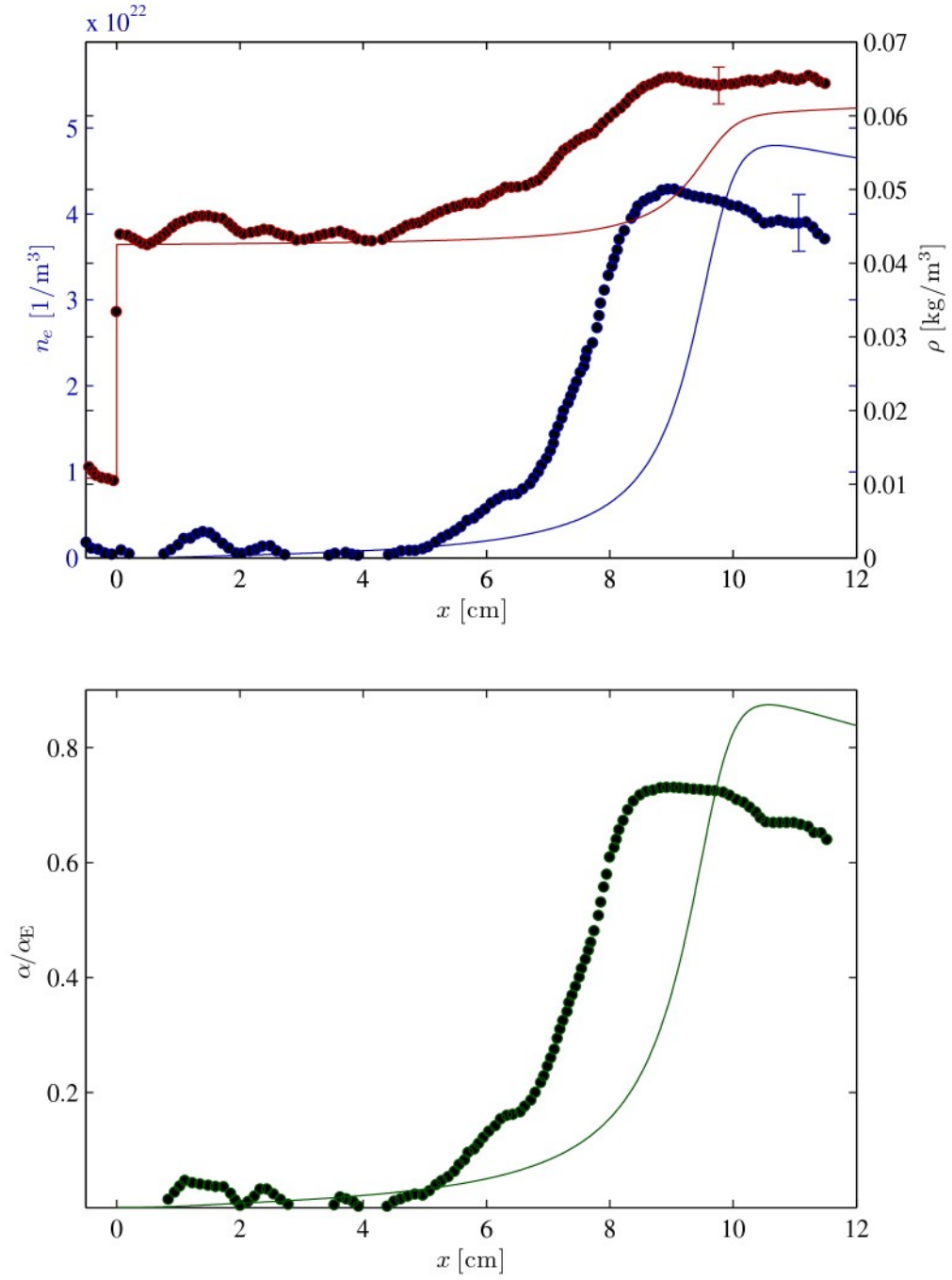


Figure E.3: Ionizing shock structure as detailed by (a)  $\rho$  and  $n_e$ , and (b)  $\alpha$  for case 4:  $p_o = 5.01$  torr,  $T_o = 296.6$  K,  $\text{Ma} = 13.0$ .

## Bibliography

- [1] H. Alfvén. On the existence of electromagnetic-hydrodynamic waves. *Arkiv för Matematik, Astronomie, och Fysik*, 29B(2):1–7, 1943.
- [2] R. L. Alpert and T. Y. Toong. Periodicity in exothermic hypersonic flows about blunt projectiles. *Acta Astronautica*, 17:538–560, 1972.
- [3] M. Arora and P. L. Roe. On postshock oscillations due to shock capturing schemes. *Journal of Computational Physics*, 130(1):25–40, 1997.
- [4] P. Atkins. *Physical Chemistry*. W. H. Freeman and Company, New York, sixth edition, 1998.
- [5] G. R. Baker and E. A. Overman II. *The Art of Scientific Computing*. The Ohio State University Bookstore, Columbus, draft xii edition, 2006.
- [6] T. J. Barth. Numerical methods for gasdynamic systems. In D. Kroner, M. Ohlberger, and C. Rohde, editors, *An Introduction to Recent Developments in Theory and Numerics for Conservation Laws*, pages 195–285. Springer-Verlag, New York/Berlin, first edition, 1999.
- [7] D. R. Bates, A. E. Kingston, and R. W. P. McWhirter. Recombination between electrons and atomic ions. I: Optically thin plasmas. *Proceedings of the Royal Society A*, 267:297–312, 1962.
- [8] D. R. Bates, A. E. Kingston, and R. W. P. McWhirter. Recombination between electrons and atomic ions. II: Optically thick plasmas. *Proceedings of the Royal Society A*, 270:155–167, 1962.



- [9] D. R. Bates, A. E. Kingston, and R. W. P. McWhirter. Collisional-radiative recombination at low temperatures and densities. *Proceedings of the Royal Society A*, 83:43–47, 1964.
- [10] T. V. Bazhenova, L. G. Gvozdeva, and M. G. Nettleton. Unsteady interaction of shock waves. *Aerosp. Sci.*, 21:249–331, 1984.
- [11] L. M. Biberman and I. T. Yakubov. Approach to ionization equilibrium behind the front of a shock wave in an atomic gas. *Soviet Physics-Technical Physics (English Translation)*, 8:1001–1007, 1964.
- [12] J. B. Boffard, G. A. Piech, M. F. Gehrke, L. W. Anderson, and C. C. Lin. Measurement of electron-impact excitation cross sections out of metastable levels of argon and comparison with ground-state excitation. *Physical Review A*, 59(4):2749–2763, 1999.
- [13] I. N. Bogatu, D. H. Edgell, J. S. Kim, R. C. Pardo, and R. Vondrasek. Argon ionization cross sections for charge state distribution modeling in electron cyclotron resonance ion source. *Review of Scientific Instruments*, 73(2):638–640, 2002.
- [14] J. U. Brackbill and D. C. Barnes. The effect of nonzero  $\nabla \cdot \mathbf{B}$  on the numerical solution of the magnetohydrodynamic equations. *Journal of Computational Physics*, 35:426–430, 1980.
- [15] S. Brassier and G. Gallice. A Roe scheme for the bi-temperature model of magnetohydrodynamics. *Computers and Mathematics with Applications*, 41:257–267, 1998.
- [16] P. I. Brimelow. An interferometric investigation of shock structure and its induced shock-tube boundary layer in ionized argon. Technical Report 187, UTIAS, July 1974.
- [17] M. Brio and C. C. Wu. An upwind differencing scheme for the equations of ideal magnetohydrodynamics. *Journal of Computational Physics*, 75:400–422, 1987.
- [18] M. P. F. Bristow and I. I. Glass. Polarizability of singly ionized argon. *Physics of Fluids*, 15(11):2066–2067, 1972.
- [19] A. Bultel, B. van Ootegem, A. Bourdon, and P. Vervisch. Influence of  $\text{Ar}_2^+$  in an argon collisional-radiative model. *Physical Review E*, 65:1–16, 2002.

- [20] J.-L. Cambier. Numerical methods for TVD transport and coupled relaxing processes in gases and plasmas. In *Proceedings of the 21st Fluid Dynamics, Plasma Dynamics, and Lasers Conference*, Seattle, WA, June 1990. AIAA.
- [21] J.-L. Cambier. Numerical simulations of a nonequilibrium argon plasma in a shock-tube experiment. In *Proceedings of the 22nd Fluid Dynamics, Plasma Dynamics, and Lasers Conference*, Honolulu, HI, June 1991. AIAA.
- [22] J.-L. Cambier, M. Carroll, and M. Kapper. Development of a hybrid model for non-equilibrium high-energy plasmas. In *Proceedings of the 35th Plasmadynamics and Lasers Conference*, Portland, OR, June 2004. AIAA.
- [23] J.-L. Cambier and S. Moreau. Simulations of a molecular plasma in collisional-radiative nonequilibrium. In *Proceedings of the 24th Plasmadynamics and Lasers Conference*, Orlando, FL, July 1993. AIAA.
- [24] J. P. Cocchi, R. Saurel, and J. C. Loraud. Some remarks about the resolution of high velocity flows near low density. *Shock Waves*, 8:119–125, 1998.
- [25] P. Colella and P. R. Woodward. The piecewise parabolic method (PPM) for gas-dynamical simulations. *Journal of Computational Physics*, 54:174, 1984.
- [26] R. Courant and K. O. Friedrichs. *Supersonic Flow and Shock Waves*. Interscience Publishers, Inc., New York, third edition, 1961.
- [27] T. G. Cowling. *Magnetohydrodynamics*. Interscience Publishers, Inc., New York, first edition, 1957.
- [28] R. K. Crockett, P. Colella, R. T. Fisher, R. I. Klein, and C. F. McKee. An unsplit, cell-centered Godunov method for ideal MHD. *Journal of Computational Physics*, 203(2):422–448, 2005.
- [29] W. Dai and P. R. Woodward. Extension of the piecewise parabolic method (PPM) to multidimensional magnetohydrodynamics. *Journal of Computational Physics*, 111:354, 1994.

- [30] W. Dai and P. R. Woodward. On the divergence-free condition and conservation laws in numerical simulations for supersonic magnetohydrodynamic flows. *The Astrophysical Journal*, 494:317, 1998.
- [31] W. Dai and P. R. Woodward. A simple finite-difference scheme for multidimensional magnetohydrodynamic equations. *Journal of Computational Physics*, 142:331, 1998.
- [32] P. J. Davis. *Circulant Matrices*. AMS Chelsea Publishing Company, New York, second edition, 1994.
- [33] P. Deb and R. Agarwal. Numerical study of compressible viscous MHD equations with a bi-temperature model for supersonic blunt body flows. In *AIAA 38th Aerospace Sciences Meeting and Exhibit, Reno NV, January 10–13, 2000*, January 2000.
- [34] H. Deutsch, K. Becker, A. N. Grum-Grzhimailo, K. Bartschat, H. Summers, M. Probst, S. Matt-Leubner, and T. D. Mark. Calculated cross sections for the electron-impact ionization of excited argon atoms using the DM formalism. *International Journal of Mass Spectrometry and Ion Processes*, 233:39–43, 2004.
- [35] H. Deutsch, K. Becker, S. Matt, and T. D. Mark. Theoretical determination of absolute electron-impact ionization cross sections of molecules. *International Journal of Mass Spectrometry and Ion Processes*, 197:37–69, 2000.
- [36] M. Van Dyke. *An Album of Fluid Motion*. The Parabolic Press, Stanford, tenth edition, 2005.
- [37] B. Einfeldt, C. D. Munz, P. L. Roe, and B. Sjogreen. On Godunov-type methods near low densities. *Journal of Computational Physics*, 92:273–295, 1991.
- [38] C. R. Evans and J. F. Hawley. Simulation of magnetohydrodynamic flows: A constrained transport method. *The Astrophysical Journal*, 332:659, 1988.
- [39] W. Fickett and W. C. Davis. *Detonation*. University of California Press, Berkeley, first edition, 1972.
- [40] H. H. Fleischmann and R. C. Dehmelt. On Drawin’s formula for ionization in atom-atom collisions. *Zeitschrift für Physik*, 252:435–442, 1972.

- [41] A. I. Gavrikov, A. A. Efimenko, and S. B. Dorofeev. A model for detonation cell size prediction from chemical kinetics. *Combustion and Flame*, 120:19–33, 2000.
- [42] I. I. Glass and W. S. Liu. Effects of hydrogen impurities on shock structure and stability in ionizing monatomic gases. Part 1. Argon. *Journal of Fluid Mechanics*, 84:55–77, 1978.
- [43] R. M. Gray. *Toeplitz and Circulant Matrices: A Review*. Now Publishers, Norwell, Massachusetts, first edition, 2006.
- [44] H. R. Griem. *Plasma Spectroscopy*. McGraw-Hill, Inc., New York, first edition, 1964.
- [45] W. Grosso. *Java RMI*. O'Reilly & Associates, Inc., New York, 2002.
- [46] A. Harten. High resolution schemes for hyperbolic conservation laws. *Journal of Computational Physics*, 49:357–393, 1983.
- [47] A. Harten. On a class of high resolution total-variation-stable finite-difference methods. *SIAM Journal on Numerical Analysis*, 21:1–23, 1984.
- [48] A. Harten. ENO schemes with subcell resolution. *Journal of Computational Physics*, 83:148–184, 1989.
- [49] K. E. Harwell and R. C. Jahn. Initial ionization rates in shock-heated argon, krypton, and xenon. *Physics of Fluids*, 7(2):214–222, 1964.
- [50] P. Haugsjaa and R. Amme. Ionization and metastable excitation in low-energy collisions of ground-state argon atoms. *Journal of Chemical Physics*, 52(9):4874–4877, 1970.
- [51] X. Y. Hu and B. C. Khoo. Kinetic energy fix for low internal energy flows. *Journal of Computational Physics*, 193:243–259, 2003.
- [52] H. T. Huynh. Accurate monotone cubic interpolation. *SIAM Journal on Numerical Analysis*, 30(1):57–100, 1993.
- [53] H. T. Huynh. Accurate upwind methods for the Euler equations. *SIAM Journal on Numerical Analysis*, 32(5):1565–1619, 1995.

- [54] H. T. Huynh. *Schemes and Constraints for Advection*, volume 490 of *Lecture Notes in Physics*, pages 498–503. Springer, Berlin, 1997.
- [55] P. Hyde. *Java thread programming*. Howard W. Sams, New York, 2000.
- [56] Jr. J. D. Anderson. *Hypersonic and High Temperature Gas Dynamics*. McGraw-Hill Book Company, San Francisco, first edition, 1989.
- [57] A. Jeffrey. *Applied Partial Differential Equations*. Academic Press, San Diego, first edition, 2003.
- [58] A. Jeffrey and T. Taniuti. *Non-Linear Wave Propagation*. Academic Press, New York, first edition, 1964.
- [59] K. Katsonis and H. W. Drawin. Transition probabilities for argon(I). *Journal of Quantitative Spectroscopy and Radiative Transfer*, 23:1–55, 1980.
- [60] A. J. Kelly. Atom-atom ionization cross sections of the noble gases—argon, krypton, and xenon. *Journal of Chemical Physics*, 45(5):1723–1732, 1966.
- [61] A. Kimura, H. Kobayashi, M. Nishida, and P. Valentin. Transition probabilities for argon(I). *Journal of Quantitative Spectroscopy and Radiative Transfer*, 34:189–215, 1985.
- [62] S. Kudriakov and W. H. Hui. On a new defect of shock-capturing schemes. *Journal of Computational Physics*, 227:2105–2117, 2008.
- [63] K. K. Kuo. *Principles of Combustion*. John Wiley & Sons, Inc., New Jersey, second edition, 2005.
- [64] H. F. Lehr. Experiments on shock-induced combustion. *Acta Astronautica*, 17:589–597, 1972.
- [65] G. Lin and E. Karniadakis. A discontinuous Galerkin method for two-temperature plasmas. *Computer Methods in Applied Mechanics and Engineering*, 195:3504–3527, 2006.

- [66] T. Linde. A practical, general-purpose, two-state HLL Riemann solver for hyperbolic conservation laws. *International Journal for Numerical Methods in Fluids*, 40:391–402, 2002.
- [67] T. Linde and P. Roe. On a mistaken notion of “proper upwinding”. *Journal of Computational Physics*, 142:611–614, 1998.
- [68] H. Lomax, T. H. Pulliam, and D. W. Zingg. *Fundamentals of Computational Fluid Dynamics*. Springer-Verlag, New York, first edition, 2000.
- [69] B. Marder. A method for incorporating Gauss’ law into electromagnetic PIC codes. *Journal of Computational Physics*, 68:48–55, 1987.
- [70] R. Matsuzaki. Quasi-one-dimensional nonequilibrium flow of partially ionized argon with different species temperatures. *Journal of the Physical Society of Japan*, 38:1488–1493, 1975.
- [71] R. P. McEachran and A. D. Stauffer. Relativistic effects in low-energy electron-argon scattering. *Australian Journal of Physics*, 50:511–524, 1997.
- [72] T. I. McLaren and R. M. Hobson. Initial ionization rates and collision cross sections in shock-heated argon. *Physics of Fluids*, 11(10):2162–2172, 1968.
- [73] D. A. McQuarrie and J. D. Simon. *Physical Chemistry: A Molecular Approach*. University Science Books, Sausalito, first edition, 1997.
- [74] B. J. McVey and T. Y. Toong. Mechanism of instabilities of exothermic hypersonic blunt-body flows. *Combustion Science and Technology*, 17:538–560, 1972.
- [75] R. Menikoff. Errors when shock waves interact due to numerical shock width. *SIAM Journal on Scientific Computing*, 15(5):1227–1242, 1994.
- [76] M. Merilo and E. J. Morgan. Ionization rates behind shock waves in argon. *Journal of Chemical Physics*, 52(5):2192–2198, 1970.
- [77] W. Merzkirch. *Flow Visualization*. Academic Press, Inc., San Diego, second edition, 1987.

- [78] M. Mitchner and C. H. Kruger. *Partially Ionized Gases*. John Wiley and Sons, Inc., New York, first edition, 1973.
- [79] M. F. Modest. *Radiative Heat Transfer*. Academic Press, San Francisco, second edition, 2003.
- [80] E. J. Morgan and R. D. Morrison. Ionization rates behind shock waves in argon. *Physics of Fluids*, 8:1608–1615, 1965.
- [81] J.-M. Moschetta and D. I. Pullin. A robust low diffusive kinetic scheme for the Navier-Stokes/Euler equations. *Journal of Computational Physics*, 133:193–204, 1997.
- [82] W. Noh. Errors for calculations of strong shocks using an artificial viscosity and an artificial heat flux. *Journal of Computational Physics*, 72:79, 1978.
- [83] E. S. Oran and J. P. Boris. *Numerical Simulation of Reactive Flow*. Elsevier Science Publishing Co., Inc., New York, first edition, 1987.
- [84] A. Orszag and C. M. Tang. Small-scale structure of two-dimensional magnetohydrodynamic turbulence. *Journal of Fluid Mechanics*, 90:129, 1979.
- [85] H. Petschek and S. Byron. Approach to equilibrium ionization behind strong shock waves in argon. *Annals of Physics*, 1:270–315, 1957.
- [86] K. G. Powell, P. L. Roe, T. J. Linde, T. I. Gombosi, and D. L. Zeeuw. A solution-adaptive scheme for ideal magnetohydrodynamics. *Journal of Computational Physics*, 154:284–309, 1999.
- [87] K. G. Powell, P. L. Roe, and R. S. Myong. An upwind scheme for magnetohydrodynamics. In *AIAA 12th Computational Fluid Dynamics Conference, San Diego, June 19-22*, pages 661–674, June 1995.
- [88] J. J. Quirk. An alternative to unstructured grids for computing gas dynamic flows around arbitrarily complex two-dimensional bodies. Technical Report ICASE-92-7, NASA, 1992.
- [89] J. J. Quirk. A contribution to the great Riemann solver debate. Technical Report ICASE-92-64, NASA, 1992.

- [90] J. J. Quirk. Godunov-type schemes applied to detonation flows. Technical Report ICASE-93-15, NASA, 1993.
- [91] J. J. Quirk. A Cartesian grid approach with hierarchical refinement for compressible flows. Technical Report ICASE-94-51, NASA, 1994.
- [92] J. J. Quirk. A contribution to the great Riemann solver debate. *International Journal for Numerical Methods in Fluids*, 18:555–574, 1994.
- [93] J. J. Quirk and U. R. Hanebutte. A parallel adaptive mesh refinement algorithm. Technical Report ICASE-93-63, NASA, 1993.
- [94] J. J. Quirk and S. Karni. On the dynamics of a shock-bubble interaction. Technical Report ICASE-94-75, NASA, 1994.
- [95] Yu. Ralchenko, A. E. Kramida, J. Reader, and NIST ASD Team. NIST atomic spectral database (version 3.1.5). <http://physics.nist.gov/asd3>, 2008.
- [96] P. L. Roe. Approximate Riemann solvers, parameter vectors, and difference schemes. *Journal of Computational Physics*, 43:357–372, 1981.
- [97] P. L. Roe and D. S. Balsara. Notes on the eigensystem of magnetohydrodynamics. *SIAM Journal on Applied Mathematics*, 56:57–67, 1996.
- [98] R. Samtaney. Computational methods for self-similar solutions of the compressible Euler equations. *Journal of Computational Physics*, 132:327–345, 1997.
- [99] R. Scott Schappe, M. Bruce Schulman, L. W. Anderson, and C. C. Lin. Measurement of cross sections for electron-impact excitation into the metastable levels of argon and number densities of metastable argon atoms. *Physical Review A*, 50(1):444–461, 1994.
- [100] K. Sermeus and H. Deconinck. An entropy fix for multi-dimensional upwind residual distribution schemes. *Computers and Fluids*, 34:617–640, 2005.
- [101] G. S. Settles. *Schlieren and Shadowgraph Techniques*. Springer-Verlag, Berlin, second edition, 2006.
- [102] A. H. Shapiro. *The Dynamics and Thermodynamics of Compressible Flow*, volume I. The Ronald Press Company, New York, first edition, 1953.



- [103] A. H. Shapiro. *The Dynamics and Thermodynamics of Compressible Flow*, volume II. The Ronald Press Company, New York, first edition, 1953.
- [104] Chi-Wang Shu and Stanley Osher. Efficient implementation of essentially non-oscillatory shock capturing schemes. *Journal of Computational Physics*, 145:458–485, 1998.
- [105] B. M. Smirnov. *Physics of Ionized Cases*. John Wiley and Sons, Inc., New York, first edition, 2001.
- [106] G. D. Smith. *Numerical Solution of Partial Differential Equations: Finite Difference Methods*. Clarendon Press, Oxford, second edition, 1978.
- [107] A. Suresh and H. T. Huynh. Accurate monotonicity-preserving schemes with Runge-Kutta time stepping. *Journal of Computational Physics*, 136(1):83–99, 1997.
- [108] M. A. Sussman and G. J. Wilson. Computation of chemically reacting flow using a logarithmic form of the species conservation equations. In *Proceedings of the 4th International Symposium on Computational Fluid Dynamics*, pages 1113–1118, Davis, CA, September 1991. AIAA.
- [109] G. W. Sutton and A. Sherman. *Engineering Magnetohydrodynamics*. McGraw-Hill Book Company, San Francisco, first edition, 1965.
- [110] J. C. Tannehill, D. A. Anderson, and R. H. Pletcher. *Computational Fluid Mechanics and Heat Transfer*. Taylor and Francis, Philadelphia, second edition, 1997.
- [111] E. F. Toro. *Riemann Solvers and Numerical Methods for Fluid Dynamics: A Practical Introduction*. Springer, Berlin, second edition, 1999.
- [112] G. Tóth. The  $\nabla \cdot \mathbf{B}$  constraint in shock-capturing magnetohydrodynamics codes. *Journal of Computational Physics*, 161:605–652, 2000.
- [113] B. van Leer. Towards the ultimate conservative difference scheme. II. monotonicity and conservation combined in a second-order scheme. *Journal of Computational Physics*, 14:361–370, 1974.

- [114] B. van Leer. Towards the ultimate conservative difference scheme. III. upstream-centered finite-difference schemes for ideal compressible flow. *Journal of Computational Physics*, 23:263–275, 1977.
- [115] B. van Leer. Towards the ultimate conservative difference scheme. IV. A new numerical approach to numerical convection. *Journal of Computational Physics*, 23:276–299, 1977.
- [116] B. van Leer. Towards the ultimate conservative difference scheme. V. A second order sequel to Godunov’s method. *Journal of Computational Physics*, 32:101–136, 1979.
- [117] J. Vlček. A collisional-radiative model applicable to argon discharges over a wide range of conditions. I: Formualtion and basic data. *Journal of Physics D: Applied Physics*, 22:623–631, 1989.
- [118] J. Vlček and V. Pelikán. Excited level populations of argon atoms in a non-isothermal plasma. *Journal of Physics D: Applied Physics*, 19:1879–1888, 1986.
- [119] J. Vlček and V. Pelikán. A collisional-radiative model applicable to argon discharges over a wide range of conditions. II: Application to low-pressure, hollow-cathode arc and low-pressure glow discharges. *Journal of Physics D: Applied Physics*, 22:632–643, 1989.
- [120] Z. U. A. Warsi. *Fluid Dynamics: Theoretical and Computational Approaches*. CRC Press, New York, second edition, 1999.
- [121] P. R. Woodward. Piecewise-parabolic methods for astrophysical fluid dynamics. In K.-H. A. Winkler and M. L. Norman, editors, *Astrophysical Radiation Hydrodynamics*, pages 245–326. D. Reidel Publishing, 1986.
- [122] Z. Xu and C.-W. Shu. Anti-diffusive flux corrections for high order finite difference WENO schemes. *Journal of Computational Physics*, 205:458–485, 2005.
- [123] A. Yanguas-Gil, J. Cotrino, and L. L. Alves. An update of argon inelastic cross sections for plasma discharges. *Journal of Physics D: Applied Physics*, 38:1588–1598, 2005.

- [124] A. L. Zachary, A. Malagoli, and P. Colella. The effect of nonzero  $\nabla \cdot \mathbf{B}$  on the numerical solution of the magnetohydrodynamic equations. *SIAM Journal on Scientific and Statistical Computing*, 15:263, 1994.
- [125] O. Zatsarinny. 2009. private communication.
- [126] O. Zatsarinny and K. Bartschat. *B*-spline Breit-Pauli *R*-matrix calculations for electron collisions with argon atoms. *Journal of Physics B: Atomic, Molecular and Optical Physics*, 37:4693–4703, 2004.
- [127] O. Zatsarinny and K. Bartschat. *B*-spline calculations of oscillator strengths in neutral argon. *Journal of Physics B: Atomic, Molecular and Optical Physics*, 39:2145–2158, 2006.
- [128] Ya. B. Zel’dovich and Yu. P. Raizer. *Physics of Shock Waves and High Temperature Hydrodynamic Phenomena*. Dover Publications, Inc., New York, third edition, 2002.

This Page Intentionally Left Blank

## Particle Motion Algorithm for Arbitrary Gyro-Frequencies

*Jean-Luc Cambier*

AFRL, Edwards AFB, CA 93524

*Oleg Batishchev*

MIT – Space Systems Laboratory, Cambridge, MA 02139

### Abstract

The transport of particles in a Particle-In-Cell (PIC) method is traditionally handled by a staggered algorithm, second-order accurate in time, originally developed by Boris [1-2]. The scheme is very efficient and although it is stable for time steps large compared to the cyclotron period (“gyro-period”), it ceases to be accurate in that case. In cases of strong applied magnetic field, this can impose an impractical time-step restriction. An alternative approach is to average over the orbital motion and consider only that of the guiding-center; this has led to so-called gyrokinetic simulations [3]. However, that approach can also lead to some inaccuracies, due to the loss of information regarding the phase of the orbital motion. Furthermore, it may also be desirable to have an algorithm that is not staggered in time, in order to guarantee exact conservation of total energy at all times. In this paper, we present an algorithm that solves the non-relativistic equation of motion exactly, and can yield exact conservation of energy for large time steps (compared to gyroperiod). The algorithm accuracy is demonstrated and compared with the Boris scheme. These preliminary results are valid for the homogenous case only, and extension to spatially-varying fields should be considered next.

## 1. Introduction

We consider the problem of solving the non-relativistic dynamical equation for charged particles in arbitrary electric and magnetic fields:

$$m\dot{\vec{v}} = q (\vec{E} + \vec{v} \times \vec{B}) \quad (1)$$

This is the basic transport process in Particle-In-Cell (PIC) codes, which is usually solved using the Boris algorithm [1], defined in Appendix A. The Boris algorithm is a computationally efficient (i.e. uses a minimum number of operations) algorithm, second-order accurate in time. Since it is a leap-frog integrator, it is also usually described as a symplectic algorithm, i.e. which conserves a discrete analog of the Hamiltonian up to second-order accuracy. This is a critically important property for PIC simulations, which usually do not have conservation properties embedded in the mathematical formulation as in continuum models, such as finite-volume or finite-difference schemes. However, it is important to exercise some caution when speaking of energy conservation in the Boris scheme; as a leap-frog algorithm, it uses position and velocity staggered in time, the kinetic and potential energies are not computed at the same time. After advancing the particle, the kinetic energy can be evaluated from the velocity field at time  $(n+1/2)$ , while the potential energy can be obtained exactly from the particle position at time  $(n+1)$ . Thus, the kinetic and potential energies are not strictly conserved at the same time.

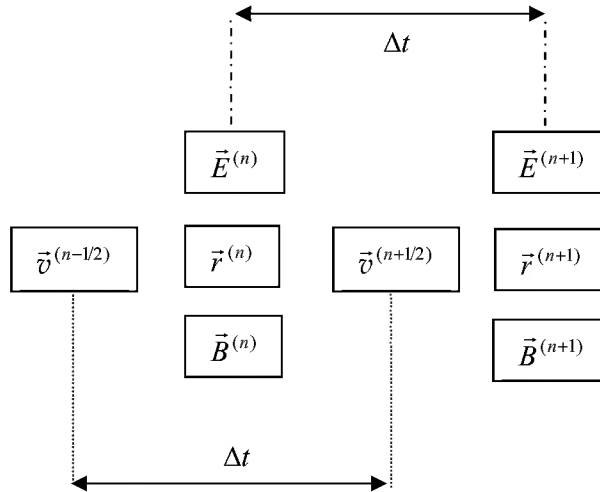


**Figure 1:** Schematic of leap-frog Boris algorithm.

In the leap-frog algorithm, the fields are used at the mid-point for advancing the velocity, i.e. fields evaluated at time  $(n)$  are needed for updating the velocity from  $\vec{v}^{(n-1/2)}$  to  $\vec{v}^{(n+1/2)}$ . In an electrostatic simulation, the electric field can be obtained from solving Poisson's equation:

$$\nabla^2 \phi = \frac{e}{\epsilon_0} (Z_i \bar{n}_i - \bar{n}_e) \quad (2a)$$

and

$$\vec{E}^{(n)} = -\nabla \phi^{(n)} \quad (2b)$$

In (2a), the particle density at a given location (grid-point) is obtained as the statistical average of the contribution of neighboring particles; this "scatter" operation maps the particles onto the grid, and various interpolation schemes can be used for this operation. We point out that this mapping uses the particle locations at time level  $(n)$ , and therefore the electro-static potential (and electric

field) are naturally synchronized with the particle positions. In electro-static simulations the magnetic field is constant and there is no concern over its synchronization. In electro-magnetic simulations, however, both fields are advanced in time and the procedure must be consistent with the Maxwell equations:

$$\epsilon_0 \vec{\nabla} \cdot \vec{E} = -\tilde{\rho}_p \quad (3a)$$

$$\epsilon_0 \frac{\partial \vec{E}}{\partial t} = -\frac{\vec{\nabla} \times \vec{B}}{\mu_0} + \vec{j}_p \quad (3b)$$

$$\frac{\partial \vec{B}}{\partial t} = -\vec{\nabla} \times \vec{E} \quad (3c)$$

$$\vec{\nabla} \cdot \vec{B} = 0 \quad (3d)$$

Equation (3a), where  $\tilde{\rho}_p$  is the charge density from the particles, is simply Poisson's equation (2a); in (3b),  $\vec{j}_p$  is the current density from the particles, and is obtained by a similar mapping of the particle velocities onto grid points. The Maxwell equations are naturally synchronized to second-order accuracy for  $\vec{r}^{(n)}, \vec{E}^{(n)}$  and  $\vec{v}^{(n+1/2)}, \vec{B}^{(n+1/2)}$ . However the leap-frog algorithm for particle transport is of the form  $\vec{v}^{(n+1/2)} = f(\vec{v}^{(n-1/2)}, \vec{E}^{(n)}, \vec{B}^{(n)})$ , and one needs to interpolate in time one of the fields for the particle push, i.e.  $\vec{B}$ . Note that the leap-frog algorithm of Figure 1 is not the unique solution: one could just as well decide to choose the fields  $\vec{r}^{(n)}, \vec{B}^{(n)}$  and  $\vec{v}^{(n+1/2)}, \vec{E}^{(n+1/2)}$  or other combinations and rely on the time-interpolation of another field (matter or particle) to re-establish second-order time accuracy. Higher-order schemes can of course be obtained with iterative methods.

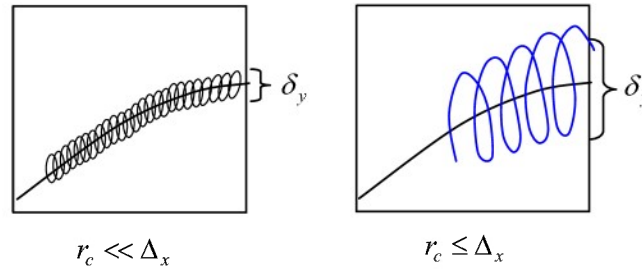


**Figure 2:** Potential positional error of drift dynamics versus gyro-radius

The Boris algorithm is stable at high values of the magnetic field, i.e. when  $\omega_c \Delta t \gg 1$ , although accuracy is lost for large time steps. Practically speaking, the time step in PIC simulations using this algorithm is restricted such that  $\omega_c \Delta t \ll 1$ ; this makes the scheme highly inefficient in cases of strongly magnetized plasmas. One could consider an alternative approach in that case, where only the motion of the guiding center is modeled; the rotation around the field line is not tracked, but averaged over several orbits. This “drift dynamics” approach is valid when the gyro-radius  $r_c \ll \Delta_x$ , the characteristic cell-size; however, significant errors can be introduced even when  $r_c \leq \Delta_x$ . Since the phase of the gyro-motion is not known in this approximation, the particle position is effectively randomized on a scale comparable to the cell size (see Figure 2). This can lead to errors at the crossing into different cells or boundaries, and errors when the field gradients on the scale of a cell size are non-negligible. Therefore, it is worth investigating the construction of an accurate particle-push algorithm that is more efficient at high cyclotron frequency, yet

remains accurate and conserves energy to a high level of accuracy. This is the object of the following study.

## 2. Exact Solution

We consider here the case of constant and uniform fields. This considerably simplifies the analysis and allows us to obtain an exact analytical solution to the non-relativistic equations of motion. The constant field approximation is valid when the time-variation of the fields is neglected during the time-step (i.e. first-order time-accuracy of the field evolution); the extension to higher-order time-dependency and non-uniform fields will be examined in the future. We will also be performing a transformation to the reference frame aligned with the magnetic field. Let us first define the laboratory frame ( $L$ ) by the italicized letters  $(\hat{x}, \hat{y}, \hat{z})$  and a rotated coordinate frame by  $(\hat{\xi}, \hat{\eta}, \hat{\zeta})$  such that the unit vector  $\hat{\zeta}$  is aligned with the magnetic field, i.e.  $\hat{\zeta} \equiv \hat{b}$ .

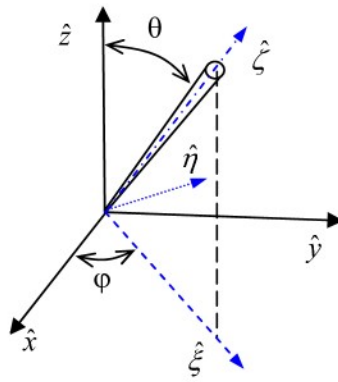


**Figure 3:** Reference frame transformation:  $\hat{\zeta}$  aligned with  $\vec{B}$ .

The rotation operators between the two reference frames are given by:

$$\hat{\mathbf{R}} = \begin{pmatrix} \xi_x & \xi_y & \xi_z \\ \eta_x & \eta_y & \eta_z \\ \zeta_x & \zeta_y & \zeta_z \end{pmatrix} = \begin{pmatrix} c_\varphi c_\theta & s_\varphi c_\theta & -s_\theta \\ -s_\varphi & c_\varphi & 0 \\ c_\varphi s_\theta & s_\varphi s_\theta & c_\theta \end{pmatrix} \quad (4a)$$

$$\hat{\mathbf{R}}^{-1} = \begin{pmatrix} \xi_x & \eta_x & \zeta_x \\ \xi_y & \eta_y & \zeta_y \\ \xi_z & \eta_z & \zeta_z \end{pmatrix} = \begin{pmatrix} c_\varphi c_\theta & -s_\varphi & c_\varphi s_\theta \\ s_\varphi c_\theta & c_\varphi & s_\varphi s_\theta \\ -s_\theta & 0 & c_\theta \end{pmatrix} \quad (4b)$$

where we have used the condensed notation of  $c_\varphi = \cos(\varphi)$ ,  $s_\theta = \sin(\theta)$ , etc. Once the rotation into the aligned frame is performed and no confusion is possible, we can use the script letters  $(x, y, z)$  to denote the components in that frame, i.e.  $(\hat{x}, \hat{y}, \hat{z}) \equiv (\hat{\xi}, \hat{\eta}, \hat{\zeta})$ . We will also denote vectors in that frame by bold-face type, i.e.:  $\mathbf{E} = \hat{\mathbf{R}} \otimes \vec{E}$ .

In this rotated frame, the equation of motion (1) can be expressed by:



$$\begin{aligned}
\dot{v}_x &= \frac{q}{m} E_x + \frac{qB}{m} v_y \\
\dot{v}_y &= \frac{q}{m} E_y - \frac{qB}{m} v_x \\
\dot{v}_z &= \frac{q}{m} E_z
\end{aligned} \tag{5}$$

In this frame, the magnetic field has a component only in the  $\hat{z}$  direction, and therefore  $B_z \equiv B$ , the magnitude of the magnetic field. We can define a normalized electric acceleration field  $\mathbf{a} = q\mathbf{E}/m$  and the cyclotron frequency  $\omega = qB/m$ , which is a *signed* quantity. The solution for the  $\hat{z}$ -component of the velocity is trivial and can be ignored for the moment. The system (5) can be reduced, for the transverse components, to:

$$\dot{\underline{v}} = \underline{a} + \begin{pmatrix} 0 & \omega \\ -\omega & 0 \end{pmatrix} \cdot \underline{v} \tag{6}$$

where the underline indicates a vector in the transverse directions only. An additional time derivative of (6) yields the following:

$$\ddot{\underline{v}} = -\omega^2 \underline{v} + \begin{pmatrix} 0 & \omega \\ -\omega & 0 \end{pmatrix} \cdot \underline{a} \tag{7}$$

The general solution of (6-7) is:

$$\underline{v} = \begin{cases} v_o \sin(\omega t + \phi) + (a_x/\omega) \sin(\omega t + \phi) + (a_y/\omega)(1 - \cos(\omega t + \phi)) \\ v_o \cos(\omega t + \phi) - (a_x/\omega)(1 - \cos(\omega t + \phi)) + (a_y/\omega) \sin(\omega t + \phi) \end{cases} \tag{8}$$

Let us denote  $\phi(t) = \omega t + \phi$ . It is to verify that the solution (8) satisfies the equations of motion:

$$\dot{\underline{v}} = \begin{cases} \omega v_o \cos(\phi) + a_x \cos(\phi) + a_y \sin(\phi) \\ -\omega v_o \sin(\phi) - a_x \sin(\phi) + a_y \cos(\phi) \end{cases} = \begin{cases} \omega v_y + a_x \\ -\omega v_x + a_y \end{cases} = \underline{a} + \begin{pmatrix} 0 & \omega \\ -\omega & 0 \end{pmatrix} \cdot \underline{v} \quad \checkmark \tag{9a}$$

$$\ddot{\underline{v}} = \begin{cases} -\omega^2 v_o \sin(\phi) - a_x \omega \sin(\phi) + a_y \omega \cos(\phi) \\ -\omega^2 v_o \cos(\phi) - a_x \omega \cos(\phi) - a_y \omega \sin(\phi) \end{cases} = \begin{cases} -\omega^2 v_x + \omega a_y \\ -\omega^2 v_y - \omega a_x \end{cases} = -\omega^2 \underline{v} + \begin{pmatrix} 0 & \omega \\ -\omega & 0 \end{pmatrix} \cdot \underline{a} \quad \checkmark \tag{9b}$$

Let us now compute the solution at an advanced time  $t + dt$ . From (8) we have:

$$\underline{v}(t+dt) = \begin{cases} v_o \sin(\phi+dt) + (a_x/\omega) \sin(\phi+dt) + (a_y/\omega)(1 - \cos(\phi+dt)) \\ v_o \cos(\phi+dt) - (a_x/\omega)(1 - \cos(\phi+dt)) + (a_y/\omega) \sin(\phi+dt) \end{cases} \tag{10}$$

Expanding the trigonometric functions we find:

$$\underline{v}(t+dt) = \begin{cases} c_\delta \cdot [v_x - a_y/\omega] + s_\delta \cdot [v_y + a_x/\omega] + (a_y/\omega) \\ -s_\delta \cdot [v_x - a_y/\omega] + c_\delta \cdot [v_y + a_x/\omega] - (a_x/\omega) \end{cases} = \underline{\Omega}(dt) \cdot \underline{v}(t) + \frac{1}{\omega} \begin{bmatrix} s_\delta & 1 - c_\delta \\ c_\delta - 1 & s_\delta \end{bmatrix} \cdot \underline{a} \tag{11}$$

where  $\delta \equiv \omega dt$  and  $\underline{\Omega}(dt)$  is the counter-rotation matrix around the magnetic field:

$$\underline{\Omega}(dt) = \begin{pmatrix} \cos(\delta) & \sin(\delta) \\ -\sin(\delta) & \cos(\delta) \end{pmatrix} \tag{12}$$

The last matrix in (11) can also be written in terms of this rotation matrix. Let us define:

$$\underline{\sigma} = \omega \begin{pmatrix} 0 & 1 \\ -1 & 0 \end{pmatrix} \quad \text{and} \quad \underline{\sigma}^{-1} = \omega^{-1} \begin{pmatrix} 0 & -1 \\ 1 & 0 \end{pmatrix} \tag{13}$$

then (11) becomes:

$$\underline{v}(t+\Delta t) = \underline{\Omega}(dt) \cdot \underline{v}(t) + \begin{bmatrix} c_\delta - 1 & s_\delta \\ -s_\delta & c_\delta - 1 \end{bmatrix} \cdot \underline{\sigma}^{-1} \cdot \underline{a} \tag{14}$$

In a compact form:

$$\Delta \underline{v} = \underline{v}(t+\Delta t) - \underline{v}(t) = [\underline{\Omega}(dt) - \underline{1}] \cdot [\underline{v}(t) + \underline{\sigma}^{-1} \cdot \underline{a}] \quad (15)$$

One should now consider the case of vanishing magnetic field. The matrix  $\underline{\sigma}^{-1}$  on the RHS of (15) is singular when  $B = 0$ . However, it can be combined with the term in brackets as follows:

$$[\underline{\Omega}(dt) - \underline{1}] \cdot \underline{\sigma}^{-1} = \underbrace{\begin{pmatrix} \frac{\sin \delta}{\delta} & \frac{1 - \cos \delta}{\delta} \\ \frac{\cos \delta - 1}{\delta} & \frac{\sin \delta}{\delta} \end{pmatrix}}_{\underline{\Delta}_1} \cdot dt \quad (16)$$

The matrix  $\underline{\Delta}_1$  is regular, since:

$$\underline{\Delta}_1 \rightarrow \begin{pmatrix} 1 & 0 \\ 0 & 1 \end{pmatrix} \quad \text{when } \omega \rightarrow 0 \quad (17)$$

One can expand (15) to the next order in  $\delta = \omega \Delta t$ , leading to:

$$\Delta \underline{v} = \begin{bmatrix} \underline{a}_x dt + \omega dt (\underline{v}_y + \frac{1}{2} \underline{a}_y dt) - \frac{1}{2} (\omega dt)^2 \underline{v}_x \\ \underline{a}_y dt - \omega dt (\underline{v}_x + \frac{1}{2} \underline{a}_x dt) - \frac{1}{2} (\omega dt)^2 \underline{v}_y \end{bmatrix} \quad (18)$$

We see that the second-order accurate ( $o(dt^2)$ ) solution is obtained by rotating a half-step advanced solution, as expected. We can also verify that this solution is identical to the Boris algorithm, by comparing (18) with (A.23b) of Appendix A.

The opposite limit of large time steps compared to the gyro-motion, i.e.  $\omega dt \rightarrow \infty$ , is also of principal interest. In that case, the trigonometric functions oscillate rapidly, but the trajectory remains bound. One can perform an averaging over a large number of gyro-motions, and eliminate all terms proportional to these functions ( $\langle \cos \rangle = \langle \sin \rangle = 0$ ). The remainder is:

$$\langle \underline{v}(t+\Delta t) \rangle = \begin{pmatrix} 0 & 1/\omega \\ -1/\omega & 0 \end{pmatrix} \cdot \underline{a} \quad (19)$$

which is independent of the time step  $\Delta t$ . This is a constant velocity, which can be easily recognized as the  $\vec{E} \times \vec{B}$  drift velocity, since (19) is equivalent to:

$$\langle \underline{v} \rangle = \begin{cases} E_y / B \\ -E_x / B \end{cases} = \frac{\mathbf{E} \times \mathbf{B}}{B^2} \quad (20)$$

Therefore, the formulation (15) automatically recovers the drift motion of the guiding center when the gyro-motion is not resolved – with a randomized rotation around the magnetic field.

Let us now look at the exact solution for the particle position. From (8), we obtain:

$$\underline{x}(t) = \frac{\underline{v}_0}{\omega} \begin{pmatrix} -\cos \phi \\ \sin \phi \end{pmatrix} + \frac{1}{\omega^2} \begin{pmatrix} -\cos \phi & -\sin \phi \\ \sin \phi & -\cos \phi \end{pmatrix} \cdot \underline{a} + \frac{1}{\omega} \begin{pmatrix} \underline{a}_y t \\ -\underline{a}_x t \end{pmatrix} + \underline{x}_0 \quad (21)$$

The expression at a later time  $t + dt$  can be expressed as function of the original phase  $\phi(t)$  and the phase difference  $d\phi \equiv \delta = \omega dt$  by:

$$\underline{x}(t+dt) = \frac{1}{\omega} \begin{pmatrix} \underline{a}_y(t+dt) \\ -\underline{a}_x(t+dt) \end{pmatrix} + \underline{x}_0 + \begin{pmatrix} c_\delta & s_\delta \\ -s_\delta & c_\delta \end{pmatrix} \cdot \begin{bmatrix} -(\underline{v}_0/\omega) c_\phi - (\underline{a}_x/\omega^2) c_\phi - (\underline{a}_y/\omega^2) s_\phi \\ +(\underline{v}_0/\omega) s_\phi + (\underline{a}_x/\omega^2) s_\phi - (\underline{a}_y/\omega^2) c_\phi \end{bmatrix} \quad (22)$$

One recognizes again the rotation matrix (12) in that expression, which allows us to write the displacement as:

$$\Delta \underline{x} = \frac{1}{\omega} \begin{pmatrix} \underline{a}_y dt \\ -\underline{a}_x dt \end{pmatrix} + [\underline{\Omega}(dt) - \underline{1}] \cdot \begin{bmatrix} -(\underline{v}_0/\omega) c_\phi - (\underline{a}_x/\omega^2) c_\phi - (\underline{a}_y/\omega^2) s_\phi \\ +(\underline{v}_0/\omega) s_\phi + (\underline{a}_x/\omega^2) s_\phi - (\underline{a}_y/\omega^2) c_\phi \end{bmatrix} \quad (23)$$

However, from (15) one can also recognize the following expression:

$$\Delta \underline{v} \equiv (\underline{\Omega}(dt) - \underline{1}) \cdot \begin{bmatrix} v_x - a_y/\omega \\ v_y + a_x/\omega \end{bmatrix} = (\underline{\Omega} - \underline{1}) \cdot \begin{bmatrix} v_o s_\phi + (a_x/\omega) s_\phi - (a_y/\omega) c_\phi \\ v_o c_\phi + (a_x/\omega) c_\phi + (a_y/\omega) s_\phi \end{bmatrix} \quad (24)$$

Inserting (24) into (23), we finally obtain:

$$\Delta \underline{x} \equiv \frac{1}{\omega} \cdot \begin{bmatrix} a_y \Delta t - \Delta v_y \\ -a_x \Delta t + \Delta v_x \end{bmatrix} \quad (25)$$

For the displacement along the magnetic field, the exact solution is of course:

$$\Delta x_{\parallel} = v_{\parallel}(t) \Delta t + \frac{1}{2} a_{\parallel} \Delta t^2 \equiv v_{\parallel}(t + \frac{1}{2} \Delta t) \Delta t \quad (26)$$

It would appear that the transverse displacement (25) has a singular behavior at vanishing magnetic field strength, due to the  $\omega^{-1}$  factor. However, a simple Taylor expansion can confirm that this is not the case: when  $\omega \rightarrow 0$  one can use (18) into (25) to verify that, as expected:

$$\Delta \underline{x} \approx \begin{bmatrix} v_x \Delta t + \frac{1}{2} a_x \Delta t^2 \\ v_y \Delta t + \frac{1}{2} a_y \Delta t^2 \end{bmatrix} + o(\omega^2) \quad (27)$$

The expression (25) is therefore valid for all non-zero values of the magnetic field. We can, as before, regularize this expression in the case of  $\omega = 0$ ; after some simple algebra, we obtain:

$$\Delta \underline{x} = \underbrace{\begin{pmatrix} \frac{s_\delta}{\delta} & \frac{1-c_\delta}{\delta} \\ \frac{c_\delta-1}{\delta} & \frac{s_\delta}{\delta} \end{pmatrix}}_{\underline{\Lambda}_1} \cdot \underline{v} \Delta t + \underbrace{\begin{pmatrix} \frac{1-c_\delta}{\delta^2} & \frac{\delta-s_\delta}{\delta^2} \\ \frac{s_\delta-\delta}{\delta^2} & \frac{1-c_\delta}{\delta^2} \end{pmatrix}}_{\underline{\Lambda}_2} \cdot \underline{a} \Delta t^2 \quad (28)$$

We have recognized the first matrix (16), and defined a second regularized matrix  $\underline{\Lambda}_2$ . Both are finite when  $\omega \rightarrow 0$ , since in that case (defining also the following  $S, C$  coefficients):

$$S_0 = s_\delta \quad S_1 \equiv \frac{s_\delta}{\delta} \approx 1 - \frac{\delta^2}{6} \quad S_2 \equiv \frac{s_\delta - \delta}{\delta^2} \approx -\frac{\delta}{6} \quad (29a)$$

$$C_0 = 1 - c_\delta \quad C_1 \equiv \frac{1 - c_\delta}{\delta} \approx \frac{\delta}{2} \quad C_2 \equiv \frac{1 - c_\delta}{\delta^2} \approx \frac{1}{2} \quad (29b)$$

Therefore, the procedure outlined above is applicable in all cases of magnetic field values.

### 3. General Algorithm

One can construct two types of algorithms. The first case is valid only for  $\delta > \varepsilon$ , i.e. does not require regularization, and is governed by the following operations:

- (1) Transform the velocity, position and acceleration vectors from the original reference frame into the rotated frame with the  $\hat{z}$  axis aligned with the magnetic field.
- (2) Compute the changes to the transformed velocity vector, separating the transverse and parallel components:

$$\Delta \underline{v} \equiv (\underline{\Omega}(dt) - \underline{1}) \cdot \begin{bmatrix} v_x - a_y/\omega \\ v_y + a_x/\omega \end{bmatrix} \quad (30a)$$

$$\Delta v_{\parallel} = a_{\parallel} \Delta t \quad (30b)$$

- (3) Compute the changes to the transformed position, separating the transverse and parallel components:

$$\Delta \underline{x} \equiv \frac{1}{\omega} \cdot \begin{bmatrix} a_y \Delta t - \Delta v_y \\ -a_x \Delta t + \Delta v_x \end{bmatrix} \quad (31a)$$

$$\Delta x_{\parallel} = v_{\parallel}(t) \Delta t + \frac{1}{2} a_{\parallel} \Delta t^2 \quad (31b)$$

(4) Transform the changes back into the original frame and add to the initial values.

In the second case, the regularized matrices are used so that the algorithm remains valid for all cases of field values, including  $\delta < \varepsilon$ . Combining transverse and parallel components<sup>\*</sup>, we can express the velocity change as:

$$\Delta \mathbf{v} \equiv \underbrace{\begin{pmatrix} -C_0 & S_0 & 0 \\ -S_0 & -C_0 & 0 \\ 0 & 0 & 0 \end{pmatrix}}_{\Delta_0} \cdot \begin{bmatrix} v_x \\ v_y \\ v_z \end{bmatrix} + \underbrace{\begin{pmatrix} S_1 & C_1 & 0 \\ -C_1 & S_1 & 0 \\ 0 & 0 & 1 \end{pmatrix}}_{\Delta_1} \cdot \begin{bmatrix} a_x \Delta t \\ a_y \Delta t \\ a_z \Delta t \end{bmatrix} \quad (32a)$$

$$\Delta \mathbf{x} = \underbrace{\begin{pmatrix} S_1 & C_1 & 0 \\ -C_1 & S_1 & 0 \\ 0 & 0 & 1 \end{pmatrix}}_{\Delta_1} \cdot \begin{bmatrix} v_x \Delta t \\ v_y \Delta t \\ v_z \Delta t \end{bmatrix} + \underbrace{\begin{pmatrix} C_2 & -S_2 & 0 \\ S_2 & C_2 & 0 \\ 0 & 0 & 1/2 \end{pmatrix}}_{\Delta_2} \cdot \begin{bmatrix} a_x \Delta t^2 \\ a_y \Delta t^2 \\ a_z \Delta t^2 \end{bmatrix} \quad (32b)$$

The transformation steps (1) and (4) remain the same.

It would appear that the proposed scheme is very expensive, since it requires the evaluation of several matrices. However, in the case of constant fields studied so far, these matrices can be determined once the fields and time step are known. The transformation matrices (4) can be incorporated into the definition of the regularized push matrices  $\Delta_0, \Delta_1, \Delta_2$ , leading to:

$$\mathbf{D}_k = \hat{\mathbf{R}}^{-1} \cdot \Delta_k \cdot \hat{\mathbf{R}}, \quad k=1,2,3 \quad (33)$$

The changes can then be computed directly in the initial (non-rotated) frame:

$$\Delta \vec{v} = \mathbf{D}_0 \cdot \vec{v} + \frac{q \Delta t}{m} \mathbf{D}_1 \cdot \vec{E} \quad (34a)$$

and

$$\Delta \vec{r} = \mathbf{D}_1 \cdot \vec{v} \Delta t + \frac{q \Delta t^2}{m} \mathbf{D}_2 \cdot \vec{E} \quad (34b)$$

#### 4. Computational Tests

The first test conducted concerns the movement of a single particle (a positron) in static fields; the initial velocity is null, the electric field is 1 kV/m in the positive  $\hat{y}$ -direction and the magnetic field is 1 Tesla in the positive  $\hat{z}$ -direction. Under such initial conditions the particle executes a cycloid movement of height equal to  $h = 2r_L = 2v_D / \omega_c$ , where  $v_D = E / B$  is the drift velocity in the  $\hat{x}$ -direction. The motion is computed for three cases of constant time steps, being respectively  $0.1 / \omega_c$ ,  $1 / \omega_c$  and  $10 / \omega_c$ . Since the Boris algorithm requires the velocity at a prior half-time step, that initial value ( $\vec{v}^{(-1/2)}$ ) is computed from the exact solution. The trajectories for the exact solution, the Boris algorithm, and the regularized algorithm of eqs. (34) are shown in Figure 4. All methods are in very good agreement for small time step. For  $\Delta t = 1 / \omega_c$ , the Boris algorithm starts to show some noticeable deviations from the exact solution; first, the Larmor radius, or height of the cycloid, is noticeably larger; second, the effective gyro-frequency is somewhat lower, leading to a growing de-phasing with the exact solution. At larger time steps (Figure 4c), the solution from the Boris algorithm is in error by close to an order of magnitude<sup>†</sup>. By contrast, the current algorithm provides a solution that is in perfect agreement with the exact solution, both in amplitude and phase.

<sup>\*</sup> The underline is eliminated, since these are now 3-dimensional variables.

<sup>†</sup> Note that the magnitude of this error is bounded, i.e. does not grow in time, a result of symplecticity.

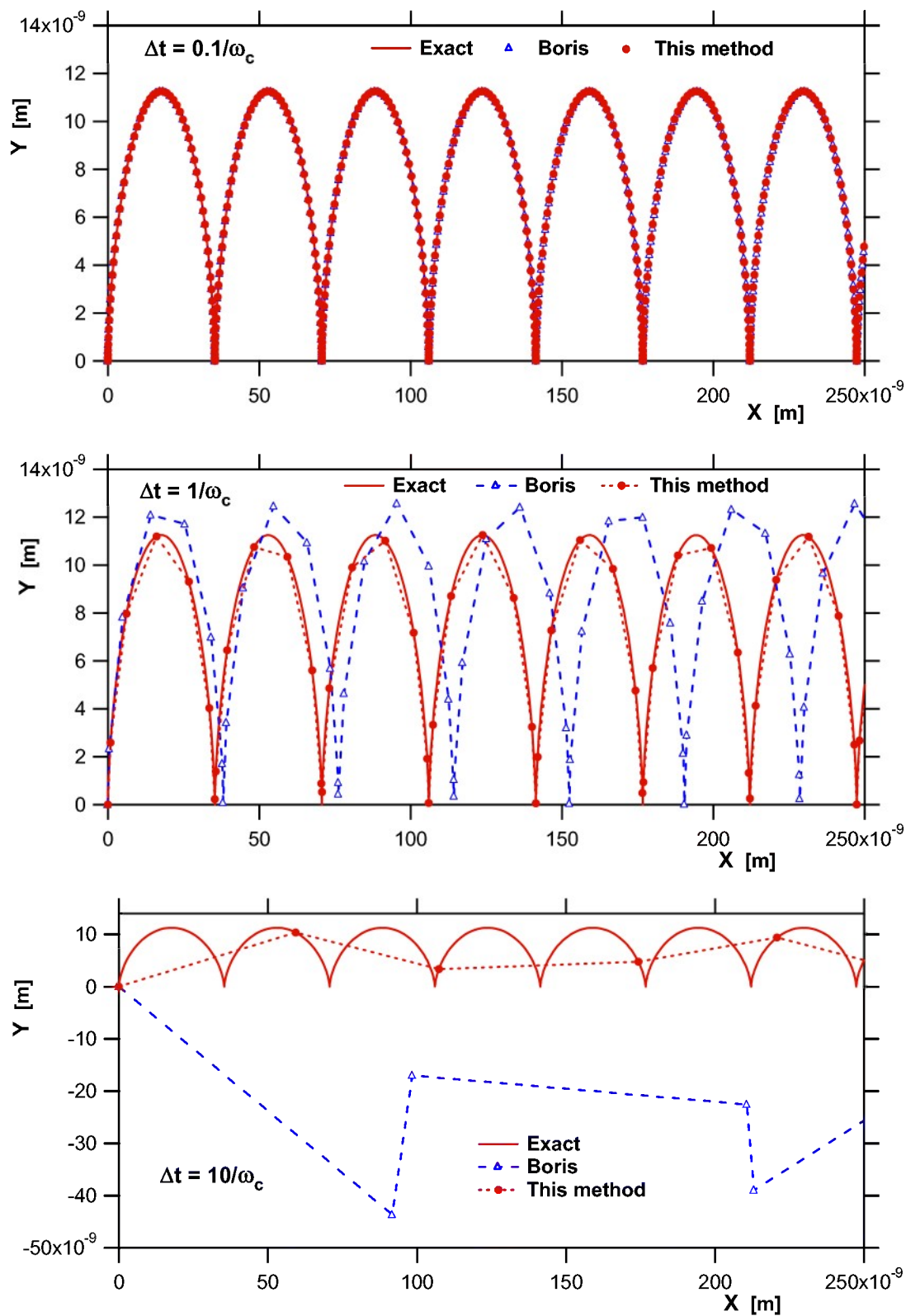


**Figure 4:** Particle trajectory for three time steps; exact solution is compared to the results from the Boris algorithm and the current scheme.

It should also be pointed out that, despite the obvious error in transverse position and rotation frequency present in the Boris algorithm, the drifting motion in the  $\hat{x}$ -direction is accurately maintained. This is evident in Figure 5, where the difference between the actual position and the expected position from the constant drift is plotted versus time. The natural oscillations are due to the cycloid motion itself and of amplitude equal to the Larmor radius; only at the largest time step does the Boris algorithm deviates from the expected behavior. The current method (Figure 5b) yields the correct drift dynamics at all time steps.

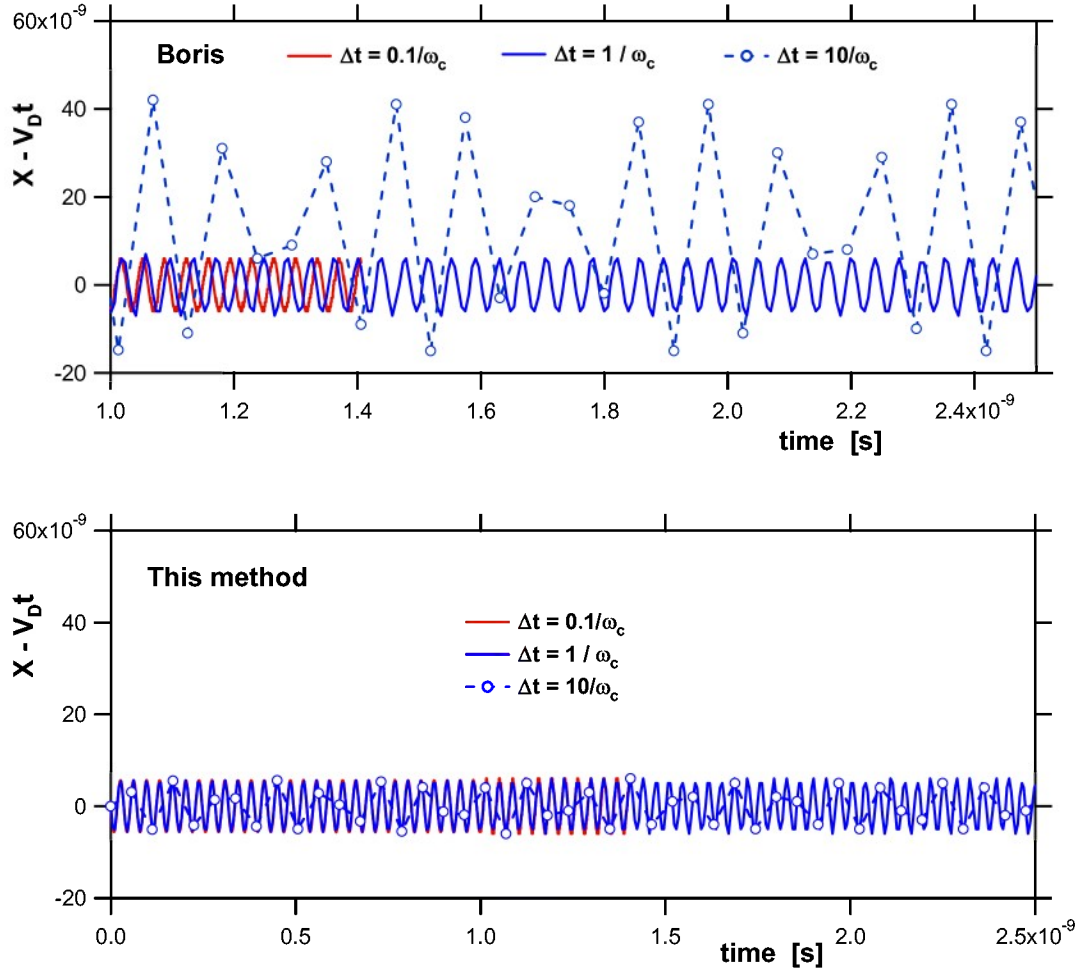


**Figure 5:** X-position versus time, normalized to theoretical position of guiding center ( $V_D t$ ).

One can now examine the impact of the errors on conservation properties, i.e. kinetic, potential and total energies. In this simple test case with an imposed external field, the potential energy per mass is simply  $e_{pot} = (qE/m) \cdot y$ , where  $y$  is the particle position along the  $\hat{y}$ -axis. It is important to point out that for the Boris algorithm, the kinetic and potential energies are evaluated at different times, i.e.:

$$e_{pot}^{(n)} = (qE/m) y^{(n)} \quad \text{and} \quad e_{kin}^{(n-1/2)} = (v^{(n-1/2)})^2 / 2 \quad (35)$$

Therefore to evaluate the total energy at a specific time (e.g.  $t^{(n)}$ ), one must interpolate one of the variables to that time level. Both kinetic and potential energies are shown as function of time for the Boris algorithm in Figure 6.

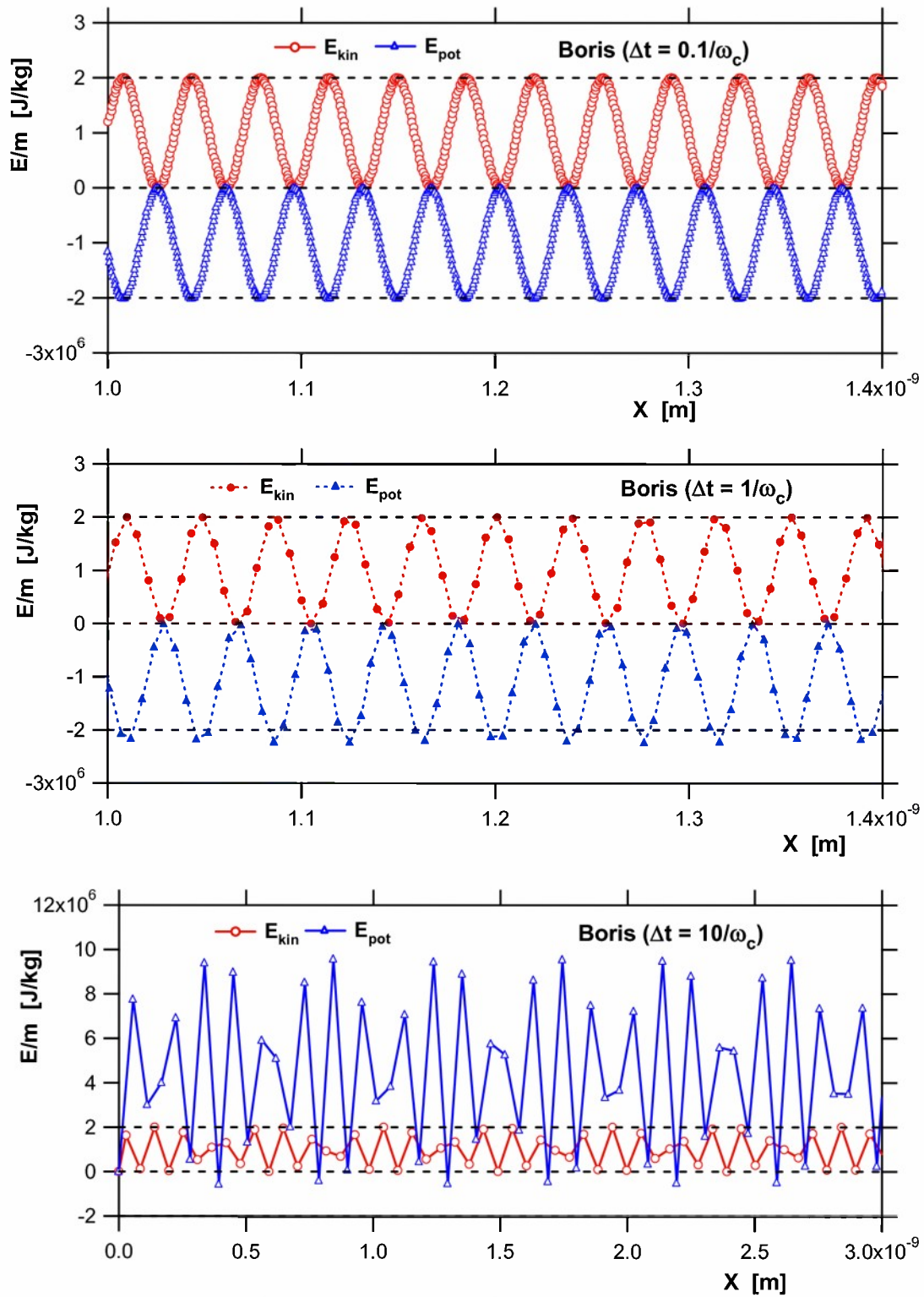


**Figure 6:** Kinetic and potential energy versus distance for Boris algorithm – all cases of time steps. Dashed horizontal lines indicate theoretical limits of variation.

It can be seen that there is a rapid degradation of the energy conservation as the time step is increased to values of the same order or beyond the gyro-period; the error in amplitude of the



particle trajectory leads to errors in potential energy which become severe for large time steps. Since the current method is in perfect agreement with the exact solution at all time steps, the energy is perfectly conserved in that case (see Figure 7).

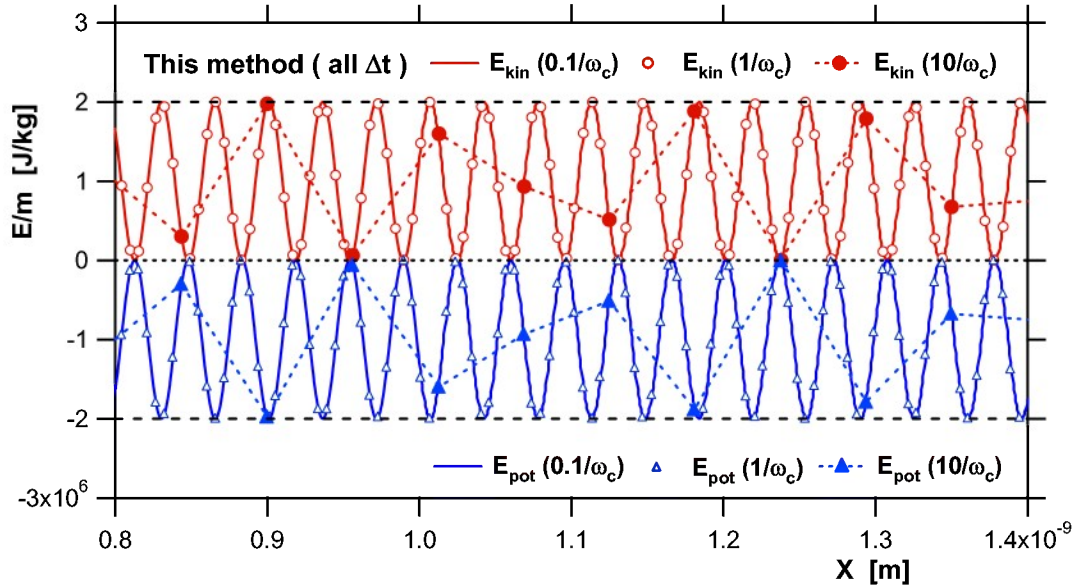


**Figure 7:** Kinetic and potential energy versus distance for current method – all time steps shown.

To evaluate the total energy, one must account for the dephasing of the velocity and position in the case of the Boris algorithm, as mentioned previously. This dephasing can be clearly seen when plotting both energies versus a single time coordinate ( $t^{(n)}$ ) in Figure 8. The shift of the two curves is a result of the leap-frog algorithm. One can correct for this by plotting the kinetic energy versus the proper time of evaluation, i.e. the set  $\{t^{(n+1/2)}\}$ , as done in Figure 7; this shifts all the points to the left, as indicated by the black arrows of Figure 8. The total energy can be evaluated at the set of times  $\{t^{(n)}\}$  by adding the potential energy at that time with the average of the kinetic energies at times  $(t^{(n-1/2)}, t^{(n+1/2)})$ . This interpolation is accurate as long as the time step is sufficiently small, i.e. such a linear approximation of the trajectory between the two times is reasonable; however, it can lead to severe errors for large time steps. This phase error of the Boris scheme is in addition to the amplitude error (effective Larmor radius) already observed, for example, in Figure 6. The average errors on total energy and position can be obtained for various values of the time step and magnetic field. The error on the total energy can

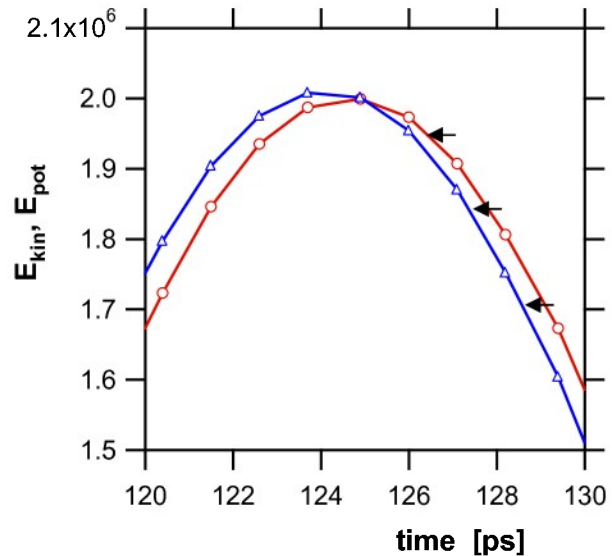


**Figure 8:** Kinetic (red) and potential (blue) energies versus a single time coordinate.



be defined here as  $err(E_{tot}) = (E_{tot} - E_{in})/E_0$ , where  $E_{in}$  is the initial total energy (at  $t = 0$ ) and  $E_0$  is a representative energy scale; here,  $E_0 = v_D^2/2$ , where  $v_D$  is the drift velocity. Similarly for the position, the error is defined as  $err(\vec{X}) = \Sigma |x_\alpha - x_\alpha^{exact}|/X_0$ ; all components of the position are contributing, and  $X_0$  is a representative length scale – in the case of cold particles here, the Larmor radius, i.e. half the height of the cycloid motion. Both errors are shown in Figure 9 for the two schemes.

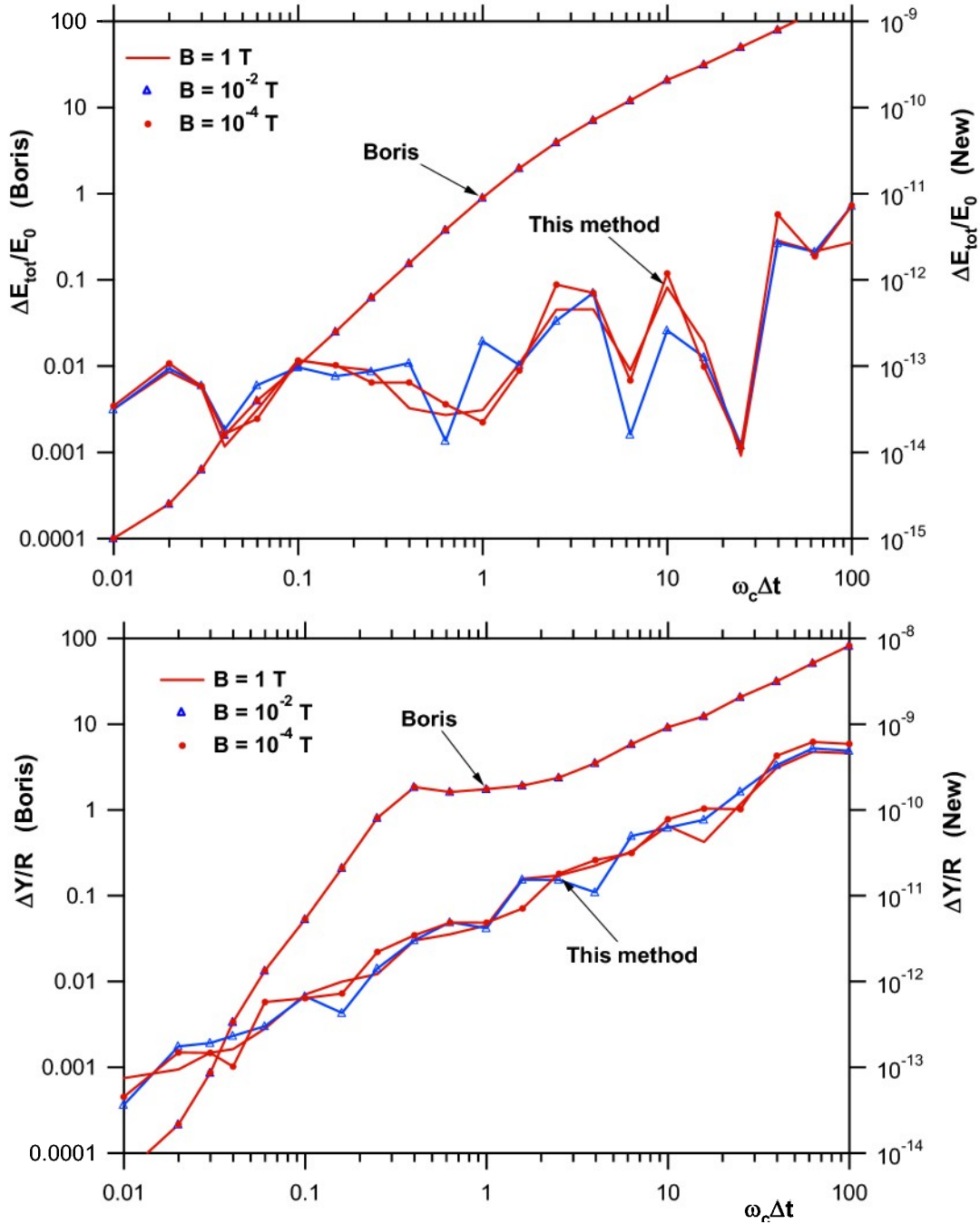


**Figure 9:** Error on energy (a) and position (b) as function of time step for several values of the magnetic field, for the Boris and our algorithms.

Note the change of scale between the left (Boris algorithm) and right axis (current algorithm); clearly, the present scheme is more accurate by several orders of magnitude.

## 5. Conclusions

We have successfully implemented and tested a new particle pusher algorithm that can effectively be used for large time steps, much larger than the gyroperiod; the method is based on the exact solution of the equations of motion, but does not require tracking the phase of the particle motion around the field line. The method can be applied to arbitrarily large time steps and yields exact (down to machine accuracy) conservation of energy and exact position. The method is currently restricted to the non-relativistic case, and to uniform fields. Extension to the relativistic regime would be very difficult, since there is no longer an analytical solution; extension to the non-uniform (magnetic) field does not present a-priori any difficulties, but this must be verified.

It would a-priori appear that the algorithm is computationally expensive, but this is not necessarily the case. The push matrices (eqs. 32) need to be computed only once for each time-step, but are the same for each particle in this case of uniform field. Thus, the method would be efficient when computing a large number of particles in such configurations, e.g. Penning traps. In the case of weakly non-uniform fields, one can also attempt a perturbation expansion, such that the computationally expensive push matrices (involving trigonometric function evaluations) are again computed once in each computational cell, while each particle is transported according to a hybrid scheme involving the one described here, and a rapid scheme such as the Boris algorithm for the small perturbation  $\delta\vec{B}$  or a similar procedure that does not involve time staggering. This can be investigated in the future.

## 6. References

- [1] J. P. Boris, "Relativistic plasma simulation – optimization of a hybrid code", *Proc. 4<sup>th</sup> Conf. Numerical. Simulation of Plasmas*, pp. 3-67, J.P. Boris and R.A. Shanny eds, Naval Research Laboratory, Wash. D.C., Nov. 2-3 1970.
- [2] C. K. Birdsall and A. B. Langdon, *Plasma Physics via Computer Simulation*, pp. 58-63, Inst. of Phys. Publ., Bristol, UK, 1991.
- [3] W. W. Lee, *Phys. Fluids* **26**(2), 556-562 (1983).

## Appendix A: Boris Algorithm

The Boris algorithm is defined by the following steps, from the velocity at  $t - \Delta t / 2$  and the fields at  $t$ :

$$1. \quad \mathbf{v}^- = \mathbf{v}(t - \Delta t / 2) + \frac{q}{m} \frac{\Delta t}{2} \mathbf{E}(t) \quad (\text{A.1})$$

$$2. \quad \mathbf{v}' = \mathbf{v}^- + \frac{q}{m} \frac{\Delta t}{2} \mathbf{v}^- \times \mathbf{B}(t) \quad (\text{A.2})$$

$$3. \quad \mathbf{v}^+ = \mathbf{v}^- + \frac{\frac{q}{m} \frac{\Delta t}{2}}{1 + \left( \frac{q}{m} \frac{\Delta t}{2} |\mathbf{B}| \right)^2} \mathbf{v}' \times \mathbf{B}(t) \quad (\text{A.3})$$

$$4. \quad \mathbf{v}(t + \Delta t / 2) = \mathbf{v}^+ + \frac{q}{m} \frac{\Delta t}{2} \mathbf{E}(t) \quad (\text{A.4})$$

The position is advanced by the additional step:

$$5. \quad \mathbf{r}(t + \Delta t) = \mathbf{r}(t) + \Delta t \mathbf{v}(t + \Delta t / 2) \quad (\text{A.5})$$

The algorithm could also be written a different way. Let us define the following vector:

$$\boldsymbol{\beta} = \frac{\omega_c \Delta t}{2} \hat{\mathbf{b}} \quad (\text{A.6})$$

where  $\omega_c = \frac{q}{m} |\mathbf{B}|$  is the cyclotron frequency (unsigned) and  $\hat{\mathbf{b}} = \mathbf{B} / |\mathbf{B}|$  is the unit vector along the magnetic field. Steps 2 and 3 can be combined into the form:

$$\mathbf{v}^+ = \mathbf{v}^- - \frac{2}{1 + \beta^2} \boldsymbol{\beta} \times \mathbf{v}^- + \frac{2}{1 + \beta^2} \boldsymbol{\beta} \times \boldsymbol{\beta} \times \mathbf{v}^- \quad (\text{A.7})$$

(with  $\beta \equiv |\boldsymbol{\beta}|$ ). The equivalent matrix form is:

$$\mathbf{v}^+ = \mathbf{v}^- + \frac{2}{1 + \beta^2} \begin{pmatrix} 0 & +\beta_z & -\beta_y \\ -\beta_z & 0 & +\beta_x \\ +\beta_y & -\beta_x & 0 \end{pmatrix} \cdot \mathbf{v}^- + \frac{2}{1 + \beta^2} \begin{pmatrix} -\beta_y^2 - \beta_z^2 & \beta_x \beta_y & \beta_x \beta_z \\ \beta_y \beta_x & -\beta_x^2 - \beta_z^2 & \beta_y \beta_z \\ \beta_z \beta_x & \beta_z \beta_y & -\beta_x^2 - \beta_y^2 \end{pmatrix} \cdot \mathbf{v}^- \quad (\text{A.8})$$

or equivalently:

$$\mathbf{v}^+ = \frac{1 - \beta^2}{1 + \beta^2} \mathbf{v}^- + \frac{2}{1 + \beta^2} \begin{pmatrix} 0 & +\beta_z & -\beta_y \\ -\beta_z & 0 & +\beta_x \\ +\beta_y & -\beta_x & 0 \end{pmatrix} \cdot \mathbf{v}^- + \frac{2}{1 + \beta^2} \begin{pmatrix} \beta_x \beta_x & \beta_x \beta_y & \beta_x \beta_z \\ \beta_y \beta_x & \beta_y \beta_y & \beta_y \beta_z \\ \beta_z \beta_x & \beta_z \beta_y & \beta_z \beta_z \end{pmatrix} \cdot \mathbf{v}^- \quad (\text{A.9})$$

The origin of the Boris algorithm is made clear by the following. Consider the rotation step as follows:

$$\delta \mathbf{v} = \mathbf{v}^+ - \mathbf{v}^- = \frac{q}{m} \frac{\Delta t}{2} (\mathbf{v}^- + \delta \mathbf{v}) \times \mathbf{B}(t) \quad (\text{A.10})$$

leading to:

$$\mathbf{v}^+ + \frac{q}{m} \frac{\Delta t}{2} \mathbf{B} \times \mathbf{v}^+ = \mathbf{v}^- - \frac{q}{m} \frac{\Delta t}{2} \mathbf{B} \times \mathbf{v}^- \quad (\text{A.11})$$

or in matrix form:

$$\underbrace{\begin{pmatrix} 1 & -\beta_z & +\beta_y \\ +\beta_z & 1 & -\beta_x \\ -\beta_y & +\beta_x & 1 \end{pmatrix}}_{\mathbf{N}_+} \cdot \mathbf{v}^+ = \underbrace{\begin{pmatrix} 1 & +\beta_z & -\beta_y \\ -\beta_z & 1 & +\beta_x \\ +\beta_y & -\beta_x & 1 \end{pmatrix}}_{\mathbf{N}_-} \cdot \mathbf{v}^- \quad (\text{A.12})$$

The matrix  $\mathbf{N}_+$  on the LHS can be inverted to yield:

$$\mathbf{N}_+^{-1} = \frac{1}{1+\beta^2} \begin{pmatrix} 1+\beta_x^2 & +\beta_z+\beta_x\beta_y & -\beta_y+\beta_x\beta_z \\ -\beta_z+\beta_y\beta_x & 1+\beta_y^2 & +\beta_x+\beta_y\beta_z \\ +\beta_y+\beta_z\beta_x & -\beta_x+\beta_z\beta_y & 1+\beta_z^2 \end{pmatrix} \quad (\text{A.13})$$

The product  $\mathbf{N}_+^{-1} \cdot \mathbf{N}_-$  is:

$$\mathbf{N}_+^{-1} \cdot \mathbf{N}_- = \frac{1}{1+\beta^2} \begin{pmatrix} 1+\beta_x^2-\beta_y^2-\beta_z^2 & +2\beta_z+2\beta_x\beta_y & -2\beta_y+2\beta_x\beta_z \\ -2\beta_z+2\beta_y\beta_x & 1+\beta_y^2-\beta_x^2-\beta_z^2 & +2\beta_x+2\beta_y\beta_z \\ +2\beta_y+2\beta_z\beta_x & -2\beta_x+2\beta_z\beta_y & 1+\beta_z^2-\beta_x^2-\beta_y^2 \end{pmatrix} \quad (\text{A.14})$$

which can be decomposed into the form:

$$\mathbf{N}_+^{-1} \cdot \mathbf{N}_- = \frac{1-\beta^2}{1+\beta^2} (\mathbf{1}) + \frac{2}{1+\beta^2} \begin{pmatrix} 0 & +\beta_z & -\beta_y \\ -\beta_z & 0 & +\beta_x \\ +\beta_y & -\beta_x & 0 \end{pmatrix} + \frac{2}{1+\beta^2} \begin{pmatrix} \beta_x\beta_x & \beta_x\beta_y & \beta_x\beta_z \\ \beta_y\beta_x & \beta_y\beta_y & \beta_y\beta_z \\ \beta_z\beta_x & \beta_z\beta_y & \beta_z\beta_z \end{pmatrix} \quad (\text{A.15})$$

We see that this is equivalent to (A.9), and therefore the steps 2 and 3 of the Boris algorithm are equivalent to a time-centered scheme for the gyro-motion (A.10).

Note that the Boris algorithm is operator-splitting the electric acceleration from the magnetic rotation. We could also look into a complete operator definition without this splitting, by considering the full time-centered algorithm:

$$\delta \mathbf{v} = \mathbf{v}_{n+1/2} - \mathbf{v}_{n-1/2} = \frac{q}{m} \Delta t \cdot \mathbf{E}_n + \frac{q}{m} \frac{\Delta t}{2} (\mathbf{v}_{n+1/2} + \mathbf{v}_{n-1/2}) \times \mathbf{B}_n \quad (\text{A.16})$$

which becomes

$$\mathbf{N}_+ \cdot \mathbf{v}_{n+1/2} = \mathbf{a}_n \Delta t + \mathbf{N}_- \cdot \mathbf{v}_{n-1/2} \quad (\text{A.17})$$

where  $\mathbf{a}_n = (q/m) \cdot \mathbf{E}_n$ . The solution is already expressed using the matrices of (A.13) and (A.15).

To simplify the notation, let us define the following:

$$\mathbf{M}_0 = \frac{1}{1+\beta^2} (\mathbf{1}), \quad \mathbf{M}_1 = \frac{1}{1+\beta^2} \begin{pmatrix} 0 & +\beta_z & -\beta_y \\ -\beta_z & 0 & +\beta_x \\ +\beta_y & -\beta_x & 0 \end{pmatrix} \quad \text{and} \quad \mathbf{M}_2 = \frac{1}{1+\beta^2} \begin{pmatrix} \beta_x\beta_x & \beta_x\beta_y & \beta_x\beta_z \\ \beta_y\beta_x & \beta_y\beta_y & \beta_y\beta_z \\ \beta_z\beta_x & \beta_z\beta_y & \beta_z\beta_z \end{pmatrix} \quad (\text{A.18})$$

then the solution is expressed as:

$$\mathbf{v}_{n+1/2} = \mathbf{N}_+^{-1} \cdot (\mathbf{a}_n \Delta t) + (\mathbf{N}_+^{-1} \mathbf{N}_-) \cdot \mathbf{v}_{n-1/2} \quad (\text{A.19})$$

with:

$$\mathbf{N}_+^{-1} = \mathbf{M}_0 + \mathbf{M}_1 + \mathbf{M}_2 \quad (\text{A.20a})$$

and

$$\mathbf{N}_+^{-1} \mathbf{N}_- = (1-\beta^2) \mathbf{M}_0 + 2 \mathbf{M}_1 + 2 \mathbf{M}_2 \quad (\text{A.20b})$$

In the case where the magnetic field is aligned along the  $\hat{z}$ -axis, considerable simplification occurs. We can easily see that (A.9) leads to the following relations for the parallel and transverse components respectively:

$$\mathbf{v}_{\parallel}^+ \equiv \mathbf{v}_{\parallel}^- \quad (\text{A.21a})$$

and

$$\mathbf{v}_{\perp}^{+} - \mathbf{v}_{\perp}^{-} = \frac{1}{1+(\delta/2)^2} \begin{pmatrix} -\delta^2/2 & \delta \\ -\delta & -\delta^2/2 \end{pmatrix} \cdot \mathbf{v}_{\perp}^{-} \quad (\text{A.22b})$$

where  $\delta = \omega_c \Delta t$ . This leads to:

$$\begin{aligned} \Delta \mathbf{v} &= \mathbf{v}_{n+1/2} - \mathbf{v}_{n-1/2} \\ &= (\cdot \mathbf{v}^{+} + \frac{1}{2} \mathbf{a}_n \Delta t) - (\cdot \mathbf{v}^{-} - \frac{1}{2} \mathbf{a}_n \Delta t) \\ &= \mathbf{a}_n \Delta t + \frac{1}{1+(\delta/2)^2} \begin{pmatrix} -\delta^2/2 & \delta & 0 \\ -\delta & -\delta^2/2 & 0 \\ 0 & 0 & 0 \end{pmatrix} \cdot (\mathbf{v}_n + \frac{1}{2} \mathbf{a}_n \Delta t) \end{aligned} \quad (\text{A.23a})$$

or, keeping terms of order  $\delta^2$  only:

$$\Delta \mathbf{v} = \begin{cases} \mathbf{a}_x \Delta t + (\omega_c \Delta t)(v_y + \frac{1}{2} \mathbf{a}_y \Delta t) - \frac{1}{2} (\omega_c \Delta t)^2 v_x \\ \mathbf{a}_y \Delta t - (\omega_c \Delta t)(v_x + \frac{1}{2} \mathbf{a}_x \Delta t) - \frac{1}{2} (\omega_c \Delta t)^2 v_y \\ \mathbf{a}_z \Delta t \end{cases} \quad (\text{A.23b})$$

This page intentionally blank

# Kinetic Modeling of Laser-Induced Fusion

**Peter Messmer  
Kevin Paul  
Peter Stoltz  
Tech-X Corporation  
5621 Arapahoe Ave., Suite A  
Boulder CO 80303**

**Jean-Luc Cambier  
AFRL/RZSA  
10 E. Saturn Blvd.  
Edwards AFB CA 93524-7680**

**September 2007**

**Special Report**

**APPROVED FOR PUBLIC RELEASE; DISTRIBUTION UNLIMITED.**



**AIR FORCE RESEARCH LABORATORY  
AIR FORCE MATERIEL COMMAND  
EDWARDS AIR FORCE BASE CA 93524-7048**

REPORT DOCUMENTATION PAGE			Form Approved OMB No. 0704-0188		
<p>Public reporting burden for this collection of information is estimated to average 1 hour per response, including the time for reviewing instructions, searching existing data sources, gathering and maintaining the data needed, and completing and reviewing this collection of information. Send comments regarding this burden estimate or any other aspect of this collection of information, including suggestions for reducing this burden to Department of Defense, Washington Headquarters Services, Directorate for Information Operations and Reports (0704-0188), 1215 Jefferson Davis Highway, Suite 1204, Arlington, VA 22202-4302. Respondents should be aware that notwithstanding any other provision of law, no person shall be subject to any penalty for failing to comply with a collection of information if it does not display a currently valid OMB control number. <b>PLEASE DO NOT RETURN YOUR FORM TO THE ABOVE ADDRESS.</b></p>					
1. REPORT DATE (DD-MM-YYYY) 01-07-2007		2. REPORT TYPE Special Report		3. DATES COVERED (From - To) 31 Jul 2002 – 24 Sep 2007	
4. TITLE AND SUBTITLE Kinetic Modeling of Laser Induced Fusion			5a. CONTRACT NUMBER RP060281		
			5b. GRANT NUMBER		
			5c. PROGRAM ELEMENT NUMBER 61102F		
6. AUTHOR(S) Peter Messmer, Kevin Paul, Peter Stoltz, Jean-Luc Cambier*			5d. PROJECT NUMBER		
			5e. TASK NUMBER		
			5f. WORK UNIT NUMBER 23040256		
7. PERFORMING ORGANIZATION NAME(S) AND ADDRESS(ES) Tech-X Corporation 5621 Arapahoe Ave., Suite A Boulder CO 80303			8. PERFORMING ORGANIZATION REPORT NO.		
9. SPONSORING / MONITORING AGENCY NAME(S) AND ADDRESS(ES) Air Force Research Laboratory (AFMC) *AFRL/RZSA 10 E. Saturn Blvd. Edwards AFB CA 93524-7680			10. SPONSOR/MONITOR'S ACRONYM(S)		
			11. SPONSOR/MONITOR'S REPORT NUMBER(S) AFRL-RZ-ED-TR-2007-0065		
12. DISTRIBUTION / AVAILABILITY STATEMENT Approved for public release; distribution unlimited. Public Affairs No. 07298A.					
13. SUPPLEMENTARY NOTES					
14. ABSTRACT Thermal neutrons are of considerable interest to the Department of Defense and for commercial applications. Unlike high-energy photons, neutrons easily penetrate high density targets, but get effectively absorbed by low density materials like paraffin, nylon or explosives. This makes them attractive complements to X-rays for radiographic applications, e.g. for the detection or inspection of explosives inside steel casings. The key challenge is to develop a compact generator for thermal neutrons with large enough flux. The limited availability of radio-isotopes, combined with the relatively short half-life, safety constraints and regulatory requirements make them unattractive for wide-spread use. An alternative design exploits the Deuterium-Tritium (D-T) fusion, which generates Alpha particles and fast neutrons. In these sources, Deuterium ions are accelerated to about 130 keV and hit a Tritium target. The acceleration of Deuterium ions is usually accomplished in a diode configuration. Recently, considerable success has been achieved in the acceleration of ions via laser-matter interaction. In this project we investigated whether laser-accelerated ions could undergo nuclear fusion in an adequately designed target and could be used for neutron sources. We therefore enhanced our proprietary plasma simulation code VORPAL with a model for fusion reactions and investigated the generation of neutrons in shaped D-T targets. We find that neutron fluxes large enough for radiographic applications can be generated by utilizing moderate ( $\approx 10^{17}$ – $10^{18}$ W/cm <sup>2</sup> ) laser intensities.					
15. SUBJECT TERMS Laser; fusion; kinetic; modeling; thermal neutrons; deuterium; VORPAL					
16. SECURITY CLASSIFICATION OF:			17. LIMITATION OF ABSTRACT	18. NUMBER OF PAGES	19a. NAME OF RESPONSIBLE PERSON Dr. Jean-Luc J. Cambier
a. REPORT Unclassified	b. ABSTRACT Unclassified	c. THIS PAGE Unclassified			19b. TELEPHONE NO (include area code) N/A



## **STINFO COPY NOTICE AND SIGNATURE PAGE**

Using Government drawings, specifications, or other data included in this document for any purpose other than Government procurement does not in any way obligate the U.S. Government. The fact that the Government formulated or supplied the drawings, specifications, or other data does not license the holder or any other person or corporation; or convey any rights or permission to manufacture, use, or sell any patented invention that may relate to them.

Qualified requestors may obtain copies of this report from the Defense Technical Information Center (DTIC) (<http://www.dtic.mil>).

AFRL-RZ-ED-TR-2007-0065 HAS BEEN REVIEWED AND IS APPROVED FOR PUBLICATION IN ACCORDANCE WITH ASSIGNED DISTRIBUTION STATEMENT.

FOR THE DIRECTOR:

\_\_\_\_//signed//\_\_\_\_  
JEAN-LUC J. CAMBIER  
Project Manager

\_\_\_\_//signed//\_\_\_\_  
INGRID J. WYSONG  
Chief, Aerophysics Branch

\_\_\_\_//signed//\_\_\_\_  
PHILIP A. KESSEL  
Technical Advisor  
Space & Missile Propulsion Division

This report is published in the interest of scientific and technical information exchange, and its publication does not constitute the Government's approval or disapproval of its ideas or findings.



# **Kinetic Modeling of Laser Induced Fusion**

## **Final Report**

**Contract # RP060281**

Peter Messmer, Kevin Paul, Peter Stoltz  
Tech-X Corporation

Jean-Luc Cambier  
AFRL

### **PREPARED BY:**

Tech-X Corporation  
5621 Arapahoe Avenue, Suite A  
Boulder, CO 80303  
Tel: (303) 448 0727, Fax: (303) 448 7756  
Email: [messmer@txcorp.com](mailto:messmer@txcorp.com)

**July, 2007**

## ***Table of Contents***

1	Introduction.....	1
2	The Plasma Simulation Framework VORPAL.....	1
2.1	Ionization Model.....	2
2.2	Fusion Reaction .....	3
2.3	Fusion of Shock-Accelerated Ions .....	4
2.4	Reverse Acceleration of Ions .....	8
2.5	Focusing of Reverse Accelerated Ions.....	9
2.6	D-T Acceleration in Shaped Targets.....	11
2.7	Neutron Generation in Shaped Target .....	14
3	Summary .....	16
4	Conclusions.....	17
5	References.....	18

## List of Figures

Figure No.	Page
1 Left panel: Example of a VORPAL Simulation, (Superconducting RF Cavity). Right Panel: Mono-Energetic Electron Beam Generated by Laser-Wakefield Acceleration.....	2
2 Left: Comparison of an Oxygen Spectrum Computed with the Kinetic Ionization Model in VORPAL [bars] with an Observed Spectrum [red stars]. ....	3
3 Energy Dependent Cross-Section for the D-T Fusion Reaction Based on the Model in [6] .....	4
4 Phase Space Projections of the D (blue) and T (red) Ions at Different Times.....	5
5 Spatial Energy Distribution of the D (blue) and T (red) Population after 0.48ps (left) and 0.96ps (right) for a Laser Intensity of $I=1.8 \cdot 10^{17}$ W/cm <sup>2</sup> .....	6
6 Phase Space Projection (left) and Ion Energy (right) for the Interaction of a 60 fs, $2.6 \cdot 10^{17}$ W/cm <sup>2</sup> Laser Pulse with a D-T Plasma .....	6
7 Left: Temporal Evolution of the Neutron Flux Generated in the Interaction of a 60 fs Laser Pulse with a D-T target. Right: Scaling of the Peak Neutron Flux with Increasing Laser Intensity.....	7
8 Reverse Acceleration of Ions in a Two Material Configuration.....	7
9 Ion Phase Space, x-y-v <sub>x</sub> , Showing an Iso-Density Surface for He <sup>2+</sup> ions (yellow) and Al <sup>+</sup> ions (green). ....	8
10 Flow Field of Reverse Accelerated Ions.....	9
11 Two Different Views of the Ion Density after 1.18 ps. ....	10
12 Evolution of the Ion Density over Time.....	11
13 Setup of Shaped Target Configuration: A High Density Shaped Tin Target (red) is Coated with an Under-Dense Deuterium Film (green) with a Tritium Ball (blue) Suspended in the Center of Spherical Mirror .....	12
14 Time Evolution of the D and T Density for a Laser Amplitude of $E=3 \cdot 10^{12}$ V/m (left) and $6 \cdot 10^{12}$ V/m (right) after 0.1ps (a), 0.3ps (b), 0.6ps (c) and 0.9ps (d). ....	13
15 Deuterium (left) and Tritium (right) Density Distribution after 1.33 ps for a Peak Electric Field of $E=3 \cdot 10^{12}$ V/m. ....	14
16 Time Evolution of the Neutron Generation for a Laser Amplitude of $E=3 \cdot 10^{12}$ V/m (left) and $6 \cdot 10^{12}$ V/m (right) after 0.3ps (a), 0.6ps (b) and 0.9ps (c) .....	15
17 Neutron Flux Evolution for Laser Amplitudes $E=1.5 \cdot 10^{12}$ V/m (dash-dotted), $E=2 \cdot 10^{12}$ V/m (dash-triple-dotted), $E=3 \cdot 10^{12}$ V/m (solid) and $E=6 \cdot 10^{12}$ V/m (dashed).....	16

***Glossary***

1D	one-dimensional
2D	two-dimensional
CFL	Courant Friedrichs Lewy
D-D	Deuterium-Deuterium
D-T	Deuterium-Tritium
PIC	Particle-in-Cell
PML	perfectly matched layer
RF	radio frequency
TNSA	Target Normal Sheath Acceleration
VORPAL	Versatile Plasma simulation code



# 1 Introduction

Thermal neutrons with energies on the order of 0.025eV are of considerable interest to the Department of Defense and for commercial applications. Unlike high-energy photons, neutrons easily penetrate high density targets, but get effectively absorbed by low density materials like paraffin, nylon or explosives. This makes them attractive complements to X-rays for radiographic applications, e.g. for the detection or inspection of explosives inside steel casings. The key challenge is to develop a compact generator for thermal neutrons with a flux of at least  $10^8$  neutrons/cm<sup>2</sup>s which is sufficient for radiographic applications.

The limited available amount of radio-isotopes like Californium 252, combined with the relatively short half-life, safety constraints and regulatory requirements make them unattractive for wide-spread use.

An alternative design exploits the Deuterium-Tritium (D-T) fusion, which generates Alpha particles and fast neutrons. In these sources, Deuterium ions are accelerated to about 130 keV and hit a Tritium target. In order to be attractive for radiographic applications, the 14.1 MeV neutrons have to be thermalized in an external moderator, for example a paraffin layer. This reduces the useful neutron flux by about two orders of magnitude. D-D reactions produce neutrons with lower energy (2.4 MeV), but one must also account for the branching ratio into charged products; i.e.,  $d(d,p)t$ , and the reduced cross-section compared to  $d(d,n)\alpha$ .

The acceleration of Deuterium ions is usually accomplished in a diode configuration. Recently, the interaction of high-power laser pulses with plasmas or solids has attracted considerable interest for the acceleration of electrons or ions [1, 2]. Especially the acceleration of ions to MeV energies opens entirely new possibilities for small scale ion accelerators and possibly for neutron sources.

In this project, we therefore investigated different target configurations for the potential use as neutron generators via numerical simulations.

## 2 The Plasma Simulation Framework VORPAL

The versatile plasma simulation code VORPAL [3] was originally designed for the investigation of laser wakefield acceleration of electrons. However, the code design is sufficiently general that it is capable to address entirely new application areas, like modeling of superconducting RF cavities, breakdown phenomena in microwaves guides or investigations of astrophysical plasmas. Figure 1 shows examples of such simulations. The code has recently been enhanced by a variety of models, including ionization processes.

The model for ionization processes is a hybrid between classical particle-in-cell [4] and the Direct-Simulation Monte-Carlo model [5]. Particles are pushed in their self-consistent

electromagnetic field. At every time-step, particles within a cell are considered for possible collision (and therefore reaction) by Monte-Carlo methods. The main parameters required in this model are energy dependent cross sections for ionization. While the model was mainly designed for ionization processes, it can relatively easily be adapted to other reaction types, including fusion.

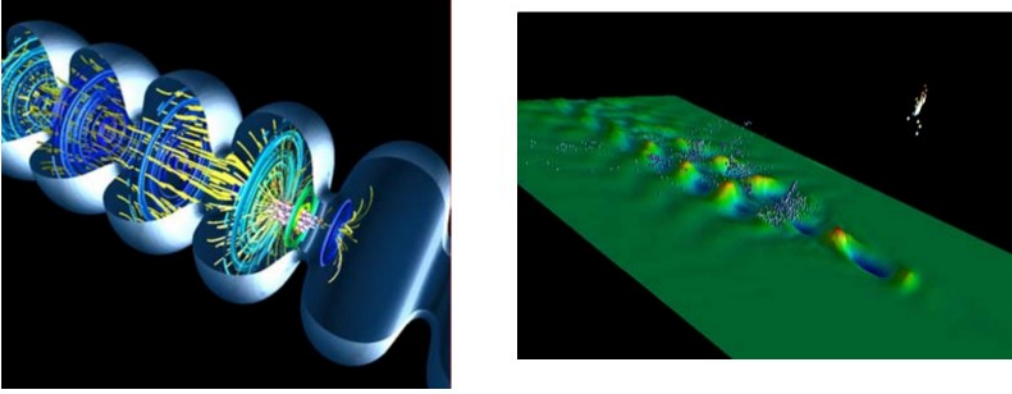


**Figure 1:** Left panel: Example of a VORPAL simulation, (superconducting RF cavity). Right Panel: Mono-energetic electron beam generated by laser-wakefield acceleration (Simulation by John R. Cary, Visualization: Peter Messmer).

## 2.1 Ionization Model

The ionization model in VORPAL was successfully used to reproduce ion spectra in Electron-Cyclotron Resonance Sources. Figure 2 shows a comparison of the kinetic impact ionization model in VORPAL with a spectrum for a hot population of oxygen measured at VENUS [7]. For experimental reasons, the spectrum was not measured for pure oxygen, but rather a mixture of Oxygen and Helium. The resulting spectrum at mass/charge ratios of 4 was therefore a blend between the oxygen and the helium contribution. The VORPAL simulation is a fully periodic box, containing atomic Oxygen,  $O^+$  and  $e^-$ . The evolution of the different charge states is shown in Figure 2 (right). For the given electron energy, the first charge state not present in the initial distribution is going to be  $O^{2+}$ , but as soon as it is available in high enough concentration, the next ionization state is being produced and the ionization rate of  $O^{2+}$  drops. The overall spectrum obtained by integrating the ionization rates in time is shown in the left panel. For comparison, the measured current at VENUS [8] is shown. Good agreement is obtained for 5 charge states. As mentioned previously, the charge state  $M/Q=4$  is mixed in the measured spectrum. We therefore plotted a token value of 0 at  $M/Q=4$ . The good agreement of the simulated with the measured spectrum indicates that the kinetic ionization model in VORPAL works as expected.

The energy dependent cross-sections for the ionization model in VORPAL are based on the semi-empirical model by Shull and Van Steenberg [9], which originates from the astrophysics community. This models predicts the energy dependent cross-sections of light elements, including, C, N, O, Ne, Mg, Si, S, Ar, Ca, Fe, and Ni.



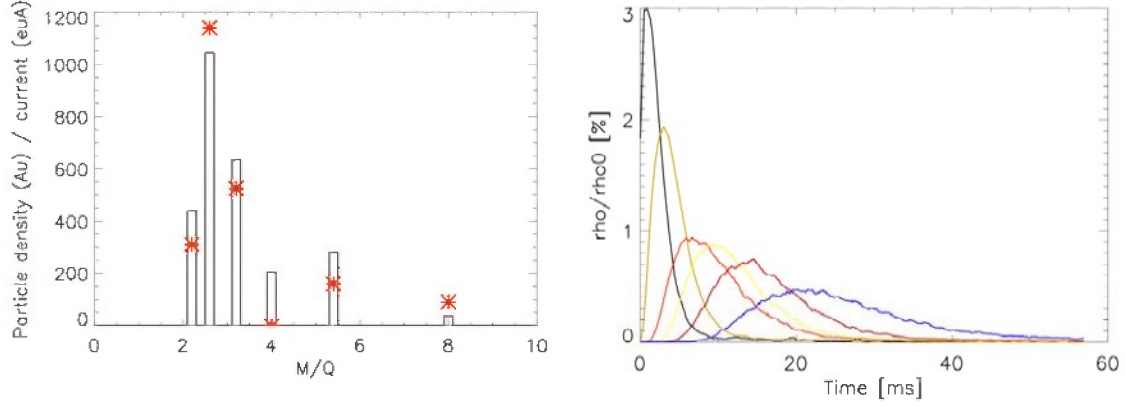


**Figure 2:** Left: Comparison of an oxygen spectrum computed with the kinetic ionization model in VORPAL [bars] with an observed spectrum [red stars]. The measurement at Oxygen 4+ was blended with Helium and therefore not shown in the picture. Right: Temporal evolution of the different charge states of Oxygen for a population starting with pure Oxygen, and O<sup>+</sup>: O<sup>2+</sup> (black), O<sup>3+</sup> (brown), O<sup>4+</sup> (orange), O<sup>5+</sup> (yellow), O<sup>6+</sup> (purple), O<sup>7+</sup> (blue).

## 2.2 Fusion Reaction

The first part of this project was to implement a cross-section model for fusion reactions into VORPAL. Due to the relatively large cross-section at low energies, we chose the Deuterium-Tritium (D-T) reaction for all further studies. We chose a parameterized cross-section model [6] of the form

$$\sigma_T(E) = \frac{A_5 + [(A_4 - A_3 E)^2 + 1]^{-1} A_2}{E [\exp(A_1 E^{-1/2}) - 1]} \quad (1)$$

with  $A_1 = 45.95$  barn keV,  $A_2 = 50200$  barn keV,  $A_3 = 3.98 \times 10^{-3}$  keV<sup>-1</sup>,  $A_4 = 1.297$  and  $A_5 = 409$  barn keV, and the total cross section  $\sigma_T$  measured in barn ( $10^{-24}$  cm<sup>2</sup>) and the energy  $E$  in keV.

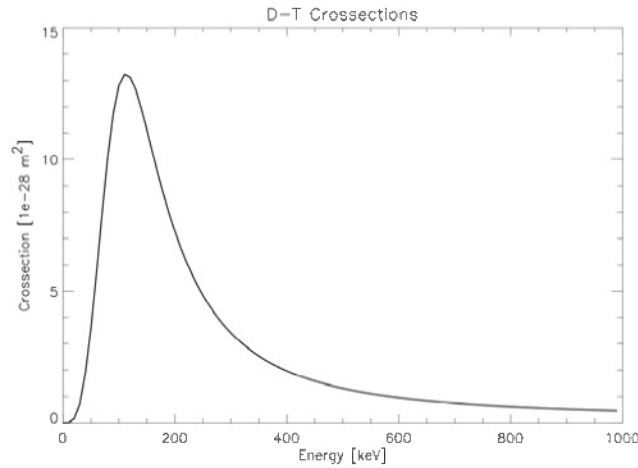
Figure 3 shows the cross-sections as a function of energy. The peak cross-section is on the order of  $10^{-27}$  m<sup>2</sup>, centered around an energy of 130 keV.

One of the main differences between the kinetic ionization model and the fusion model is the magnitude of the cross-section, which is about 7 orders of magnitude smaller for fusion than for ionization. We therefore did not track the generated <sup>4</sup>He ( $\alpha$  particles) in the simulation, but rather estimated the number of neutrons generated in the interaction based on the particle statistics. This de-coupled approximation is valid because the  $\alpha$ -particles are too few to have an impact on the plasma dynamics (i.e. energy deposition), despite the short mean free path at such high densities.

### 2.3 Fusion of Shock-Accelerated Ions

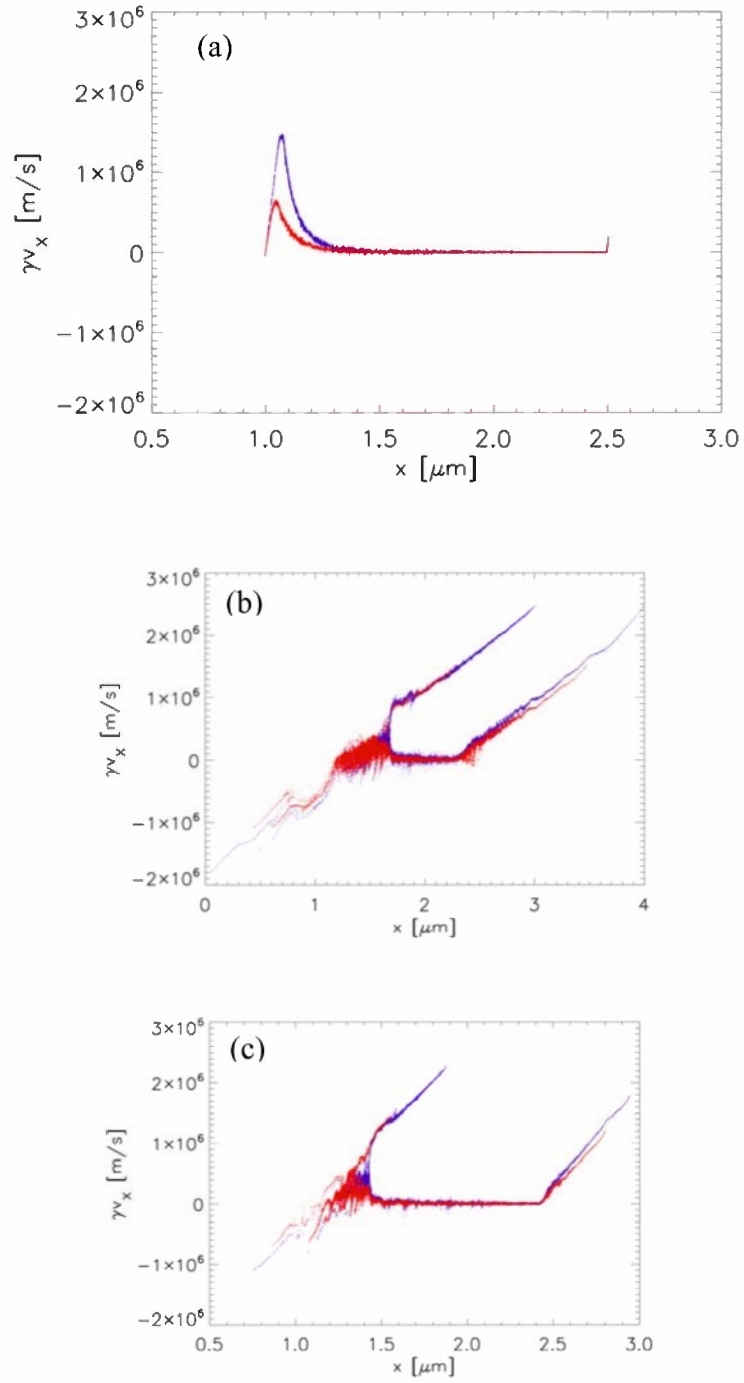
It has previously been reported that the interaction of a femto-second laser pulse with over-dense plasmas can lead to the formation of a shock wave in the target and to the acceleration of ions at this shock front [10]. In a target consisting of a D-T mix, this will therefore lead to a population of D-T ions streaming through a D-T background. If the energy of the shock- accelerated ions is large enough compared to the background ions, one expects that fusion reactions and therefore neutron generation will occur in the vicinity of the shock front

In order to test this hypothesis, we modeled the interaction of a femto-second laser pulse with a slightly over-dense D-T target. We assumed a plasma of density  $2.8 \cdot 10^{27} \text{ m}^{-3}$  being irradiated by a 60 fs,  $0.8 \text{ } \mu\text{m}$  laser pulse with an intensity of  $I = 1.8 \cdot 10^{17} \text{ W/cm}^2$  and a spot radius of  $3 \text{ } \mu\text{m}$ . The plasma was over-dense with a ratio of  $n/n_{\text{cr}} = 1.6$ . The plasma was modeled in a 2D configuration on a  $3000 \times 5$  cell grid. The grid resolution in longitudinal direction is  $1.6 \text{ nm}$  and  $10 \text{ nm}$  in transverse direction. Perfectly matched layer (PML) boundary conditions were employed along both directions of propagation and periodicity was assumed in the transverse direction.



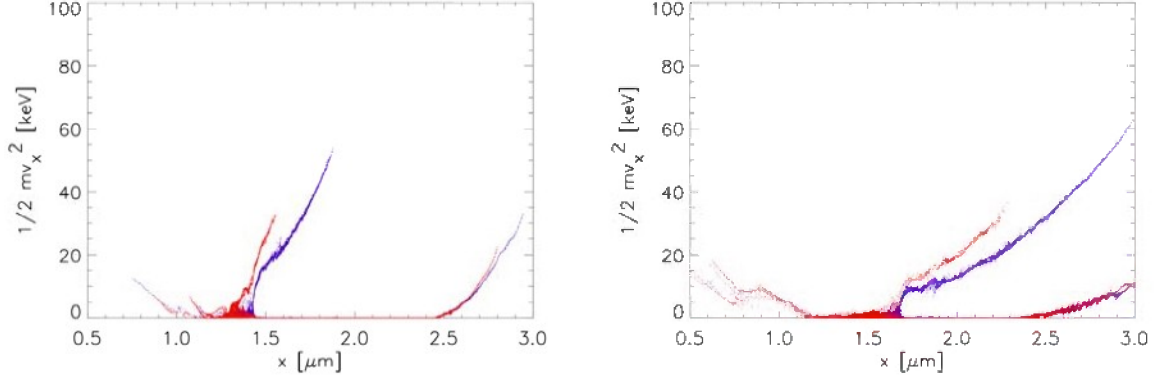
**Figure 3:** Energy dependent cross-section for the D-T fusion reaction based on the model in [6]. The peak cross-section is around 100 keV and reaches  $10^{-27} \text{ m}^2$  (10 barn).

Figure 4 shows phase space projections of the interaction at different times. Due to the lighter mass, the Deuterium ions get accelerated to higher velocities than the Tritium ions. The Target Normal Sheath Acceleration (TNSA) mechanism accelerates both D and T ions at the backside of the plasma (at  $x = 2.5 \text{ } \mu\text{m}$ ). However, in addition to the TNSA, particles are accelerated in the interior of the plasma at the shock front. This results in a fast population of D (and T) propagating forward through the background plasma.



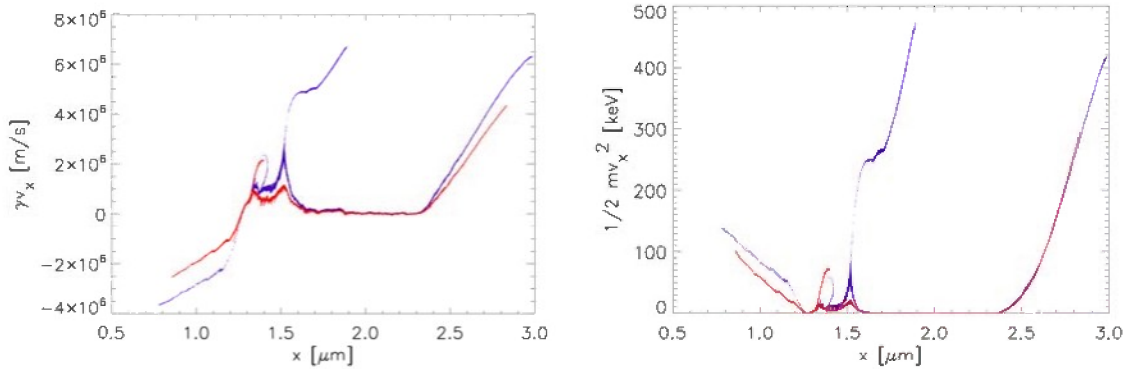
**Figure 4:** Phase space projections of the D (blue) and T (red) ions at different times: (a)- 96fs, (b)-0.48ps and (c)- 0.96ps.

Figure 5 shows the energy distribution of the ions for the above parameters. While these simulations demonstrate that a fast population of D can be generated by the laser-plasma interaction, the resulting ion energies are only on the order of 50 keV, for which the cross-section (see Figure 3) is too small to generate any significant number of fusion events.



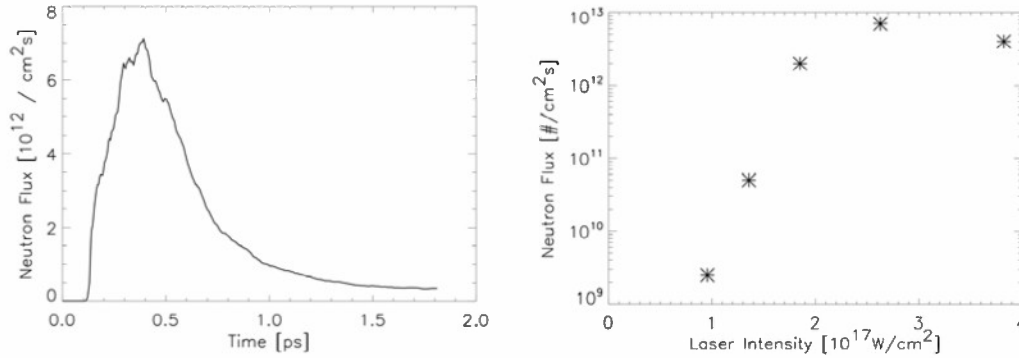
**Figure 5:** Spatial energy distribution of the D (blue) and T (red) population after 0.48ps (left) and 0.96ps (right) for a laser intensity of  $I=1.8 \cdot 10^{17}$  W/cm<sup>2</sup>.

Figure 6 shows the ion phase space and energy of an interaction with increased laser intensity of  $I = 2.6 \cdot 10^{17}$  W/cm<sup>2</sup>. All other parameters are identical to the previous simulations. The energies of the shock-accelerated ions are well above the 120 keV required for a significant number of fusion events to occur.



**Figure 6:** Phase space projection (left) and ion energy (right) for the interaction of a 60 fs,  $2.6 \cdot 10^{17}$  W/cm<sup>2</sup> laser pulse with a D-T plasma.

Using the newly developed fusion model in VORPAL, we were able to investigate the neutrons generated in this interaction. Figure 7 shows the temporal evolution of these neutrons. The peak neutron flux occurs when the shock-accelerated ions propagate through the unperturbed plasma. Once they reach the former back side of the plasma, which is now accelerated via TNSA, the relative velocity is reduced and the number of fusion events is therefore reduced.



**Figure 7:** Left: Temporal evolution of the neutron flux generated in the interaction of a 60 fs laser pulse with a D-T target. Right: Scaling of the peak neutron flux with increasing laser intensity.

The energy of the shock-accelerated ions is highly dependent on the shock velocity, which is in turn dependent on the laser intensity. As these ions are responsible for the neutron generation, the laser intensity will control the neutron flux. Figure 7 shows the scaling of the peak neutron flux as a function of laser intensity. At intensities  $> 3 \cdot 10^{17} \text{W}/\text{cm}^2$ , the target was destroyed.

In summary, using the newly developed fusion model in VORPAL, we demonstrated that the interaction of high-intensity laser pulse with an over-dense D-T target can lead to the generation of neutrons.

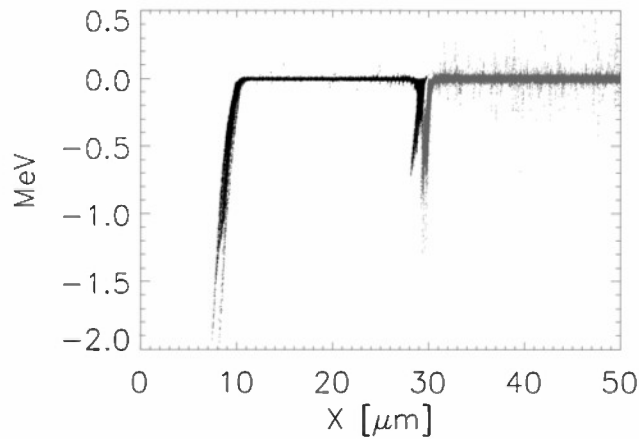


**Figure 8:** Reverse acceleration of ions in a two material configuration. Laser pulse entered from the left and accelerated the first population. At the interface of the two materials, plasma gets accelerated in backward direction.

## 2.4 Reverse Acceleration of Ions

While we demonstrated in the previous paragraph that the neutron flux generated by the interaction of a femto-second laser pulse with a D-T mix is sufficient for radiographic applications, one of the drawbacks of that configuration is the significant fraction of the D-T mix accelerated in the reverse direction (i.e. opposite to the initial laser propagation direction) which is lost to neutron generation. These back-propagating particles can be seen in the phase-space plots of Figure 4b-c, for  $x < 1.5 \mu\text{m}$ . A more efficient target design would take advantage of that ablated material as well.

One way of taking advantage of the ablated material is to optimize the target such that ions are only accelerated in the reverse direction. This can be accomplished by a target consisting of an under-dense coating applied to an over-dense material.

Figure 8 shows the ion phase space of such a two-component target, demonstrating the ion acceleration mainly in the reverse direction. This is an interesting and potentially important mechanism for this type of target, which was not previously investigated.

This mechanism is not limited to pseudo 1D simulations, but also works in 2D. Figure 9 shows the propagation of a  $10^{21} \text{ W/m}^2$ , 60 fs,  $0.8 \mu\text{m}$  laser pulse in a Helium coated aluminum target. The simulation was run on a  $640 \times 320$  cell grid, spanning a  $64 \times 32 \mu\text{m}$  domain. The neutral Helium is modeled as a gas at density of  $10^{26} \text{ \#/m}^3$ . The propagation of the laser pulse ionizes the coating and eventually accelerates the ions. This demonstrates that the reverse acceleration of ions also works in higher dimensions.

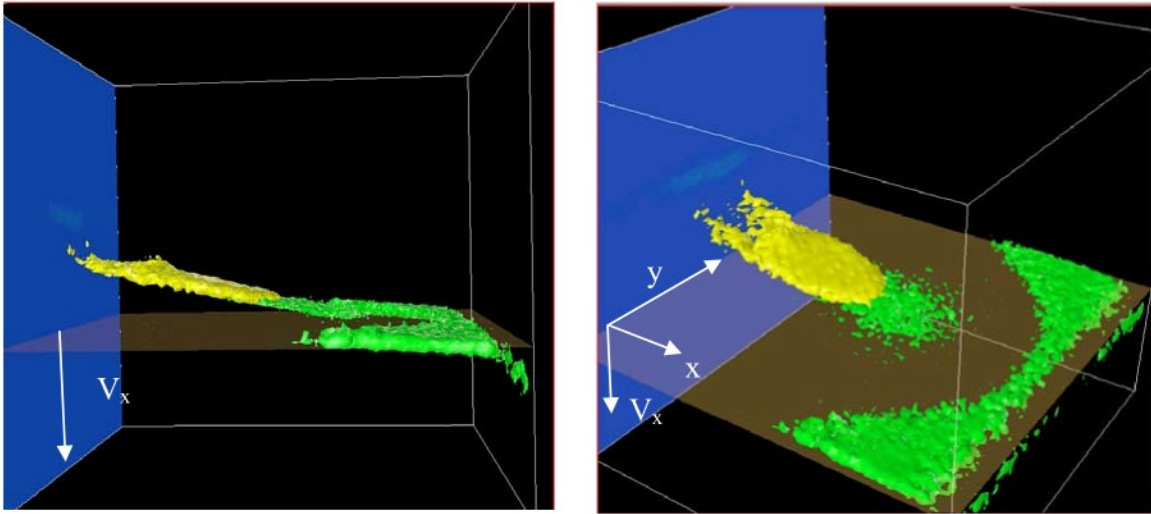


**Figure 9:** Ion phase space,  $x$ - $y$ - $v_x$ , showing an iso-density surface for  $\text{He}^{2+}$  ions (yellow) and  $\text{Al}^+$  ions (green). Negative ion velocities are plotted upwards. The laser pulse initially propagates in positive  $x$  direction, gets reflected off the Al mirror and leaves the domain in negative  $x$  direction. The  $\text{He}^{2+}$  ions initially coat the inside of the spherical Al mirror and are accelerated in reverse direction by the laser pulse.

## 2.5 Focusing of Reverse Accelerated Ions

In this section we therefore investigate whether the material ablated in the interaction of a strong laser pulse with an over-dense target can lead to a neutron flux sufficiently large for radiographic applications. An alternative application for these reverse-accelerated ions would be to use them as a driver for e.g. Inertial Confinement Fusion. In particular, one may envision a combination of forward-accelerated (sheath mechanism) and reverse-accelerated ion beams created by the same laser pulse, operating on different sides of a target, to obtain synchronized beam-beam interactions. Additionally, one may also envision the target as spherically shaped, resulting in converging beams to increase density and temperature at the beam focal point; the target would then include holes through which the laser beam can pass, similar to Hohlraum targets.

We therefore start with investigating the possibility of converging ion beams from shaped targets. We ran simulations of a  $10\text{ }\mu\text{m}$  thick foil, with a "dimple" on the near side having a radius of curvature of  $5\text{ }\mu\text{m}$ . The plate is comprised of a neutral plasma with equal numbers of electrons and singly-ionized deuterium ions. Both plasmas have a density of  $2.5 \cdot 10^{27}\text{ m}^{-3}$ . The plasma frequency is  $\omega_p = 2.825 \cdot 10^{15}\text{ rad/s}$  and the initial temperature is  $130'000\text{ K}$ , resulting in a Debye length of  $0.866\text{ nm}$ . While this leads to numerical heating of the plasma, we anticipated that the violent laser-plasma interaction will dominate and provide at least some qualitative results. For more quantitative results, we then performed subsequent simulations at higher resolution.

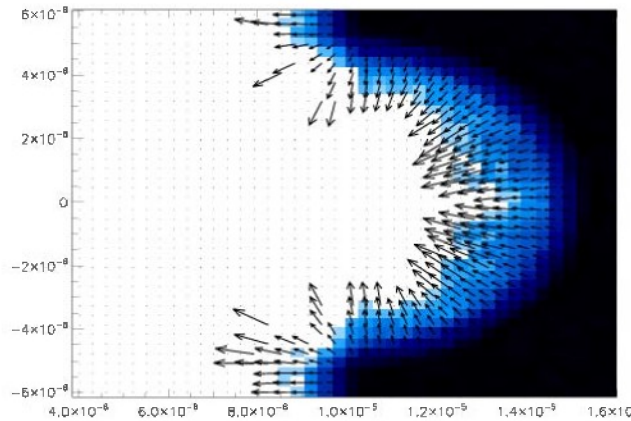


**Figure 10:** Flow field of reverse accelerated ions.

The laser has a wavelength of  $0.8\text{ }\mu\text{m}$ , for which the plasma is slightly over-dense,  $n/n_{\text{crit}} = 1.44$ . The laser field has a peak amplitude of  $1.5 \cdot 10^{12}\text{ V/m}$  (corresponding to an intensity of  $3 \cdot 10^{17}\text{ W/cm}^2$ ) and a pulse duration of  $20\text{ fs}$ .

These initial simulations were run on a  $3000 \times 2000$  cell grid spanning a physical domain of  $30\text{ }\mu\text{m} \times 20\text{ }\mu\text{m}$  ( $dx = dy = 10\text{ nm}$ ), and a time-step of  $1.73 \cdot 10^{-17}\text{ s}$ . Perfectly matched



layer boundary conditions were used along the laser propagation direction and periodic boundaries in transverse direction.

Figure 10 shows the Deuterium flow field after 1.73 ps (100'000 timesteps). The figure clearly shows the backward motion, as well as a focusing flow of the ablated material, which could eventually lead to a high density population in the center of the 'dimple'.

One of the key problems encountered in these simulations is the long timescale on which the interaction takes place. In addition, it would be highly useful to be able to fully resolve high density plasmas to avoid numerical heating, a common problem in Particle-In-Cell (PIC) simulations when the Debye length is not well resolved. In order to further investigate the focusing and to actually observe the formation of the focused ion population, we ran additional simulations, now with a finer grid resolution of 6000x4000 cells ( $dx = dy = 5\text{nm}$ ) and a time-step of  $1.17 \cdot 10^{-17}\text{s}$ . In addition to the finer grid resolution, we also applied a [1 2 1] box-car filter to smooth each component of the current deposited by the charges at every time step. This resulted in a significant reduction of numerical heating and therefore enabled simulations on long timescales. Finally, we increased the laser pulse duration from 20 fs to 50 fs.

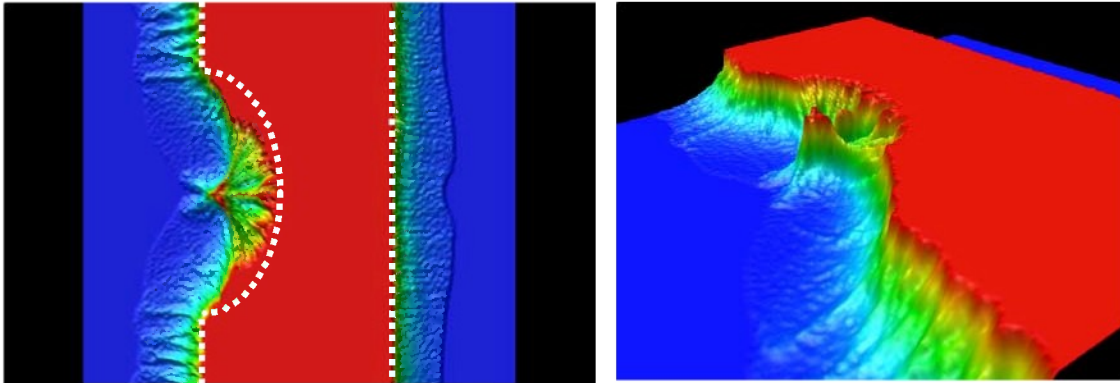


**Figure 11:** Two different views of the ion density after 1.18 ps. The laser pulse entered from the left, was reflected at the spherical mirror and left the domain to the left. The reversely accelerated ions form a high density population in the center of the mirror. The density of this population is significantly higher than the TNSA accelerated population on the right hand side of the foil. The boundaries of the initial distribution are shown as dotted lines.

The basic steps of the laser-matter interaction in these fully 2D simulations are essentially the same as in the pseudo 1D simulation in Section 2.3; i.e., TNSA. In this mechanism, the electric field of the laser pulse accelerates the electrons in the interaction region, which are rapidly accelerated into the target by the Lorentz force. The electrons stream through the foil and form a high-temperature, charged cloud out on the back side. The ambipolar field created by this cloud (sheath) accelerates the ions forward, while colder electrons are pulled back into the material (return current). If the laser pulse is long enough, the electrons return into the interaction region while the laser pulse is still on, being injected again into the foil (electron recirculation). At the same time, the ions in the interaction region start to move in reverse direction, due to the local positive charge left inside the target (reverse accelerated ions). See Figures 11 and 12.



While 1D simulations capture all these effects, they are unable to answer questions about the spatial distribution of the reversely accelerated ions, especially in a shaped target. They also do not properly capture effects from transverse gradients; for example, the return current at the periphery of the channel (outside the laser pulse envelope) can generate strong magnetic fields and affect the ion propagation.

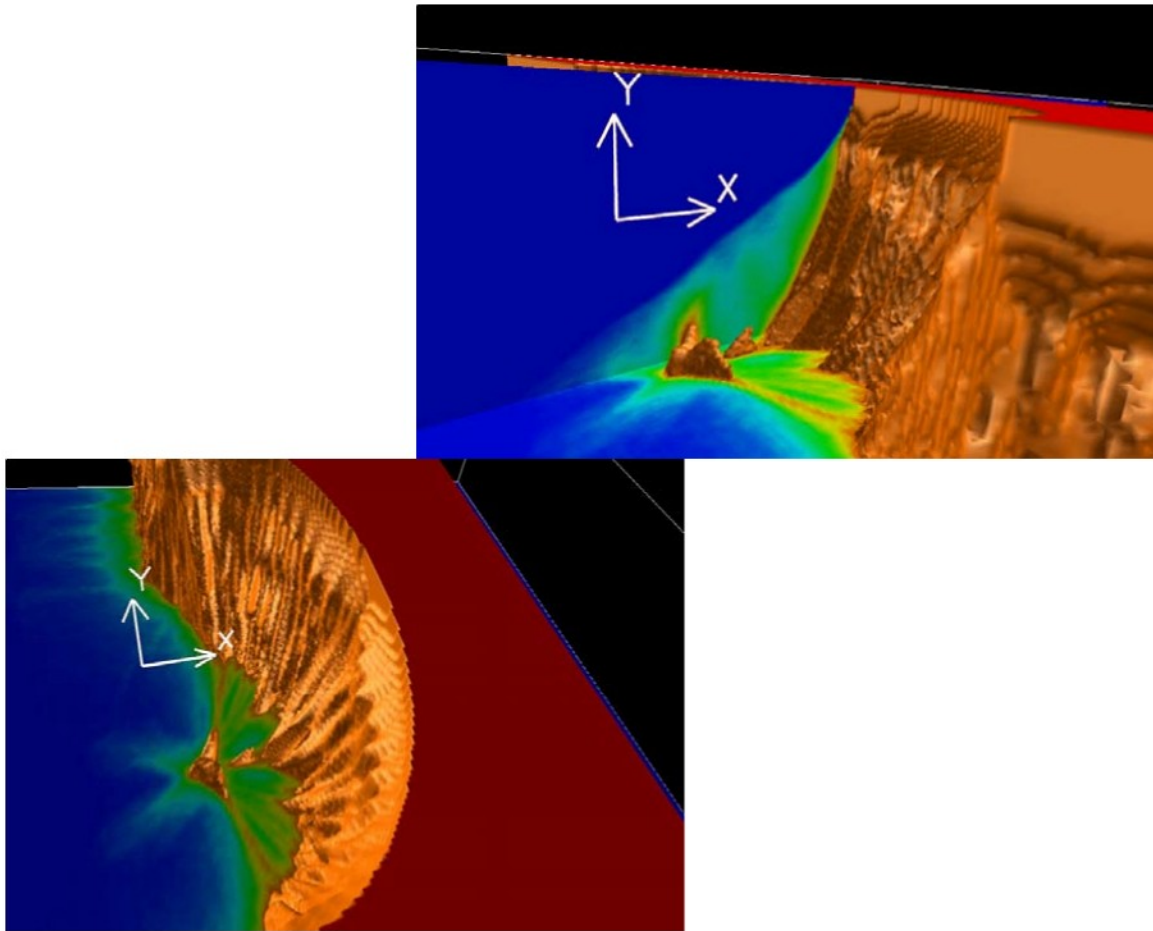


**Figure 12:** Evolution of the ion density over time. The laser pulse propagated along the x direction and got reflected at the spherical mirror. Time evolves in negative Y direction. The ‘ripples’ on the ‘canyon-wall’ show the strong filamentation of the ablated material. After about 1 ps, a high density population in the center of the mirror has formed, propagating in backward direction. This population shows strong divergence, most likely due to the high local space charge.

## 2.6 D-T Acceleration in Shaped Targets

While strong filamentation of the reverse-accelerated ion beam may prevent a good focusing for beam-beam interactions, we still need to examine the potential use of the reverse-accelerated material shown in the previous section as a driver for nuclear fusion. We tested a generic configuration where the reverse-accelerated ions can be focused onto a target. Figure 13 shows the overall setup: the main target consists of a 10  $\mu\text{m}$  thick tin

foil at a density of  $2.5 \cdot 10^{27} \text{ m}^{-3}$  with a  $5 \text{ }\mu\text{m}$  hemi-spherical cavity in the center, which acts as a mirror. The cavity is coated with an under-dense,  $2.5 \text{ }\mu\text{m}$  thick Deuterium layer at a density of  $4.4 \cdot 10^{26} \text{ m}^{-3}$ . Suspended at the focus of the mirror is a Tritium ball with  $2 \text{ }\mu\text{m}$  diameter, also at a density of  $4.4 \cdot 10^{26} \text{ m}^{-3}$ .

The  $0.8 \text{ }\mu\text{m}$  laser has a spot radius of  $2.5 \text{ }\mu\text{m}$  and an intensity ranging between  $1.5 \cdot 10^{21} \text{ Wm}^{-2}$  and  $2.4 \cdot 10^{22} \text{ Wm}^{-2}$  corresponding to peak electric fields of  $1.5 \text{ TV/m}$  to  $6 \text{ TV/m}$ . The simulation domain is  $30 \times 20 \text{ }\mu\text{m}$  covered by a computational grid of  $6000 \times 4000$  cells and a simulation time-step of  $1.06 \cdot 10^{-17} \text{ s}$ . Perfectly matched layer boundary conditions are applied in the laser propagation direction and periodic boundary conditions in the transverse direction. Similar to the simulations in the previous section, we chose an electron temperature which results in a Debye length resolved by the computational grid, as well as filtering of the currents in order to suppress numerical noise.

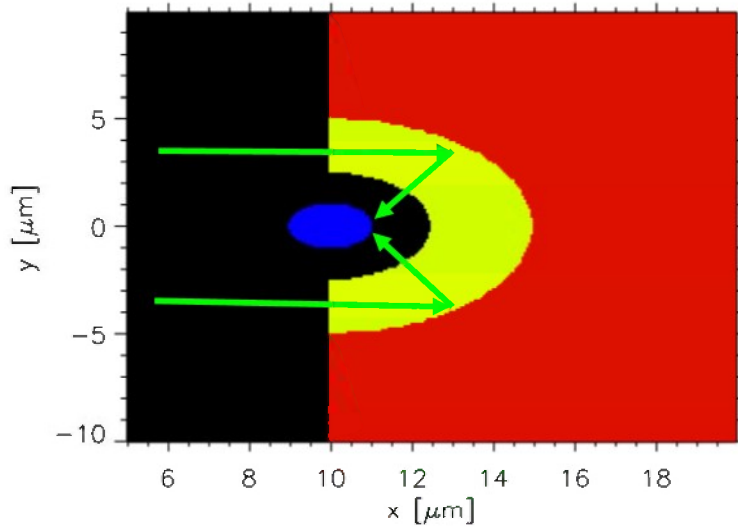


**Figure 13:** Setup of shaped target configuration: A high density shaped tin target (red) is coated with an under-dense deuterium film (green) with a Tritium ball (blue) suspended in the center of spherical mirror. The Tritium ball has a diameter of  $2 \text{ }\mu\text{m}$ , the Deuterium coating has a thickness of  $2.5 \text{ }\mu\text{m}$ . The cavity/mirror radius is  $5 \text{ }\mu\text{m}$ . The laser pulse enters from the left, is reflected off the spherical mirror and gets focused in the center of the mirror.

Figure 14 shows the development of the high density jet of ablated Deuterium. The over-dense lead foil, coated with the deuterium, is not shown. The peak density in the ejected Deuterium can reach up to 1.5 times the original Deuterium density. The Tritium ball explodes as a result of expulsion of electrons by the laser pulse (Coulomb explosion) and interacts with the counter-streaming Deuterium.

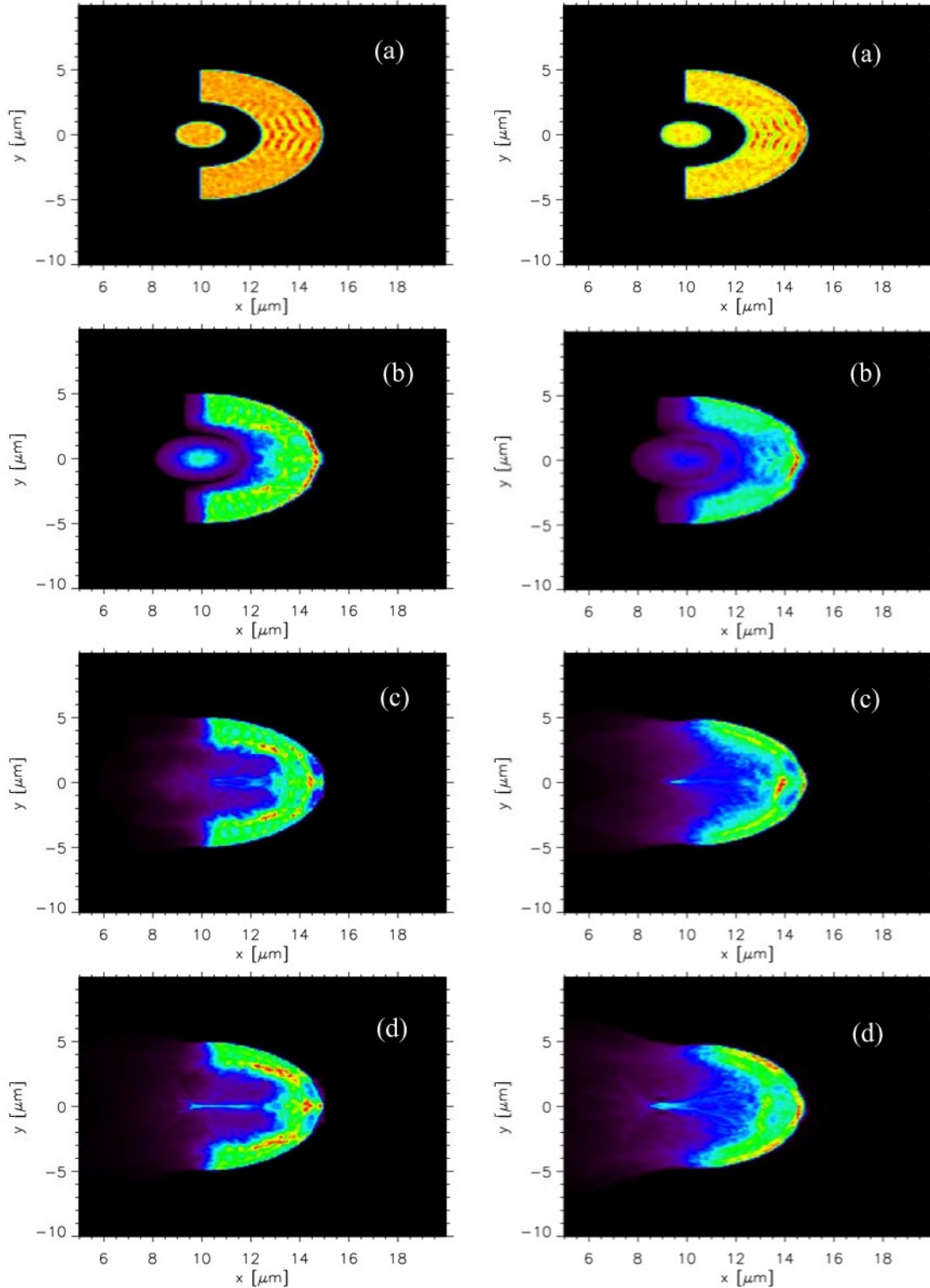


**Figure 14:** Time evolution of the D and T density for a laser amplitude of  $E=3e12$  V/m (left) and  $6e12$  V/m (right) after 0.1ps (a), 0.3ps (b), 0.6ps (c) and 0.9ps (d).

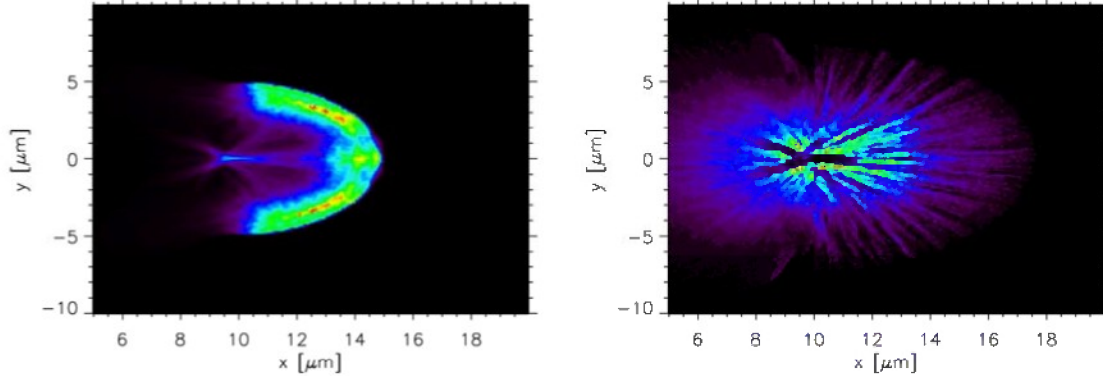


**Figure 15:** Deuterium (left) and Tritium (right) density distribution after 1.33 ps for a peak electric field of  $E = 3 \text{ TV/m}$ .

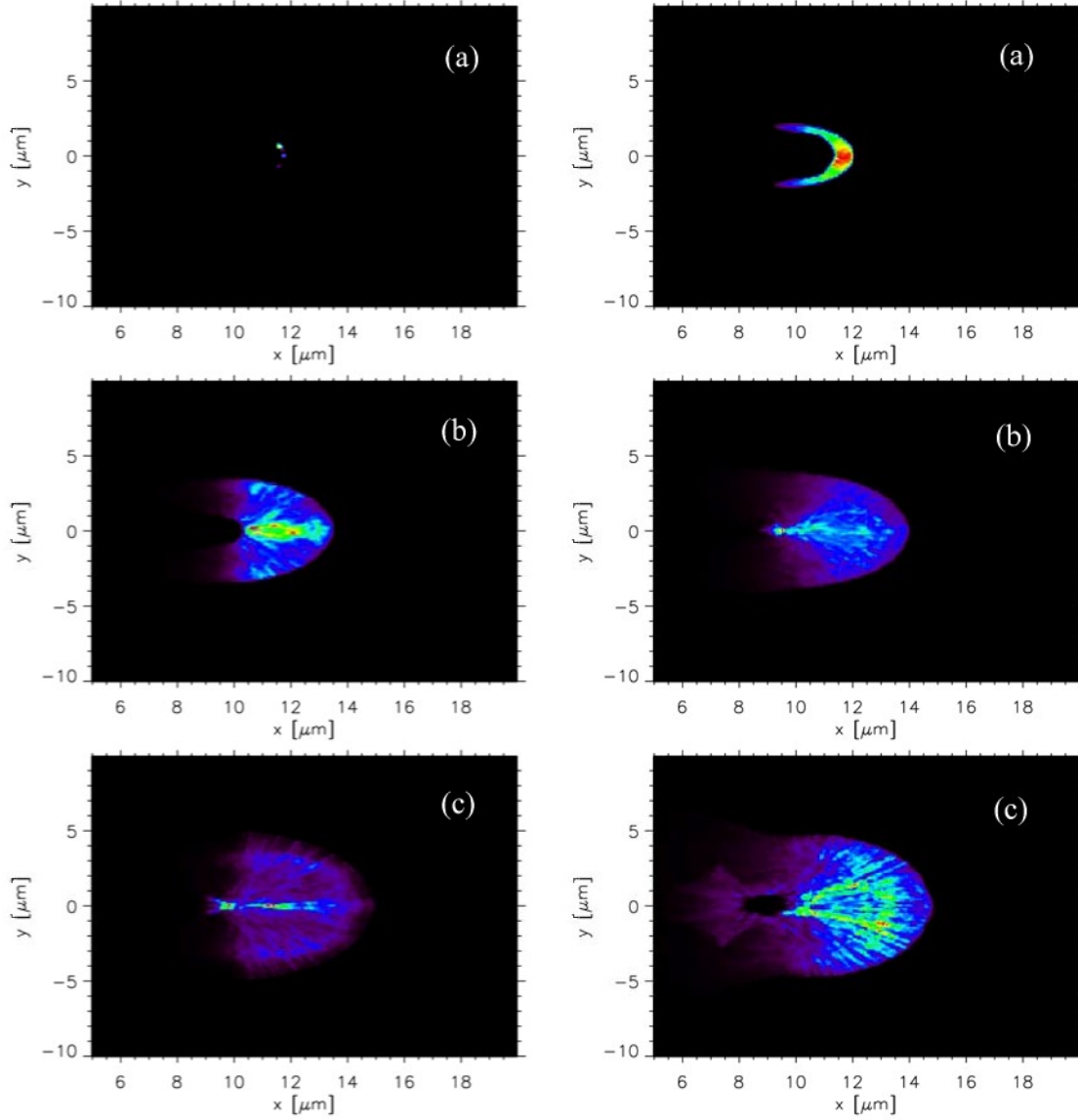
Figure 15 shows the Deuterium and Tritium density distribution after 1.33 ps. While at that time the reverse accelerated ions form a high density peak at the original location of the Tritium ball, the Tritium has been spread over a large volume due to Coulomb explosion.

## 2.7 Neutron Generation in Shaped Target

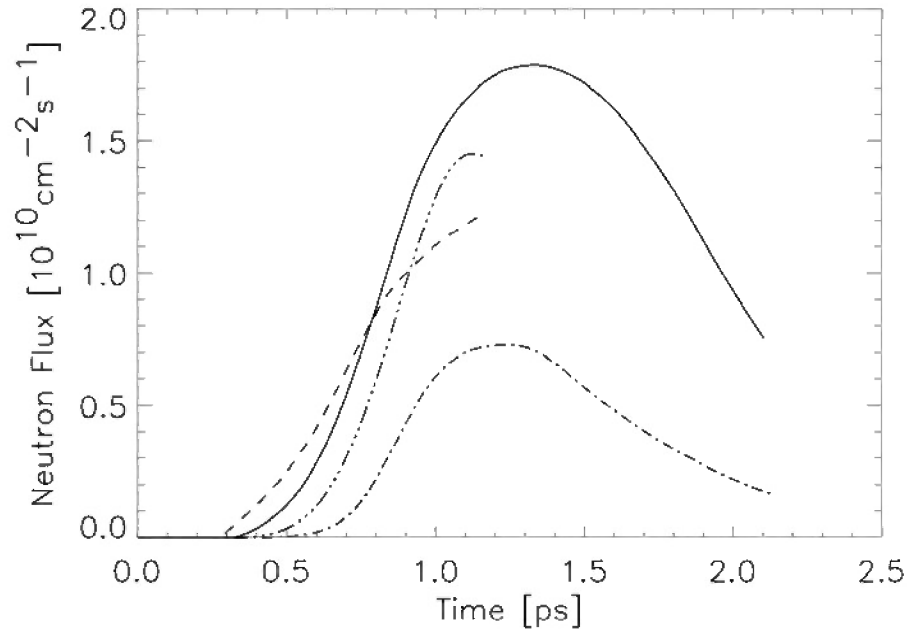
While the previous paragraph has shown that the ablated material in a shaped target can be focused and generate a high density peak, it remains to be seen whether the accelerated ions have the right energy to undergo fusion.

Figure 16 shows the temporal development of the neutron generation inferred from the Deuterium and Tritium densities and local mean velocities for two different laser amplitudes. For both amplitudes, neutron generation initially happens where the ions from the Coulomb explosion of the Tritium ball penetrate the Deuterium. Later, the interaction of the Deuterium jets creates another location of high neutron yield. Finally, the Tritium density at the original Tritium ball location becomes so low, that neutrons are no longer produced there.

Integrating the number of generated neutrons over the entire simulation domain allows estimating the total neutron flux as a function of time. Figure 17 shows the temporal evolution of the neutron flux for different laser peak electric fields. While increasing the laser peak field leads quicker to the generation of neutrons, the ions exceed the drift velocity of peak fusion cross-section. They therefore are lost to the generation of neutrons. On the other hand, for too weak a laser field, the accelerated ions are not fast enough and therefore do not lead to nuclear fusion. For the given configuration, a peak electric field of 3 TV/m maximizes the neutron flux.



**Figure 16:** Time evolution of the neutron generation for a laser amplitude of  $E=3e12$  V/m (left) and  $6e12$  V/m (right) after 0.3ps (a), 0.6ps (b) and 0.9ps (c).



**Figure 17:** Neutron flux evolution for laser amplitudes  $E=1.5$  TV/m (dash-dotted),  $E=2$  TV/m (dash-triple-dotted),  $E=3$  TV/m (solid) and  $E=6$  TV/m (dashed). Increasing the amplitude leads to an increased momentum of the accelerated ions and therefore to a relative ion energy which is beyond the peak cross-section for the D-T fusion reaction.

The neutron flux in Figure 17 is computed at a distance of 1 m away from the target. Even assuming a reduction of the flux by about two orders of magnitude due to an external moderator should lead to a sufficient flux of neutrons for radiographic applications.

### 3 Summary

In summary, we found that ions ablated in the interaction of a strong laser pulse with an over-dense plasma can be focused by shaping the target. In case of a spherically shaped target, this leads to the formation of a high density ion population in the center of the spherical mirror. Target shaping has been successfully used to focus ions accelerated via TNSA on the backside of the target. These accelerated ions are then used as drivers for Inertial Confinement Fusion. Our simulations indicate that a similar population can be generated at the interaction site, leading to a drive beam traveling in the backward direction.

We have shown that the interaction of a femto-second laser pulse with a slightly over-dense target consisting of a D-T mix can be used to generate a neutron flux sufficiently large for radiographic applications. However, a large fraction of the D-T mix does not participate in the D-T fusion reaction and is therefore lost.

In a last configuration, the laser pulse was used to strip a Tritium ball from all its electrons. The resulting Coulomb explosion was used to accelerate the Tritium ions. The

reverse ion acceleration mechanism in a shaped target generates a counter-streaming population of Deuterium ions. Depending on the peak electric field of the laser pulse, a neutron flux large enough for radiographic applications can be generated.

The above simulations pushed 40 million particles on a 6000x4000 cell grid for about 110,000 time-steps and produced about 250 GB of data and took about 500 CPU days (12,000 CPU hours). Simulations of this size are too large for performing e.g. Parameter studies. One possibility to reduce the simulation time is to employ higher-order particle shapes, which interpolate the electromagnetic field not only from the surrounding cell, but from a more extended region in space. Using the field values from three neighboring cells, it is possible to relax the constraint to resolve the Debye length and only requires resolution of the electron inertial length. This results in a grid resolution which is lower by a factor  $(c/v_{\text{therm}})^3$  which can easily exceed a factor of 1,000. In addition, this yields to an increased maximum possible time step due to its coupling via the CFL condition. Time savings of factors 10,000 and more can therefore be achieved.

## 4 Conclusions

In this project, we have implemented a kinetic model for nuclear fusion in the plasma simulation code VORPAL. We therefore extended a kinetic reaction model implemented in a different project by cross-sections for the Deuterium-Tritium nuclear reaction.

We investigated the interaction of a medium powered laser pulse with a slightly over-dense thin Deuterium/Tritium target. The interaction leads to the formation of a shock wave inside the plasma, which can accelerate particles at the shock front. This leads to the formation of a population of D (and T) streaming relative to a D/T background.

Using our newly developed fusion reaction model, we were able to compute the neutron flux generated in this interaction. The peak neutron flux was on the order of  $10^{12}$  #/cm<sup>2</sup>s, with a strong dependence on the incident laser pulse intensity.

While the overall number of particles per shot is relatively small due to the short interaction time, the high repetition rate of commercially available lasers with the required parameters can lead to high average neutron numbers.

Discussions with experimentalists have indicated that slightly over-dense thin targets can be realized using foams or gels or even using high-density gas jets. The simulation results therefore could be tested experimentally and possibly lead to the development of a compact neutron source.

We also performed simulations of reverse acceleration by laser-plasma interaction in shaped targets. We have demonstrated that a focusing of the ablated material occurs and leads to a high-density ion population propagating in reverse direction. This population could be used as a driver for Inertial Confinement Fusion.



Particle-in-Cell simulations of high-density plasmas are computationally highly demanding and algorithmic enhancements should be investigated. For example, higher order particle shapes have demonstrated that considerable time savings can be achieved compared to first order interpolation for particles.

## 5 References

- [1] B.M Hegelich, B.J. Alright, J. Cobble, K. Killipo, S. Letzring, M.Paffett, H. Ruhl, J.Schreiber, R. K. Schultze, J.C. Frenandez, ‘Laser acceleration of quasi-monoenergetic MeV ion beams’, *Nature*, 439 (26), 441, 2006.
- [2] C.G. Geddes C. Toth, J. Van Tilborg, E.Esarey, C.B. Schroeder, D. Bruhwiler, C. Nieter, J. Cary, and W.P. Leemans, *Nature*, 431, 538, 2004.
- [3] C. Nieter, J.R. Cary, ‘VORPAL: A versatile plasma simulation code’, *J. Comp. Phys*, 196, 448, 2004.
- [4] C.K. Birdsall and A.B.Langdon, ‘Plasma Simulation Using Particles’, New York, McGrawHill, 1985.
- [5] G. A. Bird, ‘Molecular Gas Dynamics and the Direct Simulation of Gas Flows’, Oxford University Press, 1994.
- [6] J.D. Huba, *NRL Plasma Formulary*, Washington DC, 2000.
- [7] D. Leitner, C. M. Lyneis, T. Loew, O. Tarvainen, D. S. Todd, and S. Virostek, *RSI* **77**, 03A302 (2006).
- [8] C. Lyneis, et al., First Results for the 28 GHz Operation o f the superconducting ECR Ion Source VENUS, *Cyclotrons* 04, 2004.
- [9] M.J. Shull, M. Van Steenberg, *Ap.J. Suppl.*, 48, 95, 1982.
- [10] L. Silva et al., Proton Shock Acceleration in Laser-Plasma Interactions, *PRL* 92, 015002, 2004.



**AFRL-RZ-ED-TR-2010-0026**

**Primary Distribution of this Report:**

AFRL/RZSS (3 CD + 1 HC)  
Jean-Luc Cambier  
1 Ara Drive  
Edwards AFB CA 93524-7013

AFRL/RZSS (1 HC - Original)  
Record Custodian  
1 Ara Drive  
Edwards AFB CA 93524-7013

AFRL/RZ Technical Library (2 CD + 1 HC)  
6 Draco Drive  
Edwards AFB CA 93524-7130

Chemical Propulsion Information Analysis Center  
Attn: Tech Lib (Mary Gannaway) (1 CD)  
10630 Little Patuxent Parkway, Suite 202  
Columbia MD 21044-3200

Defense Technical Information Center  
(1 Electronic Submission via STINT)  
Attn: DTIC-ACQS  
8725 John J. Kingman Road, Suite 94  
Ft. Belvoir VA 22060-6218